CRANFIELD UNIVERSITY

CRANFIELD POSTGRADUATE MEDICAL SCHOOL

FACULTY OF MEDICINE & BIOSCIENCES

PhD THESIS

Academic Year 2005/6

Susan Essien Etok

Structural characterisation and *in vitro* behaviour of apatite coatings and powders.

Supervisor: Prof. K. D. Rogers
Co-supervisor: Prof. A. Woodman

September 2005

Abstract

Hydroxyapatite (HAP) coatings are used in orthopaedic surgery for bone regeneration. Current methods of phase quantification of HAP coatings suffer from drawbacks. A novel methodology of quantitative phase analysis of HAP coatings has been devised and validated. This method, based on whole pattern fitting with a fundamental parameters approach, incorporates amorphous calcium phosphate (ACP) and apatite phases into structural refinements.

A comparison of the structural and chemical properties of plasma sprayed (PS) and novel electrodeposited (ED) HAP coatings has been conducted. ED coatings contained less ACP and more preferred orientation than the PS coatings, although the stoichiometry was similar.

In vitro investigations of PS and ED coatings in simulated body fluid and foetal calf serum revealed that both are bioactive. A carbonated apatite layer produced on the ED coatings was ~0.7μm thick with a stoichiometry and chemical constituents similar to that of natural bone apatite.

PS coatings produced a nanocrystalline carbonated apatite layer (~4μm). For the first time it has been possible to model crystalline HAP and nanocrystalline apatite as independent phases and obtain accurate lattice parameters for each.

A positive linear correlation has been made between microstrain and the solubility of HAP and carbonated apatites. Dissolution studies have shown that the behaviour of HAP and carbonated apatite is dominated by crystallite size at low undersaturation and by crystallite size and microstrain at high undersaturation for crystallites between ~300Å-1000Å. Metastable equilibrium occurred for crystallites ≤400Å at low undersaturation. Carbonate content did not affect the solubility or dissolution behaviour.

A novel technology for coating polymeric tape with HAP for potential use in anterior cruciate ligament reconstruction has been devised. Mechanical tests have demonstrated that no adverse properties are induced by the coating technology. Cell culture studies have shown that the HAP layer is capable of enhanced attachment, proliferation and differentiation of osteoblast cells compared to uncoated tape.

Contribution to knowledge

A fast and reliable method of non-destructive phase quantification of biphasic and triphasic apatite coatings has been devised. This novel methodology based on whole pattern fitting incorporating a fundamental parameters approach has for the first time enabled amorphous calcium phosphate and nanocrystalline apatite to be included into structural refinements. This methodology removes the error associated with internal and external standard methods. Validation of this methodology has been undertaken with reference to apatites of known composition and the measured and calculated data were in good agreement. This methodology has proved to be robust in correcting peak intensities for preferred orientation by means of a spherical harmonics function.

A novel methodology for electrodeposition of HAP coatings has been developed in conjunction with Biomet-Merck UK Ltd. For the first time, a direct comparison of the structural and chemical properties of plasma sprayed and the novel electrodeposited coatings has been undertaken. The HAP coatings produced by electrodeposition (~1.7μm) contain significantly less amorphous calcium phosphate and are of poorer crystal quality (smaller crystallite size and greater microstrain) than the plasma sprayed coatings. In addition the electrodeposited coatings have significant preferred orientation in comparison to the plasma sprayed coatings.

It has been possible for the first time to non-destructively characterise both the near surface and near substrate regions of plasma sprayed coatings. It was found that although

the stoichiometry and microstrain were identical, the amorphous calcium phosphate component was significantly larger in the near substrate region.

In vitro studies have revealed that both the plasma sprayed coatings and the electrodeposited coatings are capable of producing a carbonated apatite layer and are hence bioactive. The electrodeposited coatings produced an apatite layer (~0.7μm) that was similar in composition and stoichiometry to natural bone apatite. The plasma sprayed coatings produced a nanocrystalline calcium deficient apatite layer which was ~4μm in thickness. For the first time, it has been possible to model the nanocrystalline apatite produced by the plasma sprayed coatings as an independent phase in structural refinements and obtain relative proportions and accurate lattice parameters. The HAP component of the electrodeposited coatings dissolved entirely in water.

Synchrotron diffraction depth profiling tomography was used to investigate the HAP component of plasma sprayed coatings immersed in SBF for 21 days. It was found that the HAP was carbonated and had lower preferred orientation than the as-received coatings.

For the first time a quantitative relationship has been made between lattice microstrain and the solubility of synthetic HAP and carbonated apatite. No correlation between crystallite size and microstrain respectively with solubility has been found.

It has been demonstrated that a metastable equilibrium state exists in HAP and carbonated apatite powders with crystallite sizes less than ~400Å in SBF (high undersaturation) for 21 days. For crystallite sizes between 400Å-1000Å, dissolution suppression occurs whereby larger crystals dissolve faster than smaller crystals. The metastable equilibrium state is dependent on crystallite size and undersaturation. At higher undersaturation, the metastable equilibrium phenomenon is not observed. Dissolution is dominated by crystallite size, although microstrain has an appreciable contribution.

For the first time a rigorous diffraction approach to quantitative phase analysis and microstructural investigation of apatite coatings before and after *in vitro* testing has been undertaken. This approach has proved invaluable to the characterisation of apatites because previous work has involved qualitative and semi-quantitative analysis of diffraction patterns and FTIR spectra.

A novel coating technology for polymeric tape for the potential use in anterior cruciate ligament construction has been devised. Mechanical tests have been undertaken and it was found that the coatings produced were uniform and strongly adherent to the substrate. Cell culture studies have shown that the HAP coatings deposited on the polymeric tape enhanced attachment, proliferation and differentiation of osteoblast cells in comparison to uncoated polymeric tape.

Acknowledgements

Firstly, I would like to thank my supervisors Prof. Keith Rogers and Prof. Anthony Woodman for their continued advice and guidance throughout my PhD studies, without them this research would not have been possible.

Sincere thanks go to my family and friends for their support and encouragement during the highs and lows of my research.

I am indebted to Mrs Jenny Lovell for her assistance with FTIR analysis and to Dr. Jonathon Painter for his assistance with SEM.

Table of contents

List of figures

List of tables

Glossary

A	absorption factor
B	β_c^f / β^f
B_j	isotropic temperature factor
D	d-spacing
F	structural profile
$F_{(hkl)}$	structure factor
f_j	scattering factor of the j-th atom
G	instrument profile
H	measured profile
h, k, l	Millers indices
I	intensity
$I(hkl)\alpha$	diffraction line intensity of the test sample
$I(hkl)\beta$	diffraction line intensity of the standard
$I\alpha$	diffraction line intensity of test sample
$I\alpha 0$	diffraction line intensity of pure sample
K	Boltzmann constant
K	constant depending on crystal habit
K_d	rate constant of dissolution
L	Lorentz polarisation and multiplicity factor
M	mass formula unit
n	Order of reaction
N_j	site occupancy of the j-th atom
$P6_3/m$	space group with a six-fold symmetry axis with a three fold helix and a mirror plane
$P_{(hkl)}$	preferred orientation function
Q_y	intensity difference
R	Molar gas constant (8.314 $JK^{-1}mol^{-1}$)
R_g	rate of crystal growth
s	a function of the total number of growth sites
S	supersaturation ratio
S	scale factor
S_i	scale factor for phase i
S_p	scale factor for phase p
T	thickness
T	absolute temperature
V	number of ions in the molecule
V	unit cell volume
W	full with half maxima
W_i	inverse of Y_i
W_p	weight fraction of phase p
W_α	weight fraction of α

x_j	fractional atomic coordinate of j-th atom
$X\alpha$	weight fraction of test sample
$X\beta$	weight fraction of standard
Y_i	intensity of the i-th position of 2θ
Y_{i-b}	background intensity of the i-th data point
$Y_{i(calc)}$	calculated intensity
$Y_{i(obs)}$	observed intensity
y_j	fractional atomic coordinate of j-th atom
Z	number of formula units per cell
z_j	fractional atomic coordinate of j-th atom
α	activity of ions
β	integral breadth
β_c	integral breadth of Cauchy functions
β_c^f	integral breadth of a Cauchy function derived from the structural profile
β_c^g	integral breadth of a Cauchy function derived from the instrument profile
β_c^h	integral breadth of a Cauchy function derived from the measured profile
β^f	integral breadth from a structural profile
β_f	broadening due to structure
β_g	observed broadening
β_g	integral breadth of Gaussian functions
β_g^f	integral breadth of a Gaussian function derived from the structural profile
β_g^g	integral breadth of a Gaussian function derived from the instrument profile
β_g^h	integral breadth of a Gaussian function derived from the measured profile
β_h	broadening due to the instrument
β_{total}	broadening due to size and microstrain
β_ε	microstrain induced broadening
β_τ	size induced broadening
Δg	Gibbs free energy for dissolution
ΔG	change in Gibbs free energy
ε	microstrain
γ	activity coefficient
γ_{SL}	interfacial tension
λ	wavelength of radiation
μ	absorption coefficient
$(\mu/\rho)_m$	Mass absorption coefficient of mixture
$(\mu/\rho)_p$	Mass absorption coefficient of pure phase
θ	angle
θ_{hkl}	Bragg angle
ρ	density
σ_d	relative undersaturation (dissolution)
τ	mean column length
Ω	area occupied by each dissolution unit
AAS	atomic absorption spectroscopy
ACL	anterior cruciate ligament
ACP	amorphous calcium phosphate

AFM	atomic force microscopy
ALP	alkaline phosphatase
ANOVA	analysis of variance
BAP	biological apatite
BC	bioprosthetic coatings
BMM	biomimetic
BMU	Basic multicellular unit
CaO	calcium oxide
CDHAP	calcium deficient hydroxyapatite
CHA	carbonated apatite
CSM	Crystallographica Search Match
CVD	chemical vapour deposition
DCPD	dicalcium phosphate dihydrate
ED	electrodeposition
EDTA	ethylene diaminetetraacetic acid
EDX	energy-dispersive X-ray micro-analyser
EM	electron microscopy
ESEM	environment electron microscope
FAP	fluorapatite
FCS	foetal calf serum
FTIR	Fourier transform infrared spectroscopy
G418	geneticin antibiotic
HAP	hydroxyapatite
IC	ion chromatography
ICCD	international centre for diffraction data
IP	ionic product
IR	infrared
IRF	instrument resolution function
KBR	potassium bromide
K_{sp}	thermodynamic solubility product
$K\alpha_1$ & $K\alpha_2$	Emission lines
Log (IP)	log (ionic product)
LPA	Line Profile Analysis
Nano-HAP	nanocrystalline hydroxyapatite
NCP	non-collagenous proteins
NHS	national health service
OCP	octacalcium phosphate
OT	orthopaedic tape
OT-C	orthopaedic tape with no coating
OT-N	HAP coated orthopaedic fabricated without using a surfactant
OT-T	HAP coated orthopaedic fabricated using a surfactant
PBS	phosphate buffer solution
PCC	Pearson's correlation coefficient
PDF	powder diffraction file
PET	poly- (ethylene terepthalate)
pK_{sp}	log (solubility product)

PMMA	polymethylacrylate
PO index	preferred orientation index
PS	plasma spray
PTH	parathyroid hormone
PVD	physical vapour deposition
RPM	revolutions per minute
RS	Raman spectroscopy
R_{wp}	'goodness of fit' value
SBF	simulated body fluid
SEM	scanning electron microscopy
SG	sol-gel
Size25	hydroxyapatite synthesised at 25°C
Size55	hydroxyapatite synthesised at 55°C
Size80	hydroxyapatite synthesised at 80°C
Strain1	as-received hydroxyapatite powder
Strain2	hydroxyapatite powder ball-milled at 400rpm for 2 hours
Strain3	hydroxyapatite powder ball-milled at 400rpm for 26 hours
Ti-6Al-4V	titanium-aluminium-vanadium alloy
Triton 60	octylphenol ethoxylate
TTCP	tetracalcium phosphate
W-A	Warren-Averbach
W-H plot	Williamson-Hall plot
XPS	X-ray photoelectron spectroscopy
XRD	X-ray diffraction
α-TCP	α-tricalcium phosphate
β-TCP	β-tricalcium phosphate
0.5CHA	0.5wt% B-type carbonated apatite
1,25 DHVD	1,25-dihydroxyvitamin D
2.3CHA	2.3wt% B-type carbonated apatite
3.5CHA	3.5wt% B-type carbonate apatite

1.0 Background

The discovery of antiseptics, antibiotics, chemical water treatment, improved hygiene and vaccinations over the past century has contributed to the significant increase in human survivability in the developed world. Such an increase in human survivability means that many people outlive the quality of their osseous and connective tissue [1].

1.1 Degradation of bone tissue

The hip joint in particular, tolerates a wide range of movement during a human life cycle and is therefore subject to a range of degenerative disorders. Some of the common disorders include osteoporosis, osteoarthritis, rheumatoid arthritis, and asvascular necrosis. Figures 1.1-2 show schematic diagrams of a normal hip joint compared with a damaged hip joint.

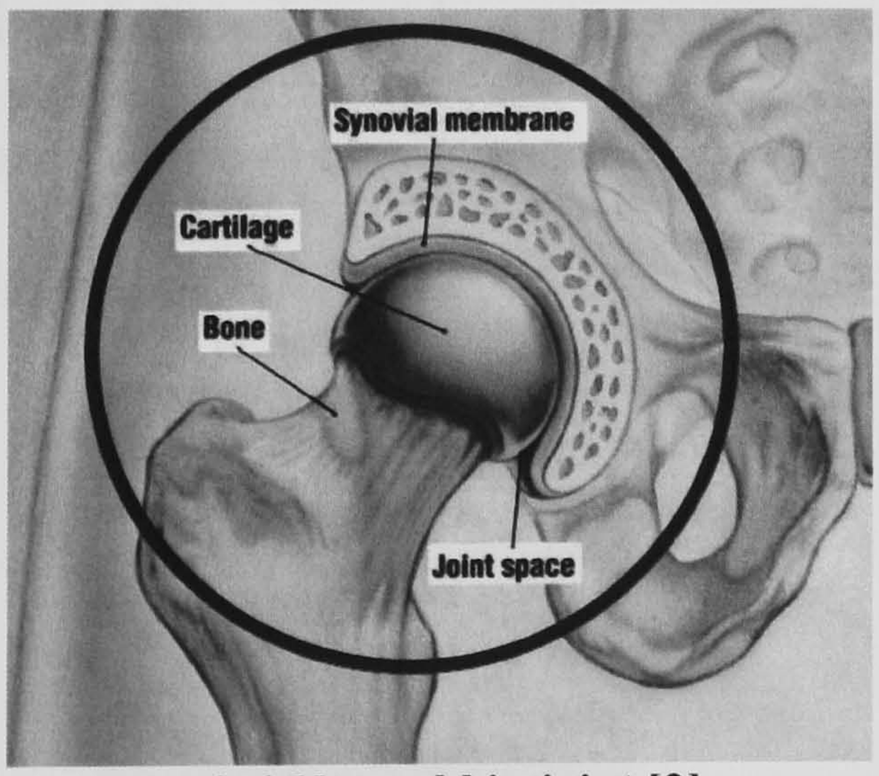

Figure 1. 1 Normal hip joint [2].

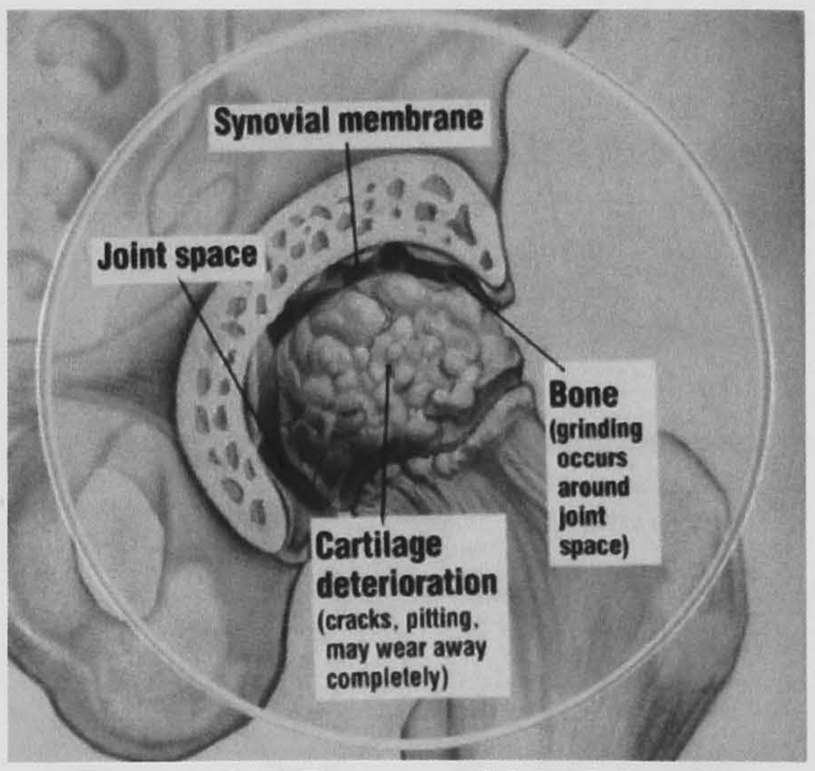

Figure 1. 2 Damaged hip joint [2].

In the UK, over 50, 000 hip replacements are performed by the NHS each year and more than half a million people have received hip implants in the last 10 years [3]. Total hip replacement is a common and highly successful operation bringing many people

restoration of mobility and relief from pain from worn or damaged hip joints as both the acetabulum and femoral head are replaced. In addition, such procedures can be life-saving as the lack of mobility resulting from a hip fracture commonly leads to deep vein thrombosis or pulmonary embolism.

The first rudimentary hip prosthesis (figure 1.3) was designed and inserted by Philip Wiles from the Middlesex hospital in the late 1930's [4]. Conventional total hip prostheses were developed and introduced in the early 1960's by the English surgeon Sir John Charnley. Charnley's design comprised of a one-piece metal stem with a 22 mm diameter head, which was cemented into the acetabulum. Incremental improvements have been made to Charnley's original design since the 1960's to improve longevity and superiority (figure1.4). There are over 100 designs of hip joint replacement, but the Charnley cemented prosthesis remains the 'gold standard' [4]. Post-operative follow-up studies of Charnley-style replacements have shown sufficient longevity and that the majority of prostheses in surviving patients are still functioning up to 10 years after implantation [5].

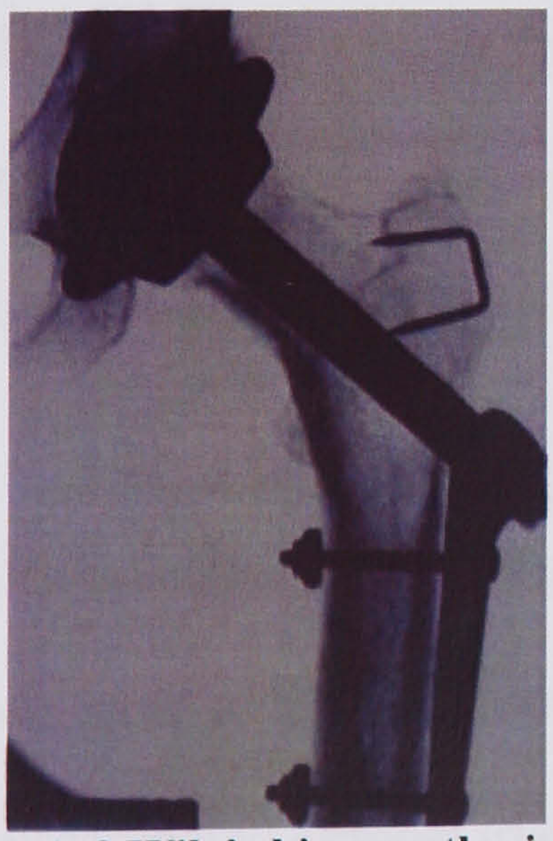

Figure 1. 3 Wile's hip prosthesis [4].

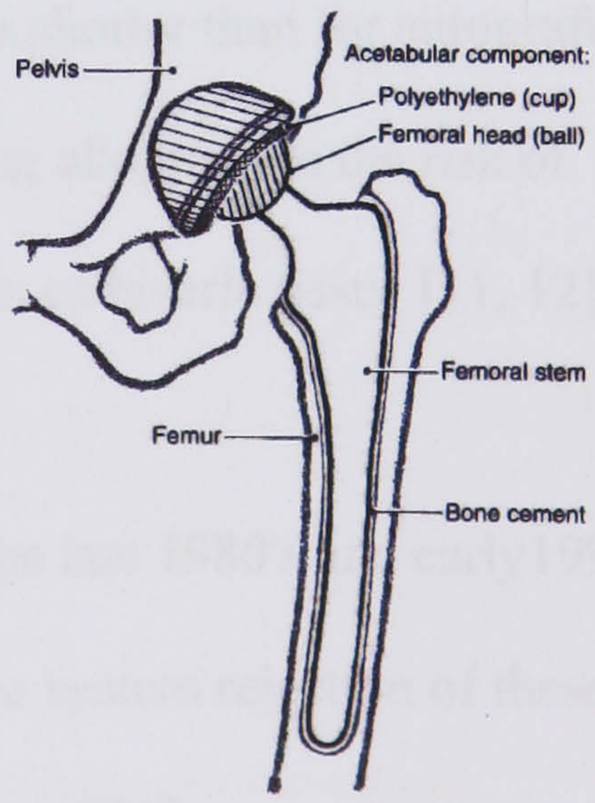

Figure 1. 4 Conventional hip prosthesis [2].

1.2 Connective tissue damage

Connective tissue disease and injury often impede daily activities and exercise. Ruptures of anterior cruciate ligaments (ACL) in particular, result in reduced mobility, pain and discomfort [6, 7]. Standard treatment used to be suturing the damaged ACL but several reports have proved this procedure ineffective [7]. Hence, several alternatives have been developed over the last 100 years for ACL reconstruction such as autogenous tissues (host tissue), allografts (human cadaveric tissue), xenografts (mammalian-derived tissue) and artificial materials (see appendix A) [6-11].

Autografts, in particular, patellar tendon grafts have been the "gold standard" for ACL reconstructions since the mid-1980's. Patellar tendon grafts have demonstrated satisfactory surgical outcomes; however harvesting them requires invasive surgery in the host tissue, thus increasing trauma and the period required for rehabilitation [8, 10-12].

Allografts, are equally as successful clinically as autografts. One feature that makes them more attractive than autografts is that no invasive surgery on the host is required to harvest the grafts. As a result the rehabilitation period is shorter than for autograft implantation. Nevertheless, the prime concern with using allografts is the risk of contracting serious infections (HIV and hepatitis B) from cadaveric tissue [11, 12].

Xenografts have been tried as ligament graft tissues in the late 1980's and early1990's. Such grafts have so far been unsuccessful due to immune system rejection of these grafts. Further research and clinical trials are currently in progress [11].

Prosthetic grafts have been pursued as a result of the inadequacies of soft-tissue grafts [6]. Synthetic grafts made from woven polymeric fibres such as poly-ethylene terepthalate (PET) have been developed to mimic native ACLs. Although, polymeric tape may not currently be the perfect substitute for native ACL, *in vitro* and *in vivo* studies have shown that they represent a forward step in knee reconstructive surgery [7, 9-11].

Generally in ACL reconstruction of the knee, isometrically positioned bone tunnels are formed respectively in the tibia and femur at a site anatomically equivalent to attachment of the ACL. Bone plugs are formed from bone tissue removed from the bone tunnels. A replacement graft having bone plugs at both of its ends is inserted through a bone tunnel to extend across the knee joint. The bone plugs are hence returned to their respective tibial and femoral bone tunnels (figure 1.5) [8]. Various surgical devices can be used to further secure bone plugs such as biodegradable bone screws, staples and washers [7-9].

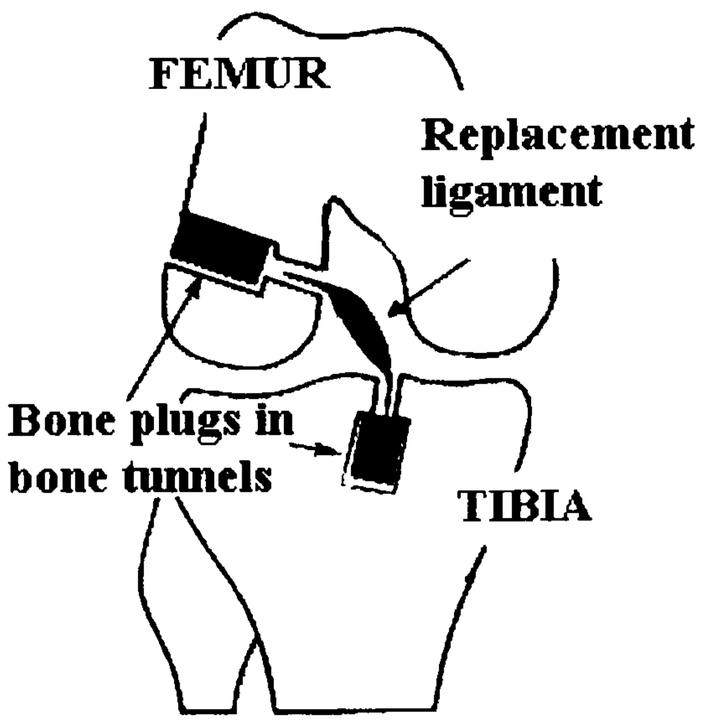

Figure 1. 5 Schematic of a typical patella tendon ACL reconstruction.

1.3 Development in orthopaedic technology

Good manufacturing protocols, international standards, government regulations and quality assurance testing minimise the probability of mechanical failure in hip arthroplasty and ligament grafts. However, most used today, suffer from problems of interfacial stability with host tissue, biomechanical mismatch of elastic moduli, production of wear debris and maintenance of a stable blood supply. The consequence of the afore-mentioned limitations is that the devices have limited lifetimes [1, 9, 13-15].

Nowadays, research in orthopaedic surgery is not solely limited to the improvement of the structural and mechanical performance of implants. Improvements are now being focused on minimising invasive surgery by modifying surgical techniques and reducing patient convalescence and rehabilitation times [8, 9, 16]. Decreasing healing times is an attractive economic option because the time necessary for hospital convalescence is minimised, thus relieving the cost burden on the health care provider. In addition it would render patients mobile earlier and alleviate malady caused by inactivity such as deep vein thrombosis, joint pain and stiffness, decline in muscle strength and cardiovascular fitness.

The lack of adequate bone fixation is the most common cause of failure of hip arthroplasty and ligament grafts [17]. Long-term function and painless fixation depends on their biological, physiochemical and mechanical characteristics [13, 18]. The binding of dissimilar materials (metal-bone or graft-bone) can be obtained by physicochemical bonding, a geometrical interference or both modalities. Since no welding or strong

enough adhesive is possible, a tenon-mortise mechanical interlock is required between the bone and the arthroplasty or graft [5].

Extensive research has been conducted in order to improve interfacial bond strengths in hip arthroplasty and the consensus is that a bioprosthetic coating with similar chemical composition and crystal structure to bone apatite is required [19]. Such coatings should be osseoconductive in nature [5, 14, 20] and promote rapid osseointegration during the early stages of implantation [14, 21, 22].

Hydroxyapatite [$Ca_{10}(PO_4)_6$ $(OH)_2$], a crystallographic analogue of natural bone mineral, was identified in the 1970's as a potential biomaterial for use in orthopaedic surgery. HAP has the capability to form strong physiochemical bonds with bone *in vivo*, while remaining stable, under the conditions encountered in physiological environments. This finding was as a result of the first X-ray diffraction study of bone published by De Jong in 1926, in which apatite was identified as the only recognizable mineral phase.

Since its introduction into the field, HAP has been the focus of numerous investigations and has been used widely as bioprosthetic coatings in medicine and dentistry [23]. However, there are a number of problems relating to deposition of HAP in the context of material quality and mechanical properties. In addition, until recently, methods of characterisation of HAP coatings have been superficial and i*n vitro* dissolution studies have been limited to chemical changes to the surrounding physiological fluid as opposed to chemical and structural changes occurring in the material.

2.0 Bone

2.1 Function of bone

Bone is a dynamic connective tissue that constitutes a significant portion of the skeleton of higher vertebrates. Biologically, bone plays an important role in calcium homeostasis and haematopoiesis in the bone marrow as well as being an ion store. Structurally, bone provides the architecture of the body and provides mechanical strength for protecting internal organs [24].

2.1.1. Mechanical function

Bones make up a structural framework, against which the muscles can contract to move the body by providing anchorage points for muscles and by acting as levers at the joints. Furthermore, they protect organs such as the brain, heart, lungs, and organs of the pelvis by forming the sturdy walls of body cavities against which they can maintain their relative position in the body [25, 26].

2.1.2 Calcium homeostasis and hormonal control

The skeleton makes up one-sixth of the body's mass, is the body's main supply of calcium, phosphate and magnesium salts. 99% of calcium, 86% of phosphate and 54% of magnesium found in the human body is contained in the bones [15, 25, 27]. Bone tissue plays a homeostatic role for calcium by aiding the regulation of the amount and consistency of physiological fluid by replenishing or removing calcium ions from it. The maintenance of serum calcium is dependent on the interaction of intestinal calcium absorption, renal excretion and skeletal mobilisation of calcium. Although serum

calcium represents less than 1% of total body calcium, the serum level is important for the maintenance of normal cellular functions [25, 27]. Serum calcium regulates and is regulated by three hormones: parathyroid hormone (PTH) 1,25-dihydroxyvitamin D (1,25 DHVD) and calcitonin (see figure 2.1). PTH is an 84-aminoacid peptide secreted by four parathyroid glands located adjacent to the thyroid gland in the neck. Calcitonin is a 32-aminoacid peptide secreted by parafollicular cells of the thyroid gland. Vitamin D, from dietary sources (vitamin D_3) or synthesised in skin (vitamin $D_{2)}$, is converted to 25-dihydroxyvitamin D in the liver and then to 1,25 DHVD in the kidney [27, 28].

PTH and 1, 25-dihydroxyvitamin D are the main regulators of calcium and bone homeostasis. Calcitonin appears to play a relatively minor role in calcium homeostasis in normal adults, despite the fact that it can directly inhibit bone resorption and enhances excretion of calcium into the urine. Mechanistically, PTH preserves blood calcium by stimulating the kidneys to increase calcium re-absorption, to produce 1,25 DHVD and to eliminate excess phosphate (phosphaturic effect). 1,25 DHVD facilitates absorption of calcium and phosphate from the small intestine and in unification with PTH, stimulates bone resorption [25, 27].

Close regulation of the level of serum calcium, PTH and 1,25 DHVD is carried out by a calcium-sensing receptor (identified in parathyroid and kidney cells) that senses extracellular calcium [27]. A low serum calcium level stimulates production of 1,25 DHVD as a result of PTH secretion. The physiological response to increasing levels of production of 1,25 DHVD and PTH is a gradual rise in serum calcium. The reverse is

true in the case of high serum levels and serum calcium is maintained within a narrow physiological margin. Disturbances in the calcium-sensing mechanisms can lead to several severe clinical states. A decrease in the level calcium in serum (hypocalcaemia) can cause the nervous system to be more active because of the increased neuronal membrane permeability with resultant muscle spasms. An increase in the calcium level in serum (hypercalcaemia) depresses the nervous system and causes the muscles to become lethargic and weak because of the effects of calcium on the muscles' plasma membrane [25, 28].

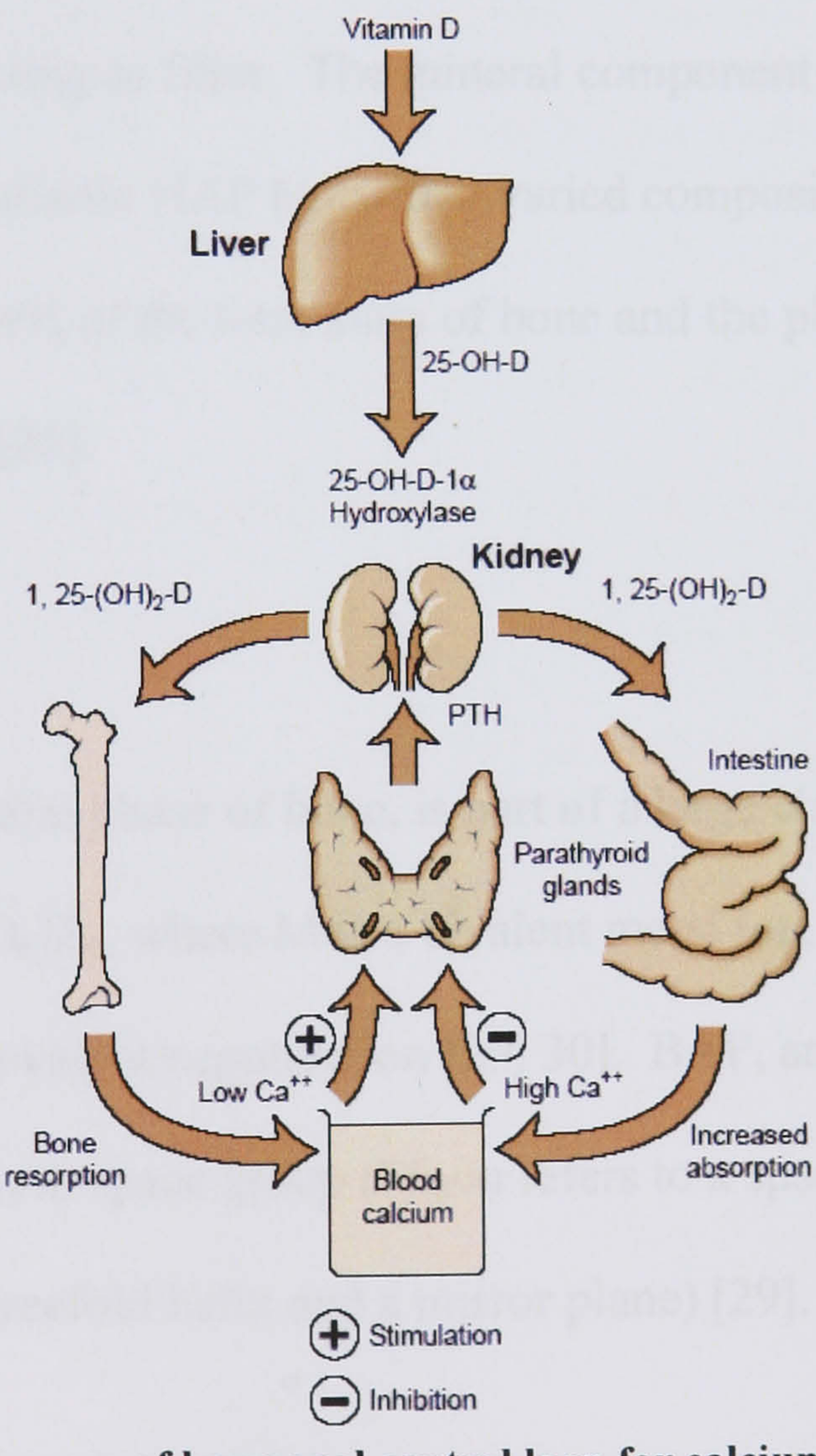

Figure 2. 1 Schematic diagram of hormonal control loop for calcium metabolism [27].

2.1.3 Immunoskeletal milieu

Bone provides a milieu (via bone marrow) for the development of the immune system. Since immune related cells also differentiate into bone related cells, the bone marrow can be thought of as an immunoskeletal milieu. Adult red bone marrow is specifically the body's main haemopoietic tissue. It is responsible for the production of erythrocytes, platelets, granular leukocytes, immature lymphocytes and monocytes [25].

2.2 Constituents of bone

Bone is a composite of collagenous organic matrix and oriented nanocrystalline calcium phosphate apatite mineral, acting as filler. The mineral component of bone has a structure that is similar to synthetic HAP but with a varied composition. The organic component accounts for 35wt% of the total mass of bone and the physiological fluids play the part of a plasticizer [26].

2.2.1 Apatite mineral

Bone apatite (BAP), the mineral phase of bone, is part of a large class of apatites, with the general formula, $M_{10}(XO_4)Z_2$, where M is a bivalent metal ion, XO_4 is a trivalent negative ion, and Z is a monovalent negative ion [29, 30]. BAP, and laboratory HAP crystallize in a hexagonal $P6_3/m$ space group ($P6_3/m$ refers to a space group with a six-fold symmetry axis with a threefold helix and a mirror plane) [29].

The lattice structure (figure 2.2) of HAP can be viewed as a three dimensional network of unconnected PO_4^{3-} tetrahedra which are linked together with Ca^{2+} ions in the space

between and a column of Z^- ions along the c-axis to balance the charge [31]. The type and location of these anions distinguish the various apatites. It has been shown [32, 33] that when pure, apatite occurs in a monoclinic form *in vitro* depending on the stoichiometry, temperature, and pressure. Pure monoclinic structure is a laboratory rarity as the preparation and storage of stoichiometric apatites is difficult because of their flexibility in accepting substitutions [34].

BAP is a nanocrystalline, non- stoichiometric carbonated apatite capable of storing variable quantities of trace elements such as Mg^{2+}, Na^+, Fe^{2+}, HPO_4^{2-}, F^- and Cl^- [30, 35, 36]. Consequently, BAP represents an important mineral reservoir for metabolic activity and hence the chemical composition of bone mineral changes with biochemical activity. Due to microstructural defects in BAP, X-ray diffraction (XRD) investigations have produced broad diffraction lines that prevent accurate phase or compositional determination. Thus, most structural models of BAP rely principally on chemical information [30, 37]. The general formula $Ca_{10-X+n}\,X_Y\,(PO_4)_{\,6-X}\,(CO_3)_X\,(OH)_{2-X+n}$ proposed by Skinner *et al* [38] accounts for the possible inclusions of ions (x), the substitution of CO_3^{2-} for PO_4^{3-}, and the presence of calcium vacancies. Apatites are discussed in more detail in chapter 3.

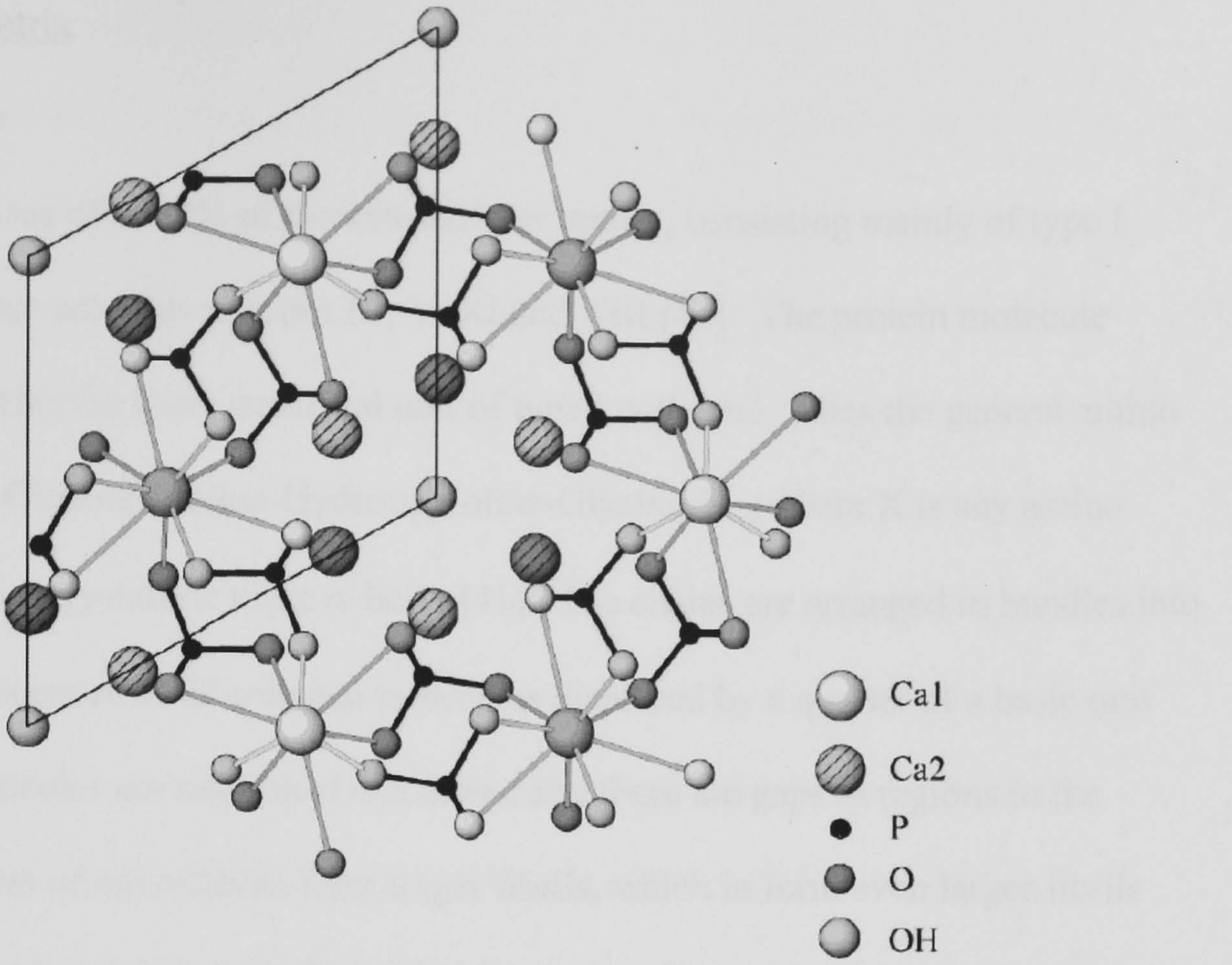

Figure 2. 2 Crystal structure of hydroxyapatite. Projection onto (001) plane [31].

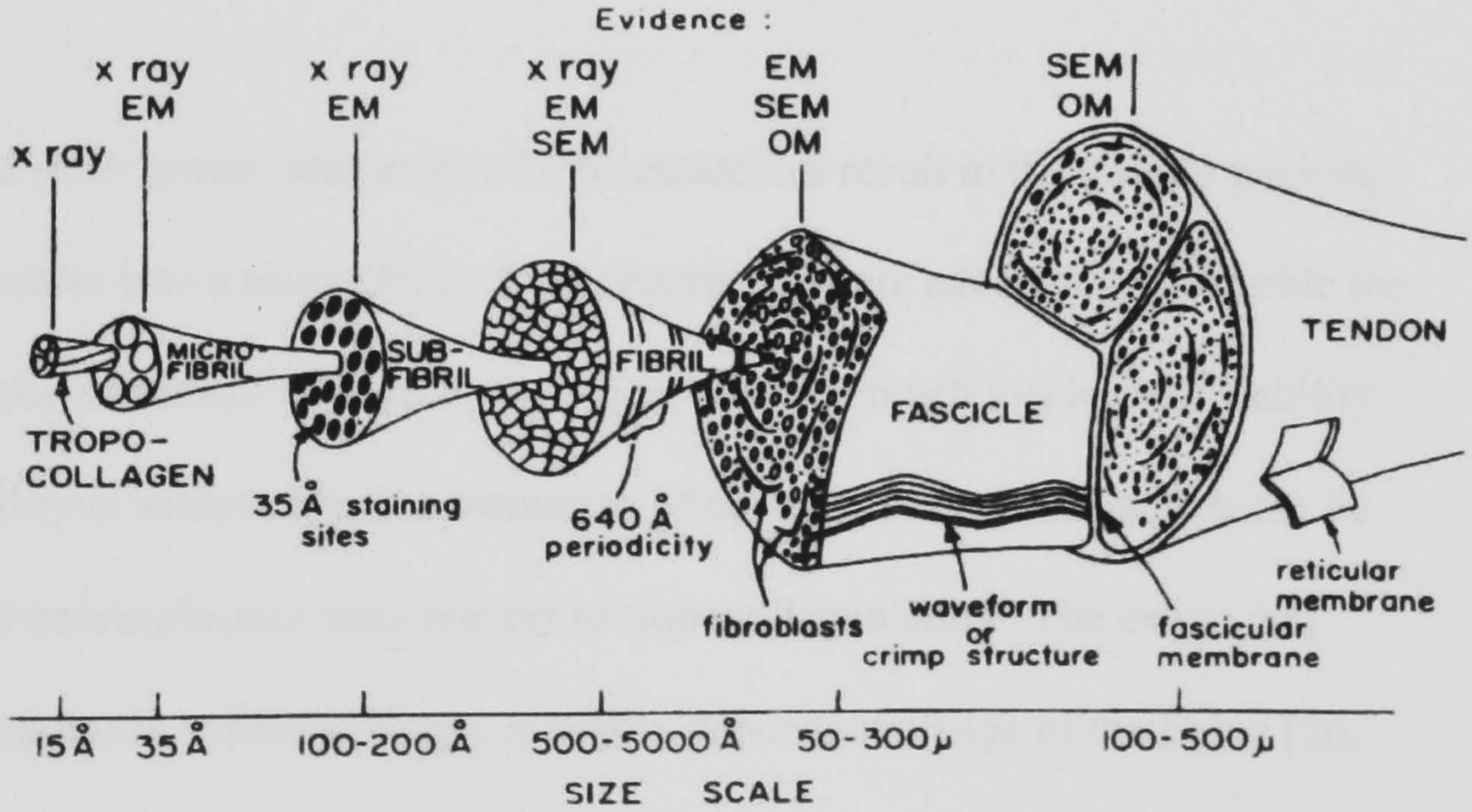

Figure 2. 3 Hierarchical structure of tendon [39].

2.2.2 Organic matrix

2.2.2.1 Collagen

Collagen comprises of 90wt% of the extracellular matrix, consisting mainly of type I collagen with trace amounts of types III, V, XI and XIII [40]. The protein molecule tropocollagen forms the basic structural unit of type I collagen. It has the general amino acid sequence: -Glycine-Proline-Hydroxyproline-Glycine-X- (where X is any amino acid) arranged in a crystalline triple α-helix [41]. The chains are arranged in bundles into microfibrils, adjacent rows of collagen molecules displaced by a quarter of a basic unit length. The molecules are not linked end to end and there are gaps in regions in the structure. Bundles of microfibrils form larger fibrils, which in form even larger fibrils (such as tendon), thus forming the hierarchical structure frequently found in natural tissue (figure 2.3) [15].

Hydrophobic and polar group interactions in the molecules result in the orderly packing of collagen molecules into a microfibril. These interactions are adequate to assemble the fibrils; however the forces are not sufficient to give collagen much mechanical stability. Mechanical stability is achieved by the formation of covalent cross-links, which can be intramolecular or intermolecular with respect to tropocollagen units. The extent and nature of cross-linking in natural collagen is highly dependent on age of the tissue [26, 42]. Reports suggest [26, 42, 43] that cross-linking increases the tensile modulus and failure stress and decreases the failure strain as well as decreasing the rate of collagen degradation. The cross-linking process provides a bridge between the mechanical and biological properties of collagen.

2.2.2.2 Non-collagenous protein (NCP)

Despite only contributing 10% of the total weight of the organic matrix, one molecule of NCP is produced per collagen unit. Hence the difference in masses is due to molecular weights of the two species. Structurally, four main groups of NCPs (table 2.1) exist within the organic matrix: proteoglycans, osteocalcin, osteonectin and osteopontin [40]. Trace amounts of growth factors and cytokines are also present in the organic matrix.

2.2.3 Collagen mineralization

The collagen matrix is laid down on the surface of bone together with other organic components forming osteiod, the non-mineralised component of bone. BAP is then deposited in the collagen initially in the 'gap regions' but then along the length of the collagen fibrils. As the plate-like mineral crystals grow, they tend to form large crystalline agglomerations and the individual mineral crystals tend to be orientated in the direction of the collagen fibrils [28, 44]. Crystal growth is not random; rather, one of the long axes of the mineral plates is always relatively well aligned with the collagen fibrils. The relationship between the mineral crystals that are inside the collagen fibrils and collagen is an intimate one. It is believed [28] that cross-linking occurs between tropocollagen chains as well as van der Waals interactions between mineral and polar groups.

Protein	Function
Proteoglycans	-contribute to the compressive strength of bone -play a role in the reservation of space for bone development - inhibits mineralization -affect binding and availability of local growth factors -affect the deposition & structuring of collagen fibrils
Osteocalcin	-essential for bone remodelling
Osteonectin	-plays a role in the regulation of calcium -binds collagen -high affinity for calcium & hydroxyapatite -localises to crystal-producing vesicles
Osteopontin	-mediates the attachment of cells to bone matrix -contains the Arg-Gly-Asp amino acid sequence, preferentially recognised by cell surface molecules

Table 2. 1 Non-collagenous proteins found in organic matrix

2.3 Macroscopic structure of bone

There are two morphologically different types of bone, namely cortical bone and cancellous bone [25]. Cortical bone is compact in structure and is mainly responsible for the support function. Cancellous bone has a large surface area compared to the volume, offering a possibility to rapidly participate in metabolism, especially in regulation of calcium homeostasis. The human skeleton consists of approximately 80wt% cortical bone and 20wt% cancellous bone. These proportions of cancellous and cortical bone vary according to the site and relate to the need of mechanical strength. Despite the fact that cancellous bone accounts for the minority of the total skeletal tissue, it is the site of greater bone turnover because its total surface area is greater than that of cortical bone [27].

2.3.1 Cortical (compact) bone

Cortical bone forms the hard and dense outer shell of human bone found principally in the shafts of long bones. Superficially, cortical bone appears solid; however, it contains cylinders of calcified bone, known as osteonal or Haversian systems. The Haversian systems (~200μm) are made up of concentric layers (lamellae: ~2-6μm thick), which give cortical bone its characteristic resistance to typical daily compressive forces [25]. In the centre of the Haversian systems are Haversian canals, longitudinal canals that contain blood vessels, nerves, lymphatic vessel and erosion cavities [25, 28]. A second system of canals, called Volkmann's canals, penetrates the bone perpendicular to its surface. These canals establish connections with the inner and outer surfaces of the bone. Vessels in Volkmann's canals communicate with vessels in the Haversian canals carrying nutrients and waste products.

2.3.2 Cancellous (trabecular) bone

Cancellous bone tissue, found mainly within the skeleton, has a sponge-like morphology filled with adipose tissue and marrow, in the form of an open-laced pattern of tiny bars "trabeculae", which withstands maximum stress and supports shifts in weight distribution. Cancellous bone has a lower stiffness and density than compact bone, but the properties of the individual trabeculae within the bone are similar to those of compact bone [28, 45]. The porosity of cancellous bone is the proportion of the total volume that is not occupied by bony tissue. Because of the high porosity in cancellous bone, the trabeculae do not form Haversian systems. HAP coatings on hip endoprostheses are required to interact with cancellous bone.

2.4 Bone cells

Bone is mutually a tissue and an organ consisting of two main permanent elements: specialised cells and intercellular substance. The four specialised cells in bone are bone-lining cells, osteoblasts, osteocytes and osteoclasts. These cells are capable of changing their roles as the needs of the body changes [25].

2.4.1 Bone-lining cells

Bone-lining cells are narrow flattened cells, which are found on the surface of most bones in the adult skeletons that are not undergoing remodelling or modelling. These lined surfaces, including the blood channels, form a thin barrier, which contributes to homeostasis by regulating the relative movement of calcium and phosphate ions between the bone and the body. On the outside of bone, the cells form the periosteum and on the inside the endosteum [28]. It is claimed [25, 26, 28, 42] that bone-lining cells are quiescent osteoblasts, derived from osteoprogenic cells, which cease their physiological activity and flatten out when on the surface of bone.

2.4.2 Osteoblasts

Osteoblasts are bone-forming cells that are present on the surface of osteoid, which contribute to appositional growth of bone by aligning themselves in a continuous layer upon the surface of mature bone. Derived from primitive mesenchymal cells, osteoblasts synthesise osteiod. Calcification of osteoid is carried out by osteopath cells, which when embodied in bone matrix are known as osteocytes [25, 26, 28, 42]. Because of their function, osteoblasts are generally located in newly forming and healing bone. Actively

forming osteoblasts secrete alkaline phosphatase (ALP), osteocalcin, osteopontin and proteoglycans, and therefore these chemicals can be used as an immunoassay for osteoblastic differentiation in cell culture systems [39, 42].

2.4.3 Osteocytes

Osteocytes play an active role in homeostasis by helping to release calcium from bone tissue into blood, thereby regulating the concentration of calcium in the blood fluids. Osteocytes are also able to keep the matrix in a stable and healthy state by secreting enzymes and maintaining its mineral content [25, 42]. Osteocytes are imprisoned in hard bone tissue and connect with neighbouring osteocytes and with bone lining cells by means of processes that are housed in small canals called canaliculi, ~ 0.2-0.3μm in diameter. The connections with neighbouring cells are by means of gap junctions that readily allow small molecules through [25, 46].

2.4.4 Osteoclasts

Osteoclasts are large multi-nucleated cells (~100 μm) derived from fused monocytes (white blood cells) circulating in the blood. Osteoclasts, when stimulated by a parathyroid hormone, resorb osteiod [25]. Osteoclasts attach themselves to the bone matrix and form a tight seal at the rim of the attachment site. The cell membrane opposite the matrix has deep invaginations forming a ruffled border. Osteoclasts empty the contents of phagosomes and residual bodies into the extracellular space between the ruffled border and the bone matrix. The released enzymes break down the collagen fibres of the matrix. Organic and mineral debris are packed into vesicles and passed through the

cell body of the osteoclasts and deposited. This is followed by cell autolysis but the mechanism is not yet fully understood [28, 42].

2.5 Bone remodelling

Bone is continually undergoing renewal or remodelling which occurs through a selective resorption of old bone and a simultaneous production of new bone. The rate of remodelling differs in different locations according to physical loading, proximity to a synovial joint or the presence of haemopoietic rather than fatty tissue in adjacent marrow. Bone remodelling follows a five-stage process (figure 2.4) where osteoclasts and osteoblasts work closely together in time and space (coupling), and they work in units called the basic multicellular unit (BMU) [39]. Proteinases derived from the bone lining cells expose the bone matrix in order for the osteoclastic matrix resorption to occur. Osteoclasts then act on the bone matrix to form an erosion cavity (Howship lacuna) by secreting lysosomal enzymes through a convulted membrane. The reversal and bone formation stage follows, whereby mononuclear cells fill in the lacuna, differentiate into osteoblasts and begin to fill in the lacuna with osteiod. The osteiod is subsequently mineralised to form new bone matrix. This process can take up to three months with mature osteoblasts secreting matrix for up to 100 days. The balanced process of bone formation and resorption (coupling) is vital to maintain the structural integrity of the skeletal system. Uncoupling of the remodelling cycle leads to skeletal diseases such as osteoporosis where net resorption is greater than formation [27, 39].

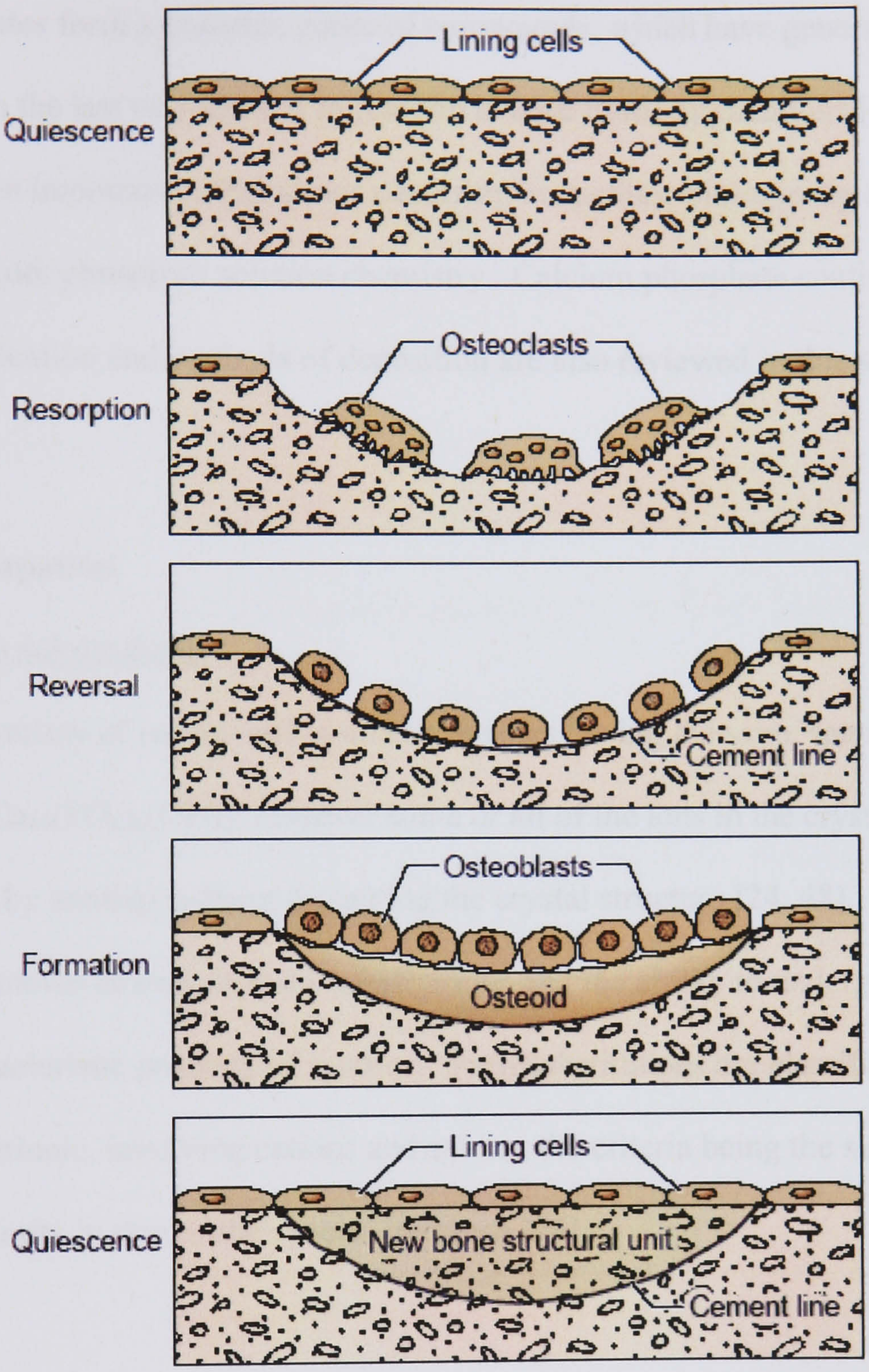

Figure 2. 4 The bone remodelling sequence.

3.0 Calcium Phosphates

Calcium phosphates form a complex genre of compounds, which have generated a great deal of interest in the last two decades in relation to hard tissue applications [47]. This section focuses on important substitutions occurring in apatites, biologically relevant apatites and calcium phosphate solution chemistry. Calcium phosphate coatings for orthopaedic application and methods of deposition are also reviewed in this section.

3.1 Substituted apatites

3.1.1 Ismorphous substitutions

There is a wide variety of natural and synthetic apatites having the same spatial arrangement as $Ca_{10}(PO_4)_6(OH)_2$, however some or all of the ions in the crystal lattice may be replaced by another without disrupting the crystal structure [24, 48]. This is phenomenon is known as isomorphous substitutions and the ability to undergo this process is a characteristic property of apatites. Such substitutions are classified as isoionic and heterionic, involving cations and anions, the criteria being the similarity in charge and proximity in size of the species involved [24].

3.1.1.1 Isoionic substitutions

Isoionic substitutions can be defined by a process whereby ions from a solid phase exchange with ions from a similar solid phase nearby it, the composition of both phases remaining unaltered [24].

3.1.1.2 Heterionic substitutions

Examples of some biologically significant heterionic substitutions include $Ca^{2+} \leftrightarrows Sr^{2+}$, $Ca^{2+} \leftrightarrows Ba^{2+}$, $Ca^{2+} \leftrightarrows Mg^{2+}$, $Ca^{2+} \leftrightarrows Pb^{2+}$, $OH^- \leftrightarrows F^-$, $PO_3^{4-} \leftrightarrows AsO_3^{4-}$. The double arrow denotes that each substitution can occur in either direction depending on the sample of apatite chosen as the seat for the occurrence of exchange [24].

3.1.1.2.1 Substitution of Ca^{2+} ions for bivalent ions

Substitution of Ca^{2+} ions for bivalent ions such as Mg^{2+}, Ba^{2+}, Sr^{2+} and Pb^{2+} ions can occur readily in both biological and synthetic apatites [49]. Ba^{2+}, Sr^{2+} and Pb^{2+} ions have larger ionic radii than Ca^{2+} and therefore cause an expansion in lattice parameters of the apatite. Although Ba^{2+}, Sr^{2+} and Pb^{2+} are minor constituents of bone mineral, in abundance they have detrimental effects on bone mineral chemistry, bone matrix mineralization homeostasis. The formation of barium HAP in the skeletal system provides a reservoir for Ba^{2+}ions, which in high doses affects the thyroid function. Lead poisoning; often know as plumbism occurs through the inhalation of lead or the absorption through the skin. The mechanism of accumulation of Pb^{2+} ions involved is isomorphous substitutions of Ca^{2+} ions by Pb^{2+} ions in the skeletal system hence forming lead hydroxyapatite [24].

Mg^{2+} ion substitution for Ca^{2+}ions causes disturbance to the apatite lattice despite no change in lattice parameters. This is due to the fact that the incorporation of Mg^{2+} ions promotes the formation of stable whitlockite, amorphous calcium phosphate and β-

tricalcium phosphate (see section 3.2)[49]. Despite the fact that the effect of Mg^{2+} is well documented [49, 50], the exact mechanisms are not fully understood.

3.1.1.2.2 Substitution of OH^- ions for monovalent ions

Apatites have a high affinity for fluoride ions as would be expected from fluorine's high electronegativity. Fluoride ions replace the similarly sized hydroxyl ions in the apatite lattice with a small reduction in the a-axis [51]. The $OH^- \leftrightarrows F^-$ exchange is of significance in explaining the prevention of dental caries. Formation of fluorapatite (FAP) on the tooth surface from a daily dose of fluorine can retard the tooth corrosion by acidogenic bacteria. This can be explained by the fact that FAP is less soluble than HAP. Fluoridation of drinking water has been practised for many years with 1 ppm being the optimal level for caries control [24]. However a higher level is toxic and has been found to lead to skeletal and dental fluorosis.

The properties of common synthetic apatites can be found in table 3.1:

	Hydroxyapatite	**Fluorapatite**	**Chlorapatite**
Formula	$Ca_5(PO_4)_3OH$	$Ca_5(PO_4)_3F$	$Ca_5(PO_4)_3Cl$
Density (gcm^{-3})	3.15	3.21	3.185
Molecular weight (g)	159.34	157.53	163.53
Formula weight (g)	502.32	504.31	520.77
Space group	$P6_3m$	$P6_3m$	$P6_3m$
Cell parameters			
a (Å)	9.424	9.367	9.628
c (Å)	6.879	6.884	6.764
Volume	529.09	523.09	543.01

Table 3. 1 Properties of common apatites [33, 52].

3.1.1.2.3 Carbonated apatites

Carbonate apatites are of particular interest in biological systems as the inorganic component of bone and teeth because of the similarity to natural bone and dental apatite [53-56]. The presence of carbonate in dental crystallites makes them more susceptible to carious attacks by acids in the mouth. This can be explained by the interference of the carbonate with the crystallisation of apatite, and its weakening effect on the bonds in the structure. Hence, there is a net increase in the dissolution rate and solubility.

Previous studies [48, 57] show that the presence of carbonate in the crystal lattice causes a reduction in crystallite size, an increase in strain [48, 58] and a change in shape of apatite crystallites [50, 59-61]. The increase in solubility of carbonate containing apatites thus reflects the increase in surface area of the mass of apatite crystallites [55].

Carbonate ions can be localised into two different sites in the apatite lattice: on the hexad axis at the OH-lattice position (type A) and the other at the PO_4^{3-} lattice position (type B) [53, 62]. It has been shown that type A carbonated apatite is produced by high temperature reactions of HAP with carbon dioxide gas resulting in an expansion of the a-axis length and a contraction of the c-axis length [56, 60, 63]. Type B carbonated apatite is produced from precipitation [60, 63] resulting in a contraction of the a-axis length and an expansion of the c-axis length.

3.2 Biologically relevant calcium phosphates

3.2.1 Amorphous calcium phosphate (ACP)

ACP is thought to play the special role of a metastable phase in biomineralization [53, 64]. In aqueous environments, because of its high solubility, ACP is readily transformed to OCP or apatitic products [53]. Like many apatites, ACP does not have a rigidly defined molecular formula. The Ca: P ratio of ACP depends largely on the conditions of preparation. Eanes *et al* [65] have shown that the composition of ACP varies less than apatites under comparable conditions and that ACP with a Ca: P ratio of 1.50 has the greater solubility. The characteristics of ACP can be seen by the absence of well-defined peaks in an XRD spectrum (figure 3.1). Unlike crystalline calcium phosphates, there is no long range, three-dimensional order of the constituent atoms [66]. However, there is a certain degree of short-range order present as can be seen from the broad diffraction maxima. In principle the phosphate tetrahedra in ACP are believed to be unitary but their positioning in relation to one another and the calcium ions is not regular [66]. The lack of periodicity of ACP and detail in the broad diffraction maxima make accurate XRD analyses of the phase challenging [66].

3.2.2 Octacalcium phosphate (OCP)

OCP has been considered as the probable precursor of biomineralisation in bones and teeth and is believed to be biocompatible, biodegradable and osteoconductive [67]. It also has a biological significance as one of the stable components in pathological calcifications of the urinary tract. Structurally, OCP is made up of apatitic layers similar to HAP separated by hydrated layers [68]. The crystal structure of OCP is monoclinic in

nature with a P 1 space group. The lattice parameters are: a=1.969 nm, b=0.952 nm, α=90.15°, β=92.54° and γ=108.65° [53].

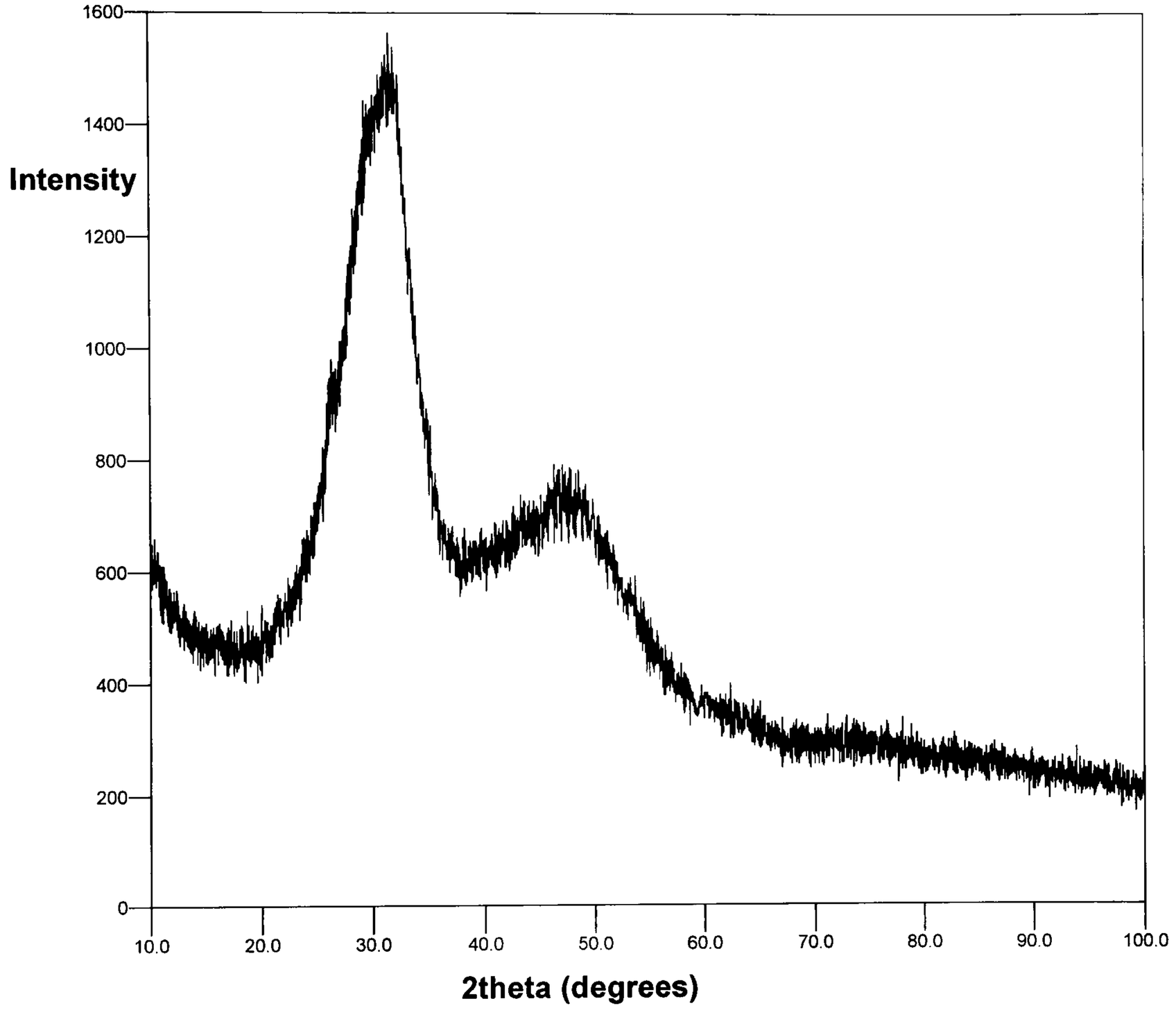

Figure 3. 1 Diffraction pattern of amorphous calcium phosphate.

3.2.3 α-Tricalcium phosphate (α-TCP)

Despite not being found in biological systems, α-TCP's role in biomineralisation is due to the fact that it easily hydrolyses to OCP *in vitro* [69]. α-TCP is a metastable phase at room temperature and is prepared from β-TCP at 1125°C. In aqueous solutions, it is readily transformed to calcium deficient hydroxyapatite (CDHAP), making α-TCP more

soluble than β-TCP [68]. Despite being more biodegradable than β-TCP, α-TCP's usage is limited to application in calcium phosphate cements [67]. α-TCP crystallises in the monoclinic space group $P2_1/a$ where a=1.288 nm, b=2.728 nm, c= 1.521 nm, β=126.20° [70].

3.2.4 β-Tricalcium phosphate (β-TCP)

β-TCP like α-TCP is not found in biological systems but its relevance to biomineralisation is due to its crystallographic similarity to the magnesium containing form whicklockite. Whitlockite is found in pathological calcifications and dental caries [67-69]. Due to its bioactivity and osteoconductive nature, β-TCP is used commercially in biphasic calcium phosphates in bone fillers and bone cements [58, 71, 72]. However, due to extremely rapid resorption rates and poorer bioactivity than HAP, β-TCP is not suitable for usage in orthopaedic reconstruction as a single phase [71, 72]. β-TCP crystallizes in the rhombohedral space group R3c with lattice parameters a=1.439 nm, c= 3.737nm [73]. It cannot be precipitated from solution, but can only be produced by calcinations of calcium deficient HAP (CDHAP) above 800°C [68]. In addition when heated at 1050°C, HAP, is partially converted to β-TCP [72].

3.2.5 Dicalcium phosphate dihydrate (DCPD)

DCPD, detected in callus, bone and pathological calcifications is a metastable compound, which can easily be hydrolysed to OCP or HAP [74]. It has been proposed that *in vivo* DCPD is transformed to bone apatite or biodegraded and replaced by bone. DCPD

crystallises in the monoclinic space group Ia with lattice parameters a=0.581 nm, b=1.518 nm, c= 0.623 nm and β=116.42° [74, 75] .

3.2.6 Tetracalcium phosphate (TTCP)

TTCP, the most basic calcium phosphate is used in self-setting calcium phosphate cements. TTCP has a much greater solubility than HAP below pH 5 and hence it is never found in biological calcifications and cannot be produced by precipitation from aqueous solutions [67, 68]. As a result, the synthesis of TTCP is achieved by solid-state reactions in dry air or nitrogen between dicalcium phosphate (DCP) and $CaCO_3$ at high temperatures, typically 1400°C [76]. TTCP crystallises in the monoclinic space group $P2_1$ with lattice parameters a=0.702 nm, b=1.198 nm, c=0.947 nm and β=90.90° [77]. The structure of TTCP is defined but can only be produced synthetically, as crystallographically, there are no known natural equivalents [74].

3.3 Basic concepts of solution chemistry of calcium phosphates

Kinetics and thermodynamics both control the dissolution and precipitation of calcium phosphates in aqueous solution. Precipitation of a calcium phosphate compound such as HAP from an aqueous solution occurs when that solution is supersaturated with respect to HAP. Dissolution in an aqueous environment, on the other hand, is a result of undersaturation with respect to HAP. The driving forces controlling dissolution and precipitation are related to respective super or undersaturation levels by means of the thermodynamic solubility product, K_{sp} [47]. The thermodynamic solubility product describes the equilibrium state between a mineral compound and an aqueous phase.

Supersaturation and undersaturation in solution can be created by a temperature change, a pH change, and an increase of ionic concentration. A high K_{sp} would suggest low solubility and higher stability at the given conditions. Table 3.2 shows solubility information for biologically relevant calcium phosphates.

Calcium phosphates are one of the most complex and ubiquitous family of materials due the existence of a multitude of phosphate compounds. Factors such changes in chemical composition and pH as well as reaction conditions (temperature, pressure and solvent) have a significant effect on the stability of calcium phosphates [78]. The dissolution and precipitation behaviour of calcium phosphates plays an imperative role in the understanding of bone regeneration [30].

Crystalline HAP is regarded as being the final thermodynamically stable product calcium phosphate [64]. At 37°C, when pH > 4.2, HAP is the most thermodynamically stable phase and all the other solid calcium phosphate phases present at that pH range will dissolve in order to allow the precipitation of HAP [79]. When pH < 4.2, DCPD is the most thermodynamically stable phase. At pH <8.5, the most soluble phase is TTCP and at pH > 8.5 the most thermodynamically stable phase is β-TCP [79, 80]. The solubility of ACP >TTCP > β-TCP > DCPD> OCP > HAP in physiological conditions.

Compound	Formula	Ca: P ratio	Solubility at 37°C, $-\log(K_{sp})$ / Mol L^{-1}	pH stability range
dicalcium phosphate dihydrate	$CaHPO_4.2H_2O$	1.00	6.63	2.0-6.0
octacalcium phosphate	$Ca_8(HPO_4)_2(PO_4)_4.5H_2O$	1.33	95.9	5.5-7.0
β-tricalcium phosphate	β-$Ca3(PO_4)_2$	1.50	29.5	[a]
amorphous calcium phosphate	$Ca_X(PO_4)_Y.nH_2O$	1.2-2.2	[b]	[a]
hydroxyapatite	$Ca_{10}(PO_4)_6(OH)_2$	1.67	117.2	9.5-12
tetracalcium phosphate	$Ca_4(PO_4)_2O$	2.0	37-42	[a]

Table 3. 2 Properties of biologically relevant calcium phosphates [47, 68, 79].
[a] These compounds cannot be directly precipitated from aqueous solution. [b] Cannot be measured precisely.

3.4 Coatings for prosthetic stems

Bioprosthetic coatings (BC) for use in orthopaedic surgery are synthetic coatings that aid in the accelerated regeneration and fixation of tissue in areas of implantation without having any detrimental effect on the existing tissue. BCs are typically applied to parts of the implant that interface with bone tissue and form a bond joining the implant to the bone tissue [81]. In the case of hip prosthesis, BC coatings are applied to the surface of the femoral stem and the outer face of the acetabular cup [14].

3.4.1 Ideal Bioprosthetic coating characteristics

In the development of bioprosthetic coatings for orthopaedic application, due consideration has to be given to how the materials integrate with the body [15]. An ideal BC would need to be bioactive, biocompatible, resorbable and capable of accelerated bone regeneration and improved fixation [14, 15, 81]. The BC must be capable of progressive dissolution to liberate the necessary calcium and phosphate ions to form physiochemical bonds with bone [14, 15].

Traditionally, prostheses have been implanted by means of thermosetting cement such as polymethylmethacrylate (PMMA) [81]. Cement fixation methods can achieve rapid fixation between bone and the implant. They are not suitable for younger (less than 50 years of age) and active patients. More stable and stronger fixation is required in these cases to prevent failure [14]. Other disadvantages include the formation of particulate debris, which can cause osteolysis and cell necrosis from the thermosetting of the PMMA [15].

Bioactive materials such as HAP can stimulate rapid bone regeneration and fixation [15]. HAP is capable of making stable physiochemical bonds with the surrounding host bone with the need of a fibrous membrane [14]. The chemical similarity of HAP to natural bone apatite suggests an intrinsic biocompatibility and osteotropism [15, 74]. In addition, HAP can develop HAP-bone bond strength that is three times larger in magnitude than a metal-bone bond strength [81].

Critical quality specifications for HAP coatings include phase composition, crystallinity, Ca/P ratio, microstructure and thickness, which all influence the mechanical properties, bioactivity and durability of the coating [14]. An ideal HAP coating must have a high degree of crystallinity, low porosity, good cohesion to the substrate and high chemical and phase stability [14, 81, 82]. The coating must be thick enough to avoid complete dissolution by physiological fluids but sufficiently thin to avoid delamination and fatigue failure under tensile loading . To have good adhesion to a metallic implant, an ideal coating would be between 50-250μm in thickness [81, 82].

3.4.2 Dental and orthopaedic athroplasty

Ti-6Al-4V alloy is currently the prime metal substrate used for dental prosthesis [14, 81]. Other materials used are 316L stainless steel, Co-Cr-Mo alloy [81] and alumina (Al_2O_3) [15]. Ti-6Al-4V alloy remains the preferred metal for fabrication of dental prosthesis because its density ($4.4gcm^{-3}$) is closer to the density of cortical bone ($2gcm^{-3}$) compared to its counterparts ($>7gcm^{-3}$) [81]. Ti-6Al-4V alloy provides good corrosion resistance and fatigue life as well as being bioinert [14]. The coating of metallic implants brings together the high torsional strength of Ti-6Al-4V alloy and the biological advantages and good compressive strength of the HAP coating [82, 83].

Of note is that the elastic moduli of Ti-6Al-4V alloy (E=110GPa) [14] and HAP (E=100GPa) [81] are similar to avoid residual stresses at the substrate coating interface [15].

3.4.3 Bone bonding and fixation

Partial dissolution of the HAP coating occurs causing the liberation of Ca^{2+} and PO_4^{3-} into the surrounding body fluid. The dissolution causes an increase in Ca^{2+} and PO_4^{3-} ion concentrations in the body fluid surrounding the coating, which promotes the calcification of the non-crystalline zones of the coating. Ion exchange continues to occur with the surrounding tissues resulting in the formation of a carbonated calcium phosphate layer. The calcium phosphate layer consists of microcrystals and macrocrystals, which can be incorporate within a collagenous matrix and promote bone growth towards the implant. Osteoclastic resorption of the normal bone occurs by the active secretion of hydrogen ions into the extracellular space, hence creating an increase in the localised pH. The osteoclastic resorption at low pH (section 2.4.4) leads to a fast dissolution of both the carbonated apatite in bone mineral and HAP in the coating. Further bone ingrowth and remodelling occurs at the bone-implant interface and biological fixation is achieved through the bi-directional growth of a bonding layer [14]. *In vivo* bone remodelling is described in chapter 2 and depicted in figure 2.4.

3.5 Coating methods

Non-ideal HAP coating characteristics have been the impetus for the modification and development of coating methods in the last twenty years. An ideal coating method would be a one step process, which is cost effective and produces thick (50-250μm), adherent and stable coatings [84]. In addition, the fabrication process would need to afford great control over the composition and microstructure of coatings [85].

3.5.1 Thermal plasma spraying (PS)

PS is the major manufacturing technology in the prosthetic implants market [14, 86-88]. The use of PS techniques to coat HAP onto implants is popular due to advantages such as simplicity, high deposition rates [89] low substrate temperature, and variable coating porosity, phase and microstructure [90-93]. Coatings produced by PS are able to bond directly to bone [94], and promote early fixation [95] and protect the surrounding bone against metal-ion release from the metal implant [14].

3.5.1.1 Thermal plasma technology

The surfaces of the implants to be coated are prepared by a variety of methods such as shot peening, electrochemical milling and grit blasting in order to increase mechanical bonding to the substrate [96, 97]. PS is a line-of-sight process [83] that involves the acceleration of highly crystalline HAP feedstock powder through mechanical transfer apparatus into a high temperature electric arc-plasma gas atmosphere at high velocity [82, 98]. An arc is struck between a cathode and an anode, with the arc heat that causes dissociation of gas to levels attaining 30 000 K [14]. The particulate HAP is passed into the plasma arc by a carrier gas such as argon

[82, 96] at velocities up to 300ms^{-1} towards the metallic substrate [89, 99, 100]. A schematic diagram of the process at the nozzle is presented in figure 3.2.

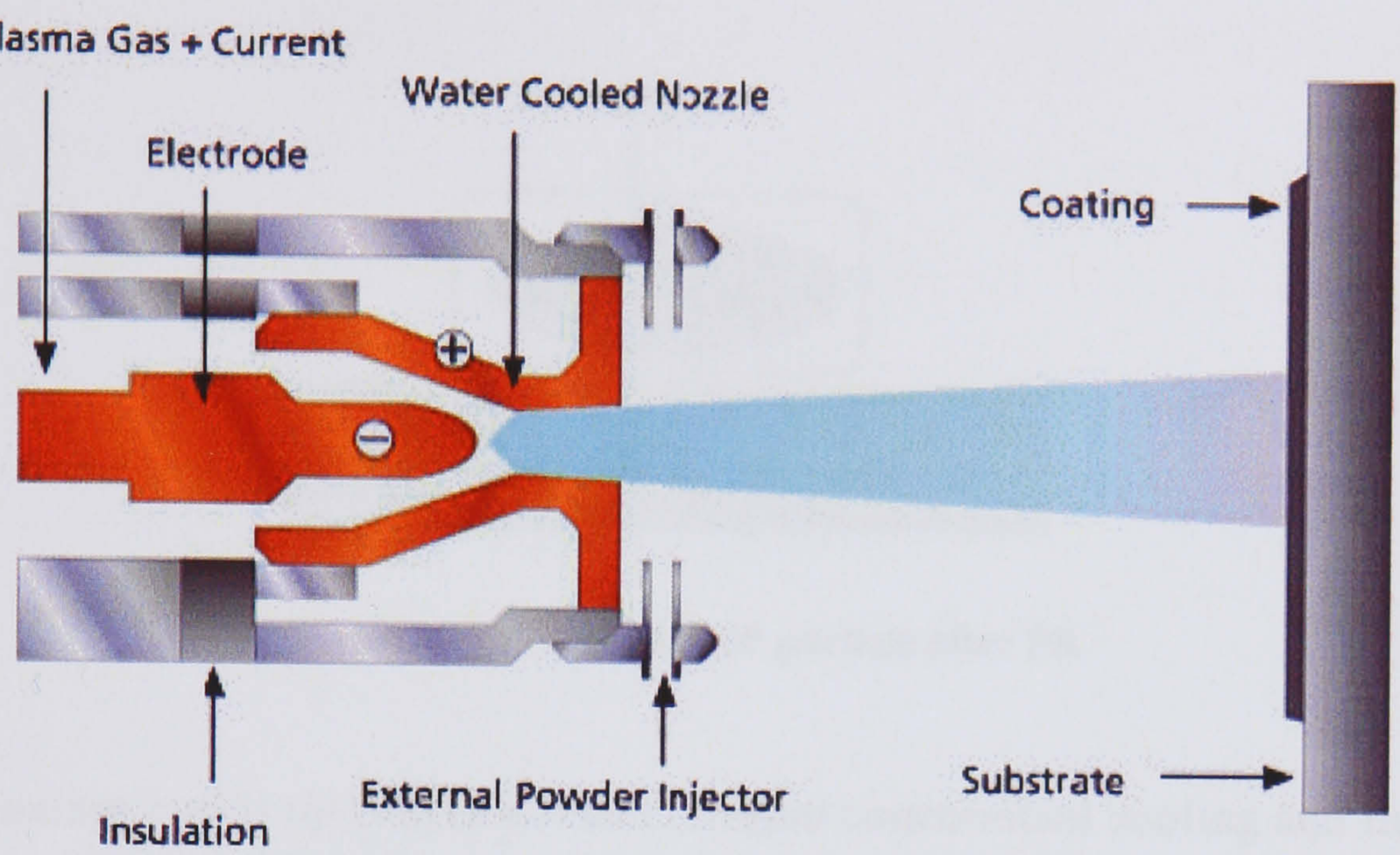

Figure 3. 2 Schematic of thermal plasma spray process [101].

3.5.1.2 Composition and microstructure of PS coatings

The high temperature attained in the plasma gun causes partial melting of HAP particles [89, 100]. On entering the plasma gun, the outer periphery of the particles melt and they lose their crystalline order. The core does not undergo this transformation and remains in a solid crystalline state. On collision with the cooler metallic substrate, rapid solidification of the HAP melt occurs producing crystalline HAP coatings with an ACP phase (figure 3.5) [14, 82, 93, 97, 99]. Other common phases that appear in PS coatings include α- and β-TCP, TTCP and CaO (discussed in section 3.2) [86, 93, 102]. The formation of extraneous phases is not only due to rapid cooling and decomposition of HAP but also due to dehydroxylation, which inherently impedes the formation of crystalline HAP [97]. The crystalline component of the coating after solidification consists of the unmolten core and recrystallised HAP

melt. Recrystallisation of the HAP melt occurs preferentially in the hydroxyl-rich regions of the ACP phase [97]. Figure 3.3 is a schematic of a typical PS coating.

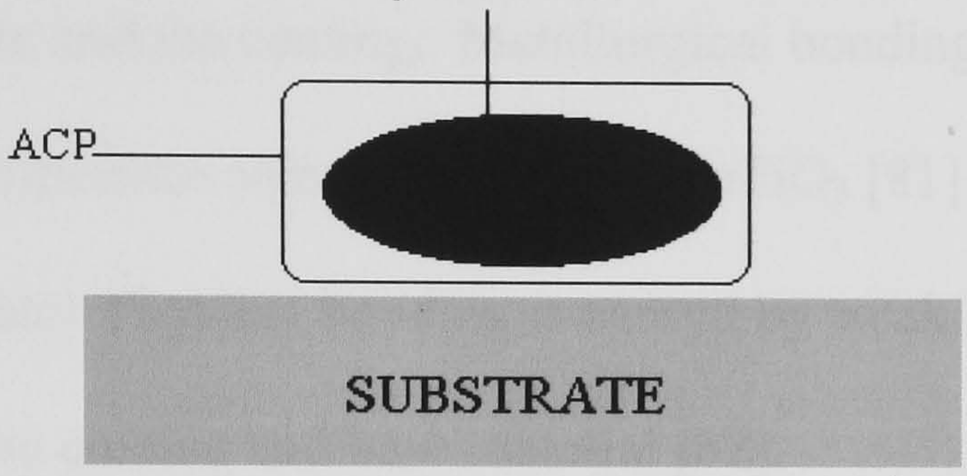

Figure 3. 3 A typical HAP particle after PS.

PS HAP coating builds up [92] as a result of rapid concomitant cooling and flattening of HAP particles. The resultant HAP coatings are stable and strongly adherent with a composition and microstructure significantly different from the feedstock powder [14, 82, 87, 103-105]. The microstructure is lamellar in nature with cracks and voids as typical defects [86, 93, 106]. HAP coatings formed commercially by PS are 50-90% crystalline [14] and are 50-100μm in thickness [14, 82, 99].

Control of coating quality can be achieved by the modification of materials characteristics and PS operating parameters. The materials characteristics include chemical composition, impurities, particle size, morphology and density. The PS operating parameters include spray stand-off distances, arc gases, powder feed and nozzle type [14, 81, 91, 107].

3.5.1.3 Adhesion mechanisms

The adhesion mechanism of PS coatings is very complex [104] and can be classified into three categories: mechanical bonding metallurgical bonding [82, 99] and Van der Waals interactions [82]. Mechanical bonding occurs when the plasma state particle hits the metallic substrate. A mechanical interlock (tenon-mortise effect) is formed between the substrate and the coating. Metallurgical bonding results from the formation of an intermediate compound such as $CaTiO_3$ [81] between the discharged HAP and the substrate. Physical bonding is caused by weak Van der Waals forces that exist between the coating and base material [82].

3.5.2 Biomimetic

Biomimetic (BMM) processes for coating prosthesis with HAP are essentially solution-based methods that mimic the mineralization of collagen in the skeletal system [108]. Typically, BMM processes involve soaking metallic implant materials in supercalcified solutions such as simulated body fluid (SBF) at physiological temperature and pH [108, 109].

Recent studies have shown that BMM coating techniques are possibly the most progressive for producing biomaterials. BMM processes are low temperature [85], cost effective techniques that produce adherent coatings of uniform thickness [110, 111]. Coatings with varying compositions can be produced with ease and growth hormones and antibiotics can be readily incorporated to stimulate bone healing [111]. The low processing temperature could be exploited to coat organic polymer implants for soft tissue replacements such as tendons, ligaments and tracheae [108, 110, 112].

Traditionally BMM coating processes have been known to be time-consuming and produce coatings of only 3-5μm. Modern BMM techniques only require immersion times of up to 24 hours and can produce coatings 30-55μm thick [108, 113]. Processing times are still lengthy compared with PS and hence, further development is required to make BMM coating methods commercially viable.

3.5.3 Sol-gel

Sol-gel (SG) processes can be characterised as any mode of producing ceramic materials from solutions. For the production of HAP coatings, chemical reactions take place between calcium and phosphate ions under controlled solution pH and temperature to form slurry. To produce a coating, the solution can be applied with dip, spin or spray coating [114]. Aqueous slurries can be readily converted to the required crystalline phase by hydrothermal methods [115, 116]. The resultant coatings are typically 1 μm in thickness, and homogenous [114]. Since the reactions occurring in SG processes are solution mediated, the particle size and morphology of the coatings produced can be manipulated to regulate nucleation, growth and ageing processes [116]. In addition, growth hormones and antibiotics can be incorporated into the coatings as is necessary clinically [117, 118].

SG methods are relatively simple low temperature wet chemical precipitation processes for the production of high purity homogeneous HAP coatings [118]. Unlike the PS process, sol-gel methods are easily applicable to substrates over a wide range of shapes and size [88, 107, 118, 119]. SG methods of producing HAP coatings are becoming increasingly popular commercially due to their versatility. However most

sol-gel coating methods are multi-step processes and are slow [88, 107, 118, 119]. Commercially, a one step process is a more attractive feature.

3.5.4 Electrochemical deposition (ED)

ED methods are emerging as a popular low temperature, non-line of sight process, by which HAP coatings can be produced in aqueous electrolytes [120, 121]. Successful electrodeposition of HAP has been demonstrated by Roessler *et al* [122], Kuo *et al* [22] and Shirkhanzadeh *et al* [121].

Electrolytes used for ED are typically produced by dissolving reagent grade $Ca(NO_3)_2$ with $NH_4H_2PO_4$ in deionised distilled water [83, 123]. The cathode used is the surface treated metallic implant to be coated, which is typically a titanium alloy or a colbalt-chromium alloy in the case of medical devices [124]. The anodes used frequently are platinum [124] or carbon. The temperature and pH of the electrolytes are maintained at specific levels depending on the concentrations of calcium phosphate ions in the system [123]. Cathodic polarisation takes place in a number of successive process cycles with current densities ranging from 0.5 $mAcm^{-2}$ to 20 $mAcm^{-2}$ [124]. The calcium phosphate material is then deposited on the cathode after numerous cathodic polarisations and drying cycles.

In some ED methods, brushite is initially deposited onto the cathode and this is then converted to HAP typically at up to 400°C [124]. Indeed there may be advantages to such a '2 stage' approach for control of film properties such as crystallite morphology through this second step, but in many cases, the conversion process is a lengthy one lasting up to 36 hours [124]. Currently, for HAP coatings produced by ED,

depositions times range from four minutes to two hours [123] at temperatures of 25-85°C [83].

Single stage electrodeposition of HAP was first reported by Shirkhanzadeh *et al* [125]. The ED mechanism of HAP deposition used is complex and involves combined electrochemical, acid–base and precipitation reactions. Some control of the coating thickness and crystallographic phase formed is afforded by the cathodic current density and interfacial pH, which has been previously investigated [22, 120, 121, 126, 127].

ED has the potential to provide dense, macroscopically homogenous coatings, with good internal cohesion and adhesion to the implant surface. It may also enable incorporation of biomolecules forming a sustained release, drug delivery system. It has been shown [123] that lysine attachment can be controlled through the number of OH polar groups (H bonding with protein molecules).

3.5.5 Alternative coating methods

Since HAP coatings were first introduced two decades ago, various novel coatings methods have been used to deposit HAP on implants. These coating methods include physical vapour deposition [92], chemical vapour deposition [81, 92], electrophoretic deposition [128, 129] and radio frequency magnetron sputter coating [14]. A comparison of these methods is summarised in table 3.3.

Method	Process details	Characteristics of coatings
Physical vapour deposition (PVD) [92, 99].	Vacuum process: Evaporation, sputtering, ion plating, ion beam processes.	Wear resistant, corrosion resistant, low friction and biocompatible. Coating thickness 1-40μm.
Chemical vapour deposition (CVD) [92, 99].	High temperature process; coating formed through chemical reaction from vapour phase.	Bioinert coatings of 1-40μm thickness.
Electrophoretic deposition [14, 128, 129].	Combination of two processes: electrophoresis and deposition.	The high temperature sintering (>1000°) can degrade the mechanical properties. Repeated deposition produces thick, uniform, crack-free HAP coating – uneconomical with low bond strength. Coating thickness can be 1-500μm.
Radio frequency magnetron sputter coating [14, 130].	Typically 400W discharge power and 5Pa Ar gas pressure.	Slow and low rate of deposition. Ca/P ratio is higher than synthetic HAP. Microstructure controllable under 1μm.

Table 3. 3 Comparison of alternative coating methods.

3.6 Summary

HAP, the most stable calcium phosphate in physiological conditions, has a chemical similarity to natural bone apatite. Therefore there is a physiochemical rationale for using HAP as a bioprosthetic coating. HAP coatings are osteoconductive in nature and promote osseointegration and stronger implant-bone fixation.

A number of novel methods for HAP deposition have been proposed offering potentially better control of film structure than traditional methods. In many cases the thickness is limited to micron dimensions presenting a concern because long-term

coating survivability is a requirement. Other methods are multi-stage processes, which are time-consuming and therefore not commercially viable.

From a practical point of view, ED is an economical alternative to traditional coating methods such as PS because it can be used to coat implants of all morphologies and can be adapted for the fabrication of other calcium phosphate phases on metallic substrates [19, 127]. The technique of choice for deposition of HAP coatings for commercial use remains PS, despite its shortcomings. Dense tightly adhered coatings of up to 100μm in thickness can be deposited within two minutes [89, 129, 131].

4.0 Structural and chemical characterisation of apatites

This section introduces the main analytical techniques used for the structural and chemical characterisation of apatite coatings and powders.

4.1 X-ray diffraction (XRD)

Since the discovery of x-rays by Rontegen in 1895 and the first experiments by Knipping and von Laue, X-ray diffraction has proved to be a valuable research tool, both for measuring wavelengths of X-rays and for the study of crystal structure [132-134]. XRD is a non-destructive and adaptable technique that allows extensive structure-property correlations [133, 135]. The information obtained from XRD is based on the diffracted intensity, I, of a specimen. The production of a diffractogram gives three main sources of information: i) the Bragg position θ_{hkl}, of the diffracted intensity which permits qualitative phase analysis and the determination of lattice parameters; ii) the relative intensities of the diffraction peaks which can be used for quantitative phase analysis and information on preferred orientation; and iii) The profile of the reflections which give information about microstructure [135].

Various types of crystalline materials can be characterised by XRD including ceramics, inorganics, organics, drugs, minerals and metals. The physical state of the samples to be analysed can be loose powders, thin films, polycrystalline and bulk materials [136].

4.1.1 X-ray absorption

When a beam of X-rays impinge on the surface of a specimen, the intensity of transmitted radiation through a layer of material with thickness, t, density, ρ, and

mass absorption coefficient, μ, at wavelength, λ_0, is given in equation 4.1 and illustrated in figure 4.1.

$$I(\lambda_0) = I_0 \exp(-\mu \rho t) \qquad (4.1)$$

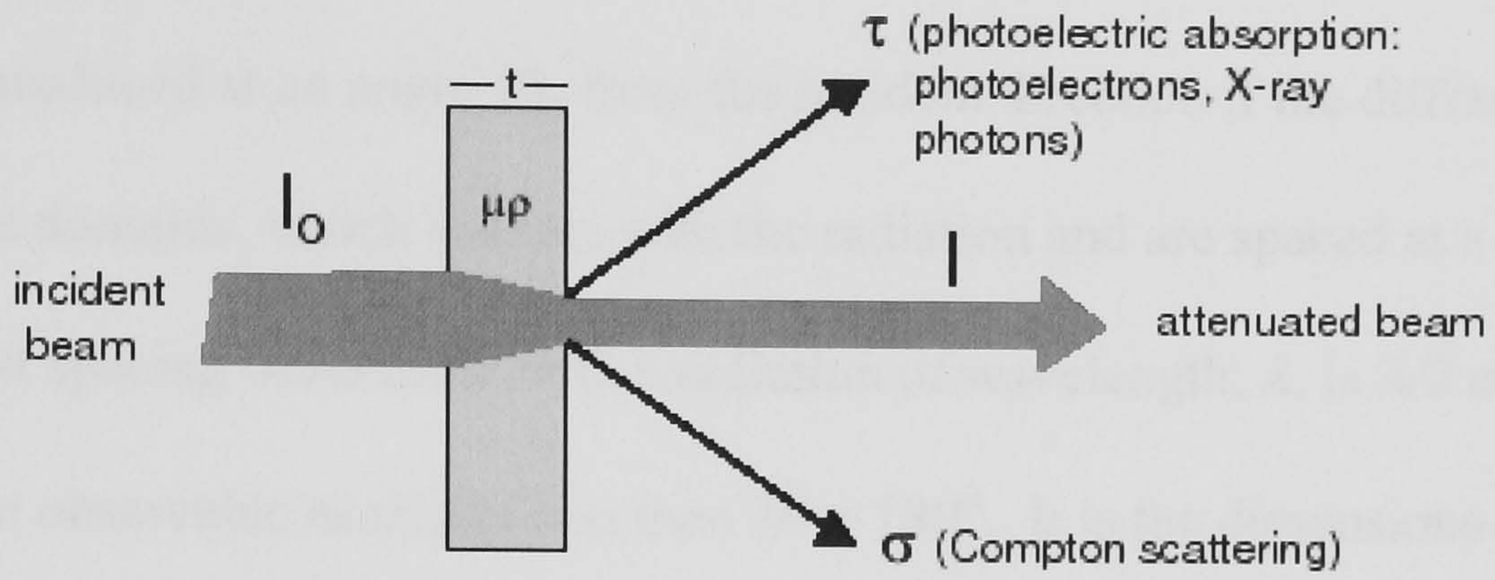

Figure 4. 1 Absorption of X-rays [137]

Attenuation of the incident beam occurs due to Compton scattering (σ) and photoelectric absorption (τ). Compton scattering diverts photons in directions different from the incident, whilst photoelectric absorption produces Auger electrons. The mass absorption coefficient is defined as a combination of Compton scattering and photoelectric scattering. Since attenuation is due to absorption from elements in the material, the mass absorption coefficient is dependent on the material as well as the wavelength of the radiation [137].

4.1.2 Principles of X-ray diffraction

If X-rays of wavelength λ, are incident on a crystal, diffracted beams of maximum intensity occur in only those directions in which constructive interference takes place between the X-rays scattered by successive layers of atomic planes. Bragg's law (see equation 4.2 & figure 4.2) describes the angular relationship for constructive

interference of monochromatic electromagnetic waves diffracted by a regularly arranged structure with a preferred separation distance, d.

$$\lambda = 2\,d \sin\theta_b \tag{4.2}$$

For an incident electromagnetic wave of monochromatic wavelength, λ, coherent waves are produced at an angle $2\theta_b$ from the incident direction if the diffracting material has domains, which interact with the radiation and are spaced at a distance d. The smallest spacing observable with a radiation of wavelength, λ, is $\lambda/2$ and larger spacings are observable at angles less than $2\theta = 180°$. It is the dimensions of the repeating cell unit (lattice parameters) of the crystal that determine the directions of the diffracted beams and the geometry of the pattern. The interference effects from the atoms in the unit cell and the lattice type determine the intensities of the diffracted beams [138].

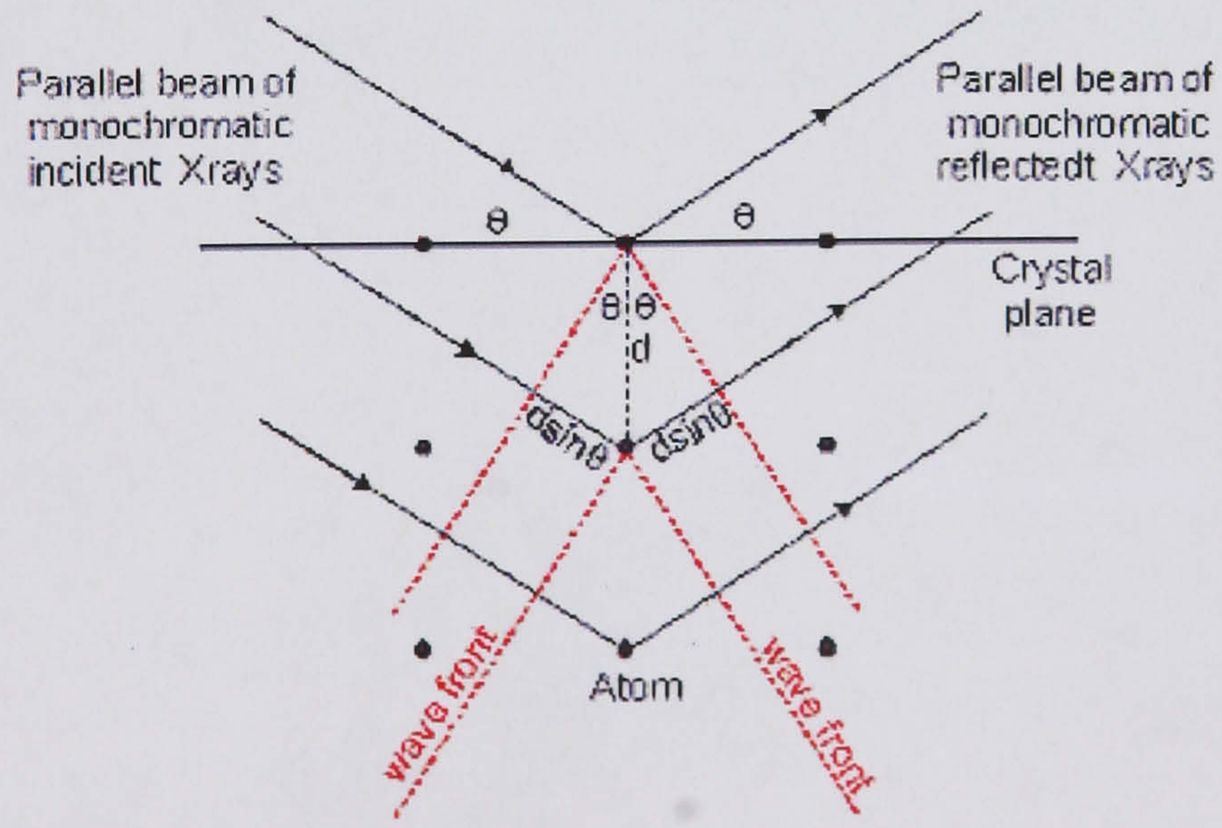

Path difference between the reflected rays is a function of the angle of incidence

Figure 4. 2 Illustration of Bragg's law [137].

4.1.3 Diffraction system

An X-ray diffraction system consists of three main parts: a radiation source comprising of an X-ray tube and generator, a diffractometer and detection and counting system. Figures 4.3 and 4.4 depict conventional XRD apparatus.

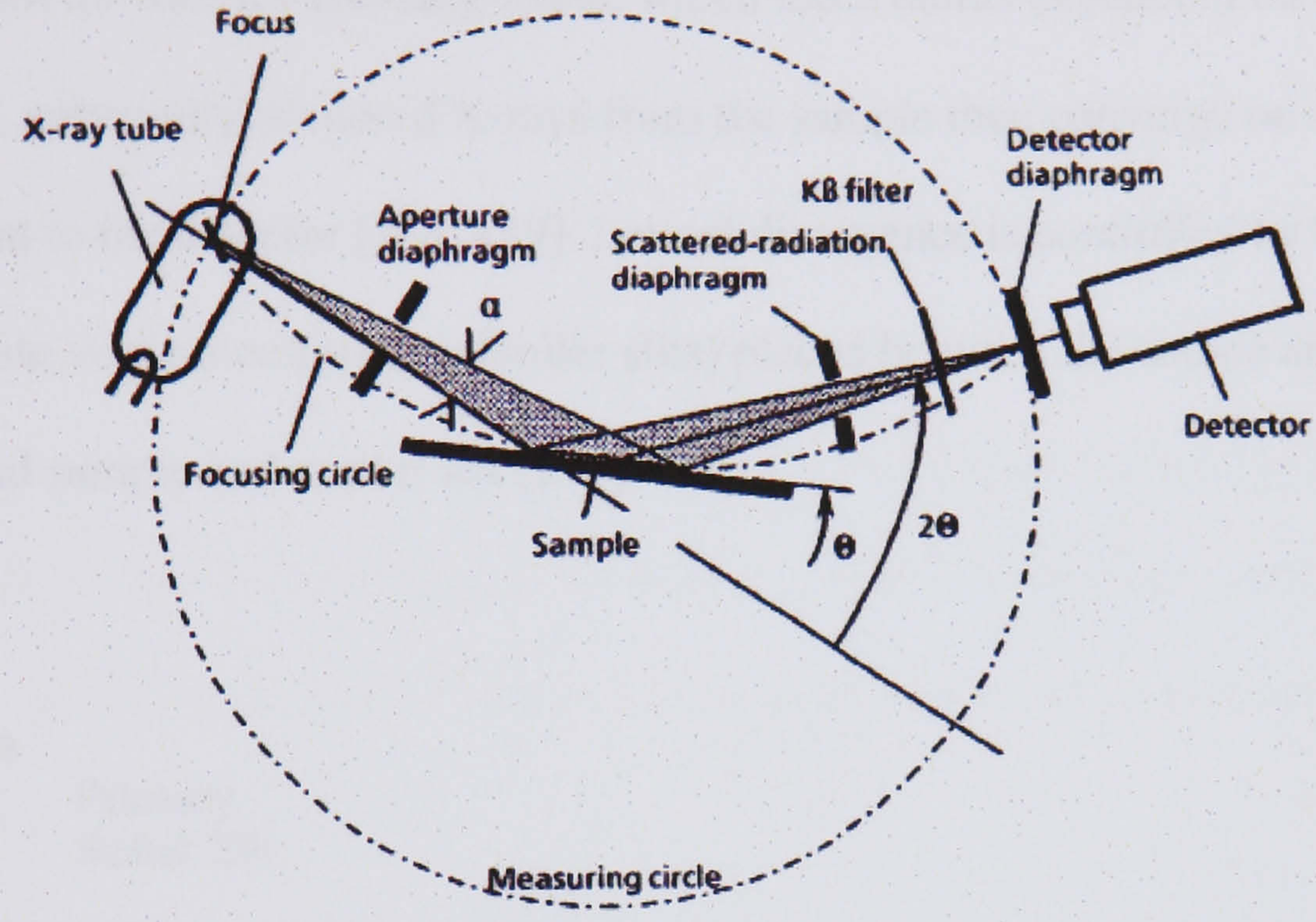

θ Glancing angle
2θ Diffraction angle
α Aperture angle

Figure 4. 3 Schematic of conventional XRD apparatus [137].

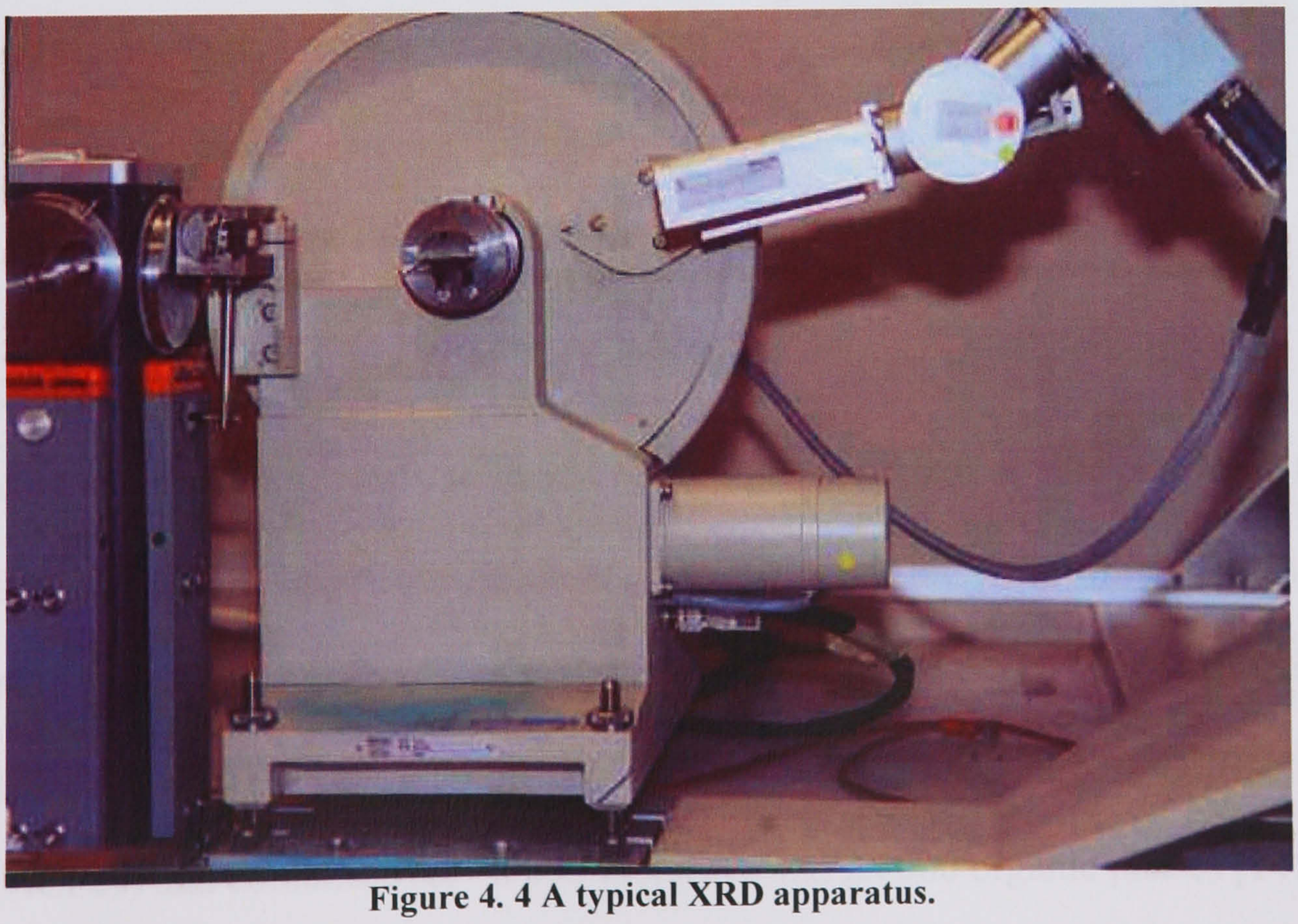

Figure 4. 4 A typical XRD apparatus.

4.1.4 Geometry

The instrumentation commonly used with a conventional divergent beam sources is Bragg-Brentano parafocusing geometry [133, 139]. Figure 4.5 illustrates the Bragg-Brentano focussing geometry of a typical diffractometer. The source, sample and receiving slit lie within a focusing circle, which has a radius dependent on θ. On irradiation, coherently scattered X-rays from the sample then converge on a receiving slit adjacent to the detector [133, 139]. Lateral divergence is controlled by two sets of parallel plate vertical collimators (soller slits) placed between the source and the sample, and sample and scatter slit [133].

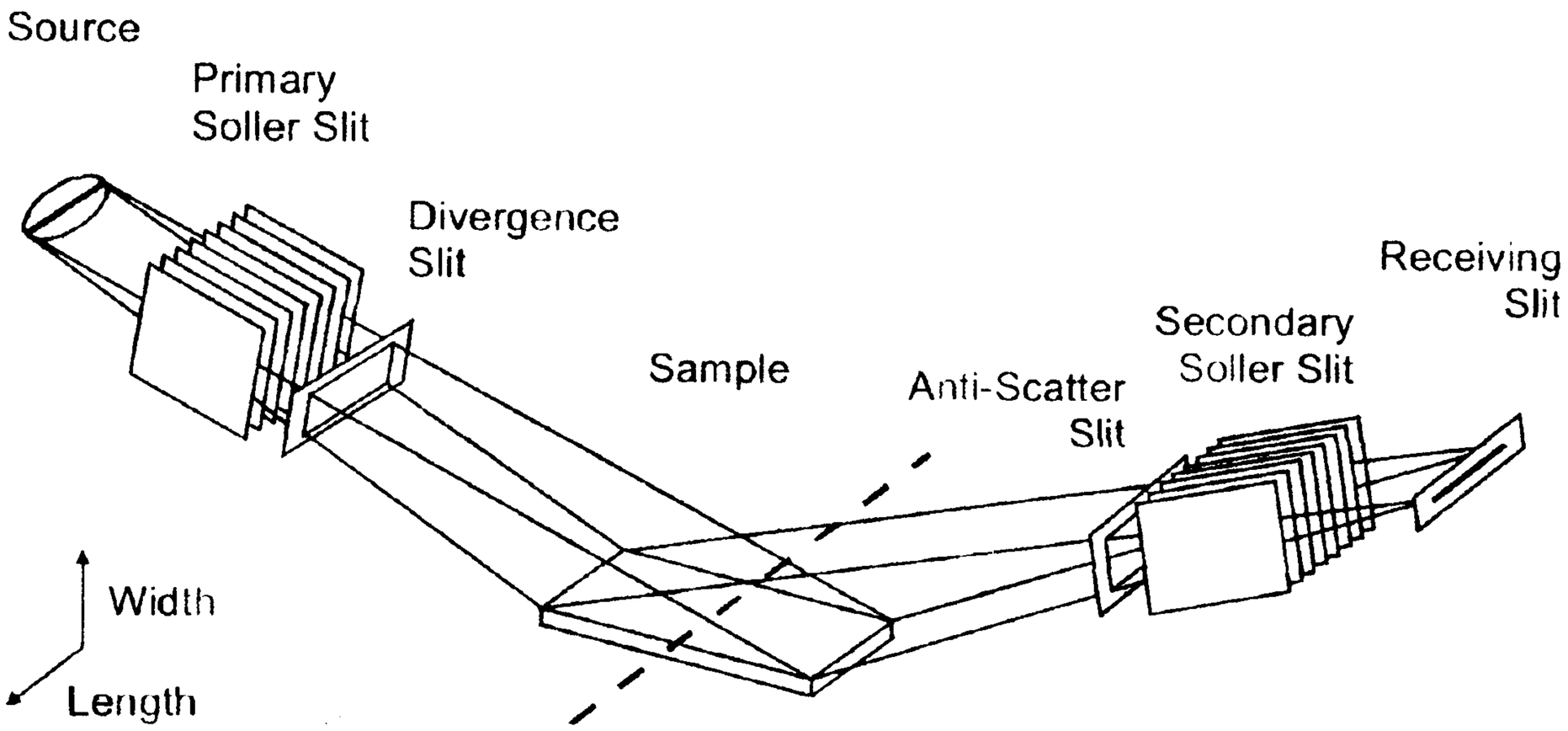

Figure 4. 5 Schematic of Bragg-Brentano geometry of a diffractometer [140].

4.1.5 Qualitative phase analysis

For samples in which crystals are randomly orientated such as apatite powders, the d-spacings and their relative intensities serves as a 'fingerprint' from which phases can be easily identified on comparison with the phases stored in the Powder Diffraction File (PDF). The PDF file is administered by the International Centre for Diffraction Data (ICDD) and contains over 70 000 inorganic and 20 000 organic phases [141-143].

4.1.6 Quantitative phase analysis

Quantitative phase analysis involves the determination of the proportion of different phases present in a multi-phase mixture [136]. The integrated intensity of Bragg reflections for a compound in a multi-phase powder diffraction pattern is related to the phase abundance in the mixture [144]. Diffraction measurements of phase abundance of apatites have previously been measured in numerous ways. Traditional methods require the use of standard reference data for each phase present in the mixture to be analysed [144]. The whole pattern analysis using a fundamental parameters approach is a technique which requires knowledge of the crystal structures of all phases present in the mixtures. In addition to quantitative phase analysis, a significant capability of the FPA is the refinement of lattice cell parameter to obtain precise lattice parameters [145].

4.1.6.1 Internal standard method

The internal standard method requires samples to be 'spiked' with known amounts of a standard to construct a calibration curve. The relationship between the diffraction line intensity of the sample under investigation, $I_{(hkl)\alpha}$, and the standard, $I_{(hkl)\beta}$, is given in equation 4.3. The constant k represents is derived from the plot of $I_{(hkl)\alpha} / I_{(hkl)\beta}$ versus X_α / X_β, and X_α where X_β represent the weight fraction of the sample and standard respectively [146].

$$\frac{I_{(hkl)\alpha}}{I_{(hkl)\beta}} = k \frac{X_\alpha}{X_\beta} \qquad (4.3)$$

The internal standard also allows the exact peak positions to be determined and any positional corrections to be made. However, the method has many limitations as it can only be used with very fine powder samples into which a crystalline standard of similar average crystallite size can be evenly mixed [146, 147]. Direct application of the internal standard method requires accurate preparation of standards to avoid errors at low concentration of standard and sample. In addition, care is needed in selection of standards as materials with simple and well-defined diffraction patterns are required [146]. The internal standard method is a destructive technique, which does not allow non-destructive structural characterisation of as-received plasma sprayed coatings

4.1.6.2 External standard methods

The external standard method provides a technique for calculating the weight fractions from the ratio of the integrated diffraction intensities of a pure sample of a phase and a mixture containing an unknown quantity of the phase. Equation 4.4 represents the working equation of the external standard method where W_α is the weight fraction; $I_{\alpha 0}$ and I_α represent the intensities of the pure sample and the sample under investigation respectively; and $(\mu/\rho)_m$ and $(\mu/\rho)_p$ the mass absorption coefficients of the mixture and the pure phase respectively [146, 147]:

$$W_\alpha = \frac{I_\alpha}{I_{\alpha 0}} x \frac{(\mu/\rho)_m}{(\mu/\rho)_p} \qquad (4.4)$$

The external standard method requires the knowledge of the mass absorption coefficient of the sample under investigation. This method is suitable for plasma

sprayed HAP coatings because the mass absorption coefficient of the pure HAP does not change regardless of phase transformations [147].

4.1.6.3 Whole pattern fitting with fundamental parameter approach (FPA)

The FPA permits computation and quantification of individual phases in a powder mix. Providing that all of the phases have been identified and their crystallographic structure information entered, there is no need for an internal, external standard or calibration process, to assay the phase mixture [144-146]. The FPA uses first principles of diffraction physics and the fundamental crystallographic parameters such as lattice parameters, oxidation states, atomic species and positions and occupancies in the unit cell. From the microstructural information, a diffraction powder pattern is calculated and its intensities are compared with the intensities obtained from XRD analysis of the powder mix. The difference in intensity is minimised by a least-squares refinement process:

$$Q_y = \sum_i W_i \left(Y_{i(calc)} - Y_{i(obs)} \right)^2 \qquad (4.5)$$

where Q_y is the intensity difference; Y_i is the intensity at the i-th position of 2θ ; and W_i is the inverse of Y_i [144, 145, 148, 149]. The iterative refinements start with a structural model whose scattering behaviour can be described by the structure factor, $F_{(hkl)}$, in equation 4.6:

$$F_{(hkl)} = \sum_j N_j f_j \exp\left[2\pi i(hx_j + ky_j + lz_{i)}\right] \exp\left[-B_j \sin^2\theta / \lambda^2\right] \qquad (4.6)$$

where N_j is the site occupancy factor of the j-th atom; f_j is the scattering factor of the j-th atom; h, k and l are the Miller indices; x_j, y_j, and z_j are the fractional atomic coordinates of the j-th atom; B_j is the isotropic temperature factor ; θ is the Bragg angle; and λ is the wavelength of radiation used [145, 149].

The calculated intensity $Y_{i\,(calc)}$, which comprises all hkl reflections, is based on the structural model as well as physical and instrument dependent parameters as shown in equation 4.7:

$$Y_{i(calc)} = S\sum_{hkl} L_{hkl} \mid F_{hkl} \mid^2 \phi\left(2\theta_i - 2\theta_{hkl}\right) P_{hkl} A + Y_{i-b} \quad (4.7)$$

where S is the scale factor; L represents the combined Lorentz, polarisation and multiplicity factor; ϕ is the reflection profile function; $P_{(hkl)}$ is the preferred orientation function; A is the absorption factor for the sample and instrument used; and $Y_{i\text{-}b}$ is the background intensity for the i-th data point [145, 149, 150]. The background, line shape, instrument-specific parameters and lattice parameter are also fitted and refined in the FPA analysis [145, 149].

The weight fraction of a phase, p, can be determined by equation 4.8:

$$W_p = \frac{S_p\left(SMV\right)_p}{\sum_{i=1}^{n} S_i\left(ZMV\right)_i} \quad (4.8)$$

where W_p is the weight fraction of the phase, p, in a mixture of n phases; S_p is the scale factors for phase p ; M is the mass of the formula unit; V is the unit cell volume; Z is the number of formula units per unit cell [145].

The FPA has many advantages over the internal and external methods because overlapped diffraction lines and patterns can be analysed. Furthermore, the usage of a whole pattern algorithm for each phase rather than a few discrete lines ensures that all lines for each phase are considered [144, 146]. Using all reflections in a diffraction pattern also ensures that effects due to preferred orientation and non-linear detection systems are minimised. Failure to consider a phase in the data analysis will yield obvious discrepancies between the observed and the calculated data and hence reveal the presence of a minor phase [144].

Despite its advantages, the FPA can only be used if the diffraction data is of high quality with few overlapping peaks. In addition, all of the phases in the materials being analysed must be identified and their structures known.

The FPA is useful for the analysis of apatite coatings by virtue of the fact that the coatings often contain extraneous phases that may affect the *in vivo* performance (chapter 3). The literature shows that quantification of the ACP content in apatite coatings using the FPA has not been successful. Quantification of ACP in apatite coatings is discussed further in chapter 5.

4.1.7 Line broadening analysis

The broadening of diffraction reflections occurs for two main reasons: microstructural properties of the material being investigated and instrument related effects. The microstructural properties can be divided into diffraction-order-independent (size) and diffraction-order-dependent (non-uniform strain or microstrain) variables [151]. The crystallites are the regions of the specimen diffracting X-rays coherently and independently, whereas the strain component is due to the non-uniform displacement of the atoms with respect to their reference position in a 'perfect' lattice [152]. Common lattice imperfections such as dislocations, as well as strain, can cause diffraction line broadening, but it is difficult to differentiate between the various structural imperfections by analysis of line broadening alone.

Microstructure is an important consideration in the design of apatite coatings because changes in microstructural properties have been reported (chapter 3) to affect both the structural and *in vitro* properties (discussed in chapter 5).

In the last five decades many elaborate, but in some cases conflicting, strain-size analyses have been devised that extract information about crystallite size and structural imperfections from diffraction line broadening [151, 153, 154]. Instrumental related contributions from radiation wavelength dispersion and instrument misalignment can cause diffraction line broadening. Therefore, accurate line size-strain analyses depend on the correction for instrument effects and the consideration of peak shape [151]. A methodology for the modelling and correction of instrument related factors using standards commonly used for analysis of apatites is

described further in chapter six. Two approaches for size-strain analysis of apatites are the integral-breadth methods and the Fourier methods [151, 152].

4.1.7.1 Integral breadth methods

The Williamson-Hall (W-H) method [155] is a semi-quantative method that allows for the separation of the crystallite size and strain components of line broadening. The method deconvolutes size and strain broadening by investigating the diffraction maxima widths as a function of 2θ. The Scherrer equation (equation 4.9) explains diffraction line broadening with relation to incident beam divergence which makes it possible to satisfy the Bragg condition for non-adjacent diffraction planes [156].

$$\beta_\tau = \frac{k\lambda}{\tau \cos \theta_{hkl}} \qquad (4.9)$$

where β_τ is the integral breadth (broadening) of a Bragg reflection, λ is the x-ray wavelength, k is a constant depending on crystal habit, τ is the a mean of the column lengths of the coherent scattering region normal to the reflecting planes (average crystallite size) and θ_{hkl} is a Bragg angle [152, 156, 157]. If broadening was due to finite crystallite size alone, then the β_τ would be independent of diffraction angle. In reality, the situation is different due to instrument broadening and strain-induced broadening [157]. The Wilson formula (equation 4.10) shows how diffraction line broadening is correlated to Bragg angle where ε is microstrain and β_ε is strain-induced broadening [154, 157, 158].

$$\beta_\varepsilon = 4\, \varepsilon \tan \theta_{hkl} \qquad (4.10)$$

For a Lorentzian peak profile, equations 4.9 and 4.10 can be derived to form equation 4.11 where β is the total line broadening:

$$\beta \cos \theta_{hkl} = \lambda/\tau + 4\,\varepsilon \sin \theta_{hkl} \qquad (4.11)$$

This is due to the fact that for a Lorentzian profile the contributions of β are additive as shown in equation 4.12 where β_{total} is integral breadth from the structural profile, β_ε is microstrain broadening and β_τ is size broadening [155]:

$$\beta_{total} = \beta_\varepsilon + \beta_\tau \qquad (4.12)$$

A W-H plot can be constructed with $\beta \cos \theta_{hkl}$ being plotted on the y-axis and 4 sin θ_{hkl} being plotted on the x-axis (in radians). If a linear fit to the data points is achieved, the average crystallite size can be obtained from the y-intercept and the average strain can be obtained from the gradient of the fit [157]. In addition, valuable information regarding the lattice direction dependency can be obtained [158].

One main limitation of the W-H method is that it assumes that it is possible to fit an analytical profile to the data even with overlapping peaks. Therefore, W-H plots only give approximate values when broadening has both size and strain dependent contribution. In addition, it is not possible to analyze solids or powders with large crystallite sizes (>2μm) with this method [131].

The W-H method is suitable for the preliminary investigation of changes in microstrain and crystallite sizes of apatite coatings used in orthopaedics as demonstrated by Roome *et al* [159, 160]. The crystallite sizes of commonly fabricated apatite coatings have been reported to be ≤ 2μm [131, 159, 160]

4.1.7.2 Fourier Methods

The Warren-Averbach (W-A) method employs a deconvolution Fourier-transform of the measured diffraction maxima and instrument broadening for the determination of the 'pure' physical line profile. The deconvolution is followed by further Fourier analysis for the evaluation of lattice imperfection [153, 156, 161]. The Fourier analysis assumes that the Fourier coefficients for the physical line profile are the products of the size and strain coefficients [153].

The W-A method is advantageous as it enables the separation of crystallite size from strain, although it considers each diffraction maxima individually and does not take into account the crystallite shape [152]. Nevertheless crystallite size distribution can be obtained and it provides a length average size rather than a volume average size. In addition it is thought to be more accurate in the separation of the instrument and sample broadening effects. Despite these advantages, the W-A method is more time consuming than the W-H method and it is prone to error when peak overlap is significant or when strains do not follow a Gaussian distribution. This is potentially a problem because with the W-A method, only a few peaks in a diffraction pattern are analysed [151, 153].

4.1.7.3 Approximate Method

The Approximate method [162] can be used to obtain the full width half maxima, w, and integral breadth, β, from a structural profile of a crystalline sample. The method assumes that the measured profile *(h)* and its components, the instrumental profile *(g)* and structural profile *(f)* can be described as a Voigt profile. Since a Voigt function is a convolution of Cauchy functions and Gaussian functions, the integral breadth β_c and β_g of the Cauchy and Gaussian functions can be represented by equations 4.13 and 4.14 [162]:

$$\frac{\beta_c}{\beta} = 2.0207 - 0.4803\left(\frac{2w}{\beta}\right) - 1.7756\left(\frac{2w}{\beta}\right)^2 \tag{4.13}$$

$$\frac{\beta_g}{\beta} = 0.6420 + 1.4187\left(\frac{2w}{\beta} - \frac{2}{\pi}\right)^{\frac{1}{2}} - 2.2043\left(\frac{2w}{\beta}\right) + 1.8706\left(\frac{2w}{\beta}\right)^2 \tag{4.14}$$

$\beta_c^{\,f}$ and $\beta_g^{\,f}$ can be obtained from equations 4.15 and 4.16 [162]:

$$\beta_c{}^f = \beta_c{}^h - \beta_c{}^g \tag{4.15}$$

$$\left(\beta_g{}^f\right)^2 = \left(\beta_g{}^h\right)^2 - \left(\beta_g{}^g\right)^2 \tag{4.16}$$

The total integral breadth of the structural profile can be obtained from equation 4.17 [162]:

$$\frac{\beta_g{}^f}{\beta_f} = \frac{-b}{2} + 0.5\left(b^2+4\right)^{\frac{1}{2}} - 0.132b\exp\left(-1.228b\right) \qquad (4.17)$$

where $b = \frac{\beta_c{}^f}{\beta_f}$.

4.2 Scanning electron microscopy (SEM).

Scanning electron microscopy is one of the most versatile and widely used tools for examining the microstructure, morphology and topography of specimens (figures 4.6 and 4.7). In addition, of the techniques available for microstructural analysis of materials, SEM is amongst those that require minimal sample preparation [41, 142].

The electron microscope is a probe system that exploits the wave nature of rapidly moving electrons to obtain a large image of a small object [142, 163]. In conventional light microscopy, the resolution is limited by the finite wavelength of light. However, high-energy electrons can be associated with shorter wavelengths (de Broglie wavelengths) than light and hence the resolving power of an SEM is in the order of one thousand times greater than that of a conventional light microscope [142, 163, 164]. For currently available SEM instruments, a resolution of approximately 5nm is attainable [142]. Figure 4.8 shows a SEM micrograph of a typical PS coating.

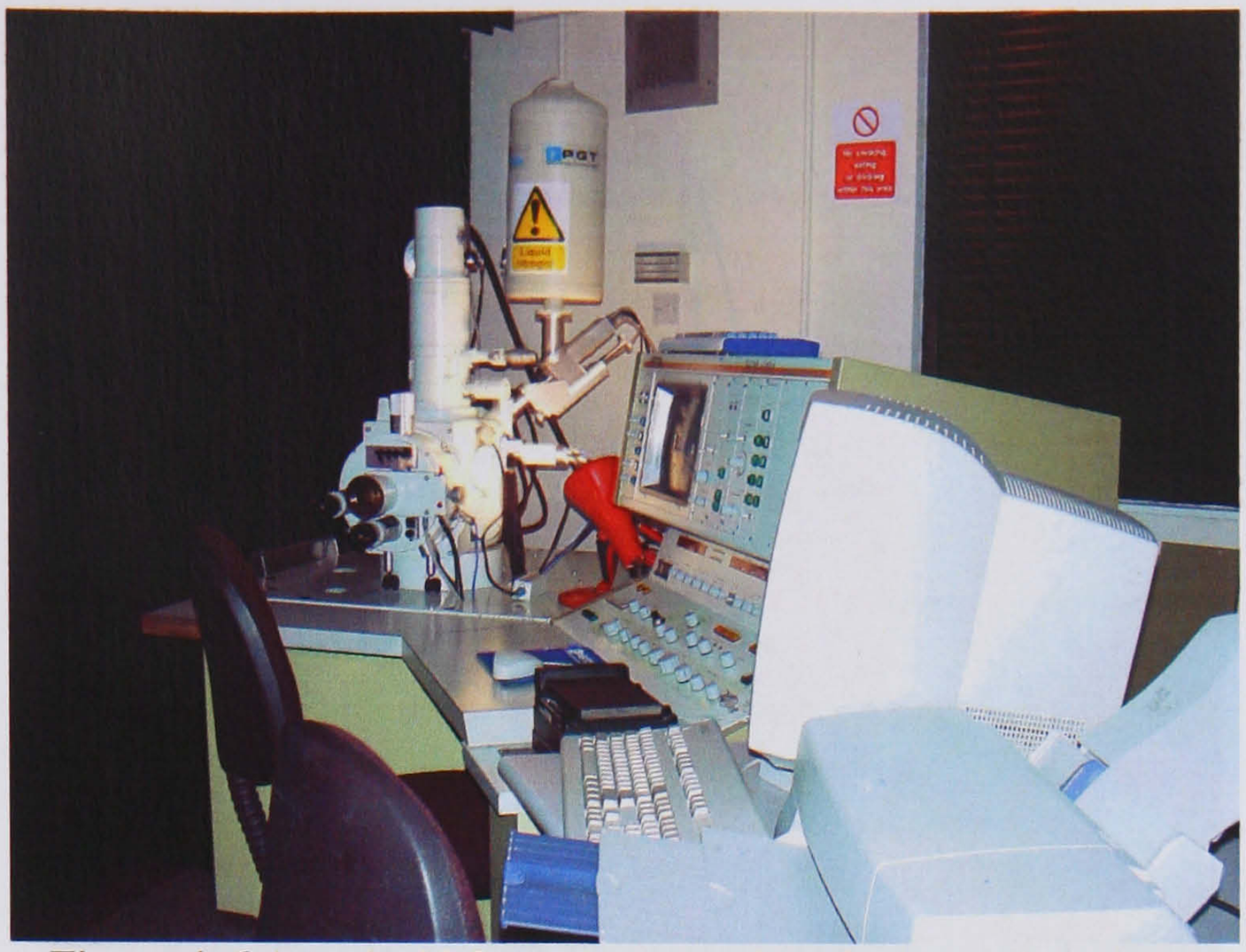

Figure 4. 6 A typical laboratory scanning electron microscope.

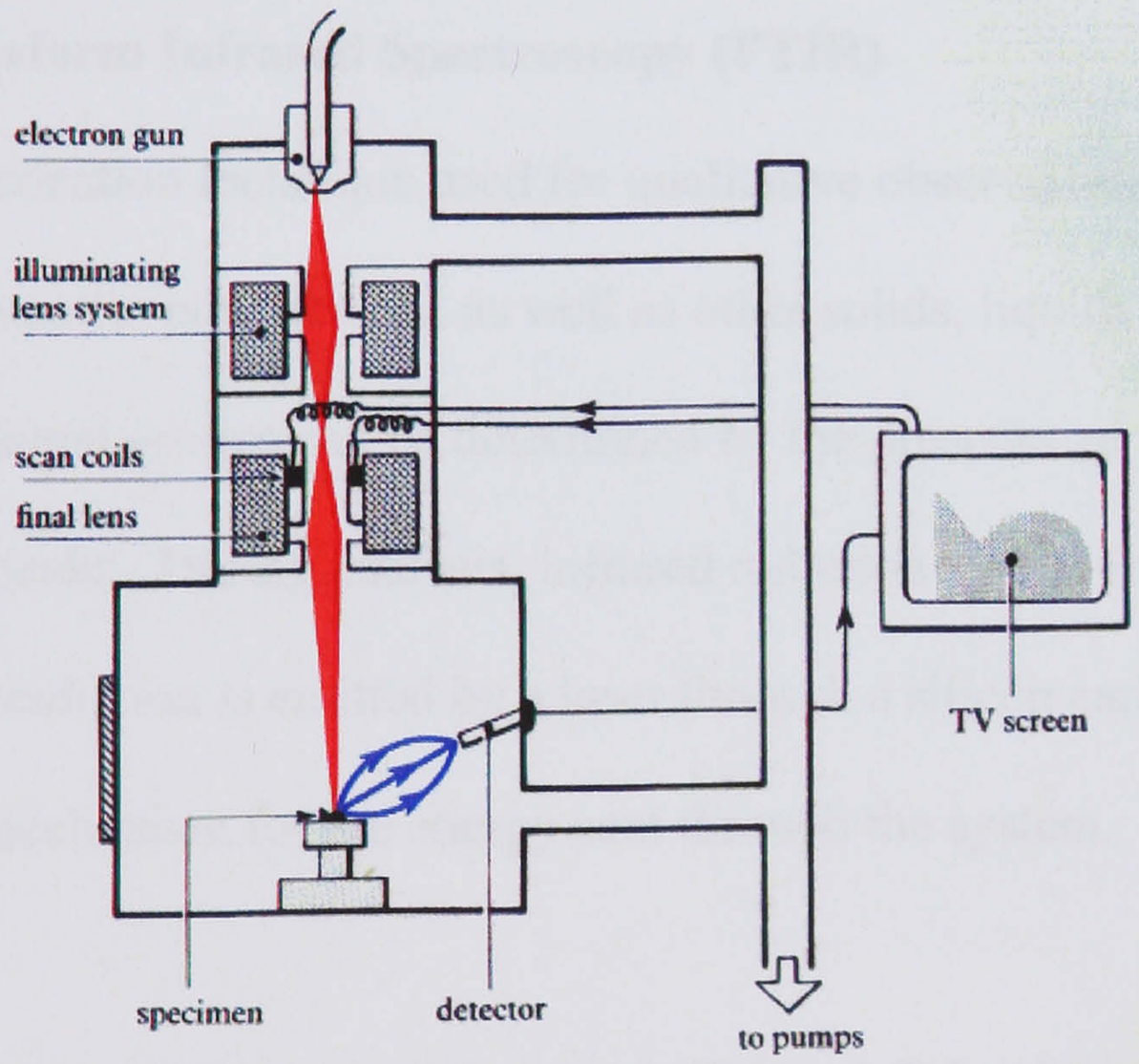

Figure 4. 7 Schematic of a typical two-scan lens SEM.

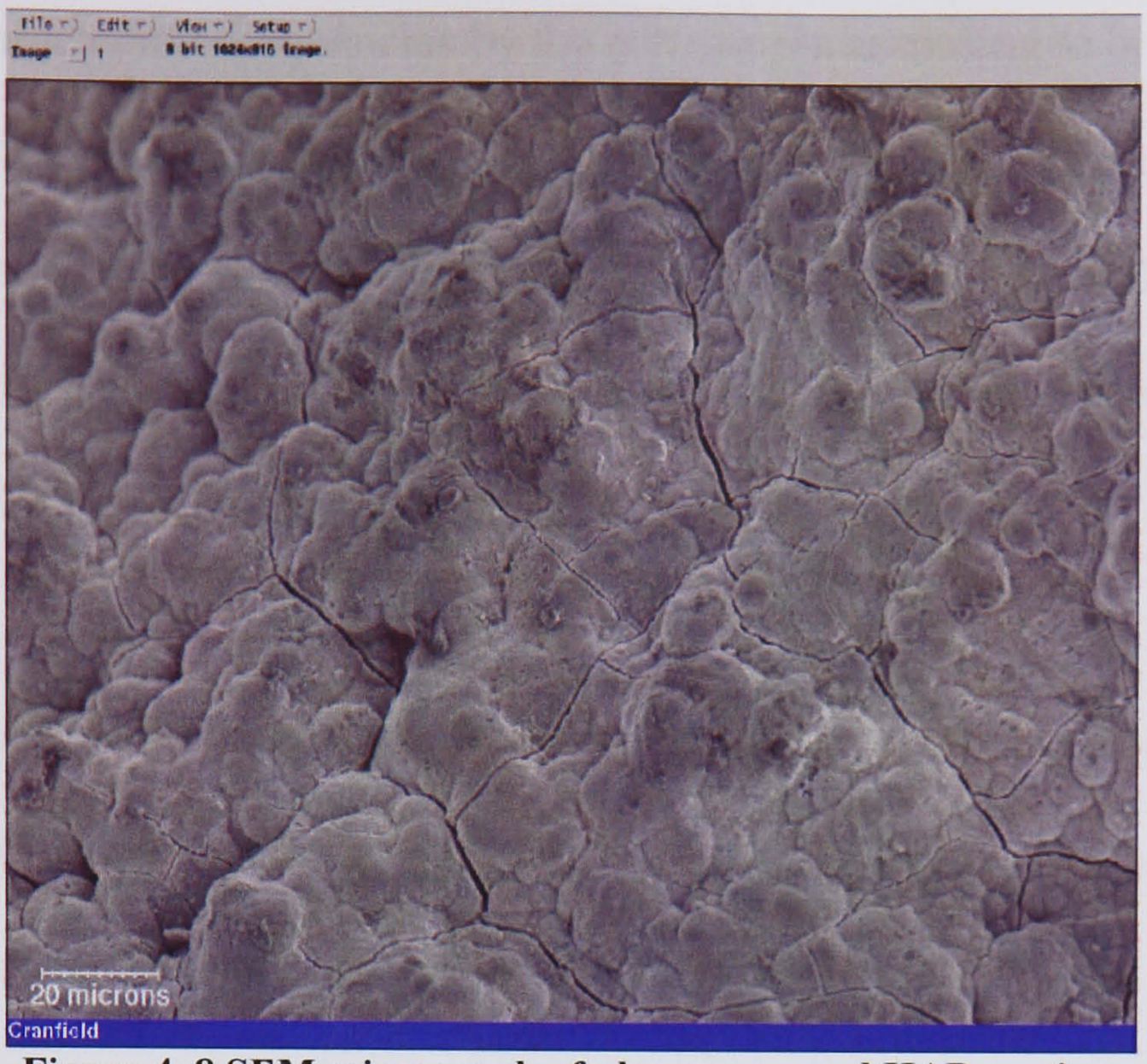

Figure 4. 8 SEM micrograph of plasma sprayed HAP coating.

4.3 Fourier Transform Infrared Spectroscopy (FTIR)

FTIR is a characterisation technique used for qualitative observations or quantitative measurements of apatite powders and as well as other solids, liquids and gases. The existence of functional groups can be determined by the presence of specific functional group peaks. During analysis, infrared radiation (IR) is channelled through a test sample. IR radiation is emitted by a laser through a silicon carbide orifice that acts as a control mechanism for the energy sent through the system.

The IR radiation is encoded by a interferometer (figure 4.9) by the creation of time-dependent, periodic intensity pattern. The movable mirror has the ability to adjust the distance between itself and the beam splitter. The intensity of the beam leaving the interferometer varies sinusoidally between a maximum intensity value (at 0° phase difference) and a minimum intensity (at 180° phase difference) value. The beam is then reflected into the sample compartment by a mirror. Some of the IR radiation is

absorbed at characteristic frequencies by the test sample according to bond strengths and chemical structure. Lattice vibrations leading to changes in dipole moments are caused by test sample absorption of IR radiation. FTIR analysis can only be carried out on test samples whose lattice vibration leads to change in dipole moments otherwise no absorption of IR radiation will occur.

The final measurement occurs when the transmitted beam enters the detector. The computer breaks down the interferogram into its sinusoidal components by Fourier transform methods. The sinusoidal component is then used to calculate the absorbance values across the spectrum. The absorbance data for a "blank" sample is subtracted from the absorbance data of a test-sample to minimize the effect of background interference and instrument related factors. The final absorbance data is then presented graphically ready for interpretation.

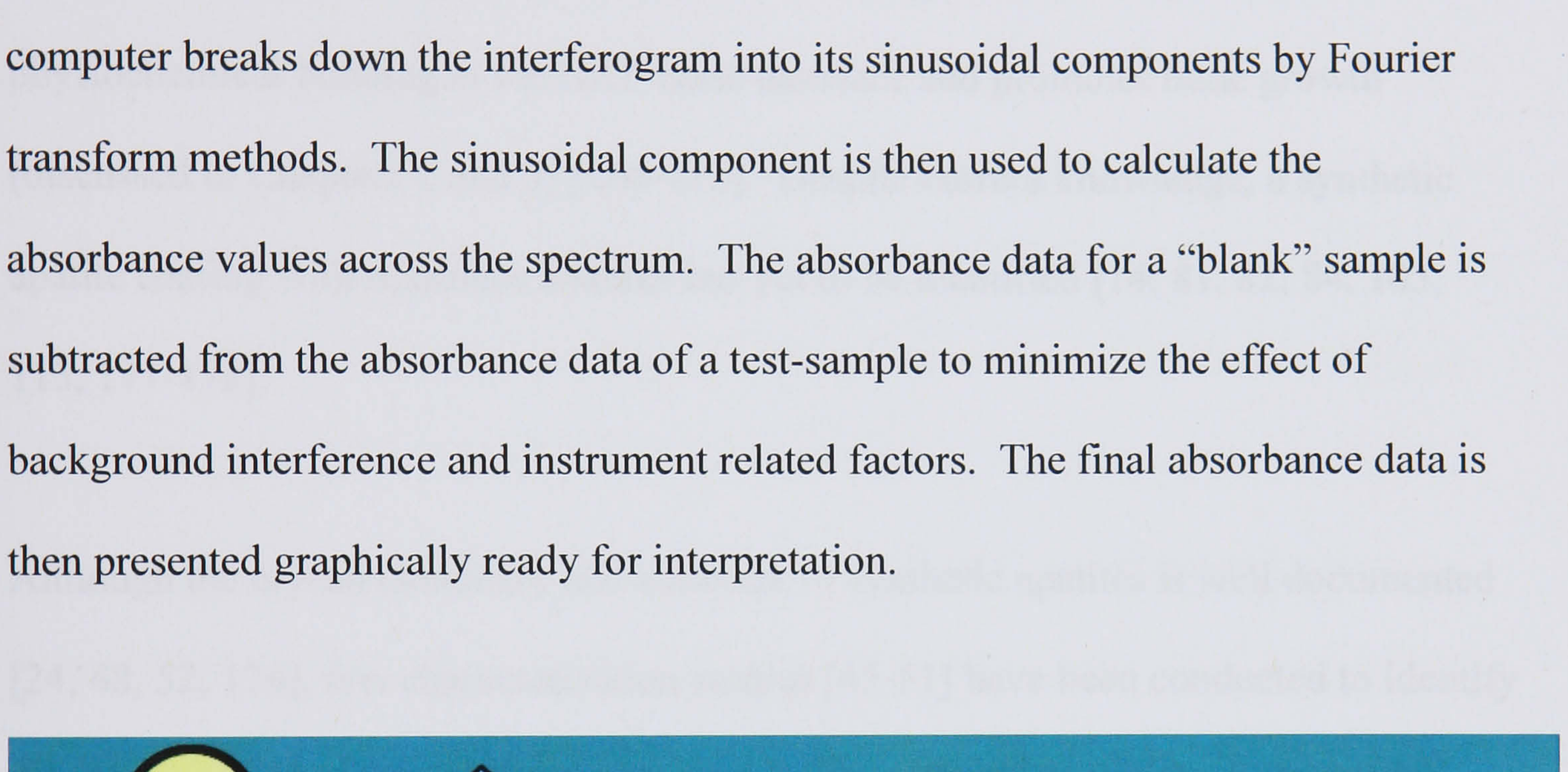

Figure 4. 9 A simplified diagram of an FTIR instrument [165].

5.0 Literature summary

The section consolidates work presented in chapters 1-4 and reviews the current literature on the use of hydroxyapatite (HAP) coatings on prostheses in particular hip joint components and ligaments.

5.1 Characterisation of apatite coatings

HAP is thought to be a particularly attractive coating material as it induces physiochemical bonding at the HAP-bone interface and promotes bone growth (discussed in Chapters 2 and 3) [166-170]. Despite current knowledge, a synthetic apatite coating with optimum features has yet to be identified [14, 81, 82, 84, 103, 113, 171-173].

Although the crystal chemistry and structure of synthetic apatites is well documented [24, 48, 52, 174], few characterization studies [45-51] have been conducted to identify the chemical and microstructural nature of HAP coatings deposited on prosthesis [131]. Recent studies [117, 175-180] have focused on the mechanical and bulk properties of apatite coatings. Others have carried out qualitative [120, 181-186] and quantitative analyses [187-189] of the crystalline phases present. Detailed chemical and structural characterisation of HAP coatings is imperative for (i) coating technology development, (ii) ensuring consistent material quality and (iii) assessing coating performance in *vivo* [190].

XRD has been used frequently in characterisation studies [82, 96, 183, 191-194] of HAP coatings but powder diffraction data patterns have not been frequently exploited to obtain information relating to microstructure such as phase composition, crystallite

size and shape, and lattice microstrain [159]. Microstructural properties may also affect actual physical and mechanical coating properties. This information is extractable from parameters such as unit cell dimensions, relative peak intensities, diffraction profiles and widths [131, 159]. Previously this information was difficult to extract with sufficient precision from diffraction data of complex mixtures containing non-crystalline phases [145, 159].

Kontoyannis *et al* [195] have developed a quantitative analytical methodology based on Raman spectroscopy for the compositional analysis of binary solid mixtures. The ratios of the relative intensities of the Raman bands corresponding to each component are used for the construction of calibration curves used for the quantitative analysis. Comparisons of this method with quantitative analysis of binary powders by internal standard methods showed that although the limit of detection was comparable (approximately 1 mol%), RS analysis offered the relative advantage of performing analyses without the need of grinding the samples, thus making it possible for the analysis of layered deposits of the minerals to be investigated [195].

The abovementioned phase quantification methods suffer from inadequacies, particularly at low concentration of non-crystalline phases. There are a number of factors limiting the accuracy of such analyses as a result of systematic errors (such as preferred orientation), random errors (counting statistics) and calibration errors. In addition, these methods are not accurate in cases where peaks overlap and where peak broadening occurs [196].

The use of whole pattern fitting methods such as Rietveld analysis (discussed in Chapter 4) could alleviate the problems associated with current methods of phase quantification of apatites [196]. Studies by Riello *et al* [197, 198] on glass-ceramic crystallisation processes have indicated that an 'ad-hoc' Rietveld analysis can be performed that includes modelling non-crystalline phases. Conventional approaches describe background intensity by means of an analytical function; however, the approach illustrated by Riello *et al* [197, 198] separates the main background components, giving a physical meaning to each of them. It is therefore possible to separate the single-phase contributions to the diffraction pattern, including the diffuse scattering from the crystalline phase. The amounts of crystalline and non-crystalline phases present in glass-ceramic materials can be measured, without the need of internal or external standards [197, 198]. Despite the theoretical justification [145, 197-199] for the 'standardless' approach, the method has yet to be validated with reference to known mixture of crystalline and amorphous calcium phosphates phases.

X-ray diffraction studies of HAP coatings using Rietveld analysis have investigated phase quantification of crystalline materials [108, 200, 201], unit cell contents [200], lattice parameters [23, 145, 200, 201] and sample-dependent contributions to line broadening (crystallite size and microstrain) [45, 51]. However, it is evident that further studies are needed, focusing on the phase quantification of HAP coatings containing ACP phases. Furthermore, characterisation studies have been limited to PS HAP coatings. In order to establish which deposition technique produces the more structurally superior coatings, comparative studies are essential.

5.2 *In vitro* behaviour of apatites

A fundamental parameter to be considered when HAP coatings are to be used for bone regeneration purposes is bioactivity. This parameter is related to the material's ability to induce the precipitation of a new carbonated apatite ''bone-like'' apatite, on the coating surface [15, 202, 203]. *In vitro*, partial dissolution of HAP coatings is initiated by a supersaturated biological fluid (with respect to HAP), causing the release of Ca^{2+}, HPO_4^{2-} and PO_4^{3-} ions and increasing the supersaturation of the environment with respect to HAP. The precipitation of the bone-like apatite results from the ions released in the partial dissolution of the HAP coating and from body fluids that contain ions such as Cl^-, CO_3^{2-} and Mg^{2+} [71, 105, 194].

The reactivity of HAP has two components: (i) physiological environment, and (ii) materials properties. Materials properties that affect the *in vivo* and *in vitro* behaviour of HAP are phase composition [14, 90, 99, 100, 204], lattice substitutions [15, 94, 99], crystallite size [99, 174, 194], particle size [99, 194], crystal imperfections [99, 174], porosity [99, 177, 194], surface roughness [14], coating thickness [14, 81, 82] and formation process [14, 81, 205].

Porosity and surface roughness of HAP coatings are critical because of their influence on the specific area in contact with the physiological medium and the physiochemical interactions at the HAP-bone interface. The porous structure of HAP essentially provides a framework for bone ingrowth into the matrix of the implant; hence an anchorage system is in place, which prevents implant loosening [99, 194]. High coating porosity and roughness increases dissolution rates *in vivo,* which may result in accelerated coating degradation, leading to delamination or fragmentation [177]. If

HAP particles remaining in the vicinity of the implant are too large, the immune system is unable to dissolve them by phagycytosis [206, 207]. In response, the local physiological pH drops in an attempt to dissolve the particles and hence rapid coating dissolution can result [14, 99].

Coating thickness affects both HAP resorption rates and mechanical properties. Coatings need to be thick enough to avoid complete dissolution by physiological fluids but sufficiently thin to avoid delamination and fatigue failure (discussed in Chapter 3). To achieve good adhesion, and avoid mechanical failure, an ideal PS coating would be between 50-250μm in thickness [81, 82]. Ideal coating dimensions for coatings produced by other fabrication methods are unknown at present.

Variations in process routes of HAP lead to differences in stoichiometry, morphology, density and microstructure [14, 99]. Low temperature synthesis and deposition of HAP produces well-crystallised, compositionally homogenous HAP [205]. High temperature methods of HAP formation lead to an increase in crystallite size through growth and reduction of the surface area [15, 97]. Sintered HAP is less soluble than biological apatite; this has been attributed to the fine crystallite size and substituted elements in biological apatite [15].

As discussed in Chapter 3, high temperature HAP deposition methods lead to the formation of ACP and metastable phases, thus increasing the solubility. This to some extent is of benefit *in vivo*, because ACP dissolution hastens fixation of implants with osseous tissue and promotes bone attachment by liberation of calcium ions and phosphate ions [14, 208]. Therefore, coatings containing ACP are of more benefit in

the early stages of bone ingrowth than a coating of 100% crystallinity [97, 209]. A higher content of ACP (>50wt%) could potentially cause disproportionate dissolution and as result compromise the reliability of coated implant [14, 85]. This would prove to be detrimental to the long-term survivability of an implant as the HAP-metal interface would come into direct contact with osseous tissue a short time after implantation [84]. Conversely, highly crystalline HAP surfaces have been reported [210] to inhibit osteoblast proliferation.

Stoichiometry has a significant influence on the physical properties of apatites. HAP lattice substitutions for carbonate [54-56, 174, 211] and strontium [212-214] increase solubility whilst substitutions for fluorine decrease solubility [174, 215, 216]. Carbonate substitution in HAP (bone-like apatite) precipitates causes a decrease in crystallite size and increase in lattice microstrain. As a result carbonated apatites are less stable than carbon-free analogues [174].

In summary, HAP coating can be degraded by six key mechanisms *in vivo*: (i) dissolution at neutral pH, (ii) osteoclastic resportion as part of normal bone remodelling, (iii) delamination due to mechanical inadequacies, (iv) abrasion due to lack of primary fixation [217], (v) lamellae cracking due to residual stresses, and (vi) preferential dissolution of ACP producing free particles that are subject to acid attack [33]. Several suggestions have been made in the literature of ideal HAP coating characteristics for optimum bioactivity, bone regeneration and fixation. Standards have been put in place for quality control purposes but it is evident that no single mechanical, microstructural or chemical property dominates in entirety.

Previous studies [218-222] have investigated the dissolution mechanisms of HAP with respect to thermodynamics and kinetics. Others [203, 223] have concentrated on morphological changes and changes in the ionic concentrations of the surrounding media. Comparative information [194, 209, 224] on the influence of microstructural (crystallite size and microstrain) and substituted elements (e.g. carbonate) on *in vitro* dissolution is scarce.

Recently, the *in vitro* formation of nanocrystalline apatite layers on crystalline HAP by immersion in SBF has been studied by XRD and X-ray photoelectron spectroscopy (XPS) [225]. A mechanism for the dissolution and subsequent precipitation of carbonated apatite was proposed based on ion exchange between the SBF and HAP. However, this work presented several curiosities including (i) a decrease in estimated HAP crystallite size with increasing immersion time, (ii) a poor fit of the scattering associated with the (002) Bragg maxima between experimental data and that calculated from a structural model and, (iii) lattice parameter changes that were interpreted as an ion exchange mechanism more commonly associated with apatites produced at high temperatures.

It has been proposed previously [171, 172, 190, 204, 225-227] that microstructural and chemical properties of coatings will change after different degrees of contact with physiological media, which will ultimately affect clinical performance. Detailed characterisation (as described in Section 5.1) of microstructural and chemical changes (and hence bioactivity) occurring in HAP coatings is lacking. HAP substituted with carbonate (<5%) is a potential candidate to be used as a bioprosthetic coating due to

its chemical similarity to bone apatite. Hence, there is a rationale for examining its *in vitro* performance.

5.3 Polymeric materials for enhanced bioactivity and fixation

The high occurrence of native anterior cruciate ligament (ACL) failures and the inadequacies of autografts, allografts and xenografts (chapter 1) have prompted much interest in synthetic grafts and fixation devices [6, 7, 9-12, 228]. The requirements of a graft are extensive. Grafts must have sufficient strength and stiffness to match the compliance of a native ligament. Durability and fatigue resistance are important considerations; as grafts are required to withstand high tensile loads for millions of cycles without wear. A graft must be biocompatible with the host tissue without rejection [6, 7, 9, 11].

Poly- (ethylene terepthalate) [PET] is one of the most common organic polymers used primarily as graft augmentation devices and in some clinical cases as synthetic grafts (appendix 1) [9, 11, 229, 230]. Increasingly, woven PET fibres are attractive candidates due to their strength and biocompatibility as demonstrated by their extensive use in arterial grafts [9, 229, 231]. In addition PET avoids the risk of tissue rejection, infection and disease associated with soft tissue-derived grafts.

Although physicians dispute the superiority of one graft type compared with another, current literature fails to show many significant differences in the clinical performances of grafts [9, 11, 228, 230, 232]. The general consensus is that the clinical success of graft constructs is dependent on a firm graft-bone interface in the bone tunnels and hence the creation of secure fixation (chapter 1). Paradoxically, in

the early post-operative period graft fixation to surrounding bone tissue is weak [9, 13, 229, 230]. This is due to the fact that bone plugs bond to bone tunnels more rapidly than the graft, hence the graft-bone interface is weak [9, 228].

Current protocols for post-operative rehabilitation emphasize the immediate return of the patient's full range of motion [9, 11]. Recent studies [9, 18] have indicated that due to rehabilitation and daily ambulation stresses, longitudinal motion of the graft within the bone tunnel can occur. Excessive motion of graft constructs impairs graft incorporation with the bony surroundings and may cause bone tunnel enlargement and lead to failure. Excessive bone tunnel enlargement complicates revision surgery because of bone loss [9].

Polymeric grafts or graft augmentation devices coated with bone analogues (such as HAP) may secure immediate fixation through the rapid formation of osseous tissue as described in section 3.4.3. Previously studies by Kokubo *et al* [112] and Tanahashi *et al* [110] have shown that PET tape can be coated with apatite by means of biomimetic processes. The resultant coatings were dense and of a uniform thickness with a bond strength of 3.48 MPa. Moreover, animal studies [110, 233] have revealed that apatite coated polymers have been successful as artificial trachea. However, as discussed in chapter 3, biomimetic process coating methods are time-consuming, despite having the capability of a great degree of control over stoichiometry. The spontaneous precipitation of HAP via a wet-chemical technique may be an alternative, provided that adequate surface wettability of PET is achieved. Detailed coating characterization, mechanical tests and cell culture studies are essential to assess the potential *in vivo* performance of PET tape coated with HAP.

6.0 Methods and Materials

In this chapter, a novel methodology of non-destructive phase quantification of multi-phase apatite coatings is introduced. A novel method of electrodeposition (ED) of HAP coatings has been developed in conjunction with Biomet-Merck UK Ltd. For the first time, coatings produced by the novel ED technique and plasma spraying (PS) have been fully characterised and their coating characteristics and dissolution behaviour compared.

Solubility and dissolution studies have been carried out to ascertain whether microstructural (crystallite size or microstrain) or chemical properties have the dominant effect on the solubility and *in vitro* dissolution.

A novel methodology for producing HAP coatings on polyester orthopaedic tape (for potential use in anterior cruciate ligament reconstruction) is introduced. Coatings have been produced using this novel technique and have been assessed for biocompatibility with osteoblast cells using a conventional cell model.

6.1 Formation and characterisation of apatites

6.1.1 Formation and structural characterisation of apatite coatings

The structural characterisation studies carried out in this section were undertaken at the X-ray diffraction laboratories at Cranfield University (Shrivenham). These laboratories are equipped with a Philips PW1830 diffractometer. The analytical software available for interpretation of diffraction data was Crystallographica Search Match (CSM: Oxford Cryosystems), TOPAS (Bruker–AXS), Profile (Bruker-AXS) and Line profile analysis (LPA: Philips) software.

6.1.1.1 Novel method of non-destructive phase quantification

This novel approach assumes that the incident beam from a CuKα source is constituted by the characteristic CuKα doublet shown by previous authors [198, 234]. Therefore the global integrated intensities from XRD data can be divided into four components: Compton scattering, air scattering, the diffuse scattering caused by the thermal disorder of atoms in the crystalline phase, and disordered scattering due to the amorphous phase (see chapter 4) [198]. Compton scattering and air scattering (ignoring fluorescence) account for the background intensity of a diffraction pattern. In studies of Y_2O_3 and amorphous silica, Riello *et al* [198, 234] have shown that once the contribution of the 'background' is subtracted from the diffraction data, the global intensity is due to both the crystalline and amorphous phases.

In order to separate the disordered scattering due to the amorphous phase and the scattering due to the crystalline phase, all incoherent scattering (Compton scattering and air scattering) has to be described. In this investigation, incoherent scatter was determined empirically through XRD analysis of an uncoated titanium test coupon (figure 6.1b). This is in contrast to traditional methods, which describe incoherent scattering by means of arbitrary analytical functions. The rationale for the use of a titanium substrate was that titanium test coupons are the substrate of the HAP coatings to be characterised in this investigative work. In addition it is important that scatter due to the amphorous phase was not misinterpreted as incoherent scatter, therefore HAP coatings on Ti substrates could not be used. Furthermore, Ti has few diffraction peaks hence making it easier to interpret incoherent scatter.

In all diffraction analysis described in this chapter, all data was collected by a conventional powder X-ray diffractometer operating at 40kV and 30mA. Data were collected in a 10^{o}-100^{o} 2θ range with a step time of 10 seconds and a step size of 0.02^{o} using a Philips PW1830 diffractometer fitted with a diffracted beam monochromator to produce diffractograms from CuKα wavelengths. A divergence slit of 1^{o}, a receiving slit of 0.1mm and an anti-scatter slit of 1^{o} were used for diffraction analysis. A large data range and step time were used, as high quality data is a prerequisite for accurate whole pattern diffraction analysis.

Incoherent scattering determined above was described by an analytical function. Several analytical functions were tested but in this case a 1^{st} order Chebychev polynomial adequately described the incoherent scatter. The choice of analytical function used to describe the 'background' is an influential parameter in the accurate determination of incoherent scattering and hence phase quantification.

TOPAS (Bruker–AXS) software capable of a whole pattern fitting approach using fundamental parameters was used to determine disordered scattering. The disordered scattering due to the amorphous phase was determined empirically using structural and atomic models fixed to that of stoichiometric HAP acquired from the Inorganic Crystal Structural Database [235] (see appendix B) but with a crystallite size of ~5 Å in magnitude. The atomic model parameters (i.e. atomic positions, thermal parameters and occupancies) were fixed throughout to that of crystalline HAP. This effectively fixed the absorption coefficient of the phase; the effect of this is discussed in chapter 8.

The instrument parameters were obtained from the manufacturer and each parameter was refined as shown in Appendix B.

The diffraction pattern obtained was significantly broadened with overlapped diffraction maxima, hence giving the appearance of that from an amorphous material. These parameter values were then refined against diffraction data (collected as described above) from laboratory ACP phase (QMW, UK). This was done in order to provide accurate and precise values of lattice parameters and apparent crystallite size. This is in contrast to work carried out by Keller *et al* [145] where only a poor fit could be obtained as the lattice parameters were fixed to stoichiometric HAP.

The novel method of non-destructive phase quantification described above was then validated and assessed for accuracy with reference to known mixtures of HAP and ACP phases shown in table 6.1 [1]. TOPAS (Bruker AXS) software was used for whole pattern fitting of the diffraction data obtained from the powder mixtures in table 6.1. The scale factors (enabling the determination of the relative phase composition, wt%), lattice parameters, and peak shapes were refined for all crystalline phases present. All of the parameter's values corresponding to the empirical structural model of the ACP phase (see Appendix B) were fixed to the values determined above (see Appendix B). After refinement the difference between calculated and observed data was inspected to ensure a good fit and hence accurate phase compositions. In all refinements conducted in this work, a 'goodness of fit' (R_{wp}) of <12% was deemed acceptable. The results are presented in section 7.1.

[1] Kindly prepared by Dr. Karen Hang, Queen Mary, University of London.

HAP	ACP	α-$Ca_3(PO_4)_2$	β-$Ca_3(PO_4)_2$
100	0	0	0
80	20	0	0
60	40	0	0
40	60	0	0
92.5	0	7.5	0
97.5	0	2.5	0
92.5	0	0	7.5
97.5	0	0	2.5

Table 6. 1 Reference powders mixtures.

6.1.1.2 Apatite coating fabrication

The HAP coatings examined in this experimental work were supported on Ti-6Al-4V alloy rectangular test coupons (~1cm X 3cm X 0.5cm) for the electrodeposited (ED) samples (figure 6.2) and surface roughened Ti-6Al-4V alloy discs (diameter ~2cm) for the plasma sprayed (PS) samples (figure 6.1b). Before coating, each substrate was cleaned in ethanol in an ultrasonic bath, rinsed off with deionised water, and dried by means of a stream of air. This was done to remove any surface debris or grease that would affect the adhesion of the coatings to the metallic substrate.

The PS coatings were produced at Biomet-Merck UK Ltd fabrication plant (Swindon, UK). The PS process consisted of high velocity and temperature spraying of a highly crystalline HAP stock powder (>98%) in air with a Plasma-Technic Type F4-MB plasma gun onto surface roughened substrates. The metallic substrate had been surfaced roughening by shot blasting in order to improve mechanical interlocking during the coating process. The primary and secondary gases used were argon and nitrogen. The precise operating parameters remain intellectual property of Biomet-Merck UK Limited.

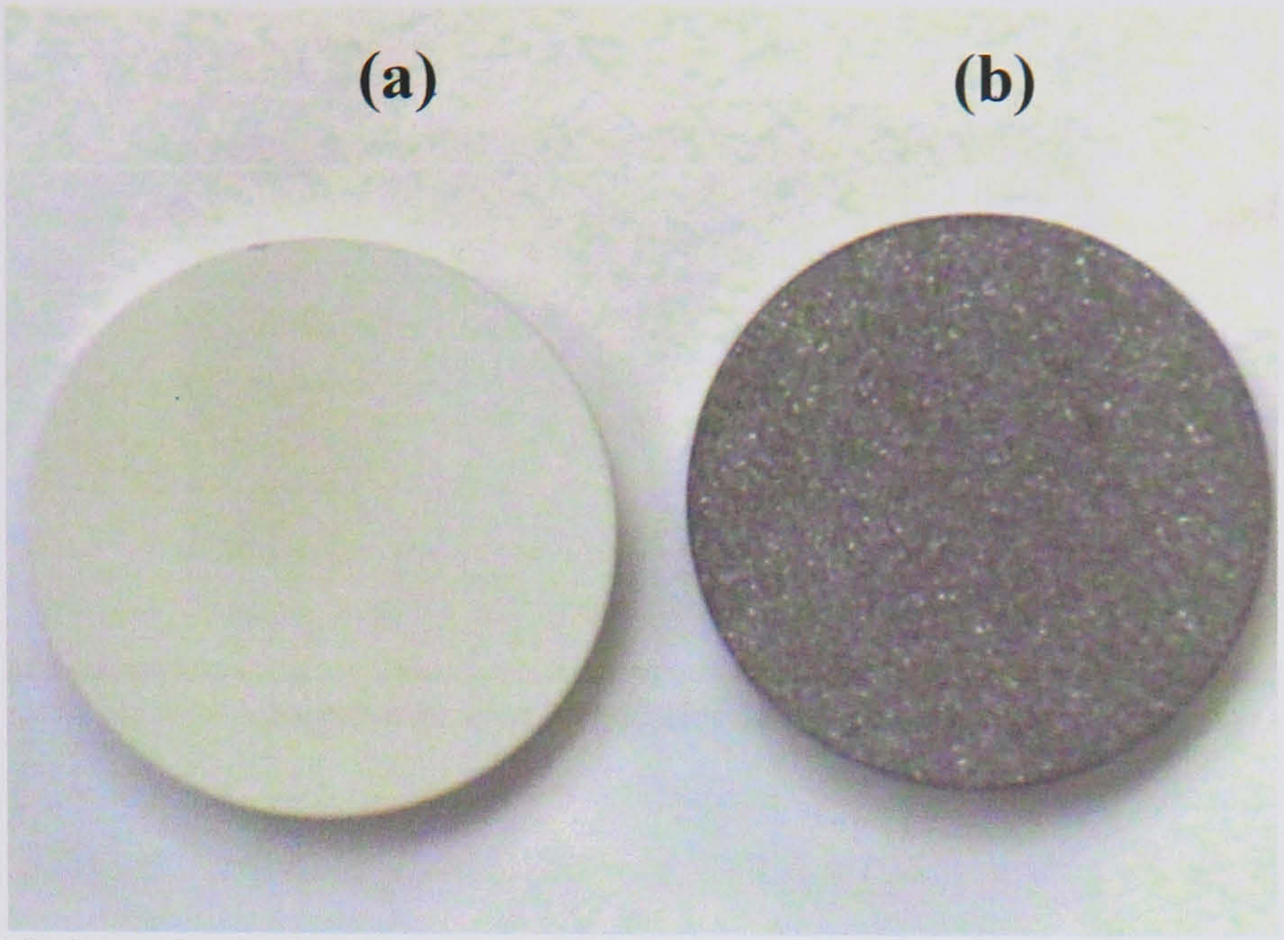

Figure 6. 1 (a) A typical plasma sprayed sample and (b) an uncoated titanium sample.

Electrodeposition of hydroxyapatite (HAP) coatings was undertaken at Biomet-Merck Europe fabrication plant (Darmstadt, Germany). The ED coatings were formed by an electrochemically assisted process within a purpose built chemical bath, using a metallic electrode and an aqueous electrolyte consisting of calcium and phosphate ions. The electrolyte liquid was prepared by dissolving 2.455g of $CaCl_2.2H_2O$ and 1.15g $NH_4H_2PO_4$ in 5 litres of deionised water to produce a solution with a Ca/P ratio of 1.67. The temperature of the electrolyte was controlled by means of a thermostat and fixed to 37°C. The pH was adjusted to 6.45 using an NH_4OH solution. The Ti substrate was polarised as the cathode and platinum gauze electrodes employed as the anode. The coating process consisted of 10 cycles, each cycle comprising of cathodic polarisation for 5 minutes with a constant current of 63 mA, rinsing for 1 minute in deionised water and then drying for 5 minutes with a fan. Specific details of the fabrication process remain intellectual property of Biomet-Merck Europe.

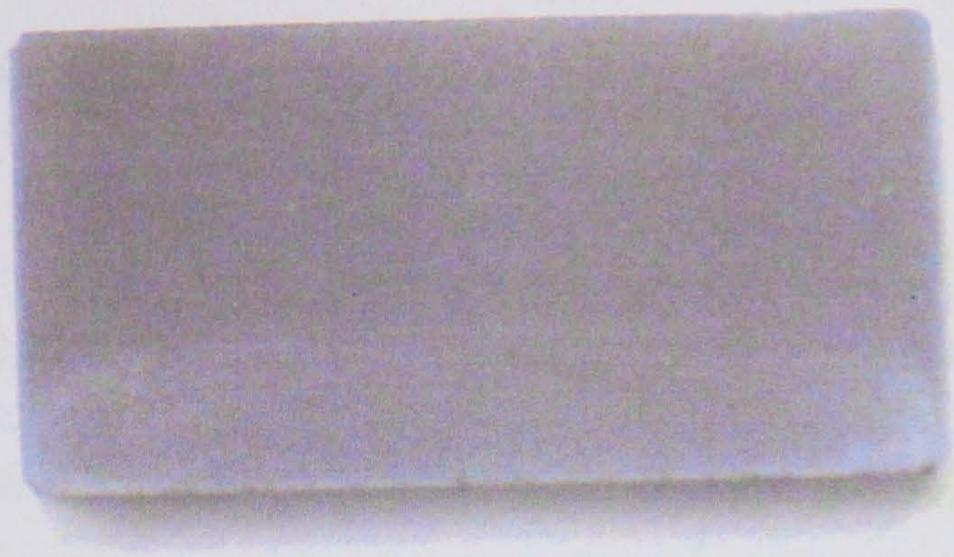

Figure 6. 2 A typical ED test sample.

6.1.1.3 Diffraction analysis

500 PS samples (and corresponding feed powder) and 40 ED samples were analysed by XRD as described in section 6.1.1.1. Crystalline phase identification was performed with reference to the database supplied by the International Centre for Diffraction Data (ICDD).

Quantitative phase analysis of the diffraction data obtained from the coatings (PS and ED) was carried out as described in section 6.1.1.1. An advantage of this approach is that preferred orientation could also be included and accounted for. In this investigation, preferred orientation was best described by a 4^{th} order spherical harmonics function.

Due to the thin nature of the HAP coatings produced by ED coatings, the dominant substrate maxima (Ti) were included as independent analytical peaks without reference to any structural model but were refined simultaneously with the crystalline and ACP phases. This effectively excluded the substrate from estimates of coating phase composition. To assess the reliability of the novel method of phase

quantification, repeated measurements were made of a PS sample. The phase composition and lattice parameters are presented in section 7.1.

In order to estimate the changes in microstructural and chemical properties of the PS coatings with depth, the PS coatings produced in section 6.1.1.2 were compared to PS coatings from a stalled manufacturing cycle [2]. The thickness of the partial coating was ~10μm and represents the material near to the coating-substrate interface as described by Rogers *et al* [131]. The results are presented in chapter 7.

6.1.1.4 Microstructural analyses

For qualitative microstructural analysis of the diffraction data obtained in section 6.1.1.3, Williamson-Hall plots were exploited as described in chapter 4. This technique offers preliminary assessments of crystallite size and microstrain contributions to the Bragg peak broadening.

To obtain peak widths, a pseudo-Voigt analytical profile ($K\alpha_1$ & $K\alpha_2$) was fitted to each of the observed diffraction maxima using profile software. Fitting quality was assessed using a chi-squared parameter and those of low quality excluded from further analyses, as were adjacent, overlapping peaks. Only the $K\alpha_1$ component was subsequently employed in further analyses. This fitting procedure provided independent estimates of peak position and integral breadth (β). Peak broadening attributable to the specimen microstructure was estimated using equation 6.1 [158].

[2] Kindly produced by Biomet-Merck UK Limited and analyzed by Professor Keith Rogers, Centre for Materials Science & Engineering, Cranfield University.

$$\beta_f = (\beta_t^2 - \beta_h^2)^{1/2} \quad (6.1)$$

Where the subscripts f, t and h refer to the specimen, observed and instrumental profiles respectively. A correction for instrumental peak broadening (IRF) in the observed data was made using of a Silicon standard reference material (NIST: NBS640C) and Levenberg non-linear regression using DataFit software. The resulting W-H plots are presented in section 7.1.

Quantitative microstructural analysis was conducted by analysis of the (002) reflection using LPA software using the approximate method (chapter 4). This in effect assumed that peak broadening was uniform in all crystallographic directions. Diffraction data from the highly crystalline feed powder (6.1.1.3) was used as standard in each case. Crystallite sizes and lattice microstrain was determined for each data set. The results are presented in chapter 7.1.

6.1.1.5 Chemical analysis

X-ray diffraction studies were complemented by a Fourier Transform Infrared spectroscopy (FTIR: VECTOR FT-IR/NIR Spectrometer with OPUS 3.1 software) study. This was carried out in order to investigate the differences in chemical nature of the test samples. The test samples were analysed in the $4000cm^{-1} - 400cm^{-1}$ region, at day 0, 7, 14 and 21 of immersion. The range used for FTIR analysis is where the characteristic absorption bands for HAP lie [236]. Spectral resolution was $2cm^{-1}$ and the number of scans used was 64, employed to ensure good data quality.

Potassium bromide (KBr) discs used for the FTIR analysis were prepared with coatings scraped from each test sample. 0.3g of KBr was mixed with 0.01g of test sample and mixed in a pestle and mortar to produce a homogeneous powder. 0.055g of the resultant powder was placed into a die and compressed with a pressure of 10 tonnes per square inch. The disk produced was then placed into the analysis chamber for analysis.

Individual band intensities and integrated areas were calculated using non-linear curve fitting using Peak fit software (Systat inc). The non-linear curve fitting procedure consisted of second derivative analysis with a Voigt function with linear baseline subtraction. The residual plots were used as an indication of goodness of fit and hence poor fits were omitted from the analysis. The results are presented in section 7.1.

6.1.1.6 Morphological analysis

Scanning electron microscopy (SEM: JEOL 100) equipped with energy-dispersive X-ray analysis (EDX) was used for morphological analysis of the HAP coatings and powders. Test samples were coated with carbon using a sputter coater and then analysed by SEM and EDX (qualitative). EDX analysis was not used to determine the Ca/P ratios of the test samples as previous work [237] has shown that this method does not produce reliable quantitative results. The SEM and EDX micrographs obtained are presented in section 7.1.

6.1.2 HAP coatings on synthetic tape

This study presents a novel method for coating polymeric tape with HAP that has a potential in orthopaedic surgery to improve internal fixation to osseous tissue (section 1.3 and chapter 5). The coatings formed have been characterised and subjected to numerous mechanical testing to assess coating quality and adhesion.

6.1.2.1 Coating method

The as-received orthopaedic tape (OT) segments used in this investigation (figure 6.3) are made from ICI Type 113 High Tenacity "Terylene" polyester with a closed weave structure. One hundred and twenty 12.5mm lengths of orthopaedic tape (RR 2840/1: Xiros PLC, Leeds, UK) were cleaned ultrasonically in laboratory grade methanol and diethyl ether for ten minutes and rinsed thoroughly in deionised water as advised by the manufacturer to remove any surface debris that could affect the coating process. The OT samples were then rinsed thoroughly in deionised water and left to dry in ambient conditions. Once dry, the OT samples were weighed (MetlerToledoB204-S) individually.

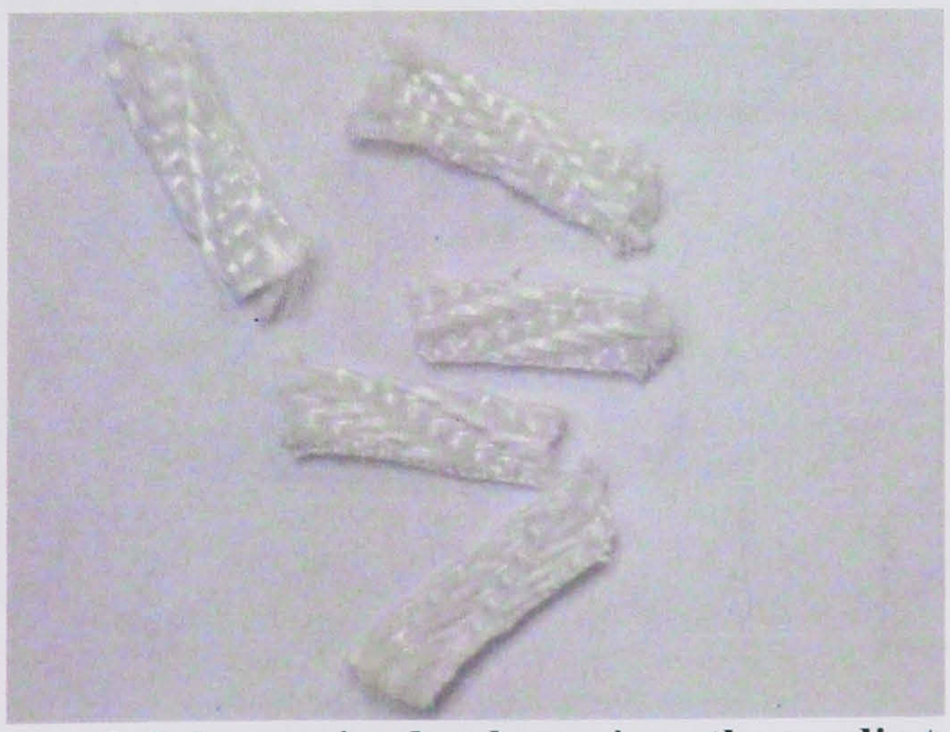

Figure 6. 3 As-received polymeric orthopaedic tape

The OT segments were divided into three batches and labelled OT-T, OT-N and OT-C samples. The OT-T samples were fully immersed in Triton 60 (Octylphenol

Ethoxylate: Sigma-Aldrich) for 5 minutes prior to coating. Triton 60 was used as a surfactant to relieve the surface tension of the fibres and increase surface wettability during the coating process. The OT-N samples were not treated with any surfactant prior to coating. The OT-C samples served as the control samples, which were not coated and subjected to any treatment with Triton 60.

Samples OT-T and OT-N were coated with HAP (see chapter 7) using a low temperature *in situ* precipitation method modified from one devised by Gilman *et al* [238]. In this modified method, equivolume tri-ammonium phosphate solution (0.125 mol dm^{-3}) and calcium nitrate solution (0.212 mol dm^{-3}) solution were slowly titrated at physiological temperature and mixed thoroughly with a Teflon coated magnetic bar as depicted in figure 6.4.

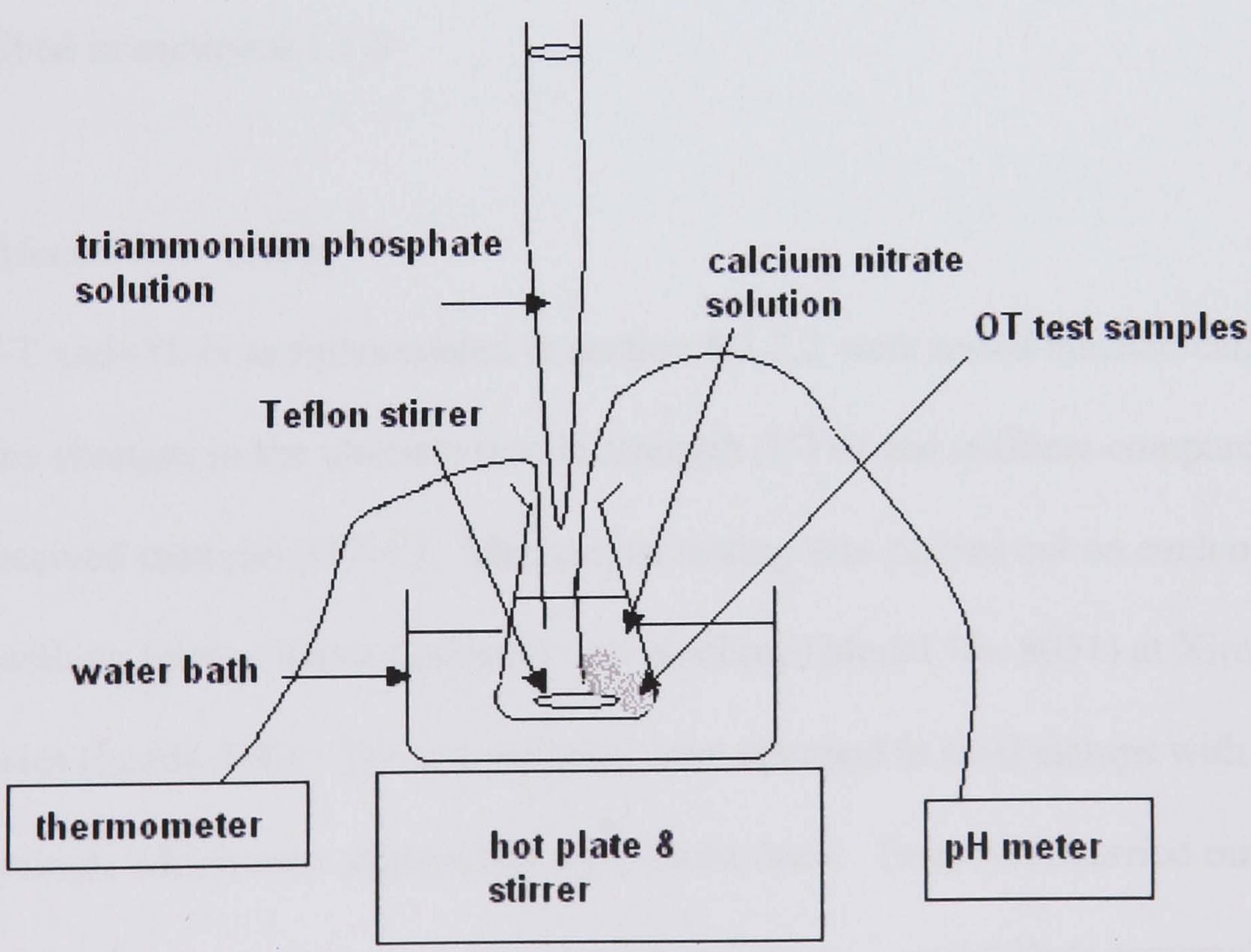

Figure 6. 4 Experimental set up of novel technology for coating polymeric tape with HAP.

The pH was maintained at 9 by the drop-wise addition of 1 mol dm^{-3} ammonium solution, monitored by a pH meter. Once the HAP started to precipitate (as observed by the cloudiness in the conical flask), the conical flask was sealed and left to stand at room temperature for 2 hour. This was in order to allow the precipitation to reach equilibrium.

After each respective coating process, the OT-T and OT-N samples were then removed from the suspension and dried at ambient temperature with a specimen dryer (Buehler Metaserv). Once dried the OT samples were weighed pending further analysis. The remaining precipitate was separated centrifugally from the solution and washed thoroughly with deionised water. The precipitate was then placed into an oven at physiological temperatures for 24 hours to dry. Once thoroughly dried, the solid sample was ground into a fine powder with a pestle and mortar and characterised as described in section 6.1.1.3

6.1.2.3 Mechanical testing

The OT-T and OT-N samples coated in section 6.1.2.2 were tested mechanically to assess any changes in the ultimate tensile strength (UTS) and stiffness compared to the as-received material (OT-C). Mechanical testing was carried out on each of the sample with an Instron Servo-hydraulic test machine (Model No. 8031) at Xiros Plc laboratories (Leeds, UK). The test samples were clamped in steel clamps with soft rubber linings, which were approximately 1-2mm thick. Tests were carried out using a uniaxial load at a constant cross-head speed of $20mms^{-1}$ until failure occurred. All tests were carried out at ambient conditions. The clamp bolts were tightened slowly to a torque of 9Nm and care was taken to ensure that the edges of both halves of each

clamp were parallel and that the test samples appeared to be evenly clamped. The initial gauge length of the test samples between the clamps was 40mm. All investigations were made in quadruplicate and numerical data is presented as mean ± standard error in chapter 7.

6.1.3 Synthesis of apatite powders

To understand the solubility and dissolution behaviour of HAP with respect to microstructural properties and chemical properties, series' of apatite powders with varying crystallite size, microstrain and carbonate content have been produced (results presented in chapter 7). In addition, dissolution investigations have been conducted to understand how changes in crystallite size, lattice microstrain and carbonate content affect long-term dissolution.

6.1.3.1 HAP powders synthesised at different temperatures

Previous investigations have shown that the average crystallite size of HAP synthesized from the reaction between calcium hydroxide and ortho-phosphoric acid is reaction temperature-dependent [239]. Therefore, an increase in reaction temperature produces an increase in average crystallite size of the HAP. HAP powders of various average crystallite size were produced using a modified version of a method devised by Kumar *et al* [239]. The method of HAP production used in this investigative work was conducted at a lower range of temperatures than cited in the literature to produce crystallite sizes in the same order of magnitude as bone mineral.

0.1 mol (7.41g) of reagent grade $Ca(OH)_2$ (Sigma-Aldrich) powder was added to 500ml of deionised distilled water in a conical flask and stirred at 400rpm at the

reaction temperature for one hour. 0.12molL^{-1} H_3PO_4 solution was added to the Ca $(OH)_2$ solution in a drop-wise manner (similar experimental setup to figure 6.4). During the addition of the acid, the pH and temperature were monitored electronically. The temperatures used for the synthesis of HAP were 25, 55 and 80 °C. The reactants were stirred thoroughly using a mechanical stirrer for a further two hours to promote precipitation. The resulting suspension left to settle at room temperature for 24 hours to allow the precipitation to reach equilibrium. The precipitates were filtered and dried in an oven at 60°C. The samples were stored in plastic sample bottles and labelled size25, size55 and size80 corresponding to the reaction temperatures.

6.1.3.2 HAP subjected to ball milling

Previous studies have shown that mechanical agitation such as ball milling has been used to induce microstrains into the crystal lattice of crystalline powders [240, 241]. High-resolution laboratory grade HAP (Fluka, Biochemika) was used as a control and labelled Strain1. 20g of laboratory grade HAP was placed into a 1litre ceramic ball mill jar and filled with 20 ceramic balls (Pascall Engineering Company) of approximately 25.8mm diameter. The jar was sealed then placed onto rotating rollers and milled at 400 rpm for two hours. The powder was retrieved and stored pending further analysis and labelled strain2. Sample strain3 was produced in the same way but using balls of approximately 12.3mm diameter and a milling time of 26 hours.

The powders produced were stored in plastic sample bottles pending further analysis.

6.1.3.3 Carbonated apatite

Low crystallinity carbonated apatite (Clarkson Chromatography Products Inc, USA) of approximately 0.5wt%, 2.3wt% and 3.5wt% carbonate substitution (B-type)[3] was used as a test sample. Apatites of low carbonate content (<5wt%) were used in this investigation to remain similar in carbonate composition to bone mineral. The samples were labelled 0.5CHA, 2.3CHA and 3.5CHA respectively and stored in plastic sample bottles pending further analysis.

6.1.3.4 Characterisation

All samples produced in sections 6.1.3.1-3 were characterised by XRD, FTIR, SEM and EDX as described in sections 6.1.1.3-6. Before any *in vitro* tests were carried out the apatite powders, it was ensured that three systematic series of apatite powders with increasing crystallite size, microstrain and carbonate content respectively had been produced. The results are presented in chapter 7.

6.2 *In vitro* testing of apatites

This study provides an assessment of the *in vitro* behaviour of PS and ED coatings; and apatite powders produced with varying microstructural and chemical properties as described in sections 6.1.3.1-3 (results are presented in section 7.1). Additionally the effect of crystallite size, microstrain and carbonate content respectively on the solubility of apatites is investigated and quantified in each case.

[3] Kindly measured by Clarkson Chromatography Products Inc, USA.

6.2.1 *In vitro* dissolution behaviour of apatite coatings and powders

6.2.1.1 Dissolution tests

In vitro testing of apatite coatings and powders was performed at the Biomaterials Laboratories located at Cranfield University (Shrivenham, UK). The media used for these analyses were deionised water, simulated body fluid (SBF) and foetal calf serum (FCS: Sigma-Aldrich). SBF and FCS were used because they have a similar ionic concentration to human blood serum [242] and, in addition, FCS contains blood proteins such as glycine, cysteine, cystine and glutamine. The three dissimilar media were chosen to be able to ascertain the *in vitro* dissolution behaviour of apatite coatings and powders with and without the presence of proteins. Deionised distilled water served as a control media in each case.

SBF was prepared by dissolving reagent grade 0.799g of NaCl, 0.350g of $NaHCO_3$, 0.224g of KCl, 0.228g of $K_2HPO_4.3H_2O$, 0.278g of $CaCl_2$, 0.071g of Na_2SO_4 and 0.305g of $MgCl_2.6H_2O$ in distilled water. The pH of the solution was adjusted to 7.4 with a mixture of $0.01 molL^{-1}$ tris(hydroxymethyl)-aminoethane $[(CH_2OH)_3CNH_2]$ and $0.01 molL^{-1}$ HCL at a temperature of $37 \pm 0.1^{o}C$ [242, 243]. The ionic concentration of the SBF solutions was checked by inductively coupled plasma-optical emission spectrometry (Liberty 200, Varian) [4] and compared to those cited in the literature [242].

PS and ED test samples were washed in deionised water to remove any surface debris and dried in air. Once dry, the test samples were weighed prior to immersion in order to detect any changes in the mass of the coatings after immersion. PS and ED test

[4] Kindly measured by Mr. Richards Andrews, Cranfield University at Silsoe (Silsoe, UK).

samples were placed into separate sterile beakers containing 300ml of deionised water, SBF and FCS respectively. The beakers were then sealed and sprayed with 70% isopropanol solution (to sterilise the outer surface of the beakers) and kept in an incubator at 37 ± 0.1°C under static and aseptic conditions. Medium without test discs served as controls to monitor changes in ionic concentration. The experimental setup for this dissolution study is depicted in figure 6.5.

At intervals of 1, 3, 7, 14 and 21 days of immersion each test sample was removed from the media and the media was refrigerated pending chemical analysis. On removal from the media, the test samples were inspected visually for any signs of coating delamination or bacteria growth. The test samples were then washed in distilled water, dried in air and re-characterised as described in sections 6.1.1.3-6.

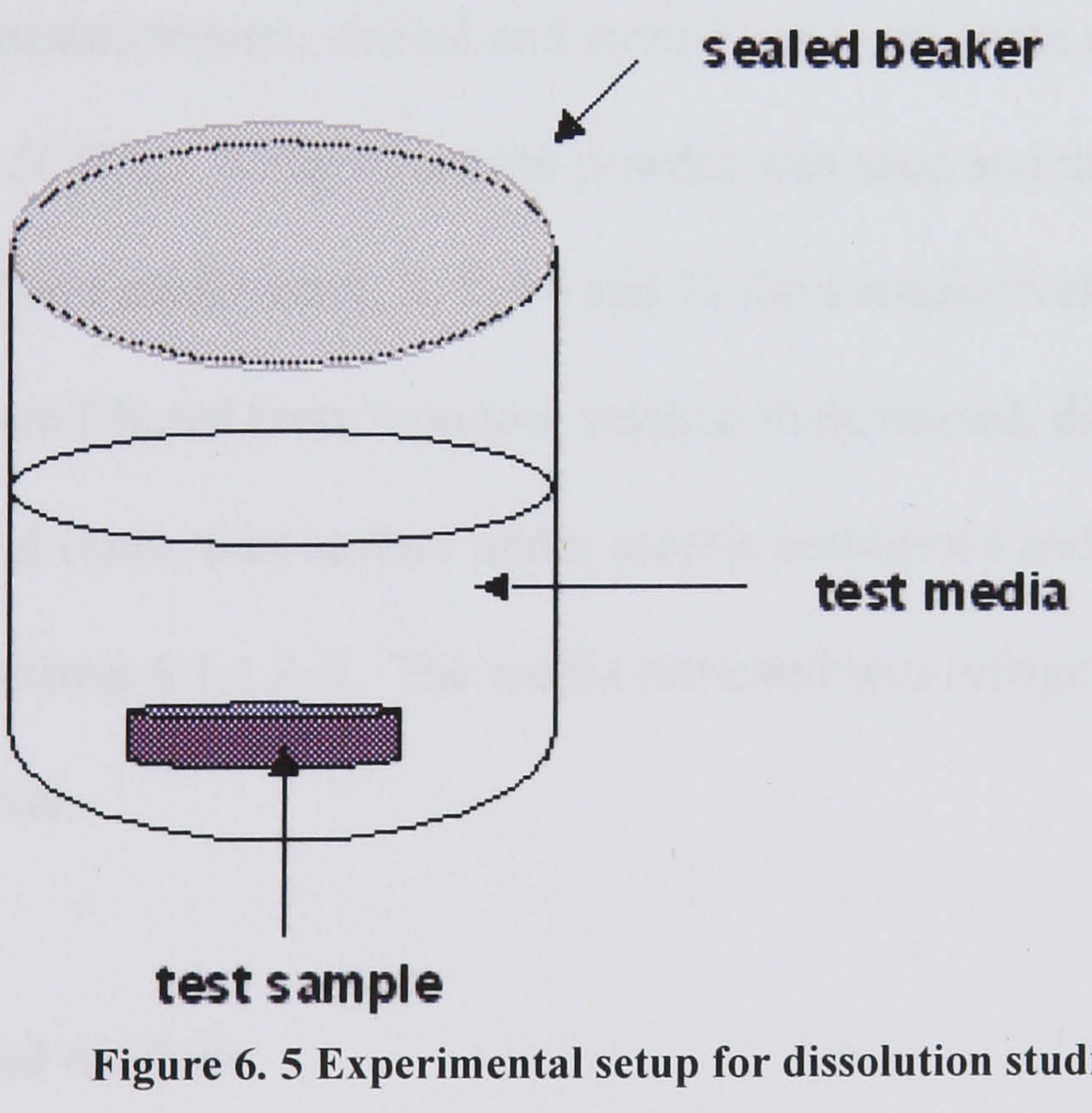

Figure 6. 5 Experimental setup for dissolution studies.

The samples were washed on removal from the media to remove remnants of the media from the surface of the coatings to avoid crystallisation of media components when the sample was air-dried. Preliminary investigations carried out for this study have revealed that dried components e.g. NaCl can affect the results of *in vitro* tests.

In addition, it was found that the washing process has no detrimental effect on the coating itself and does not influence the diffraction or chemical analyses.

An environmental scanning electron microscopy (ESEM: LEO 435VP) was used to observe the changes in coating morphology before and after each immersion period. This system enabled high quality images to be produced without having the need for application of a conductive surface layer. After characterisation, the test samples were washed in deionised distilled water and immersed in fresh media and incubated at 37 ± 0.1°C. All experiments were run in triplicate.

The abovementioned *in vitro* tests were repeated for the apatite powders produced and characterised in sections 6.1.1.3-6 with varying crystallite size (size25, size55 and size80), microstrain (strain1, strain2 and strain3) and carbonate content (0.5CHA, 2.3CHA and 3.5CHA). 0.36g of apatite powder was used and the powders were immersed in 300ml media for 1, 3, 7, 14 and 21 days respectively. After immersion, the powders were filtered from solution, washed in deionised, distilled water and allowed to dry at room temperature under aseptic conditions and then characterised as described in sections 6.1.1.3-6. The media retrieved was refrigerated pending chemical analysis.

6.2.1.2 Chemical analysis

The ionic concentrations of calcium and phosphate present in the media and controls were measured before and after the period of immersion. Calcium ion concentration was measured by atomic absorption (AAS: Perkin Elmer 3100). The instrument was calibrated with five point calibration using standards at 1, 2, 3, 4 and 5µg/ml

respectively. Strontium chloride was added to the media, controls and standards during because the measurement of calcium can be disturbed by the presence of other metal ions. Phosphate ion concentration was measured using a Dionex DX-100 ion chromatography (IC) system calibrated with four point calibration using standards at 20, 40, 60 and 80μg/ml of phosphate respectively.

The ion activity product (IP) was calculated using equation 6.2 [58], where α and γ are the activity and the activity coefficient respectively and the square brackets denote the ionic concentration. γCa^{2+}, γPO^{3-}_4 and γOH^- under the conditions in this experimental work have been taken to be 0.36, 0.06 and 0.72 respectively [244, 245]. The concentration of hydroxyl ions was calculated from the pH of the solutions at each immersion time. Equation 6.2 gives:

$$IP=(\alpha Ca^{2+})^{10}(\alpha PO_4^{3-})^{6}(\alpha OH^-)^{2} \qquad (6.2)$$

$$=(\gamma Ca^{2+})^{10}(\gamma PO_4^{3-})^{6}(\gamma OH)^{2}[Ca^{2+}]^{10}[PO_4^{3-}]^{6}[OH^-]^{2}$$

6.2.2 Solubility of apatite powders

Solubility measurements of the apatite powders were made by equilibrating 25mg of the test apatite and 250ml of deionised distilled water at 37 ± 0.1°C. This was carried out using glass (Orion 91-01) and calcium electrodes (Orion 93-200), coupled with an Ag/AgCl reference electrode (Orion 900100) in order to monitor the changes in hydrogen and calcium ion activities. The solution was left to equilibrate for 48 hours. At equilibration, the solution was filtered and calcium and phosphate concentrations of were determined by means of AAS (Perkin Elmer) and ion chromatography

(Dionex DX-100). In calculating the solubility products (K_{sp}) for each test sample, the carbonate concentration in the solution was assumed to be negligible due to the low carbonate content of each of the apatites investigated. Therefore, K_{sp} was calculated based on HAP stoichiometry using equation 6.2 where K_{sp} is the equilibrium value of IP. Solubility measurements were carried out in triplicate and are presented in chapter 7.

6.2.3 Statistical analysis.

Pearson's correlation analysis was used to interpret the data obtained from solubility measurements of the apatite powders in order to ascertain which parameter (carbonate, crystallite size and lattice microstrain) had the greatest effect on solubility. In addition changes in crystallite size, microstrain and lattice parameters obtained from the *in vitro* testing of the apatite powders were compared with solubility. Pearson's correlation analysis was assumed to be the best method of statistical analysis of this form of data.

6.3 Cell culture studies

This study assesses the osteoblastic response to polyester orthopaedic tape coated described in section 6.1.2. All cell culture studies were conducted at the Cell biology laboratories in the Institute of Biosciences and Technology, Cranfield University at Silsoe (Silsoe, UK). All cell culture preparation work was done under aseptic conditions in a laminar flow cabinet.

6.3.1 Cell culture studies

12.5 mm lengths of coated (OT-T, OT-N) and uncoated (OT-C) orthopaedic tape were irradiated at 8 kGy for 5 hours at 22°C using a colbalt 60-gamma radiation source prior to cell culture study. This treatment was carried out to ensure a sterile surface for cellular growth and proliferation.

6.3.1.1 Cell cultivation

1st passage human foetal osteoblast cells (hFOB 1.19, ATCC) were used in this study. The cells were cultivated in standard cell culture T-75 flasks in an equivolume mixture of Ham's F12 (Sigma-Aldrich) and Dulbecco's modified eagle medium without phenol red with 2.5 mML-glutamine (DMEM: Sigma-Aldrich). The media was supplemented with 0.3mg/ml G418 antibiotic, geneticin (Gibco) and 10% foetal calf serum (Sigma-Aldrich). Cultivation was conducted under standard cell conditions in an incubator at 34 °C in fully humidified atmosphere at 5% $C0_2$ in air.

In order to remove the osteoblast cells from culture, the culture flasks were first washed thoroughly with phosphate buffered saline (PBS: Sigma-Aldrich) to assure that any non-viable cells were removed. 1ml of 10X trypsin- EDTA solution was diluted with 9ml of PBS to produce a solution to detach the viable osteoblast cells from each culture flask. The resulting solution was placed into each culture flask and left to incubate for 1 minute. An inverted light microscope was used to ascertain if the cells had completely detached from the bottom of the culture flask. Once the osteoblasts had been detached from the culture flasks, the trypsin-EDTA solution was recovered and placed into centrifuge tubes containing 4ml of culture media. In order to separate the osteoblast cells and the solution, the cell suspension was centrifuged at

1300 rpm for 5 minutes at 4°C. The cell pellets obtained were resuspended in a known volume of medium and counted using a haemocytometer. Cell counts were made in sextuplicate.

6.3.1.2 Cell attachment

In order to assess the ability of osteoblast cells to adhere to OT-T, OT-N and OT-C test samples; each test sample was placed into an individual well of a 24 well culture plate. 1ml of cell suspension (5.0×10^4 cells mL^{-1}) was seeded onto each test sample and empty cell were used as controls. All investigations were conducted in quadruplicate for OT-T, OT-N and OT-C test samples respectively. The culture plates were then covered and placed in an incubator under standard cell conditions.

After 4 and 18 hours of incubation, the osteoblast cells were harvested from the OT samples and control wells and counted using a haemocytometer. The osteoblasts cells were harvested from the OT samples and culture wells using 0.5ml of trypsin-EDTA solution in PBS as described in section 6.3.1.1. Cell counts were conducted in sextuplicate and are presented as mean ± standard error in section 7.3.

6.3.1.3 Cell proliferation

In order to assess the ability of osteoblast cells to grow and proliferate on the test samples (OT-T, OT-N and OT-C) and control wells, osteoblasts were seeded at a density of 2.5×10^3 ml^{-1} in 2ml DMEM as described in section 6.3.1.1. Each test sample (OT-T, OT-N, OT-C) and control well was incubated for 7, 11, and 14 days respectively. The medium was not changed during culture in order to ascertain the net osteocalcin, intracellular protein, alkaline phosphatase and extracellular protein

production at the end of each period of culture. At the end of each period of culture, the media and osteoblast cells were harvested and counted as described in section 6.3.1.1.

6.3.1.4 Quantification of osteocalcin production

Osteoblasts were cultured on test samples and control wells as described in section 6.3.1.3 in quadruplicate. Osteocalcin production (a marker of the osteoblastic phenotype) in the medium by osteoblast cells on day 14 of incubation was determined using a commercially available kit (Intact human osteocalcin EIA kit, Biomedical Technologies, USA). The assay was conducted according to the directions of the manufacturer. All measurements were taken in sextuplicate and were reported as means ± standard error. Osteocalcin concentration in the media was expressed in ng/ml.

6.3.1.5 Total intracellular protein content

Osteoblasts were cultured on test samples and control wells as described in section 6.3.1.3 in quadruplicate. The total intracellular protein synthesised by osteoblasts cells harvested from the test samples and control wells after 14 days of incubation was determined spectrophotometrically using a commercially available kit (Pierce Chemical Company), following the manufacturer's instructions. For this purpose, each batch of osteoblast cells harvested from the test samples and controls were lysed using deionised distilled water and three freeze-thaw cycles. The cell lysates were incubated with a copper sulphate solution and bicinchoninic acid at 37°C for 30 minutes. Light absorbance of the supernatant was measured at 570nm on a microplate reader. The total intracellular protein synthesised by the osteoblast cells grown on the

test samples and control wells were expressed in mg. Measurements were made in sextuplicate.

6.3.1.6 Alkaline phosphatase activity

Evidence of enhanced osteoblast growth and proliferation was analysed by means of alkaline phosphatase (ALP) synthesis. ALP activity (p-nitrophenol conversion to p-nitrophenylate) in the cell lysates (prepared in section 6.3.1.5) was determined on day 14 using a commercially available ALP immunoassay kit (Diagnostic kit #104; Sigma-Aldrich). Light absorbance of the cell lysates was measured on a spectrophotometer (MR600 Spectrophotometric Microplate Reader, Dynatech) at 400nm according to the directions of the manufacturer. Measurements were made in sextuplicate and the total ALP activity (expressed as nano-moles of converted p-nitrophenol/min) was normalised by the total intracellular protein content and expressed as nano-moles of converted p-nitrophenol/min/mg protein.

6.3.1.7 Quantification of extracellular calcium

Osteoblasts were cultured on test samples and control wells as described in section 6.3.1.3 in quadruplicate. Media was harvested from each test sample and control well on day 2, 4, 7 and 14. Extracellular calcium production was determined by a colorimetric reaction between the harvested media and o-cresolphthaleine complexone under alkaline conditions forming a calcium-CPC-complex. Absorbance measurements were made on using a spectrophotometer at 578nm wavelength according to the manufacturer of the calcium immunoassay kit (Ecoline 25, Merck). Calcium concentrations were expressed in $mmolL^{-1}$ and measurements were conducted in quadruplicate and presented as the mean ± standard error.

6.3.1.8 Cell morphology

Osteoblasts were cultured on test samples and control wells as described in section 6.3.1.3 and harvested as described in section 6.3.1.1. The cells harvested from each batch were seeded onto plastic culture slides and left to attach for 4 hours. The slides were washed in PBS solution and the osteoblast cells fixed with 4% paraformaldehyde in PBS and stained with haematoxylin. The morphology of the osteoblast cells was observed under light microscopy and compared to osteoblasts that had not been exposed to OT test samples.

6.3.1.9 Statistical analysis

Numerical data were analysed using standard analysis of variance (ANOVA) techniques, with a minimal significance at $P< 0.05$.

7.0 Results and discussions

This section presents the findings from the experimental work outlined in this thesis (chapter 6). The findings are compared and contrasted in the context of previous work carried out in the field, and further discussed in chapter 8.

7.1 Fabrication and characterisation of apatite coatings and powders.

Various apatite coatings and powders have been fabricated and characterised. Characterisation has been undertaken by a novel methodology for non-destructive phase quantification in addition to conventional chemical, mechanical and morphological techniques.

7.1.1 Validation of novel method of quantitative phase analysis

A novel methodology of quantitative phase analysis of apatites [105, 131, 246] has been developed and described in this thesis (chapter 6). However, before any detailed structural characterisation of apatite coatings and powders could be carried out, it was imperative that this methodology was assessed to ensure accuracy and reliability. In order to assess accuracy, diffraction data from a series of HAP-ACP powder mixtures of known composition were collected and analysed. Figure 7.1 presents the diffraction data from a sample in the series. On close inspection, it can been seen that the fit is of good quality and this is further validated by the 'goodness of fit' value, R_{wp}, of ~9.8%. In all refinements conducted in this thesis, a R_{wp} of <12% was deemed acceptable as long as the visual fit was good.

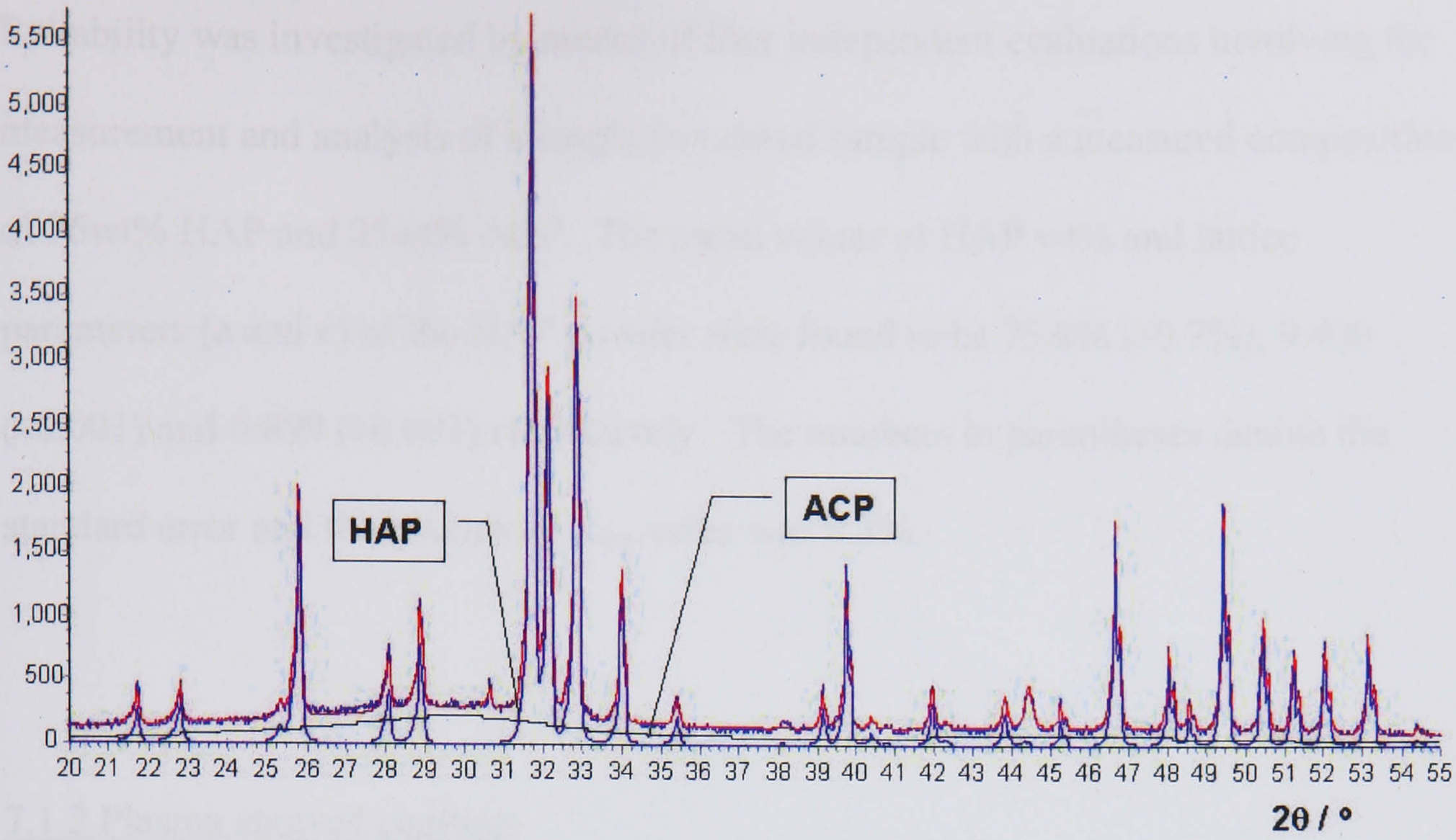

Figure 7. 1 Observed (blue) and calculated (red) diffraction data (overlaid) corresponding to a known mixture of HAP and ACP (60 wt% HAP). Each component contributing to the calculation is shown separately and marked.

Table 7.1 compares data of the measured compositions with those determined by phase analysis. All of the phases listed in table 7.1 were included in all of the analytical refinements and cases where zero is recorded denotes that the composition of that component was refined to <0.5%. In all cases, the ACP wt% corresponding to the measured and determined data was in agreement within ~ 4%.

Weighted amounts[5]				Calculated wt% from phase analysis			
HAP	ACP	α-$Ca_3(PO_4)_2$	β-$Ca_3(PO_4)_2$	HAP	ACP	α-$Ca_3(PO_4)_2$	β-$Ca_3(PO_4)_2$
100	0	0	0	97.8 ± 0.5	2.2 ± 0.5	0	0
80	20 ± 0.1	0	0	80.5 ± 0.5	19.5 ± 0.5	0	0
60	40 ± 0.1	0	0	59.8 ± 0.5	40.2 ± 0.5	0	0
40	60 ± 0.1	0	0	42.3 ± 0.5	57.7 ± 0.5	0	0
92.5	0	7.5 ± 0.1	0	92.1 ± 0.5	0	7.9 ± 0.5	0
97.5	0	2.5 ± 0.1	0	96.4 ± 0.5	0	3.6 ± 0.5	0
92.5	0	0	7.5 ± 0.1	90.1 ± 0.5	0	0	9.9 ± 0.5
97.5	0	0	2.5 ± 0.1	96.9± 0.5	0	0	3.1 ± 0.5

Table 7. 1 Comparison of measured compositions with those determined by novel quantitative phase analysis.

[5] Kindly prepared by Dr.Karen Hing, Queen Mary, University of London.

Reliability was investigated by means of four independent evaluations involving the measurement and analysis of a single powdered sample with a measured composition of 75wt% HAP and 25wt% ACP. The mean values of HAP wt% and lattice parameters (a and c) of the HAP powder were found to be 75.8% (±0.7%), 9.400 (±0.001) and 6.899 (±0.001) respectively. The numbers in parentheses denote the standard error and the maximum R_{wp} value was 8.3%.

7.1.2 Plasma sprayed coatings

7.1.2.1 Diffraction analysis

In total 500 PS coatings have been examined by XRD. The diffraction data presented here was found to be in agreement without anomalies ($P<0.05$: appendix C).

Characteristic diffraction data from randomly selected PS coatings and the fabrication feed powder is illustrated in figures 7.2-3. A summary of principal structural characteristics of the PS coatings examined is presented in table 7.2. The presented data derives from i) the feed powder used to produce the PS coatings ii) a 60μm PS coating and iii) a 10μm PS coating. It has been possible to examine typical PS surface material to a depth of approximately 16μm (the depth where 95% of the diffracted X-rays derive) and the material close to the coating-substrate interface, including the as received feed powder used in their manufacture.

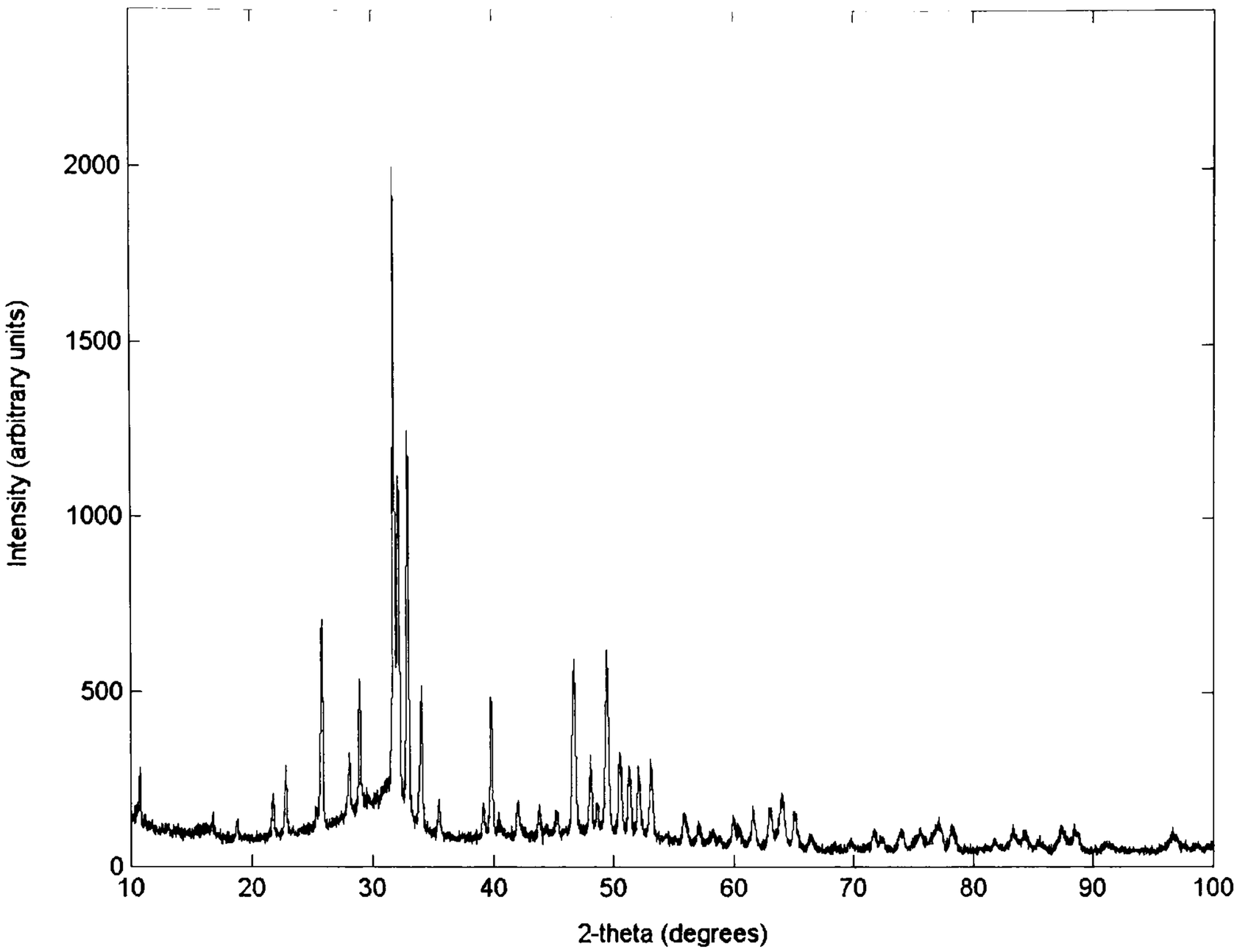

Figure 7. 2 Diffraction data from a typical 'full' thickness PS coating.

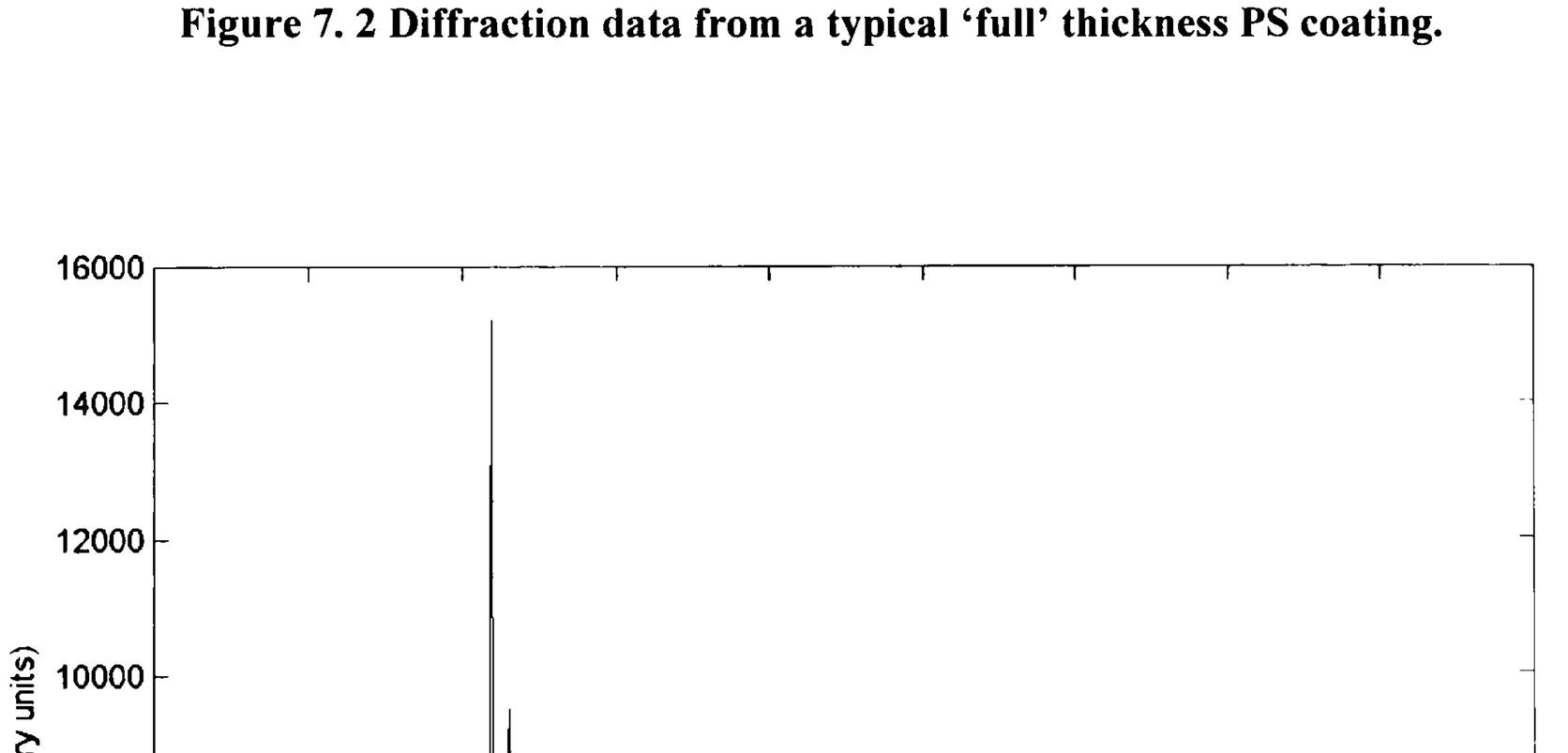

Figure 7. 3 Diffraction pattern of HAP feed powder.

Source	Composition (wt%)	β [002] (°)	a (Å)	c (Å)	PO index
Feed powder	100 ± 0.5wt% HAP	0.15 ± 1.1 X 10^{-3}	9.423 ± 1.4 X 10^{-4}	6.883 ± 1.2 X 10^{-4}	-
Full thickness coating (60μm)	72 ± 0.5wt% HAP 28 ± 0.5wt% ACP	0.15 ± 1.5 X 10^{-3}	9.411 ± 2.3 X 10^{-4}	6.891 ± 1.6 X 10^{-4}	0.72 ± 3.4%
Partial thickness coating (10μm)	32 ± 0.5wt% HAP 61 ± 0.5wt% ACP 2 ± 0.5wt% CaO 2 ± 0.5wt% β-TCP 2 ± 0.5wt% α-TCP	0.16 ± 2.4 X 10^{-3}	9.409 ± 1.6 X 10^{-4}	6.891 ± 1.9 X 10^{-4}	0.71 ± 2.9%

Table 7. 2 Principal structural characteristics of PS coatings and feed powder.

During the preliminary investigations for this study, Rogers *et al* [131] reported that the HAP/ACP ratio of 'full' and 'partial' thickness PS coatings showed periodic fluctuations with time. This time dependent behaviour corresponded to the aging and replacement of the spray nozzle and changes in chemical composition of the feed powder used for the fabrication process. Numerous equivalent reports have been found in the literature [14, 21, 93, 99, 247]. In order to counteract this effect all samples analysed in this study were taken from the same batch.

In all samples analysed, the dominant crystalline phase was found to be HAP. The diffraction pattern corresponding to the feed stock powder consisted of well-defined sharp peaks, characteristic of highly crystalline HAP [98, 147, 159, 248] as confirmed by quantitative phase analysis [248]. There were no signs indicating the presence of any metastable or amorphous phases. The diffraction patterns corresponding to the 'full' and 'partial' thickness PS coatings contained less intense peaks corresponding to HAP. In addition, a 'background' halo was observed in the diffraction data at 20°-40° / 2θ, which has previously been interpreted as an amorphous phase [131, 223, 248, 249]. The magnitude of the background halo and general peak broadening was significantly greater in the 'partial' thickness coating than in the 'full' thickness coating. This observation is further validated by quantitative phase analysis, which revealed that there was 61wt% and 28wt% ACP in the 'partial' and 'full' thickness coatings respectively. Therefore, significantly more amorphous material lays close to the coating-substrate interface compared to the surface of the coating. This observation is an important one (discussed further in chapter 8) and has a significant influence on the *in vitro* behaviour of PS coatings. Another observation that would

affect the *in vitro* behaviour of PS coatings is the presence of extraneous phases (β-TCP, α-TCP and CaO) found in the 'partial' thickness PS coatings.

The lattice parameters corresponding to the PS coatings showed small and insignificant differences in comparison to the feed powder. The results indicated that there were compression stresses in the a-axis associated with tensile stresses in the c-axis direction in the PS coatings compared with the feedstock powder. The width of the peak corresponding to the (002) reflection in HAP is similar in both the 'full' and 'partial' thickness PS coatings. This finding is an indication that the crystal size/strain along the <00l> direction is similar. In contrast, the HAP (002) peak width of the feed powder is wider than its post-fabrication counterparts. This observation has been made previously by Roome *et al* [159] and gives an indication of the smaller size of the coherently diffracting domains (crystallite size) of the feed powder.

For simplicity, a practical approach has been adopted in the quantitative determination of preferred orientation and a 'PO index' obtained. The PO index has been derived from the ratio of the integrated areas of the (002) and (300) reflections normalised to their random values. Such directions were chosen based on the fact that they are perpendicular to each other. Hence, a PO index of 1 denotes that there is no net preferred orientation. Preferred orientation was found to be similar between both of the PS coatings.

Further microstructural analyses were conducted by exploiting Williamson-Hall (W-H: figure 7.4) to provide an initial assessment of sample dependent broadening. In this case, the magnitude of microstrain and crystallite size can be determined from the

gradient and intercept of the curves respectively. An intercept at the origin is indicative of the fact that the data peaks are not broadened by finite crystallite size and such a case would occur when the crystallite sizes were greater than ~0.2μm. Good quality diffraction data with no overlapping substrate peaks had been collected; hence, numerous peaks have been exploited in this analysis. For the analysis the peaks were fitted to a pseudo-Voigt function by line profile analysis to measure values of β (integral breadth) at various 2θ positions. Peaks with a Voigt shape factor (FWHM/β) outside the range of 0.6366-0.939 were not included in the analysis, as peaks outside this range cannot be fitted with a Voigt function [158]. Within the limits of statistical error (indicated by scattered data points) [159], the data corresponding to both of the PS coatings were identical and indicated that only microstrain effects broadened the peak widths.

Further analysis by means of the single line analysis of [002] using the 'approximate method' [158] (described in chapter 4) revealed that the crystallite sizes (volume weighted) were ~0.2μm and the strain was ~0.24%. The W-H plot corresponding to the feed powder showed that although there was scatter amongst data points, the overall gradient of the best-fit line is around zero. This indicates that no significant microstrain is present in the feed powder and that broadening is due to a smaller crystallite size (~0.1μm). Roome *et al* [159] and Deram *et al* [250] have reported comparable findings in crystallite size and microstrain investigations of apatite coatings and powders.

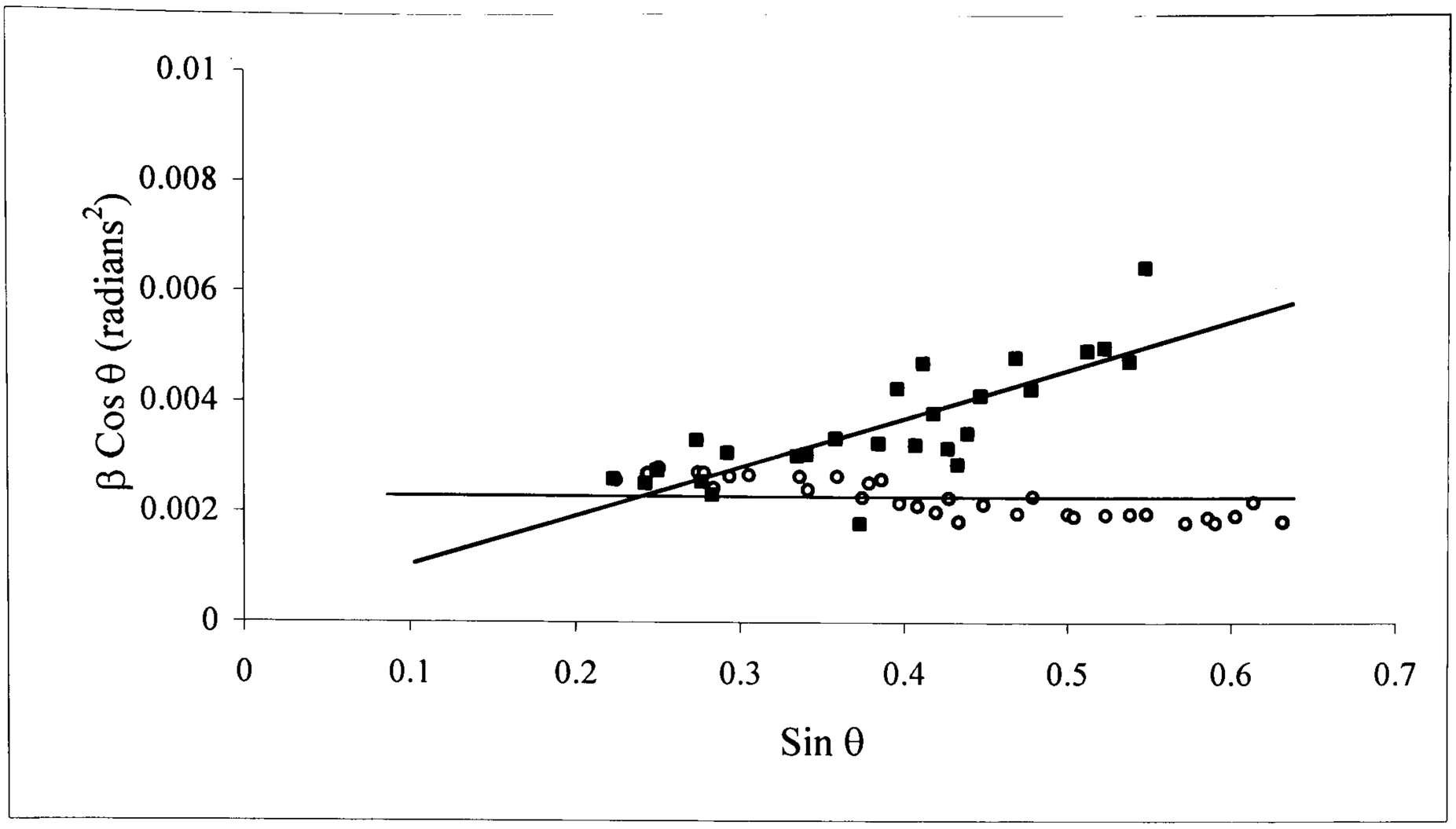

Figure 7. 4 Williamson Hall plot of feed powder (open circles), and 'full' (squares) thickness PS coatings.

7.1.2.2 Chemical analysis

Figures 7.5-6 shows FTIR spectra of the PS coatings and feed powder. All spectra contained various bands from the respective phosphate and hydroxyl groups of HAP (presented in table 7.3), which were consistent with other published data [59, 83, 239]. Of note was the fact that the intensity of the band corresponding to the OH stretching vibration (~3570cm^{-1}) was significantly smaller in the PS coatings with respect to the feed powder. In addition the band at ~630cm^{-1}, corresponding to the OH liberation band present in the feed powder, disappeared in the PS coatings. This phenomenon indicates that there is a degree of dehydroxylation in the formation of ACP during the PS process. This observation is consistent with findings by Park *et al* [248], Knowles *et al* [200] and Gross *et al* [96, 97]. In addition it was observed that the peaks in the spectra corresponding to the feed powder were more resolved than that of the 'full' thickness PS coatings. This has been attributed to the decrease in crystallinity of the HAP in the PS process, which further validates the changes in phase composition determined by XRD analysis in section 7.1.1 [131]. Gadaleta *et al*

[251] and Park *et al* [248] have reported similar findings in characterisation studies of HAP powders. Other post-fabrication changes observed in this study were the loss of the symmetric stretching mode for phosphate at 960cm^{-1}; and the disappearance of the very weak carbonate bands at 1400cm^{-1}-1500cm^{-1} and 1900cm^{-1}-2200cm^{-1}. Knowles *et al* [200] and Park *et al* [248] have made comparable observations.

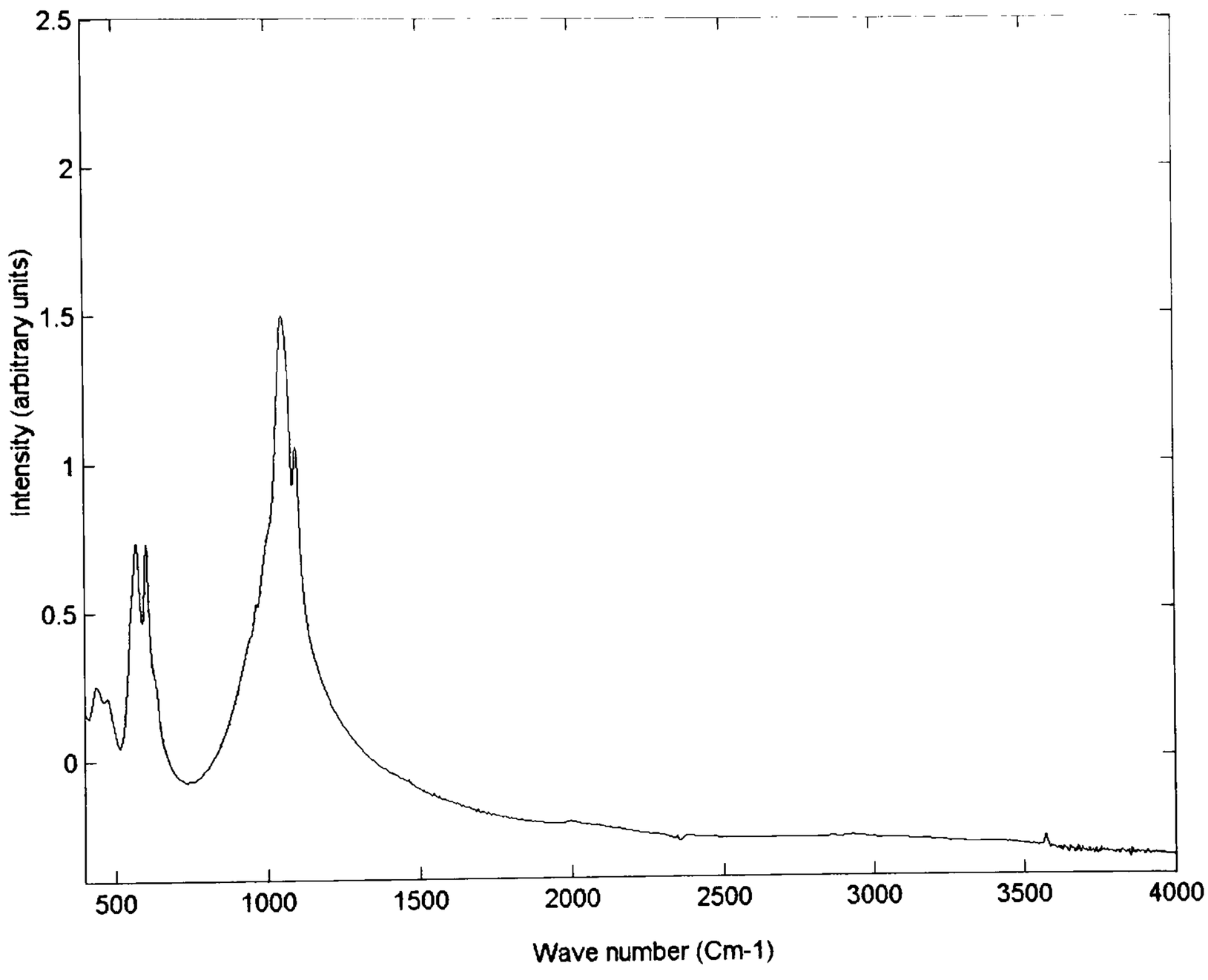

Figure 7. 5 FTIR spectra of 'full' thickness coating.

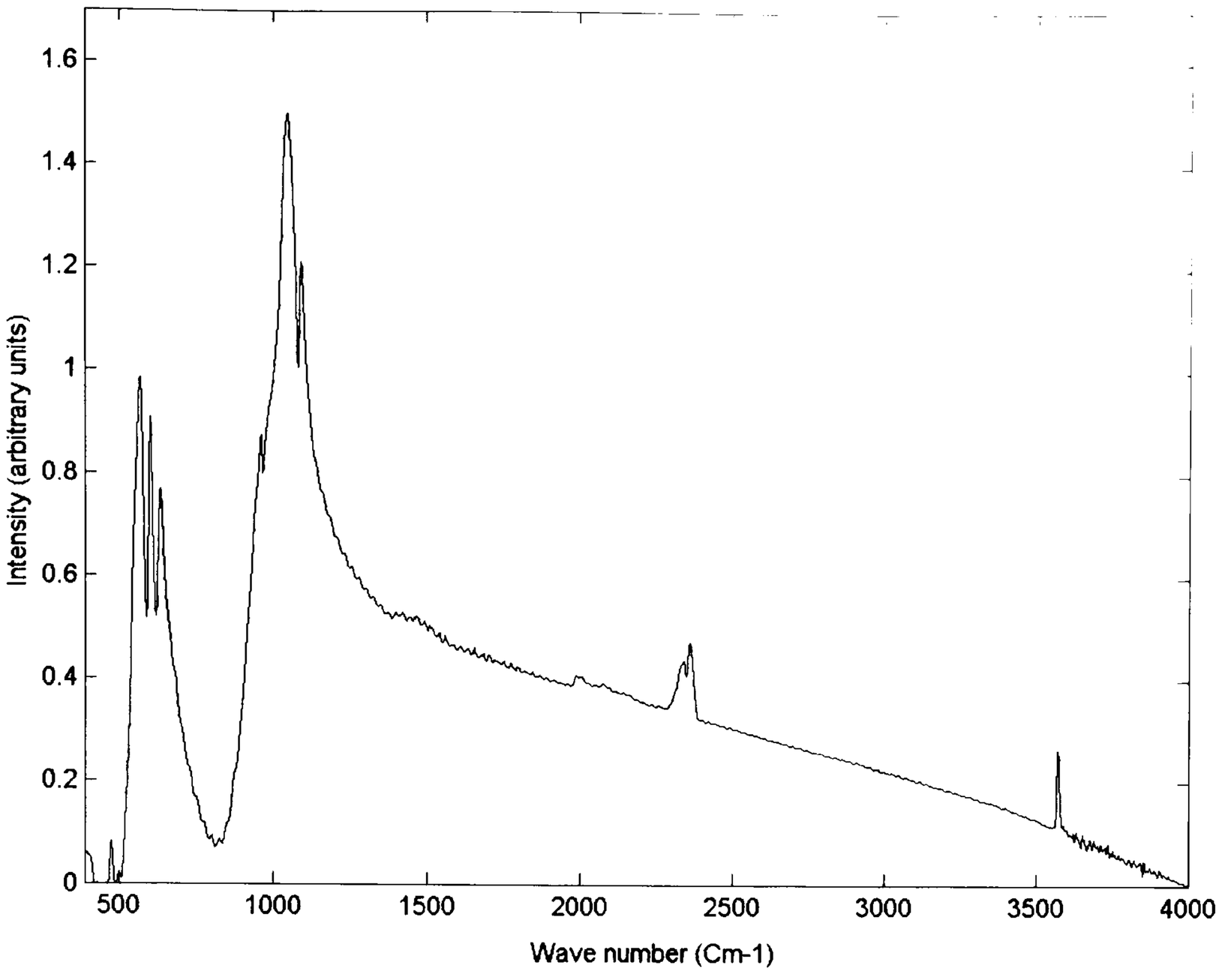

Figure 7. 6 FTIR spectra of feed powder.

Band	Feed powder (Cm^{-1})	'Full' thickness coating (Cm^{-1})
$\gamma_1 PO^3_4^-$	961	-
$\gamma_2 PO^3_4^-$	476	474
	436	438
$\gamma_3 PO^3_4^-$	1092	1092
	1043	1050
	-	990
$\gamma_4 PO^3_4^-$	602	603
	569	569
$\gamma_s OH$	3574	3575

Table 7. 3 FTIR frequencies of $PO^3_4^-$ and OH^- groups in HAP before and after plasma spraying.

7.1.2.3 Morphological analysis

SEM analysis was used to carry out a morphological assessment of 'full' thickness PS coatings and the feed stock powder. SEM analysis revealed that the 'full' thickness coatings had the typical lamellar structure associated with plasma sprayed coatings [14, 100, 105, 247, 252]. The morphological features observed were well flattened and accumulated glassy splats, spheroidized particles and unmelted or partially melted particles as shown in figures 7.7-7.10. Very few surface cracks were visible, but the microstructure was found to be porous in nature. The feedstock powder (figure 7.10) was characterised by spherical particles (5-50μm in diameter) with a porous internal structure and large holes. These features are clearly indicative of the spray dry method of manufacture [100, 250].

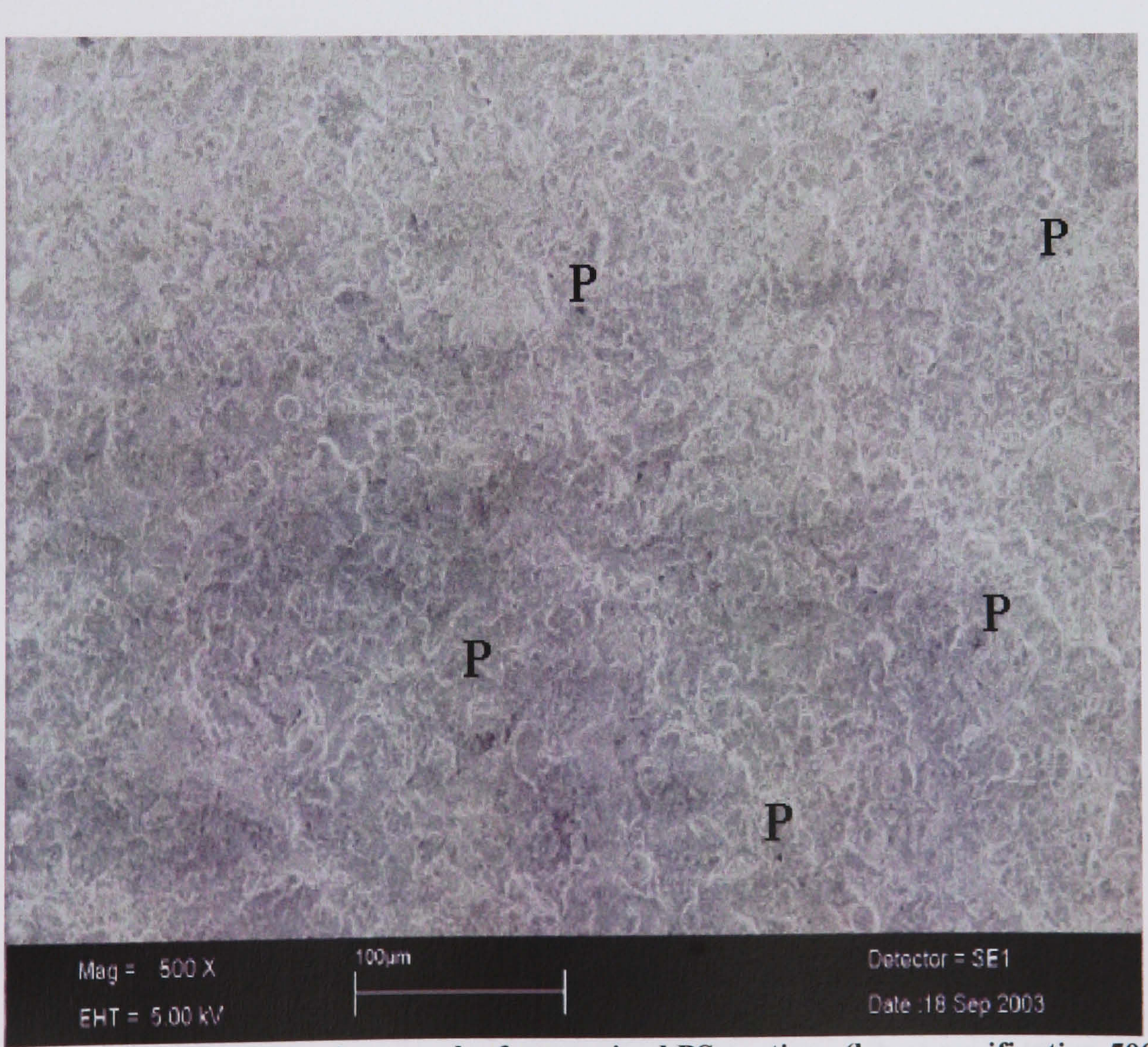

Figure 7. 7 Typical SEM micrograph of as-received PS coatings (low magnification 500X) showing porous (P) lamellar structure.

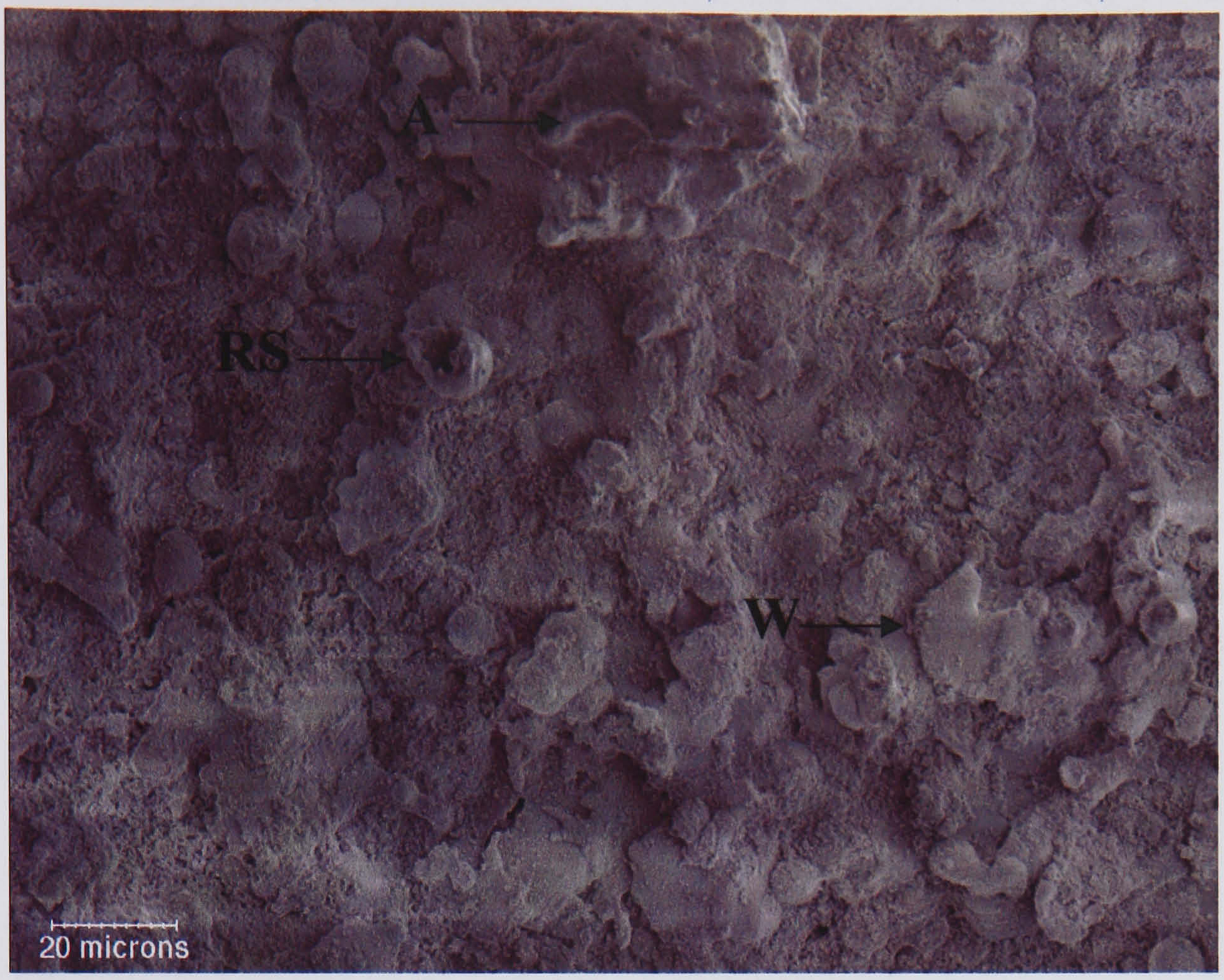

Figure 7. 8 Typical SEM micrograph of PS coatings showing re-spheroidized droplets (RS), well - flattened (W) and accumulated (A) splats.

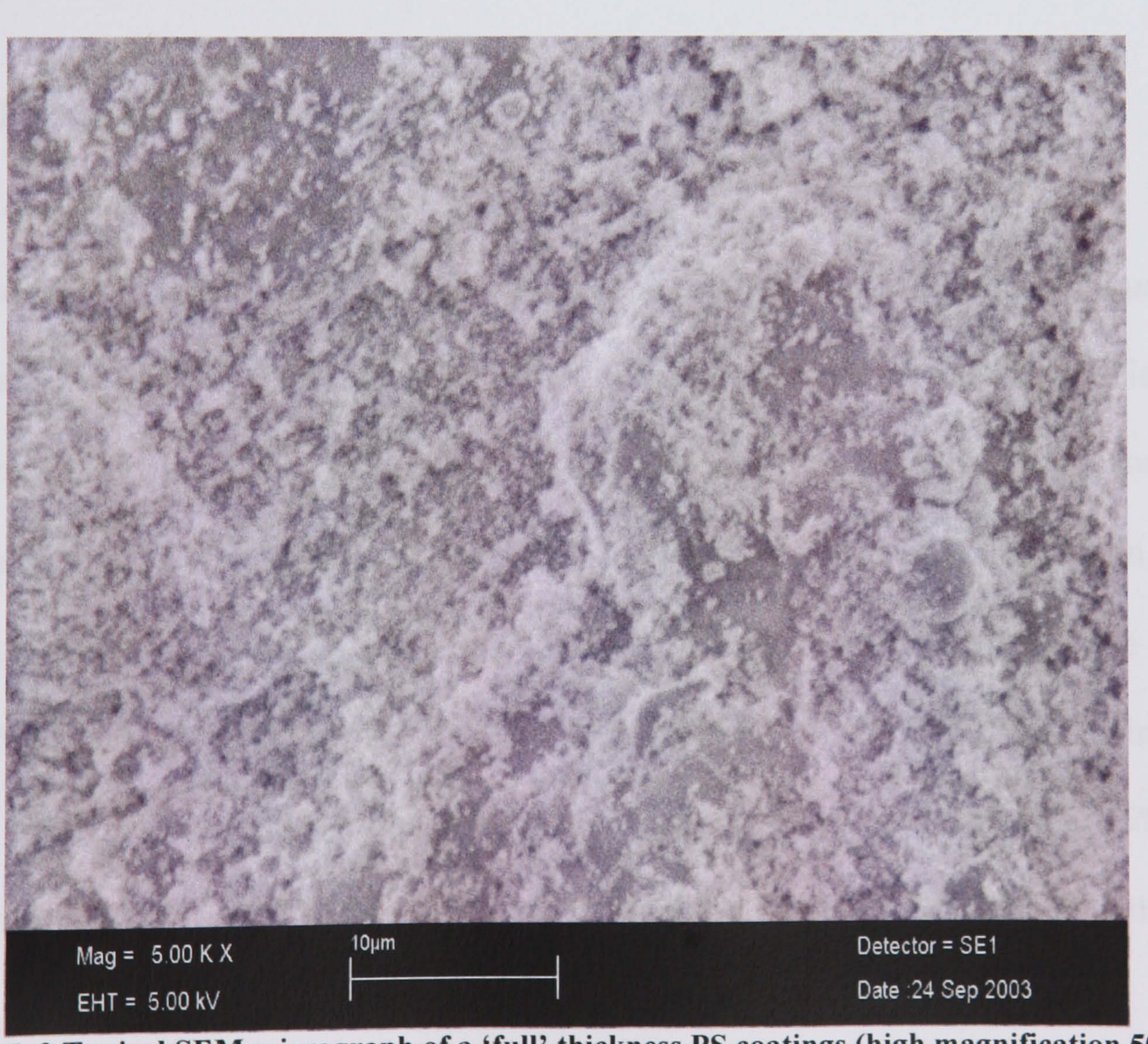

Figure 7. 9 Typical SEM micrograph of a 'full' thickness PS coatings (high magnification 5000X) showing unmelted powder particles.

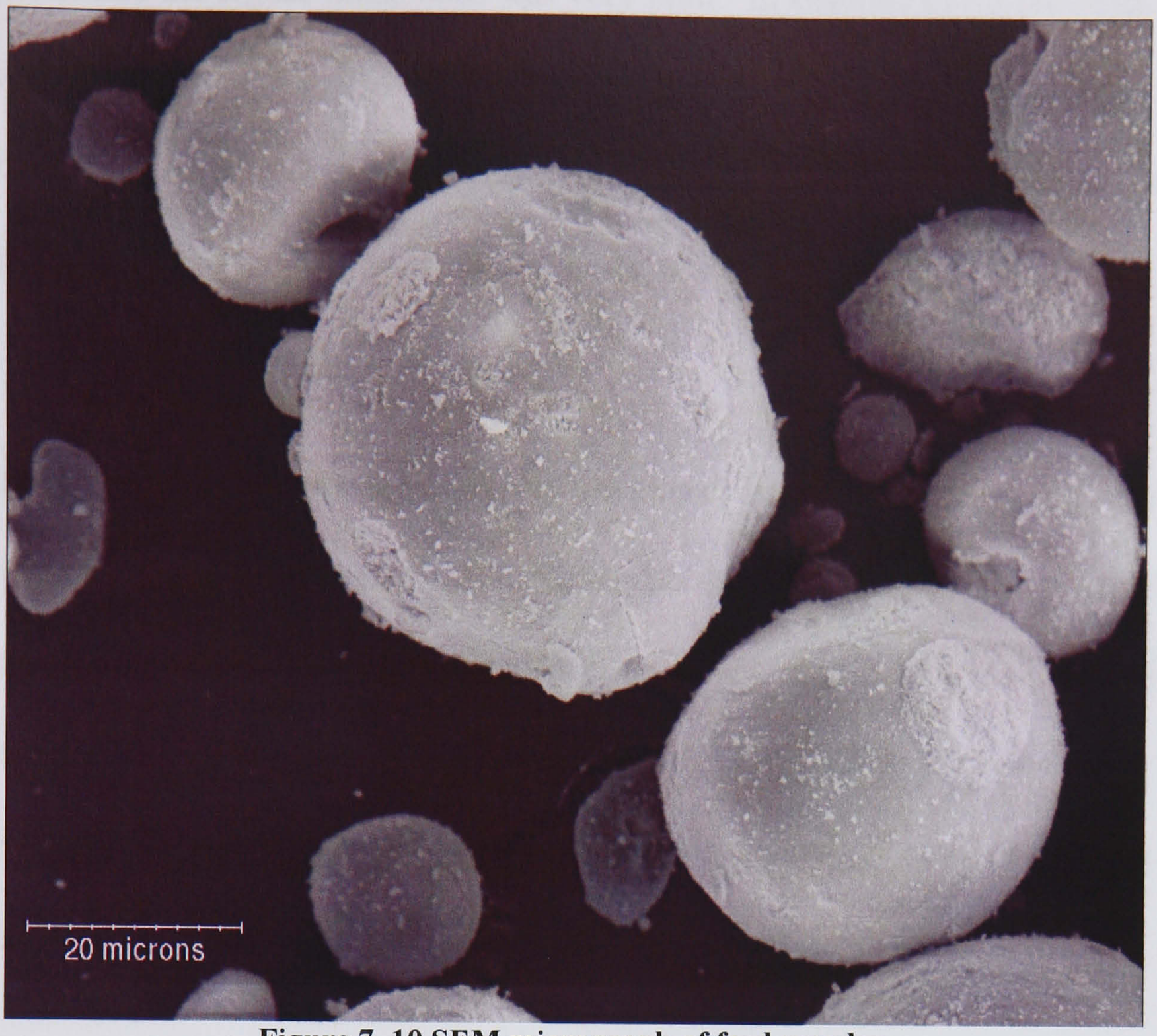

Figure 7. 10 SEM micrograph of feed powder.

7.1.3 Electrodeposited coatings.

7.1.3.1 Diffraction analyses

In total 40 ED samples were analysed by XRD and diffraction data collected found to be in agreement. A typical diffraction pattern from a randomly selected sample is presented in figure 7.11. The diffraction data is derived from a sample with a coating thickness of approximately 1.7 ± 0.17μm [253], which was measured from depth dependent data obtained by synchrotron diffraction.[6] The only crystalline phase present in the coating was HAP, but due to the limited thickness of the ED coating, peaks corresponding to the titanium substrate dominated the diffraction data (95% penetration depth). In addition, a number of the substrate peaks overlapped with the

[6] Kindly measured by Dr Anna Broadhurst, Department of Materials and Medical Sciences, Cranfield University

HAP peaks and the signal-noise ratio was very poor. In contrast to PS coatings, no significant 'background' halo was observed indicating a low ACP composition. This was observation was confirmed by quantitative phase analysis and a summary of the principal microstructural characteristics are summarised in table 7.4.

The ED coatings contained a significantly lower amount of ACP than the PS coatings. The lattice parameters showed small, but insignificant differences compared to the PS coatings. It was noted that the preferred orientation associated with the ED coatings was approximately 68% greater than the PS coatings. In addition, the peak corresponding to the (002) was 37% broader in the ED coatings compared to the PS coatings.

Peak broadening was further investigated by means of a W-H plot (figure 7.12). The poor quality (noise) and overlapping substrate peaks of the ED diffraction data meant that fewer peaks were viable to include in this analysis. Despite this disadvantage, it was possible to make a tentative estimate that peak broadening was due to both crystallite size and microstrain. However, it is difficult to draw any definitive, quantitative conclusions from the analysis with any certainty due to the limited number of suitable peaks available for analysis.

Source	Composition (wt%)	β [002] /°	a (Å)	c (Å)	PO index (arbitrary units)
ED	89± 0.5% HAP 11± 0.5% ACP	0.25 ± 0.011	9.40 ± 0.0024	6.90 ± 0.0021	2.23 ± 7.3%

Table 7. 4 Structural characteristics of typical ED coatings.

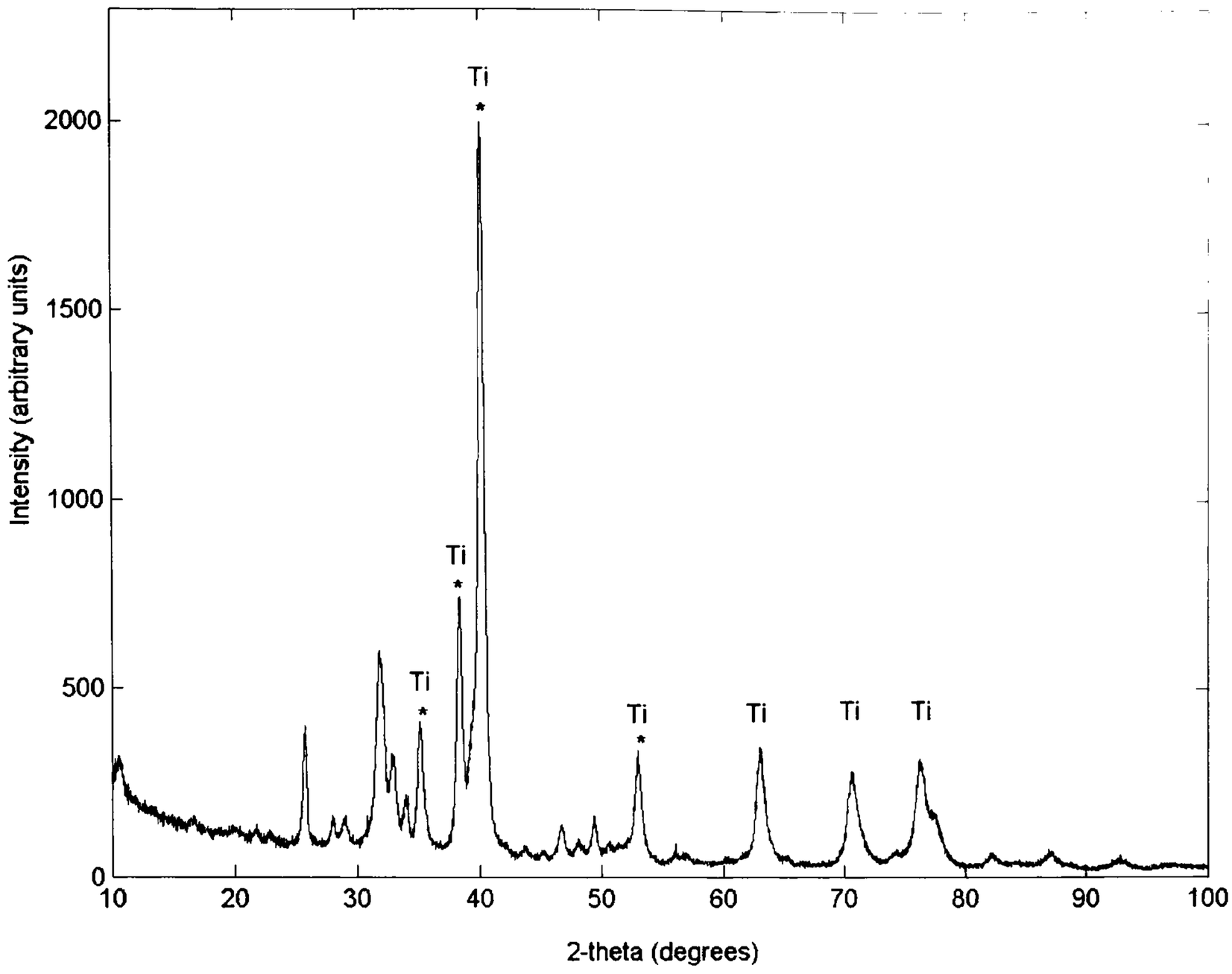

Figure 7. 11 Diffraction pattern of a typical ED coating (* denotes peaks corresponding to both Ti and HAP).

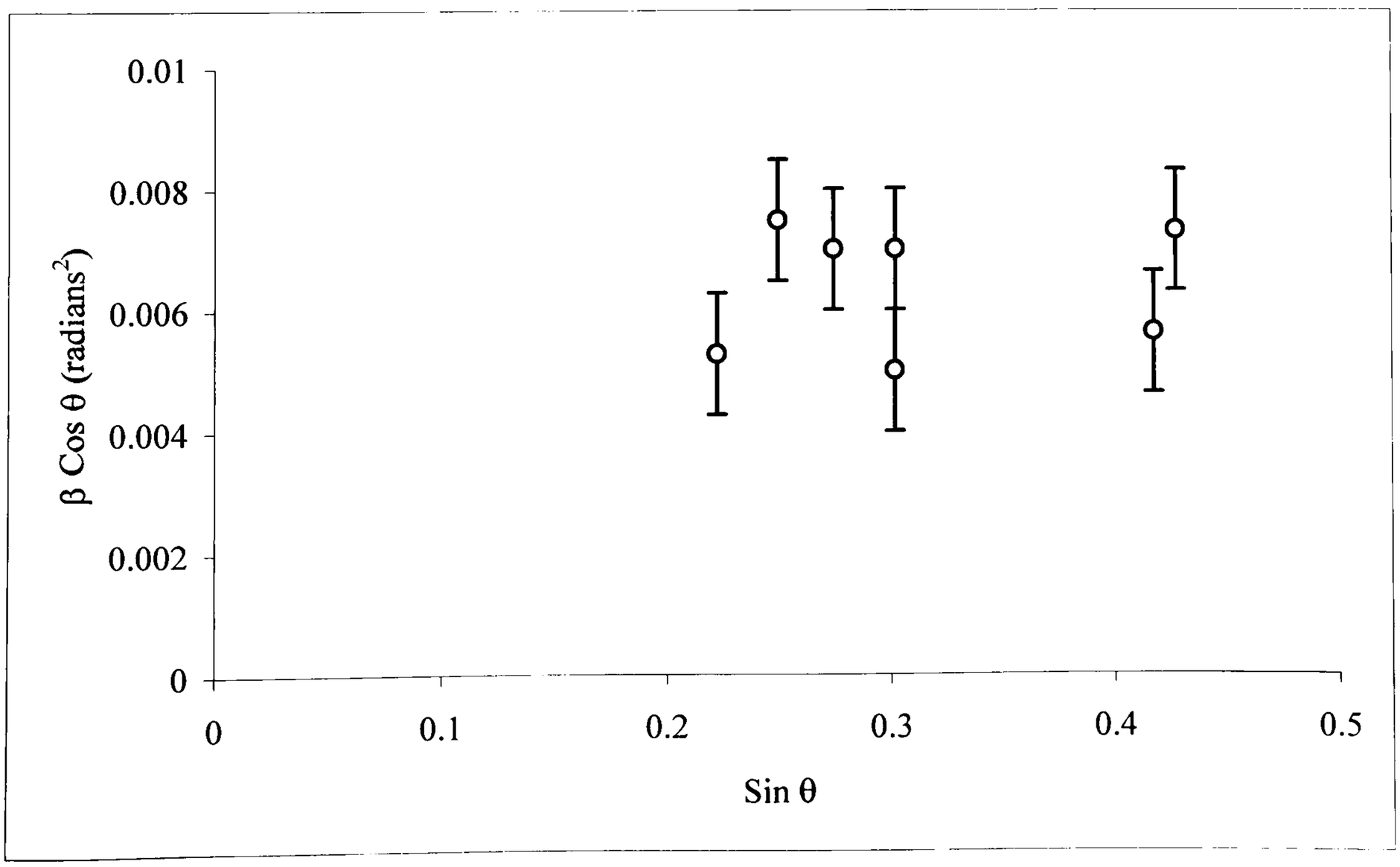

Figure 7. 12 Williamson-Hall plot of a typical ED coating.

7.1.3.2 Chemical analysis

Chemical analysis of the coatings of the coatings produced by ED was very limited within the boundaries of the analytical tools available for this investigation. The reasons for this are two-fold. Firstly, despite the coating having a thickness of ~1.7μm, adhesion to the substrate was good but it was not sufficient in mass to carry out any FTIR or Raman spectroscopy with any degree of accuracy. However, EDX analysis was conducted (figure 7.13) and Ca and P peaks corresponding to the coating were obtained. No peaks corresponding to other elements were observed indicating minimal or the complete absence of anionic or cationic substitution occurring in the apatite lattice during fabrication.

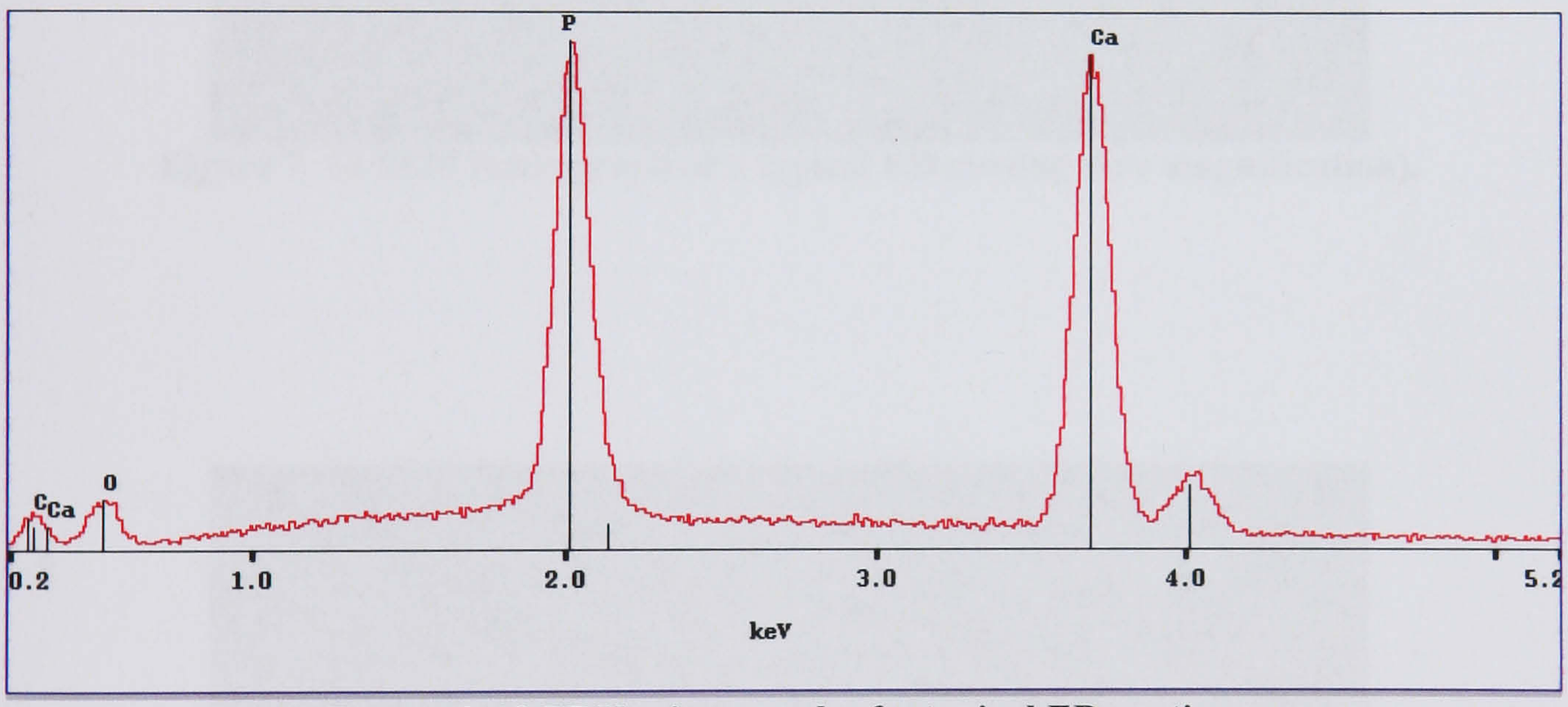

Figure 7. 13 EDX micrograph of a typical ED coating.

7.1.3.3 Morphological analysis

Examination of ED coatings at low magnification (figure 7.14) showed that the coating exhibited a relatively smooth morphology with bulbous structures (~15-90μm in diameter) embedded on the coating structure. These bulbous structures have been reported to be ACP [254]. At a high magnification (figure 7.15), it is apparent that the area between the bulbous structures is relatively smooth. It would appear that the

coating is formed by systematic layers of HAP as opposed to randomly placed HAP particles as seen in PS coatings.

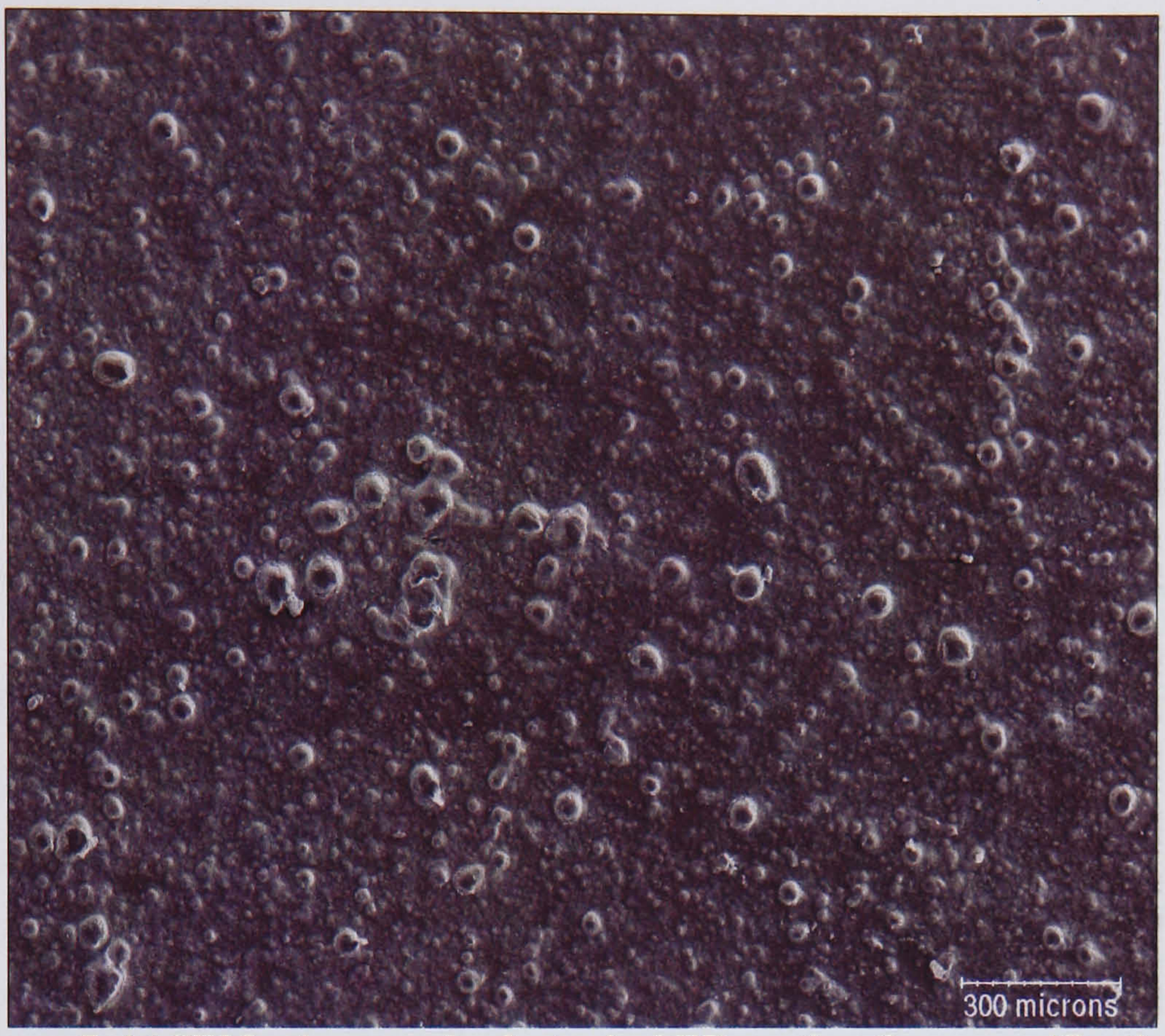

Figure 7. 14 SEM micrograph of a typical ED coating (low magnification).

Figure 7. 15 Typical SEM micrograph of ED coating showing the area between clusters of crystals.

7.1.4 HAP coatings on polymeric tape

7.1.4.1 Diffraction and chemical analysis

Diffraction and EDX analysis (table 7.5 and figures 7.16-17) confirmed the polymeric tape used in this experimental work had been coated with crystalline HAP. No extraneous phases or other elements were detected in the analyses. Data from the coatings produced with (OT-T) or without (OT-N) the use of a surfactant showed trivial differences in crystallographic properties. This indicates that the use of the surfactant has no significant effect on the phase composition of the coating produced ($P<0.05$). FTIR analysis for OT-T and OT-N coatings produced spectra typical of HAP as shown in table 7.5.

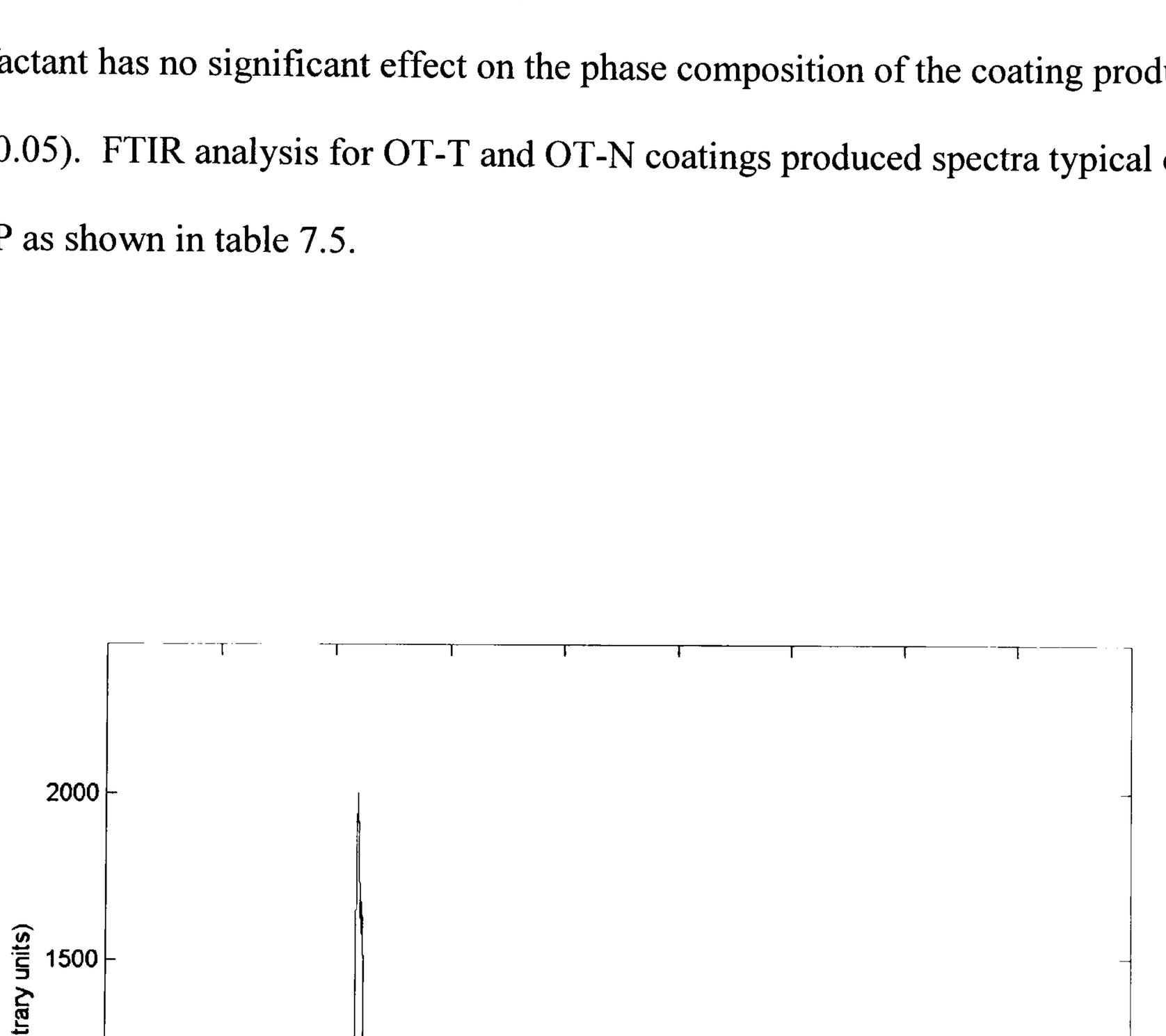

Figure 7. 16 Diffraction pattern of a typical OT-T coating scrapped from a test sample.

Source	Composition (wt%)	β [002] (°)	a (Å)	c (Å)
OT-T	91 ± 0.5wt% HAP 9 ± 0.5wt% ACP	0.27 ± 5.3 X 10^{-3}	9.432 ± 7.3 X 10^{-4}	6.892 ±5.7 X 10^{-4}
OT-N	93 ± 0.5wt% HAP 7 ± 0.5wt% ACP	0.28 ± 4.7 X 10^{-3}	9.432 ± 7.0 X 10^{-4}	6.892 ±5.5 X 10^{-4}

Table 7. 5 Principal characteristics of OT-T and OT-N coatings. The data are the mean values for a randomly selected sample ± error where n=6.

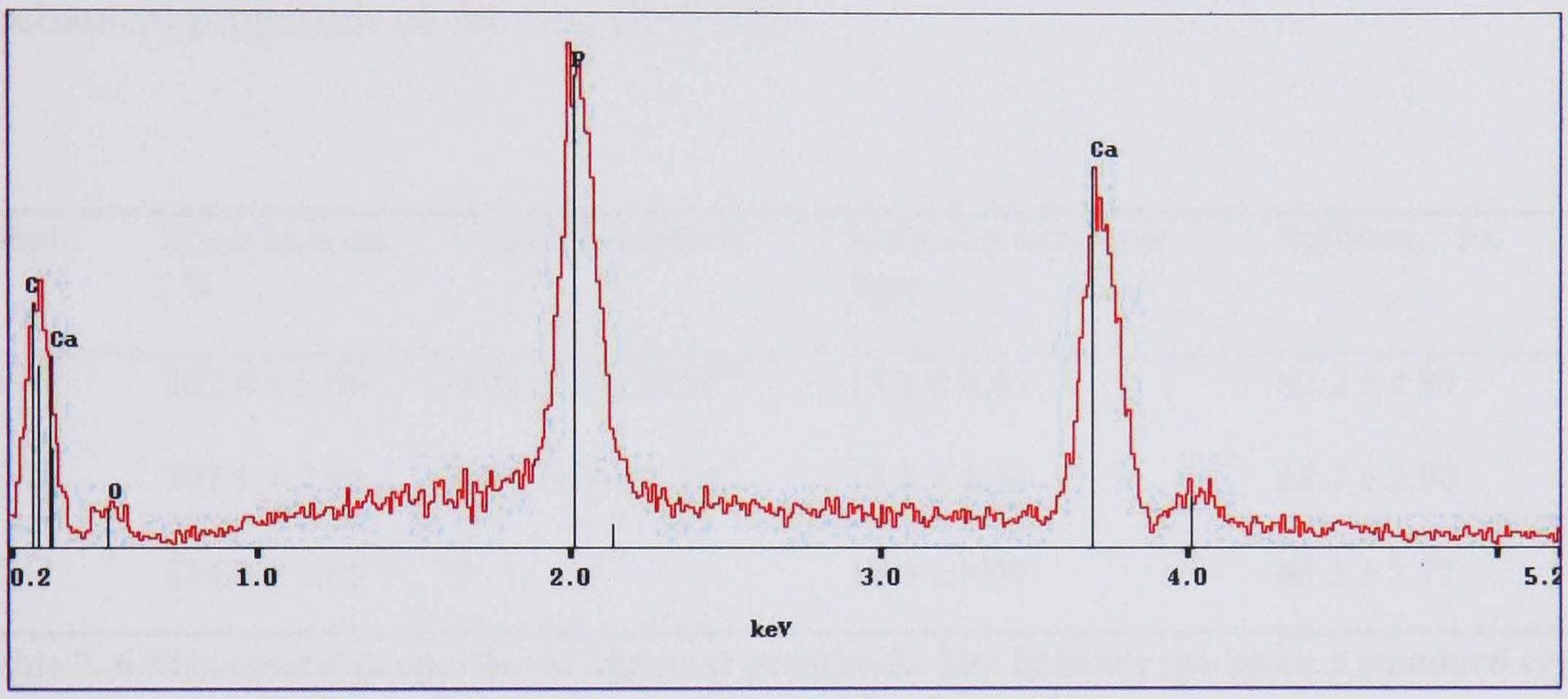

Figure 7. 17 EDX micrograph of a typical OT-T coating.

7.1.4.2 Morphological analysis

Figures 7.18-7.20 are SEM micrographs of the as-received polymeric tape (OT-C) compared to OT-T and OT-N samples. It can be seen that by using a surfactant, an even layer of HAP can be precipitated on the surface of the polymer. In contrast, the OT-N samples only had patches of HAP on their surfaces. Extensive manipulation of the OT-T and OT-N samples revealed that on average 76wt% and 57wt% of the coating stayed on the tape respectively. Figure 7.21 illustrates an OT-T sample undergoing extensive manipulation. Despite a percentage of the coating crumbling off during manipulation, the coating that was left on was strongly adhered to the

polymeric tape. It was difficult to further remove the remaining coating without the use of force. This was also the case for the coatings on the OT-N samples.

A summary of the mechanical properties of the OT samples is presented in table 7.6. Statistical analysis were carried out using ANOVA revealed that the use of a surfactant on the OT samples made a significant difference to the amount of coating adhering ($P<0.05$). The coating treatments had no significant effect on the mechanical properties of the tape ($P<0.05$).

Sample	Force to break / N	Coating weight /g	Extension to failure /mm	Stiffness / Pa
OT-T	802.6 ± 3.06	0.03 ± 1.1 X 10^{-3}	13.1 ± 0.86	62.2 ± 4.89
OT-N	797.1 ± 2.94	0.01 ± 4.1 X 10^{-4}	12.8 ± 0.34	62.7 ± 2.90
OT-C	814.8 ± 3.86	0	12.6 ± 0.49	65.3 ± 2.77

Table 7. 6 Mechanical properties of ligament prosthesis. The data are the mean ± standard error where n=6.

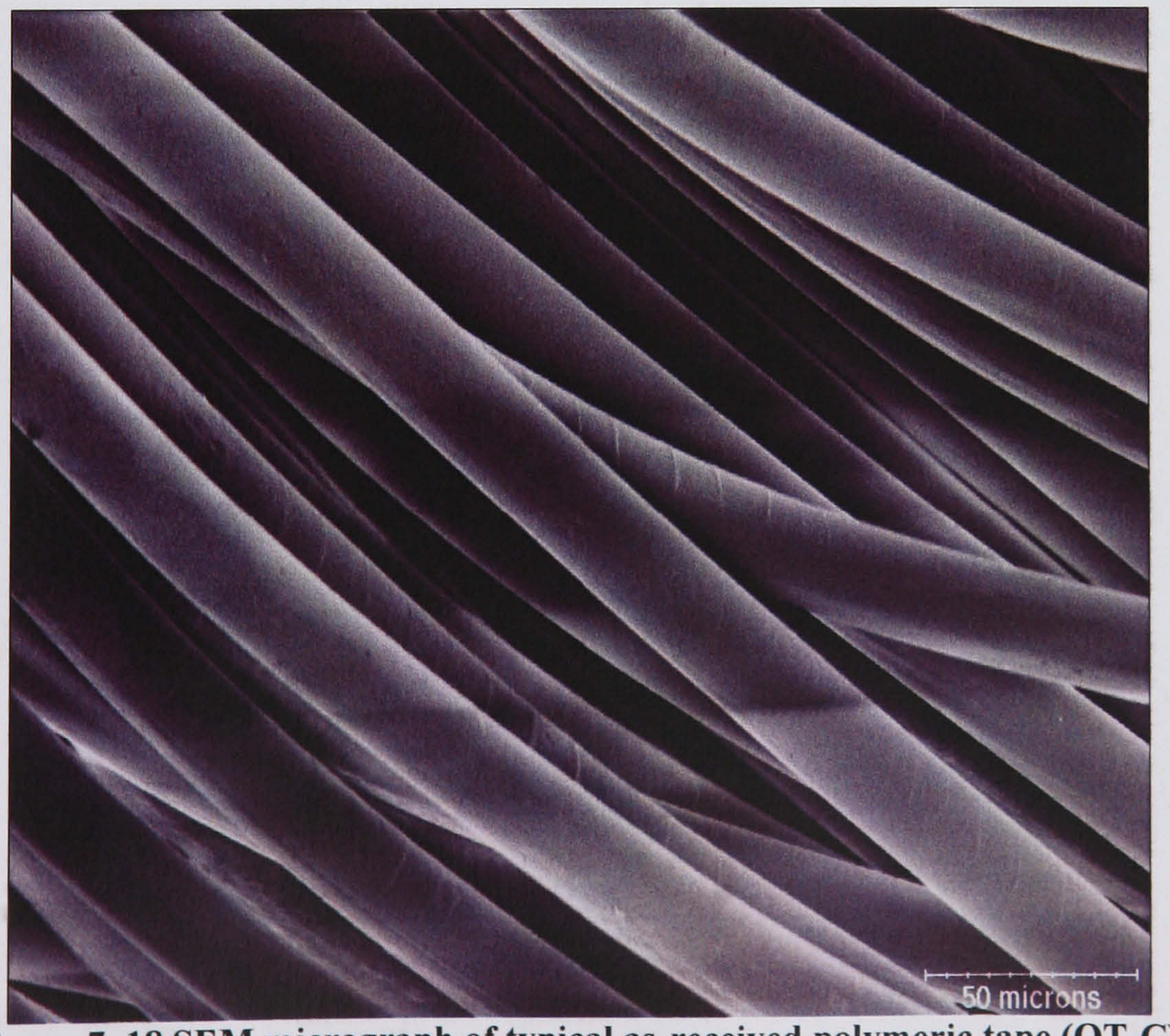

Figure 7. 18 SEM micrograph of typical as-received polymeric tape (OT-C).

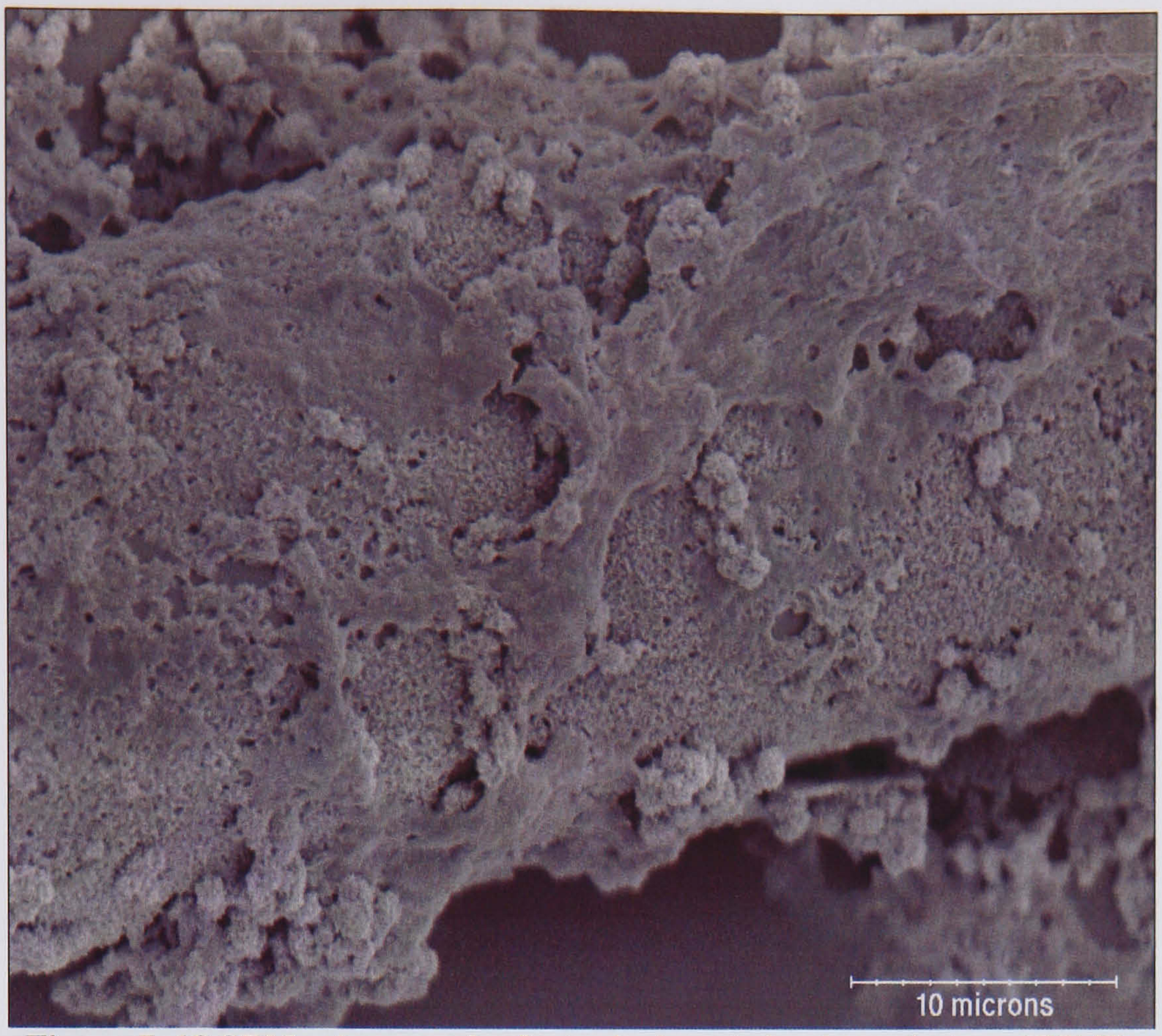

Figure 7. 19 SEM micrograph of a typical coated polymeric tape (OT-T).

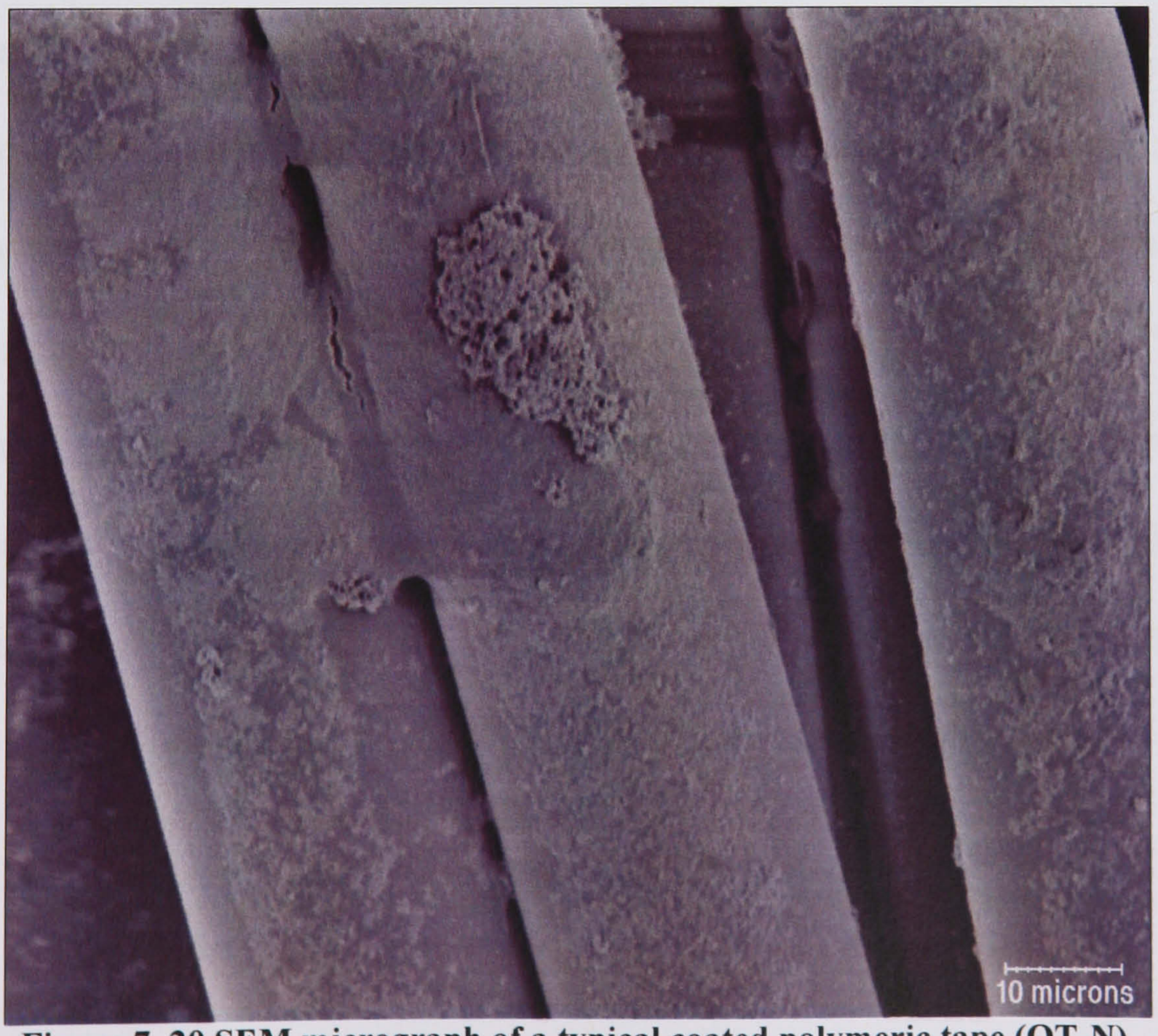

Figure 7. 20 SEM micrograph of a typical coated polymeric tape (OT-N).

Figure 7. 21 SEM micrograph of a typical coated polymeric tape (OT-T) undergoing extensive manipulation.

7.1.5 HAP precipitated at various temperatures.

Figure 7.22 shows the diffraction patterns of dried powders precipitated at different temperatures. All peaks corresponded to crystalline HAP, revealing that no extraneous phases had been produced. No significant amorphous background was visible on inspection of the peaks but whole pattern analysis (table 7.7) revealed that a small quantity of ACP (~5wt%) was present in the powder precipitated at 25° C. A small decrease in magnitude of the ACP content occurred with increasing temperature of synthesis. Furthermore, with increasing temperature of synthesis, the widths of the diffraction peaks became progressively narrower and more intense. This observation has been reported by Kumar *et al* [239] in similar characterisation studies.

A summary of the principal structural characteristics of the precipitated powders is presented in table 7.7. The lattice parameters show small changes indicating a possible deviation from stoichiometry. The a- and c-axis dimensions decreased and increased respectively. Because XRD analysis failed to reveal the cause of the small changes in lattice parameters observed, the precipitates were subjected to further FTIR analysis. The spectra obtained for each of the precipitates contained the typical bands associated with HAP. The precipitates also contained bands ($1400cm^{-1}$-$1500cm^{-1}$) attributed to B-type carbonate substitution in HAP similar to that observed in the spectra of the feed stock powder and PS coatings. However, in this case the intensity of the peaks corresponding to carbonate decreased with increasing temperature of synthesis, which is in agreement with other published data [60, 239]

W-H analysis (figure 7.23) revealed that peak broadening was predominantly due to crystallite size, although there was some broadening due to microstrain, particularly at low temperatures of synthesis. Further broadening analysis conducted on the [002] peak, revealed that with increasing temperature of synthesis, there was a systematic increase in crystallite size. In addition, lattice microstrain associated with the powdered samples decreased with increasing crystallite size and temperature of synthesis. Increased microstrain has previously been reported to be an inherent property of small crystallites produced by rapid crystallisation [131, 159].

Morphological examination of the powders revealed that with increasing temperature, there was an increase in particle size of the precipitated HAP (figures 7.24-26). With increasing temperature of synthesis the morphology of the HAP particles changed. At a low temperature of synthesis, a more needle-like morphology was observed but with

increasing temperature of synthesis, the particles became more spherical in nature. Such morphological changes with reaction temperature have been reported by Kumar *et al* [239] and Asaoka *et al* [255].

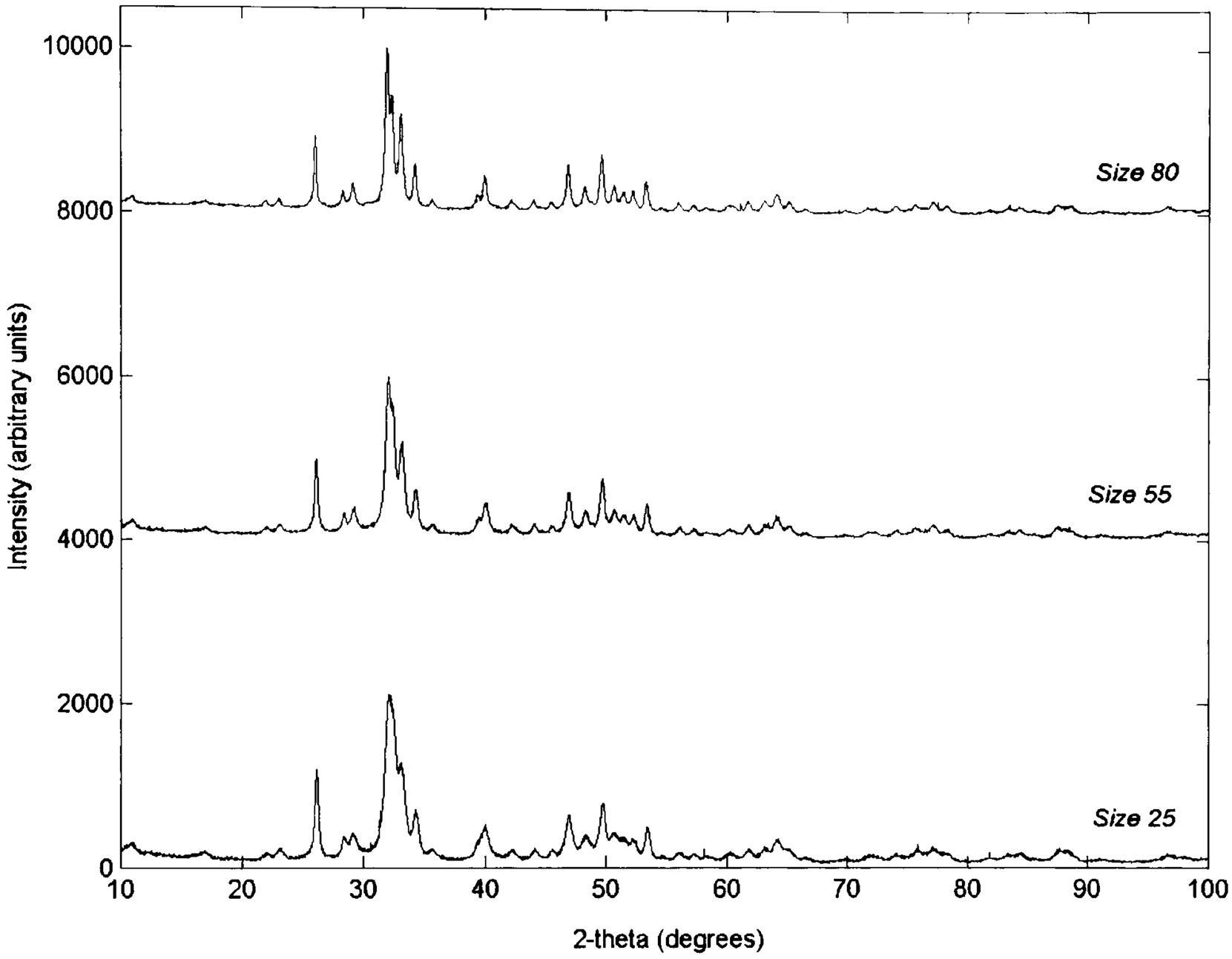

Figure 7. 22 Diffraction patterns of a series of HAP powders precipitated at various temperatures.

Sample	Composition	a (Å)	c(Å)	B [002] (°)	Crystallite size (Å)	Strain (%)
Size25	91 ± 0.5wt% HAP 9 ± 0.5wt% ACP	9.437 ± 4.9 X 10^{-4}	6.884 ± 7.4 X 10^{-4}	0.30 ± 5.8 X 10^{-3}	275 ± 21	0.25 ± 1 X 10^{-3}
Size55	95 ± 0.5wt% HAP 5 ± 0.5wt% ACP	9.430± 3.4 X 10^{-4}	6.891 ± 3.2 X 10^{-4}	0.26 ± 6.2 X 10^{-3}	388. ± 39	0.21 ± 1 X 10^{-3}
Size80	96 ± 0.5wt% HAP 4 ± 0.5wt% ACP	9.428 ± 2.2 X 10^{-4}	6.892 ± 2.2 X 10^{-4}	0.21 ± 6.2 X 10^{-3}	906 ± 68	0.16 ± 1 X 10^{-3}

Table 7. 7 Principal structural characteristics of powders precipitated at various temperatures.

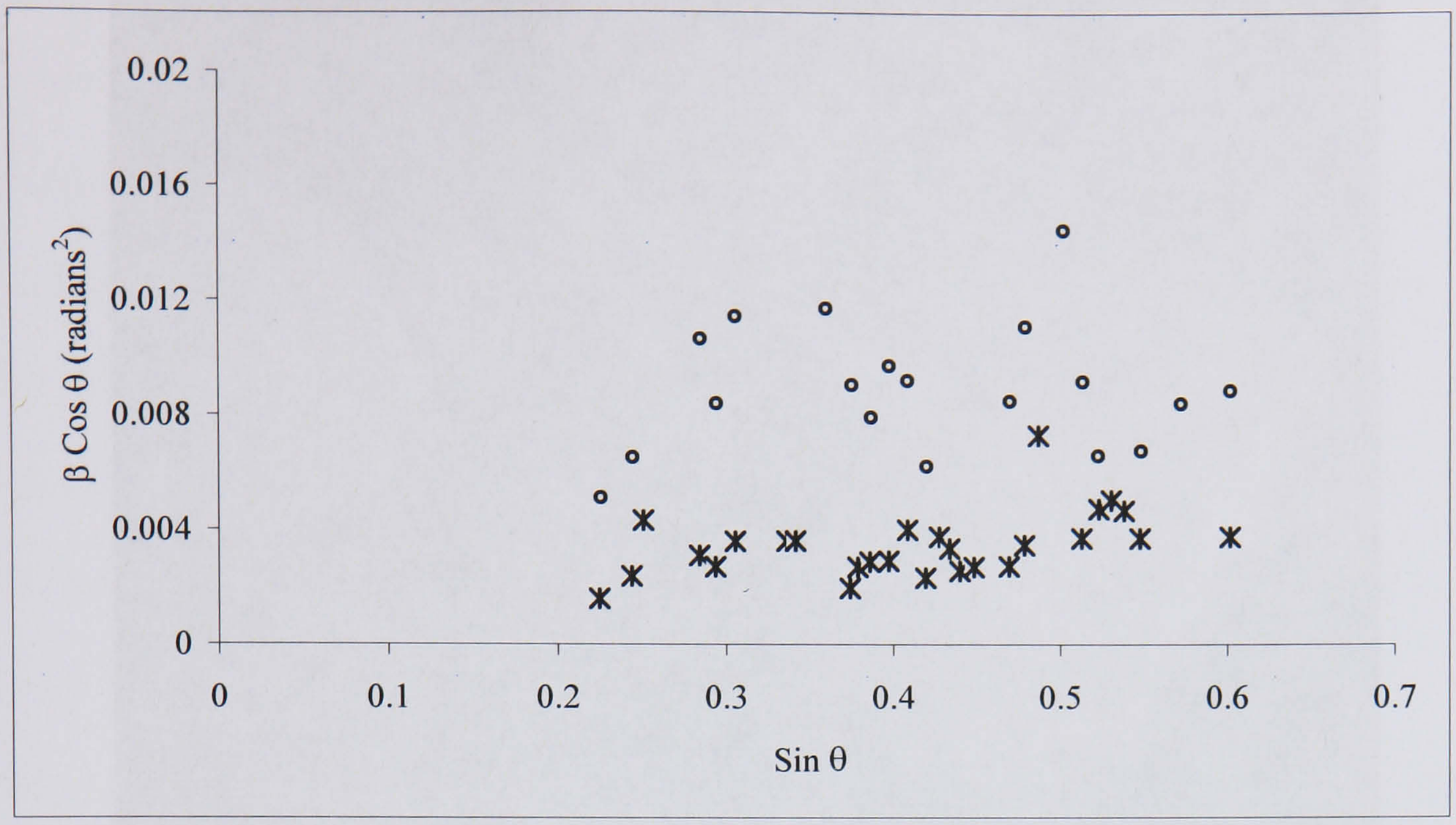

Figure 7. 23 Williamson-Hall plots of a series of HAP powders precipitated at various temperatures. Open circles and crosses denote 25°C and 80°C respectively.

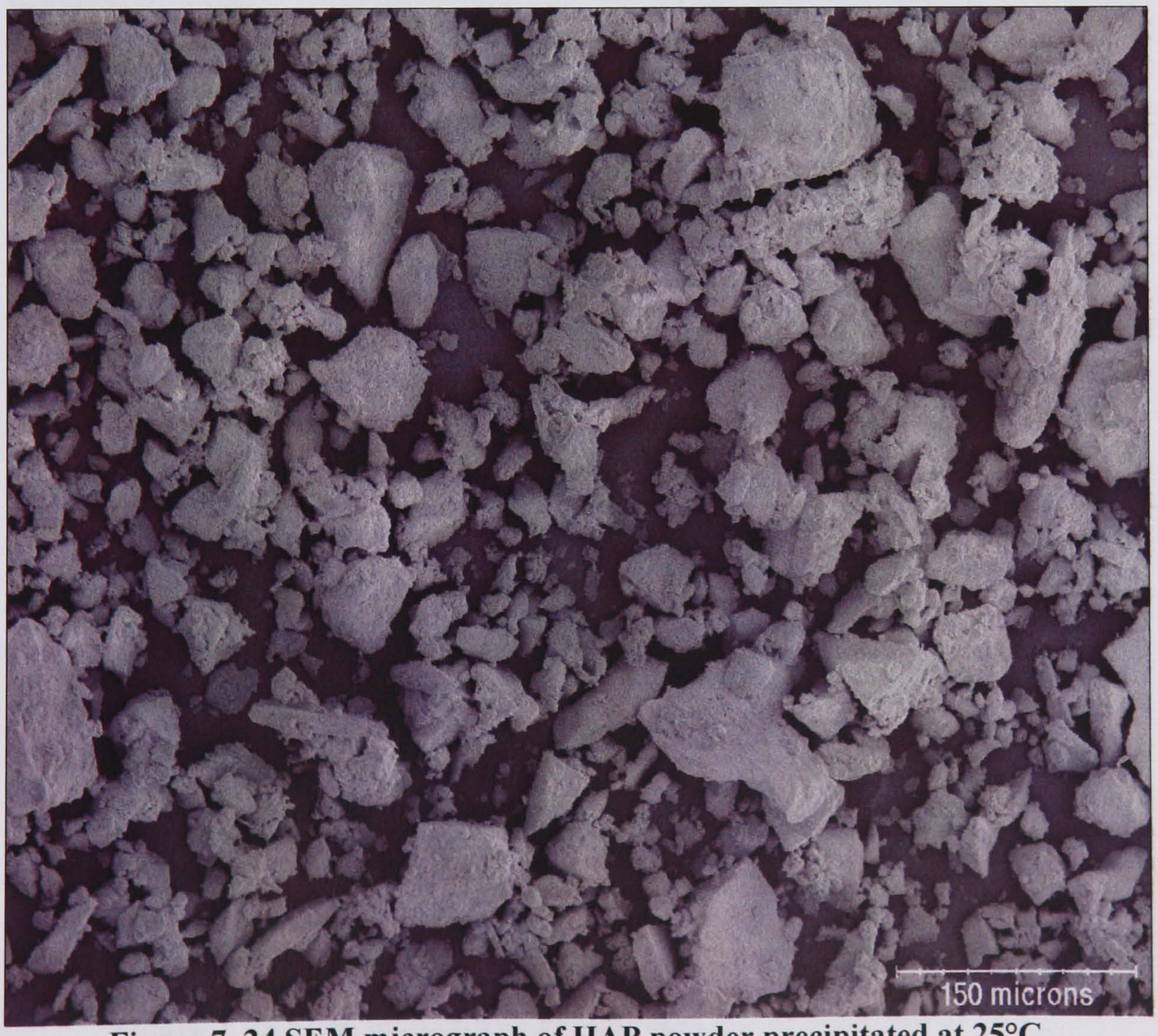

Figure 7. 24 SEM micrograph of HAP powder precipitated at 25°C.

Figure 7. 25 SEM micrograph of HAP powder precipitated at 55°C.

Figure 7. 26 SEM micrograph of HAP powder precipitated at 80°C.

7.1.6 HAP ball milled for various periods of time

Inspection of the diffraction patterns obtained from samples Strain1, Strain2 and Strain3 revealed that the diffraction peaks became broader with increasing time in the ball mill. Quantitative phase analysis (table 7.8) revealed that despite each sample having the same starting material, the amount of ACP content was highest in the sample Strain3. In addition, the lattice parameters of the powders decreased with increasing ball milling, which contradicts previous reports [240, 241]. Conversely, only the c-axis parameter of sample Strain2 increased, which is consistent with previous data [240, 241]. FTIR analysis produced spectra typical of crystalline HAP (figure 7.6) without the presence of bands corresponding to carbonate. This indicates that the small deviations in lattice parameters of the powdered samples are likely to be due to microstructural properties as opposed to deviations in stoichiometry.

W-H analyses revealed that with increasing time in the ball mill, the gradient of the W-H plot increased in magnitude, as did the intercept (figure 7.27). This infers that with increased milling, the lattice microstrain increased and the crystallite sizes decreased. An interesting observation was with increase milling time, there was a systematic increase in crystal anisotropy, which was evidenced by the increase in scatter in the W-H plot. The changes in size-strain properties of the powders were confirmed by further analysis of peak broadening associated with the [002] peak. Identical findings have been reported by in Vives *et al* [240] and Dutta *et al* [241] in size-strain analyses of ball-milled powders.

Sample	Composition	a (Å)	c (Å)	β [002] (°)	Crystallite size (Å)	Strain (%)
Strain1	100 ± 0.5wt% HAP	$9.447 \pm 3.2 \times 10^{-4}$	$6.886 \pm 2.8 \times 10^{-4}$	$0.24 \pm 7.2 \times 10^{-3}$	501 ± 38	$0.18 \pm 1 \times 10^{-3}$
Strain2	99 ± 0.5wt% HAP 1 ± 0.5wt% ACP	$9.446 \pm 2.5 \times 10^{-4}$	$6.886 \pm 2.9 \times 10^{-4}$	$0.26 \pm 6.6 \times 10^{-3}$	378 ± 28	$0.36 \pm 1 \times 10^{-3}$
Strain3	97 ± 0.5wt% HAP 2± 0.5wt% ACP	$9.442 \pm 4.3 \times 10^{-4}$	$6.885 \pm 2.1 \times 10^{-4}$	$0.30 \pm 5.7 \times 10^{-3}$	316 ± 23	$0.56 \pm 1 \times 10^{-3}$

Table 7. 8 Principal structural properties of HAP subjected to various degrees of ball milling.

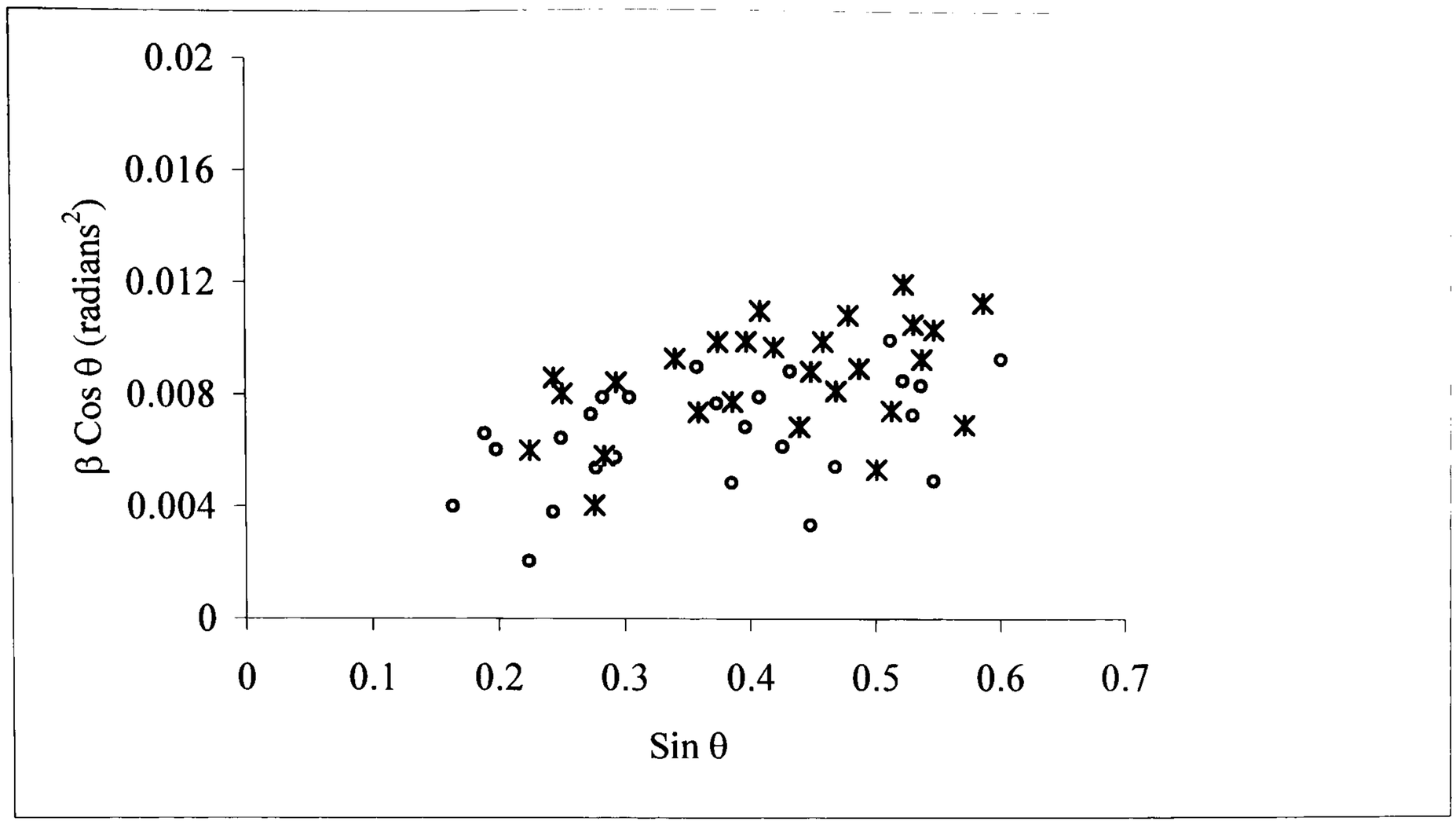

Figure 7. 27 Williamson-Hall plot of HAP powders subjected to various degrees of strain. Open circles and crosses denote sample strain1 and strain3 respectively.

7.1.7 HAP with varying carbonate content.

The principal structural and chemical properties of the carbonated apatites can be seen in table 7.9. FTIR analysis (figure 7.28) of the powders confirmed that the carbonate had occurred. Well-defined bands were seen in all samples at 1419cm^{-1} and 1464cm^{-1}, which are attributed to the stretching vibrations of carbonates [236, 248, 256]. The increases in intensity of these carbonate bands observed by FTIR were consistent with the increases in magnitude of carbonate content measured by wet chemical analyses. What's more, with increasing carbonate content, there was a decrease in the intensity of bands at 471 cm^{-1}, 562cm^{-1}, 603cm^{-1}, 960cm^{-1} and 1030cm^{-1}. The aforementioned peaks have previously been assigned to phosphate infrared modes [236, 257]. Therefore this confirms that carbonate substitution for phosphate (B-type) was the dominant substitution mechanism [256]. Conversely, a broad peak corresponding to A-type substitution was observed at 1550cm^{-1} in all samples. Evidence to show that a small degree of A-type carbonate substitution [256, 258] had occurred with increasing

B-Type substitution was seen by the slight decrease in intensity of the hydroxyl stretch vibration at 3569cm^{-1}.

As expected, there was a small decrease and increase in the dimensions of the a and c axis dimensions respectively with increasing carbonate content. This trend has been attributed to B-type carbonate substitution by previous authors [174, 216, 259, 260].

Visual inspection of the diffraction patterns revealed that there was an increase in peak broadening with increase in carbonate content. Qualitative analysis of peak broadening (figure 7.29) revealed that in each case peak broadening was due to both crystallite size and microstrain. The estimated magnitudes of microstrain and crystallite size increased and decreased respectively as evidenced by the increase in gradient and intercept on the W-H plot. Quantitative analysis of peak broadening associated with [002] peak revealed that with increasing carbonate substitution, the crystallite sizes of the samples decreased. The microstrain corresponding to each of the samples exhibited the reverse trend, which is consistent with previous work [174, 261].

Sample	Composition	Carbonate content (wt%)[7]	a(Å)	c(Å)	β [002] (°)	Crystallite size (Å)	Strain (%)
0.5CHA	98 ± 0.5wt% AP 2 ± 0.5wt% ACP	0.52 ± 0.08%	9.439 ± 3.2 X 10^{-4}	6.88 ± 4.4 X 10^{-4}	0.20 ± 5.2 X 10^{-3}	800 ± 60	0.29 ± 1 X 10^{-3}
2.3CHA	97 ± 0.5wt% AP 3 ± 0.5wt% ACP	2.25 ± 0.08%	9.437 ± 3.0 X 10^{-4}	6.89 ± 5.7 X 10^{-4}	0.25 ± 6.1 X 10^{-3}	402 ± 30	0.35 ± 1 X 10^{-3}
3.5CHA	96 ± 0.5wt% AP 4 ± 0.5wt% ACP	3.57 ± 0.08%	9.428 ± 2.5 X 10^{-4}	6.90 ± 6.8 X 10^{-4}	0.26 ± 6.3 X 10^{-3}	367 ± 28	0.44 ± 1 X 10^{-3}

Table 7. 9 Principal structural characteristics of HAP powders with varying carbonate content.

[7] Kindly measured by Clarkson Chromatography products Inc, USA.

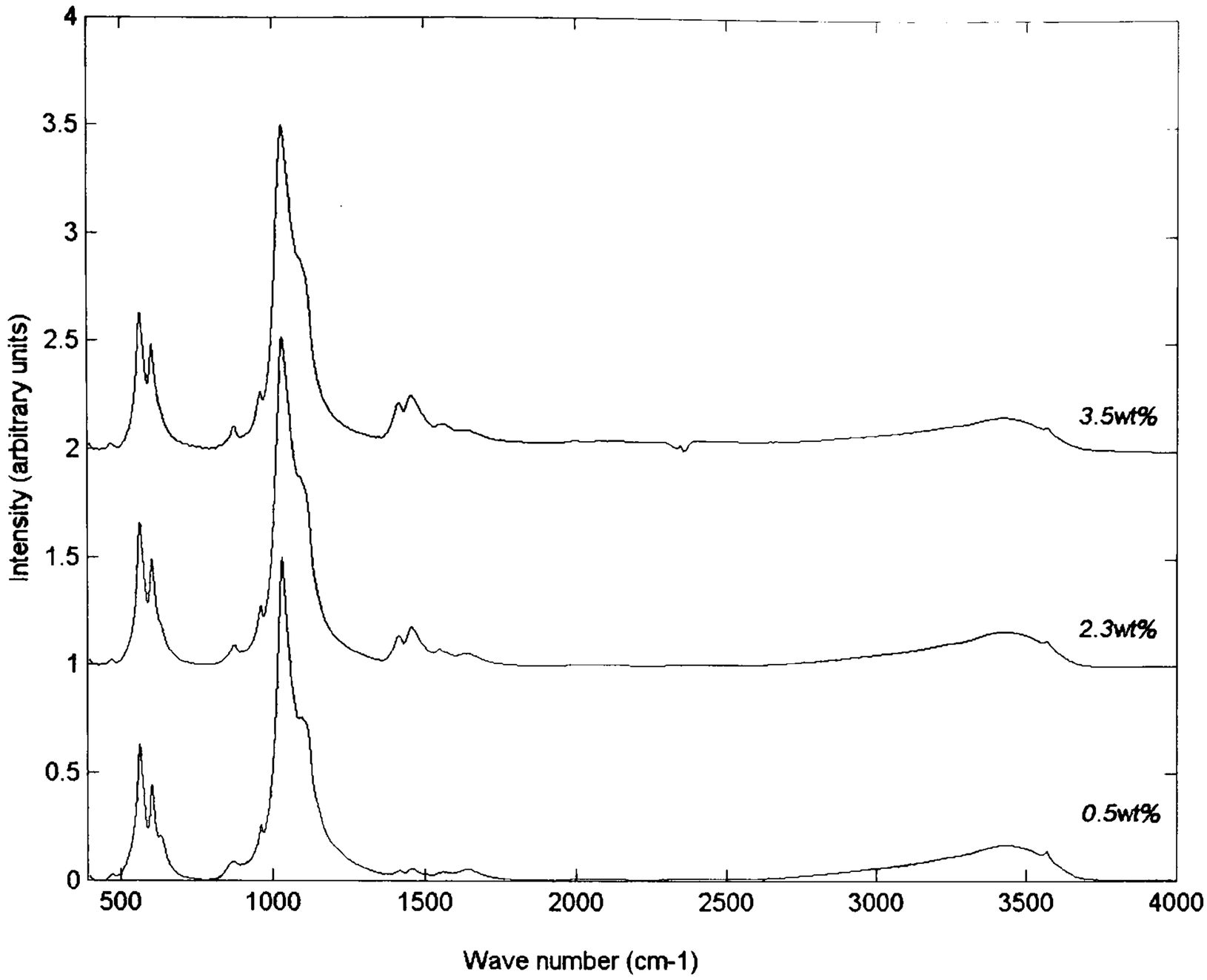

Figure 7. 28 FTIR spectra of a series of HAP powders with varying carbonate content.

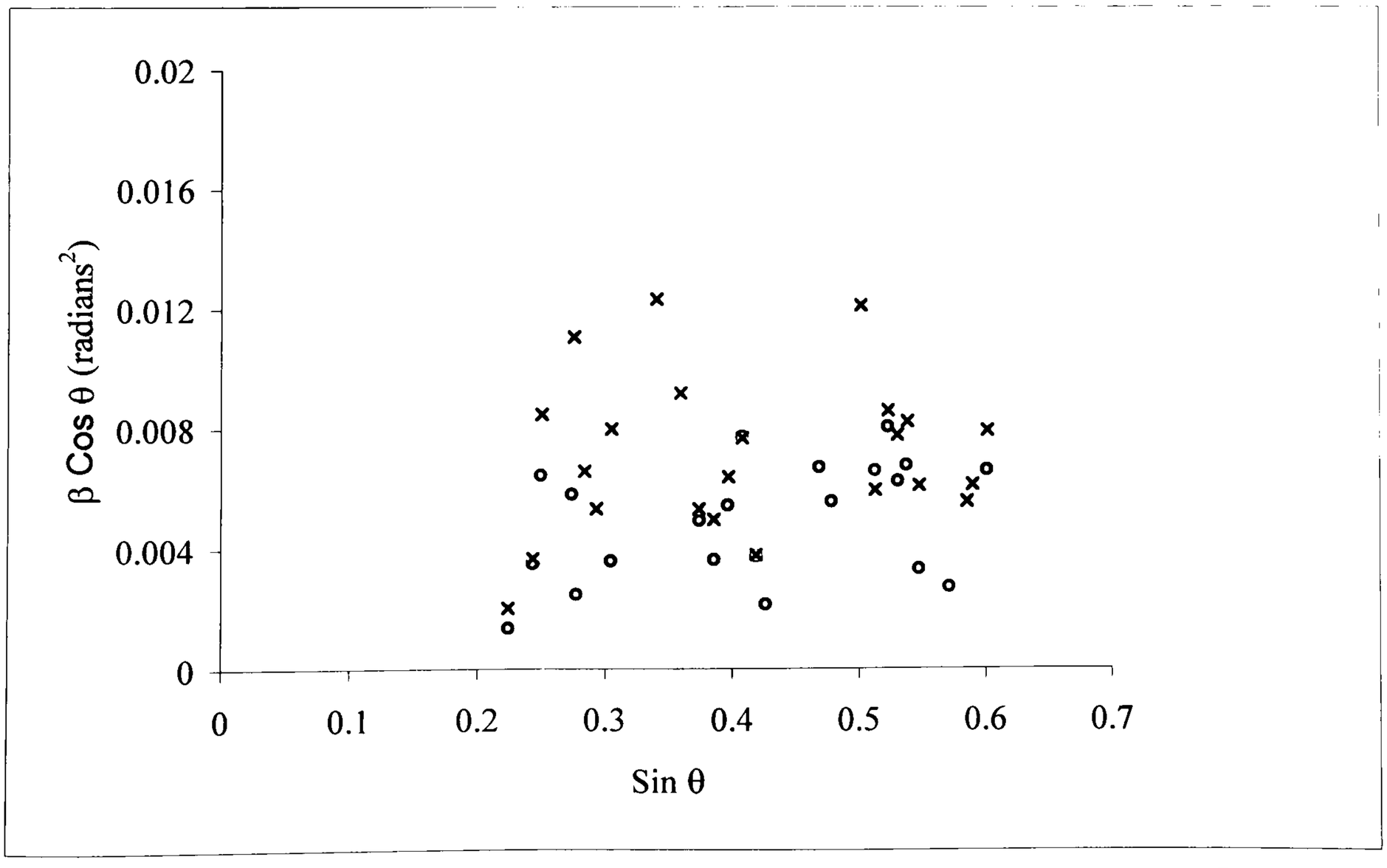

Figure 7. 29 Williamson-Hall plot of HAP powders with varying carbonate content. Open circles, closed and crosses denote samples with 0.5wt% and 3.5wt% carbonate respectively.

7.1.8 Summary

A novel methodology for structural characterisation of apatites has been validated by comparing values obtained using this technique with known compositions. The values for ACP content are in agreement within 4%.

Material from the surface and near substrate region of plasma sprayed HAP coatings have been characterised. It has been shown that the material near to the interface has a significantly higher ACP content in comparison to the surface material. The structural properties of both regions of the coating are consistent but show deviations from the initial pre-processed HAP feed powder. Size-strain analyses have revealed that diffraction peak broadening in the PS coatings is due to both crystallite size and lattice microstrain. Peak broadening associated with feedstock powder is due to crystallite size. The magnitude of crystallite size and microstrain obtained from size-strain analyses of the (002) peak is greater in the PS coatings than in the feed powder.

For the first time, electrodeposited HAP coatings have been structurally characterised. The ED coatings have a smaller crystallite size and greater degree of microstrain than the PS coatings. In addition there are small but insignificant differences in the lattice parameters of the ED and PS coatings. Of great importance is the fact that the ED coatings have a significantly higher degree of preferred orientation (PO index) compared to the PS coatings.

PET tape has been coated with crystalline HAP by means of a novel low temperature coating method. Coating coverage and adherence was greatly improved by the usage of a surfactant during the coating process. The surfactant used had no significant

effect on the chemical or structural nature of the HAP produce. No significant changes in the structural properties of the PET tape occurred on coating with HAP.

HAP powders precipitated at various temperatures have been characterised. Slight deviations in lattice parameters occurred due to contamination by carbonate ions. Crystallite size and microstrain increased and decreased respectively with increasing temperature of synthesis.

HAP powders that have been subjected to various periods of ball milling have been characterised. Small deviations in lattice parameters were noted, as were the respective decrease and increase of crystallite size and microstrain with ball milling.

HAP powders with varying degrees of carbonate substitution have been characterised. The dominant mode of carbonate substitution was B-type, although small traces of A-type substitution were present. Increased carbonate substitution resulted in the decrease of the a-axis dimension and an increase in the c-axis dimension. Crystallite size and microstrain decreased and increased respectively with increasing carbonate content.

7.2 *In vitro* behaviour of apatite coatings and powders

The *in vitro* behaviour and changes in microstructural properties of apatite coatings and powders has been investigated over a period of 21 days. The media used in this investigation was simulated body fluid, foetal calf serum and water (control). The rationale for using such media was to separate the effects of a high calcium phosphate concentration and plasma proteins respectively on the behaviour of the apatites. A static *in vitro* model has been used in this instance in order to allow for the measurement of changes in calcium and phosphate concentration in the media after each immersion period. However, a high media volume to apatite surface area ratio has been used to compensate for the static model. Media was only replenished after each period of immersion.

7.2.1 *In vitro* behaviour of plasma sprayed HAP coatings

Before immersion in the various media, the PS coatings under examination were washed thoroughly with deionised distilled water. This was to remove any surface contaminants present that may affect dissolution and precipitation of the coatings. An aseptic technique was employed in preparing the samples for immersion to avoid bacterial or viral contamination. The conditions of incubation can afford the growth of biological contaminants that can raise the pH level of the media and promote accelerated dissolution. After each period of immersion, the samples were washed thoroughly to remove any traces of media that may affect analysis of the coatings and allowed to dry in air.

7.2.1.1 Phase quantification and microstructural analyses

Figures 7.30-32 are typical diffraction patterns for test samples incubated in the different media for an increasing number of days. As with all samples, the data measured prior to immersion indicated a mix of crystalline and amorphous materials. No Bragg peaks from the titanium substrate were apparent from the depth where 99% of the signal derives (~20μm). After the first day of immersion in SBF, a sharp peak corresponding to calcite appeared in the diffraction data. It likely that formation of calcite derived from the HCO_3^- ions in the SBF. With immersion time the intensity of the calcite peak decreased and was not present by day 14. On day 7, there was a distinct change in the shape of the peaks of HAP. Each Bragg maxima appeared to develop 'tails' that increased in the relative magnitude with increasing immersion time. This feature was also apparent in the Bragg maxima of the samples incubated in water and FCS respectively, although less pronounced. This change in shape of the Bragg maxima has been interpreted as the formation of a nanocrystalline HAP (nano-HAP) phase. In addition, the amorphous halo observed in the as-received samples decreased in visibility with immersion time for all of the samples. This was most pronounced in the SBF samples.

In this investigation nano-HAP has been included in the structural models necessary for whole pattern fitting. The model used is in appendix 4. Further justification for the existence of the nano-HAP phase is presented in figure 7.33 where a substantially better fit exists between observed and calculated data on inclusion of the nano-HAP phase. The R_{wp} values of the refinements with or without the inclusion of the nano-HAP phase are 6.78 and 10.60 respectively, further confirming the improvement in

the fit. During each analysis, the lattice parameters, crystallite size and scale factors for the nano-HAP phase were refined. The model used was that of HAP.

Changes in phase composition and lattice parameters of the PS coatings in test media are demonstrated in figures 7.34-7.38. The results are based on the inclusion of all HAP, ACP and nano-HAP phases in the whole patterning fitting procedure. The HAP and ACP scale factors have been corrected for the absorption due to nano-HAP using a thickness estimate from the mass measurements of the coating and assuming a uniform coating. Density of the nano-HAP was calculated from the unit cell contents and refined lattice parameters of the nano-HAP.

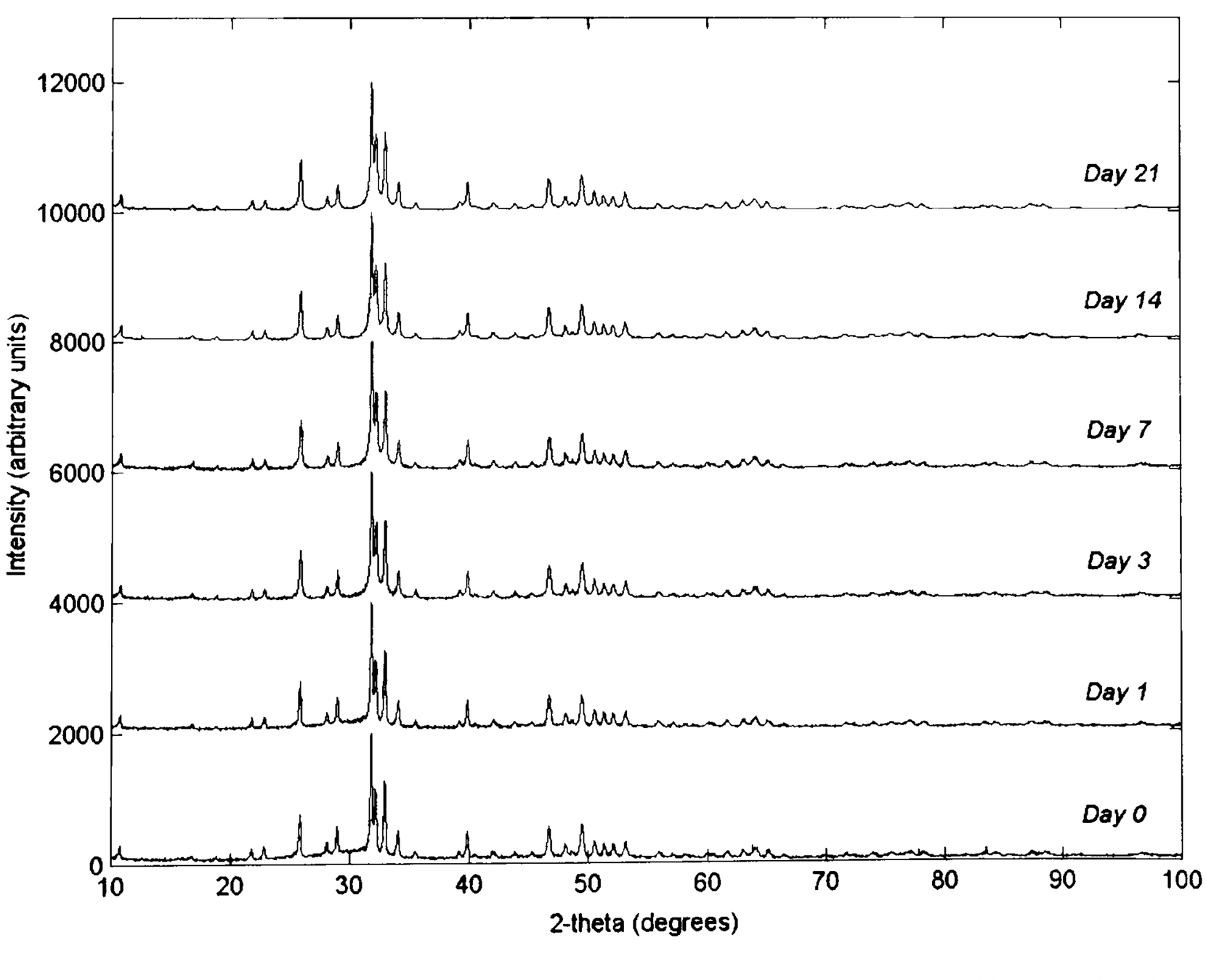

Figure 7. 30 Diffraction patterns of PS coatings after various periods of immersion in water.

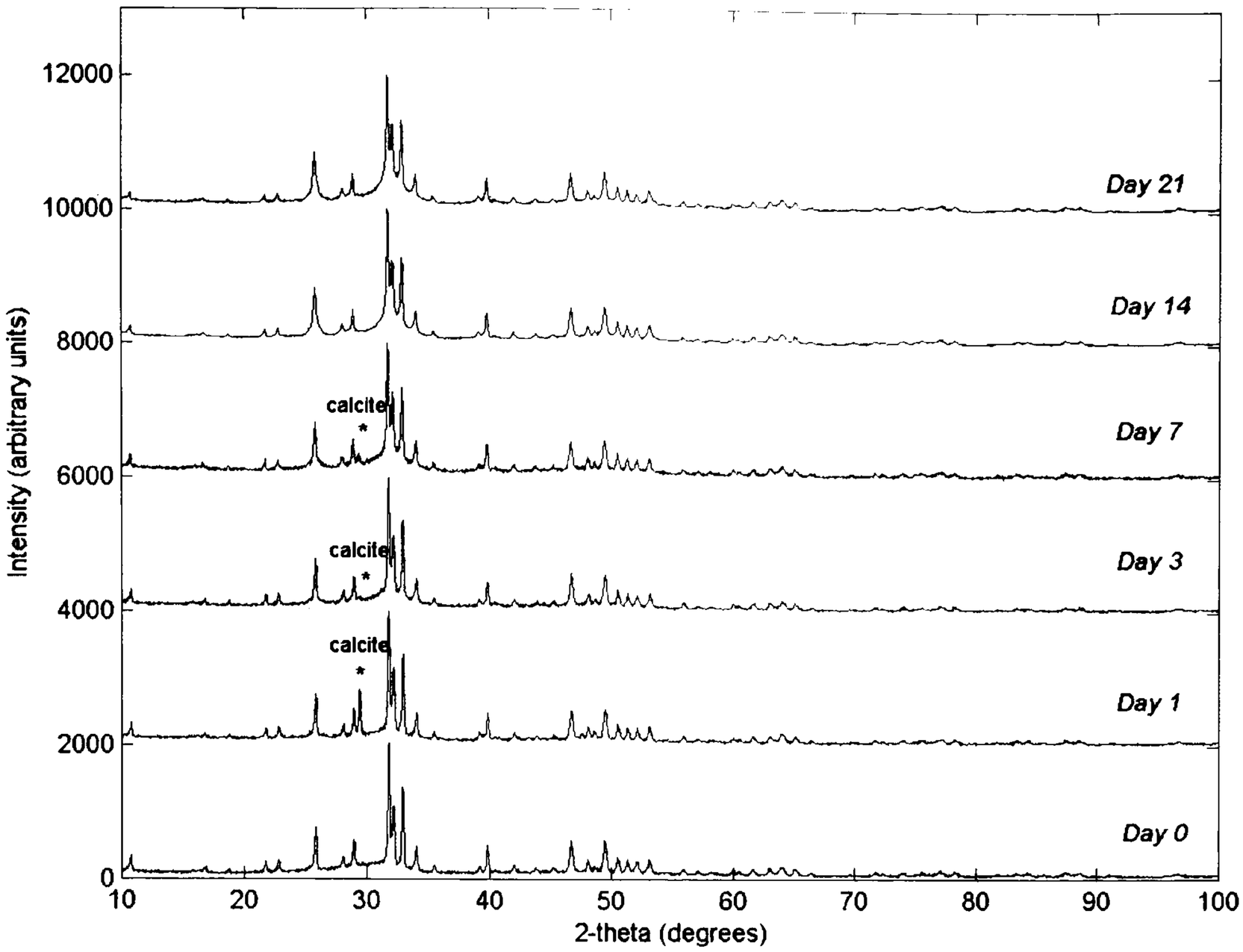

Figure 7. 31 Diffraction patterns of PS coatings after various periods of immersion in SBF.

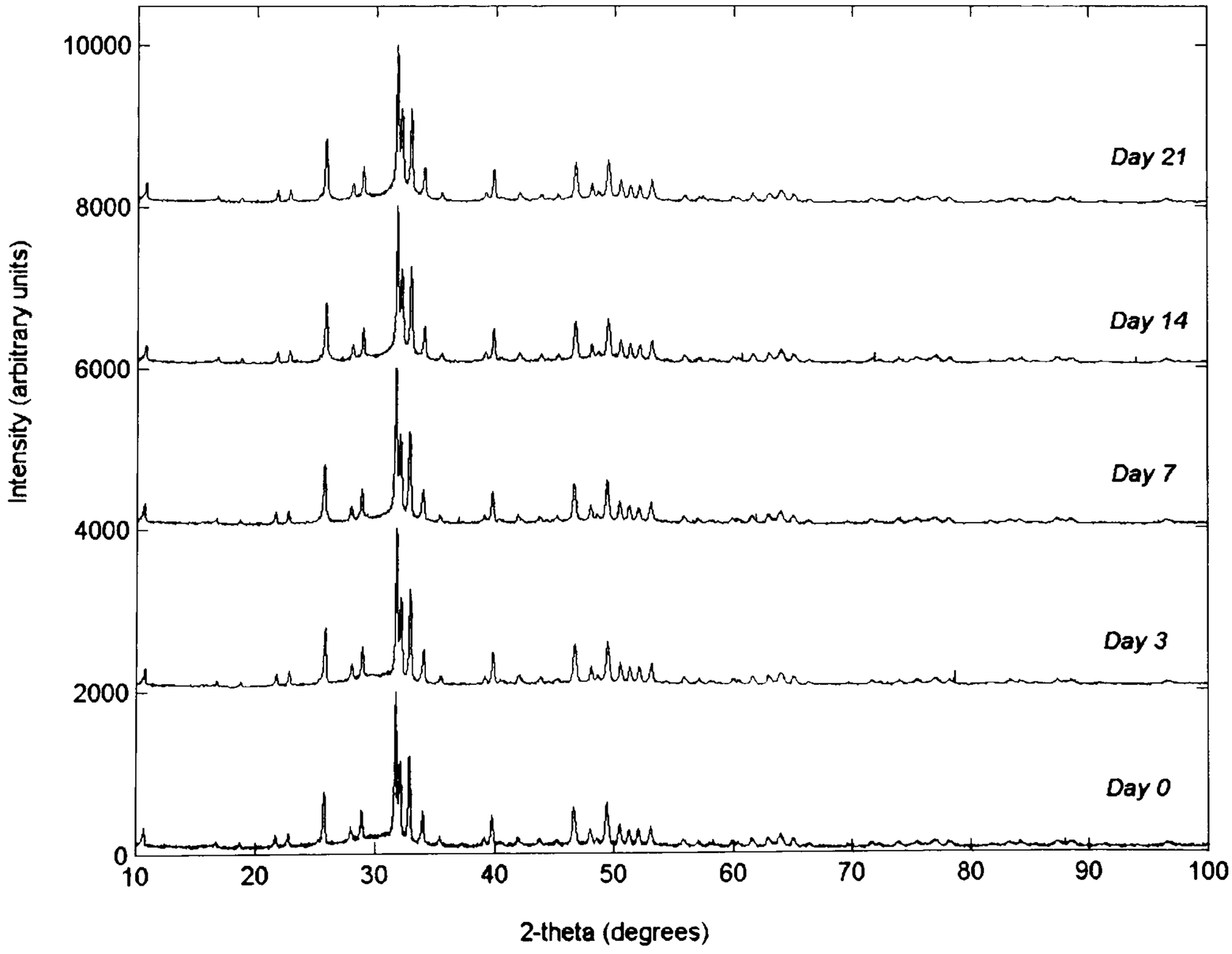

Figure 7. 32 Diffraction patterns of PS coatings after various periods of immersion in FCS (day 1 has been omitted due to similarity to day 0).

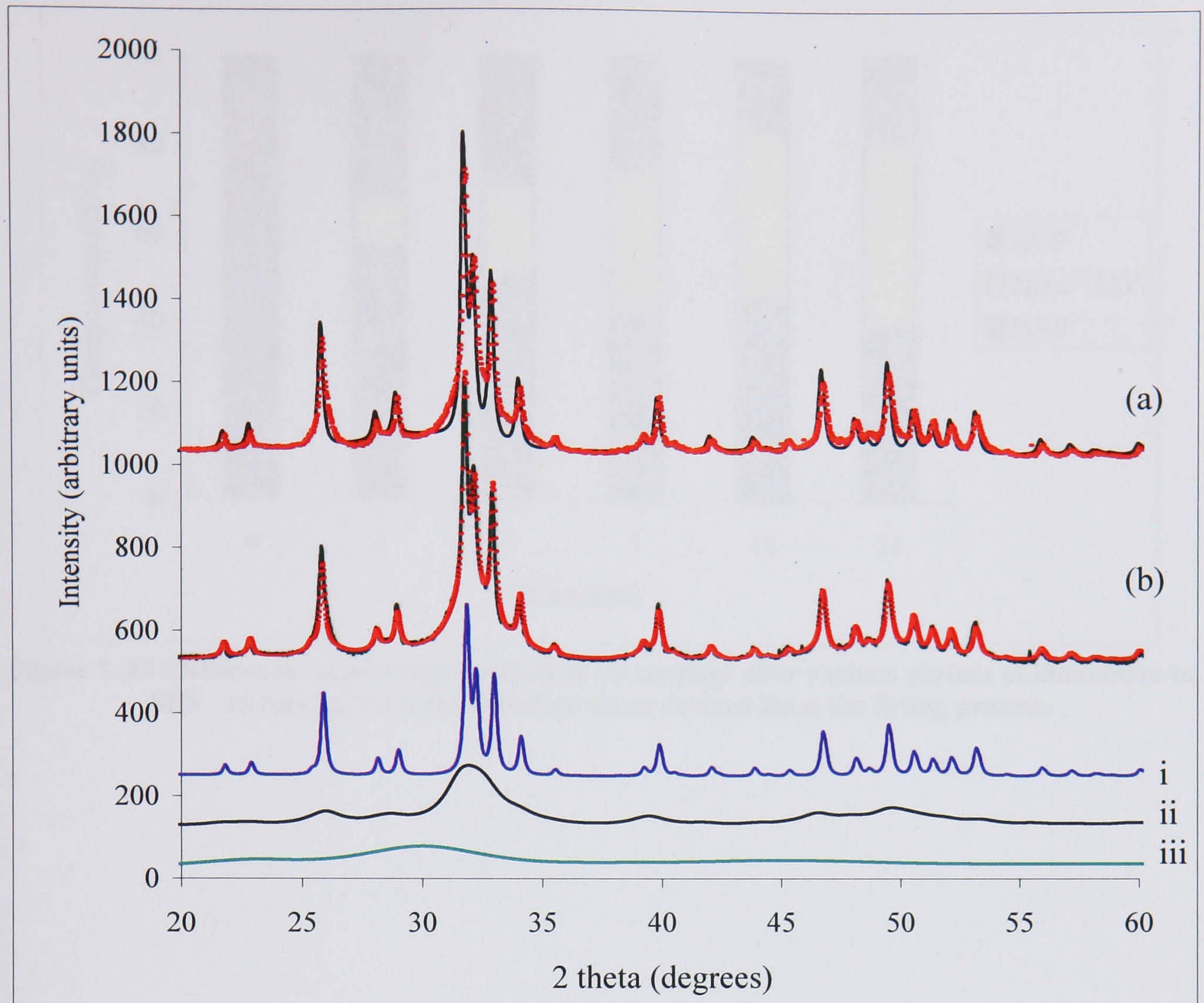

Figure 7. 33 a) Observed and calculated diffraction data (overlaid) corresponding to a PS coating following immersion in SBF for 21 days. The calculated data is derives from the sum of crystalline and amorphous components (Rwp=10.60). b) Observed and calculated diffraction data (overlaid) from the sum of i) crystalline ii) nano-HAP and iii) amorphous components (R_{wp} ~6.78).

Figure 7. 34 Changes in relative composition of PS coatings after various periods of immersion in water. Error bars are the standard error derived from the fitting process.

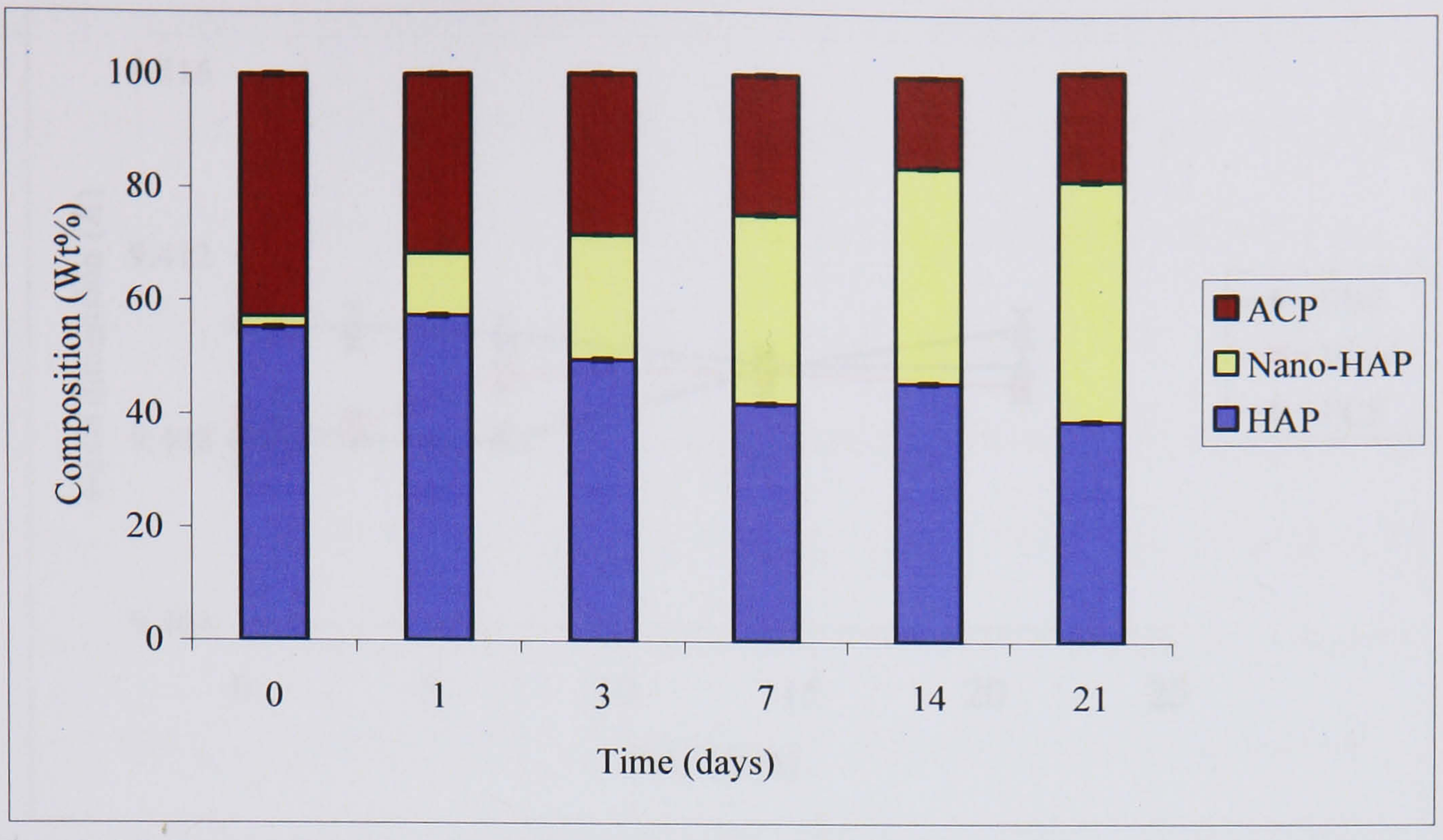

Figure 7. 35 Changes in relative composition of PS coatings after various periods of immersion in SBF. Errors bars are the standard error derived from the fitting process.

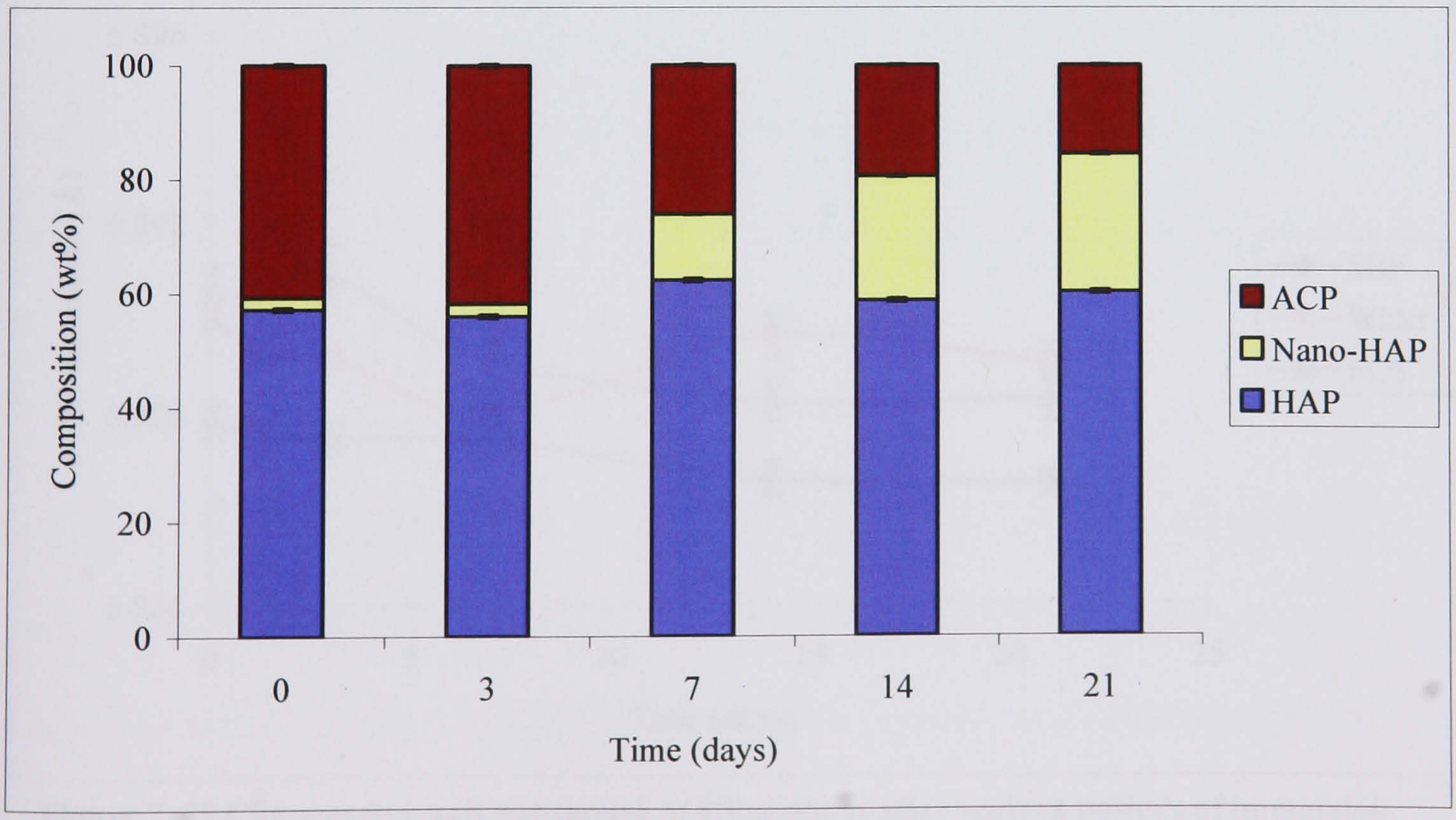

Figure 7. 36 Changes in the relative composition of PS coatings after various periods of immersion in FCS. Error bars are the standard error derived from the fitting process.

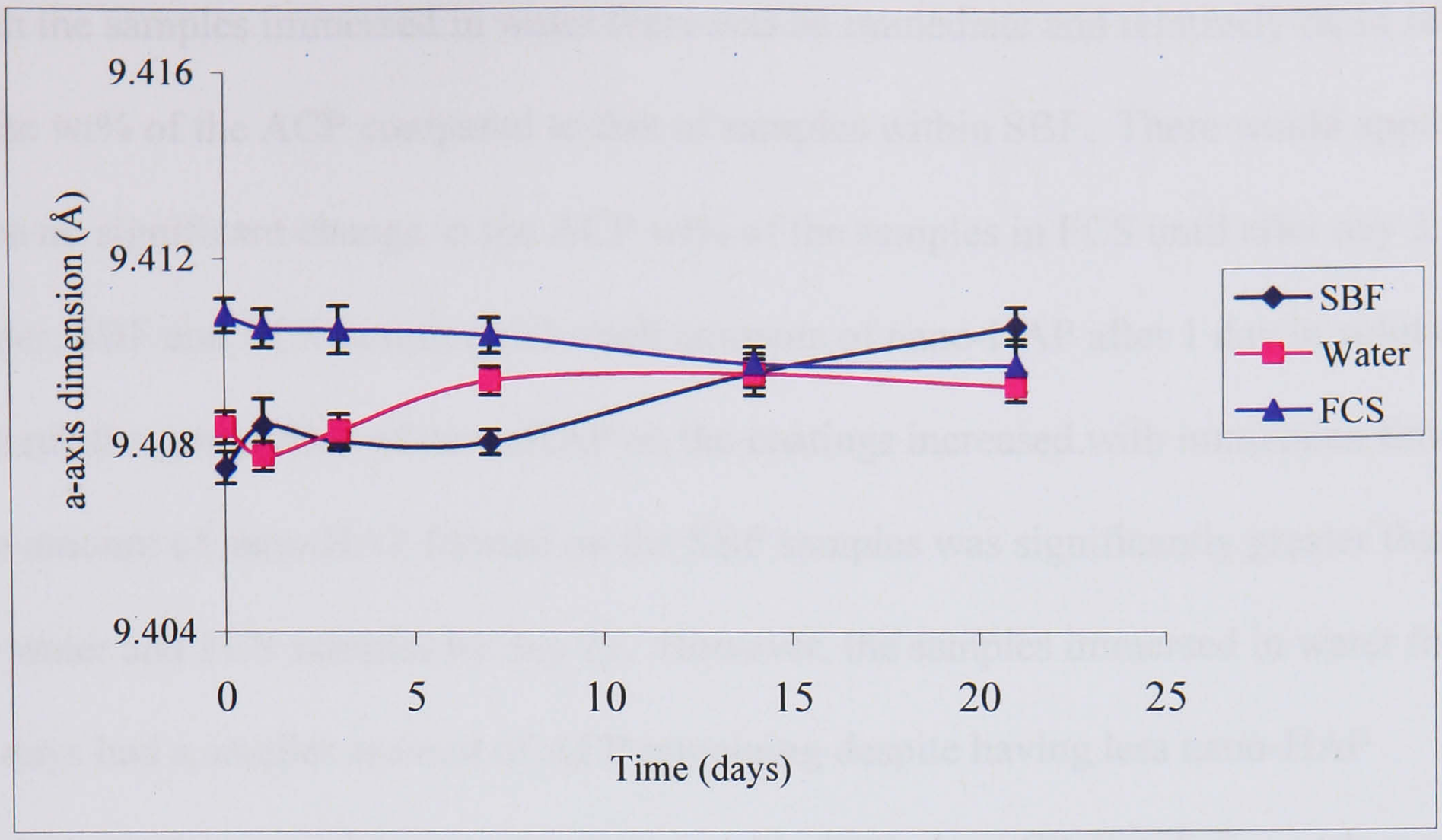

Figure 7. 37 Changes to a-axis parameter of PS coatings after various periods of immersion. Error bars are derived from the fitting process.

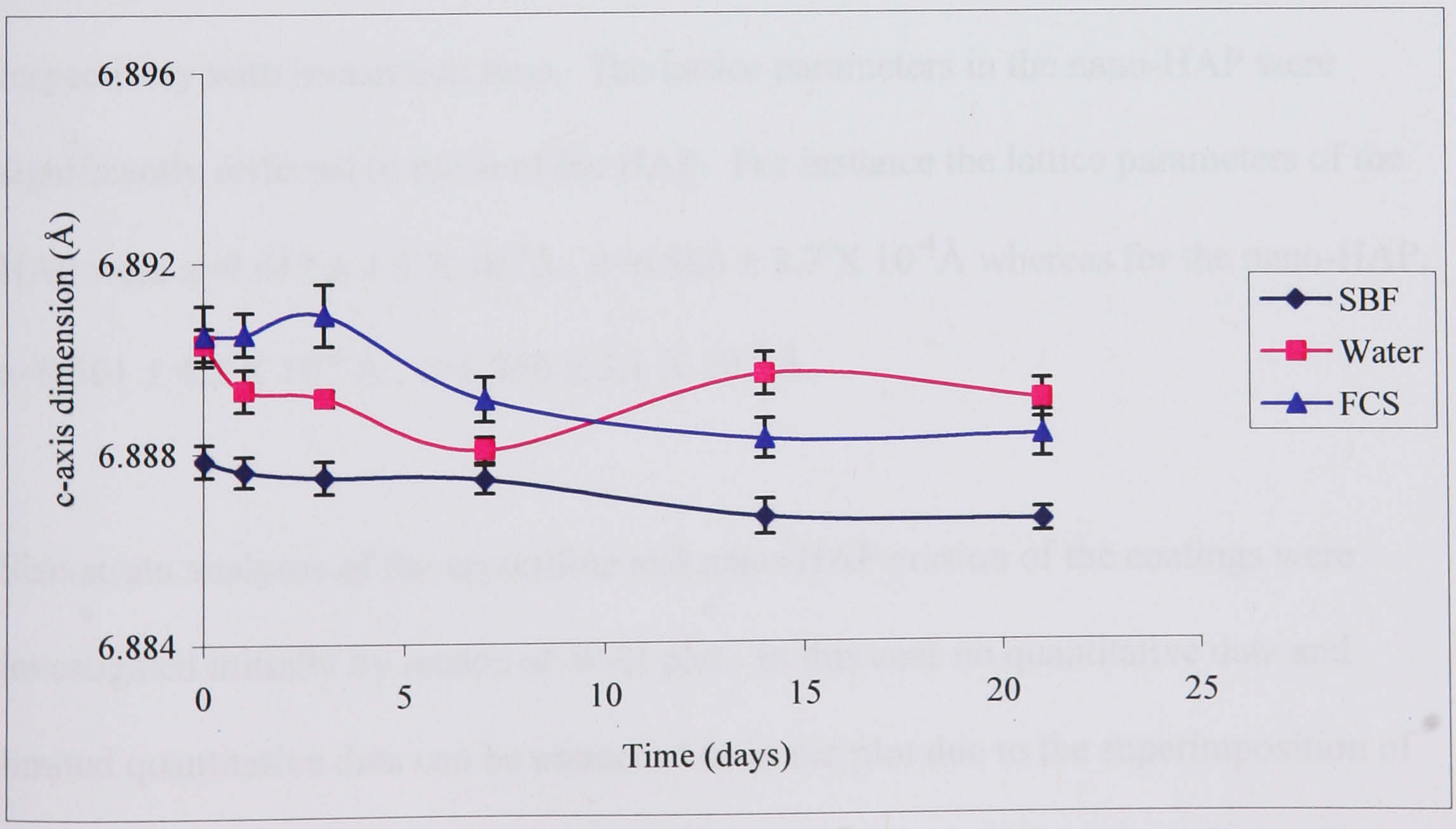

Figure 7. 38 Changes to c-axis parameter of PS coatings after various periods of immersion. Error bars the standard error derived from the fitting process.

With the samples immersed in water there was an immediate and relatively rapid fall in the wt% of the ACP compared to that of samples within SBF. There would appear to be no significant change in the ACP wt% of the samples in FCS until after day 3. Water, SBF and FCS samples had small amounts of nano-HAP after 1 day in solution. The relative proportion of nano-HAP on the coatings increased with immersion time. The amount of nano-HAP formed on the SBF samples was significantly greater than the water and FCS samples by day 21. However, the samples immersed in water for 21 days had a smaller amount of ACP remaining despite having less nano-HAP formed. In the case of the samples immersed in FCS, the ACP dissolution and nano-HAP formation was less than in both the SBF and FCS samples.

An indication of the changes in lattice chemistry was derived by inspection of the lattice parameters of the HAP and nano-HAP. In general there were only small but insignificant changes to the lattice parameters of the crystalline HAP in each of the test samples with immersion time. The a-axis and c-axis increased and decreased respectively with immersion time. The lattice parameters in the nano-HAP were significantly different to those of the HAP. For instance the lattice parameters of the HAP were $a=9.412 \pm 4.3 \times 10^{-4}$ Å , $c=6.886 \pm 3.7 \times 10^{-4}$ Å whereas for the nano-HAP, $a=9.501 \pm 4.2 \times 10^{-4}$ Å , $c=6.866 \pm 3.1 \times 10^{-4}$ Å.

Size-strain analyses of the crystalline and nano-HAP portion of the coatings were investigated initially by means of W-H plot. In this case no quantitative data and limited quantitative data can be extracted from the plot due to the superimposition of HAP and nano-HAP peaks. Therefore this analysis was merely to inspect the changes in isotropy and broadening with immersion time. Figure 7.39 represents a graph of

changes in integral breadth of the (002) and (004) peak positions with immersion time. It can be seen that in each case, the broadening associated with the (004) is consistently greater that of the (002) peak due to inherent partial overlap and smearing found at higher angles of 2θ [262]. In addition, with immersion time, size broadening increased. A similar trend was seen in the samples immersed in water (figure 7.40) but to a lesser extent. Hence there is rationale to assume that the increase in 'apparent anisotropy' is due to increased nano-HAP formation.

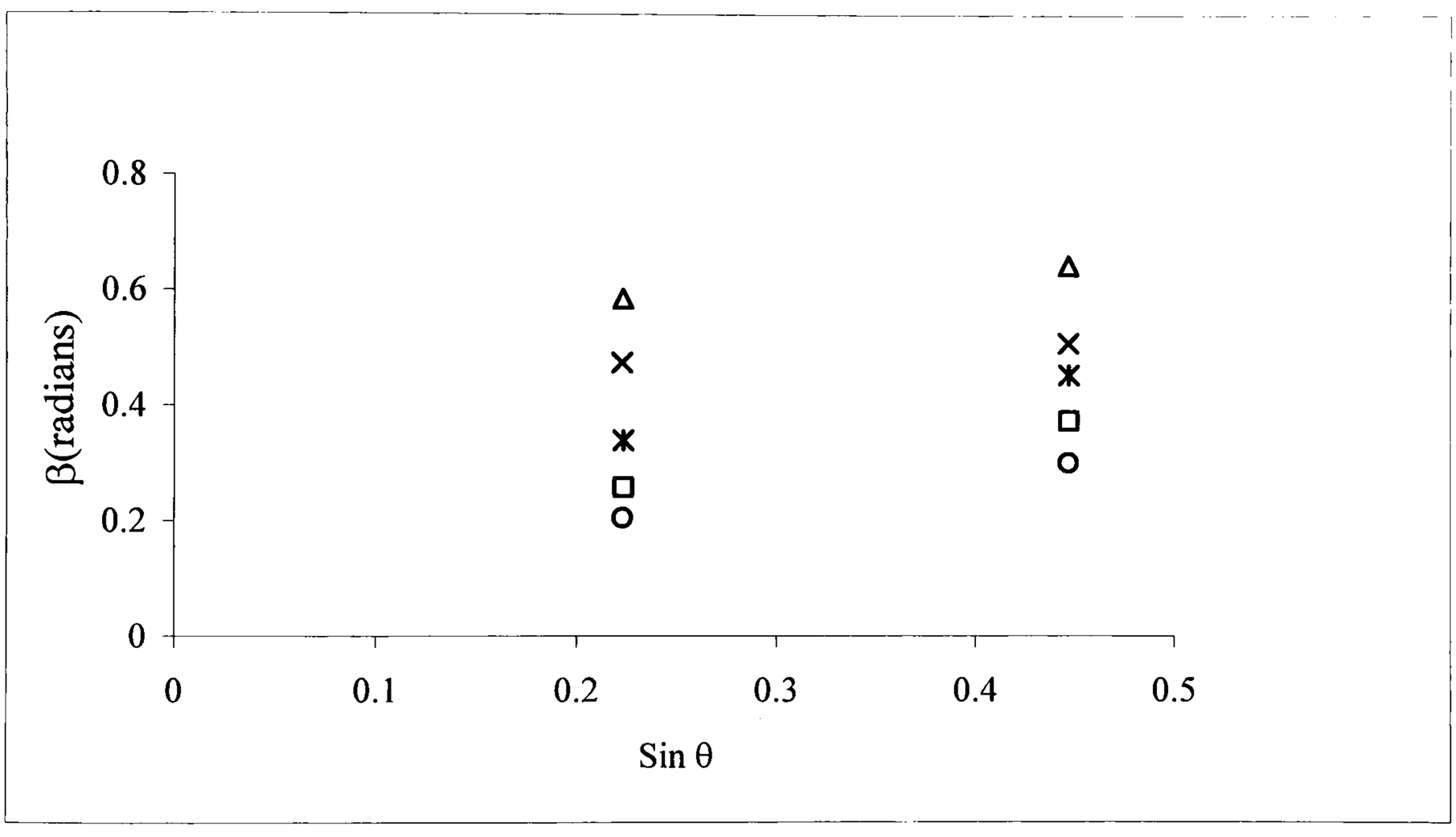

Figure 7. 39 Variation of integral breadth (β) with Sin θ in PS coatings (○) after immersion in SBF for 3 days (□), 7days (*), 14 days (×) and 21 days (Δ).

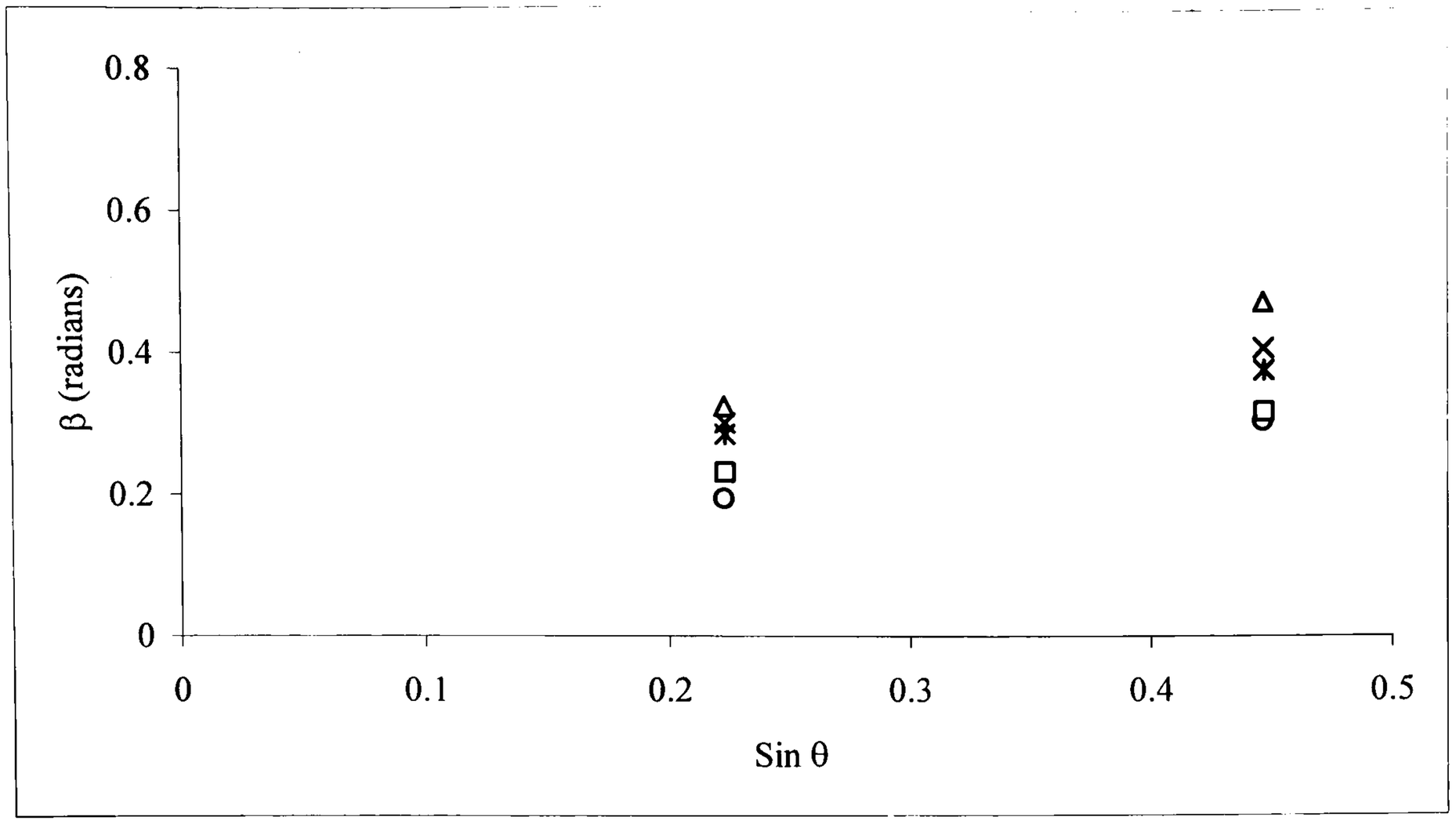

Figure 7. 40 Variation of integral breadth (β) with Sin θ in PS coatings (○) after immersion in water for 3 days (□), 7days (*), 14 days (×) and 21 days (Δ).

Additional examination of microstructural changes in the samples immersed in SBF was carried out by analysis of (002) peak at ~0.34nm. A pair of pseudo-Voigt profiles was independently fitted to the diffraction data to represent the scattering from HAP and nano-HAP in this region. This analysis excluded any contributions from ACP and provided peak positions and shapes for each phase. Figure 7.41 demonstrates the changes in (002) peak areas with immersion time in SBF. A decrease in the peak area of HAP and increase in the peak area of nano-HAP with immersion time was observed. High interphase correlations exist prior to day 7 and hence the data is conceivably unreliable before that point. This observation emphasises the strength of whole pattern fitting as opposed to single line fitting. The increase in nano-HAP area may be attributable to the increasing phase absolute mass and the decrease in HAP peak area may be attributable to both a decrease in HAP mass and increased absorption due to the formation due to the formation of surface

nano-HAP. The same trends were noted in samples immersed in water and FCS but in each case to a lesser extent.

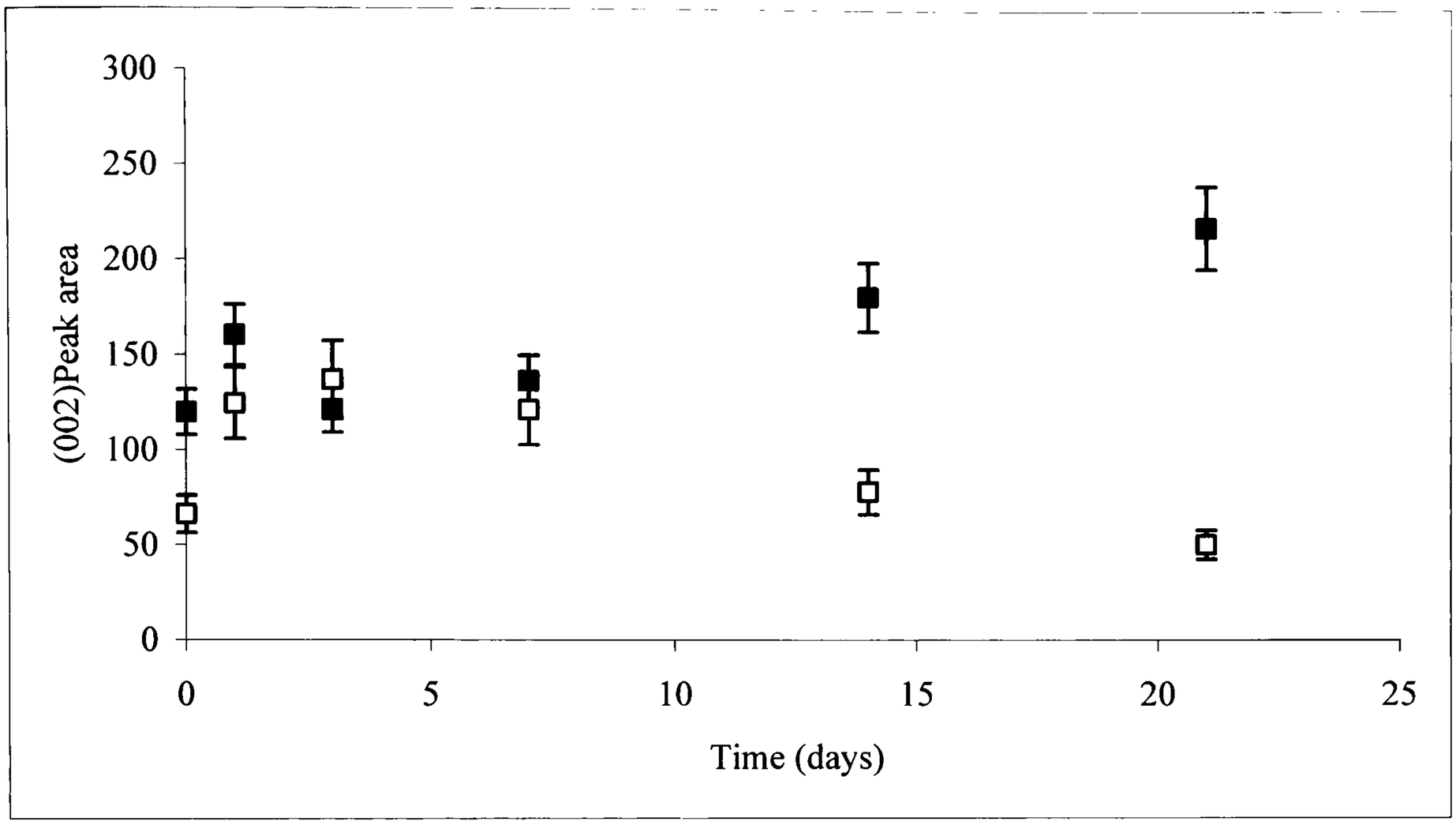

Figure 7. 41 Variation of (002) peak areas of HAP (□) and nano-HAP (■) with immersion time in SBF. Error bars are the standard error derived from the fitting process.

7.2.1.2 Chemical analysis

The changes in chemical nature of the coatings with immersion time were examined by FTIR. After each immersion time, a portion the coating was scraped off with a scalpel and used for FTIR analysis. Due care was taken to only scrape the coating off from a small section of the coating as opposed to across the whole surface of the coating. After each immersion time a different section of the coating was scrapped off. Care was taken in XRD analysis that areas, which had previously been scrapped off, did not contribute to the area of examination as depicted in figure 7.42.

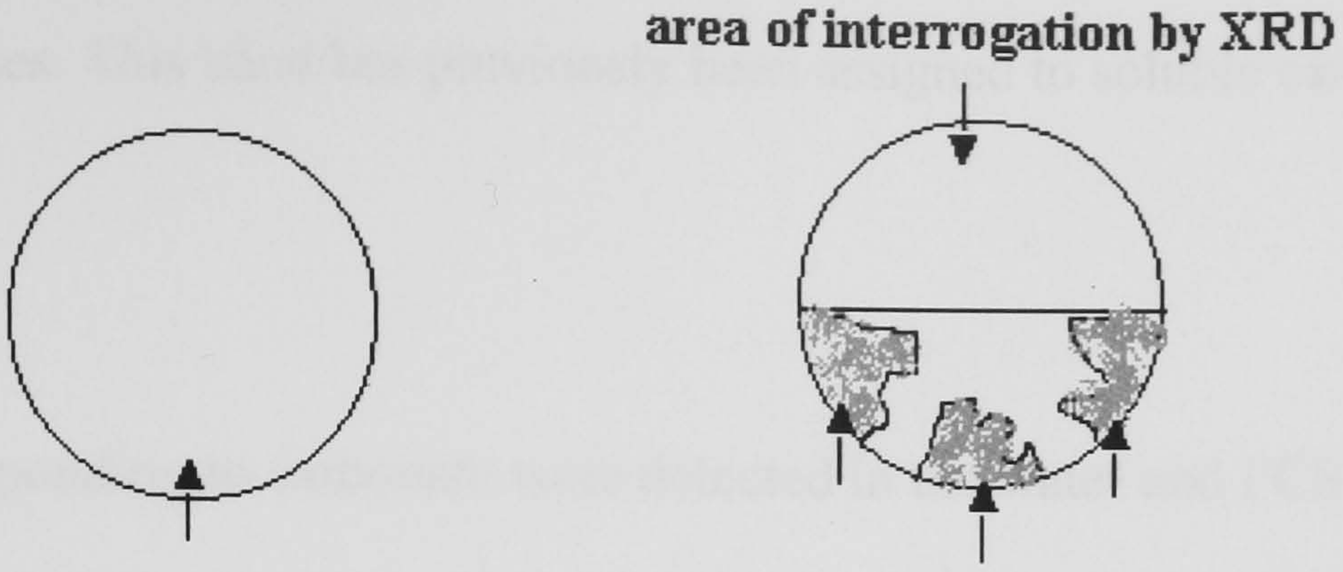

Figure 7. 42 Illustration of sample preparation for XRD and FTIR analyses.

Prior to immersion, the sample spectra were typical of those for HAP described in section 7.1. The most significant change upon immersion was the appearance of absorption bands at 970cm^{-1} and 1400-1600cm^{-1}. These can be seen most clearly in the data corresponding to immersion in SBF (figure 7.43). There was a small decrease in the resolution of the bands at 500-700cm^{-1}. This band has previously been employed as a 'splitting factor' to characterise apatites [263]. IR vibration bands peaking at 3300-3400cm^{-1} were detected in all samples after immersion. These broad bands are indicative of H_2O adsorbed in the materials. The intensity of the peaks in this region increased with immersion time, thus indicating contamination due to water. A sharp but weak hydroxyl stretch bond vibration was observed at approximately 3570 cm^{-1} in all samples before immersion. With increasing immersion time in SBF, the peak decreased and eventually disappeared by day 14. This suggests that there is a decrease in number of hydroxyl ions in the coatings. In contrast, a weak hydroxyl stretch bond vibration is visible in the samples retrieved from water and FCS, although it is reduced in comparison to the as-recieved samples. Two IR bands

peaking at approximately 2360 and 2340 cm^{-1} were detected in the as-received and immersed samples. This band has previously been assigned to soluble carbon dioxide [59].

No peaks corresponding to carbonate were detected in the water and FCS samples until day 14. In contrast, in the SBF samples, the appearance of CO_3 vibration bands at approximately 1427cm^{-1}, 1450cm^{-1} and 870cm^{-1} was observed after the first week of immersion. This indicates that carbonate-substituted calcium phosphate had been precipitated during immersion. This is consistent with results obtained previously [105, 246, 264]. The intensity of bands corresponding to CO_3 became less intense by day 21 in the samples retrieved from SBF. This suggests that there is partial dissolution of the carbonated substituted calcium phosphate formed initially, which is replaced by a one consisting of less carbonate. In contrast, the intensity of the carbonate bands increases in the samples immersed in FCS and water.

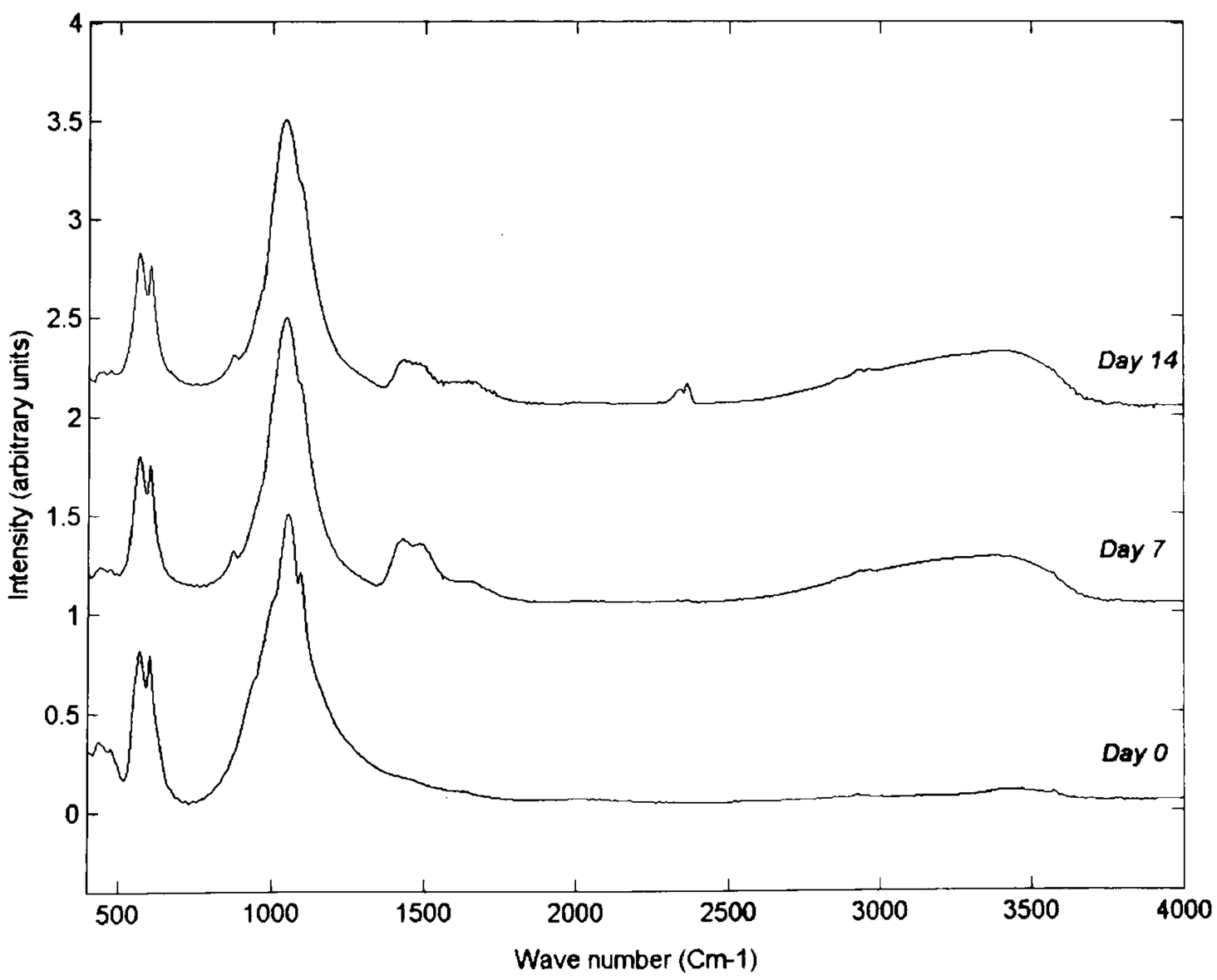

Figure 7. 43 FTIR spectra showing the changes in the chemistry of PS coatings with immersion time in SBF.

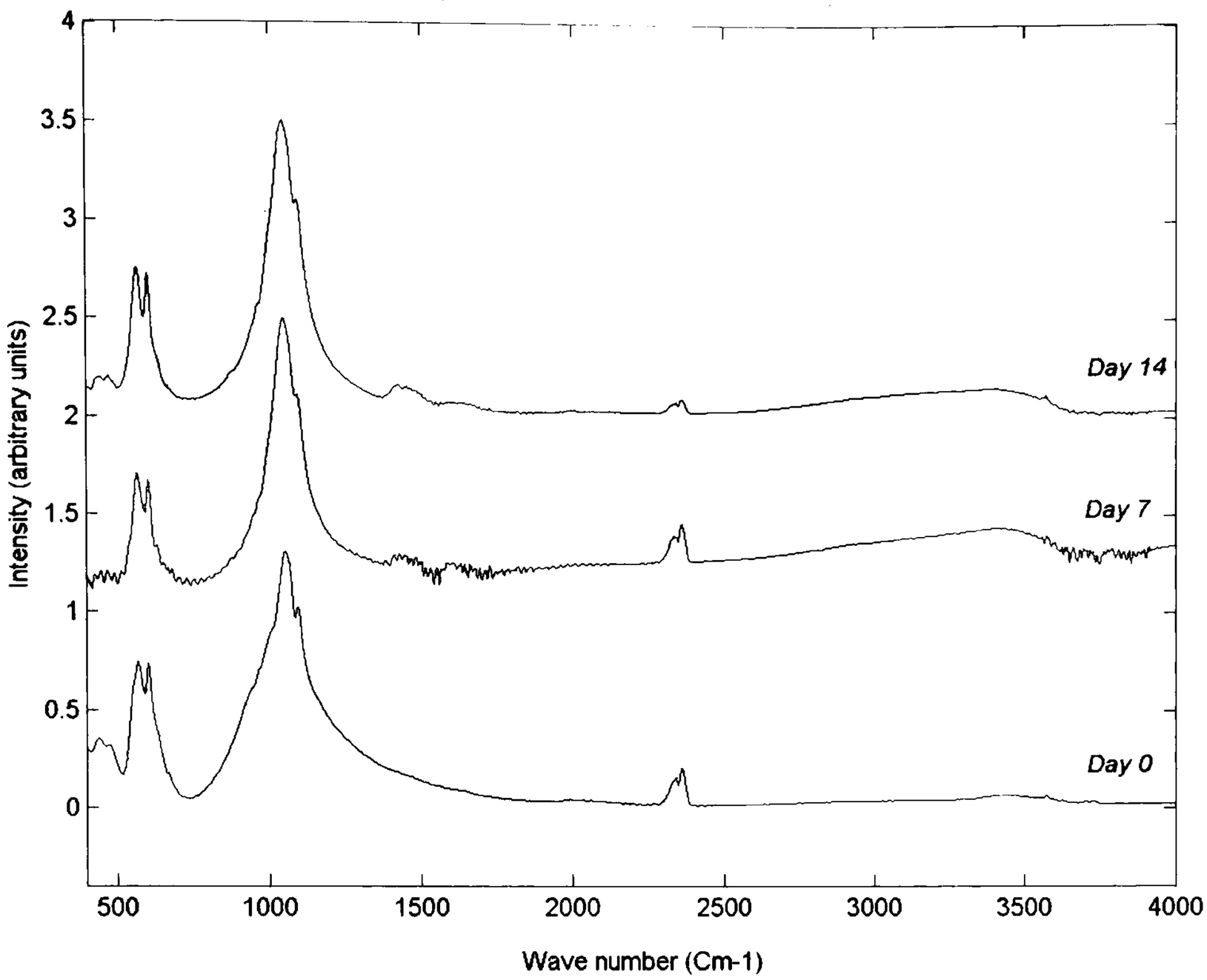

Figure 7. 44 FTIR spectra showing the changes in the chemistry of PS coatings with immersion time in water.

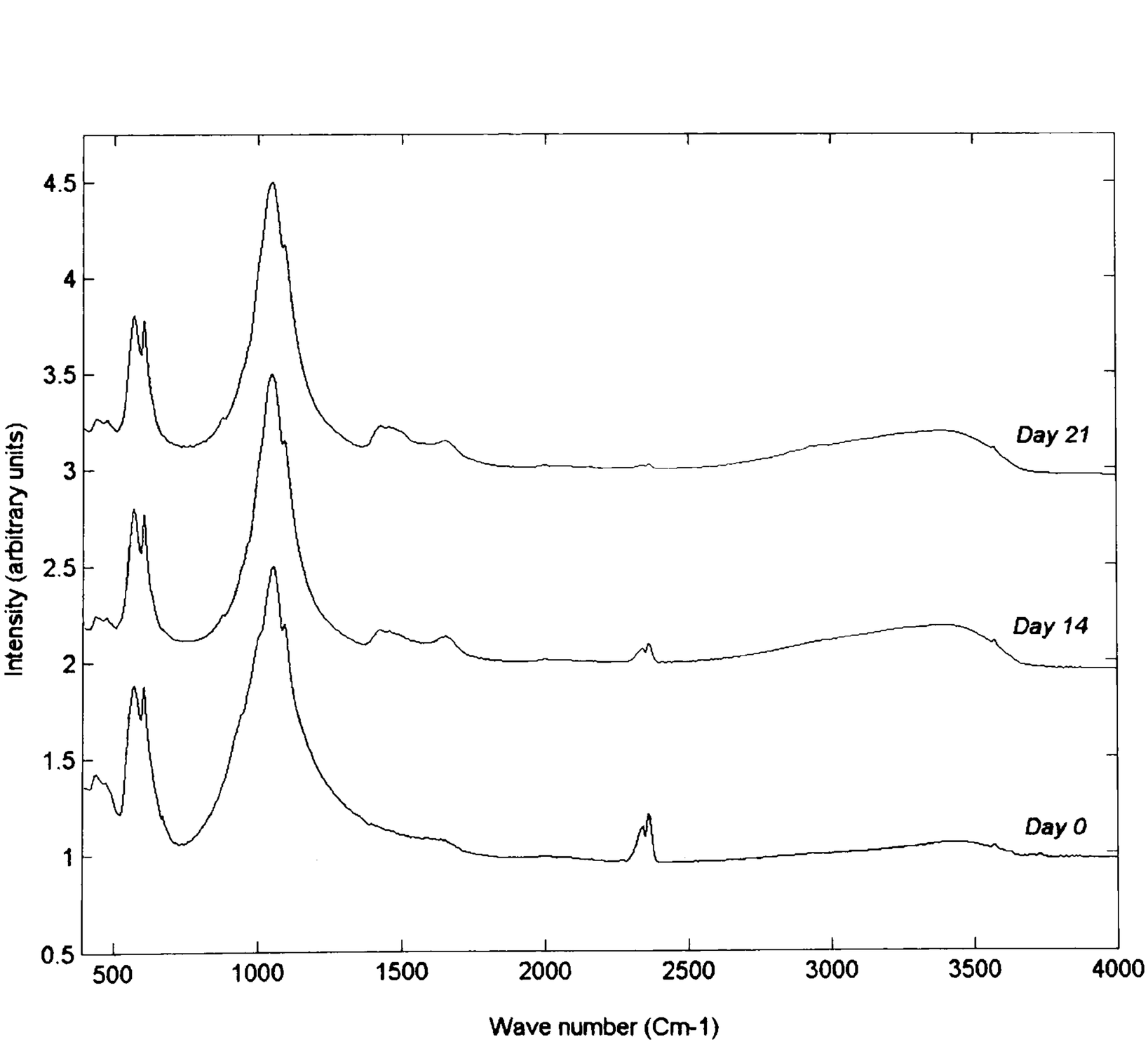

Figure 7. 45 FTIR spectra showing the changes in the chemistry of PS coatings with immersion time in FCS.

Changes in the calcium and phosphate concentration in the media after immersion time were investigated by atomic absorption spectroscopy and ion chromatography. The changes in calcium and phosphate ion concentrations and pH within the SBF determined at each inspection time are presented in figure 7.46. The calcium and phosphate ions present in the SBF and pH reached a maximum between day 1 and 3. This corresponds with the period of rapid dissolution of ACP (figures 7.35) where free calcium and phosphate ions are liberated into the media. A decrease in calcium concentration was observed between day 3 and 21,which corresponds with the period where precipitation dominates. In contrast the samples immersed in FCS showed little change in calcium and phosphate content. However, due to the large amount of interference from ions present in the media, much difficulty arose in the measurement of the changes in ionic concentration of the FCS media after immersion time (discussed further in chapter 8).

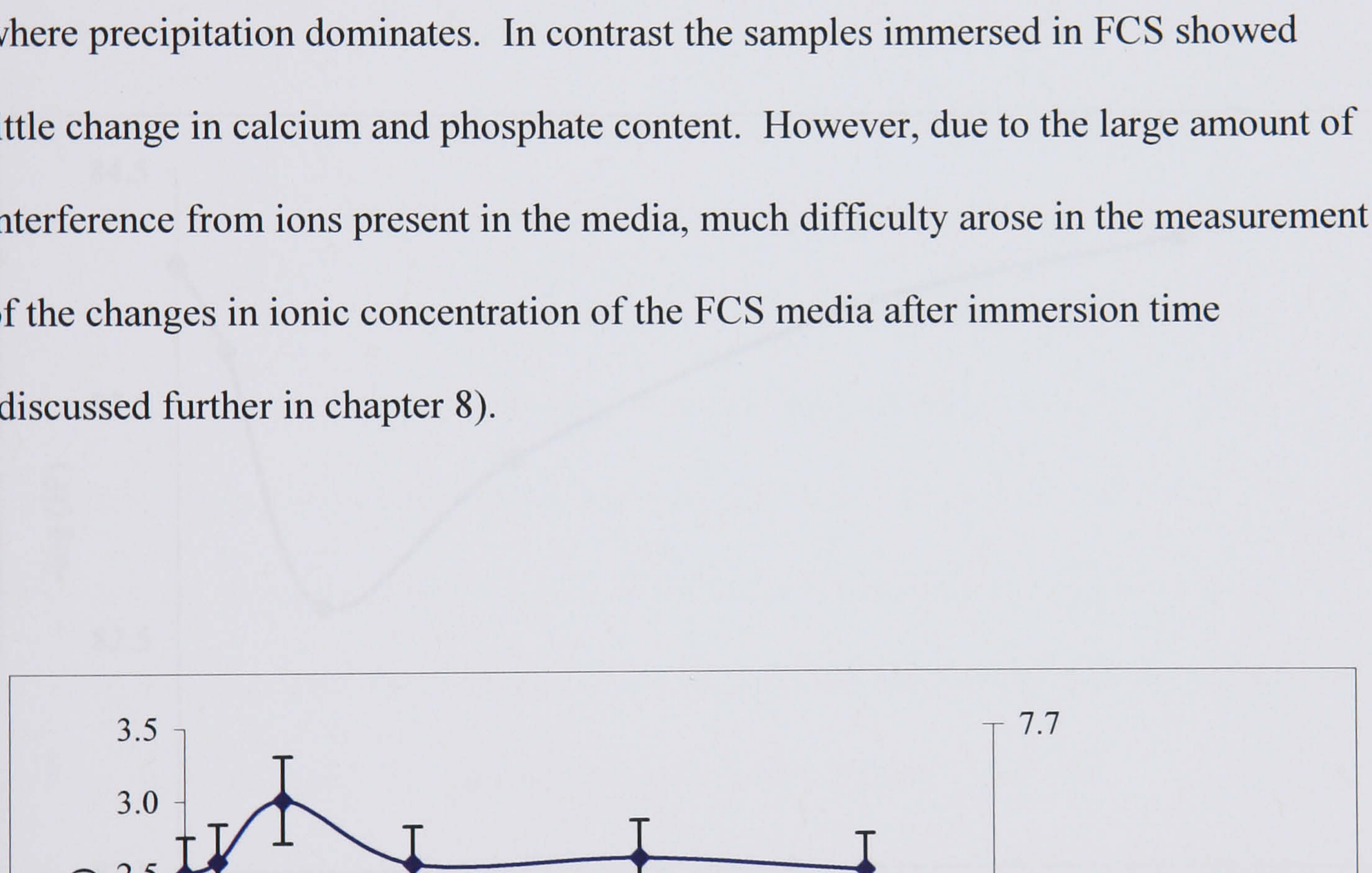

Figure 7. 46 Changes in calcium and phosphate concentration of SBF after the immersion of PS coatings. Errors are derived from the sensitivity of the equipment used.

Figure 7.47 shows the changes in -log (IP) as a function of immersion time. In the early stages of immersion the -log (IP) values decreased with an increase in immersion time. This decrease in -log (IP) is a direct result of the increase in calcium and phosphate ion concentration and pH of the SBF solution. After day three, the magnitude of -log (IP) increased quite rapidly, marking the onset of precipitation, where there is a decrease in calcium and phosphate ion concentration and pH of the SBF.

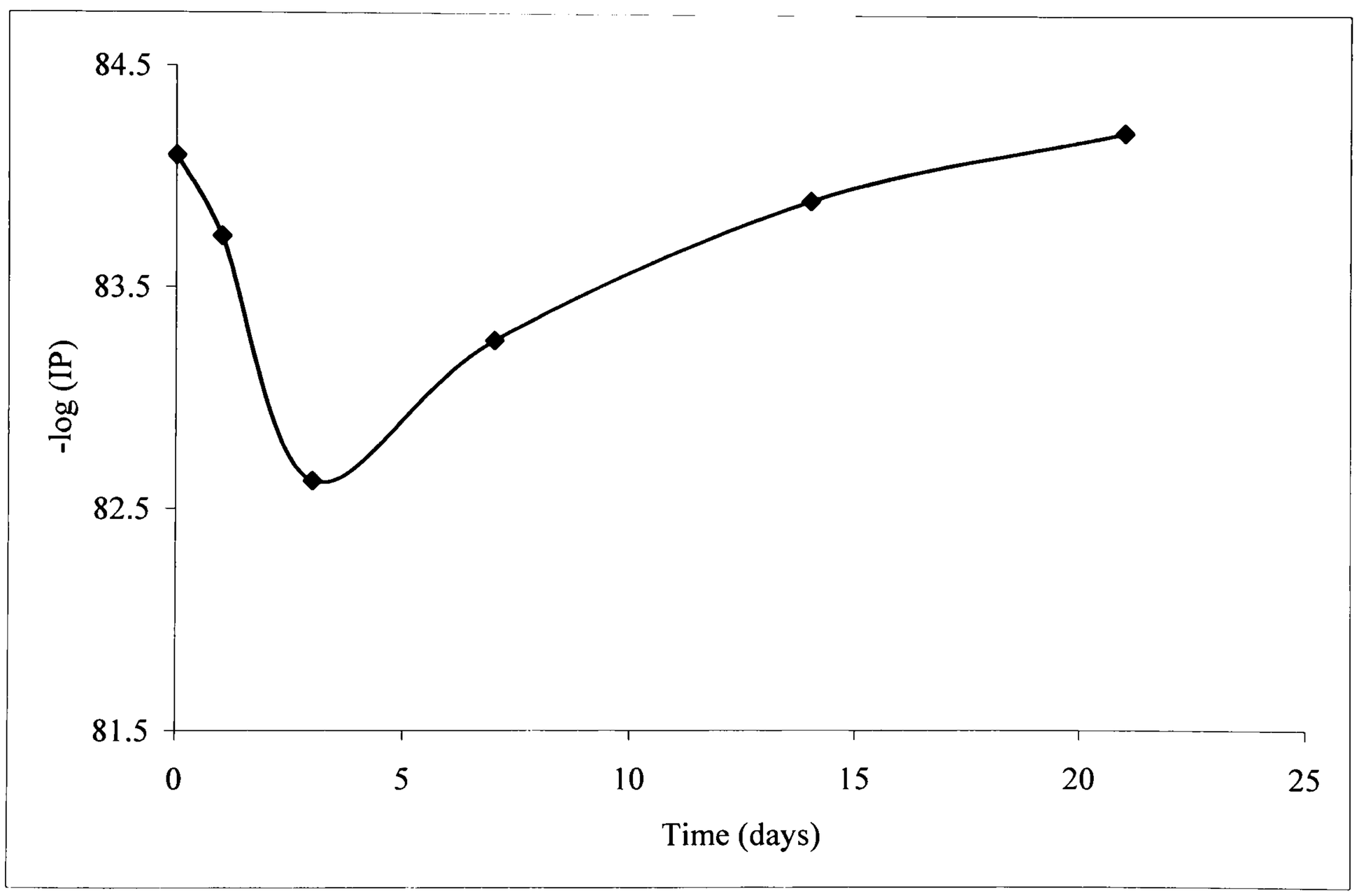

Figure 7. 47 Changes in the ionic product of the SBF as a function of soaking time.

7.2.1.3 Morphological analysis

Morphological examination of the test samples was conducted by ESEM after each immersion period and by SEM after day 21. ESEM was used to avoid the need for the samples to be coated with a conductive layer. In this way it was

possible to non-destructively analyse the samples before returning them to their respective media. SEM was used on day 21 to assess the coatings as it has been found during investigation that it has a better picture quality than ESEM with respect to analysing non-conductive coatings. It was expected that subtle surface features that were not visible by ESEM would be detected.

Figures 7.48-55 illustrate the changes in surface morphology occurring in PS coatings after immersion in SBF, water and FCS. After the first day of immersion in SBF, it was apparent that the spherical droplets and flattened splats on the surface of the coating had undergone some degree of dissolution (figure 7.48). The surface of the coating showed signs of increased roughness and micro-crack propagation. At higher magnification (figure 7.49), it was observed that the coating was covered in a newly formed layer of small granular structures. This dune-like film is characterized by numerous cracks of tortoiseshell character, which spread along the whole surface of the ceramic coating. As the immersion duration increased, the dune-like layer became denser and the granules in the layer became larger (figure 7.51) and hence more visible by day 7 at lower magnification (figure 7.50). On day 21, SEM analysis revealed that a carpet-like nanocrystals had covered the surface of the coating (figure 7.52).

ESEM analysis of the water samples on day 7 revealed a relatively smooth coating surface characterized by surface cracks (figure 7.53). This implies that dissolution of the HAP coating has occurred. No newly formed precipitates were visible on the surface of the coating. By the day 21 of immersion, by means of SEM, the extent of dissolution could be seen at low magnification (figure 7.54). Surface micro-cracks

and clusters of clusters of precipitate dominated the surface of the coating. At higher magnification small precipitates carpeted the surface the coating similar in nature to those seen on PS coatings after 21 days of immersion.

After 21 days of immersion in FCS, a small degree of dissolution occurred such as the surface cracks. In addition, small precipitates of approximately 1–3μm in diameter were visible on the surface of the coating.

Figure 7. 48 Low magnification (500X) ESEM micrograph of a PS coating after immersion in SBF for 1 day. Scale bar denotes 100μm.

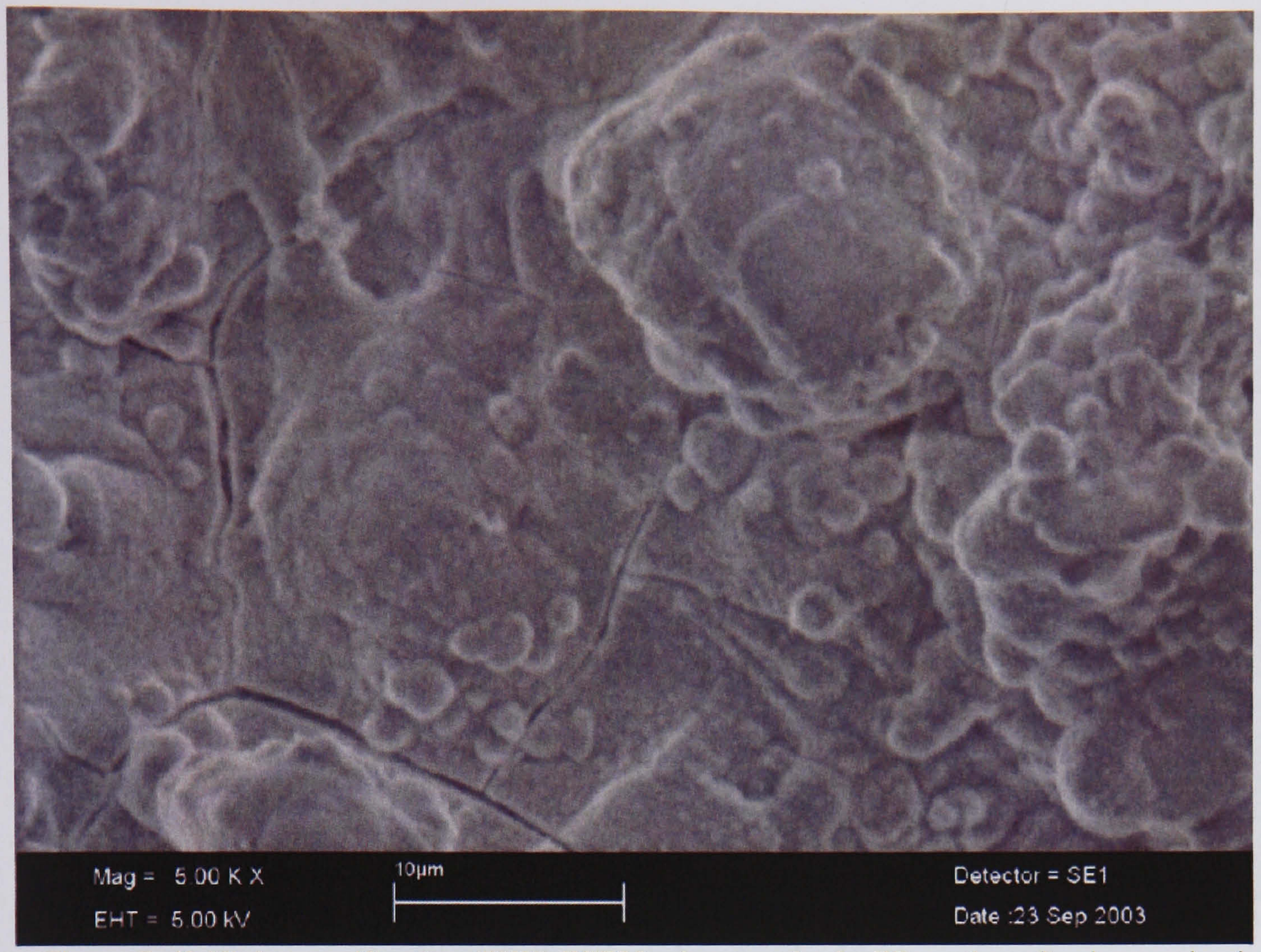

Figure 7. 49 High magnification (5KX) ESEM micrograph of a PS coating after immersion in SBF for 1 day. Scale bar denotes 10µm.

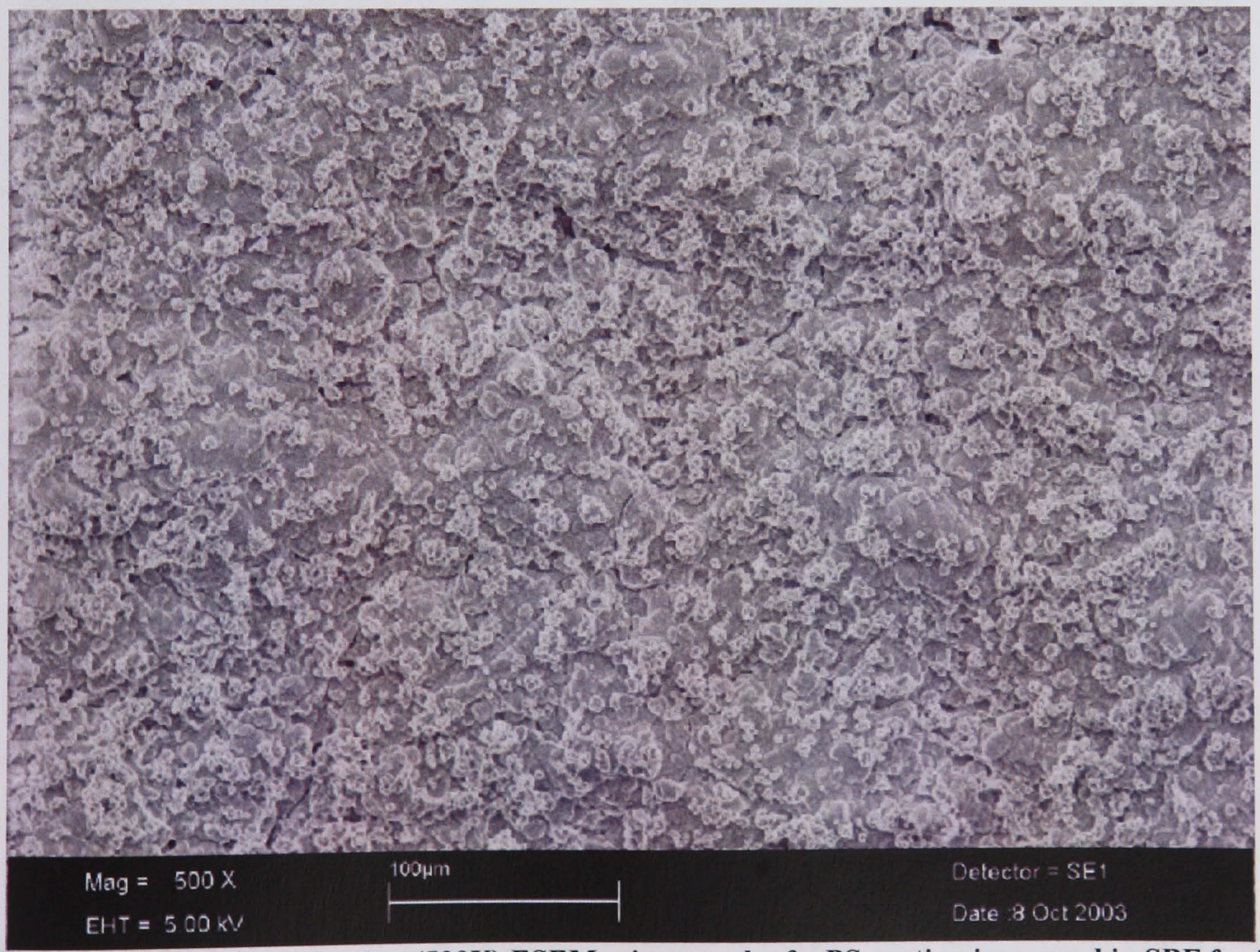

Figure 7. 50 Low magnification (500X) ESEM micrograph of a PS coating immersed in SBF for 7 days. Scale bar denotes 100µm.

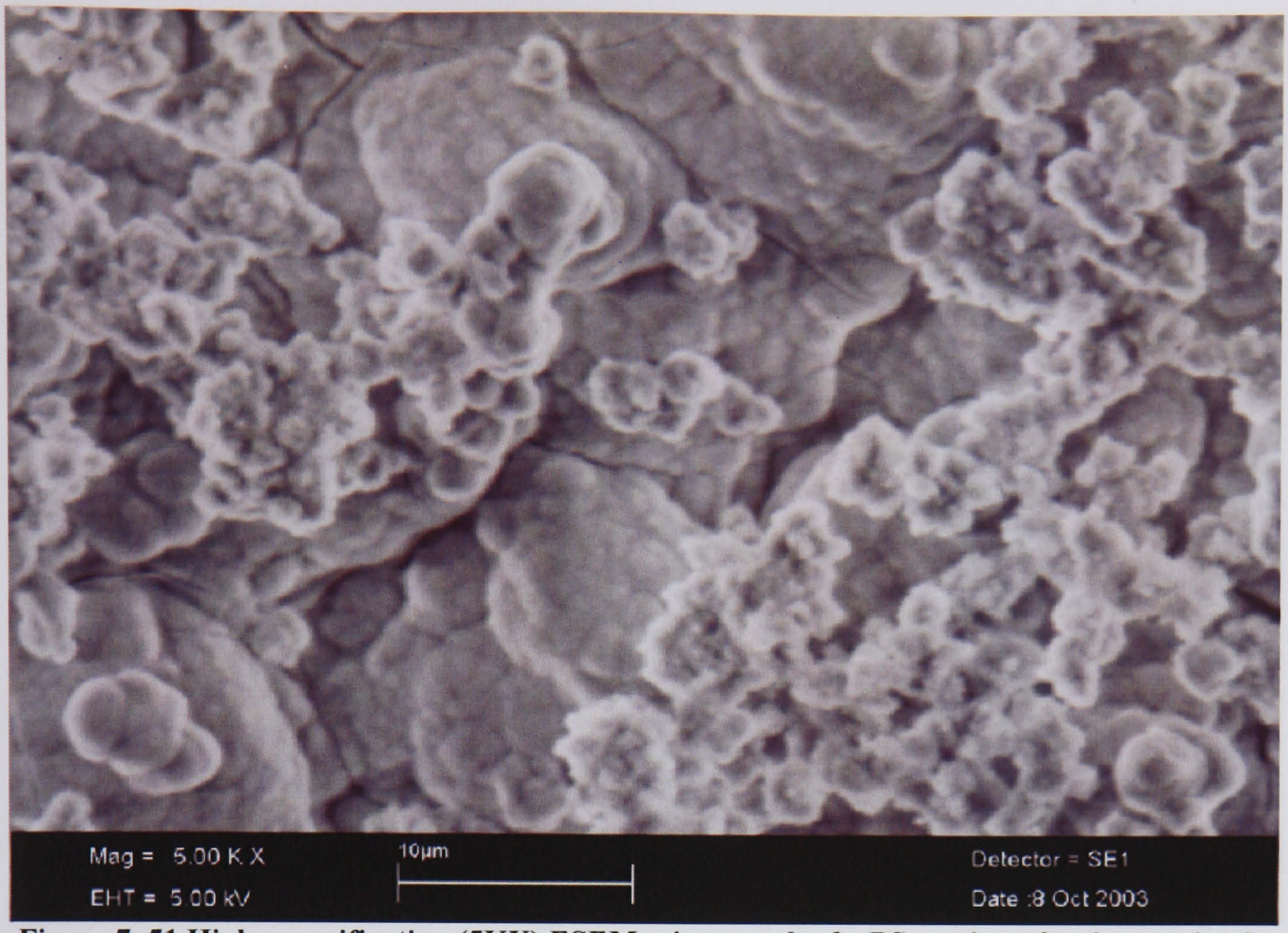

Figure 7. 51 High magnification (5KX) ESEM micrograph of a PS coating after immersion in SBF for 7 days. Scale bar denotes 10µm.

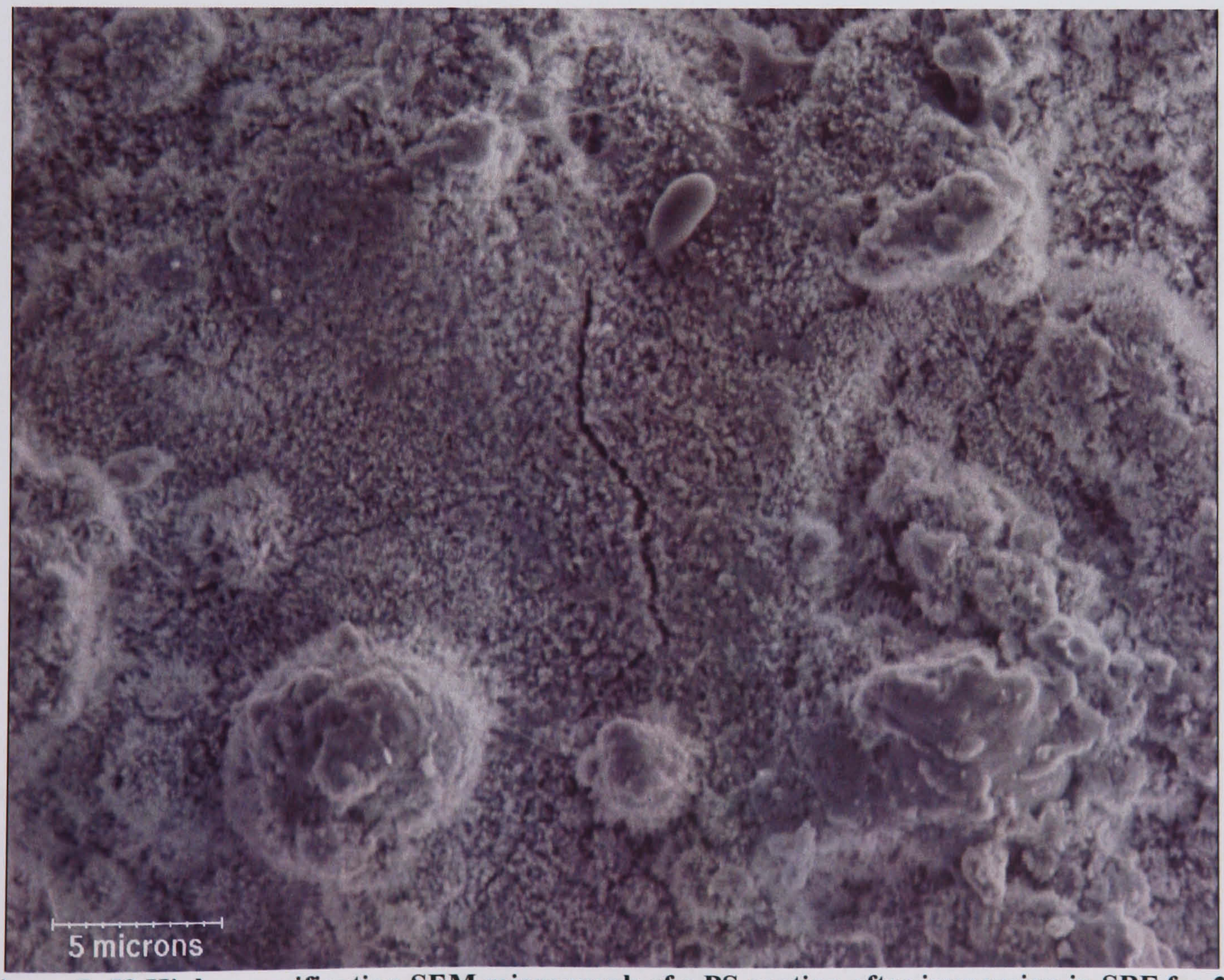

Figure 7. 52 High magnification SEM micrograph of a PS coating after immersion in SBF for 21 days. Scale bar denotes 5µm.

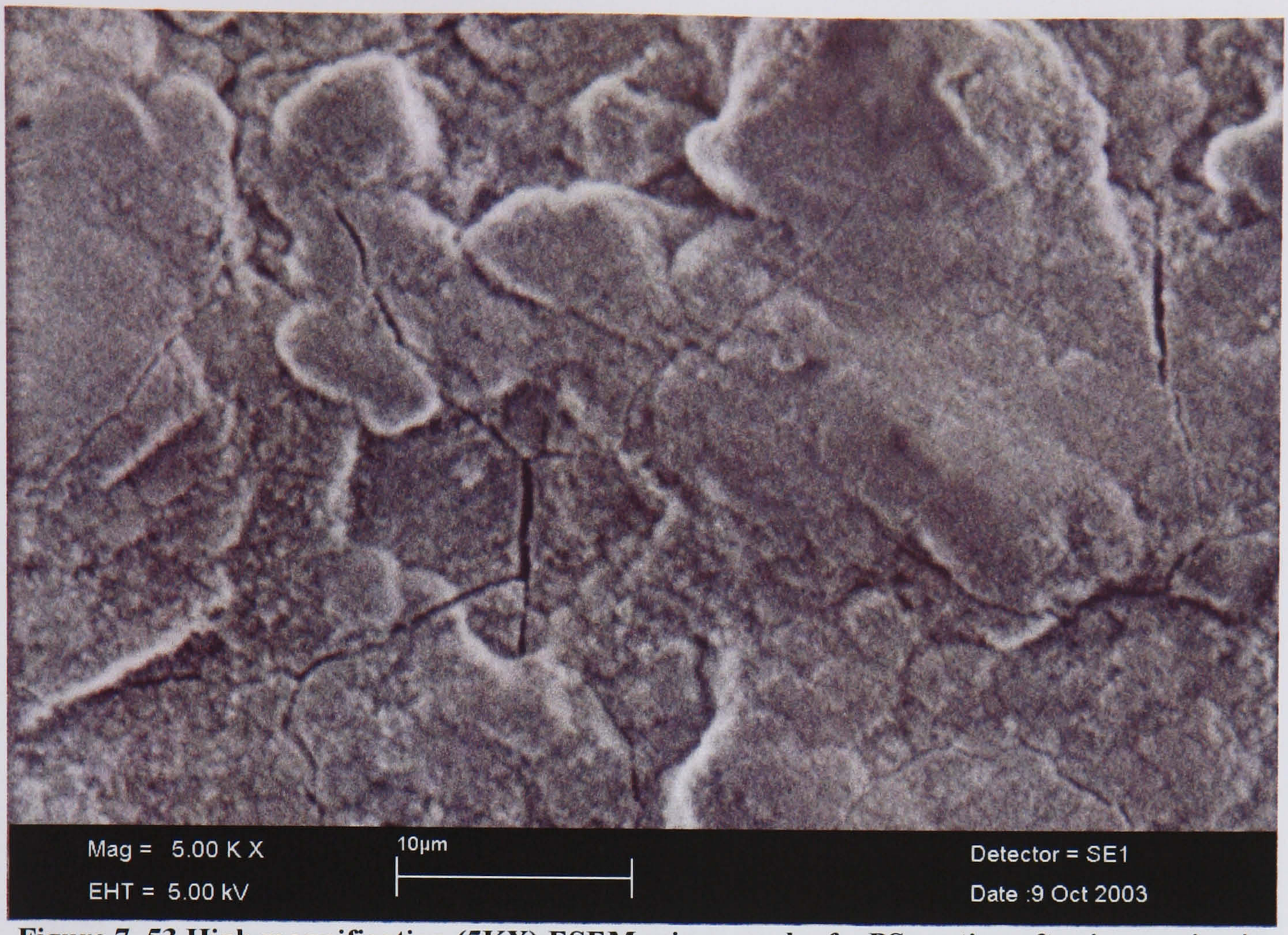

Figure 7. 53 High magnification (5KX) ESEM micrograph of a PS coating after immersion in water for 7 days. Scale bar denotes 10µm.

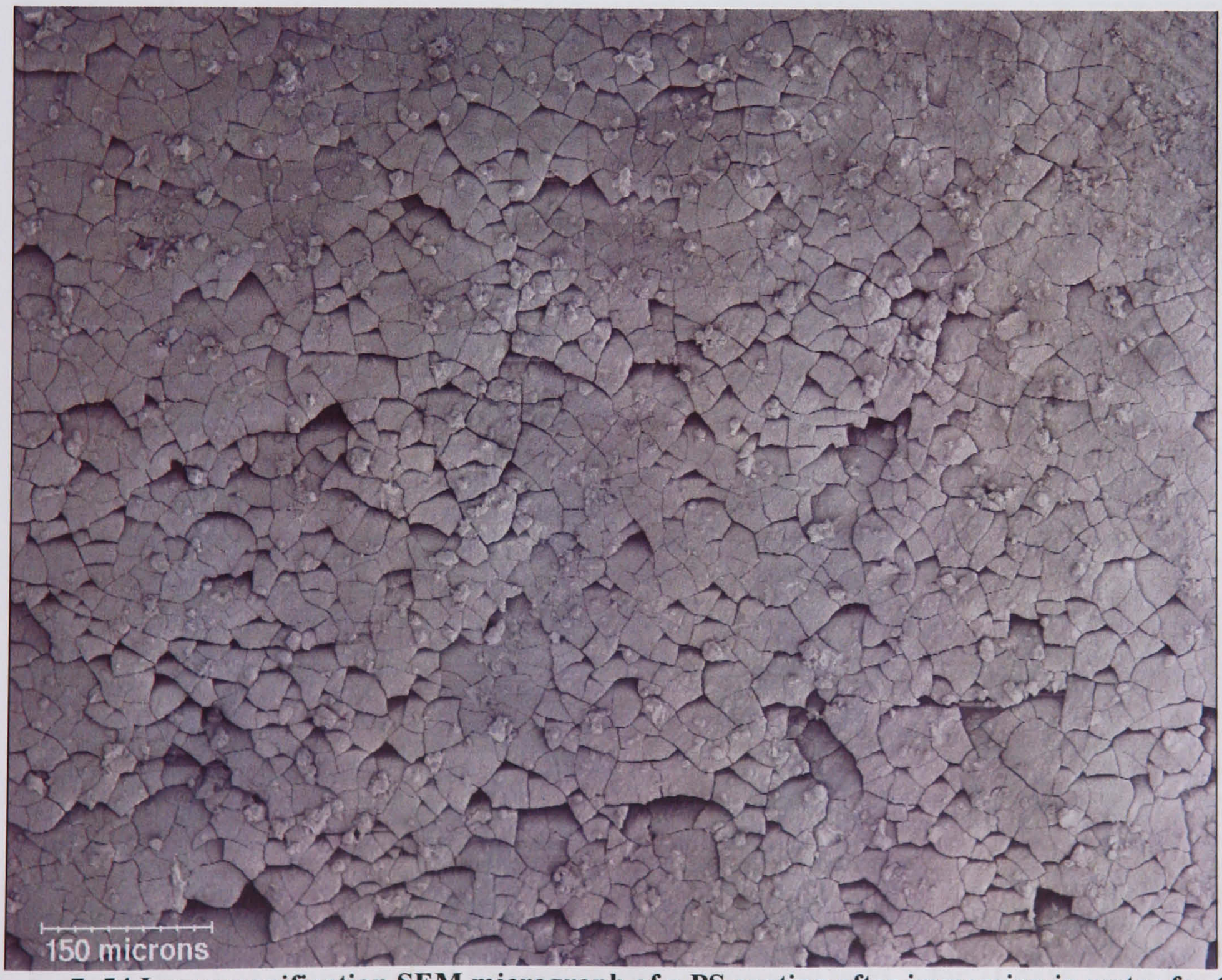

Figure 7. 54 Low magnification SEM micrograph of a PS coating after immersion in water for 21 days. Scale bar denotes 150µm.

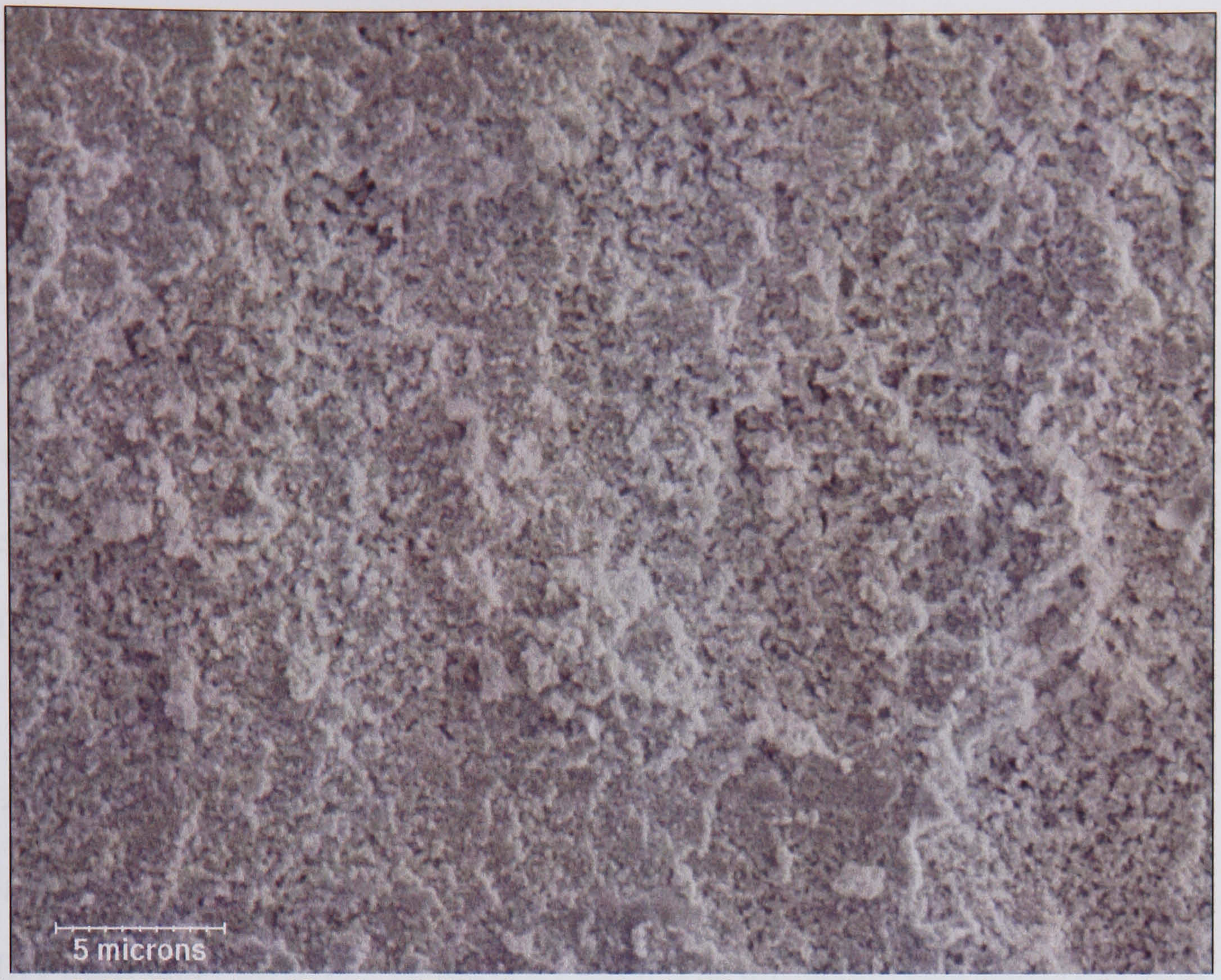

Figure 7. 55 High magnification SEM micrograph of a PS coating immersed in water for 21 days. Scale bar denotes 5μm.

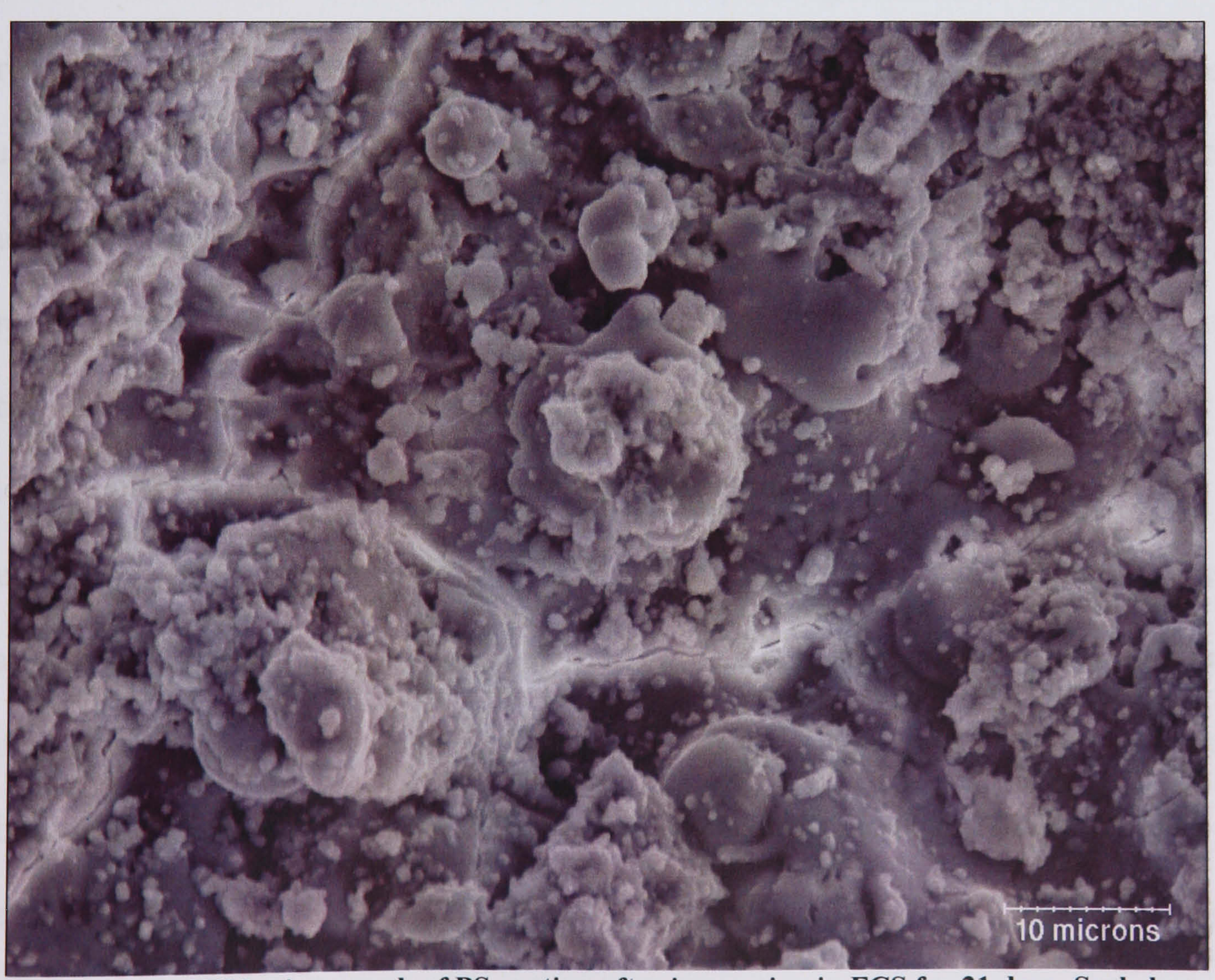

Figure 7. 56 SEM micrograph of PS coating after immersion in FCS for 21 days. Scale bar denotes 10μm.

7.2.2 *In vitro* behaviour of electrodeposited HAP coatings

The *in vitro* behaviour of ED coatings in various media has been investigated over a period of 21 days. Due to the inherent nature of ED coatings (i.e. coating covers all substrate surfaces), care was taken to ensure that the surface oriented face up in the media was analysed each time. The reason for this is that a microenvironment is created between the glass beaker and the coating at the bottom of the test sample. The behaviour in this microenvironment could not adequately model *in vivo* behaviour of ED coatings.

7.2.2.1 Diffraction analysis

Figures 7.57-7.59 illustrate the diffraction data produced for samples immersed in SBF, water and FCS over a period of 21 days. The diffraction data shows that with increased immersion time in SBF, the peaks corresponding to the HAP become broader and more intense. In addition, the intensity of the peaks corresponding to the substrate became less intense with immersion time. This same trend is observed with the samples immersed in FCS but to a lesser extent. This indicates the possible precipitation of ACP. The diffraction data did not contain any 'extended tails' as was previously observed in PS coatings exposed to similar conditions [105, 246]. This indicated the absence of the nanocrystalline phase described previously [246]. Surprisingly, coatings immersed in water behaved very differently. By day 14, it was barely possible to discern peaks corresponding to HAP. The peaks that dominated the diffraction pattern were those of the substrate. By day 21 no HAP peaks were visible. This indicates accelerated dissolution of the HAP coatings. Identical findings have been reported by Sewing *et al* [265] in solubility studies of ED coatings fabricated by the same method.

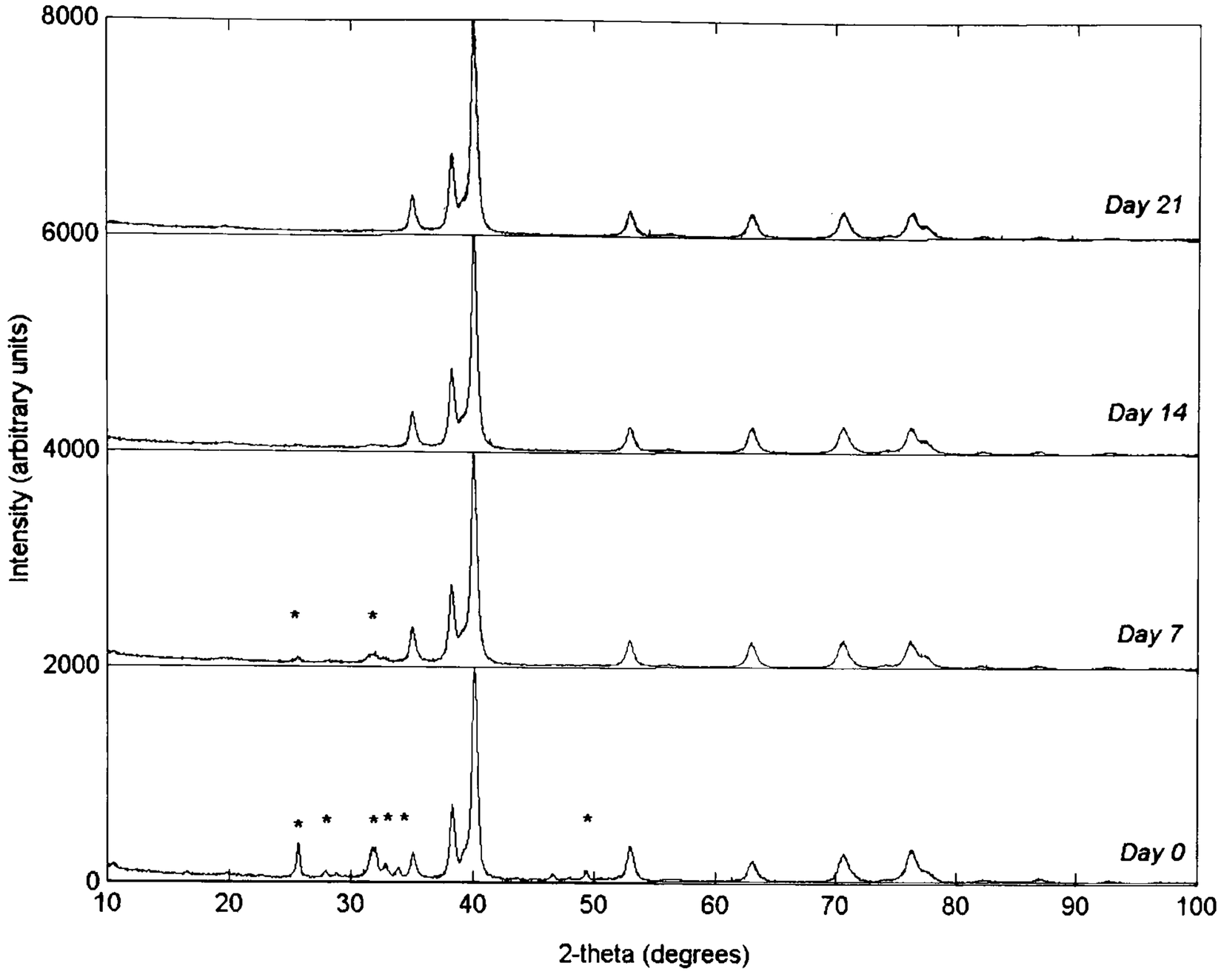

Figure 7. 57 Diffraction patterns of ED coatings after various periods of immersion in water (* denotes HAP peaks).

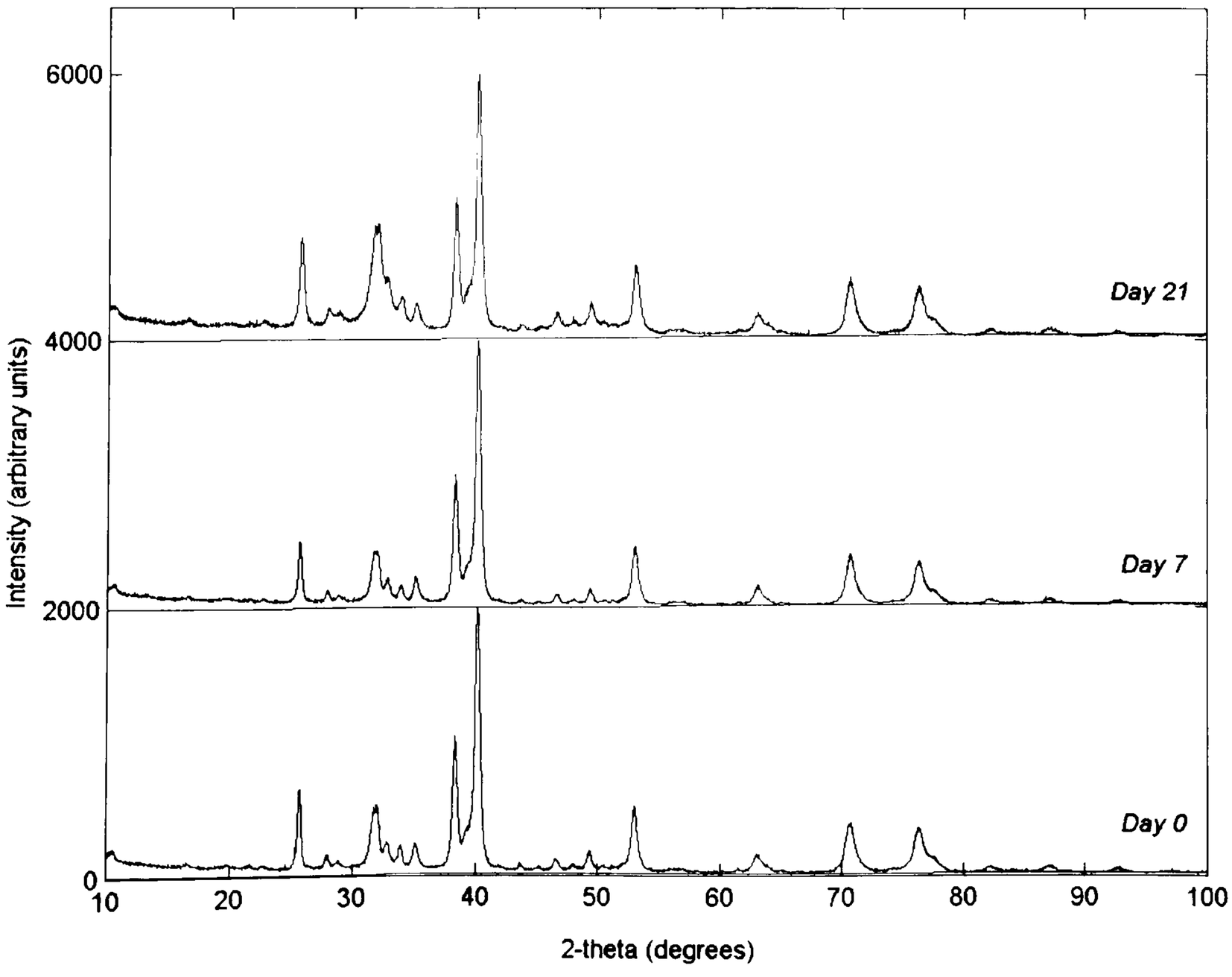

Figure 7. 58 Diffraction patterns of ED coatings after various periods of immersion in SBF.

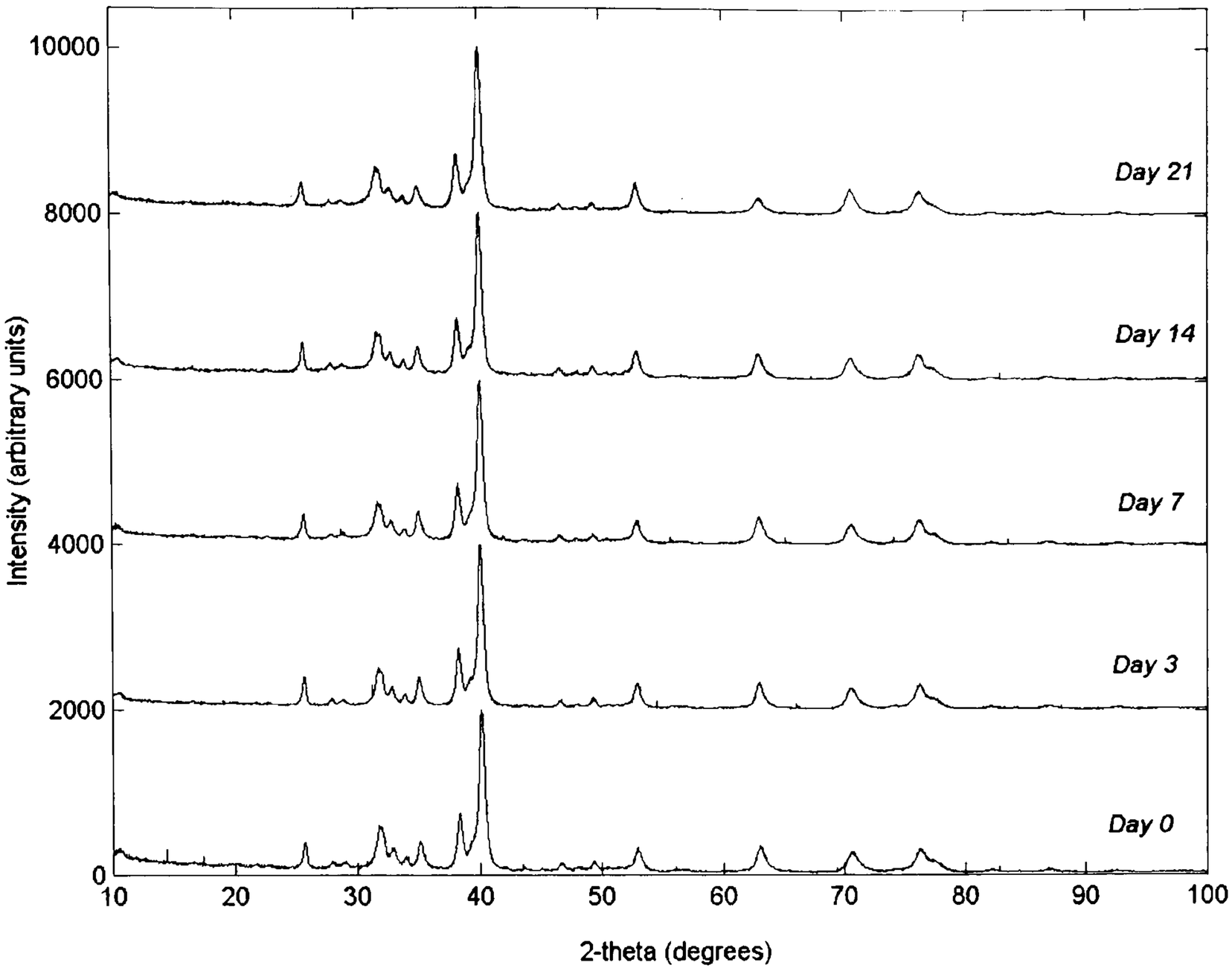

Figure 7. 59 Diffraction patterns of ED coatings after various periods of immersion in FCS.

Data from quantitative phase analysis (figures 7.60-7.62) revealed that irrespective of the media of immersion, increasing amounts of ACP was formed with immersion time. The formation of ACP was markedly high in the samples immersed in water in comparison to the samples immersed in SBF or FCS. For example, by day 21 the amount of ACP present was approximately 89wt% compared to 27wt% and 25wt% for the samples immersed in SBF and FCS respectively. The rate of ACP formation in the samples immersed in SBF and FCS was generally comparable. However prior to day 3, there was no net change in ACP content in the samples immersed in FCS, possibly due to protein inhibition of HAP dissolution. This phenomenon has been reported in previous *in vitro* investigations by Etok *et al* [246] and Bender *et al* [266].

The changes in lattice chemistry were investigation by inspection of the changes in the lattice parameters of each of the test samples (figures 7.63-64). In all cases the a-axis and c-axis dimensions increased and decreased respectively with immersion. In general the behaviour of the lattice parameters of the samples immersed in SBF and FCS were similar with immersion time. However, prior to day 3 there had been no net change in lattice parameters for the samples immersed in FCS. This indicates that there was no net change in lattice chemistry and hence reinforces the idea that no ACP formation had occurred prior to day 3. The changes in lattice parameters for the samples immersed in SBF and FCS were quite subtle, but this was not the case for samples immersed in water. Initially, the a-axis dimension behaved in the same manner as in the other test samples. Conversely between day 3 and 7, a sudden decrease occurred followed by a dramatic increase to approximately 9.52 ± 0.015Å on day 21. The c-axis parameter increased gradually between prior to day 7, but after this there was a dramatic decrease to 6.83 ± 0.017Å. Of importance to note is the fact that the errors associated with the measurements of the lattice parameters at day 14 and 21 are large and likely to be unreliable. This is due to the low scattering intensity of the HAP peaks due to low HAP content in the coatings. These changes in lattice parameters indicate a substantial modification of the lattice chemistry and hence deviations from stoichiometric HAP.

W-H analysis for the samples immersed in SBF and water showed an increase degree of crystal anisotropy with increased an immersion time. This coincides with the behaviour of PS coatings in SBF and water described in section 7.2.1 and in previous work [105]. W-H analyses were not possible for samples immersed in water. The reason for this lies with the fact the peaks corresponding to HAP overlapped and

disappeared with immersion time. No conclusive trends in size and strain behaviour have been revealed for any of the ED samples due the intrinsic poor quality of data. Low signal to noise ratios have been reported previously by Rogers *et al* [131] and Broadhurst *et al* [253, 267] in characterisation studies of HAP coatings.

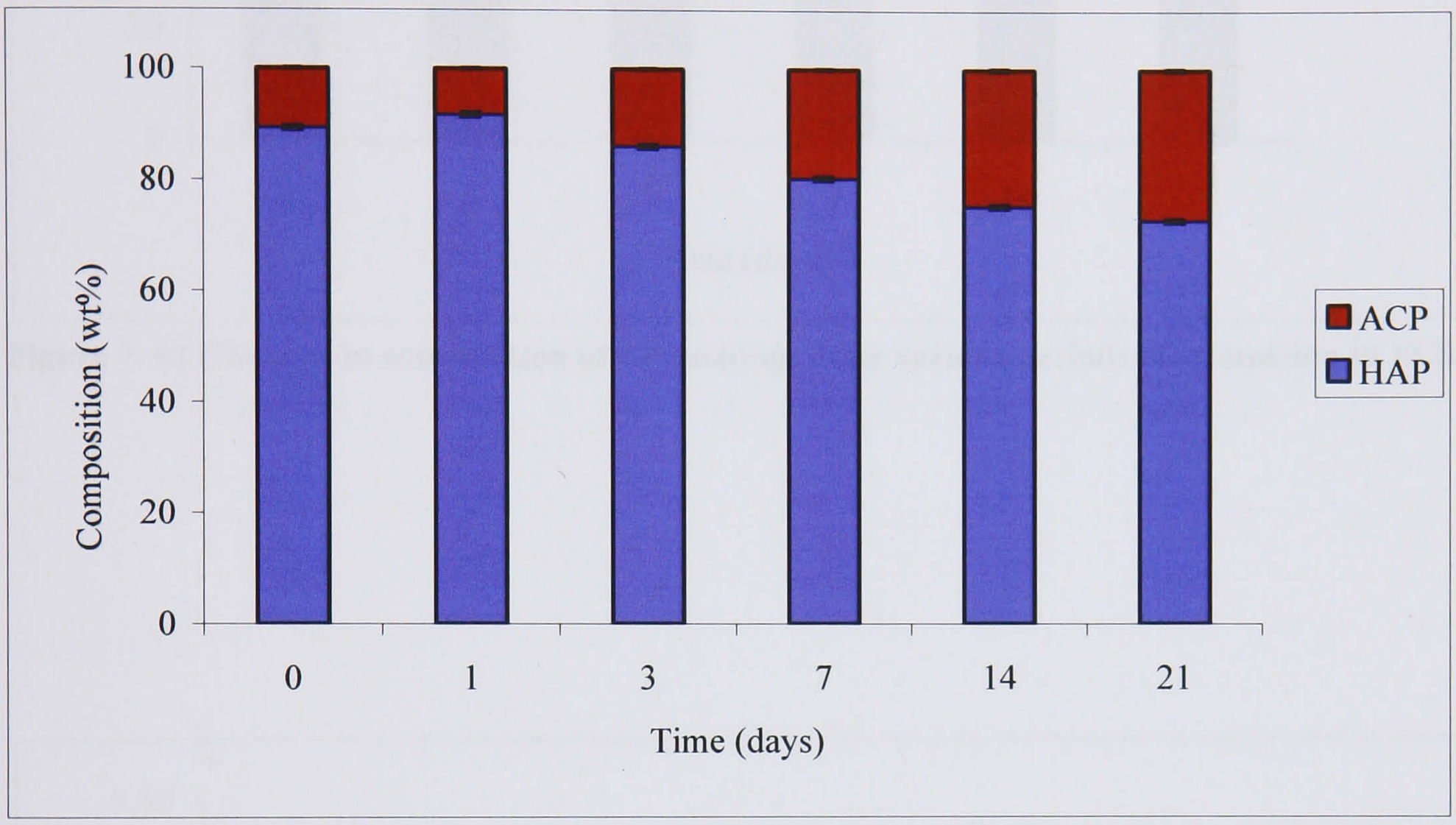

Figure 7. 60 Changes in composition of ED coatings after various periods of immersion in SBF.

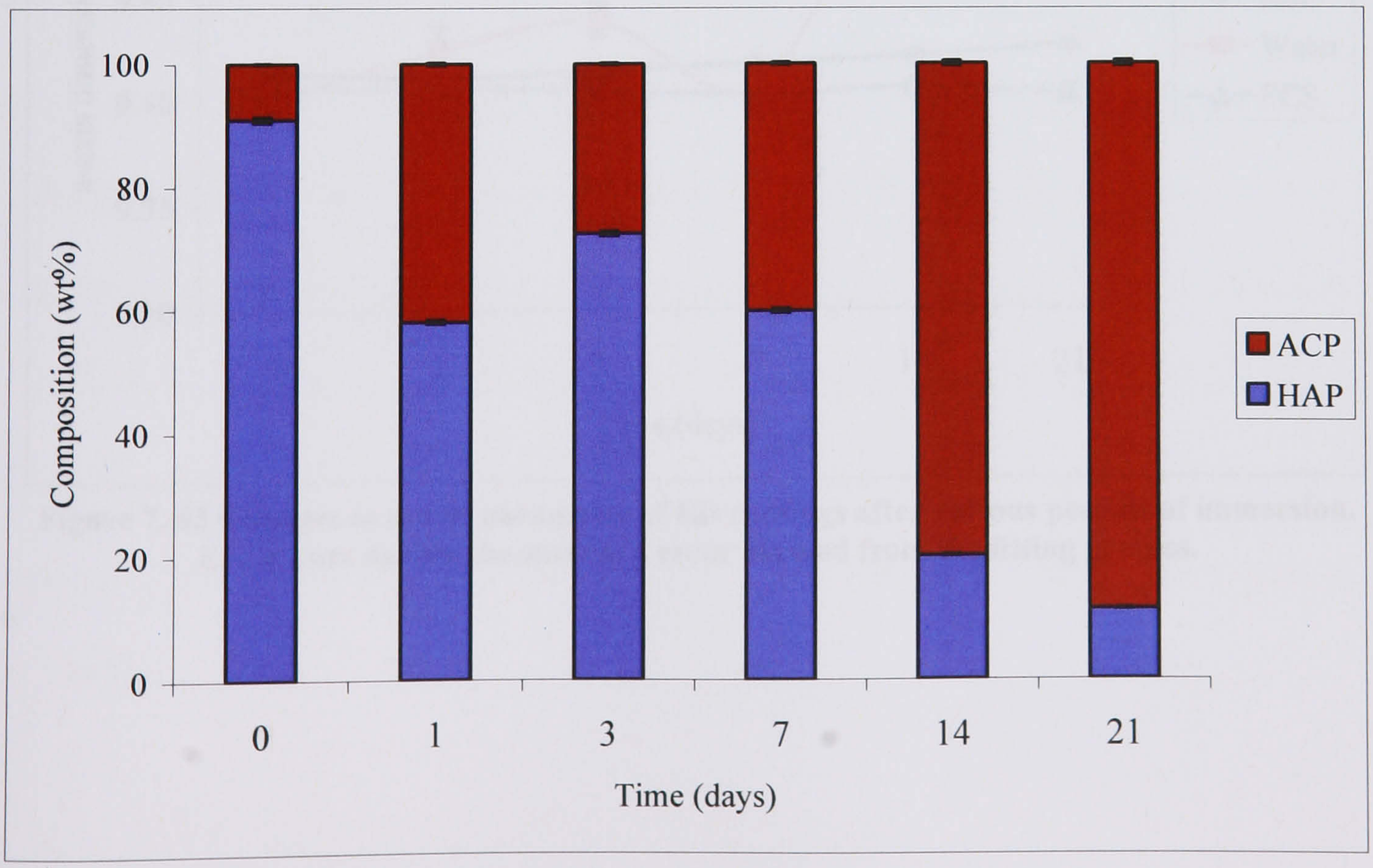

Figure 7. 61 Changes in composition of ED coatings after various periods of immersion in water.

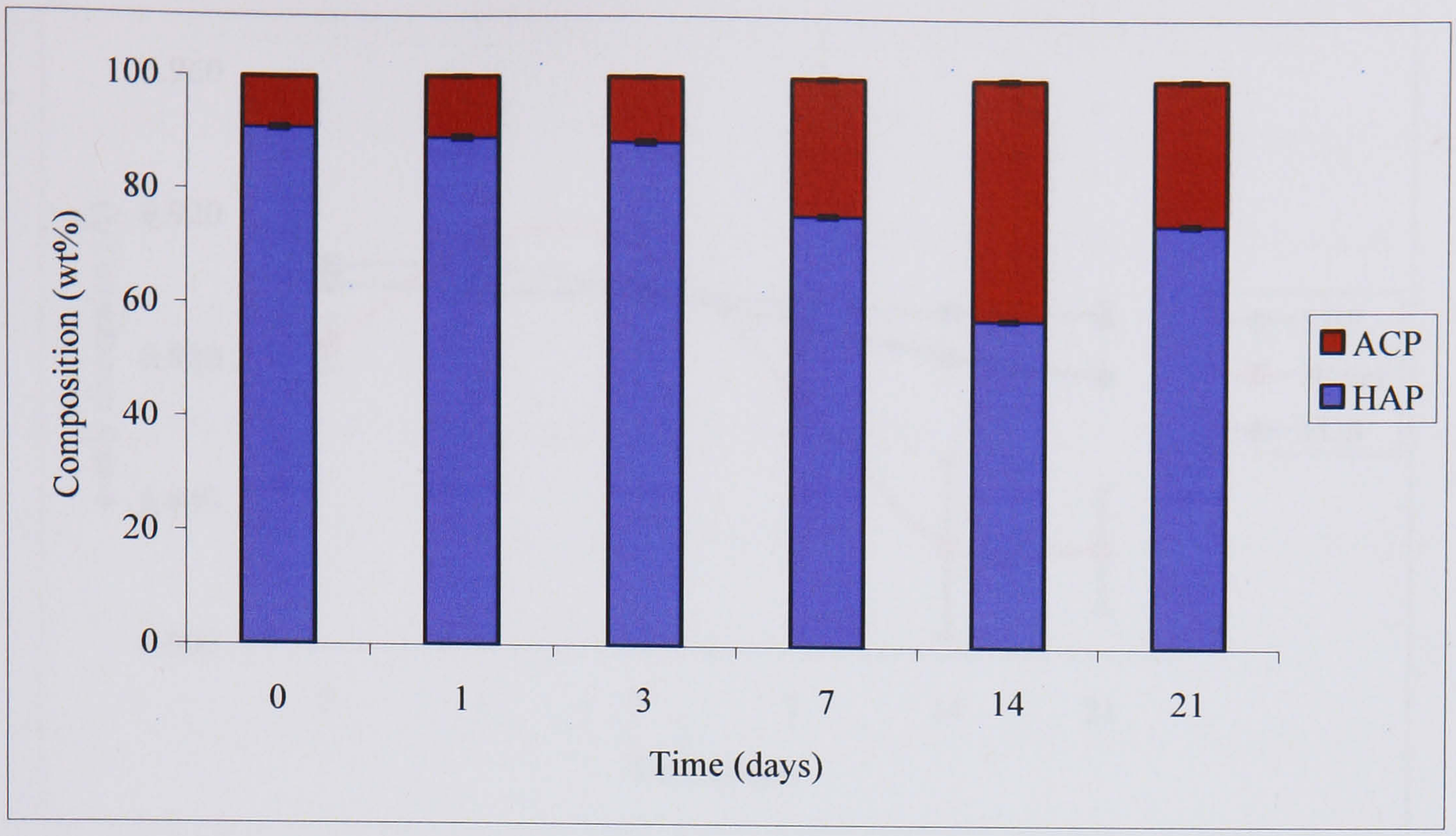

Figure 7. 62 Changes in composition of ED coatings after various periods of immersion in FCS.

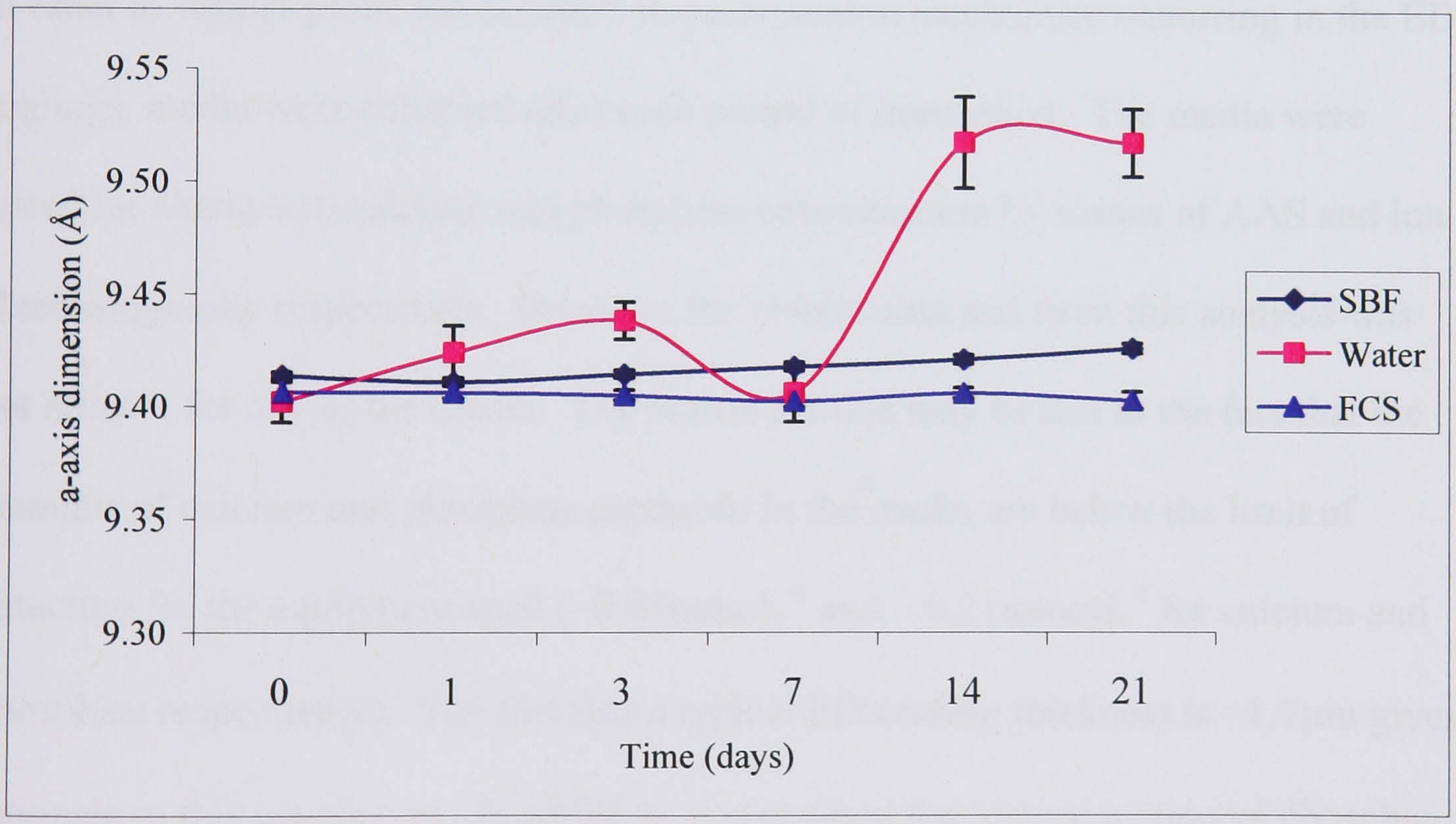

Figure 7. 63 Changes to a-axis parameter of ED coatings after various periods of immersion. Error bars denote the standard error derived from the fitting process.

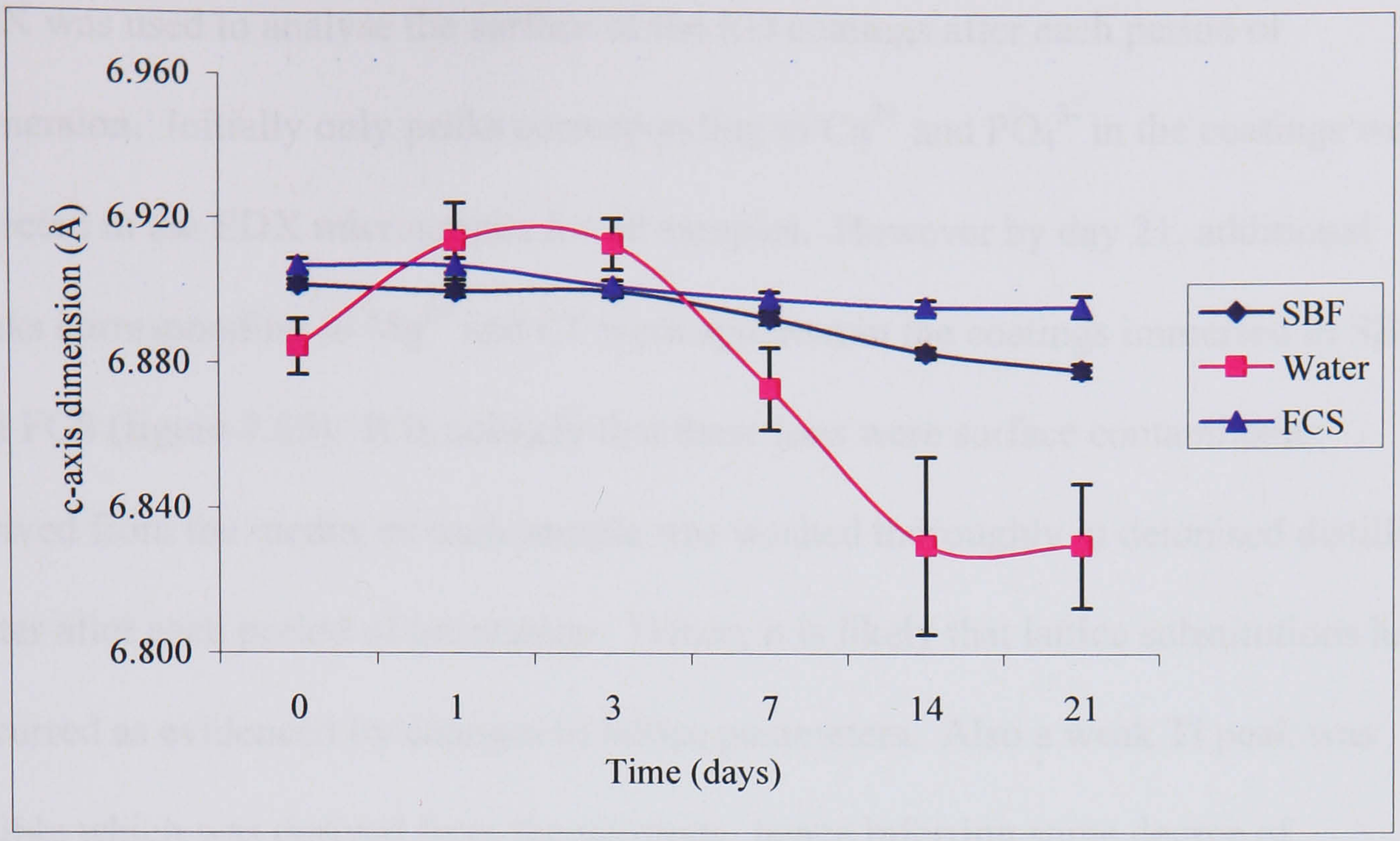

Figure 7. 64 Changes to c-axis parameter of ED coatings after various periods of immersion. Error bars denote the standard error derived from the fitting process.

7.2.2.2 Chemical analyses

In order to further probe the dissolution-precipitation mechanism occurring in the ED coatings, media were collected after each period of immersion. The media were tested for changes in calcium and phosphate concentration by means of AAS and ion chromatography respectively. However the results obtained from this analysis was not reliable for any of the media. The reason for this may be due to the fact that the amounts of calcium and phosphate produced in the media are below the limit of detection for the equipment used (~0.03mmolL^{-1} and ~ 0.21mmolL^{-1} for calcium and phosphate respectively). The fact that a typical ED coating thickness is ~1.7μm gives rationale to this conclusion. In addition, it was noted that determination of phosphate content in FCS was particularly difficult due to the interference from other anions in the media.

EDX was used to analyse the surface of the ED coatings after each period of immersion. Initially only peaks corresponding to Ca^{2+} and PO_4^{3-} in the coatings were detected in the EDX micrographs for all samples. However by day 21, additional peaks corresponding to Mg^{2+} and Cl^- were apparent in the coatings immersed in SBF and FCS (figure 7.65). It is unlikely that these ions were surface contaminants derived from the media, as each sample was washed thoroughly in deionised distilled water after each period of immersion. Hence, it is likely that lattice substitutions have occurred as evidenced by changes in lattice parameters. Also a weak Ti peak was visible which was derived from the substrate, hence inferring some degree of dissolution of these coatings had occurred. EDX analysis of the samples immersed in water revealed substrate peaks as well as weak peaks for Ca^{2+} and PO_4^{3-}.

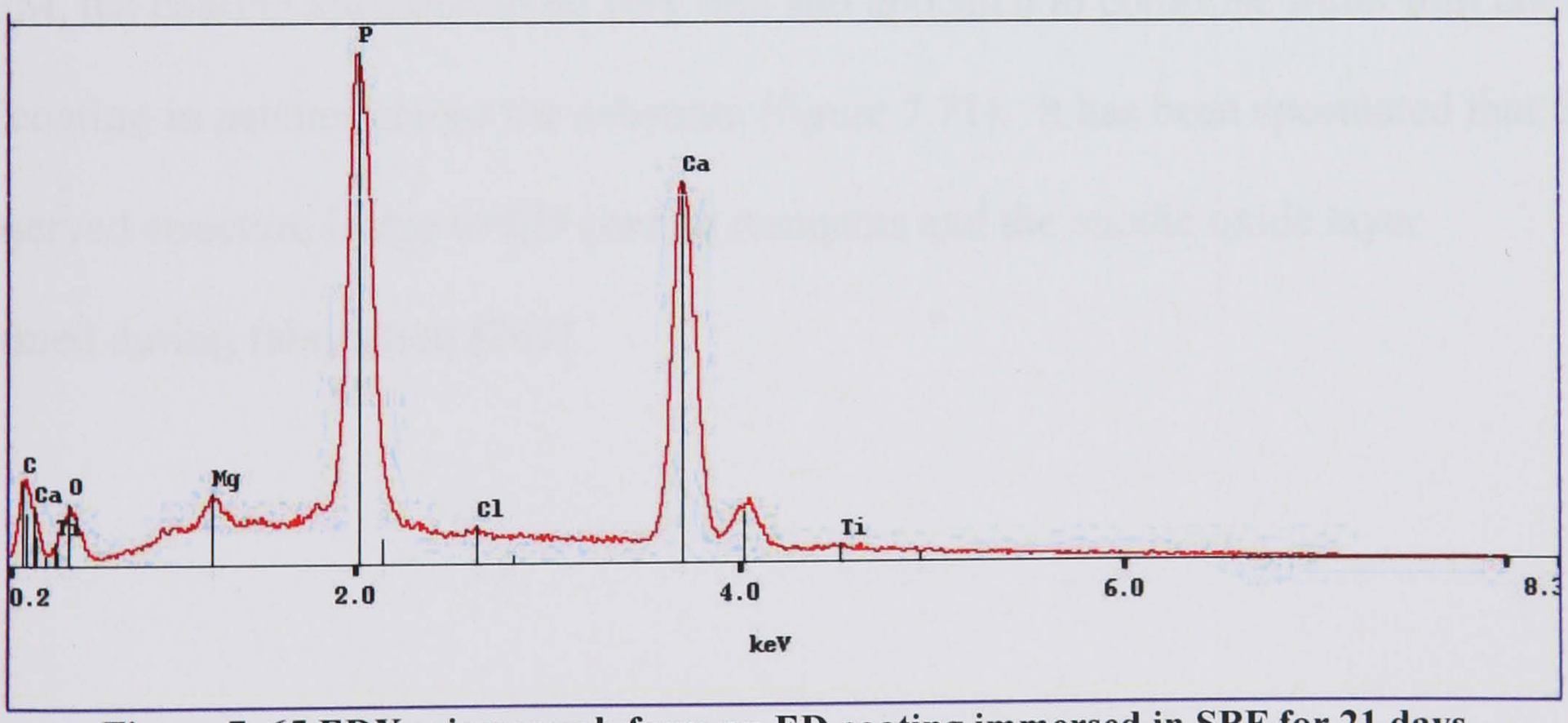

Figure 7. 65 EDX micrograph from an ED coating immersed in SBF for 21 days.

7.2.2.2 Morphological analysis

An assessment of the changes occurring in the morphology of ED coatings was conducted by SEM analysis. After three days of immersion in SBF, the coatings had cracks (figure 7.66). Some of these cracks were surface cracks and others were through-thickness cracks. By day 21 the through-thickness cracks dominated the surface of the coating (figure 7.67). Small nodular surface precipitates were visible on the surface of the coating. Other regions of the coating were characterised by tiny needle-like crystals and through-thickness pores (figure 7.68). Similar changes in coating morphology were observed for coatings immersed in FCS. Large through-thickness cracks were visible in the ED coating immersed in water on day 3 (figure 7.69). These cracks were large and it appeared that areas of the coating had come away from the substrate. Other areas of the coating were characterised by clusters of large pores, which were 1-2μm in diameter (figure 7.70). By day 21 a very superficial coating remained which could not be seen by visual inspection. Under SEM, the coating appeared to be very thin and appeared to comprise wafer thin layers of coating in patches across the substrate (figure 7.71). It has been speculated that the observed structure is due to ED coating remnants and the anodic oxide layer formed during fabrication [265].

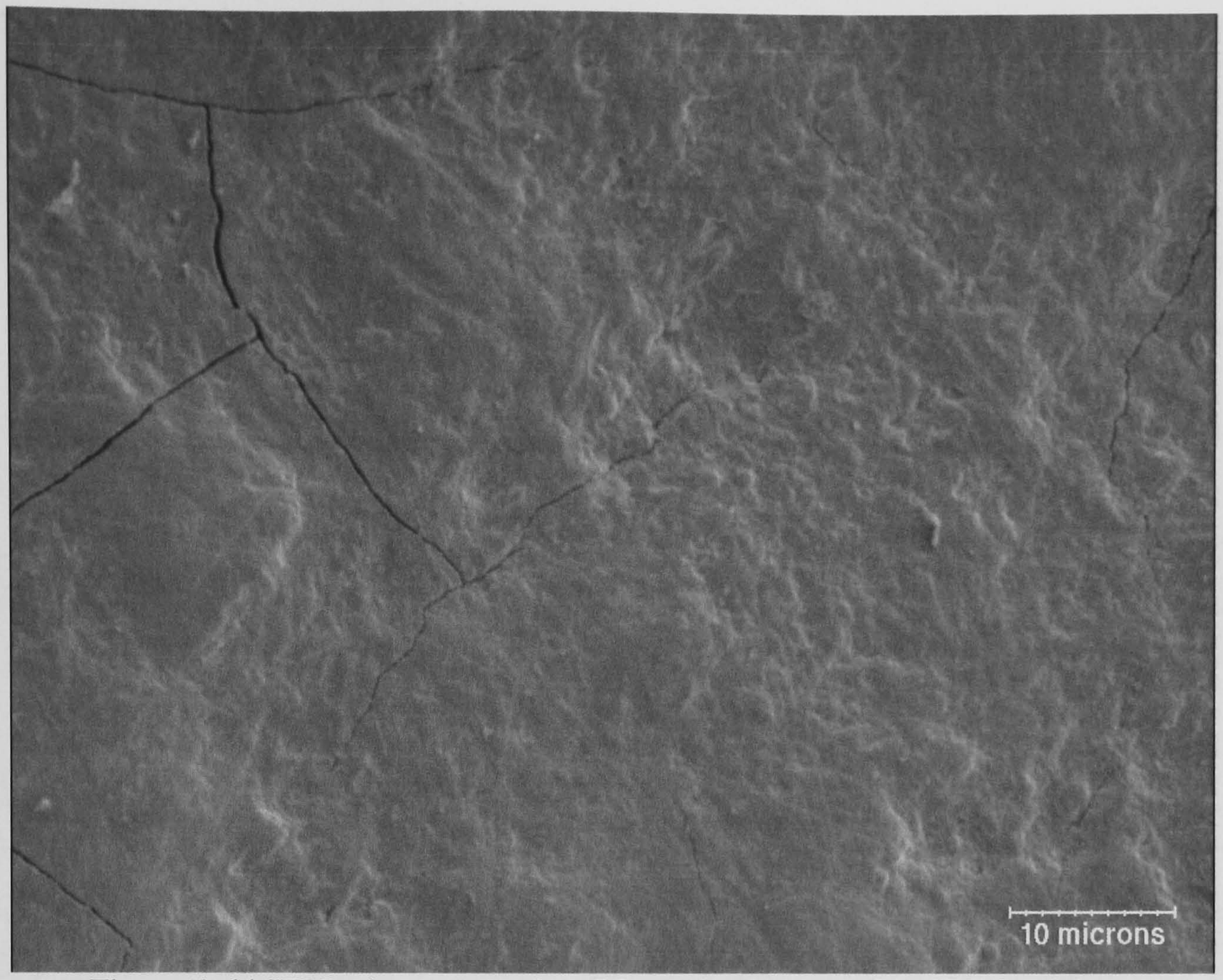

Figure 7. 66 SEM micrograph of an ED coating immersed in SBF for 3 days.

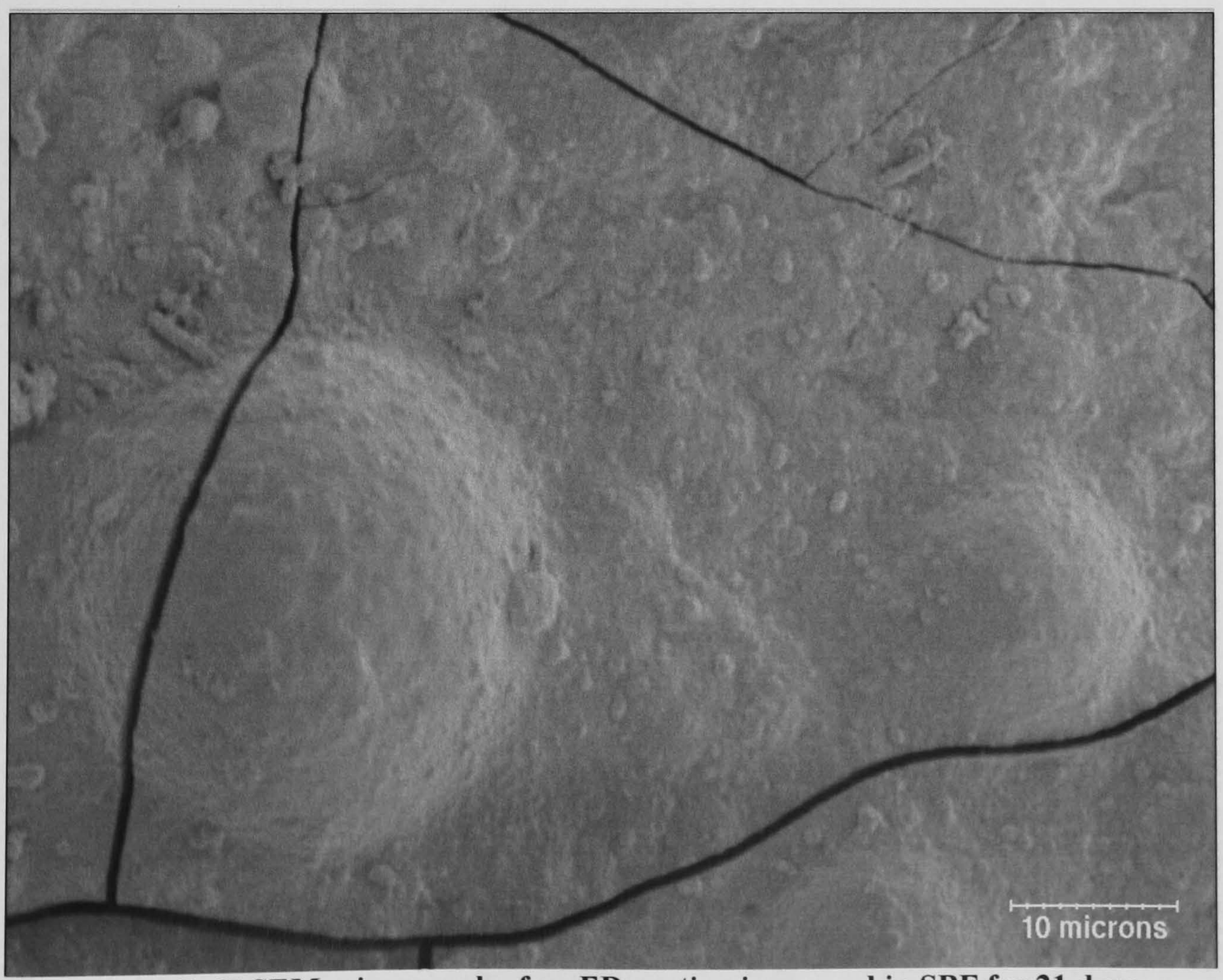

Figure 7. 67 SEM micrograph of an ED coating immersed in SBF for 21 days.

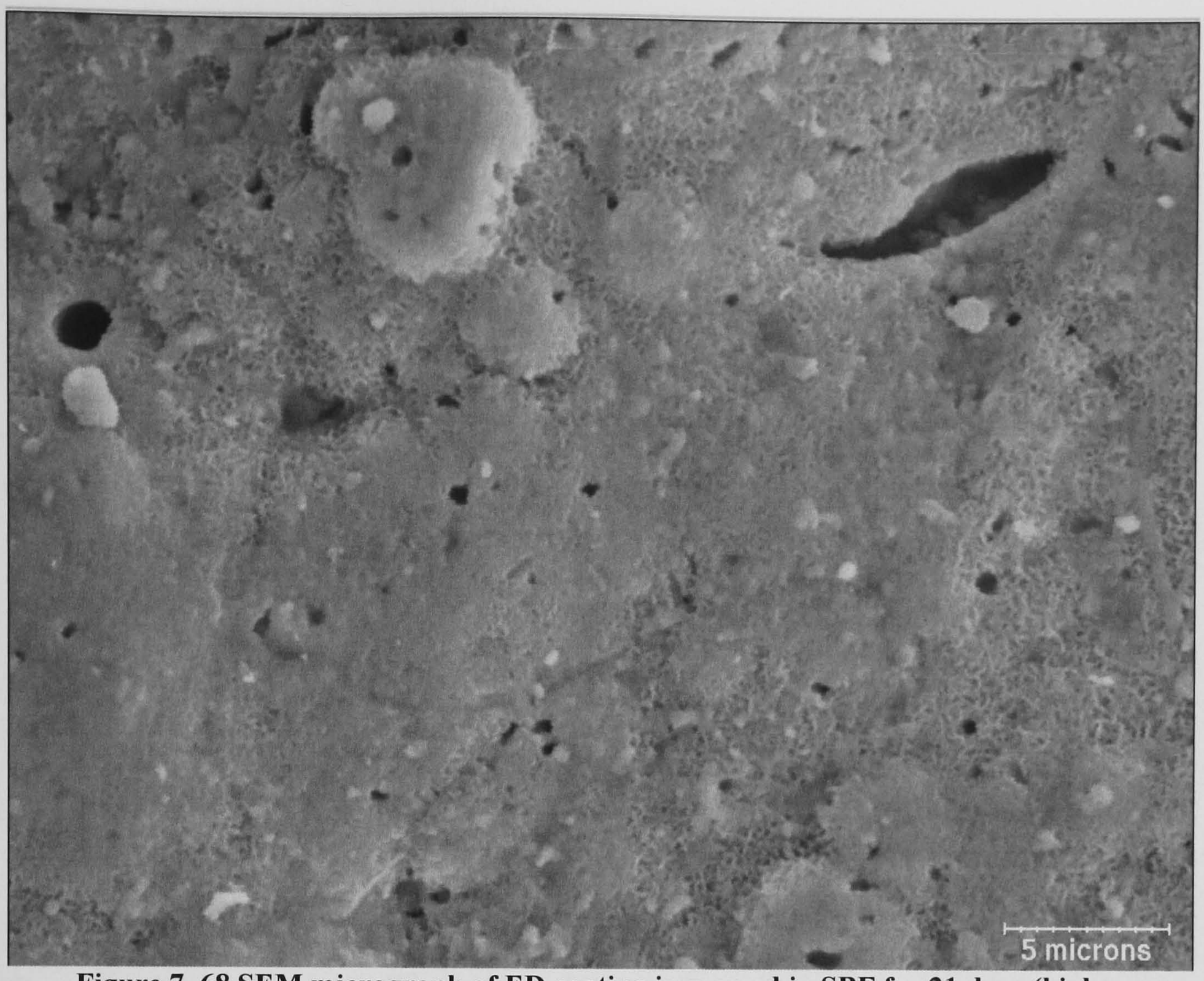

Figure 7. 68 SEM micrograph of ED coating immersed in SBF for 21 days (higher magnification).

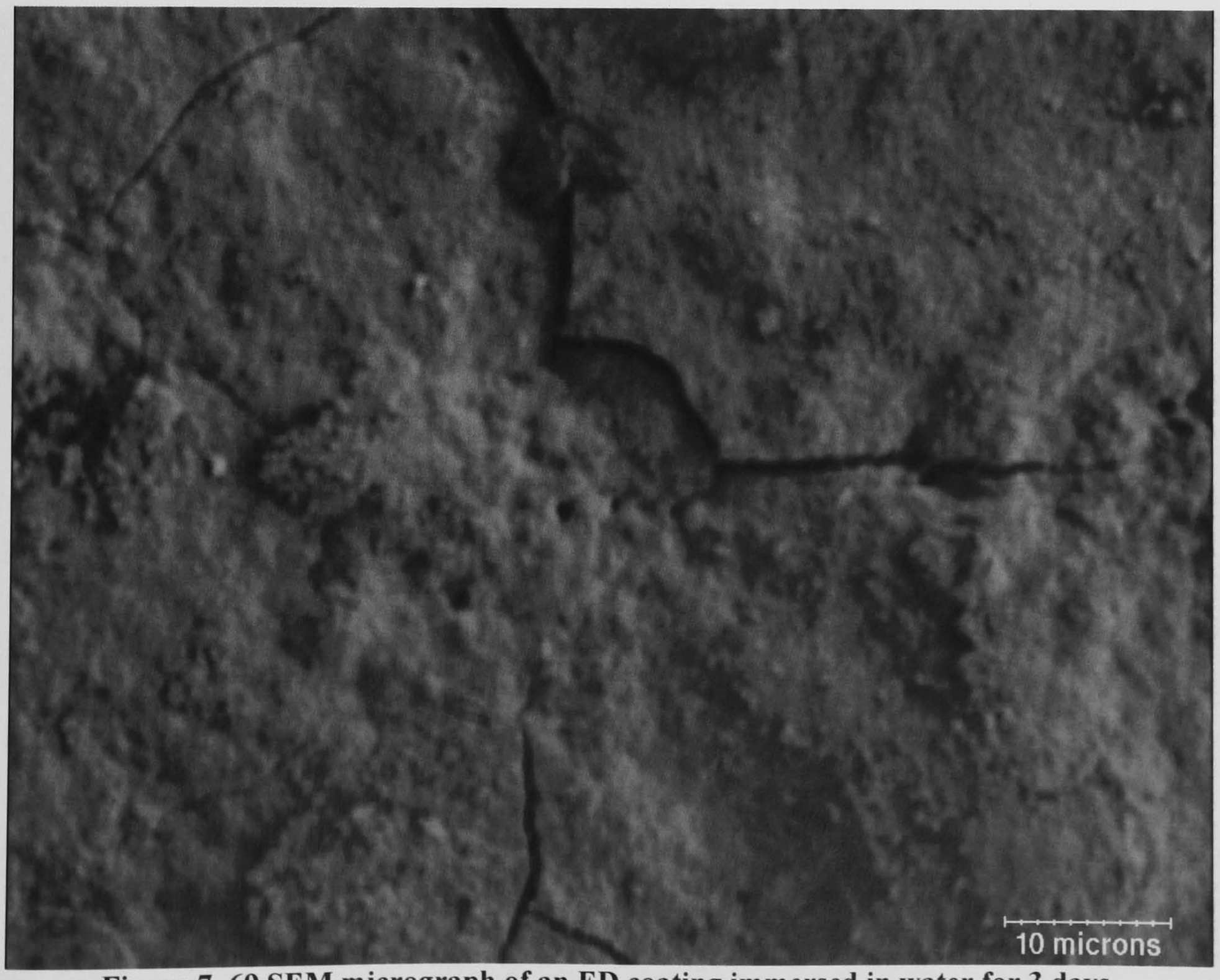

Figure 7. 69 SEM micrograph of an ED coating immersed in water for 3 days.

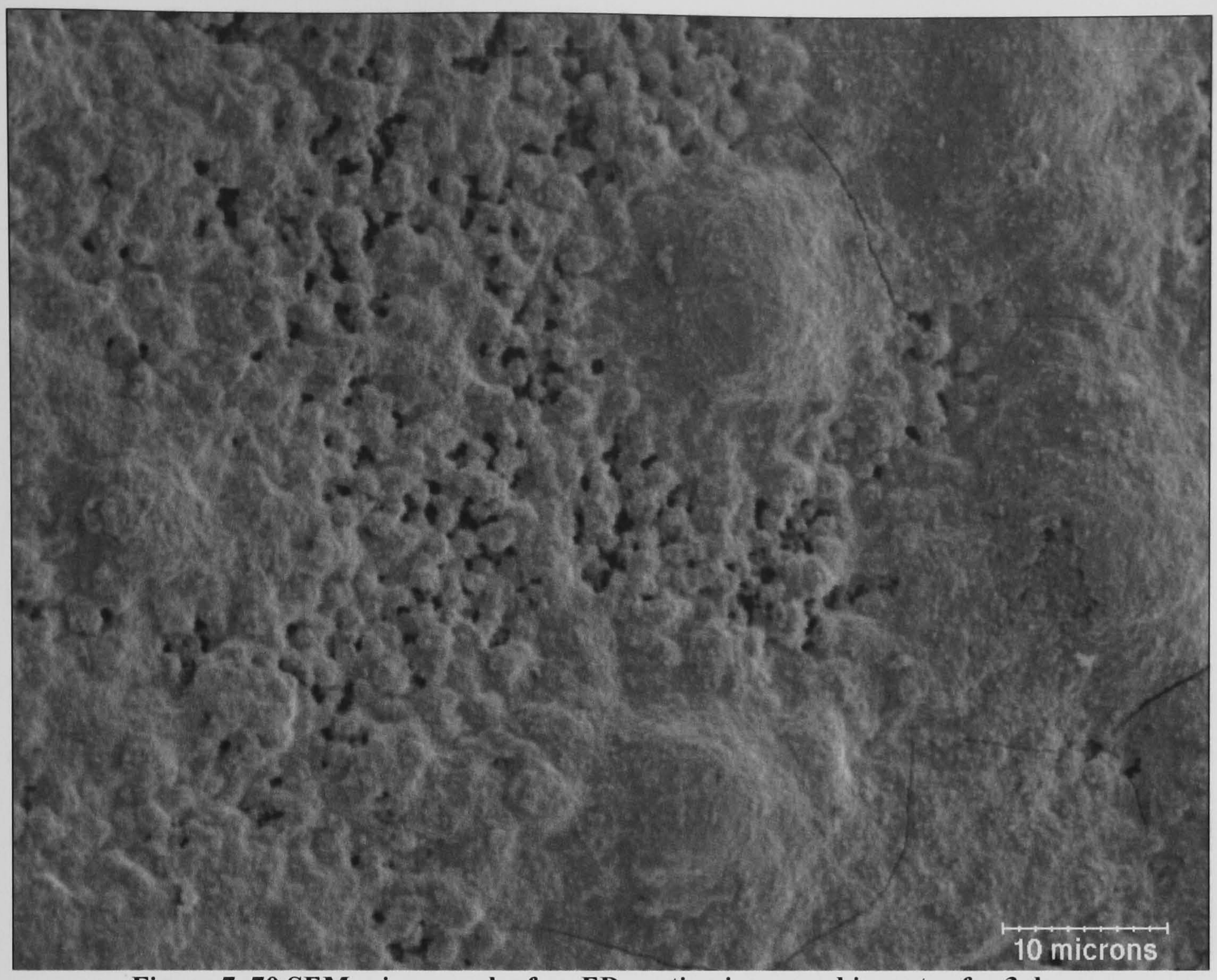

Figure 7. 70 SEM micrograph of an ED coating immersed in water for 3 days.

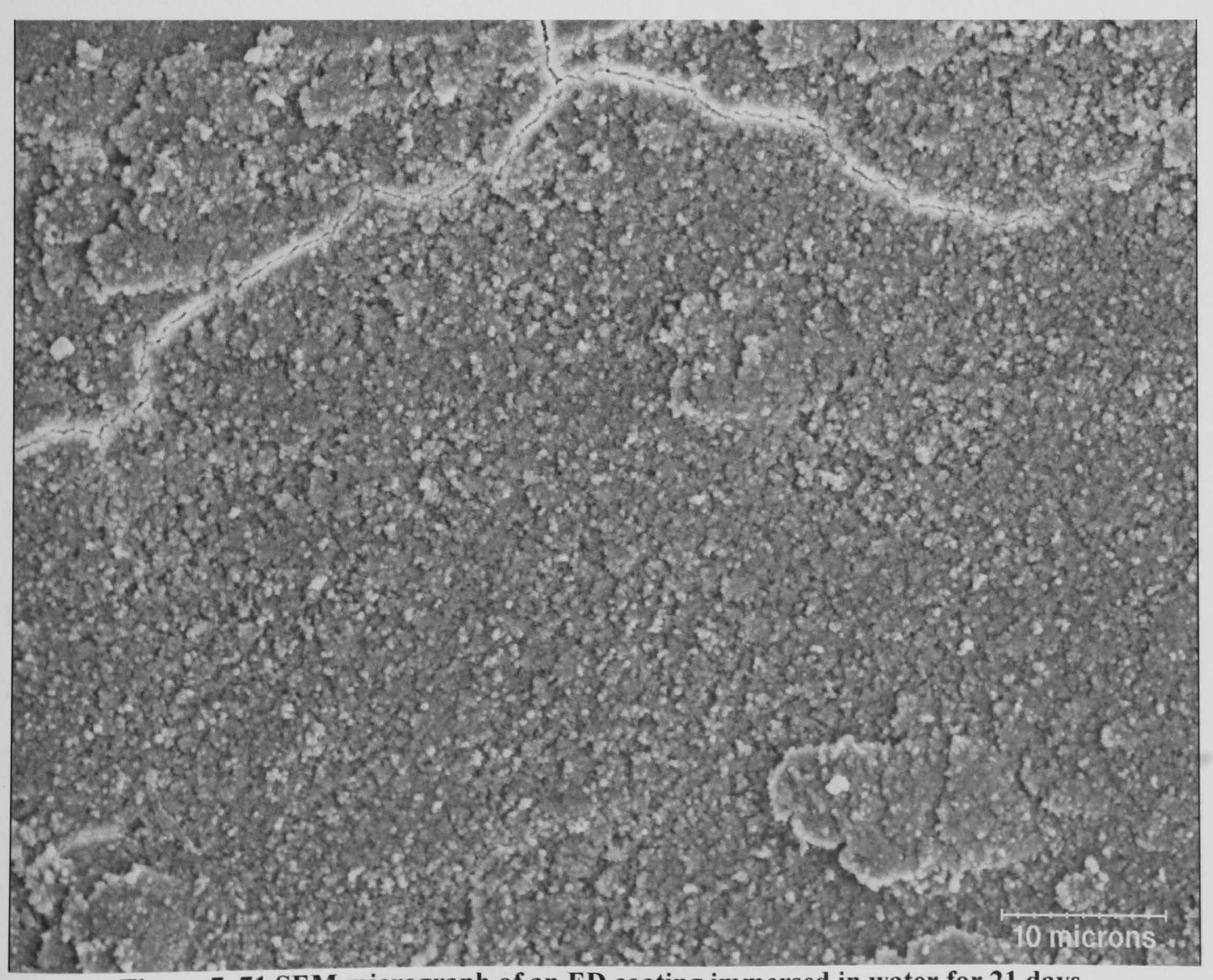

Figure 7. 71 SEM micrograph of an ED coating immersed in water for 21 days.

7.2.3 *In vitro* behaviour of apatite powders.

7.2.3.1 Solubility

A systematic series of apatite powders has been produced with varying carbonate, microstrain and crystallite size. In order to ascertain the effect each of these variables has on the solubility behaviour of HAP, solubility measurements have been made in deionised distilled water. Water (as opposed to SBF) was used as the solvent in this case in order to find the K_{sp} at physiological pH without interference from other ions such as HPO_4^{2-}, CO_3^{2-} and Mg^{2+}, which are known to disturb the apatite crystal lattice and affect solubility [56, 174]. Solubility measurements were taken after 24 hours of equilibration and K_{sp} calculations have been made using equation 6.2. Table 7.10 shows the variation of pK_{sp} with crystallite size, microstrain and carbonate content for all of the apatite powders investigated.

It can be seen from table 7.10 that as the wt% of carbonate increases so does the solubility of the apatite and sample 3.5CHA has the greatest solubility of all powders investigated. The solubility measured for samples size25, size55 and size80, showed a decrease with the increase of crystallite size. The range of values of pK_{sp} measured for the aforementioned samples was comparable to the pK_{sp} of HAP (~118) reported in the literature [222]. Samples strain1, strain2 and strain3 showed an increase in solubility with increase in strain. It can be seen from the solubility of the series of powders investigated that carbonate content, crystallite size and microstrain all appeared to have an affect on the solubility of the apatite powders.

Sample	Crystallite size (Å)	Microstrain (%)	CO_3^{2-} content (wt%)	Mean pKsp
Size25	275	0.25	0*	119.22
Size55	388	0.21	0*	119.78
Size80	906	0.16	0*	120.40
Strain1	501	0.18	0*	119.90
Strain2	378	0.36	0*	116.89
Strain3	316	0.56	0*	114.42
0.5CHA	800	0.29	0.52	116.08
2.3CHA	402	0.35	2.25	115.75
3.5CHA	367	0.44	3.57	114.29

Table 7. 10 Variation of mean pKsp with crystallite size, microstrain and carbonate content of apatite powders. (* denotes < 0.5wt%).

In order to further investigate the effect of size, strain and carbonate content on solubility, graphs of pK_{sp} versus each of the variables were constructed. It can be seen from figure 7.72 that there is a weak correlation between pK_{sp} and crystallite size. Figure 7.73 in contrast shows a strong linear correlation between pK_{sp} and microstrain. Further correlation analysis was conducted to obtain Pearson's correlation coefficients (PCC). The closer the PCC is to 1 or –1, the better the linear fit. PCC values of -0.919, -0.368 and -0.612 were obtained for pK_{sp} correlations with microstrain, crystallite size and carbonate content respectively. Interestingly, statistical analysis also revealed that carbonate content of samples 0.5CHA, 2.3CHA and 3.5CHA is strongly correlated to both crystallite size and microstrain with respective PCC values of -0.944 and 0.960. Since carbonate is strongly correlated to both crystallite size (inversely) and microstrain and microstrain is strongly correlated to solubility, it follows that the solubility increase with carbonate content is predominantly due to an increase in microstrain. Also, carbonate content alone is not

the contributing factor to changes in solubility. This is further illustrated in figure 7.74, which exemplifies the changes in solubility with carbonate content. It can be seen that although solubility increases with carbonate content for samples 0.5CHA, 2.3CHA and 3.5CHA, the differences in solubilities of strain1-3 and size25-80 samples are independent of carbonate content; hence there is no correlation. Figure 7.73 on the other hand accounts for the changes in solubility. It has therefore been demonstrated that microstrain has the greatest effect on the solubility of both HAP and carbonated apatites, although small crystallite size may make a modest contribution to solubility.

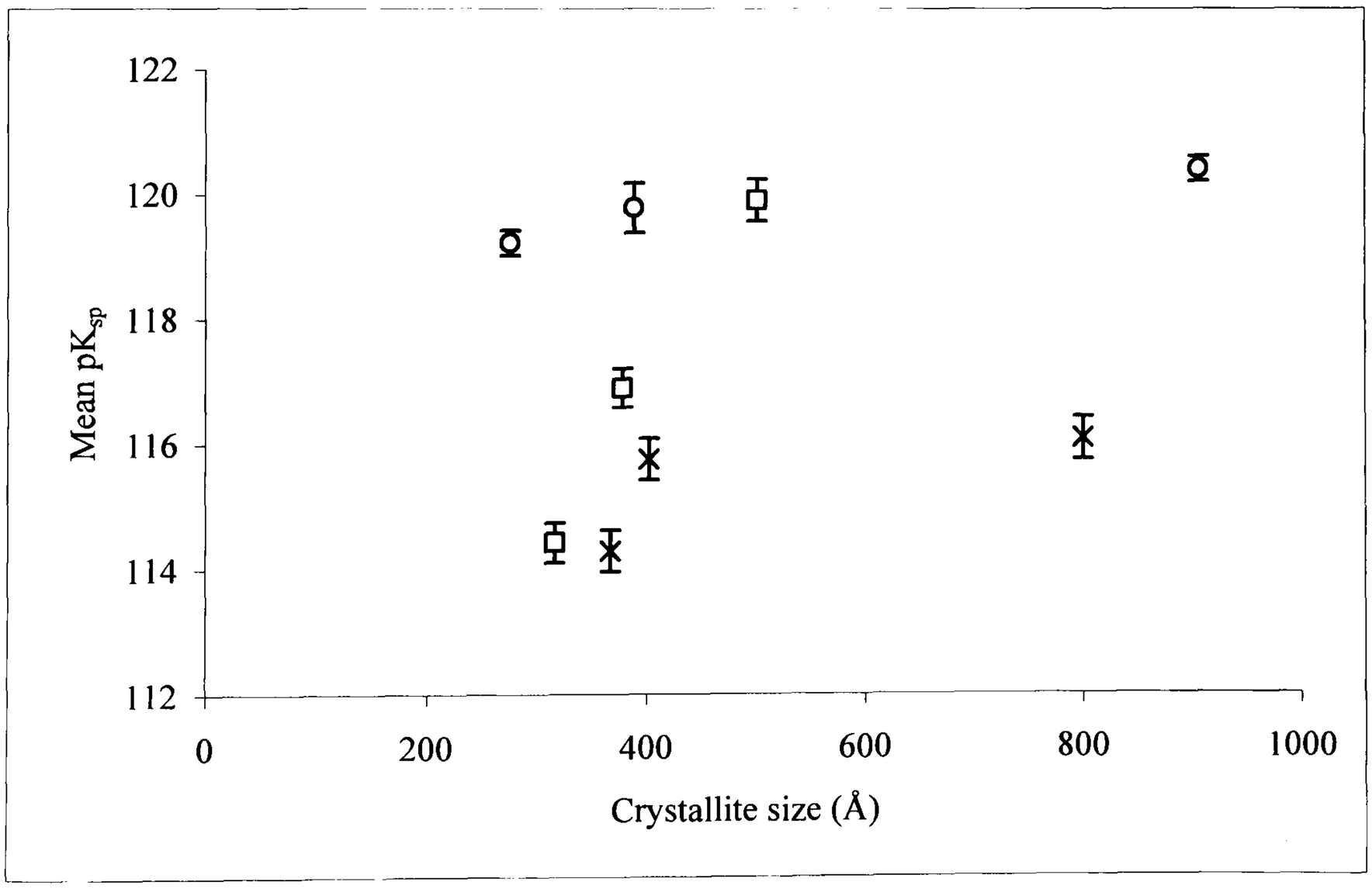

Figure 7. 72 Relationship between mean pK_{sp} and crystallite size of a series of apatites with varying crystallite size (o), strain (□)and carbonate content (X). Error bars denote the standard error.

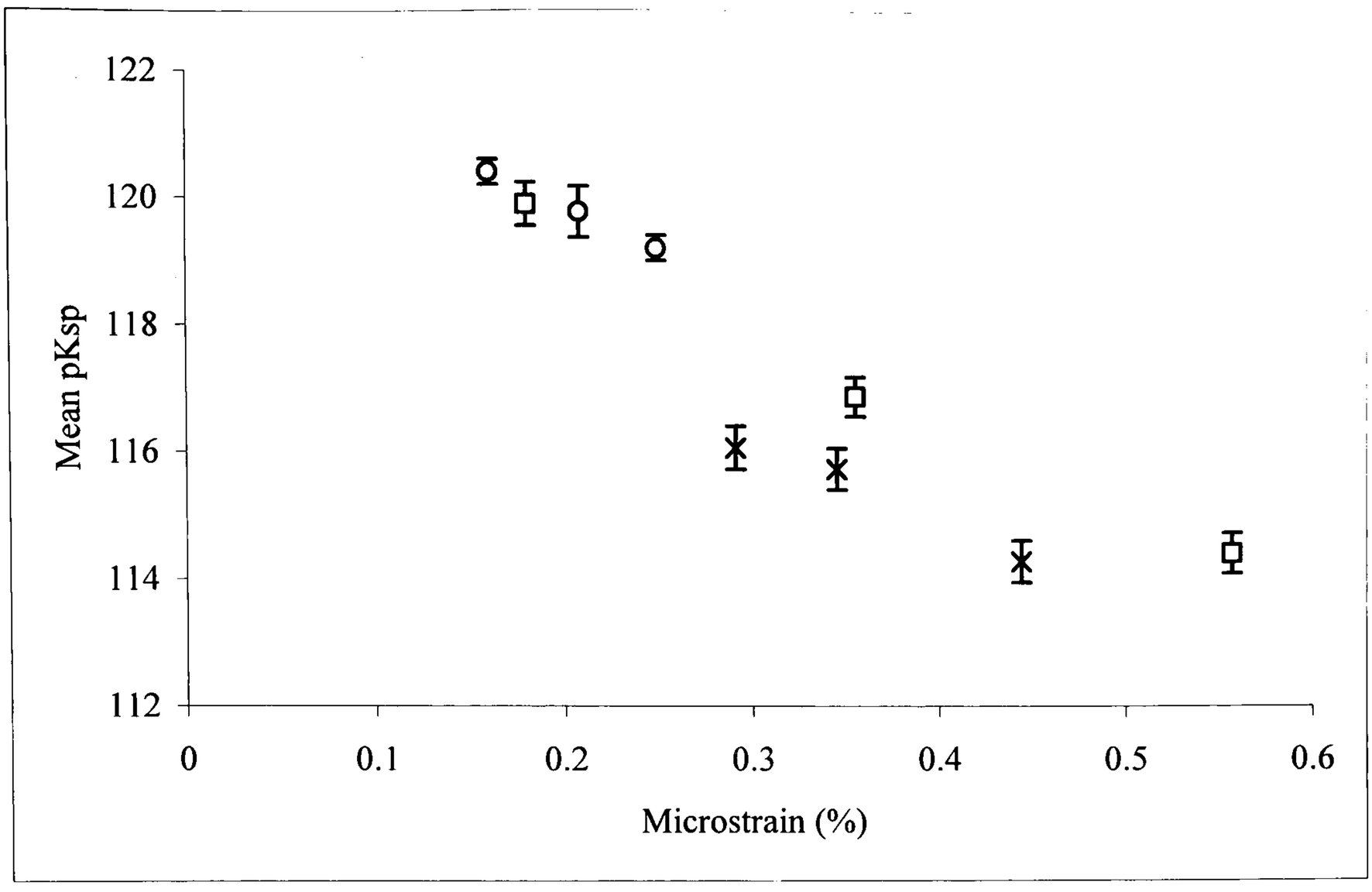

Figure 7. 73 Relationship between mean pK_{sp} and microstrain of a series of apatites with varying crystallite size (o), strain (□)and carbonate content (X). Error bars denote the standard error.

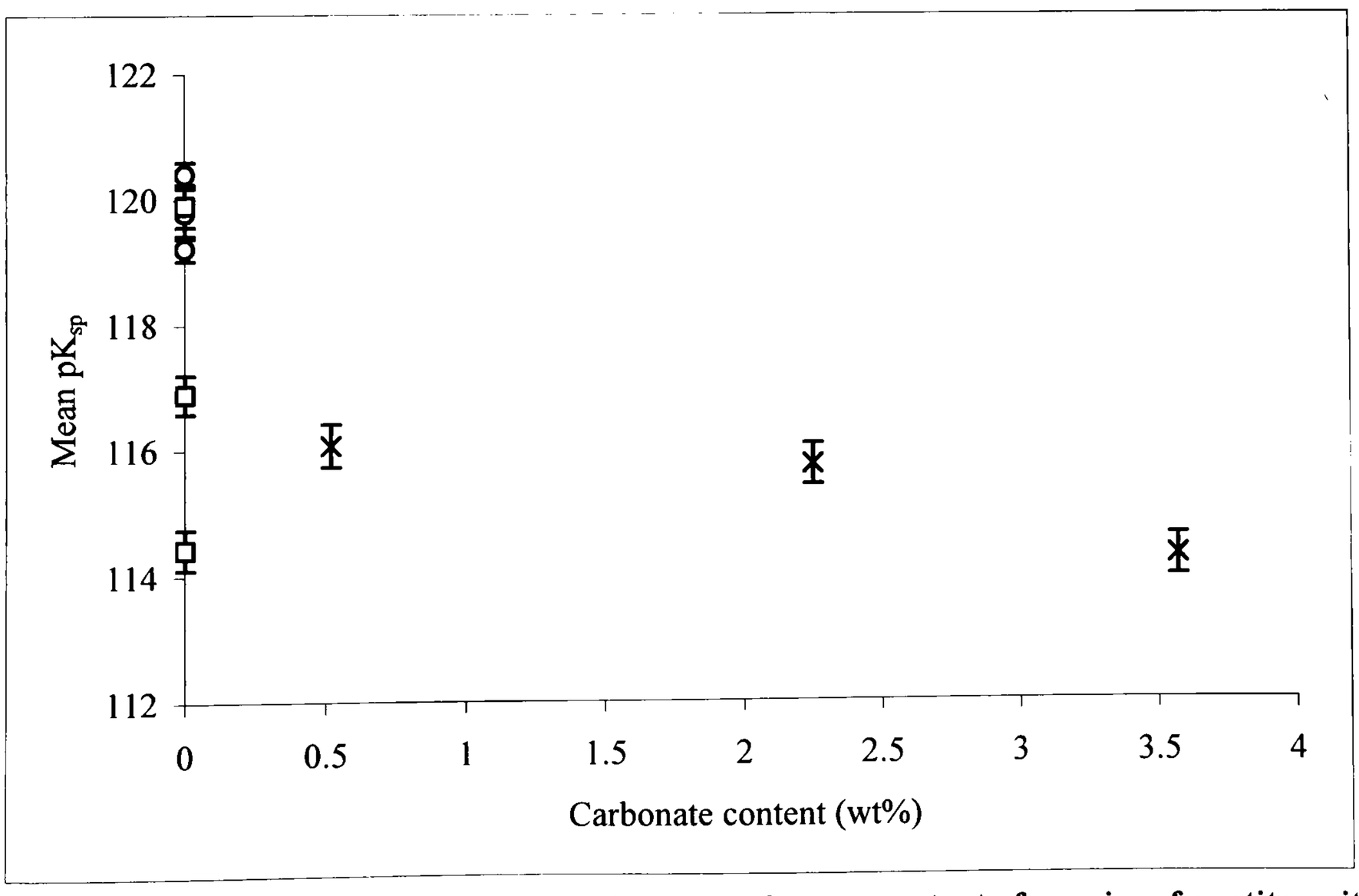

Figure 7. 74 Relationship between mean K_{sp} and carbonate content of a series of apatites with varying crystallite size (o), strain (□)and carbonate content (X). Error bars denote the standard error.

7.2.3.2 In vitro behaviour in SBF and water

In order to investigate the effect of microstrain, crystallite size and carbonate on the *in vitro* behaviour of apatites, the powders fabricated and characterised in section 7.1 were immersed in SBF for periods of up to 21 days. After each period of immersion, the powders were retrieved, washed in deionised distilled water, dried in air and characterised by means of XRD, SEM and FTIR. The chemical and structural changes occurring with immersion time in SBF has been examined. Water was used as the control to distinguish between media related changes and dissolution-precipitation related changes.

No visible changes were observed in the diffraction patterns of the respective as-received apatite samples compared to the apatite samples that had been immersed in SBF. Tables 7.11-19 show a summary of the changes in the principal structural characteristics with immersion time for each of the apatite samples. In general, for all apatite powders immersed in SBF and water respectively, there was a decrease in a-axis parameter, c-axis parameters and microstrain with immersion time. The net reduction crystallite size after immersion in SBF for 21 days did not correlate with the measured solubilities presented in table 7.10 for any of the powders investigated. In contrast, changes in the crystallite sizes appeared to be related to the initial crystallite size. The powders with the largest initial crystallite had the greatest reduction in crystal size during immersion and the samples with the smaller crystallite sizes appeared to have no net reduction in size. This suggests that the powders with the largest crystallite size underwent the greatest degree of dissolution irrespective of carbonate content, microstrain and solubility. This discovery suggests that 'crystallite size-dependent' dissolution has occurred.

Sample	Immersion time (days)	a (Å)	c (Å)	Crystallite size (Å)	Microstrain (%)	%HAP
Size25	0	$9.437 \pm 4.9 \times 10^{-4}$	$6.884 \pm 7.4 \times 10^{-4}$	275 ± 21	$0.25 \pm 1 \times 10^{-3}$	91.0 ± 0.5
	7	$9.440 \pm 4.5 \times 10^{-4}$	$6.883 \pm 4.6 \times 10^{-4}$	285 ± 21	$0.22 \pm 1 \times 10^{-3}$	99.0 ± 0.5
	14	$9.435 \pm 9.1 \times 10^{-4}$	$6.883 \pm 4.4 \times 10^{-4}$	279 ± 21	$0.18 \pm 1 \times 10^{-3}$	94.0 ± 0.5
	21	$9.437 \pm 7.9 \times 10^{-4}$	$6.883 \pm 7.0 \times 10^{-4}$	273 ± 21	$0.18 \pm 1 \times 10^{-3}$	93.1 ± 0.5

Table 7. 11 Changes in the principal structural properties of sample size25 with immersion time in SBF. Errors are the standard error derived from the fitting process.

Sample	Immersion time (days)	a (Å)	c (Å)	Crystallite size (Å)	Microstrain (%)	%HAP
Size55	0	$9.430 \pm 3.4 \times 10^{-4}$	$6.891 \pm 3.2 \times 10^{-4}$	388 ± 29	$0.21 \pm 1 \times 10^{-3}$	95.0 ± 0.5
	7	$9.436 \pm 4.9 \times 10^{-4}$	$6.890 \pm 4.5 \times 10^{-4}$	409 ± 31	$0.18 \pm 1 \times 10^{-3}$	96.0 ± 0.5
	14	$9.429 \pm 7.6 \times 10^{-4}$	$6.888 \pm 6.1 \times 10^{-4}$	398 ± 30	$0.15 \pm 1 \times 10^{-3}$	96.0 ± 0.5
	21	$9.430 \pm 6.3 \times 10^{-4}$	$6.890 \pm 4.8 \times 10^{-4}$	382 ± 28	$0.13 \pm 1 \times 10^{-3}$	95.0 ± 0.5

Table 7. 12 Changes in the principal structural properties of sample size55 with immersion time in SBF. Errors are the standard error derived from the fitting process.

Sample	Immersion time (days)	a (Å)	c (Å)	Crystallite size (Å)	Microstrain (%)	%HAP
Size80	0	$9.428 \pm 2.2 \times 10^{-4}$	$6.892 \pm 2.2 \times 10^{-4}$	906 ± 68	$0.16 \pm 1 \times 10^{-3}$	96.0 ± 0.5
	7	$9.407 \pm 3.0 \times 10^{-4}$	$6.887 \pm 3.2 \times 10^{-4}$	503 ± 38	$0.13 \pm 1 \times 10^{-3}$	100 ± 0.5
	14	$9.406 \pm 2.7 \times 10^{-4}$	$6.885 \pm 2.8 \times 10^{-4}$	491 ± 37	$0.13 \pm 1 \times 10^{-3}$	100 ± 0.5
	21	$9.411 \pm 3.0 \times 10^{-4}$	$6.888 \pm 3.1 \times 10^{-4}$	483 ± 36	$0.10 \pm 1 \times 10^{-3}$	95.5 ± 0.5

Table 7. 13 Changes in the principal structural properties of sample size80 with immersion time in SBF. Errors are the standard error derived from the fitting process.

Sample	Immersion time (days)	a (Å)	c (Å)	Crystallite size (Å)	Microstrain (%)	%HAP
Strain1	0	$9.447 \pm 3.2 \times 10^{-4}$	$6.886 \pm 2.8 \times 10^{-4}$	501 ± 38	$0.18 \pm 1 \times 10^{-3}$	100 ± 0.5
	7	$9.447 \pm 9.0 \times 10^{-4}$	$6.884 \pm 7.2 \times 10^{-4}$	348 ± 26	$0.15 \pm 1 \times 10^{-3}$	100 ± 0.5
	14	$9.443 \pm 8.9 \times 10^{-4}$	$6.883 \pm 7.2 \times 10^{-4}$	307 ± 23	$0.16 \pm 1 \times 10^{-3}$	100 ± 0.5
	21	$9.439 \pm 8.6 \times 10^{-4}$	$6.883 \pm 8.6 \times 10^{-4}$	$376. \pm 28$	$0.14 \pm 1 \times 10^{-3}$	99.0 ± 0.5

Table 7. 14 Changes in the principal structural properties of sample strain1 with immersion time in SBF. Errors are the standard error derived from the fitting process.

Sample	Immersion time (days)	a (Å)	c (Å)	Crystallite size (Å)	Microstrain (%)	%HAP
Strain2	0	$9.446 \pm 2.5 \times 10^{-4}$	$6.886 \pm 2.9 \times 10^{-4}$	378 ± 28	$0.36 \pm 1 \times 10^{-3}$	99.0 ± 0.5
	7	$9.442 \pm 9.2 \times 10^{-4}$	$6.883 \pm 0.0 \times 10^{-4}$	379 ± 28	$0.33 \pm 1 \times 10^{-3}$	100 ± 0.5
	14	$9.441 \pm 9.0 \times 10^{-4}$	$6.883 \pm 0.0 \times 10^{-4}$	397 ± 30	$0.25 \pm 1 \times 10^{-3}$	100 ± 0.5
	21	$9.440 \pm 9.0 \times 10^{-4}$	$6.884 \pm 0.0 \times 10^{-4}$	351 ± 28	$0.24 \pm 1 \times 10^{-3}$	100 ± 0.5

Table 7. 15 Changes in the principal structural properties of sample strain2 with immersion time in SBF. Errors are the standard error derived from the fitting process.

Sample	Immersion time (days)	a (Å)	c (Å)	Crystallite size (Å)	Microstrain (%)	%HAP
Strain3	0	$9.442 \pm 4.3 \times 10^{-4}$	$6.885 \pm 2.1 \times 10^{-4}$	316 ± 23	$0.56 \pm 1 \times 10^{-3}$	97.0 ± 0.5
	7	$9.442 \pm 4.9 \times 10^{-4}$	$6.885 \pm 4.7 \times 10^{-4}$	350 ± 26	$0.47 \pm 1 \times 10^{-3}$	98.5 ± 0.5
	14	$9.441 \pm 5.0 \times 10^{-4}$	$6.883 \pm 4.6 \times 10^{-4}$	343 ± 26	$0.40 \pm 1 \times 10^{-3}$	99.0 ± 0.5
	21	$9.440 \pm 9.0 \times 10^{-4}$	$6.883 \pm 7.2 \times 10^{-4}$	331.4 ± 25	$0.37 \pm 1 \times 10^{-3}$	100 ± 0.5

Table 7. 16 Changes in the principal structural properties of sample strain3 with immersion time in SBF. Errors are the standard error derived from the fitting process.

Sample	Immersion time (days)	a (Å)	c (Å)	Crystallite size (Å)	Microstrain (%)	%AP
0.5CHA	0	$9.439 \pm 3.2 \times 10^{-4}$	$6.880 \pm 4.4 \times 10^{-4}$	800 ± 60	$0.29 \pm 1 \times 10^{-3}$	98.0 ± 0.5
	7	$9.437 \pm 9.8 \times 10^{-4}$	$6.879 \pm 7.6 \times 10^{-4}$	679 ± 50	$0.28 \pm 1 \times 10^{-3}$	99.0 ± 0.5
	14	$9.435 \pm 7.8 \times 10^{-4}$	$6.879 \pm 5.9 \times 10^{-4}$	520 ± 39	$0.22 \pm 1 \times 10^{-3}$	100 ± 0.5
	21	$9.435 \pm 7.1 \times 10^{-4}$	$6.879 \pm 5.7 \times 10^{-4}$	433 ± 32	$0.18 \pm 1 \times 10^{-3}$	98.0 ± 0.5

Table 7. 17 Changes in the principal structural properties of sample 0.5CHA with immersion time in SBF. Errors are the standard error derived from the fitting process.

Sample	Immersion time (days)	a (Å)	c (Å)	Crystallite size (Å)	Microstrain (%)	%AP
2.3CHA	0	$9.437 \pm 3.0 \times 10^{-4}$	$6.890 \pm 5.7 \times 10^{-4}$	402 ± 30	$0.35 \pm 1 \times 10^{-3}$	97.0 ± 0.5
	7	$9.436 \pm 7.4 \times 10^{-4}$	$6.889 \pm 6.1 \times 10^{-4}$	436 ± 33	$0.31 \pm 1 \times 10^{-3}$	99.0 ± 0.5
	14	$9.435 \pm 8.9 \times 10^{-4}$	$6.884 \pm 6.1 \times 10^{-4}$	422 ± 32	$0.28 \pm 1 \times 10^{-3}$	99.0 ± 0.5
	21	$9.433 \pm 7.6 \times 10^{-4}$	$6.882 \pm 6.0 \times 10^{-4}$	379 ± 28	$0.27 \pm 1 \times 10^{-3}$	100 ± 0.5

Table 7. 18 Changes in the principal structural properties of sample 2.3CHA with immersion time in SBF. Errors are the standard error derived from the fitting process.

Sample	Immersion time (days)	a (Å)	c (Å)	Crystallite size (Å)	Microstrain (%)	%AP
3.5CHA	0	$9.428 \pm 8.3 \times 10^{-4}$	$6.896 \pm 6.8 \times 10^{-4}$	367 ± 28	$0.44 \pm 1 \times 10^{-3}$	96.0 ± 0.5
	7	$9.428 \pm 8.3 \times 10^{-4}$	$6.895 \pm 9.4 \times 10^{-4}$	373 ± 28	$0.43 \pm 1 \times 10^{-3}$	99.5 ± 0.5
	14	$9.427 \pm 8.3 \times 10^{-4}$	$6.894 \pm 6.7 \times 10^{-4}$	329 ± 24	$0.40 \pm 0.1 \times 10^{-3}$	100 ± 0.5
	21	$9.426 \pm 9.3 \times 10^{-4}$	$6.891 \pm 6.1 \times 10^{-4}$	336 ± 25	$0.39 \pm 1 \times 10^{-3}$	99.5 ± 0.5

Table 7. 19 Changes in the principal structural properties of sample 3.5CHA with immersion time in SBF. Errors are the standard error derived from the fitting process.

Figure 7.75 illustrates the relationship between the initial crystallite size of the apatite powders and the percentage reduction in size after immersion in SBF and water respectively for 21 days. It is apparent that there is a strong linear correlation between the initial crystallite and percentage change in crystallite size (PCC=0.971) for the apatite samples immersed in SBF. However, the relationship between initial crystallite size and reduction in size for the apatite samples immersed in water was weaker (PCC=0.879). This finding suggests that for the apatite samples investigated, the reduction in crystallite size and hence dissolution after immersion for 21 days is dependent on the level of supersaturation of the immersion media with respect to HAP. At high levels of supersaturation (SBF), dissolution appeared to be influenced by the size of the crystallites. At low supersaturation (water) dissolution was influenced by crystallite size, but to a lesser degree.

An interesting feature noticed after immersion in SBF for 21 days was that the crystallite sizes of all of the apatite powders were approximately the same size after immersion (~273-483Å) irrespective of the size of the initial crystallites (~275-900Å). This finding suggests that there is a critical crystallite size (≤400Å) below which dissolution is inhibited (or in equilibrium) in SBF. It can be seen that the magnitude and range of sizes of the resultant crystallites after immersion in water (~215-350Å) was smaller than that of the SBF samples. This may indicate that the critical size for dissolution inhibition or suppression may be lower for water (<200) than SBF. Worth mentioning is the fact that this speculative 'critical crystallite size' is in the same order of magnitude as that of bone

mineral. The significance of this finding with respect to the stability of synthetic and natural apatites *in vitro* and *in vivo* is discussed in chapter 8.

No relationship was found between percentage reduction in crystallite size and strain in the control samples. However, figure 7.76 shows the correlation between change in size reduction between samples immersed in SBF and water and microstrain (PCC=0.942). This finding suggests that the difference in size reduction in the water samples relative to the SBF samples is proportional to the initial strain. As the initial microstrain increases, the difference in size reduction between the water and SBF samples increases. This implies that in this system, although crystallite size dominates dissolution behaviour at low supersaturation, microstrain also makes a modest contribution to dissolution behaviour. The increased effect of microstrain is further evidenced in figure 7.76. Figure 7.77 shows that at low supersaturation, the change in microstrain after dissolution correlated more with the initial microstrain (PCC=0.972) than at high supersaturation (PCC=0.724). Although Tang *et al* [268], has previously observed size dependency in the dissolution of brushite seeds in constant composition studies under acidic conditions, no reports have been made on size-microstrain effects on dissolution. A possible mechanism for the observed size-microstrain effects on dissolution at the different supersaturations are discussed in chapter 8 and compared to traditional dissolution theories.

Figure 7.78 shows how the changes in the a-axis dimension of the apatite powders after immersion in SBF and water for 21 days vary with the initial crystallite size. The

changes in a-axis dimensions have a linear correlation with the initial crystallite size with a Pearson's correlation coefficient of 0.780 and 0.775 respectively for the water and SBF samples. For crystallite sizes below ~380 Å, the difference in a-axis parameters between the water and SBF samples was not significantly different ($P<0.05$). However, above a crystallite size of ~380 Å, the change in a-axis parameter was higher for the samples immersed in SBF than the samples immersed in water. This may be due to precipitation of substituted HAP derived from alien ions from the SBF due to the media being supersaturated with respect to HAP.

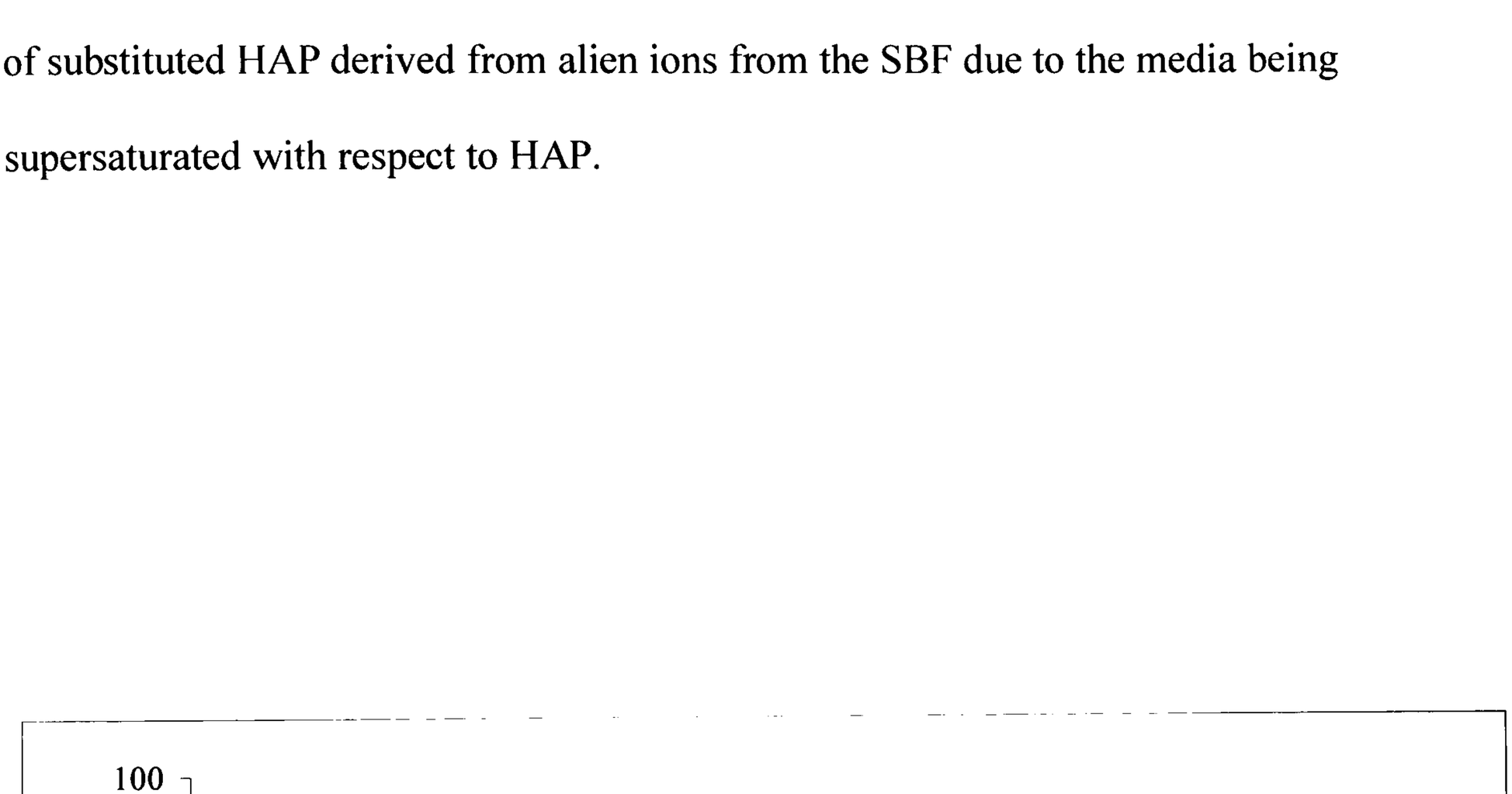

Figure 7. 75 Relationship between the initial crystallite size and the change in crystallite size of apatite powders after immersion in SBF and water for 21 days respectively. Error bars are the standard error derived from the fitting process.

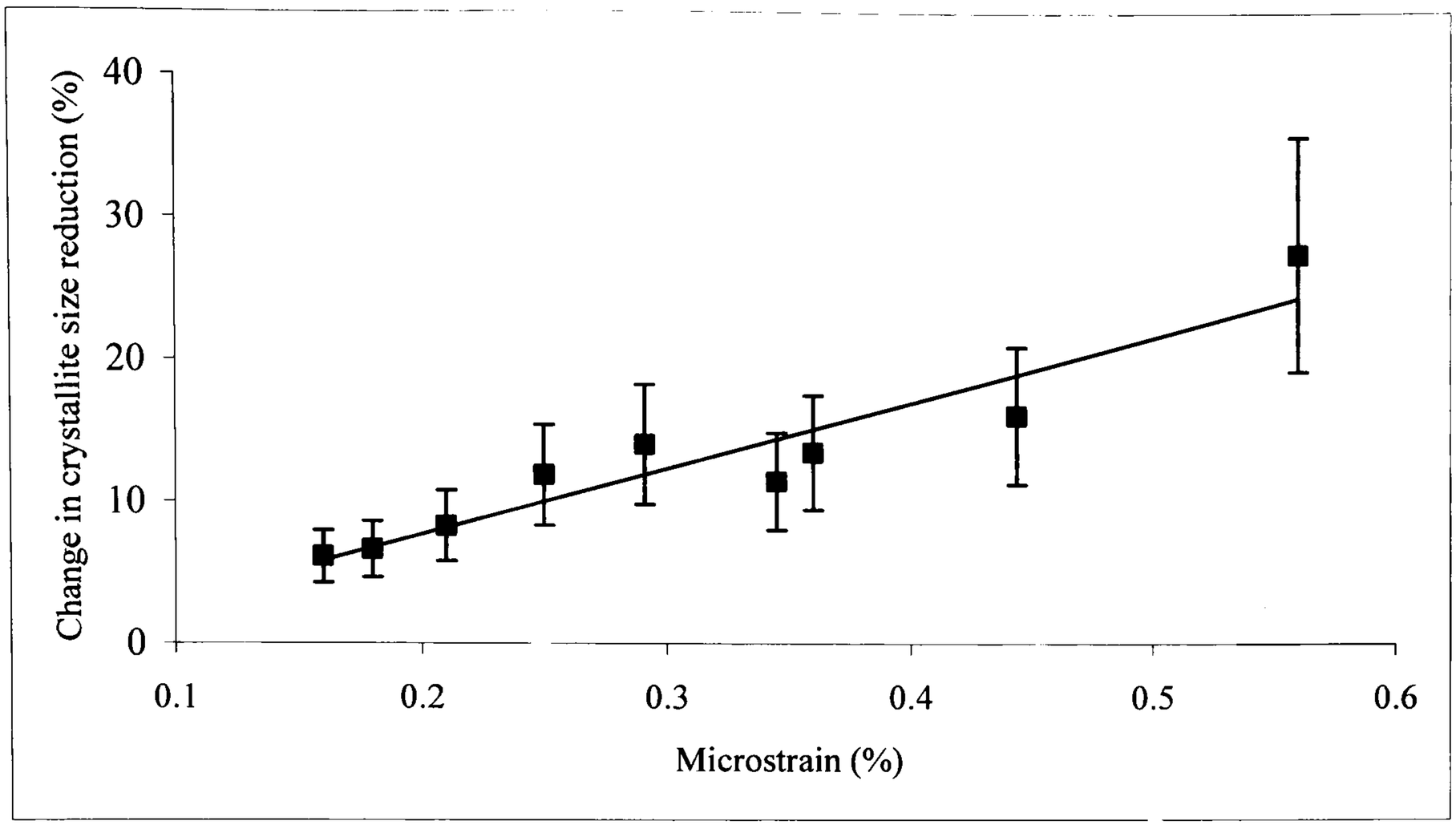

Figure 7. 76 Relationship between the difference in crystallite size reduction of apatite powders immersed in SBF and water for 21 days and microstrain. Error bars are the standard error derived from the fitting process.

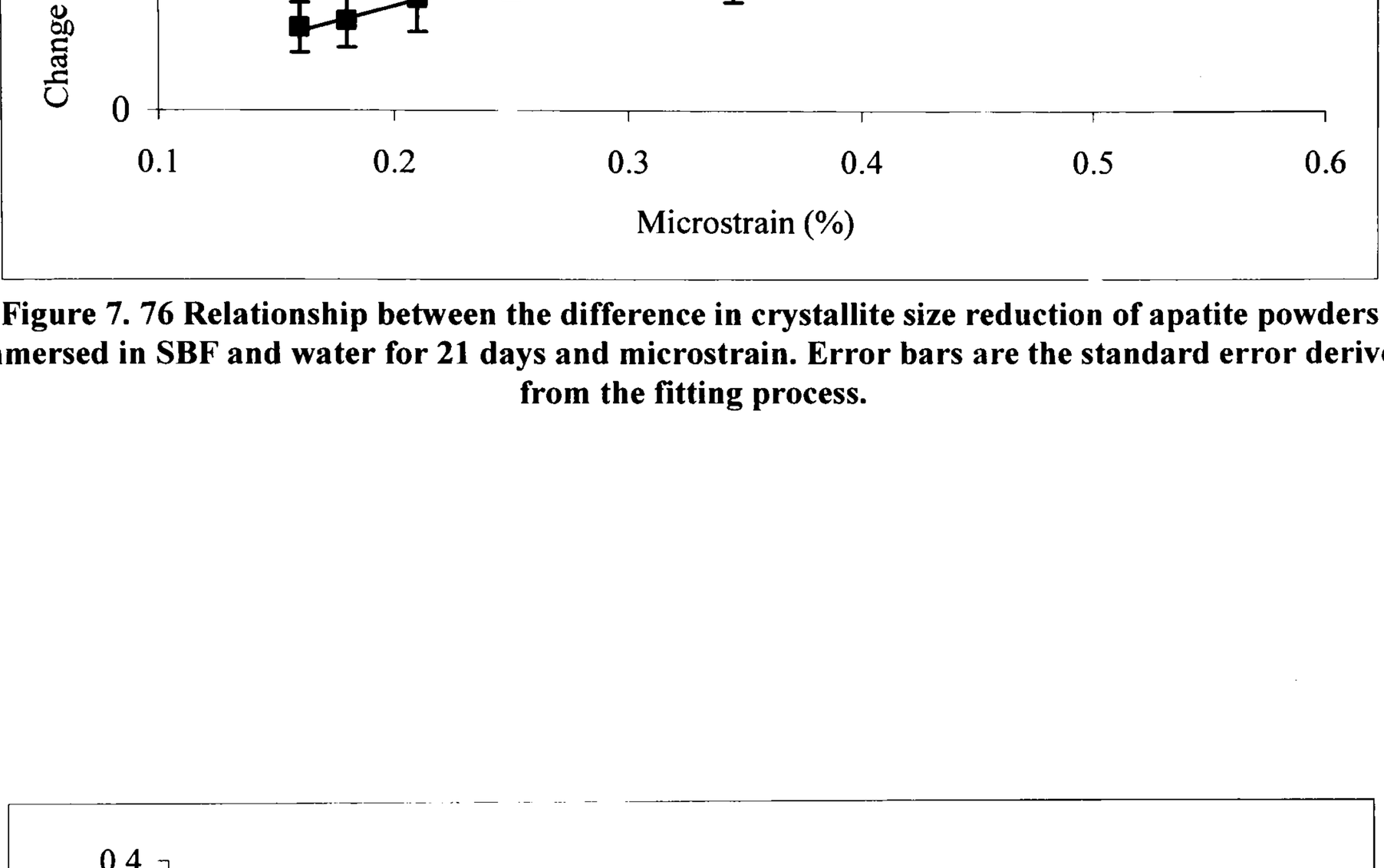

Figure 7. 77 Relationship between the initial microstrain and the change in microstrain of apatite powders after immersion in SBF and water respectively for 21 days.

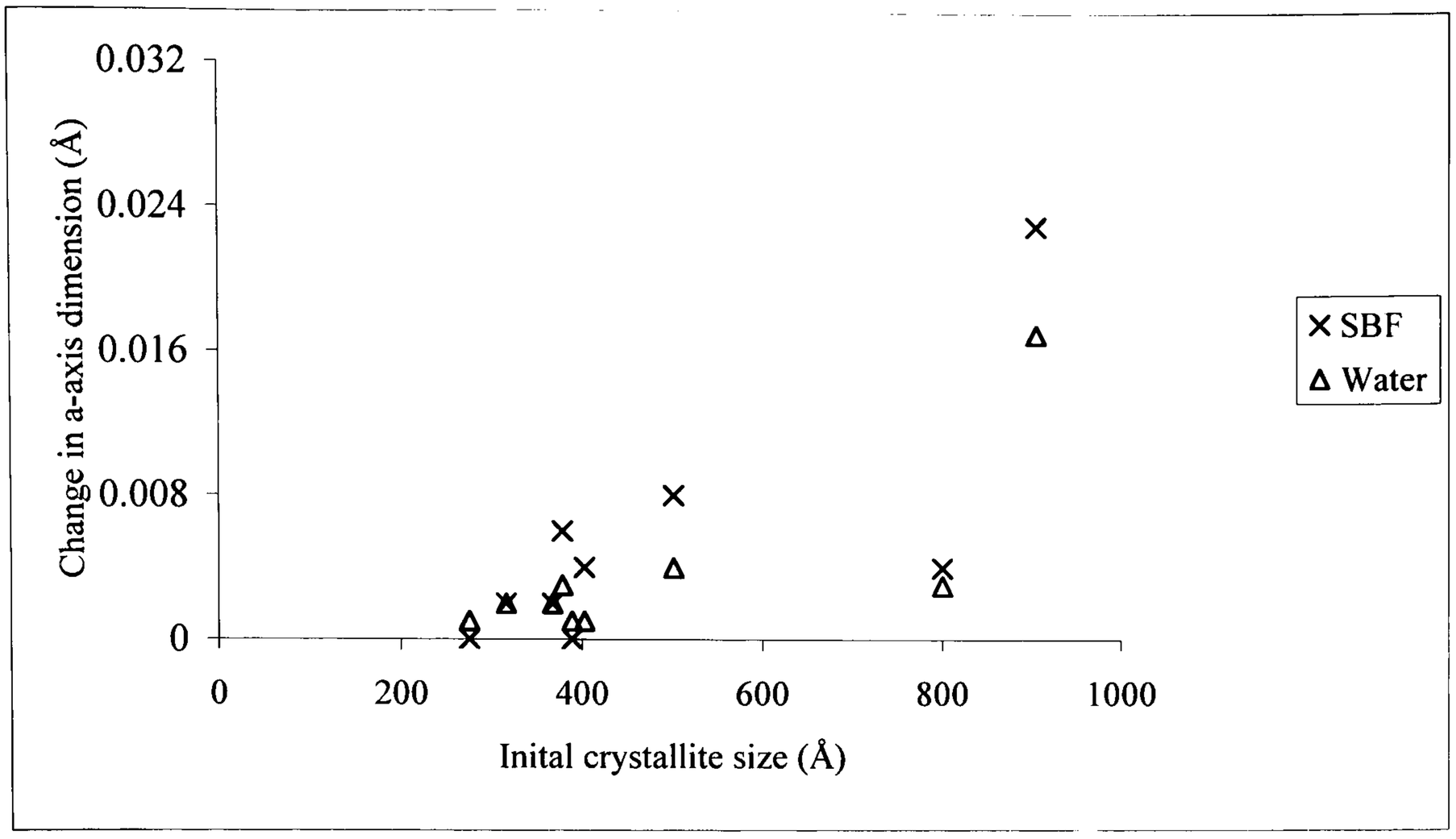

Figure 7. 78 Relationship between the initial crystallite size and change in a-axis dimension of apatite powders after immersion in SBF and water respectively for 21 days.

In order to further investigate the change in the chemical nature of the apatite powders after immersion in SBF and water respectively, FTIR analysis was conducted. Figures 7.79-81 and table 7.20-28 summarise the changes in the FTIR spectra. All of the apatite powders, except for the carbonated samples had an increase in area corresponding to the carbonate ν_3 band between 1300-1650 cm^{-1} for samples immersed in SBF and water respectively. An increase in the peak area of the hydroxyl stretch band at 3570 cm^{-1} and hydroxyl liberation band at 630 cm^{-1} was observed in all of the apatite samples. These changes in hydroxyl bands have previously been attributed to of the decrease in A-type carbonation [269]. Consequently this serves as confirmatory evidence that the increase in the area of the carbonate ν_3 band was due to the increase of B-type carbonation. This would suggest for all apatite samples, except the carbonated apatite samples that precipitation of newly formed B-type carbonated apatite had occurred. The degree of

carbonation of the newly formed precipitates was greater for the samples immersed in SBF as a result of its higher HCO_3^{2-} content. The newly formed precipitates on the carbonated samples after immersion in SBF and water respectively was not carbonated. This has been observed previously [258] in dissolution studies of carbonated apatites in SBF.

The 'splitting factor' of the phosphate ν_4 band calculated from the ratio of the peaks intensities at $603cm^{-1}$ and $563cm^{-1}$ has previously [270] been correlated to crystallinity (crystallite size/perfection) of bone mineral. From tables 7.20-28, it is evident that the splitting factor of each of the apatites decreased after immersion time in SBF and water for 21 days respectively. The decrease in splitting factor was more pronounced in the apatites with the largest crystallite sizes after immersion in water. This observation may be due to the greater degree of dissolution and hence crystallite size reduction that occurred as evidenced by the diffraction data. Other authors [271] have interpreted the reduction in the splitting factors of phosphate bands as the precipitation of poorly crystalline apatite. It is plausible that the reduction of the splitting factor observed in this case could be a combination of both modalities as the dissolution of the apatite powders can induce precipitation of poorly crystallised apatite.

Figures 7.82-83 illustrate the relationship between the splitting factor [603/563] measured from the FTIR data and the integral breadth of the (002) peak measured from the XRD data of all of the apatite powders before and after immersion in SBF and water respectively for 21 days. It is apparent from the good fit of the data points that the

splitting factor and the broadening (crystallite size and microstrain effects) of the (002) peak are inversely proportional. This linear relationship between the splitting factor and peak broadening provides corroboratory evidence for the size dependent dissolution effects observed from XRD analysis. Explicitly, that after immersion in SBF and water the crystallinity (crystal size/perfection) as evidenced by increased peak broadening and decrease of splitting factor, decreased in all apatite samples. However, decrease in crystallinity was greatest for the apatite powders with the largest crystals after immersion in water (size80). The powders with the smallest crystals had the least decrease in crystallinity after immersion in SBF (size25).

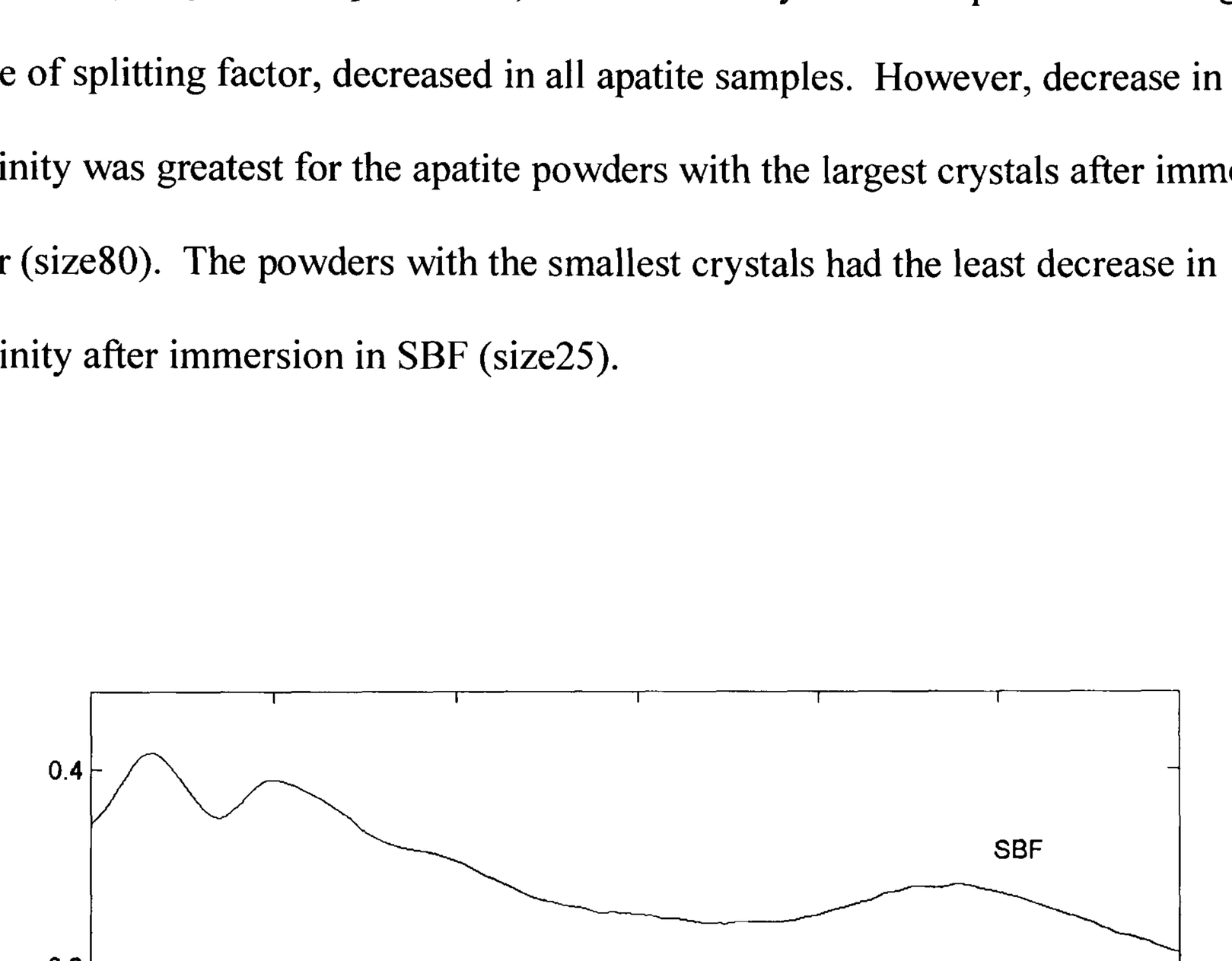

Figure 7. 79 Typical appearance of the carbonate ν_3 band (1400-1650 cm^{-1}) of apatite powders before and after immersion in SBF and water respectively for 21 days.

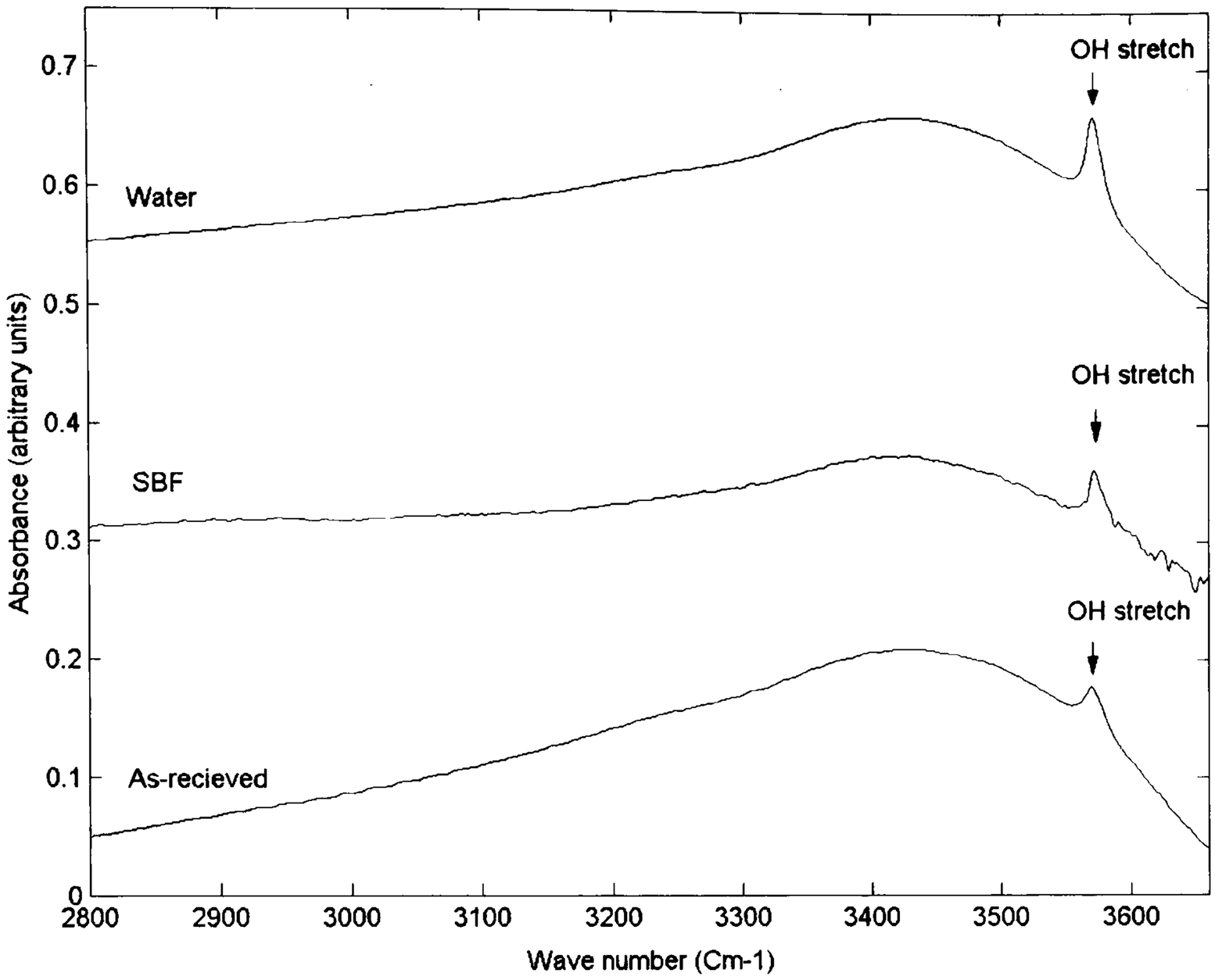

Figure 7. 80 Typical appearance of OH stretch band (~3570 cm^{-1}) of apatite powders before and after immersion in SBF and water for 21 days respectively.

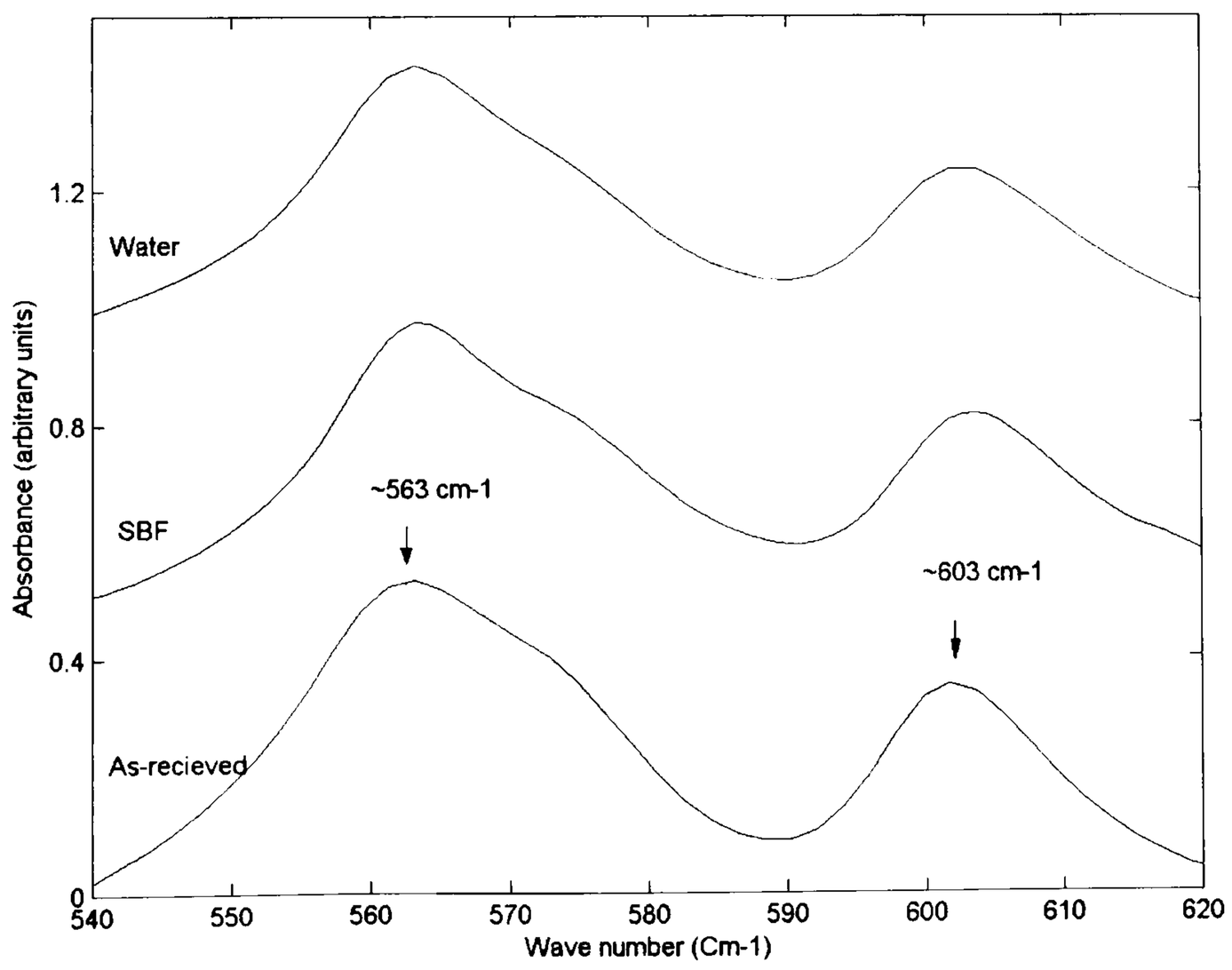

Figure 7. 81 Typical appearance of the splitting of the phosphate ν_4 band of apatite powders before and after immersion in SBF and water respectively for 21 days.

	size25 (as-received)	size25 (SBF)	size25 (water)
Peak area carbonate ν_3 (1300-1650)	4.7 ± 0.35	5.6 ± 0.28	5.6 ± 0.18
Peak area hydroxyl stretch (~3570)	0.6 ± 0.03	1.5 ± 0.02	2.0 ± 0.02
Splitting factor phosphate ν_4 (603/563)	0.5 ± 0.04	0.5 ± 0.04	0.5 ± 0.05

Table 7. 20 Peak areas and splitting factors of apatite powders precipitated at 25°C, before and after immersion in SBF and water respectively. Errors denote the standard error derived from the fitting process.

	size55 (as-received)	size55 (SBF)	size55 (water)
Peak area carbonate ν_3 (1300-1650)	4.1 ± 0.30	5.7 ± 0.31	4.7 ± 0.44
Peak area hydroxyl stretch (~3570)	0.6 ± 0.03	0.7 ± 0.02	0.9 ± 0.02
Splitting factor phosphate ν_4 (603/563)	0.7 ± 0.07	0.7 ± 0.08	0.6 ± 0.07

Table 7. 21 Peak areas and splitting factors of apatite powders precipitated at 55°C, before and after immersion in SBF and water respectively. Errors are the standard error derived from the fitting process.

	size80 (as-received)	size80 (SBF)	size80 (water)
Peak area carbonate ν_3 (1300-1650)	2.4 ± 0.44	4.4 ± 0.20	2.5 ± 0.29
Peak area hydroxyl stretch (~3570)	1.5 ± 0.01	1.6 ± 0.01	1.7 ± 0.01
Splitting factor phosphate ν_4 (603/563)	0.80 ± 0.08	0.7 ± 0.07	0.7 ± 0.06

Table 7. 22 Peak areas and splitting factors of apatite powders precipitated at 80°C, before and after immersion in SBF and water respectively. Errors are the standard error derived from the fitting process.

	strain1 (as-received)	strain1 (SBF)	strain1 (water)
Peak area carbonate ν_3 (1300-1650)	3.2 ± 0.28	5.8 ± 0.58	4.1 ± 0.23
Peak area hydroxyl stretch (~3570)	1.8 ± 0.03	2.2 ± 0.03	2.7 ± 0.03
Splitting factor phosphate ν_4 (603/563)	0.7 ± 0.06	0.6 ± 0.05	0.6 ± 0.05

Table 7. 23 Peak areas and splitting factors of apatite powders (not subjected to milling) before and after immersion in SBF and water respectively. Errors denote the standard error derived from the fitting process.

	strain2 (as-received)	strain2 (SBF)	strain2 (water)
Peak area carbonate ν_3 (1300-1650)	4.3 ± 0.61	8.0 ± 0.36	7.49 ± 0.273
Peak area hydroxyl stretch (~3570)	1.2 ± 0.02	1.4 ± 0.02	1.8 ± 0.02
Splitting factor phosphate ν_4 (603/563)	0.7 ± 0.08	0.7 ± 0.083	0.7 ± 0.053

Table 7. 24 Peak areas and splitting factors of milled apatite powders (at 400 rpm for 2 hours) before and after immersion in SBF and water respectively. Errors denote the standard error derived from the fitting process.

	strain3 (as-received)	strain3 (SBF)	strain3 (water)
Peak area carbonate ν_3 (1300-1650)	4.6 ± 0.19	6.4 ± 0.24	5.9 ± 0.22
Peak area hydroxyl stretch (~3570)	1.2 ± 0.02	1.3 ± 0.03	1.6 ± 0.02
Splitting factor phosphate ν_4 (603/563)	0.5 ± 0.04	0.5 ± 0.04	0.4 ± 0.06

Table 7. 25 Peak areas and splitting factors of milled apatite powders (at 400 rpm for 26 hours) before and after immersion in SBF and water respectively. Errors are the standard error derived from the fitting process.

	0.5CHA (as-received)	0.5CHA (SBF)	0.5CHA (water)
Peak area carbonate ν_3 (1300-1650)	6.8 ± 0.24	6.3 ± 0.34	6.2 ± 0.32
Peak area hydroxyl stretch (~3570)	1.6 ± 0.04	1.6 ± 0.03	1.7 ± 0.03
Splitting factor phosphate ν_4 (603/563)	0.7 ± 0.06	0.7 ± 0.05	0.6 ± 0.08

Table 7. 26 Peak areas and splitting factors of 0.5wt% carbonated apatite powders before and after immersion in SBF and water respectively. Errors are the standard error derived from the fitting process.

	2.3CHA (as-received)	2.3CHA (SBF)	2.3CHA (water)
Peak area carbonate ν_3 (1300-1650)	25.0 ± 0.41	13.6 ± 0.58	7.9 ± 0.56
Peak area hydroxyl stretch (~3570)	1.4 ± 0.01	1.5 ± 0.01	1.6 ± 0.01
Splitting factor phosphate ν_4 (603/563)	0.7 ± 0.08	0.7 ± 0.05	0.6 ± 0.05

Table 7. 27 Peak areas and splitting factors of 2.3wt% carbonated apatite powders before and after immersion in SBF and water respectively. Errors are the standard error derived from the fitting process.

	3.5CHA (as-received)	3.5CHA (SBF)	3.5CHA (water)
Peak area carbonate ν_3 (1300-1650)	30.6 ± 0.37	15.4 ± 0.43	13.8 ± 0.29
Peak area hydroxyl stretch (~3570)	1.0 ± 0.01	1.0 ± 0.02	1.2 ± 0.02
Splitting factor phosphate ν_4 (603/563)	0.7 ± 0.06	0.7 ± 0.08	0.7 ± 0.06

Table 7. 28 Peak areas and splitting factors of 3.5wt% carbonated apatite powders before and after immersion in SBF and water respectively. Errors are the standard error derived from the fitting process.

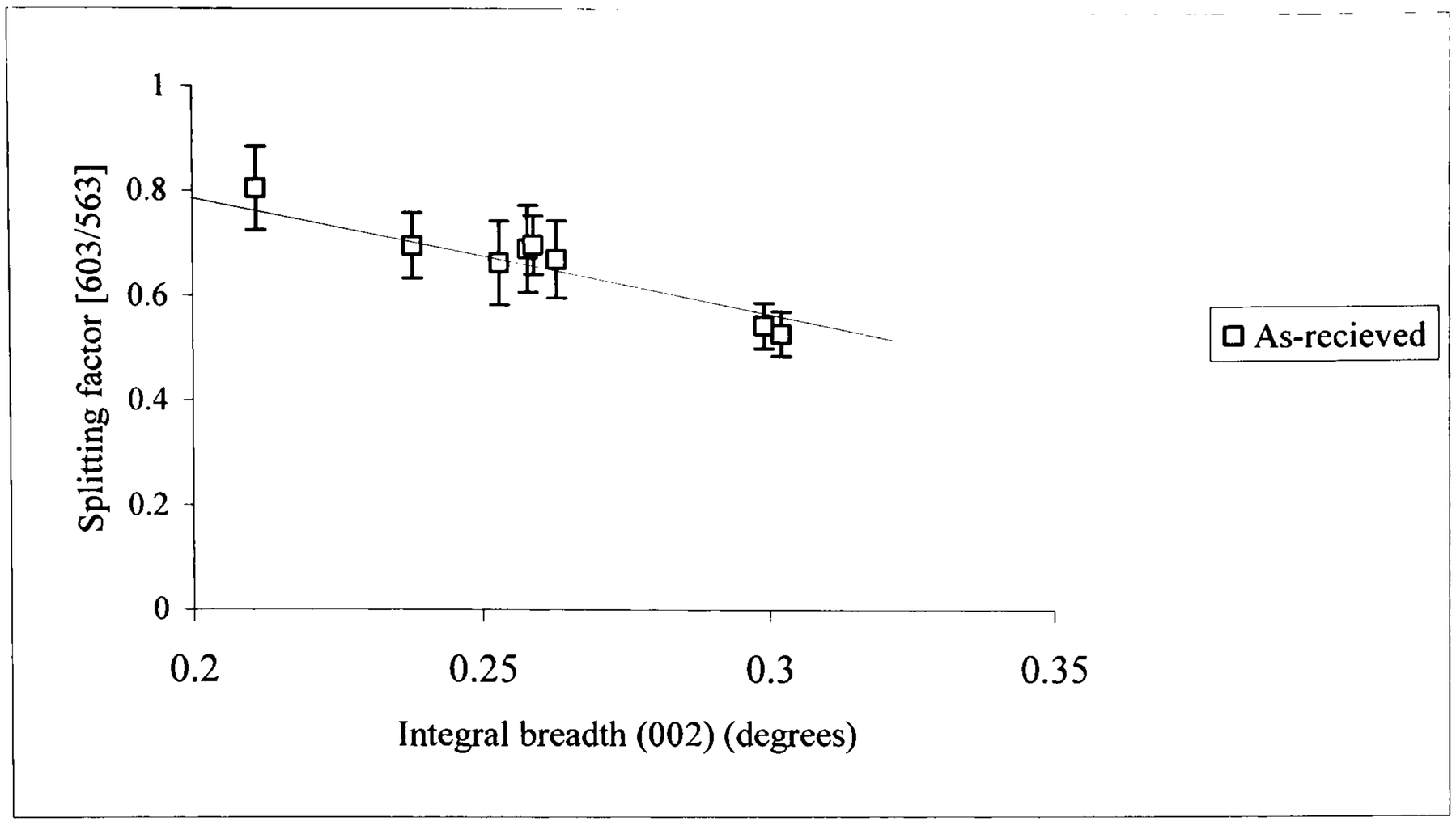

Figure 7. 82 Splitting factor [603/563] as a function of the integral breadth of the (002) peak of apatite powders before immersion (PCC= -0.900). Error bars are the standard error derived from the fitting process.

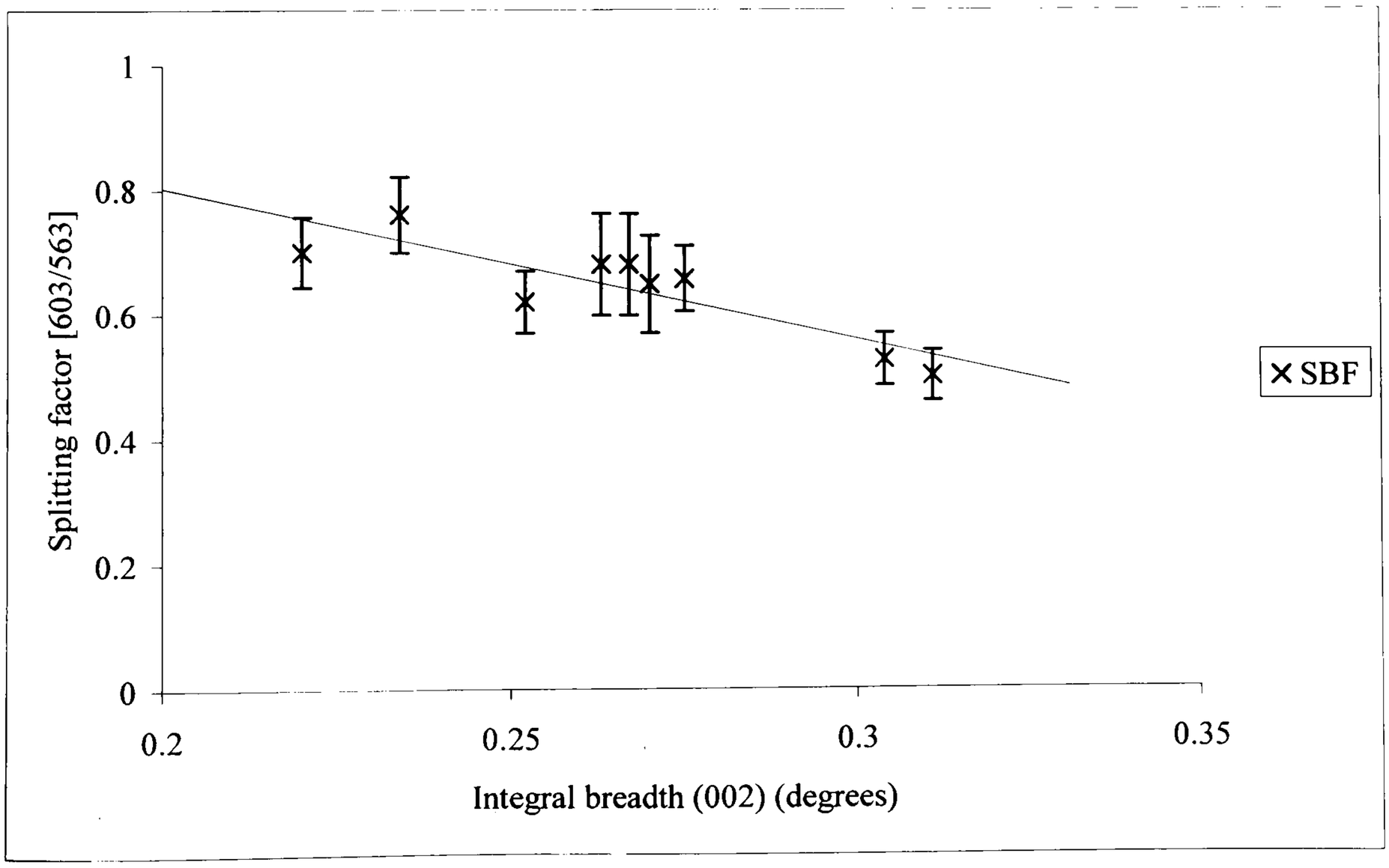

Figure 7. 83 Splitting factor [603/563] as a function of the integral breadth of the (002) peak of apatite powders after immersion in SBF for 21 days (PCC= -0.869). Error bars are the standard error derived from the fitting process.

The changes in the morphology of the apatite powders after immersion in SBF and water respectively were investigated by SEM analysis. In general no significant changes in morphological profile and size were noted for samples with an initial crystallite size of less than ~400Å after immersion in either media. In contrast, powders with crystallite sizes larger than this did show signs of dissolution.

As described in section 7.1, figures 7.24-27 illustrate the morphological profile of samples size25-80 before immersion. After immersion in SBF, no significant changes were noted in the size and shape of the resultant particles of samples size25 and size50. Even at higher magnification, there was no significant change in the morphology of the particles. This observation is in agreement with the diffraction data indicating that little or no dissolution of samples size25 (crystallite size ~275Å) and size55 (crystallite size ~388Å) had occurred. In contrast, sample size80 showed a decrease in average particle size (50-300μm) and change in the morphology of the surface of particles. Before immersion (figure 7.84), the surface of the particles was covered in small granules, however, after immersion, the majority of these granules were absent or partially dissolved (figure 7.85). This is an observation consistent with the diffraction data, which indicates that dissolution had occurred by virtue of the larger crystallite size (~906Å).

No difference in morphology or size distribution was observed in comparison to the control samples. This confirmed the XRD analysis, which showed that the differences in crystallite size reduction between the water and SBF samples were small in magnitude with respect to the initial size of the crystallites.

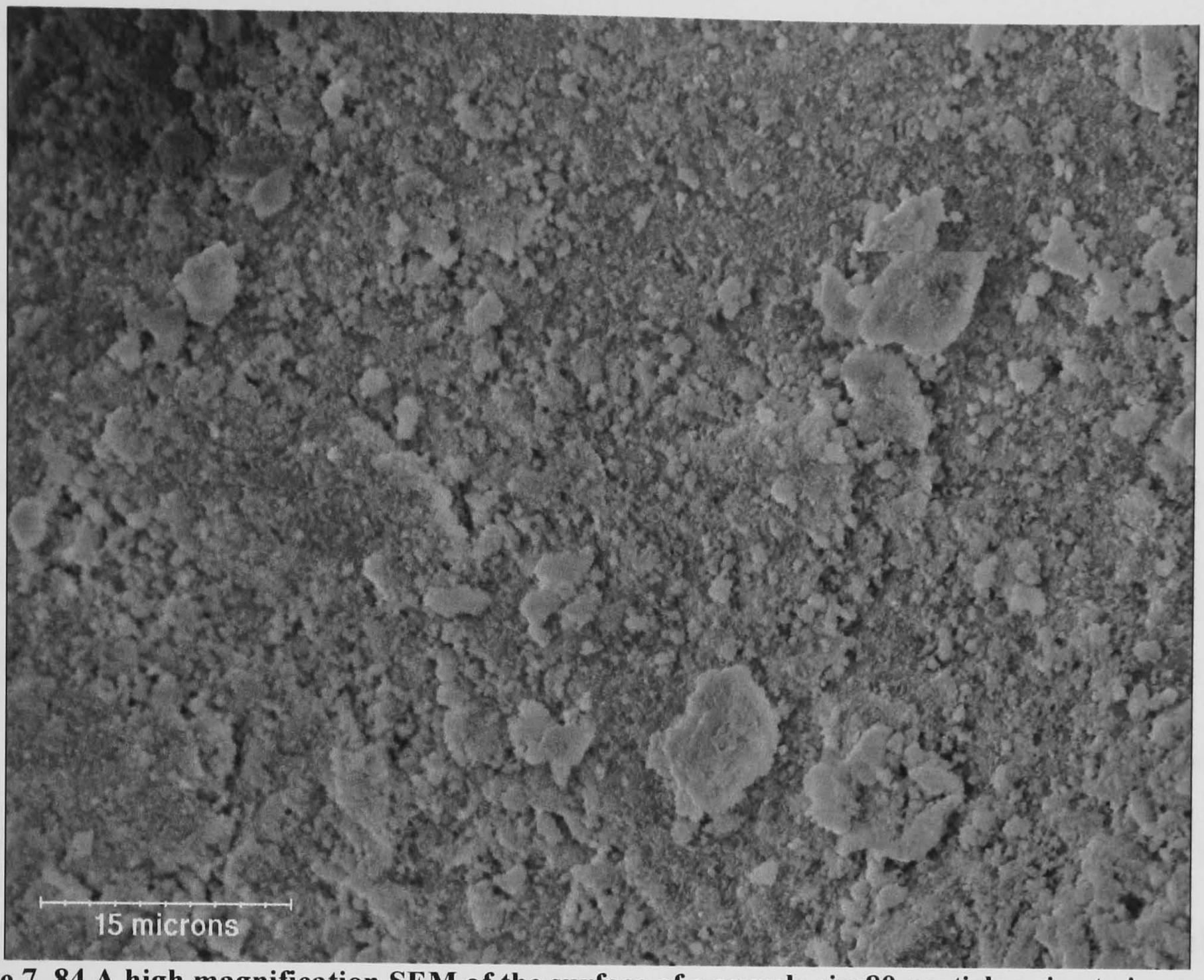

Figure 7. 84 A high magnification SEM of the surface of a sample size80 particle prior to immersion in SBF. The scale bar denotes 15μm.

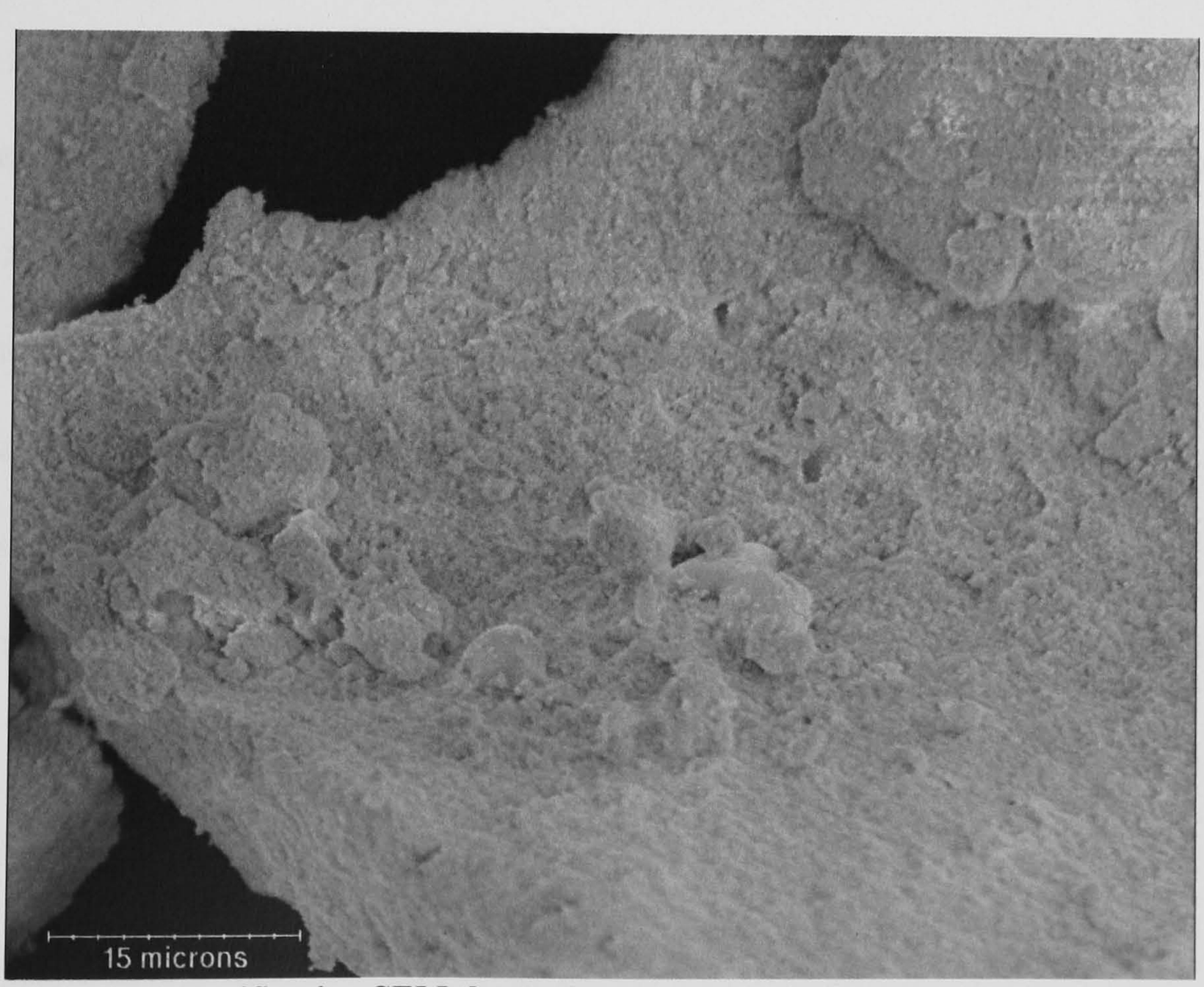

Figure 7. 85 A high magnification SEM the surface a sample size80 particle after immersion in SBF for 21 days. The scale bar denotes 15μm.

The morphology of samples strain1-3 before immersion in SBF is illustrated in figures 7.86-89. The crystals in sample strain1 were well-formed flat diamond-shaped particles approximately 25-100μm in length and 15-25μm in width. At higher magnification, it was evident that the surfaces of the particles were covered in small spherical granules. Due to ball milling, the particles in samples strain2 and strain3 were significantly smaller, comprising of shattered diamond-shaped crystals approximately 25-55μm and 10-20μm in length respectively. The surfaces of the particles in each of these samples were decorated with small granules and pulverised particles. After immersion in SBF for 21 days, the size of the particles in sample strain1 (~ 501Å) had decreased to approximately 15-30μm in length and 10-30μm in width (figure 7.90-1). Furthermore, the resultant particles had become less angular in character, hence confirming that dissolution had occurred which is consistent with the diffraction data. Inspection at higher magnification revealed the presence of tiny needle-like structures on the surface of the particles, which may have been derived from precipitation. In contrast, the size of the particles and morphological profile of samples strain2 (~378Å) and strain3 (~316Å) had not changed. These findings are consistent with the data obtained from diffraction analysis, hence substantiating the conclusion that no or only a small degree of dissolution had occurred in samples strain2 (figure 7.92) and strain3 after immersion in SBF. No difference in morphology or size distribution was observed in comparison to the control samples.

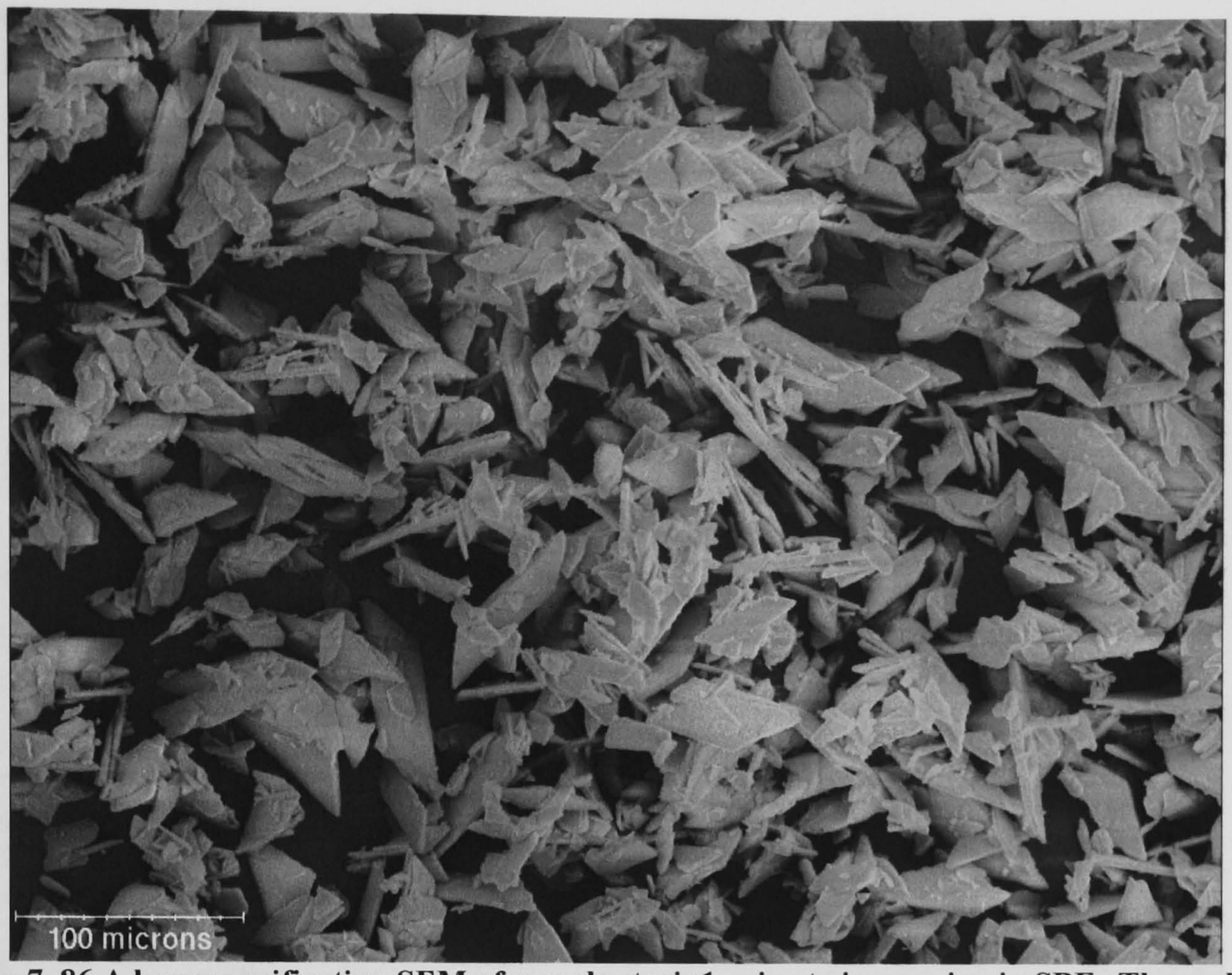

Figure 7. 86 A low magnification SEM of sample strain1 prior to immersion in SBF. The scale bar denotes 100μm.

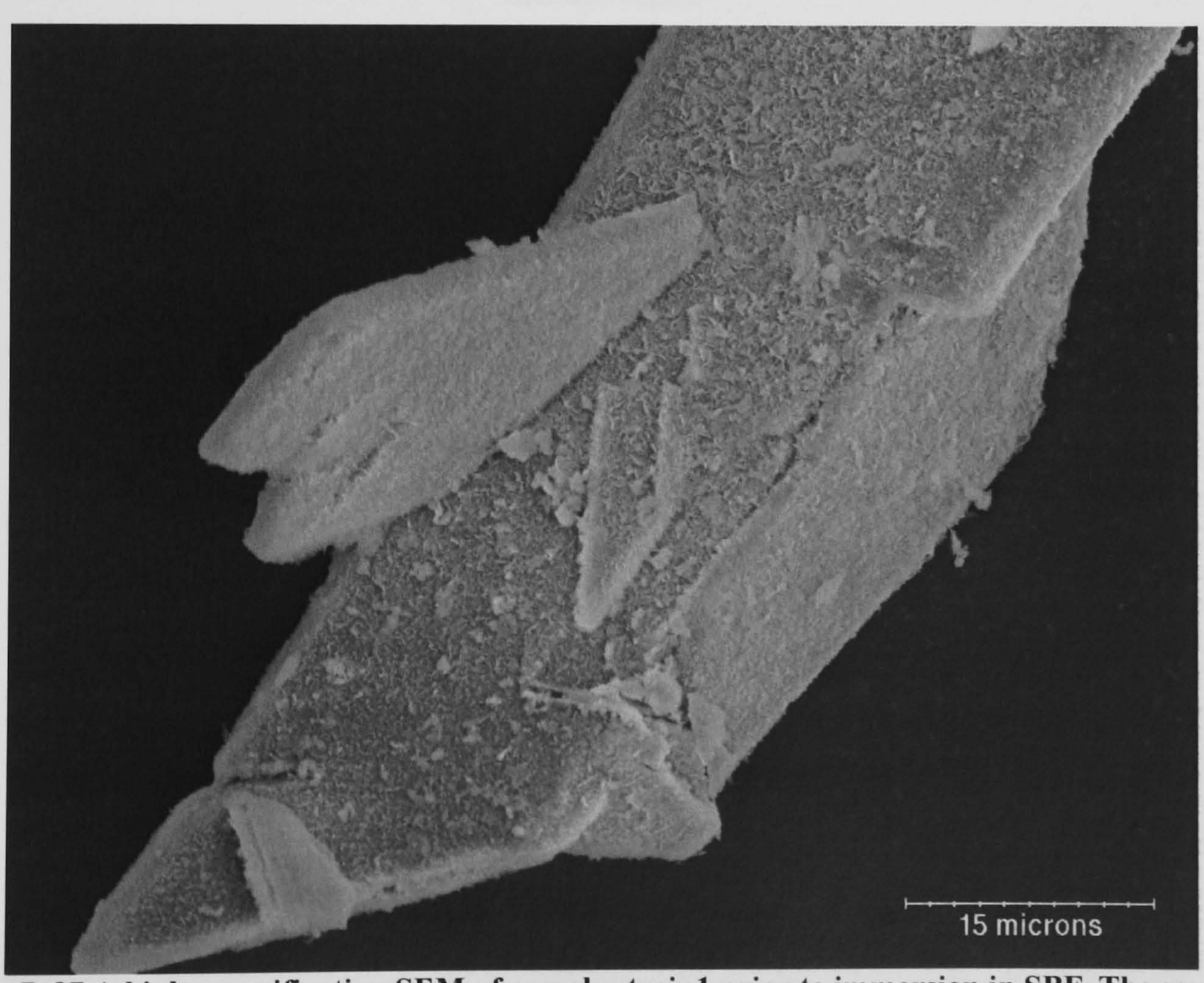

Figure 7. 87 A high magnification SEM of sample strain1 prior to immersion in SBF. The scale bar denotes 15μm.

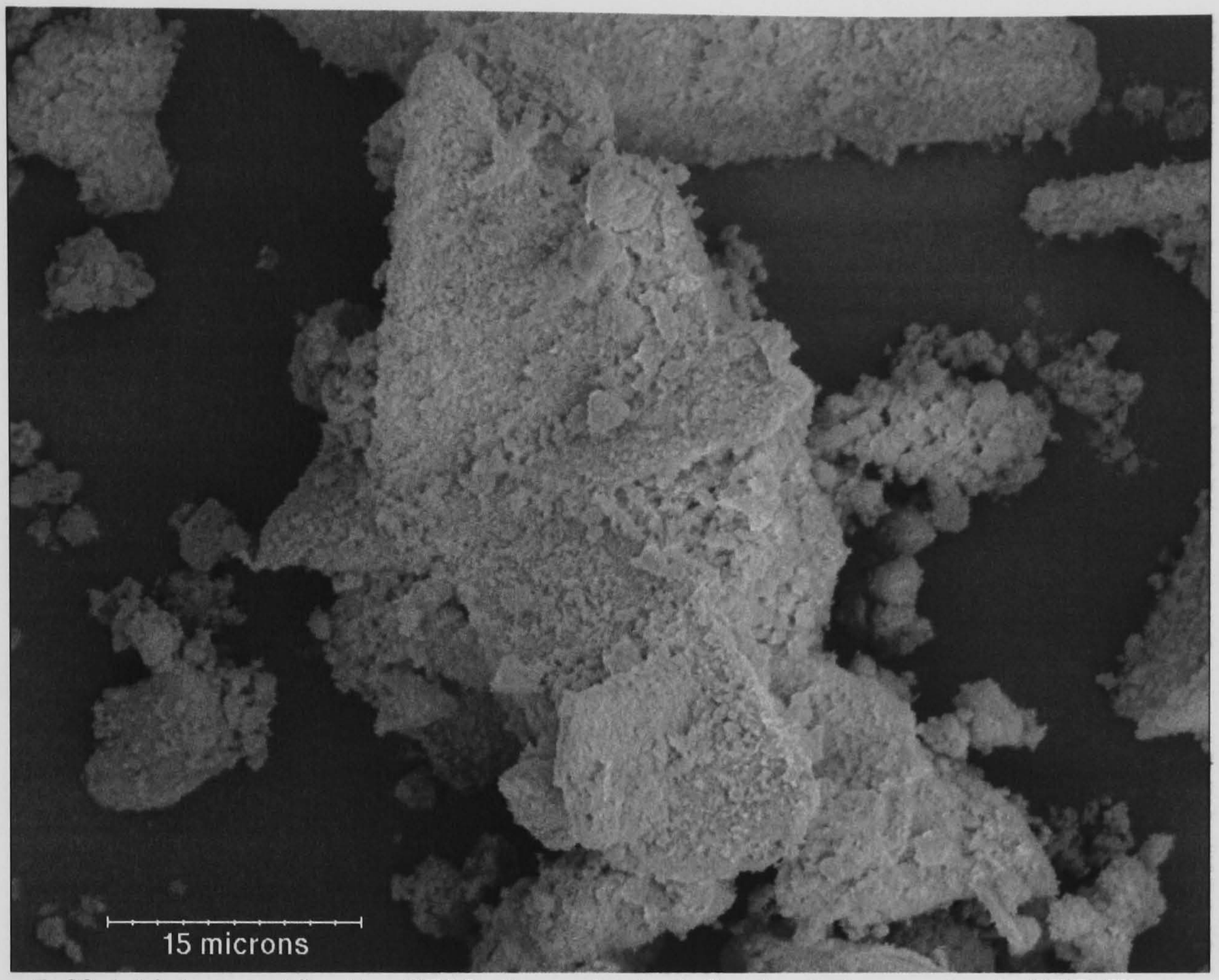

Figure 7. 88 A high magnification SEM of sample strain2 prior to immersion in SBF. The scale bar denotes 15μm.

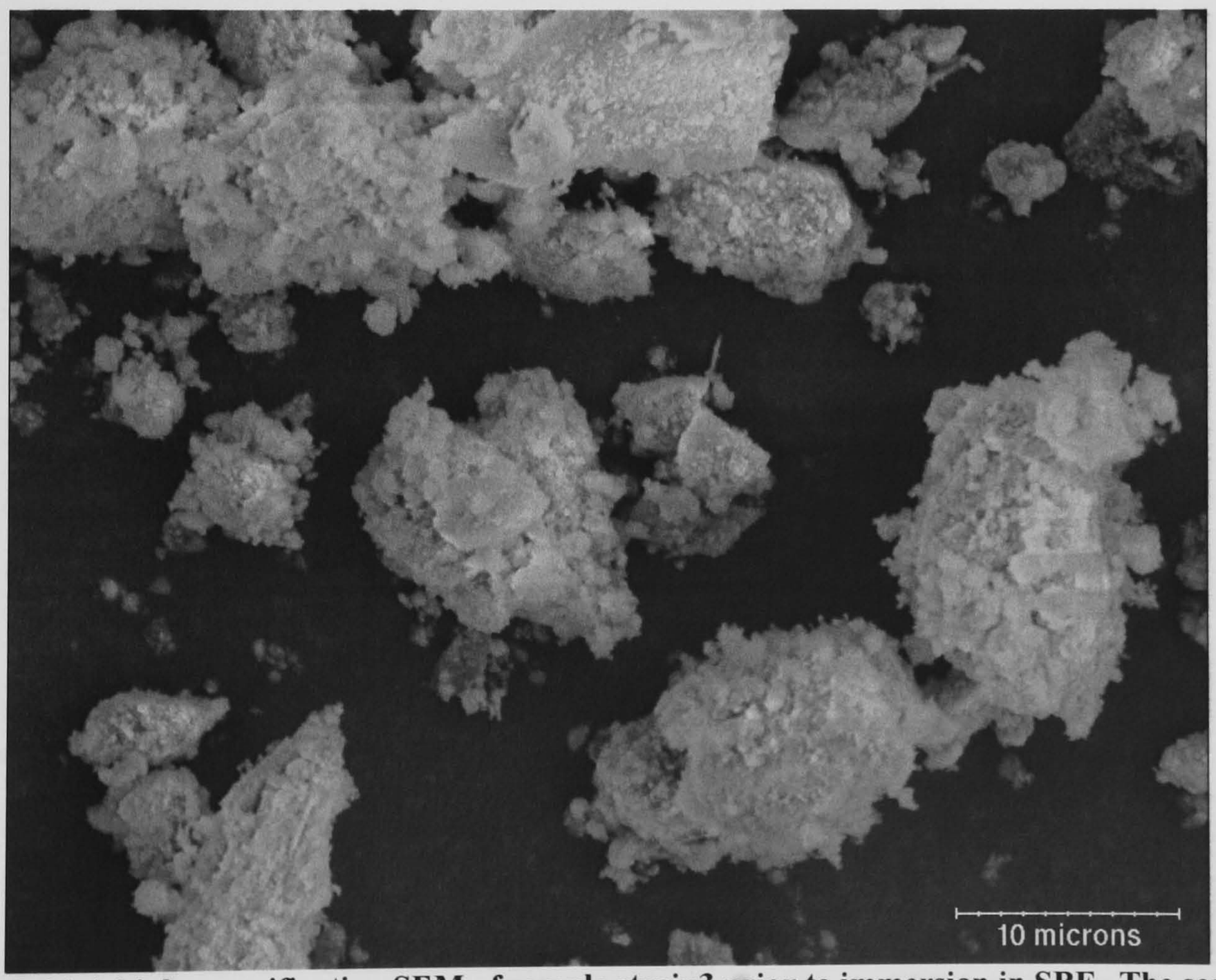

Figure 7. 89 A high magnification SEM of sample strain3 prior to immersion in SBF. The scale bar denotes 10μm.

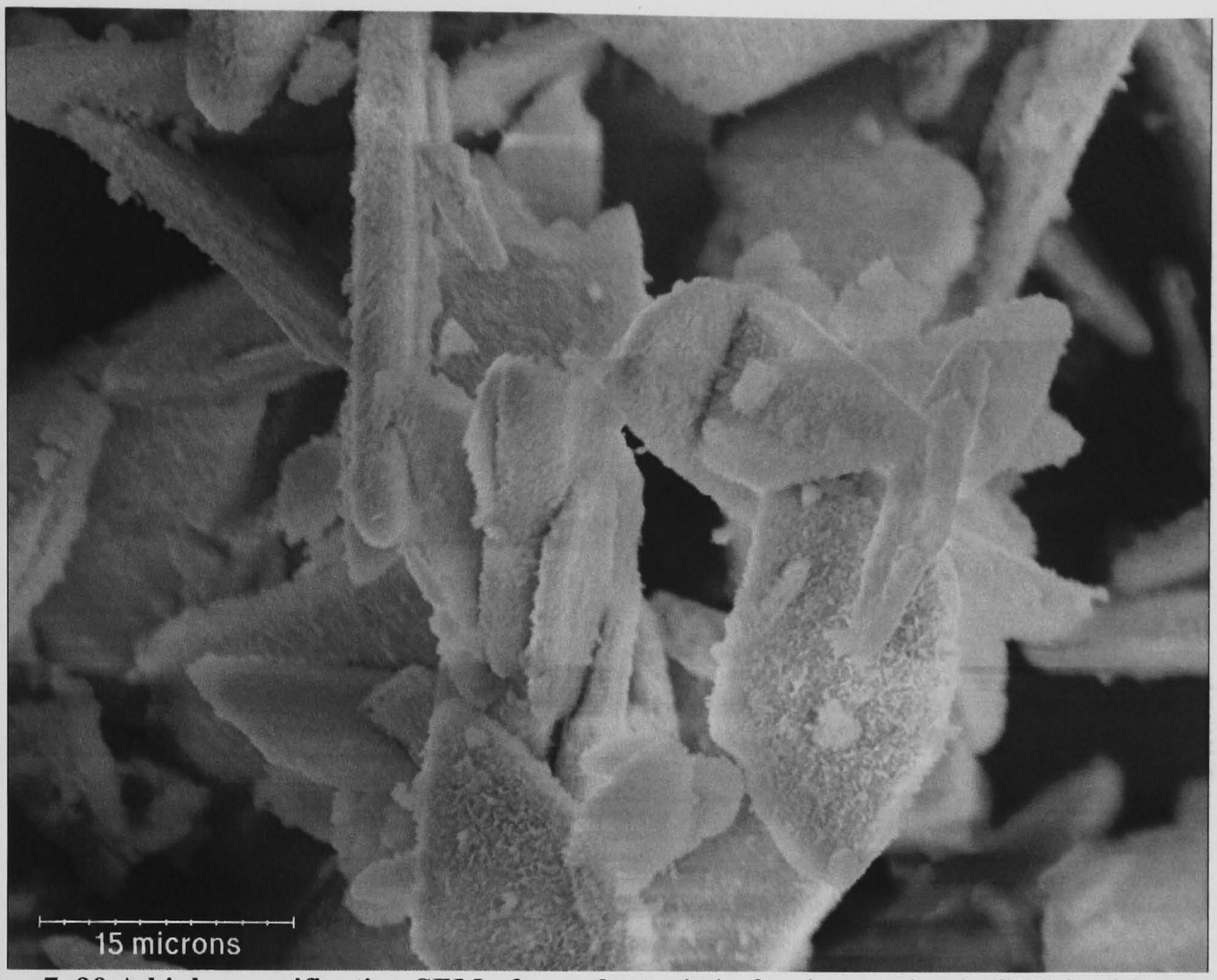

Figure 7. 90 A high magnification SEM of sample strain1 after immersion in SBF for 21days. The scale bar denotes 15μm.

Figure 7. 91 A high magnification SEM of strain1 after immersion in SBF for 21 days. The scale bar denotes 5μm.

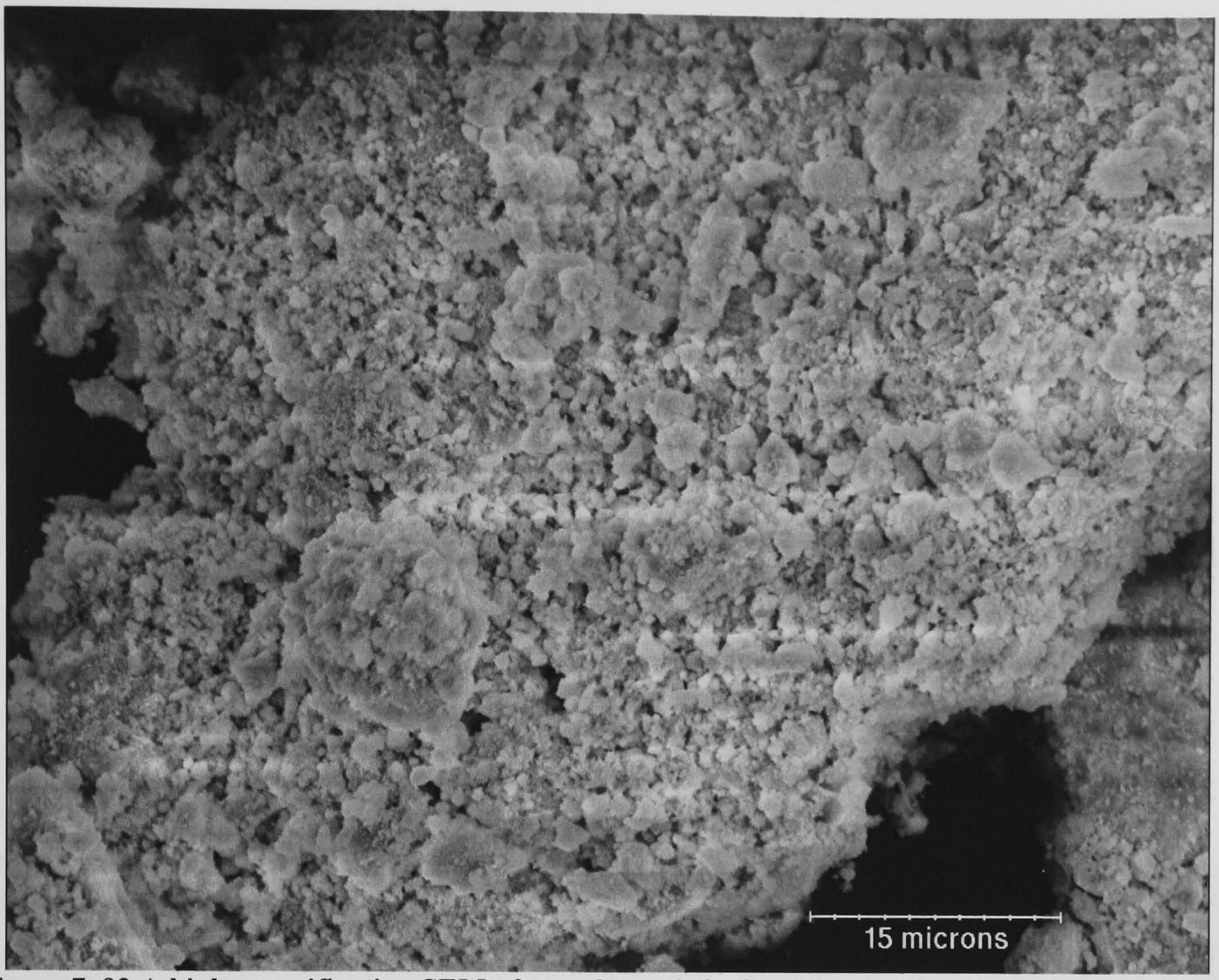

Figure 7. 92 A high magnification SEM of sample strain2 after immersion in SBF for 21 days. The scale bar denotes 15μm.

Figure 7.93 depicts the morphology of a typical particle from sample 0.5CHA (crystallite size ~ 800Å) prior to immersion in SBF. The particles are spherical structures approximately 60-85μm in diameter with a rough surface. Figure 7.94 depicts the morphology of a typical particle from sample 2.3CHA (crystallite size 402Å). The particles are small spherical structures approximately 3-20μm in diameter. The surface of the particles was covered with small clusters of particles. Sample 3.5CHA (crystallite size ~367Å) had an identical morphology and size distribution as sample 2.3CHA.

Figure 7.95 shows the morphology of sample 0.5CHA particles after immersion in SBF. After immersion, the particles were approximately 20-45μm. The surfaces of the particles were carpeted with small granules, which may have been derived from precipitation. In contrast the particles from sample 2.3CHA (figure 7.95) and 3.5CHA were approximately 3-20μm in diameter indicating no net change in particle size. The small clusters of particles that were present on the surface of 2.3CHA and 3.5CHA samples before immersion in SBF were absent in the immersed samples, suggesting that a small degree of dissolution had occurred, hence corroborating the diffraction data. No difference in morphology or size distribution was observed in comparison to the control samples.

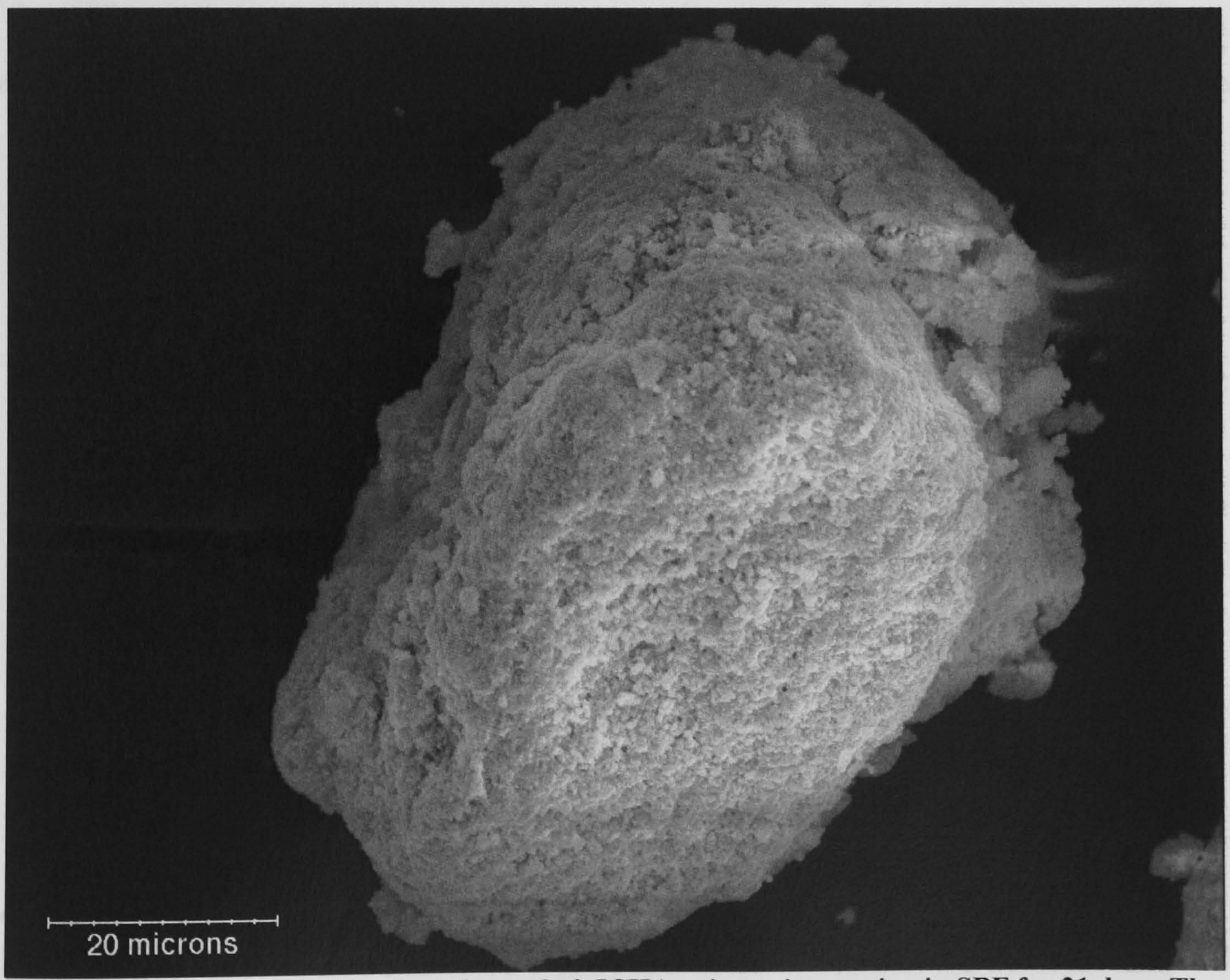

Figure 7. 93 A high magnification of sample 0.5CHA prior to immersion in SBF for 21 days. The scale bar denotes 20μm.

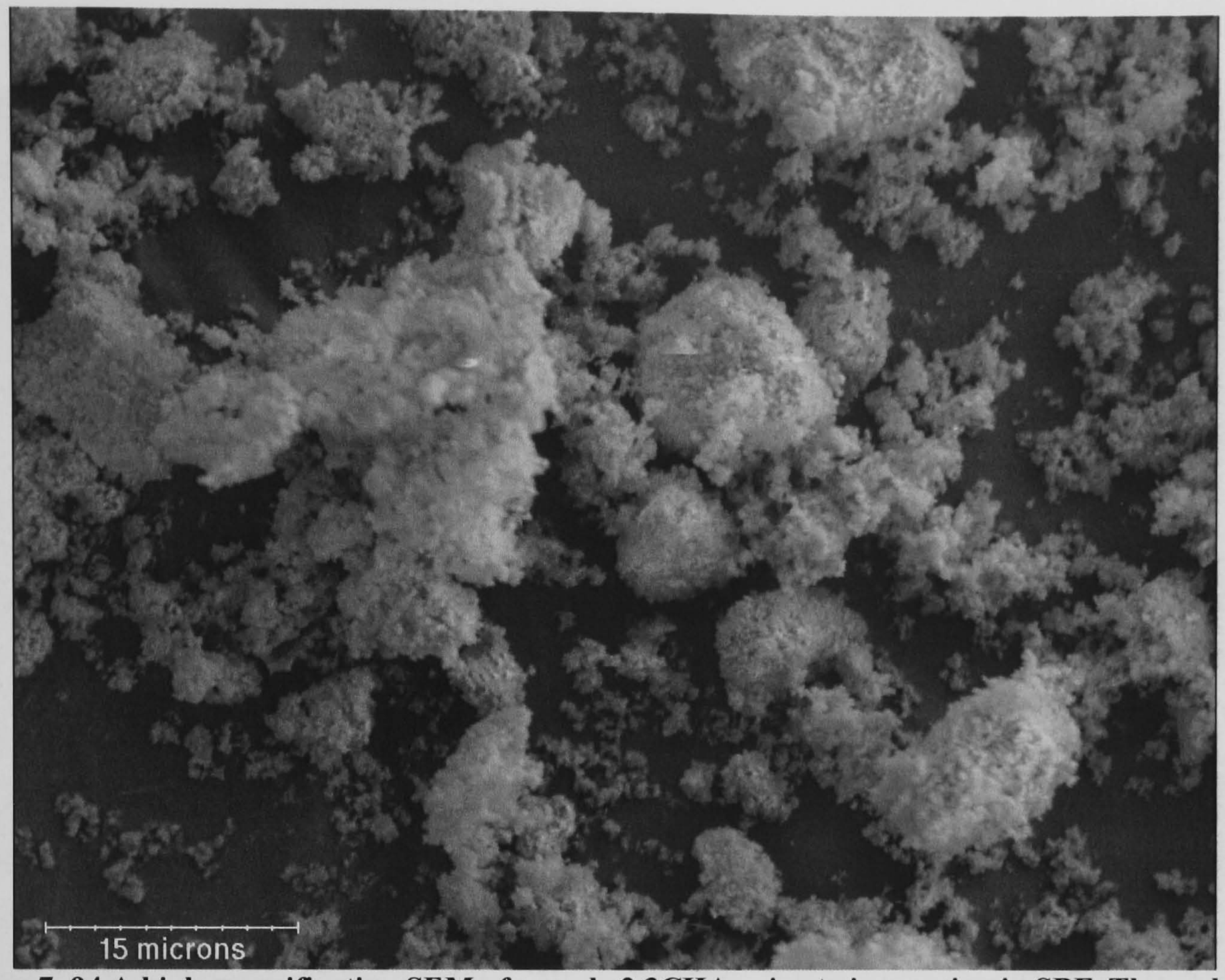

Figure 7. 94 A high magnification SEM of sample 2.3CHA prior to immersion in SBF. The scale bar denotes 15μm.

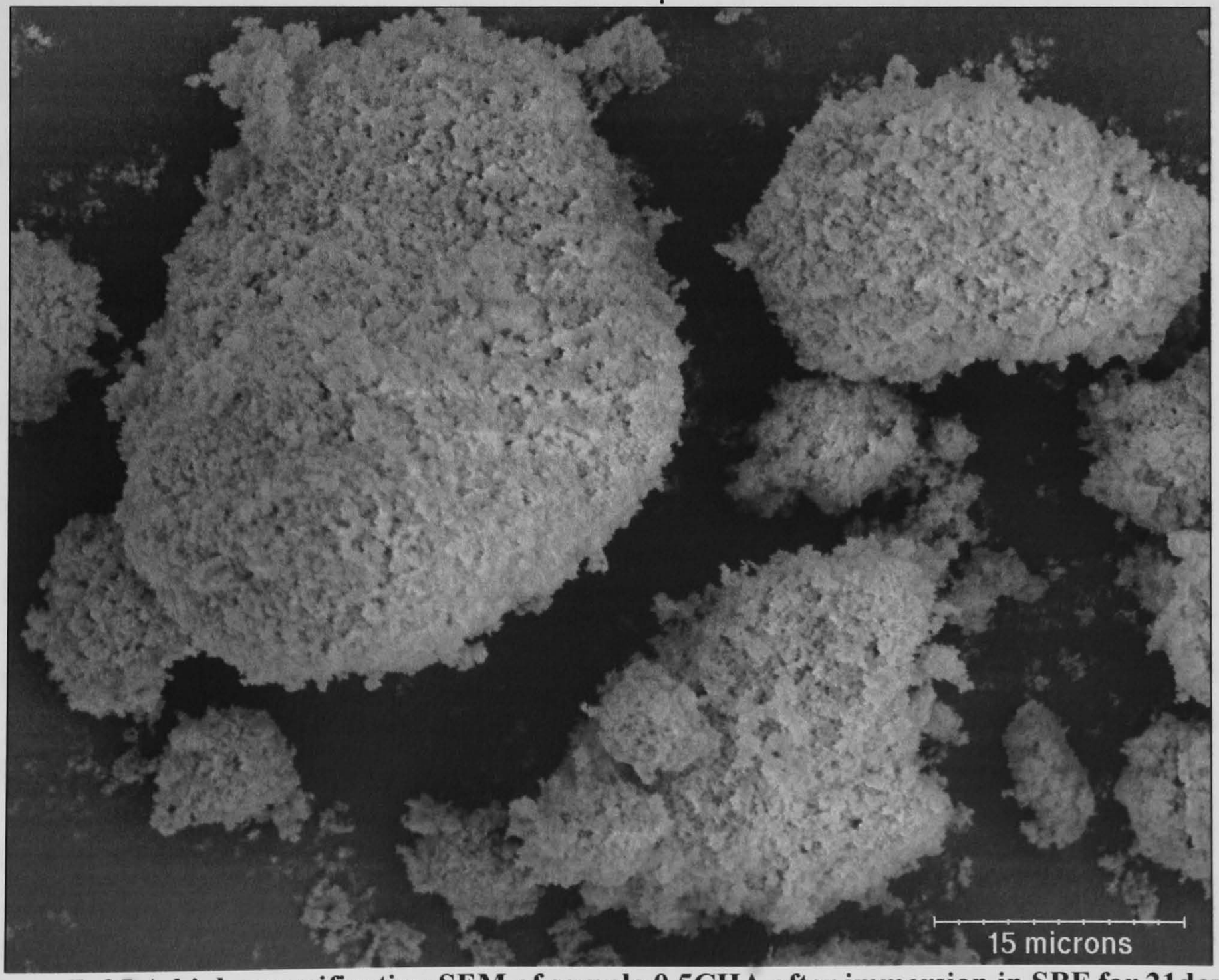

Figure 7. 95 A high magnification SEM of sample 0.5CHA after immersion in SBF for 21days.

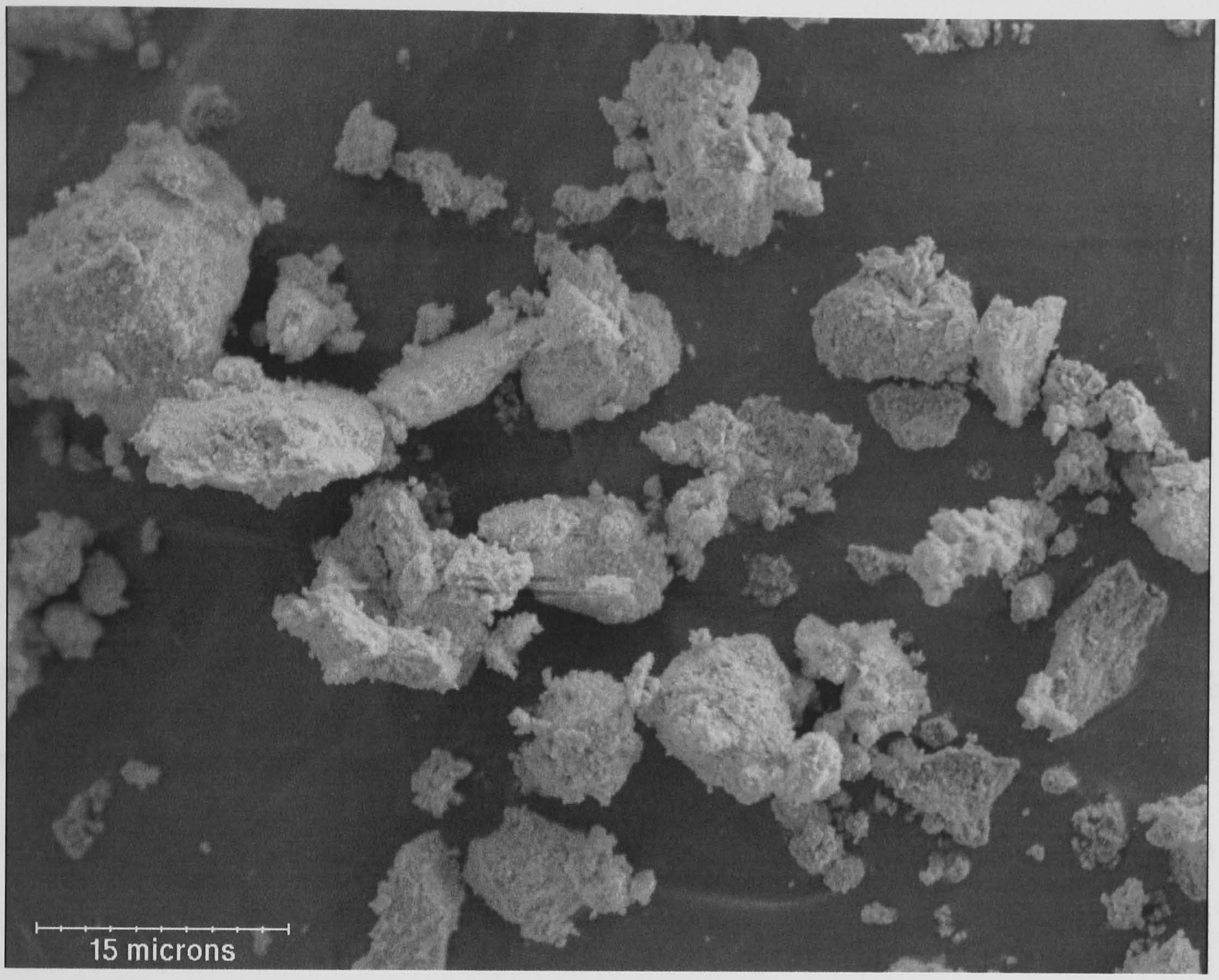

Figure 7. 96 A high magnification SEM of sample 2.3CHA after immersion in SBF for 21 days. The scale bar denotes 15μm.

7.2.4 Summary

The *in vitro* behaviour of PS and ED coatings has been assessed in water, SBF and FCS respectively using a novel method of non-destructive characterisation of apatites. The results have indicated the formation of a nano-crystalline phase on the surface of the PS coatings, which occurred to greater extent in SBF than FCS and water. For the first time, it has been possible to incorporate a nanocrystalline apatite phase into structural refinements in order to obtain structural information and examine changes with immersion time. This novel diffraction approach has allowed for changes in weight

proportions of HAP, ACP and nano-HAP components of HAP coatings to be characterised independently to allow for a deeper understanding of the interaction between HAP coatings and the various media. Such an understanding can allow for a prediction of likely *in vivo* behaviour (discussed further in chapter 8).

The *in vitro* behaviour of the ED coatings was dissimilar to the PS coatings despite having significantly less ACP in the as-received state. The results emphasize the importance of 'crystal quality' on the *in vitro* behaviour of HAP coatings. This was demonstrated most clearly by the unexpected enhanced dissolution of crystalline HAP observed in the ED coatings after immersion in water for 21 days and rapid dissolution of ACP in the PS coatings (discussed further in chapter 8). In addition, the formation of nano-HAP occurring only on PS coatings, which was absent in the ED coatings gives an indication of the effect of ACP on the precipitation products and hence bioactivity of HAP coatings (discussed in chapter 8). For the first time a comparative investigation of the *in vitro* behaviour of HAP coatings produced by plasma spraying and an electrodeposition coating has been conducted using a rigorous diffraction approach. This diffraction approach has enabled subtle changes in lattice parameters; crystal quality and chemistry of both PS and ED coatings to be identified in order to assess their suitability to *in vivo* applications. The diffraction approach outlined in this thesis has also aided in furthering the understanding of the relationship between coating technology and dissolution-precipitation behaviour.

In vitro investigations of apatite powders in SBF suggest that in the system used in this investigation, crystallite size effects dominate the dissolution behaviour of apatites over carbonate content and lattice microstrain. Contrary to previous work [211, 222, 258], the results from this investigation show that dissolution suppression occurred in apatite powders with crystallite sizes ≤1000Å when immersed in SBF for 21 days. In addition dissolution of apatite powders with crystallite sizes ≤400Å were inhibited. This finding reveals that the mechanism of dissolution of apatites is more complex (discussed in chapter 8) than previously reported and that dissolution does not occur continually until true equilibrium is reached or when solid phases cease to exist. Conversely, when the degree of saturation (with respect to HAP) is near to equilibrium, there appears to be a critical crystal size below which dissolution of apatites is suppressed or in equilibrium with the solution irrespective of solubility. The implications of these findings are discussed further in chapter 8.

In vitro investigations of the dissolution behaviour of apatite powders in water have revealed that in the system used in this investigation, at low supersaturation, size-dependent dissolution occurs, but to a lesser extent than at high supersaturation. Hence the crystallite sizes of the resultant apatites are smaller after immersion in water than after immersion in SBF. It would appear that dissolution inhibition in water occurs in apatite powders with a crystallite size ≤200Å.

For the first time it has been demonstrated that despite the fact that crystallite size dominates the dissolution of apatite powders with crystallite sizes <1000Å, microstrain has a modest contribution to the dissolution of the apatite powders at low supersaturation.

For the first time, a quantitative relationship has been established between the solubility of different apatite powders in water and crystallite size and lattice microstrain. Contrary to previous work [18, 19], which has attempted to correlate chemical stability of carbonated HAP to carbonate content, microstrain is the dominant factor governing the apparent solubility of apatites in water. The results suggest that the increase in apparent solubility observed with increasing carbonate content is due to the increase in microstrain as opposed to chemical effects. It has also been demonstrated that crystallite size also has a diminutive effect on the solubility of apatites with respect to microstrain. The possible mechanisms of microstrain and crystallite size effects on solubility and hence dissolution are discussed further in chapter 8.

Of note is the fact that no dissolution suppression due to size-effects was observed in the solubility investigations. This suggests that the dissolution suppression (or equilibrium) observed on prolonged immersion in SBF may not be a spontaneous mechanism, but may come into place after 24 hours; hence after solubility measurements had already been made. No reports of size-effects have been made in previous solubility studies [54, 56, 222, 272]. The discrepancy between trends in apparent solubility and the observed dissolution behaviour is discussed further in chapter 8.

7.3 Cell culture studies

A cell culture approach has been taken to assess the biological feasibility of HAP coated polymeric tape for potential use in ACL reconstruction. A novel low temperature coating technique (described in chapter 6) has been used to coat the polymeric tape used in this investigation. The coatings produced have been characterised structurally and chemically prior to commencement of the cell study (appendix D).

7.3.1 Cell attachment

Osteoblast cells have been cultured on HAP coated polymeric OT samples and controls. The number of cells adhering on each substrate has been counted using a haemocytometer. Figure 7.97 presents the number of osteoblast cells attaching to the surfaces of the plastic wells, polymeric OT samples after 4 and 18 hours of incubation in culture media. Osteoblast cell attachment to plastic culture wells was significantly higher than on OT-T, OT-N and OT-C samples ($P<0.05$) after 4 hours of cell culture. In addition, osteoblast attachment to OT-T samples was significantly higher than to OT-N and OT-C ($P<0.05$) samples. Cell attachment to OT-N surfaces was higher than to OT-C surfaces; however the difference was not significant.

The number of osteoblast cells attaching to the surfaces of each of the samples increased with incubation time and all groups were significantly different. At 18 hours of incubation, it was apparent that OT-T surfaces had promoted the fastest rate of increase in cell attachment, whilst the plastic culture wells had the slowest rate of increase in cell attachment with time. Nevertheless, the plastic culture wells had the most cells attached to its surface. Regardless of the difference in cell attachment to the plastic culture wells

and OT-T surfaces decreasing with incubation time, the difference remained significant ($P<0.05$) after 18 hours of incubation. The number of osteoblasts attaching to OT-N was significantly higher than OT-C ($P<0.05$).

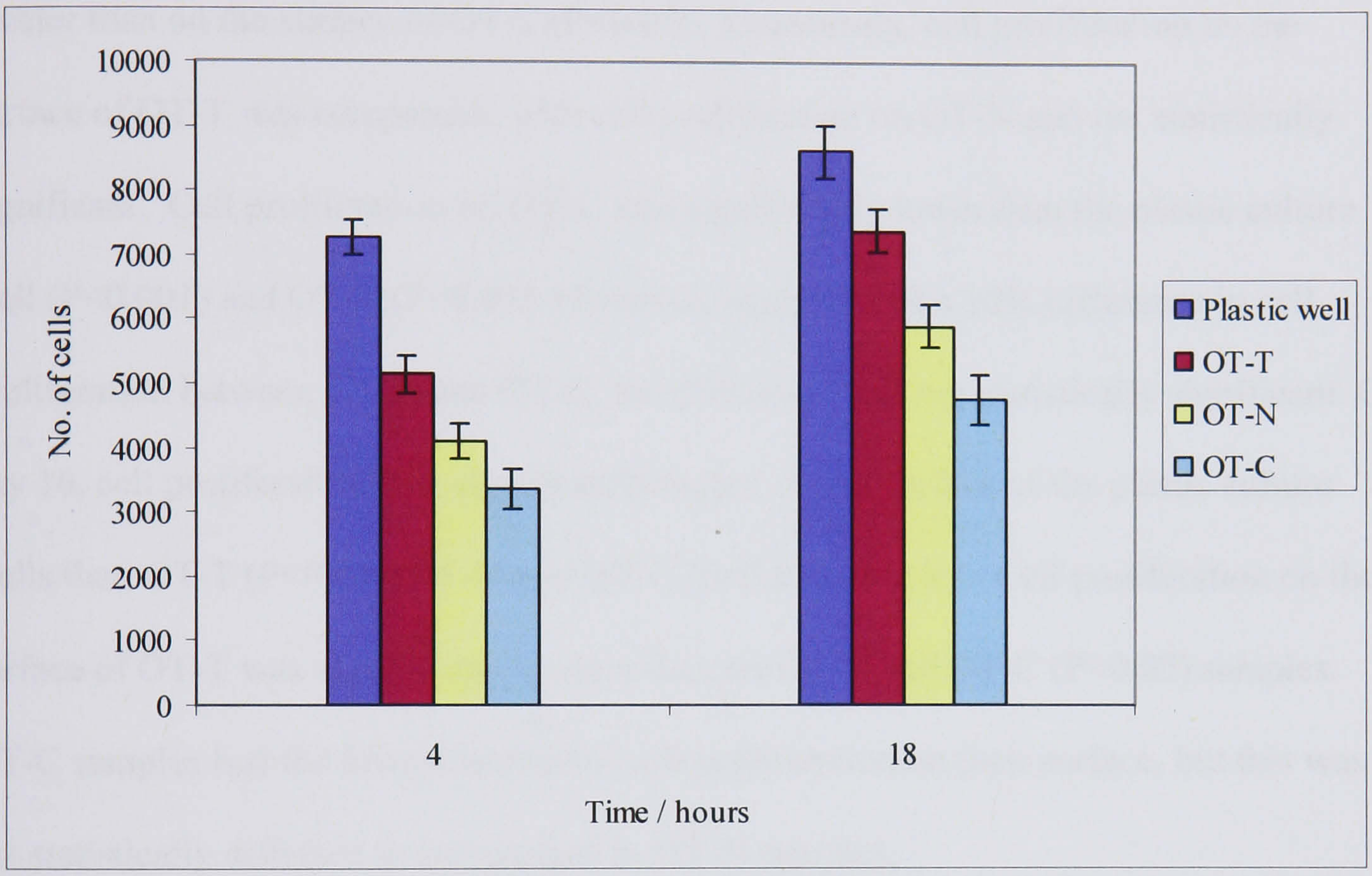

Figure 7. 97 Attachment of osteoblast cells to plastic culture wells or polymeric tape after 4 and 18 hours of incubation in culture media. The data are the mean ± standard error (n=24).

7.3.2 Cell proliferation

Figure 7.98 summarises the changes in osteoblast cell proliferation on plastic wells and polymeric OT samples between 7 and 16 days of incubation in culture media. On day 7, cell proliferation on the surface of the plastic wells and OT-T samples was similar and the difference was not statistically significant. Similarly, cell proliferation on the surfaces of OT-N and OT-C samples was not significantly different.

On day 11, osteoblast cell proliferation on the surface of OT-T samples was 17% greater than on the surface of the plastic wells ($P<0.05$). However, proliferation on the surface on OT-C samples was higher than on OT-N samples, but this difference was not statistically significant. On day 14, cell proliferation on the plastic culture well was 37% greater than on the surface of OT-T ($P<0.05$). Conversely, cell proliferation on the surface of OT-T was comparable with cell proliferation on OT-N and not statistically significant. Cell proliferation on OT-C was significantly lower than the plastic culture well ($P<0.001$) and OT-T ($P<0.01$). However, regardless of a 20% difference in cell proliferation between OT-N and OT-C, the difference was not statistically significant. On day 16, cell proliferation was significantly higher on the surface of the plastic culture wells than OT-T ($P<0.05$), OT-N and OT-C ($P<0.05$) samples. Cell proliferation on the surface of OT-T was significantly greater than on OT-N and OT-C ($P<0.05$) samples. OT-C samples had the lowest amount of cell proliferation on their surface, but this was not statistically different in comparison to OT-N samples.

Plastic culture wells promoted a fastest rate of cell proliferation between day 7 and day 16. However, the initial increase in cell proliferation between day 7 and day 11 was limited, but it accelerated more rapidly after day 11. On day 7, osteoblast proliferation on OT-T was initially comparable with that of the plastic culture well, but, by day 11, proliferation on OT-T was higher than on the plastic culture wells. After day 11, cell proliferation on OT-T remained lower than on the plastic culture well. Osteoblast proliferation on OT-N and OT-C remained comparable between day 7 and day 16.

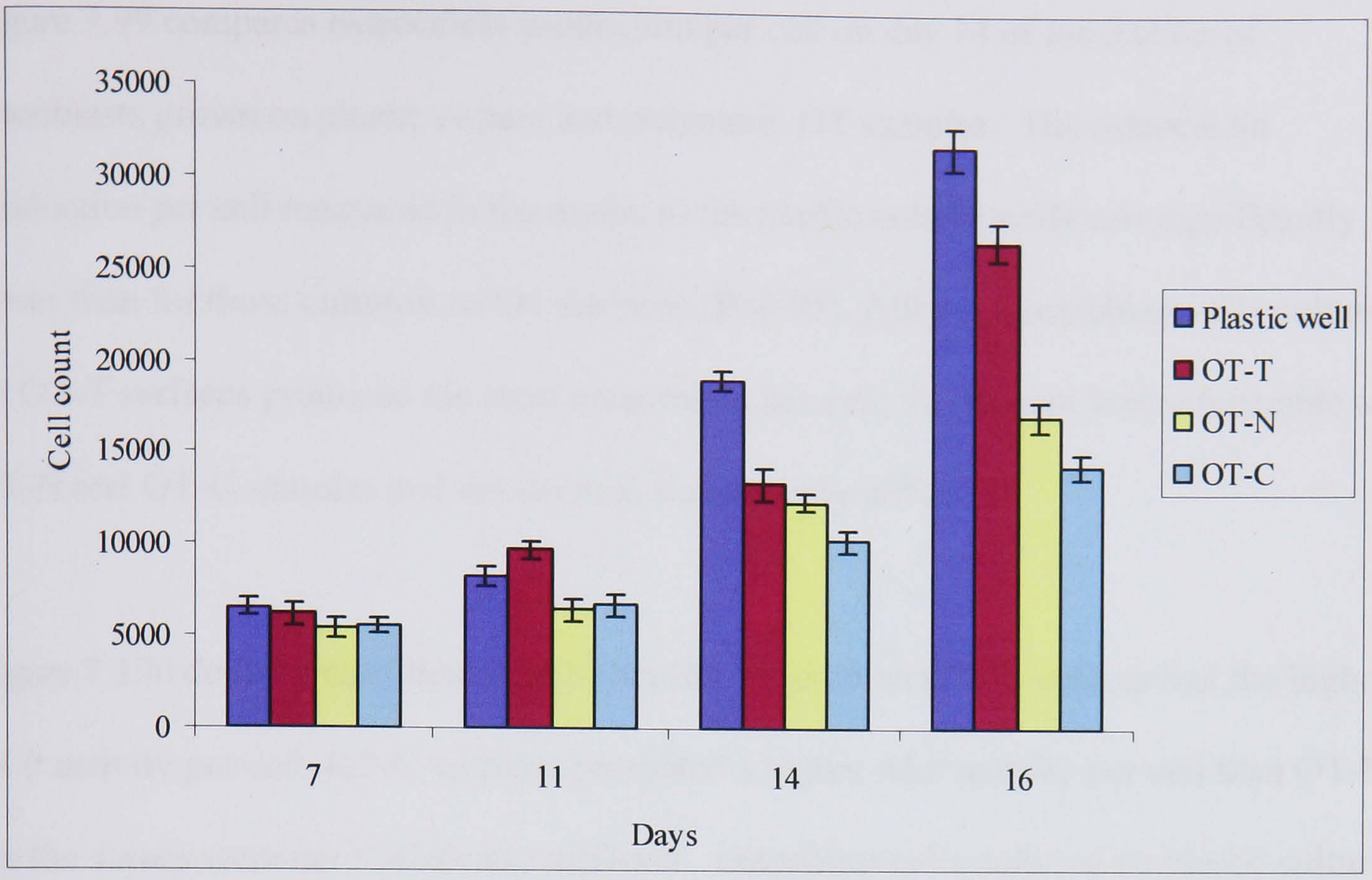

Figure 7. 98 Proliferation of osteoblast cells on plastic culture wells or polymeric tape after 7, 11, 14 and 16 days of incubation in culture media. The data are the mean ± standard error (n=24).

7.3.3 Osteocalcin production and ALP activity

Osteocalcin and ALP activities were used as differential markers of osteoblasts. Table 7.29 compares the production of osteocalcin and ALP activity of osteoblast cells after 14 days of incubation on plastic wells and polymeric OT samples in culture media. Osteoblast cells cultured on OT-T surfaces had the highest osteocalcin production and ALP activity. However, ALP activity amongst the groups was not significantly different. Conversely, the quantity of osteocalcin produced by the osteoblast cells grown on plastic culture wells was significantly lower than that of the other surfaces ($P<0.001$). Osteoblasts cultured on OT-N and OT-C surfaces produced comparable quantities of osteocalcin that were not significantly different.

Figure 7.99 compares osteocalcin production per cell on day 14 of incubation of osteoblasts grown on plastic culture and polymeric OT samples. The osteocalcin production per cell measured in the media in the plastic culture wells was significantly lower than for those cultured on OT surfaces ($P<0.05$). Although osteoblast cells cultured on OT-T surfaces produced the most osteocalcin per cell, the amount was comparable to OT-N and OT-C samples and not deemed significantly different.

Figure 7.100 demonstrates that osteoblast cells cultured on OT-T surfaces had the highest ALP activity per cell. OT-C surfaces promoted a higher ALP activity per cell than OT-N, but the values were not statistically different. Osteoblast cells cultured on plastic culture wells produced the lowest ALP activity per cell, which was 40% lower than for cells grown on OT-T surfaces.

Sample	Osteocalcin (ng mL^{-1})	ALP activity (nmol min^{-1} mg^{-1} of protein)
Plastic well	1.7 ± 0.05	0.3 ± 0.04
OT-T	6.5 ± 0.12	0.5 ± 0.08
OT-N	5.0 ± 0.20	0.3 ± 0.05
OT-C	4.6 ± 0.27	0.2 ± 0.04

Table 7. 29 Osteocalcin production (ng mL^{-1}) and ALP activity (nmol min^{-1} mg^{-1} of protein) of osteoblast cells in culture media after 14 days of incubation on plastic wells or polymeric tape. The data are the mean ± standard error (n=6).

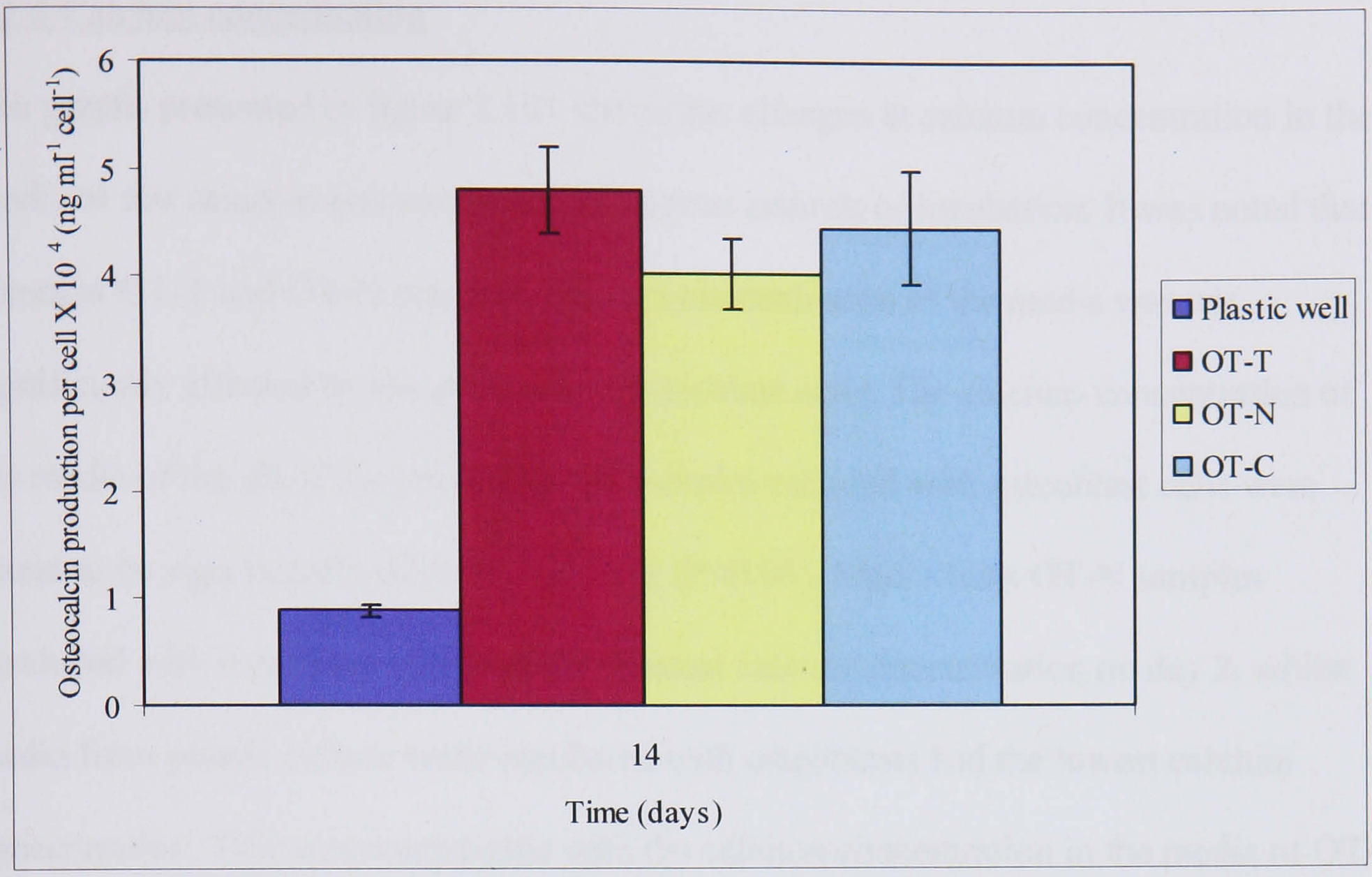

Figure 7. 99 Osteocalcin production per cell X 10^4 (ng mL^{-1} $cell^{-1}$) after 14 days of incubation in culture media. The data are mean ± standard error (n=24).

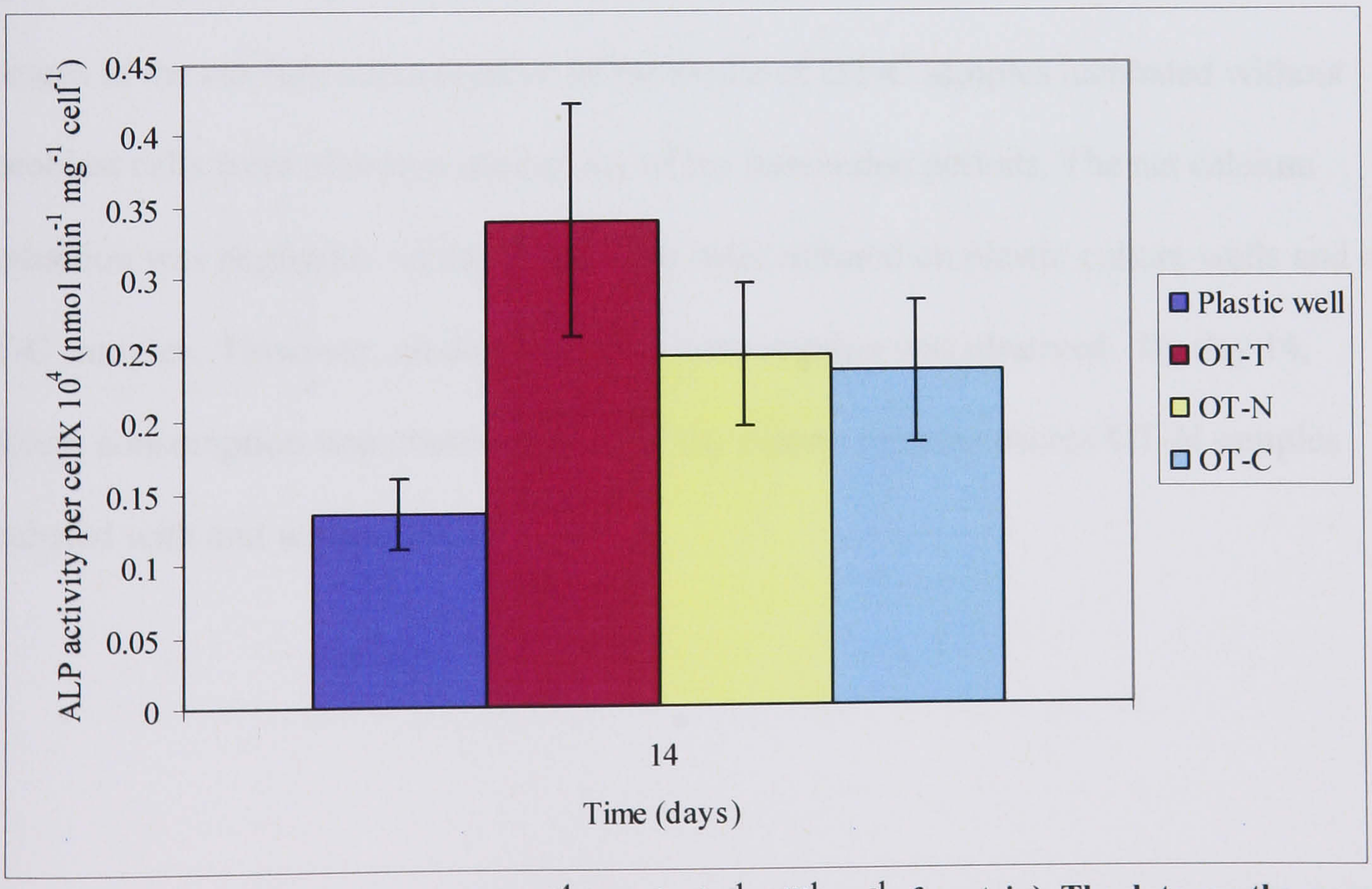

Figure 7. 100 ALP activity per cell X 10^4 (nmol min^{-1} $cell^{-1}$ mg^{-1} of protein). The data are the mean ± standard error (n=6).

7.3.4 Calcium concentration

The graphs presented in figure 7.101 shows the changes in calcium concentration in the media of test samples and controls after various periods of incubation. It was noted that amongst OT-T and OT-N samples, calcium concentration of the media was not significantly affected by the presence of osteoblast cells. The calcium concentration of the media of the all of the polymeric OT samples cultured with osteoblast cells were found to be significantly different on day 2 ($P<0.05$). Media from OT-N samples incubated with osteoblast cells had the greatest calcium concentration on day 2, whilst media from plastic culture wells incubated with osteoblasts had the lowest calcium concentration. This was comparable with the calcium concentration in the media of OT-C samples and was not found to be statistically different.

Figure 7.102 presents the net changes in concentration of calcium in the media. No net changes in the calcium concentration of the media of OT-C samples incubated without osteoblast cells were observed during any of the immersion periods. The net calcium production was negligible on day 2 and 4 for cells cultured on plastic culture wells and on OT-C samples. However, on day 7 calcium consumption was observed. By day 14, calcium consumption was observed in all of the culture systems except OT-N samples incubated with and without cells.

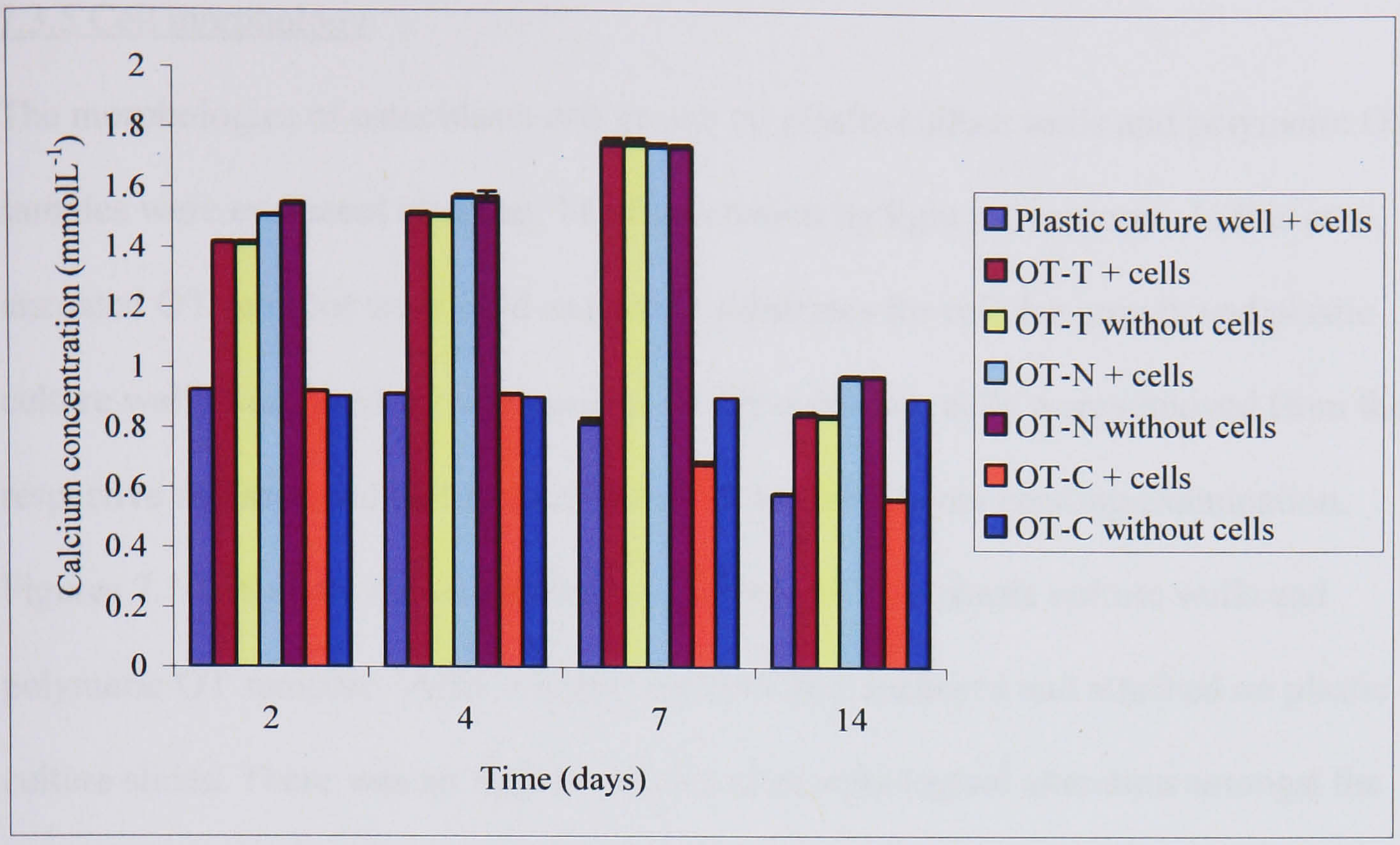

Figure 7. 101 Calcium concentration of media after different periods of incubation. The data are the mean ± standard error (n=24).

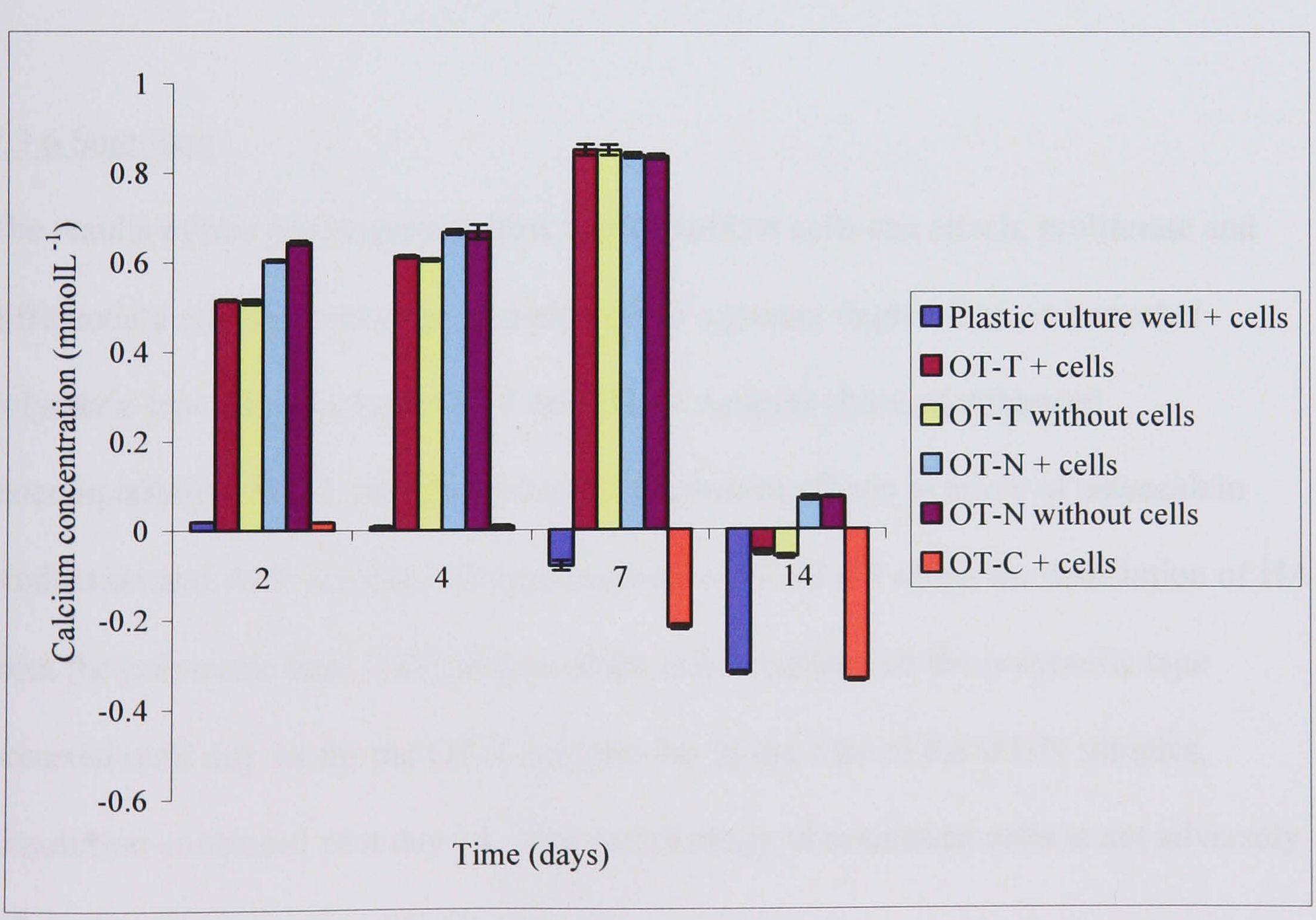

Figure 7. 102 Net changes in calcium concentration in the media of test samples and controls after different periods of incubation. The data are the mean ± standard error (n=24).

7.3.5 Cell morphology

The morphologies of osteoblasts cell grown on plastic culture wells and polymeric OT samples were evaluated after day 14 of incubation by light microscopy. In this case, uncoated OT samples were used as control substrates for cellular growth and plastic culture wells were used for comparison. After culturing, cells were removed from their respective surfaces and cultured on plastic slides for 4 hours pending examination. Figures 7.103-6 show the morphology of cells grown on plastic culture wells and polymeric OT samples. After 4 hours, the cells had anchored and attached on plastic culture slides. There was no sign of toxicity or morphological alteration amongst the groups. The osteoblasts cells had retained their morphology, and were elongated with long cytoplasmic processes and regular shaped nuclei and no 'giant cells' were observed.

7.3.6 Summary

The results of this investigation show that osteoblast cells can attach, proliferate and differentiate on HAP coated polymeric tape to a greater degree than on uncoated polymeric tape. Despite both OT-T and OT-N samples showing enhanced biocompatibility, OT-T samples induced the greatest effects in terms of osteocalcin production and ALP activity. The presence of cells did not affect the dissolution of HAP from the polymeric tape. Dissolution of the HAP coatings on the polymeric tape occurred until day 14 for the OT-T samples but in the case of the OT-N samples, dissolution continued past day 14. The morphology of osteoblast cells is not adversely affected by the presence of HAP.

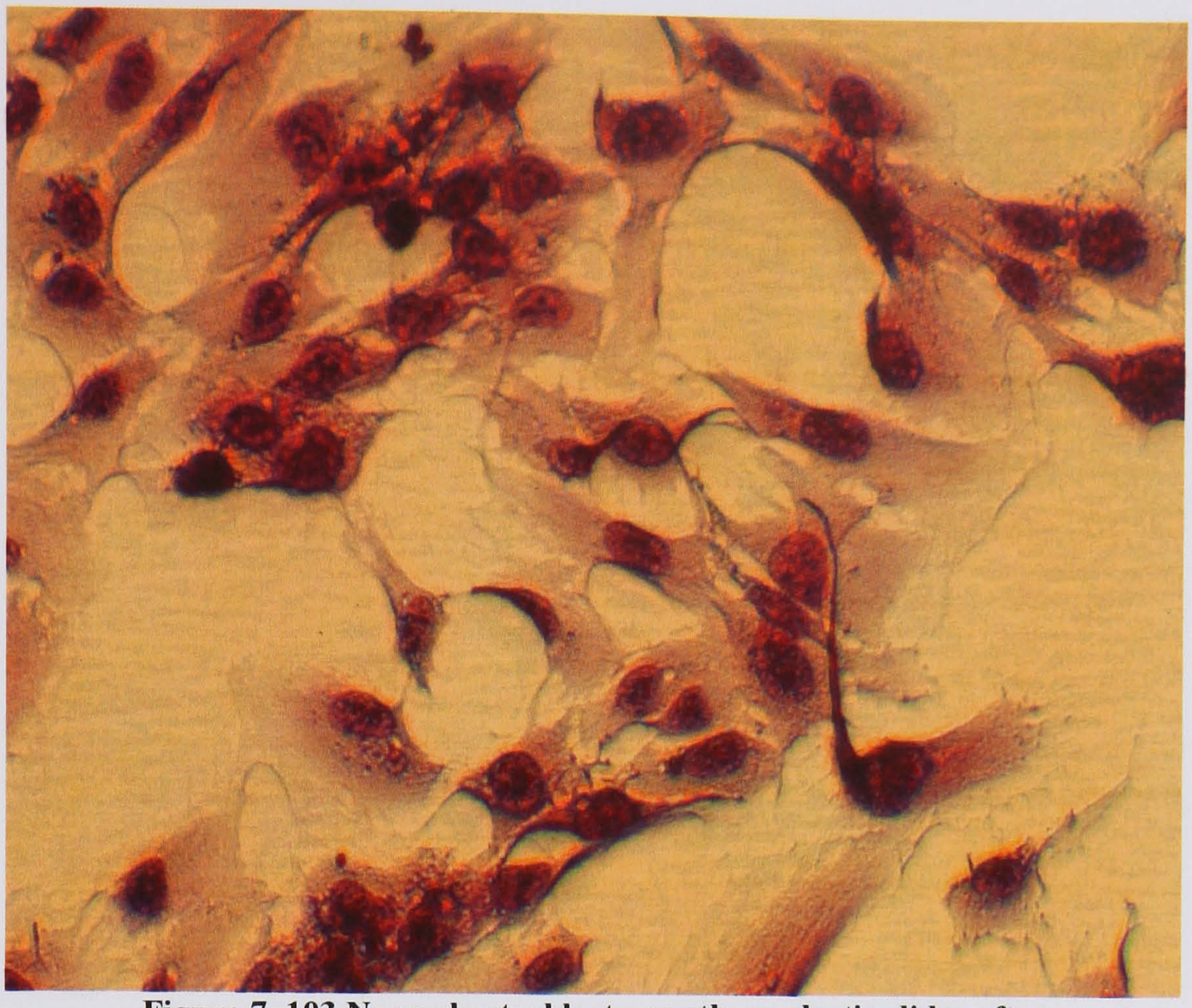

Figure 7. 103 Normal osteoblast growth on plastic slides after exposure to plastic culture wells for 14 days.

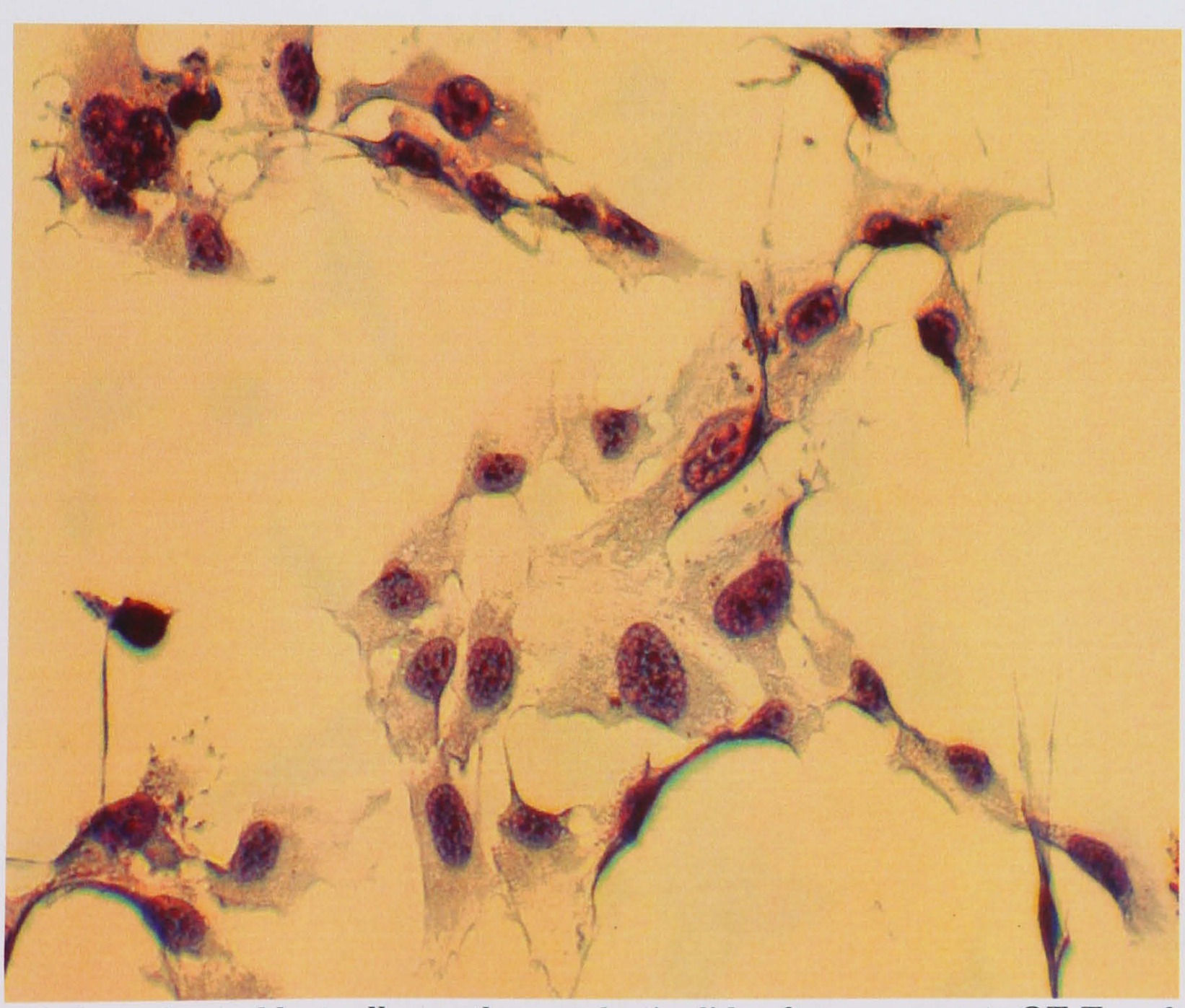

Figure 7. 104 Normal osteoblast cell growth on a plastic slide after exposure to OT-T surfaces for 14 days.

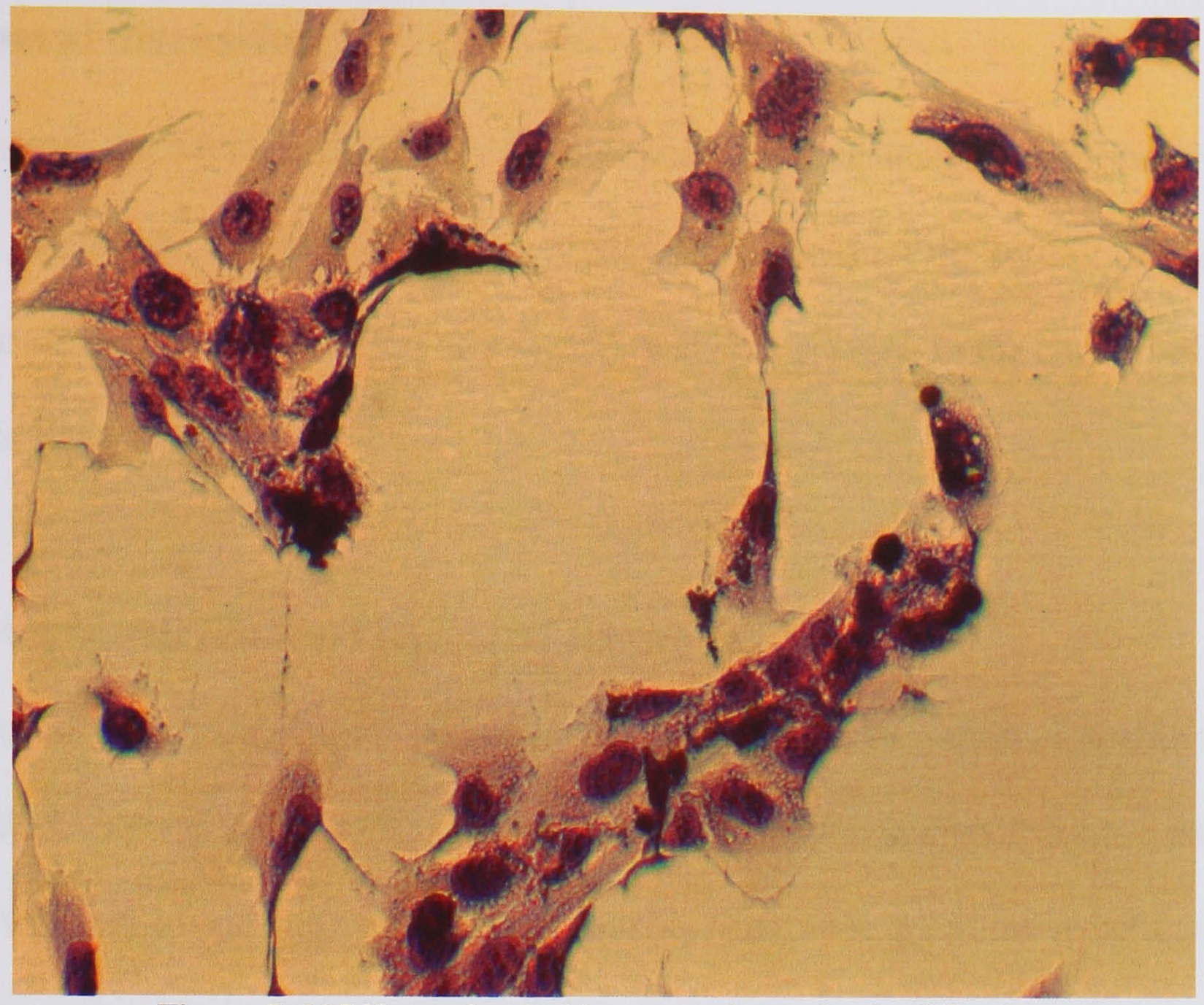

Figure 7. 105 Normal osteoblast growth on plastic slide after exposure to OT-N surfaces for 14 days.

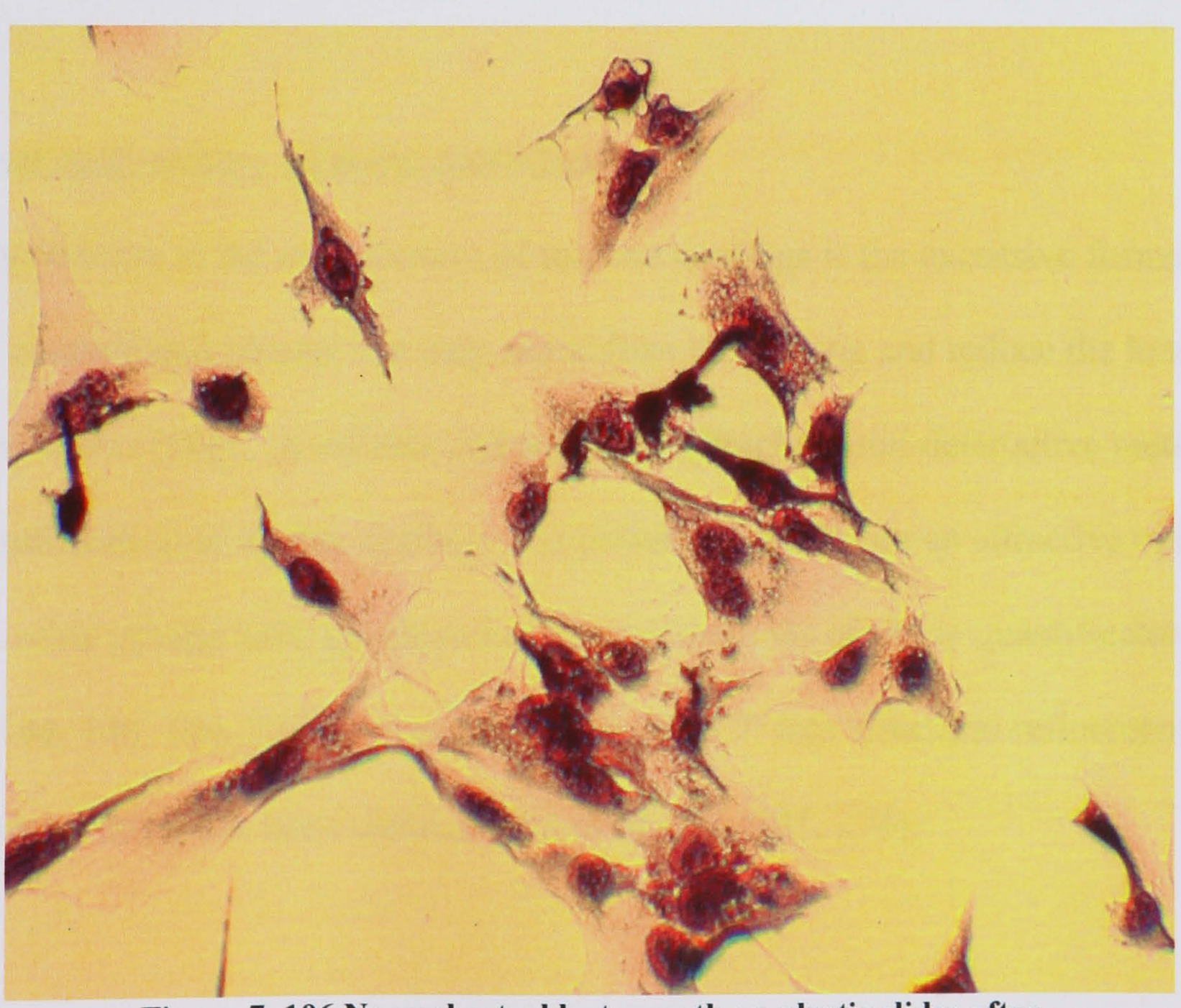

Figure 7. 106 Normal osteoblast growth on plastic slides after exposure to OT-C surfaces for 14 days.

8.0 General discussion

In this chapter the novel methodology for quantitative phase analysis described in chapter 6 will be discussed. In addition the underlying mechanisms for the solubility and *in vitro* behaviour of the apatite coatings and powders will be discussed in the context of traditional theories.

8.1 Phase quantification and structural characterisation

A rigorous diffraction approach has been taken to the characterisation of apatite coatings and powders. This is in contrast to previous characterisation studies that have used methods that rely on external or internal standards to provide quantitative compositional information. Previous methodologies have not been able to tolerate very thin coatings or coatings with preferred orientation such as electrodeposited coatings.

8.1.1 Novel methodology of phase quantification

A primary concern in the manufacture of implant coatings is the excessive formation of ACP and contaminant phases that may destabilize the coating and reduce the longevity of the device *in vivo* [145]. A reliable and accurate diffraction non-destructive method of phase quantification of apatite coatings and powders is therefore an attractive option. Although other groups have developed numerous methods of phase quantification of apatites [144, 146, 196, 273], the incorporation of ACP into structural refinements for whole pattern fitting has been unsuccessful until now [145, 274].

A novel methodology for phase quantification of biphasic apatites coatings and powder *in situ* has been described in chapters 6 and 7. This method is a customized Rietveld approach that enables scattering contributions from HAP and ACP phases to be separated and the relative quantities evaluated without the need of internal or external standards. For the first time, an ACP phase has been included in structural refinements of biphasic apatites enabling the determination of the crystalline-amorphous ratio. It has been demonstrated that this technique is capable of reliably and accurately providing quantitative phase information and hence eliminating the sample destruction and calibration errors associated with internal standards and systematic errors associated with external standard methods [196].

Keller *et al* [275] have previously attempted to include an amorphous phase into structural refinements of biphasic HAP coatings. However, only a poor fit of observed and calculated diffraction data was obtained as the lattice parameters were fixed to that of stoichiometric HAP.

Riello *et al* [234] have successfully conducted phase quantification of semi-crystalline poly-(ethylene terephthalate) [PET] and $ZrOCl_2$ by separating scattering from amorphous and crystalline components. The methodology used by Riello et al [234] has a similar theoretical basis as the novel methodology described in this thesis. However the method described by Riello *et al* [234] was not robust enough to tolerate preferred orientation despite the use of a March-Dollase correction function. A more recent study by Riello *et al* [198] entailed the quantitative phase analysis of Y_2O_3/silica and hence materials with

phases containing different chemical compositions. This method showed discrepancies between Y_2O_3/silica of known and measured compositions. This was a result of the difference in the linear absorption coefficients that were not fully accommodated in this analysis.

In contrast to other methods of phase quantification [100, 147, 180, 196, 200] currently employed, this methodology proved robust particularly in light of the preferred orientation present in the ED coatings by means of a 4^{th} order spherical harmonics correction. Previously, the presence of preferred orientation has posed a problem for methods that rely on the measurement of relative peak intensities [147, 196, 276]. To reduce the effects of preferred orientation, Prevey [98] has employed integrated intensities of several diffraction peaks rather than one. However, in a multiphase system where the peaks are severely broadened, this method is not robust.

In order to achieve a satisfactory fit for each refinement, it was necessary to adopt an complex background function [147]. It was important that the background function did not coincide with the scattering maxima of the amorphous component and that it differs markedly from the HAP coating. Therefore, the background (incoherent scattering) was determined empirically using a Ti substrate without a coating. A Ti substrate was used to find the incoherent scattering as opposed to a fully crystalline HAP coating due to the fact that the Ti substrate has fewer peaks and the incoherent scattering is decipherable more clearly. The quality of each fit was assessed visually and by means of the 'goodness of fit' value R_{wp}. In all of the refinements an R_{wp} value of <12% and a good visual fit

was obtained. The good fit between observed and calculated diffraction patterns gives further strength to the validity of the methodology.

According to Tong *et al* [277] fixing the refineable parameters of the ACP phase (except scale factors) in structural analysis of HAP coatings may simplify the precise shape of scattering from the amorphous component. The affect of lattice parameters on the shape of the ACP scattering was investigated further for the system used in this study. It was found that the shape of the ACP scattering was affected by changes in lattice parameters. However, the novel methodology introduced and validated in this thesis, can provide an approximate value for the density of the non-crystalline phase as well as accurate and precise quantitative information.

A possible limitation to this methodology is the fact that in the first instance (before refinement), the atomic model of the ACP phase was based on that of HAP. It may have been more appropriate to model the ACP phase on $Ca_3 (PO_4)_2$, as it is closer in stoichiometry than to HAP. Since the ACP phase in the coatings used in all of the investigative work carried out derived from HAP, there was rationale for using a HAP atomic model. An assessment of the accuracy of the methodology, by comparing known and measured compositions showed that in all cases the values of ACP were in agreement with 4wt% (section 7.1). Therefore in this case, using a HAP model as opposed to $Ca_3 (PO_4)_2$ provided an appropriate base for accurate and precise phase quantification.

Additionally, for each refinement, the atomic parameters (atomic positions, thermal parameters and occupancies) were fixed to that of stoichiometric HAP. This effectively fixed the linear absorption coefficient, which is different for HAP and ACP [131]. The difference in linear absorption coefficient may have introduced small errors into the system but these errors did not affect the robustness of the model as evidenced by the good correlation between measured and calculated compositions.

This method is a powerful for performing quantitative analysis on biphasic materials. It is anticipated that this technology could be applied to a wide range of materials, although materials with larger differences in linear absorption coefficient and chemical constituents may be more complicated [198, 234].

8.1.2 Lattice parameters

The whole pattern approach to diffraction analysis incorporating instrument related factors and sample-dependent factors used in the investigative work documented in this thesis has proved to be a powerful method. The accuracy and reliability of the whole pattern approach to determine accurate and precise lattice parameters has been well documented [145, 148, 150]. In order to assess the reliability of the approach in the system used throughout the investigative work, repeated measurements of a single sample was made. A good quality fit was achieved each time and the standard error associated with the measurement of each of the lattice parameters was $\leq 0.011\%$.

8.1.3 Microstructural analysis

Discrepancies arise when values of 'crystallite size' are quoted on an absolute scale. The main source of disagreement arises in the different definition of the parameter 'crystallite size' and the method of determination. In this thesis the terminology 'crystallite size' denotes the average volume weighted column height as explained in chapter 4. This is due to the fact that actual crystallite sizes cannot be measured directly by XRD. For true values of crystallite size to be determined, the mean shape of crystallites must be identified in order to derive and apply a correction to the column height of each hkl [140].

Other methods, such as the Warren Averbach methods, liberate area weighted column heights and mean-square microstrain averaged over a distance perpendicular to the diffracting planes. Therefore there is great difficulty in making direct comparisons between absolute values quoted in the literature. Consequently the values of average volume column heights (length of coherently scattering domains along the c-axis) and microstrain quoted in this thesis principally provide indications of systematic changes in the microstructure of HAP. Alternative methods such as transmission electron microscopy may be better suited to accurate measurement of crystallite sizes [152].

The values of crystallite size (average volume weighted column height) and microstrain calculated in this thesis by the approximate method (chapter 4) are likely to be precise but not accurate. Only the (002) reflection is exploited in this analysis hence giving the length of coherently scattering domains in the c-axis direction only, as opposed to the an

average crystallite size based on all reflections. The Warren-Averbach method would perhaps be a more suitable method of size-strain determination but this would require multiple order reflections [152] e.g. (002), (004) and (006), which is not possible for the diffraction data obtained in this experimental work due to peak overlapping. Microstrain values obtained by the approximate method (chapter 4) are the upper limit (maximum).

For size-strain estimation using Williamson-Hall plots, an analytical profile shape function (pseudo-Voigt) has been fitted to observed diffraction peaks corresponding to HAP peaks. This method has allowed determination of parameters such as shape factor (ϕ), integral breadth, and peak positions. The shape factor is an important consideration in analytical profile fitting using a pseudo-Voigt function. As a pseudo-Voigt function is a convolution of Lorentzian and Gaussian functions [150, 158], a shape factor outside the limits of Lorentzian and Gaussian is not accurately described by a Voigt function [158] and was therefore omitted from analyses. A chi-squared parameter was used in order to assess the quality of fitting. Peak fits of low quality were excluded from further analyses.

A pseudo-Voigt function was used in this analysis to describe peak shapes because in preliminary studies for the experimental work carried out in this thesis, it was found that the pseudo-Voigt function adequately describes the peak profiles of the diffraction data. Pseudo-Voigt functions are known to be suitable for least-squares refinements and to give a better fit due to their flexibility in shaping the profile.

Williamson-Hall plots have been employed in a first qualitative estimation to observe changes in size and strain in accordance with previous work [155, 158, 159, 240]. More accurate values of size and strain were obtained by the approximate method (chapter 4). Values of crystallite size obtained directly from W-H plots have been reported to be high compared to other methods such as Warren-Averbach analysis [240]. This may be due to the fact that W-H analyses assumes uniform crystallite size in all crystallographic directions.

8.2 Characterisation of apatite coatings

Characterisation of apatite coatings is of great importance in the development and improvement of coatings and coating technologies. The studies outlined in this thesis have enabled a direct structural comparison of HAP coatings fabricated by plasma spraying and electrodeposition.

8.2.1 Plasma sprayed coatings

As discussed in chapter 5, during the PS process, HAP particles will melt partially or wholly. The melt may solidify to ACP, recrystallise to HAP or form impurity phases [100]. The formation of ACP in the PS process is a result of the interaction of HAP particles with plasma gases, the cooling rate of the melted droplets and the temperature of the substrate onto which the melted droplets fall [97, 100].

The melted droplets that impinge on the substrate at the start of the PS process experience rapid cooling. This is due to the large difference in thermal conductivity between the substrate and the droplets and spreading of the droplets on the substrate. Therefore the molten droplets dissipate heat to the substrate and rapid cooling of the molten droplet occurs. The rapid cooling of HAP melt produces a 'liquidus temperature effect' allowing the melt to cool to a lower temperature before solidification, and increasing the likelihood of ACP formation. Dehydroxylation of the HAP melt occurs during the PS process, as evidenced by the decrease in the intensity of the OH stretch band at ~3574cm^{-1} and absence of the OH liberation band at ~630cm^{-1} (see table 7.3). This is as a result of partial temperature degradation of HAP. Dehydroxylation of the melt has been reported

to create a barrier to nucleation of HAP from the melt because of the lattice distortions and vacancies associated with it. Therefore the production of ACP is thermodynamically more viable [100]. The tendency to form ACP is further accentuated by the complexity and structure of HAP. Crystallisation to form the intricate structure of HAP requires more time for diffusion of the atoms or groups to lattice sites [97]. This is explanatory evidence of why a greater amount of ACP was observed in the 'partial thickness' coating than the 'full thickness' coatings (see table 7.2).

Successive droplets build up the coating and as layers form, the temperature gradient between layers decreases, hence decreasing the cooling rate. In addition the roughness of successive layers of HAP impedes the spreading of molten droplets and therefore decreases the cooling rate. The decreased cooling rate provides a thermodynamic driving force for the recrystallisation of molten HAP droplets or prior- formed ACP to occur [100]. During the PS process, the temperature of the substrate can increase to ~1000°C as a result of the heat transfer from the plasma flame and the HAP melt. As coating layers build up, the heat energy from the substrate and coatings ultimately leads to recrystallisation of the HAP melt and some of the prior-formed ACP, as the recrystallisation temperature of ACP is 500-700°C [97, 278]. It has been reported [278] that the time interval between deposition of droplets is ~0.1 seconds, compared to 10^{-5}-10^{-7} seconds for solidification. Therefore, the prior-formed ACP may incorporate hydroxyl ions from the surrounding air and therefore become rehydroxylated at temperatures above ~400°C, hence promoting recrystallisation [100, 278, 279]. As a result of the aforementioned mechanisms of recrystallisation, the material at the surface

of PS coatings contains less ACP than at the coating-substrate interface as observed in the diffraction data in this investigation. In addition, dehydroxylation observed in figure 7.5 was as a result of ACP formation.

Previous authors have attributed the increase in broadening in the diffraction maxima of PS coatings, relative to the initial feed powder, to the formation of recrystallised HAP melt during PS. The results of this investigation show that this phenomenon is unlikely. Although the peak widths of the full and partial coating are larger than those of the feed powder, they are not attributable to small crystallite size as evidenced by microstructural analyses (see table 7.3). If the increase in peak widths had been attributable to recrystallisation (small crystallite size), the peak widths of the 'full thickness' coatings would be greater than that of the 'partial thickness' coatings. This is due to the fact that recrystallisation is greater in the 'full thickness' coatings than the 'partial thickness' coatings. Williamson-Hall analysis of the full thickness coatings (figure 7.4) and the partial thickness coatings [131] the peak width increase was as a result of increased lattice microstrain. In addition, it was found that the average crystallite size measured using the (002) reflection had increased. The W-H plot corresponding to the feed powder indicated the absence of microstrain as evidenced by the horizontal best-fit line (figure 7.5).

The likely causes of increased microstrain are the presence of lattice distortions (phosphate and hydroxyl) and vacancies arising from fast heating and cooling cycles, which become 'frozen' in the structure on solidification. Distortion of the PO_4 tetrahedra

is evidenced by the absence of the symmetric stretching mode for PO_4 at ~960cm^{-1}. Further evidence of lattice distortions can be seen in table 7.3 where small shifts in the position of the maxima of all of the principal bands are observed compared to the feed powder. Lattice distortions may also be a result of rapid crystal growth (evidenced by increase crystallite size) as a result of the temperature gradient in the coatings.

Roome *et al* [159] have attributed the presence of microstrain in the PS coatings to the difference between the thermal expansion coefficients of HAP and the Ti substrate. This would imply that microstrain would be localised at the HAP-Ti interface. The results obtained in study were contrary to this. Microstrain was found to be uniform as evidenced by the similar values of microstrain in the near substrate and near surface regions of the coating.

Another possible explanation for the existence of microstrain in the PS coatings may be the reaction of deposited HAP with airborne components such as water, oxygen and carbon dioxide. In addition, small quantities of impurities may lie on the surface of the feed powders and on melting of the HAP particles; the impurities become incorporated into the structure on cooling. No such elements were detected by EDX, although they may still have been present.

The results show that estimated microstrain (~0.24%) and crystallite size (~0.2μm) for both the 'full and partial thickness' coatings were similar in magnitude [131]. This would suggest that there is no significant size/strain gradient through the thickness of the

PS coating. The value of crystallite size for the PS coatings was close to the instrument resolution function (IRF) and may hence have had a great error attached to it. The instrument would not be sensitive to crystallites larger than 0.2μm and no further decrease in peak broadening would occur as the result of larger crystallite size.

Of interest is the fact that the partial PS coating contained small amounts of contaminant phases such as α-TCP, β-TCP and CaO that were absent in the 'full thickness' PS coating. These contaminant phases exist as a result of the partial decomposition of crystalline HAP as a result of the high temperature associated with the P.S process. Dehydroxylation of the HAP melt decreases the temperature at which HAP decomposes to metastable compounds [100]. The 'partial thickness' coatings contained a greater relative proportion of metastable compounds than the 'full thickness' due to the fact that closer to the substrate more dehydroxylation and hence decomposition of HAP occurred as a result of rapid heating and cooling of HAP. The absence of impurity phases in the 'full thickness' coating may be due to the recrystallisation of dehydroxylated melt as a result of decreased cooling rates or hydroxyl build up between layers of coatings.

The chemical nature of the PS coatings was dissimilar to the initial feed powder. From the diffraction data, subtle differences in the lattice parameters were discernable. The differences in the lattice parameters in the 'full and partial thickness' PS coating compared to the initial feed powder may be attributed to the vaporisation of carbonate ions (see figure 7.5-6) from the coating and the possible inclusion of small quantities of airborne alien ions into the crystal lattice (causing macrostrain). The removal of the

carbonate ions from the feed powder during the PS suggests that the carbonate ions may be loosely bound carbonate ions, possibly adsorbed to the powder surfaces [248]. Lattice parameter changes (macrostrain) may also be the result of the formation of dehydroxylated apatite and/or the recrystallisation of the HAP melt during the PS process. The recrystallisation of the HAP melt may also account for the small but insignificant differences in the lattice parameters of the 'full and partial thickness' coatings by virtue of the different degrees of dehydroxylation and recrystallisation. The 'partial thickness coatings' have the greatest deviation in lattice parameters from that of the feed powder. This may be explained by the greater degree of dehydroxylated apatite and less recrystallised HAP.

The preferred orientation observed by measurement from (002) and (300) peak intensities was as a result of recrystallisation of the HAP melt. When recrystallisation occurs, diffraction peaks increase in intensity and become well defined. In this case, recrystallisation was direction dependent and the intensity of peaks corresponding to the <00l> direction increased faster than the <h00> direction as a result of preferred recrystallisation. As a result the intensities of peaks in the <00l> direction became exaggerated with respect to the <h00> direction.

8.2.2 Electrodeposited coatings

The main difficulty experienced in the characterisation of the ED coatings was the limited thickness of the coating and hence low intensity of HAP peaks. The diffraction data was dominated by the presence of peaks corresponding to the titanium substrate. In addition much information relating to HAP was lost due to the titanium peaks overlapping with the HAP peaks. Therefore limited information was obtained with respect to the microstructural properties of the coatings. For example, only a few data points could be exploited for the construction of a W-H plot (section 7.1.2). A tentative estimation of size and strain was difficult due to scattering and the limited number of the data points. In addition, as a result of a poor signal to noise ratio, the errors associated to the measurement of the lattice parameters were significantly higher than those corresponding to the PS coatings.

The crystallinity index, the inverse of the integral breadth of the (002) HAP peak, of the ED coatings was ~3.7 compared to ~7.81 for PS coatings. This indicates that the ED coatings have a poorer crystal quality in comparison to the PS coatings. The poor crystal quality is derived from both crystal imperfections and small crystallite size associated with the fabrication process.

It is probable that the microstrain (~0.39%) is a result of the stacking faults, vacancies, substitutions or dislocations associated with the direct growth on the titanium substrate during cathodic deposition [280, 281]. No ionic substitutions were detected by EDX,

therefore it is likely that the deviation from stoichiometry observed in the lattice parameters was a consequence of macrostrain.

It is expected that during coating build up with each subsequent coating layer the dislocation density (length of dislocation line per unit volume of crystal) and microstrain are reduced due to the release of stress in the film. The cumulative effect of decrease in dislocation density and microstrain may cause a gradual reduction of stacking faults with coating build up [280]. Therefore, it would be expected that the highest concentration of dislocation density, microstrain and stacking faults would be found nearer to the coating substrate interface.

The smaller crystallite size (~0.11μm) in comparison to that of the PS coatings is perhaps a result of the slow growth of crystals during the deposition period as result of lower temperature. Mahalingham *et al* [280] have reported a functional dependency of crystallite size on temperature in ZnTe thin films produced by electrodeposition. In addition, the small crystallite size observed in ED coatings investigated may be due to the short deposition cycles in the fabrication process. Mahalingham *et al* [280] have found a positive correlation between deposition cycle time and average crystallite of ZnTe produced by electrodeposition.

A characterisation study using non-destructive structural tomography has been carried out by Broadhurst *et al* [253, 267] on the ED coatings prepared for the investigative work described in this thesis. The results of the analysis have shown that crystallite size of the

HAP (measured from the (002) peak) increases with coating thickness (distance from substrate). Similar observations have been made in thin films deposited by electrodeposition for solar cell applications [280, 281]. Although no formal mechanism of the changes in crystallite size with depth has been proposed in the literature, it may be due to the fact that as the coating becomes thicker (and hence denser), successive layers build up a resistance to the cathodic current, were as a consequence, the current density in the adjacent areas increase. It has been reported previously that the time required for crystallization and growth of HAP decreases quasi-hyperbolically as a function of current density [122].

Of note was the fact that only a small quantity of ACP was present in the ED coatings (~10wt%). One could argue that the presence of ACP as measured using the novel methodology for quantification was an artefact of the background. This was found not to be the case as spherical structures (section 7.2), which have been identified previously [122, 254] as clusters of ACP, were observed on the surface of the coatings by SEM.

The presence of ACP in the ED coatings characterised in this investigative work is expected. The reason is that the electrodeposition process, introduced in section 3.5, involves the deposition of ACP (at near physiological temperature and pH), which is then converted to HAP. The electrochemical deposition of HAP is based upon the diffusion and migration processes in the electrolyte and the pH solubility of the calcium phosphate phases involved [122, 254]. During the cathodic polarisation of the substrate (cathode) in the electrolyte, alkalisation (reduction of water, proton discharge, reduction of dissolved

oxygen) occurs close to the surface of the cathode. This chemical activity results in the production of hydroxyl ions close to the surface of the cathode. Alkalisation results in the precipitation of the ACP in the form of spherical structures [122]. With increase in polarisation time during the fabrication process, needle-like HAP crystals begin to form and the dissolution of the ACP structures occurs. Dissolution of the ACP structures is the onset of the transformation of ACP to HAP. Depending on the length of the polarisation time, a complete ACP to HAP transformation may occur [122, 254]. The ED coatings produced in this work contained small weight proportions of ACP, indicating that complete transformation had not occurred. The sequence of deposition of HAP presented in this investigative work (via a low activation energy intermediary phase) occurring at physiological temperature and pH mimics *in vivo* biomineralisation. Therefore, the process conditions are considered to be biomimetic [122, 254] and hence are expected to undergo resorption and remodelling processes similar to those found *in vivo*.

The chemical and microstructural properties and phase composition of the HAP coating produced can be tailored by altering the electrochemical parameters (current density, polarisation time, pH and temperature) [122, 254]. This feature makes the deposition process favourable in comparison to PS due to the degree of flexibility that it affords.

The greater degree of preferred orientation observed in the ED coatings is an intrinsic characteristic of thin films produced by cathodic deposition due to slow growth process involved. Slow crystal growth, allows for the crystals to become aligned in a preferred orientation. Although the presence of preferred orientation, can pose problems

(systematic errors) in the structural analysis of ED coatings, it is still not know whether it affects the *in vivo* stability of the coating.

In summary, for the first time a direct comparison between commercially fabricated PS and ED coatings have been conducted. A rigorous diffraction approach has been adopted in this case, which has incorporated a novel methodology of non-destructive phase quantification of the coatings. Despite the chemical and microstructural properties of PS being well documented [20, 86, 97, 102, 250, 252, 282], most have focused on qualitative analysis of coatings. This study has adopted a quantitative perspective to the determination of the principal structural and chemical characteristics of PS coatings.

Electrodeposition of HAP coatings is still in its infancy and hence the characterisation studies that exist are either exploratory [120, 121, 123, 125, 283] or semi-quantitative [122, 254] with respect to phase composition and microstructure. This is the first time that phase quantification and structural analysis of ED deposited HAP coatings have been conducted and the findings presented signify an advancement in knowledge in the field of biomaterials science.

Despite the fact that the nature of the ED HAP coatings produced by other groups differs to the ones presented in this study by virtue of fabrication (and hence growth procedure of HAP), characterisation studies are important to allow for direct comparison and assessment of their *in vivo* suitability and performance. In addition, characterisation allows for improvements and development in coating characteristics and technologies.

The advantages of electrodeposition over plasma spraying are evident. Composition and microstructural control are afforded due to the relatively low temperature of fabrication. Also there are many variables that can be used to control the deposition process and properties of the coatings formed. The advantage that the ED coatings characterised in this investigative work have over other documented ED technologies [123, 125, 283] is that they are 'biomimetic' in nature and do not require post fabrication annealing or conversion in order to obtain suitable coating quality or characteristics.

8.3 *In vitro* behaviour of apatite coatings

This study has enabled a direct comparison of the *in vitro* behaviour of PS and ED HAP coatings. Such a study allows for the prediction of the probable *in vivo* behaviour of the coatings. In addition, for the first time, it has been possible to monitor and account for the chemical and microstructural changes occurring in the coating with immersion time.

8.3.1 Plasma sprayed coatings

It has been demonstrated the novel method of phase quantification introduced in chapter 6 and 7, has enabled the crystalline, semi-crystalline and amorphous components of 'treated' PS to be modelled simultaneously as independent phases. Changes in microstructural and chemical nature of the coatings with immersion time have thus been quantified.

The *in vitro* behaviour of PS coatings was investigated following immersion in deionised water, SBF and FCS for periods of up to 21 days. Samples immersed in water had rapid

dissolution of ACP compared to the SBF and FCS samples followed by a subsequent precipitation of carbonated nano-HAP. The rapid dissolution of ACP in the water samples is as a result of the degree of undersaturation with respect to HAP. According to Brown *et al* [219] and Paschalis *et al* [284] when an excess of HAP is placed into an undersaturated solution with respect ($S<1$; $K_{sp} > IP$) to HAP, the HAP will dissolve and the solution will become enriched in calcium and phosphate ions. The rate of dissolution may be interpreted in terms of an empirical kinetic equation 8.1 where R_d is the rate of dissolution; K_d is the rate constant; n is the order of reaction; and σ_d the relative undersaturation, equal to {1-S} [285, 286].

$$R_d = K_d \, \sigma^n_d \qquad (8.1)$$

As emphasised by equation 8.1, the rate of dissolution is proportional to the degree of undersaturation. The calculated ionic product (IP) for SBF and FCS was ~ 1×10^{-84}. In contrast, the K_{sp} of HAP in water is ~5.5×10^{-118} at 37.5°C [222], which indicates that SBF and water are already highly supersaturated (low undersaturation) with respect to HAP as seen in equation 8.2 [285] where S is supersaturation ratio, IP is the ionic product, Ksp is the solubility product and v is the number of ions in the molecule (18 for HAP).

$$S = \left(\frac{IP}{K_{sp}} \right)^{\frac{1}{v}} \qquad (8.2)$$

Therefore the rapid dissolution of ACP observed in the water samples compared to in SBF and FCS respectively is in agreement with this dissolution model (equations 8.1 and 8.2). ACP dissolved preferentially due to the fact that it is least thermodynamically stable phase is in the PS coatings under the experimental conditions in this system (pH 7.4; 37.5°C) [65, 287].

As the dissolution of ACP proceeded with time in the water samples, nucleation, precipitation and growth of nano-HAP (carbonated nanocrystalline HAP) was promoted. Nucleation occurred as a result of an increase in supersaturation with respect to HAP in the water due to the rapid dissolution of ACP. The nucleation stage corresponds to the production of nuclei from which crystal growth can occur. The initial nucleation process has been reported to determine the size, number and morphology of precipitating crystals [285]. As nucleation proceeds, nuclei aggregate until a critical nuclei size is formed. Nuclei larger than the critical size will have a tendency to grow by crystal growth. Since the rate of formation of the critical nucleus is proportional to $(\ln S)^{-2}$, where S is the supersaturation ratio [288], nucleation is sensitive to the degree of supersaturation.

The driving force for crystal growth is described by equation 8.3 [285] where R_g is the rate of crystal growth; K_g is the rate constant; n is the order of reaction; s is a function of the total number of growth sites; and σ_g the relative supersaturation, equal to (S-1):

$$R_g = K_g\, s\, \sigma_g^n \qquad (8.3)$$

As can be seen from equation 8.3, the rate of crystal growth is proportional to supersaturation. Therefore, at higher supersaturations with respect to HAP, faster crystal growth is expected. The dependency of nucleation and growth rates on supersaturation explains the differences in the proportion of nano-HAP produced in the SBF and water samples.

Further evidence for the observed differences in the proportion of nano-HAP produced can be seen in equation 8.4 where ΔG is the change in Gibbs free energy; R is the molar gas constant (8.314 $JK^{-1}mol^{-1}$); T is the absolute temperature; n is the number of ion units in a HAP molecule; and S is the supersaturation.

$$\Delta G = - \frac{RT}{n} \ln(S) \qquad (8.4)$$

The Gibbs free energy available for the formation of HAP is proportional to the degree of supersaturation. The more negative the Gibbs free energy, the stronger the driving force for formation of HAP. Therefore, the driving force for formation of HAP is greater for the SBF system than the water system; hence the formation of nano-HAP is greater in the SBF samples than the water samples after immersion for 21 days as measured from the diffraction data. This is emphasised by the greater proportion of nanocrystals observed by SEM on the SBF samples than the water samples (section 7.2).

There was a difference in the behaviour of the SBF and FCS samples. Although both media had similar chemical compositions, the presence of plasma proteins in the FCS

appeared to act as a retardant for HAP dissolution. No significant dissolution occurred during the first three days of dissolution. This was evidenced by the constant lattice parameters during this period. After seven days of immersion, there was a gradual dissolution of ACP and formation of nano-HAP. This may have been due to the denaturation of the plasma protein after ~ 4 days. In order to check this hypothesis, additional samples were immersed in FCS and the media was changed daily. Under these conditions, dissolution of ACP and the formation of nano-HAP was observed after ~ 4 days of immersion. Hence it can be concluded that in this system, the plasma proteins have a 'temporary shielding effect' on the dissolution of PS coatings. Studies [266, 289, 290] on the interaction of proteins on HAP have revealed that some proteins bind to a specific face of HAP crystals thus controlling dissolution mechanics and morphogenesis of such crystals. In addition, a study carried out on ACP powders by Blumenthal *et al* [291] showed that the conversion of ACP to HAP was slower in the presence of serum proteins due to the absorption of proteins on to the surface of HAP. However, no protein absorption bands were detected in the FTIR spectra of the samples immersed in FCS, so protein adsorption may not have been the mechanism that occurred in this case.

Apatite crystal growth from ACP aqueous systems has been well documented [219, 287, 292-294]. ACP is isothermally metastable and if allowed to exist within a solution, will spontaneously convert to an isothermally more stable product with a chemical stoichiometry approaching that of crystalline HAP [294]. The nature of apatite formed as a result of the dissolution of ACP is partly dependent on the degree of dissolution, the stoichiometry of the ACP, pH and temperature. Hence, for *in vivo* considerations the

proportion of ACP or the stoichiometry of ACP within the coating could be used to control the nature of the HAP material being precipitated. This is further emphasised by the difference in the *in vitro* behaviour of the ED coatings (discussed in section 7.3.2).

The structural refinements made incorporating the nano-HAP phase produce a good fit in all cases both after visual inspection and on consideration of the R_{wp} values (<12%). The peaks with extended tails were as a result of the superimposition of broadened peaks (corresponding to the nano-HAP) and sharp peaks (corresponding to the crystalline HAP). Other groups have not previously reported this phenomenon in diffraction studies and hence this is the first time that a nano-crystalline HAP phase has been included in structural refinements to investigate changes in apatite coatings.

A recent parallel investigation conducted by Rogers *et al* [190] on the day 21 SBF samples from this study further justifies the existence of the nano-HAP phase. Rogers *et al* [190] employed, synchrotron depth profiling tomography (described elsewhere [253, 267]) in conjunction with conventional XRD to obtain the structural characteristics of the post-immersion coatings with depth. It was shown that the nano-HAP material is confined to the upper regions of the coating (co-existing with HAP) where there is little ACP. In contrast, at 20μm depth into the coating, there was significant ACP, but no nano-HAP. The thickness of the nano-HAP film on the day 21 SBF samples was estimated to be ~ 4μm which is in good agreement with the estimation made in chapter 7. Combining the results from the parallel investigation [190] and the results obtained in this investigation, there is further evidence to show that the formation of nano-HAP is

formed principally from the preferred dissolution of ACP and re-precipitation as a thin film.

Figures 8.1-2 show the variation in preferred orientation (calculated as described in chapter 6) and d-spacing with depth of the crystalline HAP obtained in the study by Rogers *et al* [190]. It is evident from figure 8.1 that at the surface of the coating there was no net preferred orientation. Between the surface and a depth of 2mm, the preferred orientation increases and reaches at a plateau a depth of ~4μm, with a PO index of ~0.7, which corresponds with the PO index of the as-received coating (chapter 6). This finding is further evidence that the nano-phase thickness is ~4μm. In addition, the results suggest that the nature of the HAP that co-exists with nano-HAP increases in texture magnitude. The impact of the increase in texture on the coating performance is not yet known.

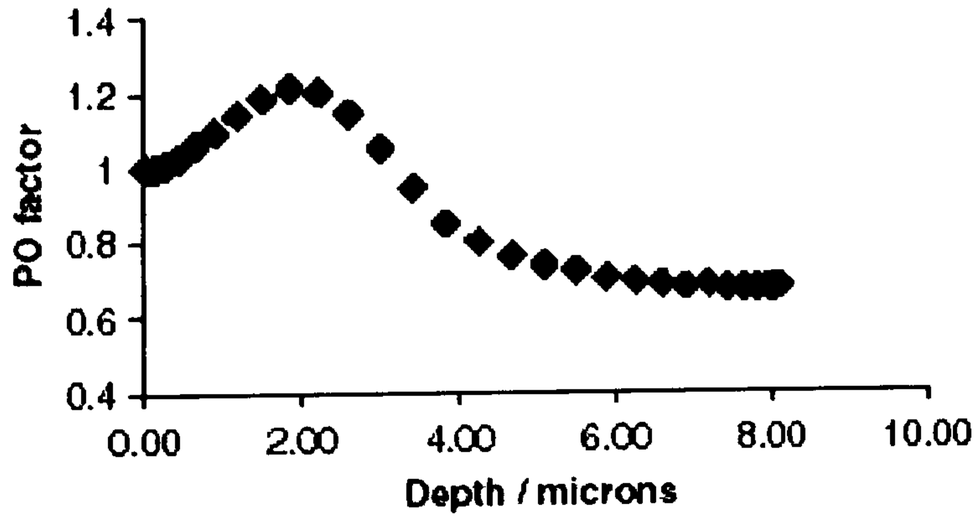

Figure 8. 1 Preferred orientation of crystalline HAP with depth into coating [190]

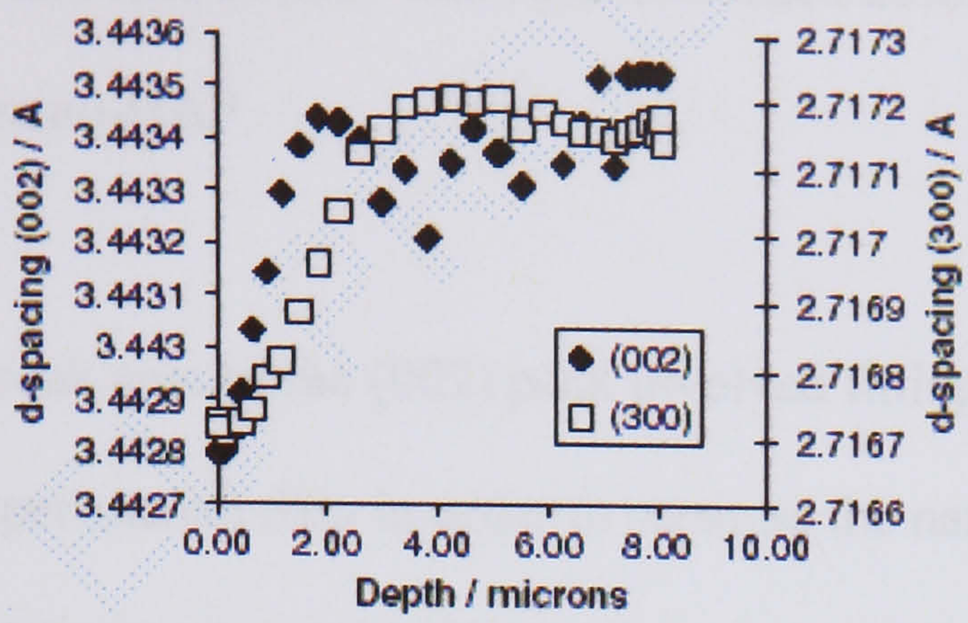

Figure 8. 2 d-spacing of (002) and (300) of HAP with depth into the coating [190].

Figure 8.2 shows that the d-spacing (and hence lattice parameters) of the (002) and (003) increase with coating depth until a depth of ~4μm coating. After this the d-spacings of both reflection remain constant. The initial increase (between the surface and 4μm depth) may be a result of the decrease of carbonate content in the lattice with depth as indicated by FTIR analysis (section 7.2). This shows that the uppermost HAP layer that co-exists with nano-HAP changes in stoichiometry with depth into the coating.

The peak areas for nano-HAP and HAP determined in section 7.2 indicated that with immersion time the crystallinity of the nano-HAP increased whilst the crystallinity of the HAP decreased. The increase in the peak area of the nano-HAP was perhaps as a result of the increase in crystallite size and increase in crystal perfection with immersion time. The increase in peak area of the HAP was perhaps due to the decrease in crystallite size due to partial dissolution and decrease in crystal perfection as a result of lattice substitutions. On the other hand, the increase in nano-HAP peak area may be attributable to increasing phase absolute mass and the decrease in HAP peak area may be

attributable to both a decrease in HAP mass and increased absorption due to the formation of surface nano-HAP.

Measurement of the peak area of the (002) peak involved fitting two independent pseudo-Voigt peaks to the experimental data in order to separate the nano-HAP component from the HAP component (chapter 6 and 7). The peak areas are only suitable to assess the changes in nature of the nano-HAP and HAP qualitatively. This is due to the fact that prior to day 7, only small proportions of nano-HAP were present in the coating and therefore the data suffers from high interphase correlations (between HAP and nano-HAP). Therefore it should be appreciated that although the data is precise, its accuracy is likely to be limited.

Overall, the results indicate the formation of an adherent; nanocrystalline HAP phase, which is formed from the dissolution and re-precipitation of the plasma, sprayed coating material in SBF, FCS and water respectively. It is apparent from the difference in the lattice parameters between the nano-HAP from the HAP components of the coating that the newly precipitated phase is not stoichiometric HAP. Possible reasons for the deviation in stoichiometry are calcium deficiency [19, 258], macrostrain [295] and carbonate ion inclusion in the crystal lattice (section 7.2.1).

Many groups [204, 227, 258, 296] have characterised apatite coatings and powders post-immersion in SBF. However these studies have been qualitative in nature or morphological and in most case diffraction data has not been exploited. Studies have

also focused on the chemical changes occurring in the media. Therefore little information is known about the changes in the structural and chemical properties of the coating itself.

Monteiro *et al* [258] have conducted non-quantitative FTIR studies on various apatite powders immersed in SBF. Although some carbonate inclusions were reported, no other changes were probed. Changes in phase composition and crystallinity were assessed by visual inspection of diffraction patterns.

Gu *et al* [225] attempted to elucidate the biological behaviour of PS coatings immersed in SBF. The study focused on the morphological changes occurring in the PS coatings, which are already well documented [203, 271, 297]. Although in this investigation Gu *et al* [225] tried to assess changes in phase composition and microstructure by diffraction, interpretation of the diffraction data was conducted by visual inspection only. Similar attempts have been made by Liu *et al* [107] and Weng *et al* [298].

Gu *et al* [299] is the only other group that have used XRD quantitatively to characterise the precipitates on plasma sintered HAP coatings, however the results obtained are questionable. The starting materials used in the aforementioned investigation were reported to be HAP with traces of β-tricalcium phosphate (β-TCP) without a trace of an amorphous phase. However the Bragg maxima corresponding to the as-received material, has peak ratios that do not correspond to HAP. It is appreciated that due to the difference in starting materials, the dissolution kinetics and thermodynamics would differ

when compared to this study. However, despite having SEM evidence to clearly suggest the presence of a nano-HAP phase, little evidence of its presence was observed on inspection of the Bragg maxima. In addition, close inspection of the calculated and experimental Bragg maxima revealed a very poor fit between calculated and observed data, particularly the (002) peak. Gu *et al* [299], have attributed this observation to preferred orientation. Further inspection reveals that a good fit is obtained in the (004) crystal plane, which is parallel to the (002) plane. It is therefore clear that the poor fit is not due to preferred orientation, but likely to be due to the presence of a nano-HAP phase. Quantitative estimations of the crystallographic parameters made by Gu *et al* [299] are likely to be erroneous, as the nano-HAP and HAP phases have been modelled as one phase. This is due to the 'depth effect' phenomena whereby more enhanced signals corresponding to the surface of the coating are obtained. However, careful separation of independent phases is necessary to obtain accurate crystallographic parameters.

Gu *et al* [299] have also made estimations of crystallite size using the Scherrer equation (chapter 4), because of the failure to separate the nano-HAP and HAP phase, the estimations quoted are likely to be incorrect.

In summary, the early stage of immersion in SBF was generally dominated by dissolution. This can be seen by the decrease in ACP content between day 1 and day 7 and the increase in calcium and phosphate ions in the SBF (figure 7.46). When the precipitation process caught up speed and eventually formed an apatite layer that

effectively sealed the underneath surface, the dissolution process declined [192, 203]. This effect can be seen clearly in figure 7.46 and the corresponding SEM images (figure 7.48-51). In addition, Figure 7.46, a plot of the variation in log (IP) of the SBF with soaking time confirms the change in mechanism. When dissolution was the dominant mechanism, log (IP) values were low and when precipitation was the dominant mechanism, log (IP) values were high. Gu *et al* [299] has reported similar trends in log (IP) values with immersion time.

Crack propagation, increased porosity and surface roughness on the surface of the ceramic materials were a result of the diffusion of ions from the coating surface and the surrounding media. It is believed that the surface roughness of the ceramic coatings due to dissolution of the amorphous component provided nucleation sites for apatite precipitation. Microcracks and pores may have provided a suitable microenvironment where for high supersaturation could be reach with ease.

The results of this investigation emphasis that the plasma sprayed coatings exhibit an ability to promote the formation of carbonated nano-HAP (bone-like apatite) layer. The formation of the carbonated layer appears to be accelerated by the presence of free calcium and phosphate ions in the media.

8.3.2 Electrodeposited coatings

The coatings thickness of the as-received ED samples probed in this investigation varied from 1-2μm (average ~1.7μm) and preferred orientation. Variable coating thickness and preferred orientation is an intrinsic property of ED coatings between batches despite

identical electrochemical parameters. It was anticipated that the variation in coating thickness and preferred orientation might cause a discrepancy in the behaviour of the coatings in each media. In order to access this, multiple samples were used for each of the media used in this investigation. The response of the ED coatings irrespective of sample thickness and preferred orientation was in agreement for each of the media used.

In comparison to the PS coatings, the ED coatings behaved in a dissimilar way. No extended tails were visible in the diffraction data. Indicating that there had the nano-HAP phase was absent. When a nano-HAP phase was included in the structural refinements of the ED to test this hypothesis, none was detected. The absence of the nano-HAP phase was perhaps a direct result of the low proportion of ACP in the as-received coatings.

Surprisingly, the diffraction analysis revealed that with immersion time in SBF and FCS, the proportion of ACP increased. This was not so apparent on visual inspection of the diffraction pattern corresponding to the FCS samples at day 21. This was due to the limited coating thickness.

After 21 days of immersion, the peaks of the SBF and FCS samples were broadened and more intense in comparison to the as-received samples. It can be concluded that low crystallinity (size/crystal perfection) near stoichiometric HAP had been precipitated due to the lattice parameters. SEM analysis revealed the existence of need-like crystals on the surface of the ED coatings in after immersion in SBF (figure 7.68).

The increase in intensity and broadening of the HAP peaks of the FCS samples at day 21 were not as pronounced as the SBF samples, therefore less HAP had been precipitated. This was expected as it has previously [266, 290] been shown that plasma proteins retard HAP dissolution and precipitation.

EDX analysis of the SBF and FCS samples indicated the presence of Mg^{2+}, CO_3^{2-} and Cl^- ions. These contaminant ions are derived from the immersion media (chapter 6). FTIR would have been able to establish the position of the CO_3^{2-} ions in the lattice. However, due to the limited coating available for analysis, this technique was not used. It is likely CO_3^{2-} ion substitutions for PO_4^{3-} (B-Type carbonation) had occurred due to the low temperature used in the investigative work. B-type carbonation has been reported [300] to occur at low temperatures (>100°C). Although carbonated apatite has the same thermodynamic driving force as stoichiometric HAP, it is kinetically more favourable due to the decrease in crystal order [301].

B-type carbonation and Cl^- ion inclusion each have the opposite effect on the lattice parameters [174, 259, 300] the net increase in the a-axis and decrease in the c-axis parameter may be due to the fact that Cl^- ion substitution was more abundant. Mg^{2+} ions (ionic radius ~0.66Å) [174], which normally substitute for Ca^{2+} ions, have a similar ionic radius as Ca^{2+} ions (~ 0.99Å) [174], therefore not net change in lattice parameters would occur due to Mg^{2+} ions inclusion into the lattice.

The increase in ACP observed in the SBF and FCS samples may be due to the inclusion Mg^{2+} ions into the lattice. Mg^{2+} ions in solution have been reported [55, 174] to cause considerable disturbance in the crystallisation of HAP promoting the formation of stable ACP (with more short range order). ACP formation was not observed in the PS samples after immersion in SBF or FCS. This is due to the fact that during immersion, the Mg/Ca ratio was lower in the solution for the PS samples due to the rapid dissolution of ACP and hence liberation of Ca^{2+} ions [174]. In contrast, the ED samples did not undergo such rapid dissolution due to the low ACP content in the as-received samples and hence the Mg/Ca ratio was high. High Mg /Ca ratios in aqueous CaP systems have been reported to promote ACP formation [174].

The peak broadening observed in the diffraction data of the may have been a result of increased aniostropic microstrain and crystallite size as a result of HAP crystal lattice inclusions. The insignificant changes in the c-axis and hence d-spacing (0.5c) showed that no significant isotropic strain had occurred in the lattice.

With increasing immersion time in SBF and FCS, the PO index decreased to (~1.1 and 1.3 respectively) significantly. This would suggest that the newly precipitated HAP were more randomly orientated than the initial HAP deposited in the fabrication process. This decrease in PO was observed in the PS samples.

An interesting point to note is that despite ACP formation in the ED coatings, the HAP that was precipitated was closer to stoichiometric HAP than the nano-HAP precipitated

on the PS coatings. This is due to the fact that in the ED coatings, precipitation was initiated by the slow dissolution of the thermodynamically more stable HAP as opposed to the dissolution of ACP in the PS coatings. The dissolution of HAP from the ED coatings creates a greater degree of supersaturation with respect to HAP than the dissolution of ACP. Therefore the thermodynamic driving force (Gibbs free energy) for the nucleation and growth of HAP in SBF and FCS is greater for ED coatings hence increasing the likelihood of precipitation of carbonated HAP as opposed to carbonated nano-HAP.

After the first day of immersion in SBF, the proportion of ACP decreased slightly. The existence of dissolution was confirmed by the through thickness cracks in the coatings (figures 7.66-7). In order to ascertain that the cracks were through thickness EDX analysis was used to probe the crack. Signals corresponding to the Ti substrate were detected. This dissolution of ACP may have been the initial driving for HAP precipitation. However, due to the limited proportion of ACP in the initial coating, it is estimated that dissolution of HAP was the principal driving force for HAP precipitation. Since dissolution-precipitation is a dynamic process and the net ACP proportion after each interval increased with immersion time, the coating component contributing to precipitation was not reflected in the results of quantitative phase analysis. Despite the lack of 'dynamic' information, the increase in coating thickness as evidenced by the increase in HAP peak intensity relative to the substrate peaks shows that HAP was precipitated.

Due to the solubility of ACP than HAP, it is anticipated that the dissolution and precipitation occurring in the PS coatings was more rapid than in the ED coatings. After 21 days of immersion in SBF, the PS coatings produced a precipitation layer of ~4μm whereas the ED coatings produced a precipitation layer of ~0.7μm. Therefore the PS coatings have are more active than the ED coatings i.e. they have a greater ability to produce carbonated HAP.

Despite having a low ACP content, it is probable that the HAP component of the ED coatings was more soluble than well-crystallised stoichiometric HAP as result of poor crystal quality (small crystallite size and increase microstrain). If the ED coatings had comprised of the highly crystalline HAP then little dissolution and hence bioactivity would have occurred. Highly crystalline HAP coatings have been reported to exhibit low crystallinity [14].

The water samples showed dissimilar behaviour. After immersion for 21 days, no peaks corresponding to HAP were visible. Quantitative phase analysis revealed that the coating consisted principally of ACP and non-stoichiometric HAP as evidenced by the lattice parameters. Worth mentioning, the lattice parameters of the HAP in the coating on day 21 were close to those of the nano-HAP observed in the PS coatings, however no nano-crystals were observed on the surface of the substrate. In contrast, the ED coatings compromised of thin and inhomogeneous wafer layers with areas of the anodic oxide layer substrate exposed. This shows that rapid dissolution of the ED coatings had occurred. Similar observations have been made by Sewing *et al.*, [265] in preliminary quality control assessments of the ED coatings used in this investigative work. Only

qualitative solubility studies have been carried out previously by Sewing *et al* [265] and no data regarding the changes in chemical and structural properties of the coating have been investigated.

The ACP and non-stoichiometric HAP were not visible in the diffraction data of the water samples on day 21. This is due to the fact that the coating was >0.5μm in thickness and the Ti peaks dominated the diffraction data. The higher proportion of ACP at the coating-substrate interface is as expected. This is by virtue of the fabrication process as explained in chapter 6 and section 8.2.2. In the initial stages of fabrication, spheres of ACP form on the substrate. Depending on the charge density and polarisation time, the ACP dissolves and re-precipitates as HAP and the coating builds up as result of HAP precipitation [122, 254]. As demonstrated in section 7.1.3, the ACP spheres in the coatings produced in this investigation did not completely dissolve. Therefore the coating-substrate interface is to be dominated by ACP.

The rapid dissolution of the ED coatings in water emphasises the poor crystal quality. Water is a corrosive environment for HAP due to the high undersaturation and hence greater thermodynamic driving force for dissolution. During immersion in water, dissolution was the dominating mechanism. Since the thickness of ED coatings was limited and the relative proportion of ACP was low in comparison to the PS coatings supersaturation with respect to HAP was very low even at day 21 in water (supersaturation was not reached). Therefore the Gibbs free energy for precipitation of

HAP was unattainable. This is would explain why no net HAP precipitation occurred [122, 254].

Chemical analysis of the media after each immersion time would give valuable information on the dissolution-precipitation mechanism. However, it was not possible to obtain accurate or precise results by AAS and ion chromatography for any of the media investigated. The calcium and phosphate in the water after each immersion time was below the detection limit as explained in section 7.2.2. The results corresponding to the SBF after each immersion time showed no net changes within the limits of experimental error as demonstrated previously by Sewing *et al* [265].

High crystallinity coatings, which have only a small amount of amorphous material holding the particles together, exhibit poor cohesion and adhesion to the substrate, and a high level of porosity [14]. Previous authors [14, 223, 302] have suggested that ACP content (~30-40%) is a perquisite for a coating, which is required to be bioactive, and osteoconductive. However, this study has provided evidence to show that this is not necessarily the case. It has been shown that ED coatings (~11% ACP) can induce the formation of a bone-like apatite layer (~4.7 x $10^{-3}m^{-1}$) despite the low ACP content compared to ~1.27 x $10^{-2}m^{-1}$ for the PS coatings. The formation of the bone-like apatite layer in the ED coatings is a result the dissolution of HAP of poor crystal quality. The lattice parameters of the newly formed apatite layer of the ED coatings (a=9.426Å;c=6.879Å) are closer to bone apatite (a=9.417Å;c=6.880Å) [174] than the nano-HAP layer precipitated on the PS coatings (a=9.501Å;c=6.866Å).

The formation of ACP in the ED coatings observed in SBF and FCS may be an attractive feature. This may be due to the fact that the dissolution of the ACP formed would increase the bioactivity of the coating. This was not observed in the ED coatings immersed for in SBF or FCS for 21 days, however ACP dissolution may occur outside the after immersion for more than 21 days.

Electrodeposited coatings are an attractive alternative to PS coatings. This is due to the fact that the manufacturing process (electrochemical parameters) can be easily adjusted to tailor the coatings produced in terms of stoichiometry, porosity and thickness. In addition, the process has a low energy cost and can be used to coat irregular shaped substrates. The low temperature of synthesis supports the inclusion of growth factors and antibiotics that may benefit the donor site.

From the investigations carried out in this thesis, it is estimated that ED coatings may have a similar or better performance than the PS coatings *in vitro* in terms of biocompatibility. This is due to the fact that the stoichiometry of the apatite layer is closer to bone-apatite than the PS coatings. Although, the rate of bioactivity (thickness of apatite layer formed per square metre of substrate) and hence osseoconductivity of the ED coatings is be lower than that of the PS coatings, it may be suitable for *in vitro* purposes. According to current knowledge [14, 303], an ideal ceramic coating for bone-induction purposes is one, which exhibits slow, uniform resorption, at a rate that allows the bone to replace the absorbed coating. Cell culture studies are needed to further

investigate bioactivity and biocompatibility. The electrochemical parameters can be adjusted to increase apatite layer precipitation should it be necessary.

Despite the superficial understanding of the exact mechanisms involved, *in vivo* coating resorption can be categorised as two simultaneous processes; namely dissolution-precipitation at neutral pH (between bone and the coating through ionic species, Ca^{2+}, OH^-, PO_4^{3-}, carried by body fluid) and osteoclastic bone modelling [90, 176, 296, 301]. This investigation has concentrated on ascertaining the response of the ED and PS coatings in the physiological environment. The results show that both types of would be bioactive under physiological conditions.

8.4 Apatite poders

The solubility and dissolution behaviour of apatite coatings has been measured in order to elucidate the microstructural and chemical factors dominating dissolution. Explicating the factors affecting dissolution is invaluable for the design of an optimum calcium phosphate coating. In addition, it gives further information regarding the dissolution mechanism occurring. The results are discussed in the context of conventional dissolution theories.

8.4.1 Characterisation

In order to assess the effect of crystallite size, microstrain and carbonate content on solubility and dissolution behaviour, it would have been more appropriate to engineer series of materials in which the only parameter that differed was the one being probed. However this is a very difficult goal to achieve, due to the fact that increased microstrain and reduced crystallite size are intrinsic properties carbonated apatites. In addition, smaller crystallite sizes are associated with large microstrain due to lack of crystal perfection.

The values of crystallite size and strain were the 'best estimates' obtained using the approximate method (chapter 4). The Warren-Averbach would have been more appropriate because it uses data from several orders of reflection. However due to peak overlap at higher values of 2θ, this was not possible. Hence size and strain approximations were made from the (002) HAP peak.

The HAP powders precipitated at different temperatures produced crystals with different sizes, and stoichiometry. The differences in stoichiometry were small and were a result of carbonate inclusion. Carbonate production presence in HAP is an intrinsic property of synthetic HAP precipitated at low temperatures [239]. However, the carbonate content was <0.5wt% and was considered negligible.

The difference in crystallite sizes of the HAP powders precipitated at different temperatures was a result of faster growth as a result of the increase Gibbs free energy of formation associated with the higher temperature systems [239].

Determination of B-type carbonate content was carried out by infrared spectroscopy and chemical analyses by Clarkson chromatography products Inc (S. Williamson, USA). Although the contribution of A- and B-type carbonation was separated A-type carbonation in was ignored as it was ~ <0.5wt% for each of the carbonated samples (CHA). B-type carbonation in the HAP samples was also ignored due to the fact that it was ≤0.5wt%.

For the series of increasing strain (strain1, strain2 and strain3), it was noted that although the a-axis showed a systematic decrease, the c-axis did not. This possibly due to contamination from debris during the ball milling process. The most probable contaminant is CO_3^{2-} and this is evidenced by the decrease in the a-axis parameter and increase in c-axis parameter in sample strain2.

The increase in microstrain observed with milling time was principally due to dislocations and perhaps CO_3^{2-} contamination. The nature of the dislocations was not probed further in this investigation.

The reduction in crystallite size in the (002) direction observed in the strain samples is due to the deformation/fracture of crystals as evidenced by SEM (figures 7.87-89). A reduction in crystallite size of ball-milled ceramics and metallic powders has been reported previously by Tromans *et al* [304], Dutta *et al* [241] and Vives *et al* [240].

W-H analysis revealed that with increased milling time, lattice microstrain and crystal size became more anisotropic in nature. This was due to the fact that during milling, anisotropic deformation (reduction in crystallite size and increase in microstrain) of the different crystallographic direction occurred. This has phenomenon has been previously reported by Dutta *et al* [241] in characterisation studies of ball-milled V_2O_5.

The HAP/ACP ratio of the milled samples decreased with milling time. This is due to fact that during the ball milling process the powders are plastically deformed under high energy and pressure between the balls and the walls of the mill. Ceramic powders processed by milling undergo several mechanochemical phase transformations hence producing metastable phases [241].

8.4.2 Statistical analysis

The series of apatites fabricated for this analysis were the best alternative possible and statistical analysis was necessary to separate the effects of each parameter probed. Pearson's correlation analysis (Microsoft Excel) and multiple regression analysis (Minitab) were used to assess the degree of correlation between the parameters being probed with solubility and dissolution behaviour. Pearson's correlation analysis was used to determine the extent of the linear relationship one of the variables being probed and an *in vitro* response (changes in solubility and microstructural properties). Multiple regression analysis was used to find linear relationships between all the parameters probed and an *in vitro* response.

8.4.3 Solubility measurements

Solubility measurements were made using conventional techniques [56], in water at 37°C in order to compare the results obtained in this investigation with published values in the literature.

The results from both Pearson's correlation and analysis and multiple regression showed that, microstrain is the dominant factor affecting the solubility behaviour of apatite powders over crystallite size and carbonated content. With increased microstrain, there is an increase in solubility (decrease in pK_{sp}). The increase in solubility with increased carbonate content is a result of microstrain, which is an inherent property of carbonated apatite as shown in section 7.2.3. This is in accordance with Baig *et al* [54] who have

previously shown that the differences in solubility between carbonated apatites were due to microstructure.

The measurements of microstrain and crystallite size were based on the intrinsic sample broadening from the <002> direction. This is a best estimate of the average microstrain and crystallite size for the all the crystallographic directions. Hence, the exclusion of the other crystallographic directions from the microstructural analyses is not anticipated to have a significant affect on the correlation of microstrain.

Baig *et al* [272] are the only other group that have investigated the relationship between crystallite size, microstrain and carbonate content and solubility in enamel and CHA. Their results have indicated that microstrain is the parameter that dominants the apparent solubility of enamel and synthetic CHA as opposed to crystallite size and carbonate content.

The results of this investigation are comparable to the results obtained by Baig *et al* [272]. However, the focus has been on synthetic apatites and has encompassed both carbonated and non-carbonated apatites. The rationale for this was to ascertain whether the differences in solubility of carbonated apatites were due to both microstrain and the chemical properties of natural apatite and CHA. In addition, the carbonated apatites probed by Baig *et al* [272] were synthesised by a wide range of methods possibly imparting difference HAP/ACP ratios. No information relating to the phases present in the CHA were reported and hence, it would appear that HAP/ACP ratios were ignored.

The presence of ACP, could considerably affect the apparent solubility of CHA powders investigated.

For the first time it has been possible to demonstrate a quantitative relationship between microstrain and the apparent solubility of synthetic CHA and HAP powders.

8.4.4 Dissolution behaviour

Dissolution studies have been carried out on HAP and CHA powders with varying crystallite sizes, carbonate content and lattice microstrain in SBF and water respectively. Comparisons have been made between the resultant powders of each series, however the as-received powders had different starting materials. As explained in section 8.3.2, it is difficult to engineer HAP materials and change only one variable. However, with the use of statistical analysis, comparisons have been possible.

According to the results obtained, dissolution of the HAP and CHA powders in SBF and water was dominated by crystallite size. Hence, the powders with the largest crystallite sizes underwent the greatest degree of dissolution as evidenced by the difference in crystallite size before and after investigation. The degree of dissolution was greatest in water, which indicates that the dissolution of the powders was correlated to undersaturation. This was as expected as it is in agreement with traditional dissolution theories [305, 306].

Powders with crystallites below ~400Å did not undergo any significant degree of dissolution in SBF. This would suggest that the crystallites were in 'equilibrium' with the media. This evidenced by the fact that the powders with crystallite size > 400Å had a crystallite size ~ 400Å after dissolution. This would suggest that the critical crystallite size at which crystallites are in equilibrium with SBF was ~ 400Å. This was higher than the critical crystallite size in water (~200Å).

The observed dissolution behaviour cannot be attributed to biological factors due to the fact that no proteins or other biological species were present within the media. In addition, multiple experimental runs were conducted and identical dissolution inhibition/suppression was observed in these cases, hence the results were reproducible. The preparation of the media was conducted under aseptic conditions to prevent the growth of microbes or other organisms in the media that could affect the pH of the media and hence dissolution behaviour.

Tang *et al* [268, 286] has recently proposed a dissolution model for apatite powders that explains the unconventional dissolution behaviour exhibited by the apatite powders in this investigation. Tang *et al* [224, 268, 286] has confirmed by experiment using atomic force microscopy that dissolution occurs through a mechanism that is analogous with crystallisation but with the participation of critical conditions involving dissolution etch pits as opposed to nuclei. For crystallisation to occur, nuclei (clusters of crystals) or dislocation sources on the crystal surface or driving force (supersaturation) must reach a critical value [224, 285, 305]. Correspondingly, dissolution is a result of surface etch pit

formation followed by the spreading of dissolution steps in the etch pits. Dissolution can only occur once etch pits become active and only etch pits larger than the critical pit size are active. The steps within the etch pits formed act as dislocation lines, their movement contributing to dissolution. The density of etch pits on the surface and spreading velocities determines the rate of dissolution. This poly-pitting dissolution mechanism with a kinetic rate dominated by the formation of two-dimensional pits has been confirmed experimentally by Tang *et al* [224, 268, 286], although further investigations are in progress [307].

Tang *et al* [224, 268, 286] has observed that for sparingly soluble solids like HAP when the sizes of dissolving crystals approach the critical etch pit size; dissolution may be suppressed or completely inhibited. Real time *in situ* studies [224, 268, 286] have revealed that when the crystallite size approaches the critical etch pit size, fewer etch pits contribute to dissolution. Only when the crystallite size is greater ~50 times the critical etch pit size does normal dissolution behaviour occur [268].

The critical size of a two-dimensional etch pit can be described by equations 8.5 and 8.6 [286, 305] where γ_{SL} is the interfacial tension; k is the Boltzmann constant; T is the absolute temperature; Ω is the area occupied by each dissolution unit; Δg the Gibbs free energy for dissolution; and S is the supersaturation ratio.

$$r^* = \frac{\gamma_{SL}\, 2\Omega}{|\Delta g|} \tag{8.5}$$

$$\Delta g = kT \ln S \tag{8.6}$$

The dissolution model proposed by Tang *et al* [224, 268, 286] and equations 8.5 and 8.6 are in good agreement with the results obtained in this investigation. As the crystallite sizes decreased, the dissolution decreased as observed by a decrease in changes in crystallite size, lattice parameters and microstrain. The dissolution observed in water was greater than in SBF. This is in agreement with equations 8.5 and 8.6 where it is shown that as undersaturation decreases, the Gibbs free energy required for dissolution increases and hence the critical crystal size and etch pit size increase.

The results obtained have shown that although undersaturation (water) induces dissolution, decreasing the crystallite size increased dissolution suppression. However, dissolution inhibition did not occur even with the smallest crystallite size (273Å).

It has been shown that the critical crystallite size is a function of undersaturation (equations 8.5 and 8.6) and the resultant crystallite sizes after dissolution are close to the critical crystallite size for each media. There the resultant crystallite size is related only to undersaturation. This is in good agreement with previous work [224, 268, 286]. Values of crystallite size have not been compared with previous work [224, 268, 286] due to the differences in method of measurement. However, Tang *et al* [286] suggested that the dissolution inhibition (metastable equilibrium) phenomenon is apparent in apatite crystallites between 10-10^3nm, which is in good agreement with the results presented here.

In addition, for the first time it has been shown that for apatite crystallites with sizes of 200Å-1000Å, crystallite size is the dominating factor controlling dissolution in SBF. Statistical analysis has shown that microstrain and carbonate have no effect on the dissolution of the powders in SBF within this size region.

The dissolution of the apatites immersed in water was dominated by crystallite size, but to a lesser extent than the SBF samples. This is in accord with work by Tang *et al* [224, 268, 286]. Also, it has been shown that microstrain contributed to dissolution at high undersaturation. This is in accord with Baig *et al* [272] and the results from the solubility investigation discussed in section 8.3.3. Carbonate content had no effect on the dissolution behaviour of the apatite powders investigated.

For crystallites sizes further away from the metastable equilibrium, it is probable that both dissolution and precipitation occurred concurrently in SBF and water respectively by day 21. This evidenced by the decrease in crystallite size and microstrain (dissolution) and the changes in lattice parameters and SEM micrographs (precipitation).

For crystallites close to the critical crystallite size the metastable equilibrium phenomenon, it is likely that by day 21, precipitation was the only mechanism occurring. This was not reflected in the crystal sizes of the residues at day 21 perhaps because nucleation and crystal growth was slow. Although within experimental error, no net

changes in lattice parameters were observed, FTIR analysis did reveal a small increase in carbonate content, indicative of bone-like apatite formation.

FTIR analysis revealed that carbonated apatite (B-type) had been precipitated after 21 days of immersion in SBF and water respectively. The level of B-type carbonation was more pronounced in the SBF samples due to the greater concentration of CO_3^{2-} in the media. The CHA samples produced a non-carbonated apatite. The low efficiency of CHA producing bone-like apatite has been reported in a recent dissolution study [258].

This is the first time that such dissolution studies have been attempted. Previous studies that have investigated the roles of crystallite size, microstrain and carbonate content on the dissolution properties of apatites [54, 272] have used solubility data alone.

It was observed that the dissolution behaviour of the HAP and CHA powders was different to the solubility behaviour of the powders. It would appear that the metastable equilibrium phenomenon observed in the dissolution experiments does not occur spontaneously when apatite crystals are put into solution. In the initial stages of immersion, the thermodynamic factors dominated. During the solubility experiments the apatite powders were not thermodynamically stable (i.e. undersaturation is the driving force for dissolution) and hence 'normal' dissolution behaviour occurred. With immersion time (> 24 hours), the powders with smaller crystallite size became dynamically stable (no dissolution) due to fewer active etch pits and hence metastable equilibrium occurred.

This may be due to 'normal' dissolution behaviour occurring as a result of the initial structural defects on the surface of the crystallites (causing lattice microstrain) that provide natural dissolution sites [268, 307]. Tang *et al* [268] have reported that reported that only the newly created etch pits rather than the existing dissolution sites provide permanent dissolution sites. Therefore it is likely that after a period of immersion (>24 hours), the rate of formation and growth of new etch pits in the larger crystals overtook the growth of the existing dissolution steps in the apatite crystals. In the smaller crystals, the newly formed etch pits are close to the critical etch pit size. This is due to the fact that the formation of etch pits on smaller surfaces is difficult. In addition the growth and spreading of etch pits is strongly inhibited by limited crystallite size. Therefore dissolution is suppressed or completely inhibited due to the lower number of active etch pit (etch pits greater than the critical size) in the smaller crystals than the larger ones. Therefore the dominance of microstrain on dissolution is overridden by crystallite size once the growth of the initial dissolution sites diminishes.

The decrease in lattice microstrain with immersion time was proportional to the initial microstrain. This shows firstly that microstrain was perhaps was concentrated at the surface of the apatite crystals and that the more strained component of the crystals dissolved preferentially. This is further evidence to show that the initial stages of dissolution of the apatite powders in SBF and water was dominated by microstrain.

It may be the case that for this system, the higher solubility of the smaller HAP crystals may be due to the intrinsic microstrain only that is associated with smaller crystals and

not crystal size. Investigations by Tromans *et al* [304] have revealed that the enhanced dissolution of defective crystallites arising from surface microtopography effects (etch pits) are more pronounced when crystals are in the sub-micron region. This is contrary to the Ostwald-Freundlich model, which assumes that smaller crystals are more soluble than larger crystal. No linear relationship has been demonstrated in this investigation between crystallite size and microstrain.

Tang *et al* [268] have indicated when crystals are in the metastable equilibrium state; dissolution can resume at any time due to the fact that the crystallites are thermodynamically unstable. This may suggests that the metastable equilibrium state is temporary.

It is the opinion of the author that the values of solubility obtained in this investigation are accurate and precise as evidenced by the good agreement with values published in the literature and the trends correspond to those obtained by Baig *et al* [272]. Although no other group has conducted solubility and *in vitro* tests of this nature, solubility data exists for some B-type carbonated apatites [56, 272] and HAP.

8.4.5 *In vivo* considerations

The implication of the results of the solubility and dissolution investigations of apatite coatings and powders is that for large crystallites greater than 1000Å lattice microstrain dominates the solubility and dissolution behaviour of both HAP and CHA. When crystallite sizes are in the region of 200Å-1000Å metastable equilibrium may be

observed. Therefore, for bioactive osseoconductive coatings, crystallite sizes <1000Å should be avoided as the dissolution behaviour is metastable and hence unpredictable.

HAP coatings can be tailored for increased/decreased solubility most efficiently by varying the lattice microstrain. This can be done through carbonate substitution or by the temperature of synthesis of the HAP coating. Although the carbonate substitution has no chemical contribution to the solubility of HAP [54, 272], the efficiency of bone-like apatite formation from CHA is low and hence synthetic CHA is not a suitable material to enhance bioactivity and osseoconductivity *in vivo*.

The crystallite sizes of the apatites powders investigated are of the same order of bone mineral and dental enamel [174]. Therefore in biological systems metastable equilibrium is of advantage as a defence mechanism against acidic attack and fluctuating physiological fluids. Biominerals become insensitive to dissolution even in undersaturated environments. This is strongly supported by dissolution studies conducted by Tang *et al* [286].

8.5 PET tape

8.5.1 Coating and characterisation

HAP has successfully been coated on to PET woven tape for potential use in anterior cruciate ligament reconstructions. The use of Triton 60 surfactant improved the amount and coverage of HAP on the PET tape. PET is a hydrophobic polyester with a low surface wettability. Surface wettability is directly related to surface energy, an

energetically more stable surface results in a less wettable surface [308]. Surfactants such as Triton 60 act on PET tape by reducing the surface tension of the woven fibres, increasing the surface wettability.

The improvement in surface wettability of the treated tape (with surfactant) was evident on comparison with the untreated tape. Triton 60 is a water-soluble surface-active agent comprised of a hydrophobic portion (long alkyl chain) attached to hydrophilic functional groups. On contact with the tape in solution, the hydrophobic portion of the molecule attaches itself to each fibre leaving the hydrophilic functional group at the surface of the fibre hence improving the surface wettability [308].

The ultrasonic cleaning process in methanol and diethyl ether that was conducted on all of the samples coated in this work may have also improved the surface wettability of the as-received PET tape. This is evidenced by the fact that the tapes, which were not treated by the surfactant (OT-N), had a thin but reasonable coverage of HAP. This was because the cleaning process removed surface debris and any waxy residues that may have been deposited during the fabrication process of the PET tape.

The adhesion to the treated PET tape is likely to be through mechanical interlocking as a result of the improved surface wettability and the microfibre structure. The microfibre structure provided a scaffold or matrix for HAP precipitation, which is analogous to the mineralization of collagen by bone apatite *in vivo*. Due to the fact that PET have an ester

group, it is probable that a fairly strong bond between the polar ester group and the hydroxyl group or calcium ion of the apatite [110].

The coating process did not affect the mechanical properties of the coated PET tape with or without the use of a surfactant. In addition the stoichiometry of the HAP produced was not affected by the presence of the surfactant in the fabrication process. This would suggest that the surfactant did not degrade to produce undesirable contaminants and is relatively inert with respect to the chemical solution from which HAP precipitated.

Quantitative phase analysis revealed that the HAP produced was relatively phase pure with ~9% ACP. EDX analysis showed that the HAP precipitated was carbonated in nature. The carbonate may have been derived from dissolved carbon dioxide from the air. No other contaminant ions were detected.

Microstructural analysis of the coatings was not possible due to the fact that the coating was scrapped from the PET substrate and the coating texture and crystal quality altered. *In situ* XRD analysis of the coating was not conducted as it as the scattering from the PET would have dominated the diffraction data. In addition, a poor signal-noise ratio was anticipated.

8.5.2 Cell culture study

Events occurring at the interface between a graft material and the surrounding osseous tissue in bone tunnels are the direct result of cellular, physiological and mechanical

reactions evoked by the presence of biomaterials [309, 310]. Since *in vivo* investigations do not afford the investigation of specific cell behaviour, osteoblast cell behaviour when in contact with HAP surfaces can be assessed and quantified by cell culture techniques.

A decrease in cell population after exposure to test materials can be used as a marker of toxicity. A decrease in growth rate could be due to an increase in death rate or mitotic rate [311]. Osteoblast cells undergo a temporal sequence of gene expression during the development of a fully differentiated osteoblastic phenotype. The sequence includes: proliferation, differentiation and mineralization periods [312]. The proliferative phase is characterised by an increase in cell number and by the synthesis of extracellular matrix. This followed by the expression of high levels of ALP. Hence, the level of ALP activity in osteoblast cells reflects the level of cellular differentiation from non-calcium mineral-depositing cells to calcium mineral-depositing cells. Amendments to the extracellular matrix promote the deposition of apatite crystals. The mineralization phase is characterised by the synthesis of osteocalcin, a bone-specific protein that binds to HAP and represents the peculiar marker of final osteoblast differentiation and plays a fundamental role in bone remodelling [313].

The objective of this study was to investigate the osteoblastic behaviour to PET orthopaedic tape coated with HAP. In addition because a surfactant had been used during the coating process, it was imperative to ascertain if this would promote any adverse effects. Hence, osteoblast behaviour on these surfaces was compared with osteoblast behaviour when cultured on HAP coated PET surfaces without the use of a surfactant,

uncoated PET surfaces; and plastic culture wells as a control. Before cell culture, all PET surfaces were irradiated to create a sterile environment for the growth of osteoblast cells. According to Lovell [314], the irradiation process used has no adverse affect on the PET tape.

A number of different parameters have been chosen to monitor the behaviour of osteoblast cells in the early stages of colonisation. To evaluate whether each surface could support the attachment and proliferation of osteoblast cells, the number and morphology of attached cells was determined at different periods of cell culture. The level of ALP was assumed as a reliable marker of cellular differentiation since it is a product of osteoblast cells. Osteocalcin production was monitored to assess mineralization occurring within the osteoblast cells.

Cells from a single culture were used in determination of cell differentiation and mineralization in order to eliminate cell origin and maturation effects. Cell counts were made of viable cells only and viability was ascertained using haematoxylin dye.

Cell attachment after 4 and 18 hours of incubation was greatest on the plastic culture wells. This was as expected due to the fact that the culture wells are engineered to have the optimum surface topography to enhance cell attachment and growth in the short term [315-317]. On comparing cell attachment to the PET tapes, the tape coated with HAP using a surfactant (OT-T) had the greatest cell attachment after 4 and 18 hours of incubation.

Cell proliferation was similar on the plastic culture wells and OT-T samples in the early stages of incubation (day 1-11). However, by day 16, proliferation was greater on the plastic culture wells. This would suggest that the HAP coatings enhance cell growth in the short-term. This is in accord with previously published data [316, 317].

Osteocalcin production and ALP activity per cell on day 14 was significantly greater on the OT-T samples than on the plastic culture wells, indicating that differentiation and mineralization was greater for cells cultured on OT-T samples. Although more cells proliferated on contact with the plastic culture wells, the level of cell differentiation and mineralization was low. This emphasises that although cell attachment and proliferation was reduced on contact with HAP, differentiation and mineralization were promoted. The data indicate that mineralization was predominantly a physiochemical process as opposed to a cell-mediated process since osteocalcin production was significantly greater ($P<0.05$) on contact with the OT-T samples than the plastic culture wells. This is contrary to data published by Hott [316].

Osteocalcin production and ALP activity per cell was not significantly different on cell contact with the PET tape coated with a surfactant (OT-N) and the uncoated PET tape (OT-C) despite the greater cell attachment and proliferation observed on the OT-N samples. This would suggest that differentiation and hence mineralization is inhibited by the OT-C samples perhaps due to partial delamination of the coating [318]. This may explain why there was significantly less cell attachment and proliferation of cells on

contact with OT-C samples compared to OT-T samples. This has demonstrated the strength of the use of a surfactant for deposition of HAP on PET tape.

ALP activity was very sensitive and displayed a high standard error. Results by other authors using human osteoblast cells showed similar variability [317]. This is due to the fact that ALP activity is measurement of enzyme kinetics of transformation of p-nitrophenylphosphate into p-nitrphenol, which varied greatly between measurements, as it is a dynamic process.

Calcium concentration was not affected by the presence of osteoblast cells.

Measurements of calcium concentration that the OT-T and OT-N samples with and without cells underwent a degree of dissolution until day 14. On day 14 the calcium concentration in the media decreased indicating that calcium uptake had occurred. The calcium uptake in for the OT-T samples was significantly greater than for the OT-N samples. The calcium concentration of the cell culture media of the OT-T samples with and without cells was less than that of the as-received cell culture media. This was also the case for the media of the cells cultured in the plastic culture wells. Therefore calcium uptake was due to both cellular uptake of calcium and to calcium precipitation. By day 14 the calcium concentration in the media of the OT-N samples was higher than that of the OT-T samples perhaps indicating that cell uptake of calcium was less for cells cultured on OT-N samples. It is more likely that more coating dissolution had occurred in the OT-N samples than from the OT-T samples.

The data showed that PET tapes coated with HAP with a surfactant (OT-T) to improve surface wettability and are capable of promoting attachment, proliferation, differentiation and mineralization. Light micrographs show that osteoblast cells grown on PET tape with or without HAP have normal osteoblast morphology. Overall the PET tapes coated with HAP without using a surfactant (OT-N) showed no advantages over the uncoated PET tapes (OT-C). This may have been due to the poor coverage and adhesion of the HAP coating to the substrate. In addition, it has been shown that enhanced attachment and proliferation of osteoblasts on plastic culture wells (induced by surface engineering), no advantages in terms of differentiation and mineralization.

Various groups [110, 112, 319] have deposited apatites on polymers for potential use in orthopaedic surgery. Tanahashi *et al* [110] have coated organic polymers with apatite coatings using a biomimetic process for potential use as ligaments. Despite the fact that an adherent layer of bone-like apatite was formed, the deposition process was multi-phase and apatite growth was slow. However, no cell biocompatibility studies have been reported.

Yamamoto *et al* [319] has precipitated HAP onto PET films that have been polymerised by anionic monomers to further understand the ultrastructure of the material/bone interfaces *in vivo*. Osteoblast cell adhesion and differentiation was enhanced in comparison to untreated films, which is in good agreement with the results presented here.

Kokubo *et al* [112] has deposited bone-like apatites onto organic polymers using a biomimetic process. Despite the formation of a dense uniform coating, the induction period for apatite nucleation was long and the coating process took 24 hours. This lengthy fabrication process would not be viable commercially.

8.5.3 Tissue engineering approach

A good tissue engineering approach for ligament constructs is provided by blending HAP with a polymer to form a composite material that combines the mechanical strength and osseoconductivity of HAP with the high affinity to cells of polymers. This system is analogous to the collagen and bone apatite *in vivo* systems. The presence of HAP crystals within the polymeric matrix (PET tape) are likely to participate in the biological remodelling process *in vivo* as demonstrated in the cell culture study. The gradual dissolution of HAP provides a source of calcium for consumption by a nearby cell population as demonstrated in this cell culture study. In vivo, the dissolution of HAP and liberation of calcium and phosphate ions could lead to the re-precipitation of bone-like apatite thus enhancing bone osseoconductivity and osseointegration.

The advantage of the novel coating technology described here, is that it is a rapid and reproducible low temperature method of depositing bone-like apatite on polymeric tape. Due to the low temperature of synthesis, growth factors and antibiotics can be incorporated into HAP with ease. In addition, the stoichiometry and microstructural properties of the HAP produced can be easily tailored by changing parameters such as

temperature, relative proportion of reactants and pH. Coating thickness can be controlled by reaction time.

9.0 Conclusion

This section draws conclusions on the findings of this research work.

9.1 Non-destructive phase quantification

A novel methodology for the quantitative phase analysis of multiphase apatite coatings has been devised. The methodology allows for the incorporation of crystalline and amorphous phases into refinements and hence gives quantitative estimates of each.

Validation of the technique was conducted with reference to known mixtures and it has been shown that the methodology is accurate within ~4%. The methodology has proved to robust for the analysis of apatite coatings even in the presence of preferred orientation.

9.2 Characterisation of apatite coatings

A novel methodology for the electrodeposition of HAP coatings for use on hip arthroplasty has been introduced. Comparative investigations have revealed that ED and PS technologies produce HAP coatings with dissimilar chemical and microstructural properties.

Typical PS coatings were ~60μm in thickness and contained ~28wt% ACP at the surface and ~61wt% ACP at the coating-substrate interface compared to ~1.7μm thickness and 11wt% ACP for a typical ED coating. The ED coatings did not contain any metastable crystalline phases, however the PS contained ~2wt% of CaO, β-TCP and α-TCP near to the coating-substrate interface. The ED coatings had significantly more preferred orientation (~2.23) than the PS coatings (~0.72) by virtue of the manufacturing

technology (discussed in chapter 8). The coatings produced by ED possessed smaller crystallite sizes and a greater degree of microstrain than the PS coatings.

9.3 *In vitro* behaviour of apatites

9.3.1 Apatite coatings

The diffraction approach outlined in this research has aided in furthering the understanding of the relationship between coating technology and dissolution-precipitation behaviour of HAP. PS coatings are bioactive in nature, capable of producing an apatite layer at both high and low supersaturation. ED coatings are bioactive at high undersaturation but at low supersaturation they undergo rapid corrosion as a result of poor crystal quality (small crystallites and microstrain).

PS coatings are more bioactive in nature than ED coatings at high supersaturation perhaps by virtue of the greater composition of ACP in the PS coatings. The bioactivity of ED coatings is a result of poor crystal quality whilst ACP content has a dominant effect on the bioactivity of PS coatings.

The nature of the bioactive layers produced on the PS and ED coatings were dissimilar in nature. After 21 days of immersion in SBF, the PS coatings produced nano-HAP (a=9.501Å;c=6.866Å). The ED coatings produced a carbonated apatite substituted with Mg^{2+} and Cl^{-} ions (a=9.426Å;c=6.879Å), which is crystallographically more similar to bone mineral (a=9.417Å;c=6.880Å) than nano-HAP. Despite a difference in the *in vitro* behaviour, PS and ED coatings may be equally of benefit *in vivo*.

9.3.2 Apatite powders

A quantitative relationship has been established between the solubility of apatite powders and crystallite size and lattice microstrain. Microstrain has the most dominant effect on the solubility of apatites and not carbonated as previously believed, although crystallite size has a modest effect.

For the system used in this research, crystallite size dominated the dissolution behaviour of apatites over carbonate content and lattice microstrain. Dissolution suppression occurred in apatite powders with crystallite sizes ≤1000Å when immersed in SBF for 21 days. In addition dissolution of apatite powders with crystallite sizes ≤ 400Å was inhibited.

At low supersaturation (water), size-dependant dissolution occurred, but to a lesser extent than at high supersaturation (SBF). For apatite powders with crystallite sizes <1000Å, microstrain had a modest contribution to the dissolution of the apatite powders at low supersaturation.

9.4 HAP coated PET tape

A novel methodology for the deposition of HAP coatings on PET tape (for use in orthopaedic surgery) has been introduced. Mechanical tests revealed that the coating process did not significantly affect the mechanical properties of the tape. In addition, it has been shown that a uniform adherent HAP coating can be produced on the PET tape.

Short-term cell culture studies have shown that the HAP coatings produced on the PET tape support the normal growth and differentiation of osteoblast cells. In addition, it has been demonstrated that coated PET tape promote enhanced differentiation of osteoblast cells and mineralization compared to uncoated PET tape.

10.0 Future work

This research work has highlighted a number of observations concerning the use of HAP coatings for bone regeneration purposes. Recommendations for future work are made in this section.

10.1 Atomic refinements

All structural refinements of apatites conducted in this research assumed that atomic positions remained constant as discussed in chapters 7 and 8. To further understand the chemical changes occurring in apatite coatings and powders *in vitro,* refinement of atomic parameters is necessary (Rietveld refinement). Changes in atomic positions, bond lengths and occupancies within the apatite lattice can be obtained and such information can allow for a deeper understanding of the dissolution and precipitation mechanisms.

10.2 Chemical analysis of ED coatings

Chemical analyses are essential to further investigate the chemical nature of electrodeposited (ED) and plasma sprayed (PS) coatings produced in this work (chapter 6). As discussed in chapter 7, FTIR analysis of ED coatings was not possible due to the limited thickness of the coatings. Raman spectroscopy is recommended in this case for analysis, as it requires only a small quantity of sample for analysis.

10.3 *In vitro* behaviour of apatite coatings and powders

In the dissolution studies carried out in this research, monitoring the changes in ionic concentration of the media of ED coatings and apatite powders was difficult. This is due

to the fact that the calcium and phosphate levels in the media were below the detection limit of the instrument used.

Changes of the ionic concentration of the dissolution media are essential to understand the mechanism by which dissolution and precipitation occur. Therefore it is recommended that an instrument with higher sensitivity is identified and dissolution studies repeated.

10.4 TEM studies of HAP crystallites

X-ray diffraction (XRD) has been used in this research in order to determine the size of coherent scattering domains of apatites. Absolute values of crystallite sizes and morphology are difficult to determine by XRD (chapter 8). Therefore, TEM studies are recommended to assess the changes in crystallite sizes of apatite powders before and after dissolution. TEM analysis will enable a deeper understanding of any changes in shape or size of HAP crystals as a result of dissolution or precipitation.

10.5 AFM analysis of etch pit formation

In situ dissolution studies of apatite powders using AFM analysis would enable a better understanding of etch pit formation and it's affect on dissolution of nanosized apatite powders. This technique would also facilitate real-time measurement of etch pit growth (polypitting) processes of apatite crystals in solution.

10.6 Cell culture studies on ED and PS coatings

ED HAP coatings for orthopaedic usage are in their infancy. Whilst, the *in vitro* behaviour of PS coatings is well documented, there are no reports in the literature of studies assessing the biocompatibility and osseoconductivity of ED coatings. Therefore cell culture studies are recommended to investigate the ability of ED coatings to support the growth of osteoblast cells and aid in the prediction of the likely *in vivo* performance. A direct comparison between ED and PS coatings would then be possible.

Long-term cell culture (>14 days) would give an insight into whether PS and ED coatings are more effective in long term or short term culture. This could have implications on the future design of HAP coatings. In addition more detailed analysis of HAP coatings after cell culture would give an insight to the changes occurring in the coatings and the nature of the calcium minerals being deposited.

References

1. Hench, L.L., *Biomaterials: a forecast for the future.* Biomaterials, 1998. **19**: p. 1419-1423.
2. Bellamy, P. *Hip implant.* 2002 [cited 07/01/05]; Available from: www.hipimplants.com.
3. NICE, *Guidance on the use of metal hip resurfacing athroplasty*. 2002, National Institute for Clinical Excellence: London.
4. McMinn, D. and Treacy, R. *Total hip replacement*. 2004 [cited 09/07/04]; available from: www.midmedtec.co.uk/hip_arthroplasty.htm.
5. Munting, E.D., *Prosthetic Design and surface characteristics: the keys to implant fixation.* Hydroxylapatite coatings in orthopaedic surgery, ed. Geesink, R.G.T., Manley, M.T.,. 1993, New York: Raven press Ltd.
6. Altman, G.H., Horan, R.L., Lu, H.H., Martin, I., Richmond, J.C., and Kaplan, D.L., *Silk matrix for tissue engineered anterior cruciate ligaments.* Biomaterials, 2002. **23**: p. 4131-4141.
7. Matsumoto, H. and Fujikawa, K., *Leeds-Keio artificial ligament: a new concept for the anterior cruciate ligament reconstruction of the knee.* Keio Journal of Medicine, 2001. **50**(3): p. 161-166.
8. McGuire, D.A. and Paterson, R., *Methods for precisely forming bone tunnels in cruciate ligament reconstruction of the knee*, in *US Patent and Trademark Office*. 2005: USA.
9. Brand, J., Weiler, A., Caborn, D.N.M., Brown, C.H., and Johnson, D.L., *Graft fixation in cruciate ligament reconstruction.* The American Journal of Sports Medicine, 2000. **28**(5): p. 761-774.
10. Vacanti, C.A., Cao, Y.L., Langer, R.S., Vacanti, J.P., Paige, K., and Upton, J., *Tissue engineered tendons and ligaments*, in *US Patent and Trade Mark Office*. 2005, Massachusetts Institute of technology: USA.
11. Avery, L. *Anterior Cruciate Ligament (ACL) Graft Options*. 2004 [06/09/04]; available from: http://www.orthoassociates.com/ACL_grafts.
12. Bonfiglio, M. and Jeter, W.S., *Immunological responses to bone.* Clinical Orthopaedics, 1972. **87**: p. 19-27.
13. Montanaro, L., Aricola, C.R., Campoccia, D., and Cervellatia, M., Biomaterials, 2002. **23**: p. 3651-3659.
14. Sun, L.B., C.C; Gross, K.A; Kucuk A., *Material Fundamentals and Clinical Performance of Plasma sprayed Hydroxyapatite Coatings: A Review*. 2001, Centre for Thermal Spray Research, University of New York at Stony Brook: New York. p. 570-592.
15. Gross, K.A. and Berndt, C.C., *Materials applications: Biomedical applications of apatites*, in *Phosphates: Geochemical, geobiological, and materials importance*, Kohn, M.J., Rakovan, J., and Hughes, J.M., Editors. 2002, Mineralogical society of America: Washington DC, USA631-672.
16. Lloyd, A., *Interfacial Bioengineering to enhance surface biocompatibility.* Medical device technology, 2002: p. 18-21.

17. Lee, I., Kim, H., and Kim, S., *Studies on calcium phosphates.* Surface and Coatings Technology, 2000. **131**: p. 181-186.
18. Graham, S.M. and Parker, R., *Clinical Orthopaedics and Related Research.* 2002. **402**: p. 64-75.
19. Gu, Y.W., Loh, N.H., Khor, K.A., Tor, S.B., Cheang, P., *Spark plasma sintering of hydroxyapatite powders.* Biomaterials, 2002. **23**: p. 37-43.
20. Chang, C., Huanq, J., Xia, J., and Ding, C., *Study on crystallization kinetics of plasma sprayed hydroxyapatite coating.* Ceramics International, 1999. **25**: p. 479-483.
21. Yang, Y.C., Wang, B.C., Chang, E., Wu., J.D, *The influences of plasma spraying parameters on the characteristics of hydroxyapatite coatings: a quantitative study.* Journal of Materials Science, 1995. **6**: p. 249-257.
22. Kuo, M.C., Yen, S.K.,, *The process of electrochemical deposited hydroxyapatite coatings on biomedical titanium at room temperature.* Materials Science & Engineering, 2002. **C20**: p. 153-160.
23. Guo, L., Huang, M., and Zhang, X., *Effects of sintering temperature on structure of hydroxyapatite studied with Rietveld method.* Journal of materials science: Materials in medicine, 2003. **14**: p. 817-822.
24. Narasaraju, *Review. Some physico-chemical aspects of hydroxylapatite.* Journal of Materials Science, 1996. **31**: p. 1-21.
25. Carola, R., Harley, J.P., and Noback, C., *Human anatomy & physiology*. 2nd Edition. ed. 1992: McGraw-Hill, Inc, USA.
26. Lawson, A.C. and Czernuszka, J.T., *Collagen-Calcium phosphate composites.* Proceeds of the Institution of Mechanical Engineers., 1998. **212**(H): p. 413-425.
27. Sambrook, P., *Bone structure and function in normal and disease states.*, in *The musculoskeletal system*. 2001, Elsevier.p.68-84.
28. Currey, J.D., *Bones*. 2002, Princeton, New Jersey: Princeton University Press.
29. de Groot, K., Klein, C.P.A.T., Wolke, J.G.C., and de Blieck-Hogervorst, J.M.A., *Chemistry of calcium phosphate bioceramics*, in *CRC handbook of bioactive ceramics*, Yamumuro, T., Hench, L.L., and Wilson, J., Editors. 1990, CRC Press: Boca Raton, FL,3-15.
30. Meneghini, C., Dalconi, M.C., Nuzzo, S., Mobilio, S., and Wenk, R., *Rietveld refinemet on X-ray diffraction patterns of bioapattie in human fetal bones.* Journal of Biophysics, 2003. **84**: p. 2021-2029.
31. Ivanova, T.I., Frank-Kamenetskaya, O.V., Kol'tsov, A.B., and Ugoolkov, V.L., *Crystal structure of calcium deficient carbonated hydroxyapatite. Thermal decomposition.* Journal of Solid State Chemistry, 2001. **160**: p. 340-349.
32. Elliot, J.C., *Monoclinic space group of hydroxyapatite.* Nature, 1971. **230**: p. 72.
33. Elliot, J.C., Mackie, P.E., and Young, R.A., *Monoclinic hydroxyapatite.* Science, 1973. **180**: p. 1055.
34. Calderin, L. and Stott, M.J., *Electronic and crystallographic structures of apatites.* Physics review, 2003. **B67**(134106): p. 1-7.
35. Tadic, D., Peters, F., and Epple, M., *Continuous synthesis of amorphous carbonated apatites.* Biomaterials, 2002. **23**(12): p. 2553-2559.

36. Elliot, J.C., *The Problems of the compostion and structure of the mineral components of the hard tissues.* Clinical Orthopaedics and related research., 1973. **93**: p. p313-330.
37. Driessens, F.C. and Verbeeck, R.M., *Biominerals*. 1990, Florida: CRC Press: p 81-82.
38. Skinner, H.C.W., *Mineral and human health*, in *Enviromental mineralogy. EMU notes in mineralogy.*, Vaughan, D.J. and Wogelius, R.A., Editors. 2000, Eotvos University Press: Budapest. p.383-412.
39. Slomianka, L. *Blue histology-skeletal tissue-bone*. 2002 [cited 16/10/03]; Available from www.lab.anhb.uwa.edu.au/.../Bone/images.
40. Salo, J., *Bone resorbing osteoclasts reveal two basal plasma membrane domains and transcytosis of degraded matrix material*, in *Department of Anatomy and Cell Biology*. 2002, University of Oulu: Oulu.
41. Walker, P., Braithwate, N.,Lewis, P., Reynolds, K., Weidman, G.W.,, *Materials science and technology dictionary.* 1999: Chambers Harrap, UK.
42. Hughes, S. and McCarthy, I., *Sciences basic to orthopaedics*. 1996, WB Saunders company Ltd, UK: London: p. 10-15.
43. Weadon, K., Olson, R.M., and F.H, S., *Evaluation of collagen cross-linking techniques* . Biomat Med Dev & Artifical organs, 1984. **11**(4): p. 293-318.
44. Stryer, L., *Connective tissue proteins*, in *Biochemistry*. 1981, Freeman: San Francisco59-65.
45. Gibson, I.R. and Bonfield, W., *Novel synthesis and characterization of an AB-type carbonate-substituted hydroxyapatite.* Journal of Biomedical Materials Research, 2002. **59**(4): p. 697-708.
46. Currey, J.D., *Mechanical Adaptations of bones*. 1984, Princeton, New Jersey: Princeton University press: p.52-60.
47. Fernandez, E., Gil, F., Ginebra, M.P., Driessens, F.C., and Planell, J.A., *Calcium phosphate bone cements for clinical aplications. Part I: Solution chemistry.* Journal of Mater Sci: Mater in Med, 1999. **10**: p. 169-176.
48. Carlstrom, D., *X-ray crystallographic studies on apatites and calcified structures*. 1955, Karolinska Institutet, Sweden: Stockholm. p. 8-58.
49. Le Geros, R.Z., *Apatites in biological systems.* Crystal Growth Characterisation, 1981. **4**: p. 1-45.
50. Le Geros, R.Z., *Properties of osteoconductive biomaterials: calcium phosphates.* Clinical Orthopaedics & Related Research, 2002(395): p. 81-98.
51. Elliot, J.C., *Mineral components of hard tissue.* Clinical orthopaedics and related research, 1973. **93**: p. 326-344.
52. Young, R.A., *Biological apatite vs hydroxyapatite at atomic level.* Clinical Orthopaedics and related research., 1975: p. 249-263.
53. Mathew, M. and Takagi, S., *Structures of biological minerals in dental research.* Journal of research of the national institute of standards technology, 2001. **106**(6): p. 1035-1044.
54. Baig, A.A., Fox, J., Hsu, J., Wang, Z., and Otsuka, M., *Effect of carbonate content and crystallinity on the metastable equilibrium solubility behaviour of carbonated apatites.* Journal of Colloid and interface science, 1996. **179**: p. 608-617.

55. LeGeros, R.Z., Trautz, O.R., Legeros, J.P., and Klein, E., *Apatite crystallites: Effects of carbonate on morphology.* Science, 1967. **155**: p. 1409-1411.
56. Tang, R., Henneman, Z.J., and Nancollas, G.H., *Constant composition kinetics study of carbonated apatite dissolution.* Journal of crystal growth, 2003. **249**: p. 614-624.
57. Nelson, D.G.A. and Featherstone, J.D.B., *Preparation, analysis, and characterisation of carbonated apatites.* Calcified Tissue International, 1982. **34**: p. S69-S81.
58. Uchida, M., Kim, H.M., Kokubo, T., Miyaji, F., and Nakamura, T., *Bonelike apatite formation induced on zirconia gel in a simulated body fluid and its modified solutions.* Journal of American Ceramic Society, 2001. **84**(9): p. 2041-4.
59. Panda, R.N., Hsieh, M.F., Chung, R.J., and Chin, T.S., *FTIR, XRD, SEM and solid state NMR investigations of carbonate-containing hydroxyapatite nano-particles synthesized by hydroxide-gel technique.* Journal of Physics and Chemistry of Solids., 2003. **64**: p. 193-199.
60. Barralet, J., Best, S.M., and Bonfield, W., *Carbonate substitution in hydroxyapatite: An investigation into the effects of reaction temperature and bicarbonate ion concentration.* Journal of Biomedical Materials Research, 1998. **41**: p. 79-86.
61. Le Geros, R.Z., Trautz, O.R., Le Geros, J.P., and Klein, E., *Apatite crystallites: effects of carbonate on morphology.* Science, 1967. **155**: p. 1409-1411.
62. Xu, G., Aksay, I., and Groves, J.T., *Continuous crystalline carbonate apatite thin films. A biomimetic approach.* J. Am. Chem. Soc., 2001. **123**: p. 2196-2203.
63. Chickerur, N.S., Tung, M.S., and Brown, W.E., *A mechanism for incorporation of carbonate into apatite.* Calcified Tissue International, 1980. **32**: p. 55-62.
64. Skrtic, D., Antonucci, J.M., and Eanes, E.D., *Amorphous calcium phosphate-based bioactive polymeric composites for mineralized tissue regeneration.* J.Res. Natl. Inst. Stand. Technol., 2003. **108**: p. 167-182.
65. Eanes, E.D., Gillessen, I., and Posner, A.S., *Intermediate states in the precipitation of hydroxyapatite.* Nature, 1965: p. 365-367.
66. Posner, A.S., *Crystal chemistry of bone mineral.* Physiological reviews, 1969. **49**(4): p. 760-792.
67. Vanderschoot, P., *Spine fractures: Treatment options and development of a vertebral replacement implant.*, in *Dept of Traumatology*. 2002, Universitair Ziekenhuis te Leuven: Leuven , Belgium. p. 195.
68. Dorozhkin, S. and Epple, M., *Biological and medical significance of calcium phosphates.* Angew. Chem. In. Ed., 2002. **41**: p. 3130-3146.
69. Calvo, C. and Gopal, R., *The crystal structure of whitlockite from palmero quarry.* American Mineral., 1975. **60**: p. 120-133.
70. Mathew, M., Schroaeder, L.W., and Brown, W.E., *The crystal structure of α–$Ca_3(PO_4)_2$.* Acta Crystallogr, 1977. **B33**: p. 1325-1333.
71. Simske, S.J., Ayers, R.A., and Bateman, T.A., *Porous Materials for Bone Engineering.* Materials science forum, 1997. **250**: p. 151-182.
72. Vallet-Regi, M. and Gonzalez-Calbet, J.M., *Calcium phosphates as substitution of bone tissues.* Progress in solid state chemistry, 2004. **32**: p. 1-31.

73. Dickens, B., Schroeder, L.W., and Brown, W.E., *Crystallographic studies of the role of Mg as a stabilizing impurity in β–$Ca_3(PO_4)_2$. I. The crystal structure of pure β–$Ca_3(PO_4)_2$.* J. Solid State Chem, 1974. **10**: p. 232-248.
74. Osborn, J.F. and Newesely, H., *The material science of calcium phosphate ceramics.* Journal of Biomaterials, 1980. **1**: p. 108-111.
75. Curry, N.A. and Jones, D.W., *Crystal structure of brushite, calcium hydrogen orthophosphate. A neutron-diffraction investigation.* Journal of Chemical Society, 1971. **A**: p. 3725-3929.
76. Elliot, J.C., *Structure and chemistry of apatites and other calcium orthophosphates.* 1994, Amsterdam: Elsevier: p. 29.
77. Dickens, B., Brown, W.E., Kruger, G.J., and Stewart, J.M., *$Ca_4(PO_4)_2O$, tetracalcium diphosphate monoxide. Crystal structure and relationships to $Ca_5(PO_4)_3OH$ and $K_3Na(SO_4)_2$.* Acta Crystallogr, 1973. **B29**: p. 2046-2056.
78. Kumta, P., Sfeir, C., Dong-Hyun, L., Olton, D., and Choi, D., *Nanostructured calcium phosphates for biomedical applications: novel synthesis and characterization.* Acta Biomaterialia, 2005. **1**: p. 65-83.
79. Fernandez, E., Gil, F., Ginebra, M.P., Driessens, F.C., and Planell, J.A., *Calcium phosphate bone cements for clinical applications. Part II: Precipitate formation during setting reactions.* Journal of Materials Science: Materials in Medicine, 1999. **10**: p. 177-183.
80. Hench, L.L., *Bioceramics.* Journal of American Ceramic society, 1998. **81**(7): p. 1705-1728.
81. Berndt, C.C., Haddad, G.N., Farmer, A.J.D., and Gross, K.A., *Review Article: Thermal spraying for bioceramic applications.* Materials Forum., 1990. **14**: p. 161-173.
82. Le Geros, R.Z., B. Bonel, and R. Legeros, *Types of H_2O in human enamel and in precipitated apatites.* Calcified Tissue Research, 1978. **26**: p. 111-118.
83. Stoch, A., Brozek, A., Blazewicz, S., Jastrzebski, W., Stoch, J., Adamczyk, A., and Roj, I., *FTIR study electrochemically depoited hydroxyapatite coatings on carbon materials.* Journal of Molecular Structure., 2003. **651-653**: p. 389-396.
84. Yang, Y.C. and Chang, E., *Influence of residual stress on bonding strength and fracture of plasma spray hydroxyapatite coatings on Ti-6Al-4V substrate.* Biomaterials, 2001. **22**: p. 1827-1836.
85. Li, F., Feng, Q.L., Cui, F.Z., Li, H.D., and Schubert, H., *A simple biomimetic method for calcium phosphate coating.* Surface and coatings technology, 2002. **154**: p. 88-93.
86. Guipont, V., Espanol, M., Borit, F., Llorca-Isern, N., Jeandin, M., and Khor, K.A., *High-pressure plasma spraying of hydroxyapatite powders.* Materials Science and Engineering, 2002. **A325**: p. 9-18.
87. Lee, I., Whang, C., Kim, H., Park, J., Song, J.H., Kim, S., *Various Ca/P ratios of thin calcium phosphate films.* Materials Science & Engineering, 2002(C22): p. 15-20.
88. Pilliar, R.M., Filiaggi, M.J., *New calcium phosphate coating methods.*, in *Bioceramics*, Ducheyne, P., Christiansen, D., Editor. 1993, Butterworth-Heinemann Ltd: Philadelphia165-171.

89. Serekian, M.S., ed. *Process applications of hydroxyapatite coatings.* Hydroxyapatite coatings in Orthopaedic surgery, ed. Geesink, R.G.T. and Manley, M.T. Vol. 81-88. 1993, Raven Press Ltd: New York.
90. Sun, L., Berndt, C.C., Khor, K.A., Cheang, H.N., and Gross, K.A., *Surface characteristics and dissolution behaviour of plasma-sprayed hydroxyapatite coating.* Journal of Biomedical Materials Research, 2002. **62**: p. 228-236.
91. Gerdeman, D.A., Hecht, N.L., *Arc Plasma Technology*, in *Materials Science*. 1972, Spring-Verlag: New York, USA
92. Vuoristo, P., *Coating structure and techniques for bio applications*, in *Euroceram Seminar Biotechnical Engineering*. 2001: Tampere, Finland.
93. Cheang, P. and Khor, K.A., *Addressing problems associated with plasma spraying of hydroxyapatite.* Biomaterials, 1996. **17**(5): p. 537-544.
94. Anselme, K., Sharrock, P., Hardouin, P., and Dard, M., *In vitro growth of human adult bone-derived cells on hydroxyapatite plasma-sprayed coatings.* Biomedical Materials Research, 1997. **34**(2): p. 247-259.
95. Ducheyne, P., Bianco, P.D., and Kim, C., *Bone tissue growth enhancement by calcium phosphate coatings on porous titanium alloys: the effect of shielding metal dissolution product.* Biomaterials, 1992. **13**(9): p. 617-624.
96. Gross, K.A. and Berndt, C.C., *Structural changes of plasma sprayed hydroxyapatite coatings during in-vitro testing.*, in *Characterization and performance of calcium phosphate coatings for implants*, Horowitz, E. and Parr, J.E., Editors. 1994, ASTM: Philadelphia, USA125-137.
97. Gross, K.A. and Berndt, C.C., *Amorphous phase formation in plasma-sprayed hydroxyapatite coatings.* Journal of Biomedical Materials Research, 1998. **39**: p. 407-414.
98. Prevey, P.S. and Rothwell, R.J., *X-ray diffraction characteristics of percent crystallinity and contaminants in plasma sprayed hydroxyapatite coatings*. Characterisation and performance of calcium phosphate coatings for implants, ed. Horowitz, E. and Parr, E. 1994, Philadelphia: ASTM.
99. Berndt, C.C., Haddad, G.N., Farmer, A.J.D., and Gross, K.A., *Thermal spraying for bioceramics applications.* Materials Forum., 1990. **14**: p. 163-173.
100. Sun, L., Berndt, C.C., and Grey, C.P., *Phase, structural and microstructural investigations of plasma sprayed hydroxyapatite coatings.* Materials Science & Engineering, 2003. **A360**: p. 70-84.
101. Athanasou, N.A. *Hydroxyapatite crystals/ Prosthetic coating.* 1996 [cited 2002 14/03/02]; Available from: http://www.medmedia.com/o2/436.htm.
102. Klein, C.P.A.T., Wolke, J.G.C., de Blieck-Hogervost, J.M.A., de Groot, K.,, *Calcium phosphate plasma sprayed coatings and their stability.* Journal of Biomedical Materials Research, 1994: p. 909-917.
103. Yamada, K., Imamura, k., Itoh, H., Iwata, H., and Maruno, S., *Bone bonding behaviour of the hydroxyapatite containing glass-titanium composite prepared by the Cullet method.* Biomaterials, 2000. **22**: p. 2207-2214.
104. Kumar, R.R. and Wang, M., *Functionally graded bioactive coatings of hydroxyapatite/titanium oxide composite system.* Biomaterials, 2001.
105. Etok, S.E. and Rogers, K.D., *Structural and chemical changes to plasma sprayed hydroxyapatite coatings in simulated body fluid*, in *Bioceramics: Materials and*

Applications V, Rusin, R., Editor. 2004, American Ceramic Society: Indianapolis, USA
106. Chen, J., Wolke, J.G.C., De Groot, K.,, *Microstructure and crystallinity in hydroxyapatite coatings.* Biomaterials, 1994. **15**(5): p. 396-399.
107. Liu, X., Tao, S., and Ding, C., *Bioactivity of plasma sprayed dicalcium silicate coatings.* Biomaterials, 2002. **23**: p. 963-968.
108. Li, H., Khor, K.A., Kumar, R., and Cheang, P., *Characterization of hydroxyapatite/nano-zirconia composite coatings deposited by high velocity oxy-fuel (HVOF) spray process.* Surface and Coatings Technology, 2004. **182**(2-3): p. 227-236.
109. Barrere, F., Layrolle, P., van Blitterswijk, C.A., and De Groot, K., *Biomimetic coatings on titanium: a crystal growth study of octacalcium phosphate.* Journal of Materials Science, 2001. **12**: p. 529-534.
110. Tanahashi, M., Yao, T., Kokubo, T., Minoda, M., Miyamoto, T., Nakamura, T., and Yamamuro, T., *Apatite coating on organic polymers by a biomimetic process.* Journal of American Ceramic Society, 1994. **11**: p. 2805-2808.
111. Li, H., Khor, K.A., and Cheang, P., *Properties of heat-treated calcium phosphate coatings deposited by high-velocity oxy fuel (HVOF) spray.* Biomaterials, 2002. **23**(10): p. 2105-2112.
112. Kokubo, T., *Apatite formation on organic polymers by a biomimetic process.* European Journal of Solid State Inorganic Chemistry, 1995. **32**: p. 819-827.
113. Barrere, F., Stigter, M., Layrolle, P., van Blitterswijk, C.A., and De Groot, K., *In vitro dissolution of various calcium phosphate coatings on Ti6Al4V.* Key Engineering Materials, 2001. **192-195**: p. 67-70.
114. Ben-Nissan, B.C., C; Evans, L., *Crystallographic and spectroscopic characterization of morphology of biogenic and synthetic apatites*. Encyclopaedic handbook of biomaterials and bioengineering., ed. Wise, D.L. Vol. Part B. 1995, New York: Marcel Dekker.
115. Lopatin, C.M., Alford, T.L., Pizziconia, V.B., and Laursen, T., *Hydroxyapatite powders and thin films prepared by a sol-gel technique.* Thin solid films, 1998. **326**: p. 227-232.
116. Riman, R.E., Suchanek, W.L., Byrappa, K., Chen, C.-W., Shuk, P., and Oakes, C.S., *Solution synthesis of hydroxyapatite designer particulates.* Solid State Ionics, 2002. **151**(1-4): p. 393-402.
117. Lopatin, C.M., Alford, T.L., Pizziconia, V.B., and Laursen, T., *A new technique for characterization of pore structures in materials application to the study of hydroxyapatite thin films.* Materials Letters, 1998. **37**(4-5): p. 211-214.
118. Kaciulis, S., Mattogno, G., Pandolfi, L., Cavalli, M., Gnappi, G., and Montenero, A., *XPS study of apatite-based coatings prepared by sol-gel technique.* Applied Surface Science, 1999. **151**: p. 1-5.
119. Hwang, K. and Lim, Y., *Chemical and structural changes of hydroxyapatite films by using a sol-gel method.* Surface and Coatings Technology, 1999. **115**: p. 172-175.
120. Manso, M., Jimenez, C., Morant, C., Herrero, P., and Martinez-Duart, J.M., *Electrodeposition of hydroxyapatite coatings in basic conditions.* Biomaterials, 2000. **21**: p. 1755-1761.

121. Shirkhanzadeh, M., *Electrochemical preparation of bioactive calcium phosphate coatings on porous substrates by the periodic pulse technique.* Journal of Materials Science Letters, 1993. **12**: p. 16-19.
122. Roessler, S., Sewing, A., Stolzel, M., Born, R., Scharnweber, D., Dard, M., and Worch, H., *Electrochemically assisted deposition of thin calcium phosphate coatings at near-physiological pH and temperature.* Journal of Biomedical Materials Research, 2003. **64A**: p. 655-663.
123. Shirkhanzadeh, M., *Direct formation of nanophase hydroxyapatite on cathodically polarized electrodes.* Journal of Materials Science: Materials in Medicine, 1998. **9**: p. 67-72.
124. Kotte, B., Hofinger, J., and Hebold, T., *Apatite-coated metallic materials, process for its preparation, and its use*, in *US Patent and Trademark Office*. 2003, Biomet-Merck GmbH: USA.
125. Shirkhanzadeh, M., *Bioactive calcium phosphate coatings by electrodeposition.* Journal of Materials Science Letters, 1991. **10**(1991): p. 1415-1417.
126. Zhang, J.M., Lin, C.J., feng, Z.D., and Tian, Z.W., *Mechanistic studies of electrodeposition for bioceramic coatings of calcium phosphates by an in-situ ph-microsensor technique.* Electroanalytical Chemistry, 1998. **452**: p. 235-240.
127. Therese, G.H.A., Kamath, P.A., and Subbanna, G.N., *Novel electrosynthetic route to calcium phosphate coatings.* Journal of Materials Chemistry, 1998. **8**(2): p. 405-408.
128. Wang, C.X., Wang, M., and Zhou, X., *Electrochemical impedance spectroscopy study of the nucleation and growth of apatite on chemically treated titanium.* Langmuir, 2002. **18**: p. 7641-7647.
129. Stoch, A., Brozek, A., Kmita, G., Stoch, J., Jastrzebski, W., Rakowska,A, *Electrophoretic coating of hydroxyapatite on titanium implants.* Journal of Molecular Structure., 2001(596): p. 191-200.
130. Odezi, K., Yuhta, T., Fukui, Y, *A functionally graded titanium/hydroxyapatite film obtained by sputtering.* Journal of materials science: Materials in medicine, 2002. **13**: p. 253-258.
131. Rogers, K.D., Etok, S.E., and Scott, R., *Structural characterisation of apatite coatings.* Journal of Materials Science, 2004. **39**: p. 5747-5754.
132. Raju, K.S., *Structural characterisation of materials.*, in *Handbook of advanced materials testing.*, Cheremisinoff, N.P. and Cheremisinoff, P.N., Editors. 1995, Marcel Dekker, Inc: New York, USA849-870.
133. Jenkins, R. and de Vries, J.L., *An introduction to X-ray powder diffractometry.* 1990: N.V Philips: p. 1-18.
134. Stout, G. and Jensen, L., *X-ray structure determination - A practical guide*. 1989, Washington D.C: John Wiley and Sons: p. 14-138
135. Ermrich, M., *Use of X-ray diffraction in properties testing.*, in *Handbook of advanced materials testing*, Cheremisinoff, N.P. and Cheremisinoff, P.N., Editors. 1995, Marcel Dekker, Inc: New York, USA181-193.
136. Louer, D. and Mittemeijer, E.J., *Powder diffraction in materials science*. 2000, Universite de Rennes: Rennes, France. p. 1-6.
137. Wittke, J.H. *Primary Absorption.* 2005 [cited 13/06/05]; Available from: www.jan.ucc.nau.edu.

138. Hammond, C., *Introduction to crystallography*. Royal Microscopy Society Microscopy Handbooks. 1992, Oxford: Oxford University Press: p16-24.
139. David, W.I.F., Shankland, K., McClusker, L.B., and Baerlocher, C., eds. *Structure determination from powder diffraction data.* IUCr monographs on Crystallography. 2002, Oxford University Press, Inc: New York, USA.
140. Bruker, A., *Topas: General profile and structure analysis software for powder diffraction data*. 2001, Bruker Advanced X-ray solutions: Germany. p. 1-202.
141. Hammond, C., *The basics of crystallography and diffraction*. IUCr texts on crystallography, ed. Coppens, P., Glazer, A., Glusker, J.P., Larsen, S., Kuchitsu, K., Robertson, J.H., and Simonov, V.I. 1997, Oxford: Oxford University Press: p. 73-75.
142. Flewitt, P.E. and Wild, R.K., *Physical methods for materials characterisation*. Institute of physics series in materials science and engineering. 2003, Bristol and Philadelphia: Institute of physics publishing: p.164-5.
143. Artioli, G. *Conventional and advanced diffraction techniques*. in *Workshop on engineering mineralogy of ceramic materials*. 2001. Certosa di Pontignano, Italy.
144. Esteve, V., Ochando, L.E., Reventos, M.M., Peris, G., and Amigo, J.M., *Quantitative phase analysis of mixtures of three components using Rietveld and Ruis standardless methods : comparative results.* Crystal research technology, 2000. **35**(10): p. 1183-1192.
145. Keller, L., *X-ray powder diffraction patterns of calcium phosphates analyzed by the Rietveld method.* Journal of Biomedical Materials Research, 1995. **29**: p. 1403-1413.
146. Connolly, J.R., *Introduction to qunatitative diffraction methods.* 2003, University of New Mexico: Albuquerque, USA. p. 1-14.
147. Prevey, P.S., *X-ray diffraction characterization of crystallinity and phase composition in plasma sprayed hydroxyapatite coatings.* Journal of thermal spray technology, 2000. **9**(3): p. 369-376.
148. Rodriguez-Carvajal, J., *Structural analysis from powder diffraction data: The Rietveld method.* 1997, CEA/Saclay: Gif sur Yvette, France. p. 1-25.
149. Masciocchi, N., *The contribution of powder diffraction methods to structural crystallography: Rietveld and ab-inito techniques.* The Rigaku journal, 1997. **14**(2): p. 9-16.
150. Toraya, H., *Whole-powder-pattern decomposition method.* The Rigaku journal, 1989. **6**(2): p. 28-34.
151. Balzar, D., Auderbrand, N., Daymond, M.R., Fitch, A., Hewat, A., Langford, J.I., Le Bail, A., Louer, D., Masson, O., McCowan, C.N., Popa, N.C., Stephens, P.W., and Toby, B.H., *Size-strain line broadening analysis of the ceria round-robin sample.* Appl. Crystallography, 2004. **37**: p. 911-924.
152. Bigi, A., Boannini, E., Gazzano, M., Kojdecki, M., and Rubini, K., *Microstructural investigation of hydroxyapatite-polyelectrolyte composites.* Journal of materials chemistry, 2004. **14**: p. 274-279.
153. Marinkovic, B., de Avillez, R.R., Saavedra, A., and Assuncao, F.C.R., *A comparison between the Warren -Averbach method and alternative methods for X-ray diffraction microstructure analysis of polycrystalline specimens.* Materials Research, 2001. **4**: p. 71-76.

154. Danilchenko, S.N., Moseke, C., Sukhodub, L.F., and Sulkio-Cleff, B., *X-ray diffraction studies of bone apatite under acid demineralization.* Crystal research technology, 2004. **1**: p. 71-77.
155. Williamson, G.K. and W.H, H., *X-ray line broadening from filed aluminium and wolfram.* Acta Metallurgica, 1953. **1**: p. 22-31.
156. Meier, M., *Crystallite size measurement using X-ray diffraction.* 2005, University of California, Davis: Davis, USA. p. 1-6.
157. Rosenburg, Y., Machavaariani, V., Voronel, A., Garber, S., and Rubshtein, A., *Strain energy density in the X-ray powder diffraction from mixed crystals and alloys.* Journal of Physics: Condensed matters., 2000. **12**: p. 8081-8088.
158. Langford, J.I., *The use of the voigt function in determining microstructural properties from diffraction data by means of pattern decomposition.*, in *Accuracy in powder diffraction II - NIST special publication No. 846*, Prince, E. and Stalick, J.K., Editors. 1992: Gaithersburg, USA
159. Roome, C.M. and Adam, C.D., *Crystallite orientation and anisotropic strains in thermally sprayed hydroxyapatite coatings.* Biomaterials, 1995. **16**: p. 691-696.
160. Roome, C.M. and C.D. Adam, *Synchrotron radiation powder diffraction studies of thermally deposited coatings of hydroxylapatite.* Nuclear Instruments and Methods in Physics Research B, 1995. **97**: p. 308-311.
161. Warren, B.E., *X-ray diffraction.* 1969, Reading: Addison-Wesley: p. 8-12.
162. Philips, *Theory of line profile analysis*, in *Line Profile analysis for Windows user's guide*. 1996, Philips: UK. p. A1-A27.
163. Isaacs, A., ed. *A concise dictionary of physics*. 1990, Oxford University Press: Oxford, UK.
164. Martin, E., ed. *Oxford concise colour medical dictionary*. 1998, Oxford University Press: Oxford..
165. Jasco. *FTIR Seminar.* 2004 [cited 03/06/05]; Available from: www.jascofrance.fr/pdf/ftir.pdf.
166. Cerroni, L., Filocamo, R., Fabbri, M., Piconi, C., Caropreso, S., and Condo, S.G., *Growth of osteoblast-like cells on porous hydroxyapatite ceramics: an in vitro study.* Biomolecular Engineering, 2002. **19**(2-6): p. 119-124.
167. Nagano, M., Nakumura, T., Kokubo, T., Tanahashi, M., and Ogawa, M., *Differences of bone bonding ability and degradation in vivo between amorphous calcium phosphate and highly crystalline hydroxyapatite coating.* Biomaterials, 1996. **17**: p. 1771-1777.
168. Strnad, Z., Strnad, J., Povýsil, C., and Urban, K., *Effect of plasma-sprayed hydroxyapatite coating on the osteoconductivity of commercially pure titanium implants.* The International Journal of Oral & Maxillofacial Implants, 2000. **15**(4): p. 483-490.
169. Tonino, A., Romanini, L., Rossi, P., Borroni, M., Greco, F., Garcia-Araujo, C., Garcia-Dihinx, L., Murcia, A., Hein, W., and Anderson, J., Clinical Orthopaedics and Related Research, 1995. **312**: p. 211.
170. Courteney-Harris, R.G., Kayser, M.V., and Downes, S., *Comparison of the early production of extracellular matrix on dense hydroxyapatite and hydroxyapatite-coated titanium in cell and organ culture.* Biomaterials, 1995. **16**(6): p. 489-495.

171. Klein, C.P.A.T., Driessens, A.A., and De Groot, K., *Relationship between the degradation behaviour of calcium phosphate ceramics and their physical-chemical characteristics and ultrastructural geometry.* Biomaterials, 1984. **5**(3): p. 157-160.
172. Wolke, J.G.C., van der Waerden, J.P.C.M., Schaeken, H.G., and Jansen, J.A., *In vivo dissolution behaviours of various RF magnetron-sputtered Ca-P coatings on roughened titanium implants.* Biomaterials, 2003. **24**: p. 2623-2629.
173. Tong, W., Chen, J., and Zhang, X., *Initial investigation on the internal stress in plasma sprayed hydroxyapatite coatings.*, in *In Biomedical Materials Research*, Zhang, X. and Ikada, Y., Editors. 1993, Kobunshi Kankokai: Kyoto, Japan
174. LeGeros, R.Z., *Apatites in biological systems.* Crystal growth characterisation., 1981. **4**: p. 1-45.
175. Dalton, J.E., Cook, S.D.,, *In vivo mechanical and histological characteristics of HA coated implants vary with coating vendor.* Journal of Biomedical Materials Research, 1995. **29**(2): p. p239-245.
176. Sergo, V., Sbaizero, and Clarke, D., *Mechanical and chemical consequences of residual stresses in plasma sprayed hydroxyapatite coatings.* Biomaterials, 1997. **18**: p. 477-482.
177. Tsui, Y.C., Doyle, C., Clyne, T, *Plasma sprayed hydroxyapatite coatings on titanium substrates. Part 1: Mechanical properties and residual stress levels.* Biomaterials, 1998. **19**: p. 2015-2029.
178. Werner, J., Linner-Krcmar, B., Friess, W., and Greil, P., *Mechanical properties and in vitro cell compatibility of hydroxyapatite ceramics with graded pore structure.* Biomaterials, 2002. **23**(21): p. 4285-4294.
179. Gauthier, O., Bouler, J.M., Aguando, E., Pilet. P., Daculsi, G., *Macroporous biphasic calcium phosphate ceramics: influence of macropore diameter and macroporosity percentage on bone ingrowth.* Biomaterials, 1998. **19**: p. 133-139.
180. Tong, W., Chen, J., Li, X., Feng, J., Cao, Y., Yang, Z., and Zhang, X., *Preferred orientation of plasma sprayed hydroxyapatite coatings.* Journal of Materials Science, 1996. **31**: p. 3739-3742.
181. Kalita, S.J., Bose, S., Hosick, H.L., and Bandyopadhyay, A., *CaO-P2O5-Na2O-based sintering additives for hydroxyapatite (HAP) ceramics.* Biomaterials, 2004. **25**(12): p. 2331-2339.
182. Lower, S.K., Maurice, P.A., and Traina, S.J., *Simultaneous dissolution of hydroxylapatite and precipitation of hydroxypyromorphite: direct evidence of homogeneous nucleation.* Geochimica et Cosmochimica Acta, 1998. **62**(10): p. 1773-1780.
183. Sridhar, T.M., Kamachi Mudali, U., and Subbaiyan, M., *Preparation and characterisation of electrophoretically deposited hydroxyapatite coatings on type 316L stainless steel.* Corrosion Science, 2003. **45**(2): p. 237-252.
184. Katto, M., Kurosawa, K., Yokotani, A., Kubodera, S., Kameyama, A., Higashiguchi, T., Nakayama, T., and Tsukamoto, M., *Poly-crystallized hydroxyapatite coating deposited by pulsed laser deposition method at room temperature.* Applied Surface Science, 2005. **ARTICLE IN PRESS**.

185. Yang, D., Yang, Z., Li, X., Di, L., and Zhao, H., *A study of hydroxyapatite/calcium sulphate bioceramics.* Ceramics International, 2005. **ARTICLE IN PRESS**.
186. Rapacz-Kmita, A., Paluszkiewicz, C., Slósarczyk, A., and Paszkiewicz, Z., *FTIR and XRD investigations on the thermal stability of hydroxyapatite during hot pressing and pressureless sintering processes.* Journal of Molecular Structure., 2005. **ARTICLE IN PRESS**.
187. Sung, Y., Lee, J., and Yang, J., *Crystallization and sintering characteristics of chemically precipitated hydroxyapatite nanopowder.* Journal of Crystal Growth, 2004. **262**(1-4): p. 467-472.
188. Petrov, O.E., Dyulgerova, E., Petrov, L., and Popova, R., *Characterization of calcium phosphate phases obtained during the preparation of sintered biphase Ca-P ceramics.* Materials Letters, 2001. **48**(3-4): p. 162-167.
189. Marin Rusu, V., Ng, C., Wilke, M., Tiersch, B., Fratzl, P., and Peter, M.G., *Size-controlled hydroxyapatite nanoparticles as self-organized organic-inorganic composite materials.* Biomaterials, 2005. **26**(26): p. 5414-5426.
190. Rogers, K.D., Etok, S.E., Broadhurst, A., and Scott, R., *Enhanced analysis of biomaterials by synchroton diffraction.* Nuclear Instruments and Methods in Physics Research A, 2005. **ARTICLE IN PRESS**.
191. Wang, C.X., Chen, Z.Q., Guan, L.M., Liu, Z.Y., Wang, P.L., Zheng, S., and Liao, X., *Structural characterisation of ion beam sputter deposited calcium phosphate coatings.* Surface and coatings technology, 2000. **130**: p. 39-45.
192. Ding, S.J., Su, Y.M., Ju, C.P., and Chern-Lin, J.H., *Structure and immersion behavior of plasma-sprayed apatite-matrix coatings.* Biomaterials, 2001. **22**: p. 833-845.
193. Huaxia, J.I., Ponton, C.B., and Marquis, P.M., *Microstructural characterisation of hydroxyapatite coating on titanium.* Journal of Materials Science: materials in Medicine, 1992. **3**(283-287).
194. Shi, D., Jiang, G., and Bauer, J., *The effect of structural characteristics on the in vitro bioactivity of hydroxyapatite.* Journal of Biomedical Materials Research, 2002. **63**(1): p. 71-78.
195. Kontoyannis, C.G., Bouropoulos, N.C., and Koutsoukos, P.G., *Raman spectroscopy: A tool for the quantitative analysis of mineral components of solid mixtures. The case of calcium oxalate monohydrate and hydroxyapatite.* Vibrational Spectroscopy, 1997. **15**: p. 53-60.
196. Wandt, M.A.E. and Rodgers, A.L., *Quantitative X-ray diffraction analysis of urinary calculi by the use of the internal-standard method and reference intensity ratios.* Clinical Chemistry, 1988. **34**(2): p. 289-294.
197. Riello, P., Canton, P., Comelato, N., Polizzi, S., Verita, M., Fagherazzi, G., Hofmeister, H., and Hopfe, S., *Nucleation and crystallization behavior of glass-ceramic materials in the Li2O-Al2O3-SiO2 system of interest for their transparency properties.* Journal of Non-Crystalline Solids, 2001. **288**(1-3): p. 127-139.
198. Riello, P., Caton, P., and Fagherazzi, G., Journal of Allied Crystallography, 1998. **31**: p. 78.

199. Rietveld, H., *A profile refinement method for nuclear and magnetic structures.* Journal of Applied Crystallography, 1969. **2**: p. 65-71.
200. Knowles, J.C., Gross, K.A., Berndt, C.C., and Bonfield, W., *Structural changes of thermally sprayed hydroxyapatite investigated by Rietveld analysis.* Biomaterials, 1996. **17**(6): p. 639-645.
201. Kim, H., Kishimoto, K., and Miyaji, F., Journal of Materials Science: Materials in Medicine. **11**(7): p. 421-426.
202. Cao, W., Hench, L.L,. *Bioactive materials.* Ceramics International, 1996. **22**: p. 493-507.
203. Ding, S.J., Ju, C.P., and Lin, J.H., *Morphology and immersion behaviour of plasma-sprayed hydroxyapatite / bioactive glass coatings.* Journal of Materials Science: Materials in Medicine, 2000. **11**: p. 183-90.
204. Barrere, F., Stigter, M., Layrolle, P., Van Blitterswijk, C.A., and De Groot, K. *In vitro dissolution of various calcium phosphate coatings on Ti6AL4V.* in *13th International symposium on ceramics in Medicine*. 2000. Bologna, Italy: Trans Tech Publications.
205. Yoshimura, M. and Suda, H., *Hydrothermal processing of hydroxylapatite: Past present and future*, in *Hydroxylapatite and related materials*, Brown, P., W and Constanz, B., Editors. 1994, CRC Press: Boca Raton, Florida45-72.
206. Bauer, T.W., Geesink, R.C.T., Zimmerman, R., and McMahon, J.T., *Hydroxyapatite-coated femoral stems. Histological analysis of components retrieved at autopsy.* Journal of Bone Joint Surgery, 1991. **80B**: p. 267-272.
207. Wang, J.S., Goodman, S., and Aspenberg, P., *Bone formation in th presence of phagocytostable hydroxyapatite particles.* Clinical Orthopaedics and Related Research, 1994. **304**: p. 272-279.
208. Le Geros, R.Z., Zheng, R., Kijkowska, R., Fan, D., and Le Geros, J.P., eds. *Variations in composition and crystallinty of hydroxyapatite preparations.* Characterisation and performabce of calcium phosphate coatings for implants, ed. Horowitz, E. and Parr, J.E. 1994, American Society for testing and materials: Philadelphia, 1994.
209. Ducheyne, P., Radin, S., and King, L., *The effect of calcium phosphate ceramic composition and structure on in vitro behaviour: I Dissolution.* Journal of Biomediccal Materials Research, 1993. **17**: p. 25-34.
210. Lo, W.-J., Grant, D.M., Ball, M.D., Welsh, B.S., Howdle, S.M., Antonov, E.N., Bragratashvili, V.N., and Popov, V.K., *Physical, chemical, and biological characterization of pulsed laser deposited and plasma sputtered hydroxyapatite thin films on titanium alloy.* Biomedical Materials Research, 1999(50): p. 536-545.
211. Hankermeyer, C.R., Ohasi, K.L., Delaney, D.C., Ross, J., Costantz, B.R,, *Dissolution rates of carbonated hydroxyaptite in hydrochloric acid.* Biomaterials, 2002. **23**: p. 743-750.
212. Christoffersen, J., Christoffersen, M.R., Kolthoff, N., and Barenholdt, O., *Effects of strontium ions on the growth and dissolution of hydroxyapatite and on bone mineral detection.* Journal of Bone, 1997. **20**(1): p. 47-54.

213. LeGeros, R.Z., Kijkowska, R., Tung, M., and Legeros, J.P. *Effect of strontium on some properties of apatites.* in *Tooth enamel V. Proceedings of 5th International symposia*. 1989.
214. Shpak, A.P., Karbovskii, V.L., and Vakhney, A.G., *Electronic structure of isomorphically substittued strontium apatite.* Journal of Electron Spectroscopy and Related Phenomena, 2004. **137-140**: p. 585-589.
215. Kim, H., Y. Koh, S. Seo, and H. Kim, *Properties of fluoridated hydroxyapatite-alumina biological composites densified with addition of CaF_2.* Materials Science and Engineering: C, **ARTICLE IN PRESS**.
216. LeGeros, R.Z., *Properties of osteoconductive biomaterials: calcium phosphates.* Clinical Orthopaedics and Related Research, 2002(395): p. 81-98.
217. Bauer, T.W., *Hydroxyapatite: Coating controversies.* Orthopaedics, 1995. **18**: p. 389-395.
218. Fulmer, M.T., Ison, I.C., Hankermayer, C.R., Constantz, B.R., Ross, J.,, *Measurements of the solubilities and dissolution rates of several hydroxyapatites.* Biomaterials, 2002. **23**: p. 751-755.
219. Brown, W.E. and Chow, L.C., *Thermodynamics of apatite crystal growth and dissolution.* Journal of Crystal Growth, 1981. **53**: p. 31-34.
220. Christoffersen, M.R., Christoffersen, J., and Arends, J., *Kinetics of dissolution of calcium hydroxyapatite.* Journal of Crystal Growth, 1984. **67**: p. 107-114.
221. Dorozhkin, S., *Surface reactions of apatite dissolution.* Journal of Colloid and Interface Science, 1997. **191**: p. 489-497.
222. McDowell, H., Gregory, T.M., and Brown, W.E., *Solubility of $Ca_5(PO_4)_3OH$ in the system $Ca(OH)_2$-H_3PO_4-H_2O.* Journal of Research of the National Bureau of Standards -A. Physics and Chemistry., 1977. **81A**(2 & 3): p. 273-281.
223. Weng, J., Lui, Q., Wolke, J.G.C., Zhang, D., and De Groot, K., *The role of amorphous phase in nucleating bone-like apatite on plasma sprayed coatings in simulated body fluid.* Journal of Materials Science Letters, 1997. **16**: p. 335-337.
224. Tang, R., Wang, L., and Nancollas, G.H., *Size-effects in the dissolution of hydroxyapatite: an understyanding of biological demineralizaation.* Journal of Materials Chemistry, 2004. **14**(14): p. 2341-2346.
225. Gu, Y.W., Khor, K.A., and Cheang, P., *In vitro studies of plasma-sprayed hydroxyapatite/Ti-6Al-4V composite coatings in simulated body fluid (SBF).* Biomaterials, 2003. **24**(9): p. 1603-1611.
226. Leadley, S.R., Davies, M.C., Castro Ribeiro, C., Barbosa, M.A., Paul, A.J., and Watts, J.F., *Investigation of the dissolution of the bioceramic hydroxyapatite in the presence of titanium ions using ToF-SIMS and XPS.* Biomaterials, 1997. **18**(4): p. 311-316.
227. Zhang, Q., Chen, J., Feng, J., Cao, Y., Deng, C., and Zhang, X., *Dissolution and mineralization behaviors of HA coatings.* Biomaterials, 2003. **24**(26): p. 4741-4748.
228. Rodeo, S.A., Amoczky, S.P., and Torizilli, P.A., *Tendon-healing in a bone tunnel. a biomechanical and histological study in the dog.* Journal of Bone Joint Surgery, 1993. **75A**: p. 1795-1803.

229. Dunn, M.G., *Anterior cruciate ligament prosthesis.*, in *Encyclopaedia of Sports Medicine and Sciences.*, Fahey, T.D., Editor. 1998, Internet Society for Sport Science
230. Fu, F., Bennett, C.H., Lattermann, C., and Ma, B., *Current trends in anterior cruciate ligament reconstruction; Part 1: Biology and biomechanics of reconstruction.* American Journal of Sports in Medicine, 1999. **27**(6): p. 821-830.
231. McLoughlin, S.J. and Smith, R.B., *Clinical Orthopaedics and Related Research.* 1992. **283**: p. 215-222.
232. Steiner, M.E., Necker, A.T., and Brown, C.H., *Anterior cruciate ligament graft fixation: Comparison of human hamstring and patellar tendon grafts.* American Journal of Sports in Medicine, 1994. **22**: p. 240-247.
233. Suzuki, K., Kobayashi, R., Yokoyama, Y., Harada, Y., and Kokubo, T., *Experimental study of an artificial trachea made of polymers coated with hydroxyapatite*, in *Bioceramics*, Ducheyne, P. and Christiansen, D., Editors. 1993, Butterworth-Heineman: Guildford, UK
234. Riello, P., Fagherazzi, G., and Canton, N., *Determining the degree of crystallinity in semicrystalline materials by means of Rietveld analysis.* Journal of Applied Crystallography, 1995. **28**: p. 121-126.
235. Fletcher, D.A., McMeeking, R.F., and Parkin, D., *The United Kingdom chemcial database service.* Journal of Chemical Information Computer Science, 1996. **36**: p. 746-749.
236. Rehman, I. and Bonfield, W., *Characterization of hydroxyapatite and carbonated apatite by photo acoustic FTIR spectroscopy.* Journal of Materials Science: Materials in Medicine, 1997. **8**: p. 1-4.
237. Payne, C.M. and Cromey, D.W., *Limitations of ZAF correction factors in the determination of calcium/phosphorous ratios: Important forensic science considerations relevant to the analysis of bone fragments using scanning electron microscopy and energy-dispersive X-ray microanalysis.* Journal of Forensic Sciences, 1990. **35**(3): p. 560-568.
238. Gilman, H. and Hukins, D.W.L., *Seeded growth of Hydroxyapatite in the presence of dissolved albumen at constant composition.* Journal of Inorganic Biochemistry, 1991(55): p. 31-39.
239. Kumar, R., Prakash, K.H., Cheang, P., and Khor, K.A., *Temperature driven morphological changes of chemically precipitated hydroxyapatite nanoparticles.* Langmuir, 2004.
240. Vives, S., Gaffet, E., and Meunier, *X-ray diffraction line profile analysis of iron ball milled powders.* Materials Science & Engineering, 2004. **A366**: p. 229-238.
241. Dutta, H. and Pradhan, S.K., *Microstructure characterization of high energy ball-milled nanocrystalline V_2O_5 by Rietveld analysis.* Materials Chemistry & Physics, 2002. **77**: p. 868-877.
242. Kokubo, T., Kushhitani, H., Kitsugi, S., and Yamamuro, T., *Solutions able to reproduce in vivo surface changes in bioactive glass-ceramic A-W.* Journal of Biomedical Materials Research, 1990. **24**: p. 721-734.
243. Zhang, L., Feng, X., Liu, H., Qian, D., Zhang, L., Yu, X., and Cui, F.Z., *Hydroxyapatite/collagen composite materials formation in simulated body fluid environment.* Material Letters, 2004. **58**: p. 719-722.

244. Ohtuski, C., Kokubo, T., and Yamamuro, T., *Mechanism of apatite formation on CaO-SiO_2-P_2O_5 glasses in a simulated body fluid.* Journal of Non-crystalline Solids, 1992. **143**: p. 84-92.
245. Kokubo, T., Kushhitani, H., Ohtuski, C., and Sakka, S., *Chemical reaction of bioactive glass and glass-ceramics with a simulated body fluid.* Journal of Materials Science, 1992. **3**: p. 79-83.
246. Etok, S.E., Rogers, K.D., and Scott, R., *Dissolution of behaviour of plasma sprayed apatite coatings.* Journal of Materials Science, **ARTICLE IN PRESS**.
247. Taylor, M.P., Chandler, P., and P, M. *The influence of powder morphology on the microstructure of plasma-sprayed hydroxyapatite coatings.* in *6th International symposium on ceramics in Medicine*. 1993. Philidelphia, USA: Butterworth-Heinemann Ltd.
248. Park, E., Condrate, R., Lee, D., Kociba, K., and Gallagher, P.K., *Characterization of hydroxyapatite: Before and after plasma spraying.* Journal of materials science: Materials in medicine, 2002. **13**: p. 211-218.
249. Yan, L., Leng, Y., and Weng, L., *Characterization of chemical inhomogeneity in plasma hydroxyapatite coatings.* Biomaterials, 2003. **24**: p. 2585-2592.
250. Deram, V., Minichiello, C., Vannier, R.-N., Le Maguer, A., Pawlowski, L., and Murano, D., *Microstructural characterizations of plasma sprayed hydroxyapatite coatings.* Surface and Coatings Technology, 2003. **166**: p. 153-159.
251. Gadaleta, S.J., Paschalis, E.P., Betts, F., Mendelsohn, R., and Boskey, A.L., *Fourier transform infrared spectroscopy of the solution-mediated conversion of amorphous calcium phosphate to hydroxyapatite: new correlations between X-ray diffraction and infrared data.* Calcified Tissue International, 1996. **58**: p. 9-16.
252. Kweh, S.W.K., Khor, K.A., and Cheang, P., *High temperature in-situ XRD of plasma sprayed coatings.* Biomaterials, 2002. **23**: p. 381-387.
253. Sewing, A., Lakatos, M., Scharnweber, D., Roessler, S., Born, R., Dard, M., and Worch, H. *Influence of Ca/P ratio on electrochemical assisted deposition of hydroxyapatite on titanium.* in *Bioceramics 16*. 2003. Porto, Portugal.
254. Asaoka, N., Best, S.M., Knowles, J.C., and Bonfield, W., *Bioceramics*. Vol. 8. 1995, Oxford: Butterworth.
255. Apfelbaum, F., Diab, H., Mayer, I., and Featherstone, J.D.B., *An FTIR study of carbonate in synthetic apatites.* Journal of Inorganic Biochemistry, 1992. **45**: p. 277-282.
256. Park, E., Condrate, R., and Lee, D., *Infrared spectral investigation of plasma spray coated hydroxyapatite.* Materials Letters, 1998. **36**: p. 38-43.
257. Monteiro, M., da Rocha, N.C.C., and Rossi, A.M., *Dissolution properties of calcium phosphate granules with different compositions in simulated body fluid.* Journal of Biomedical Materials Research, 2003. **65A**: p. 299-305.
258. Chiranjeevirao, S.V., Voegel, J.C., and Frank, R.M., *A method of preparation and characterisation of carbonato-apatites.* Inorganica Chimica Acta, 1983. **78**: p. 43-46.
259. Sampath Kumar, T.S., Manjubala, I., and Gunasekaran, J., *Synthesis of carbonated calcium phosphate ceramics using microwave irradiation.* Biomaterials, 2000. **21**(16): p. 1623-1629.

260. Heslop, D.D., Bi, Y., Baig, A.A., Otsuka, M., and Higuchi, W.I., *A compararative study of the metastable equilibrium solubility behaviour of high-crystallinity and low crystallinity carbonated apatites using pH and solution strontium as independent variables.* Journal of Colloid & Interface Science, **ARTICLE IN PRESS**
261. Lucy, D. and Pollard, A.M. *Chemical study of degraded dentine by resolution enhanced infra-red spectroscopy.* in *Proccedings of the conference on the applications of scientific techniques to the study of archaeology.* 1995. Liverpool: Oxbow Books.
262. Queiroz, A.C., Santos, J.D., Monteiro, F.J., and Prado da Silva, M.H., *Dissolution studies of hydroxyapatite and glass-reinforced hydroxyapatite ceramics.* Materials Characterization, 2003. **50**(2-3): p. 197-202.
263. Sewing, A., *Solubility of BoneMaster HA coatings in buffer solution.* 2004, Biomet Merck Biomaterials GmbH: Daamstradt, Germany. p. 1-4.
264. Bender, S.A., Bumgardner, J.D., Roach, M.D., Bessho, K., and Ong, J.L., *Effect of protein on the dissolution of HA coatings.* Biomaterials, 2000. **21**: p. 299-305.
265. Broadhurst, A., Rogers, K.D., Lowe, T.W., and Lane, D.W., *Determination of depth-dependent diffractin data: a new approach.* Acta Crystallographica, 2004. **A61**: p. 139-146.
266. McDowell, H., Gregory, T.M., and Brown, W.E., *Solubility of Ca5 (PO4)3 OH in thr system Ca(OH)2-H3PO4-H2O.* Journal of research of the national bureau of standards -A. Physics and Chemistry., 1977. **81A**(2 & 3): p. 273-281.
267. Landi, E., *Nucleation of biomimetic apatite in synthetic body fluids: dense and porous scaffold development.* Biomaterials, 2005. **26**(26): p. 2835-2845.
268. Miller, L.M., Vairavamurthy, V., Chance, M.R., Menelsohn, R., Paschalis, E.P., Betts, F., and Boskey, A.L., *In situ analysis of mineral content and crystallinity in bone using infrared micro-spectroscopy of the $v_4 PO_4^{3-}$ vibration.* Biochimica et Biophysics Acta, 2001. **1527**: p. 11-19.
269. Kweh, S.W.K., Khor, K.A., and Cheang, P., *An in vitro investigation of plasma sprayed hydroxyapatite (HA) coatings produced with flame-spheroidized feedstock.* Biomaterials, 2002. **23**: p. 775-785.
270. Baig, A.A., Fox, J.L., A, Y.R., Hsu, J., Higuchi, W.I., Chhettry, A., Zhuang, H., and Otsuka, M., *Relationship among carbonate apatite solubility, crystallite size and microstrain parameters.* Calcified Tissue International, 1999. **64**: p. 437-449.
271. Le Geros, J.P., Le Geros, R.Z., Burgess, A., Edwards, B., and Zitelli, J., *X-ray diffraction method for the quantitative characterisation of calcium phosphate coatings*, ed. Horowitz, E. and Parr, E. 1993.
272. Richardson, J.W., *Background modelling in Rietveld analysis*. IUCs Monographs on crystallography 5, International Union of Crystallography. 1993: Oxford University Press.
273. Keller, L. and Lyengar, S., F04.13.05, A.c., Editor. 1993: Dallas.
274. Keller, L. and Rey-Fessler, P., *Non-destructive characterisation of hydroxyapatite-coated dental implants by XRD method.* Characterisation and performance of calcium phosphate coatings for implants, ed. Horowitz, E. and Parr, E. 1994, Philadelphia: ASTM.

275. Tong, W., Yang, Z., Zhang, X., Yang, A., Feng, J., Cao, Y., and Chen, J., *Studies on diffusion maximum in x-ray diffraction patterns of plasma-sprayed hydroxyapatite coatings.* Journal of Biomedical Materials Research, 1998. **40**: p. 407-413.
276. McPherson, R. and Gane, N., Journal of Biomedical Materials Research, 1995. **29**: p. 327-334.
277. Mahalingham, T., John, V.S., Ravi, G., and Sebastian, P.J., *Microstructural characterization of electrosynthesized ZnTe thin films.* Crystal Research Technology, 2002. **37**(4): p. 329-339.
278. Pal, U., Samanta, D., Ghoral, S., Samantaray, B.K., and Chaudari, A.K., *Structural characterization of cadmium selenide thin films by X-ray diffraction and electron microscopy.* Journal of Physics D: Applied Physics, 1992. **25**: p. 1488-1494.
279. Carayon, M.T. and Lacout, J.L., *Study of Ca/P atomic ratio of the amorphous phase in plasma-sprayed hydroxyapatite coatings.* Journal of Solid State Chemistry., 2003. **172**(2): p. 339-350.
280. Shirkhanzadeh, M., *Calcium phosphate coatings prepared by electrocrystallisation from aqueous electrolytes.* Journal of Materials Science: Materials in Medicine, 1995. **6**: p. 90-93.
281. Paschalis, E.P., Zhao, Q., Tucker, B.E., S, M., Bearcroft, J.A., Beals, N.B., Spector, M., and G.H, N., *Degradation potential of plasma-sprayed hydroxyapatite-coated titanium implants.* J Biomed Mater Res, 1995. **29**: p. 1499-1505.
282. Nancollas, G.H., *In vitro studies of calcium phosphate crystallisation*, in *Biomineralization, chemical and biomechanical perspectives*, Mann, S., Webb, J., and Williams, R.J.P., Editors. 1989, VHC Verlagsgesellscaft: Weinheim, Germany157-187.
283. Eanes, E.D. and Posner, A.S., *A note on the crystal growth of hydroxyapatite precipitated from aqueous solutions.* Mater Res Bull, 1970. **5**(6): p. 377-383.
284. Garside, J., in *Biological mineralisation and demineralisation*, Nancollas, G.H., Editor. 1982, Springer: Berlin 23.
285. Rees, S.G., Hughes-Wassell, D.T., Shellis, R.P., and Embrey, G., *Effect of serum albumin on glycosaminoglycan inhibition of hydroxyapatite formation.* Biomaterials, 2004. **25**: p. 971-977.
286. Kawasaki, K., Kambara, M., Matsumura, H., and Norde, W., *A comparision of the adsorption of saliva proteins and some typical proteins onto the surface of the hydroxyapatite.* Colloids and Surfaces B: Biointerfaces, 2003. **32**: p. 321-334.
287. Blumenthal, N.C., Betts, F., and Posner, A.S., *Effect of carbonate and biological macromolecules on formation and properties of hydroxyapatite.* Calcified Tissue International, 1975. **18**: p. 81-90.
288. Asada, M., Miura, Y., and Osaka, A., *Hydroxyapatite crystal growth on calcium hydroxyapatite cermaics.* Journal of Materials Science, 1988. **23**: p. 3202-3205.
289. Brown, W.E., *Crystal growth of bone mineral.* Clin. Orthopaedics, 1966. **44**(205).
290. Eanes, E.D. and Posner, A.S., *Kinetics and mechanism of conversion of non-crystalline calcium phosphate to crystalline hydroxyapatite*, in *Transactions of the New York Academy of Sciences*. 1965: New York. p. 233-241.

291. Rogers, K.D., *Dissolution and precipitation of hydroxyapatite in various media*, Etok, S.E., Editor. 2005: Shrivenham, UK.
292. Mavropoulos, E., Rossi, A.M., da Rocha, N.C.C., Soares, G.A., Moreira, J.C., and Moure, G.T., *Dissolution of calcium-deficient hydroxyapatite synthesized at different conditions.* Materials Characterization, 2003. **50**(2-3): p. 203-207.
293. Liu, X. and Ding, C., *Morphology of apatite formed on surface of wollastonite coatings soaked in simulatd body fluid.* Materials Letters, 2002. **57**: p. 652-655.
294. Liu, X., Tao, S., Ding, C.,, *Bioactivity of plasma sprayed dicalcium silicate coatings.* Biomaterials, 2002. **23**: p. 963-968.
295. Weng, J., Liu, Q., Wolke, J.G.C., Zhang, X., and De Groot, K., *Formation and characteristics of the apatite layer on plasma-spray hydroxyapatite coatings in simulated body fluid.* Biomaterials, 1997. **18**: p. 1027-1035.
296. Gu, Y.W., Khor, K.A., and Cheang, P., *Bone-like apatite layer formation on hydroxyapatite prepared by spark plasma sintering (SPS).* Biomaterials, 2004. **25**: p. 4127-4134.
297. Clasen, A.B. and Ruyter, I.E., *Quantitative determination of type A and type B carbonate in human decidious and permanent enamel by means of fourier transform infrared spectrometry.* Advances in Dental Research, 1997. **11**(4): p. 523-527.
298. Lu, X. and Leng, Y., *Theoretical analysis of calcium phosphate precipitation in simulated body fluid.* Biomaterials, 2005. **26**: p. 1097-1108.
299. Maxian, S.H., Zawadsky, J.P., Dunn, M.G.,, *Mechanical and histological evaluation of amorphous calcium phosphate and poorly crystallised hydroxyapatite coatings on titanium implants.* Journal of Biomedical Materials Research, 1993. **28**: p. 909-917.
300. Soballe, K. and Overgaard, S., *The current status of hydroxyapatite coating of prostheses.* Journal of Bone joint surgery, 1996. **78B**: p. 689-690.
301. Tromans, D. and Meech, J.A., *Enhanced dissolution of minerals: Modeling conjoint effects of particle size and microtopography.* 2001, University of British Colombia: Vancouver, Canada.
302. Boistelle, R. and J.P, A., *Crystallization mechanisms in solution.* Journal of Crystal Growth, 1988. **90**: p. 14-30.
303. Nielson, A.E., *Kinetics of precipitation.* 1964, New York: Macmillan.
304. Oktem, T., Seventekin, N., Ayan, H., and Piskin, E., *Modication of polyester and polyamide fabrics by different in situ plasma polymerization methods.* Turkish Journal of Chemistry, 2000. **24**: p. 275-285.
305. Andrade, J.D., *Interfacial phenomena and biomaterials.* Medical Instrumentation, 1973. 7: p. 110-120.
306. Sun, J.-S., Ysuang, Y.-H., Chang, W., Li, J., Liu, H., and Lin, F., *Effect of hydroxyapatite particle size on myblasts and fibroblasts.* Biomaterials, 1997. **18**.
307. Lian, J.B., *The developmental stages of osteoblast growth and the differentiation exhibit selective responses of genes to growth factors and hormones.* Journal of Oral Implantology, 1993. **19**: p. 5-105.
308. Lovell, K.V., *Irradiation of PET tape*, Etok, S.E., Editor. 2003: Shrivenham, UK.
309. ATCC, *Product information sheet for CRL-11372.* American Type Culture Collection, 2001: p. 1-3.

310. Hott, M., Noel, B., Bernache-Assolant, D., Rey, C., and Marie, P.J., *Proliferation and differentitation of human trabecular osteoblastic cells on hydroxyapatite.* Journal of Biomedical Materials Research, 1997. **37**(4): p. 508-516.
311. Deligianni, D.D., Katsala, N.D., Koutsoukos, P.G., and Missirlis, Y.F., *Effect of surface roughness of hydroxyapatite on human bone marrow cell adhesion, proliferation, differentiation and detachment strength.* Biomaterials, 2001. **22**(1): p. 87-96.
312. Yamamoto, M., Kato, K., and Ikada, Y., *Ultrastructure of the interface between cultured osteoblasts and surface modified polymer substrates.* Journal of Biomedical Materials Research, 1997. **37**(1): p. 29-36.
313. Woo, S.L., Hollis, J.M., and Adams, D.J., *Tensile properties of human femur-anterior cruciate ligament-tibia complex: The effects of specimen age and orientation.* American Journal of Sports in Medicine, 1991. **19**: p. 217-225.
314. Cunniff, J., Fossey, S., Song, J., Auerbach, M., Kaplan, D.L., Eby, R., Adams, W., and Vezzie, D., *Mechanical and thermal properties of Nephila clavipes drag-line silk.* Polymer Advanced Technology, 1994. **5**: p. 401-410.
315. Cooper, D.E., Deng, X.H., and Burstein, A.L., *The strength of the central third patella tendon graft: A biomechanical study.* American Journal of Sports in Medicine, 1993. **21**: p. 818-824.
316. Scherping, S.C., Schimdt, C.C., and Georgescu, H.I., *Effect of growth factors on the proliferation of ligament fibroblasts from skeletally mature rabbits.* Connective Tissue Research, 1997. **36**: p. 1-8.
317. Staubli, H.U., Schatzmann, L., and Brunner, P., *Quadriceps tendon and patellar ligament: Cryosectional anatomy and structural properties in young adults.* Knee Sung Traumatology Arthroscopy, 1996. **4**: p. 100-110.
318. Nomura, E., Otani, T., Kawakubo, M., Fujikawa, K., Takeda, T., Iseki, F., and Aihara, S., *Bone fixation methods of a substitute for the anterior cruciate ligament reconstruction of the knee: effect of double stapling.* Journal of Tokoyo Knee Society, 1988. **9**: p. 325-335.
319. Barber, F.A., Elrod, B.F., and McGuire, D.A., *Preliminary results of an absorbable interference screw.* Arthroscopy, 1995. **11**: p. 537-548.
320. Pierz, K., Baltz, M., and Fulkerson, J., *The effect of Kurosaka scre divergence on the holding strength of bone-tendon-bone grafts.* American Journal of Sports in Medicine, 1995. **23**: p. 332-335.

Bibliography

1. Giacovazzo, C., et al., *Fundamentals of crystallography*. IUCr Texts on Crystallography 2. 1992, New York: Oxford University Press.

2. Kern, A. and A. Coelho, *A new fundamental parameters approach in profile analysis of powder data*. 1998, London: Allied Publishers Ltd.

3. Woodman, A., *A brief guide to methods, practices and rules*, in *Introduction to mammalian cell culture*. 1998, Cranfield University at Silsoe: Silsoe. p. 1-9.

4. Akbari, M., M. Nikbakht, and A. Sobhani, *Expression of alkaline phosphatase during osteogenic differentiation of rat bone marrow cells*. 2002, Tehran Medical Sciences University: Tehran. p. 1-7.

5. Wilson, R.M., J.C. Elliot, and S.E.P. Dowker, *Rietveld refinement of the crystallographic structure of human dental enamel apatites.* American Mineralogist, 1999. **84**: p. 1406-1414.

6. Jarcho, M., *Calcium phosphate ceramics as hard tissue prosthetics.* Clinical Orthopaedics, 1981. **157**: p. 259-78.

Publications

1. Etok, S.E., K.D. Rogers, and R. Scott, *Dissolution of behaviour of plasma sprayed apatite coatings.* Journal of Materials Science, 2005. **Article in Press**.
2. Rogers, K.D., S.E. Etok, A. Broadhurst, and R. Scott, *Enhanced analysis of biomaterials by synchrotron diffraction.* Nuclear Instruments and Methods in Physics Research A, 2005. **548**: p. 123-128.
3. Etok, S.E. and K.D. Rogers, *Structural and chemical changes to plasma sprayed hydroxyapatite coatings in simulated body fluid*, in *Bioceramics: Materials and Applications V*, R. Rusin, Editor. 2004, American Ceramic Society: Indianapolis, USA.
4. Rogers, K.D., S.E. Etok, and R. Scott, *Structural characterisation of apatite coatings.* Journal of Materials Science, 2004. **39**: p. 5747-5754.
5. Etok, S.E. and K.D. Rogers. *A novel technique for characterisation of plasma sprayed coatings*. in *World Congress on Medical Physics & Biomedical Engineering*. 2003. Sydney, Australia: IFMBE.
6. Etok, S.E. and K.D. Rogers. *Osteoblastic response to hydroxyapatite coated polymeric fibres for potential application in orthopaedic surgery*. in *World Congress on Medical Physics and Biomedical Engineering*. 2003. Sydney, Australia: IFMBE.

Appendix A

Many types of grafts exist for anterior cruciate ligament reconstruction: autografts, allografts, xenografts, synthetic grafts and tissue engineered grafts [1-6]. Table A.1 gives a comparison of grafts types commonly used grafts.

Graft type	Source	Advantages	Disadvantages
Autograft [4, 7, 8]	Patellar tendon, hamstring tendon, quadriceps tendons of host.	Good bone-tendon interface (patellar tendon grafts). Mechanical properties. No risk of tissue rejection.	Donor site morbidity. Prolonged rehabilitation. Bone tunnel motion. Limited bone graft-fixation.
Allografts [4, 7]	Tendons or ligaments human cadavers.	Mechanical properties. No pain or risks associated with harvesting grafts. No risk of tissue rejection.	Risk of infection from cadaveric tissue. Limited bone-graft fixation.
Xenografts [4, 7]	Tendons or ligaments mammalian cadavers.	Mechanical properties. No pain or risks associated with harvesting grafts.	Risk of infection from cadaveric tissue. Risk of tissue rejection.
Synthetic grafts (Polymers) [2, 7-9]	Synthesised *in vitro.*	Mechanical properties. Biocompatibility. Osseoconductive properties.	Limited elasticity. Stress shielding. Limited bone graft fixation. Wear debris.
Tissue engineered grafts (silk matrix) [4, 10]	Synthesised *in vitro.*	Mechanical properties. Biocompatibility.	Fast degradation of mechanical properties with time. Limited *in vivo* performance tests.

Table A. 1 Comparison of commonly used grafts in ACL reconstruction.

Table A.2 shows the mechanical properties of commonly used grafts in ACL reconstruction.

Graft type	Failure strength *in vivo* (N)	Stiffness (Nmm^{-1})
Native ACL [1]	2160 ± 157	242 ± 28
Patellar tendon [11, 12]	2376 ± 151	455
Quadriceps tendon [12, 13]	2352 ± 495	326
Polyester (Leeds-Keio) [9]	2061-2350	151-294
Silk matrix [4]	2337 ± 72	354 ± 26

Table A. 2 Mechanical properties of commonly used grafts in ACL reconstruction.

Fixation devices can be divided into direct and direct methods. Direct methods include interference screws, washers and staples. These methods are used to fix grafts mechanically to bone tissue [6]. Preliminary, the mechanical strength of fixation is from the fixation device, but long-term fixation is achieved through the biological osseointegration between the bone plug and bone tunnel [9]. Indirect methods or graft augmentation devices were developed to protect biological grafts from high loads in the early postoperative period of graft weakness. These devices are typically implanted in parallel with a biological graft to share the mechanical loads. An example of a graft augmentation device using a titanium button and a looped polymeric is shown in figure A.1 [8]. Table A.3 gives a summary of the *in vivo* properties of common fixation devices used in ACL reconstruction.

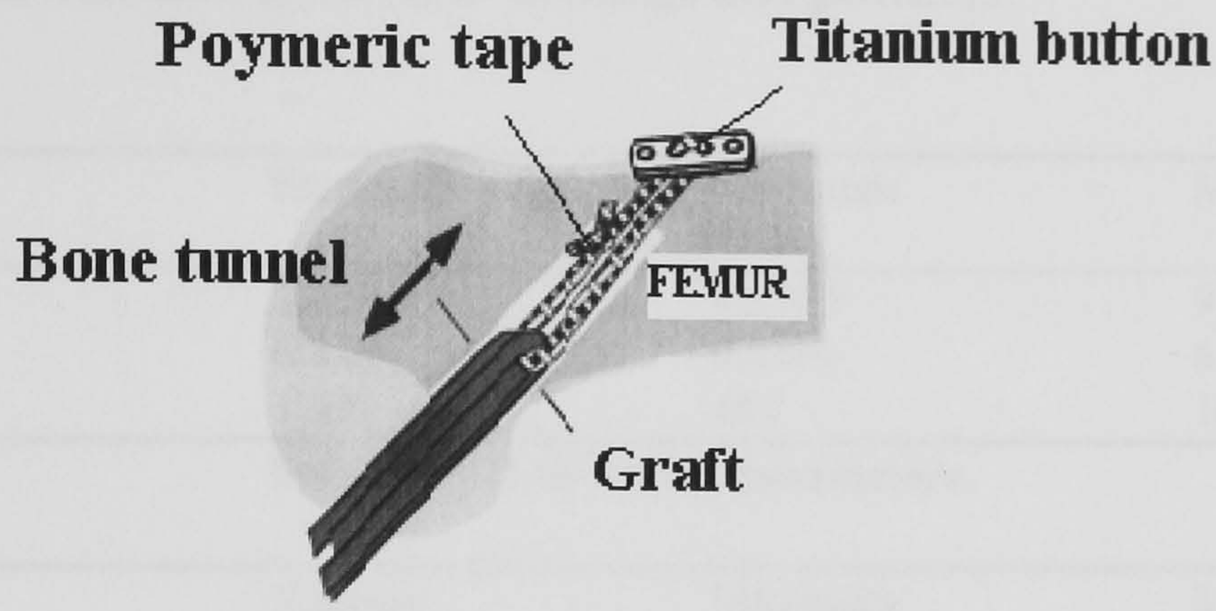

Figure A. 1Graft augmentation device.

Fixation devices	Failure strength *in vivo* (N)	Advantages	Disadvantages
Double staple [14]	647 ± 25	Stiffness.	Potential bone plug breakage.
Single staple [8, 14]	253 ± 68	None reported	Limited strength & stiffness. Painful.
Biodegradable polymeric interference screw [8, 15]	341 ± 163	No revision surgery necessary for removal	Potential breakage on insertion
Biodegradable polymeric screw & metal washer [3]	821 ± 219	Mechanical properties.	Potential breakage on insertion
Metal screw (7mm) [16]	640 ± 201	Mechanical properties.	Metal ion release. Laceration of graft.
Endobutton-Endotape (Smith & Nephew) [8]	520	Mechanical properties.	Relative motion in bone tunnel.

Table A. 3 Common fixation devices used in ACL reconstruction.

Appendix B

Tables B.1-B.4 show the structural and instrument parameters used for the whole pattern fitting of the diffraction data from HAP coatings and powders.

	Starting	Minimum	Maximum
a (Å)	9.4230	9.3300	9.5180
c (Å)	6.8800	6.8300	6.9200
Crystallite size	1000	45	1000

Table B. 1 HAP lattice parameters.

	Starting	Minimum	Maximum
a (Å)	9.9491	9.3300	10.2000
c (Å)	7.7488	6.5000	8.0000
Crystallite size	1000	1	1000

Table B. 2 ACP lattice parameters.

Atom	x	y	z	Occupancy	B (A^2)
O1	0.15640	0.67180	0.25000	1	1.03
O2	0.87760	0.41240	0.25000	1	1.57
O3	0.34330	0.25790	0.07040	1	1.52
P	0.97000	0.60170	0.25000	1	0.68
Ca1	0.33333	0.66667	0.49870	1	0.89
Ca2	0.74660	0.75350	0.25000	1	0.83
O4	0.00000	0.00000	0.30220	0.5	1.75
H	0.00000	0.00000	0.43920	0.5	3.64

Table B. 3 Atomic coordinates (X, Y, Z) and isotropic thermal parameters (B) for HAP and ACP.

	Value	Refine / Fix
Primary radius /mm	173	Fix
Secondary radius /mm	173	Fix
Receiving slit width /mm	0.1	Fix
Fixed divergence slit angle /°	1	Fix
Source length /mm	12	Fix
Sample length /mm	15	Fix
Receiving slit length /mm	2.3	Refine
Primary soller /mm	2.3	Refine

Table B. 4 Instrument parameters.

Table B.5 shows the emission profile for Cu Kα radiation used in the diffraction analysis.

Area	Emission lines	Wavelength (Å)	Lorentzian HW (mÅ)
0.0159	Satellites	1.534753	3.6854
0.5791	Ka_{1a}	1.540596	0.4370
0.0762	Ka_{1b}	1.541058	0.6000
0.2417	Ka_{2a}	1.544410	0.5200
0.0871	Ka_{2b}	1.544721	0.6200

Table B. 5 Emission profile of CuKα radiation

Appendix C

Table C1 shows structural and composition information of typical as-received plasma sprayed coatings.

Sample	a (Å)	Error (Å)	c(Å)	Error (Å)	R_{wp} (%)	HAP (wt%)	Error (wt%)	ACP (wt%)	Error (wt%)
1	9.411085	0.00046	6.89065	0.00036	10.189	56.42	0.5	43.58	0.5
2	9.411750	0.00045	6.89095	0.00037	12.409	62.80	0.5	37.20	0.5
3	9.409830	0.00039	6.89052	0.00033	10.750	59.66	0.5	40.34	0.5
4	9.413480	0.00053	6.89330	0.00040	11.044	60.80	0.5	39.02	0.5
5	9.412540	0.00043	6.89190	0.00040	9.131	54.39	0.5	45.61	0.5
6	9.414140	0.00049	6.89160	0.00040	9.511	48.86	0.5	48.16	0.5
7	9.413890	0.00051	6.89240	0.00040	10.967	58.09	0.5	41.90	0.5
8	9.413690	0.00052	9.89368	0.00040	10.333	58.95	0.5	41.05	0.5
9	9.412500	0.00039	9.89279	0.00038	10.799	55.13	0.5	44.87	0.5

Table C. 1 Structural and composition information of typical as-received plasma sprayed coatings.

Table C.2 shows the structural information of Nano-HAP used in the refinements of PS coatings after soaking.

	Starting	Minimum	Maximum
a (Å)	9.48114	9.3300	9.9000
c (Å)	6.86776	6.8300	7.0000
Crystallite size	6.2	3	50

Table C. 2 Nano-HAP unit parameters.

Appendix D

Tables D.1-3 show the mechanical properties of OT samples before and after coating with HAP.

Sample	UTS (N)	Ext to failure (mm)	Stiffness (Nmm^{-1})
OT 1	825.7	11.4	72.43
OT 2	812.7	12.9	63.00
OT 3	807.7	12.2	66.20
OT 4	813.2	13.7	59.36

Table D. 1 Mechanical properties of OT-C samples. Four measurements were taken per sample.

Sample	Coating weight / g	UTS (N)	Ext to failure (mm)	Stiffness (Nmm^{-1})
OT-T 1	0.0027	810.5	10.6	76.46
OT-T 2	0.0025	795.8	14.1	56.44
OT-T 3	0.0022	800.8	14.3	55.94
OT-T 4	0.0026	803.1	13.4	59.93

Table D. 2 Mechanical properties of OT-T samples. Four measurements were taken per sample.

Sample	Coating weight /g	UTS (N)	Ext to failure (mm)	Stiffness (Nmm^{-1})
OT-N 1	0.008	795.6	12.7	56.10
OT-N 2	0.009	789.8	13.1	64.2
OT-N 3	0.009	803.7	11.9	69.8
OT-N 4	0.010	799.3	13.4	60.6

Table D. 3 Mechanical properties of OT-N samples. Four measurements were taken per sample.

Tables D.4-D.7 show the changes in cell count on test and control samples with incubation time. Tables D.8-D11 demonstrate the differences in osteocalcin concentration in the media of test and control samples. Table D.12 compares the ALP activity in the media of test and control samples. Table D.13 shows the proliferation rates of cells incubated on test and control samples. Tables D.14-D.20 shows the changes in calcium concentration in the media of test and control samples.

Sample	Cell count at 4 hours	Cell count at 18 hours
Plastic well 1	7.50×10^3	1.16×10^4
	6.40×10^3	1.02×10^4
	9.40×10^3	9.10×10^3
	8.70×10^3	8.40×10^3
	6.10×10^3	9.30×10^3
	6.90×10^3	9.40×10^3
Plastic well 2	6.70×10^3	7.90×10^3
	5.50×10^3	8.20×10^3
	5.70×10^3	7.10×10^3
	6.10×10^3	8.70×10^3
	4.70×10^3	7.50×10^3
	9.10×10^3	9.50×10^3
Plastic well 3	6.60×10^3	1.10×10^4
	7.80×10^3	1.03×10^4
	6.20×10^3	8.50×10^3
	7.30×10^3	8.30×10^3
	9.00×10^3	1.00×10^4
	6.70×10^3	8.80×10^3
Plastic well 4	5.30×10^3	7.00×10^3
	8.60×10^3	8.70×10^3
	9.50×10^3	7.70×10^3
	8.20×10^3	8.90×10^3
	8.70×10^3	9.80×10^3
	7.60×10^3	1.09×10^4

Table D. 4 Attachment of osteoblast cells to plastic wells after 4 and 18 hours of incubation in culture media. Six measurements were taken per well.

Sample	Cell count at 4 hours	Cell count at 18 hours
OT-T 1	5.10×10^3	8.60×10^3
	4.30×10^3	6.00×10^3
	3.70×10^3	9.90×10^3
	3.90×10^3	5.70×10^3
	4.70×10^3	8.00×10^3
	3.50×10^3	7.50×10^3
OT-T 2	6.90×10^3	8.80×10^3
	3.60×10^3	5.50×10^3
	5.70×10^3	5.80×10^3
	5.10×10^3	7.30×10^3
	3.30×10^3	1.07×10^4
	5.50×10^3	8.10×10^3
OT-T 3	4.10×10^3	5.90×10^3
	7.90×10^3	9.10×10^3
	5.90×10^3	7.40×10^3
	6.40×10^3	5.00×10^3
	5.80×10^3	7.70×10^3
	4.90×10^3	8.90×10^3
OT-T 4	3.60×10^3	9.80×10^3
	7.10×10^3	6.70×10^3
	5.50×10^3	8.50×10^3
	4.70×10^3	4.70×10^3
	4.20×10^3	5.10×10^3
	8.00×10^3	6.90×10^3

Table D. 5 Attachment of osteoblast cells to OT-T samples after 4 and 18 hours of incubation in culture media. Six measurements were taken per sample.

Sample	Cell count at 4 hours	Cell count at 18 hours
OT-N 1	3.30×10^3	4.20×10^3
	2.60×10^3	6.70×10^3
	3.70×10^3	3.90×10^3
	2.90×10^3	4.90×10^3
	2.10×10^3	4.10×10^3
	3.90×10^3	5.70×10^3
OT-N 2	2.40×10^3	4.00×10^3
	5.40×10^3	7.30×10^3
	6.50×10^3	6.60×10^3
	4.20×10^3	6.10×10^3
	6.10×10^3	5.90×10^3
	2.60×10^3	4.40×10^3
OT-N 3	5.20×10^3	5.80×10^3
	3.70×10^3	3.80×10^3
	5.80×10^3	6.30×10^3
	3.20×10^3	8.10×10^3
	4.80×10^3	4.80×10^3
	3.60×10^3	7.80×10^3
OT-N 4	2.00×10^3	9.60×10^3
	5.30×10^3	8.00×10^3
	4.70×10^3	7.70×10^3
	5.80×10^3	5.50×10^3
	4.90×10^3	6.30×10^3
	4.00×10^3	4.50×10^3

Table D. 6 Attachment of osteoblast cells to OT-N samples after 4 and 18 hours of incubation in culture media. Six measurements were taken per sample.

Sample	Cell count at 4 hours	Cell count at 18 hours
OT-C 1	3.40×10^3	5.60×10^3
	1.50×10^3	6.40×10^3
	2.40×10^3	9.60×10^3
	3.90×10^3	3.70×10^3
	5.70×10^3	2.70×10^3
	1.80×10^3	7.10×10^3
OT-C 2	5.10×10^3	5.00×10^3
	3.90×10^3	7.90×10^3
	4.20×10^3	4.30×10^3
	6.10×10^3	3.60×10^3
	1.70×10^3	6.30×10^3
	2.50×10^3	3.00×10^3
OT-C 3	4.90×10^3	2.40×10^3
	1.10×10^3	4.20×10^3
	2.20×10^3	5.50×10^3
	3.60×10^3	2.00×10^3
	1.90×10^3	3.70×10^3
	4.20×10^3	4.30×10^3
OT-C 4	2.00×10^3	3.20×10^3
	5.50×10^3	4.90×10^3
	3.80×10^3	2.90×10^3
	3.50×10^3	6.90×10^3
	4.30×10^3	4.10×10^3
	1.30×10^3	5.20×10^3

Table D. 7 Attachment of osteoblast cells to OT-C samples after 4 and 18 hours of incubation in culture media. Six measurements were taken sample per sample.

Sample	Day 14
Plastic well 1	1.8
	1.8
	1.8
	1.7
	1.7
	1.7
Plastic well 2	1.4
	1.4
	1.4
	1.5
	1.5
Plastic well 3	1.6
	1.5
	1.6
	1.6
	1.6
	1.7
Plastic well 4	1.9
	1.9
	1.9
	2.0
	2.1
	2.2

Table D. 8 Osteocalcin production (ng ml^{-1}) of osteoblast cells on plastic wells after 14 days of incubation in culture media. Six measurements were taken per well.

Sample	Day 14
OT-T 1	5.4
	5.4
	5.6
	5.6
	5.6
	5.7
OT-T 2	7.1
	7.1
	7.1
	7.1
	7.1
OT-T 3	6.8
	6.9
	6.7
	6.7
	6.7
	6.7
OT-T 4	6.3
	6.5
	6.4
	6.4
	6.4
	6.4

Table D. 9 Osteocalcin production (ng ml^{-1}) of osteoblast cells on OT-T samples after 14 days of incubation in culture media. Six measurements were taken per sample.

Sample	Day 14
OT-N 1	5.1
	5.1
	5.3
	5.4
	5.4
	5.4
OT-N 2	4.7
	4.9
	4.8
	4.9
	4.9
	4.9
OT-N 3	6.1
	6.2
	6.3
	6.3
	6.4
	6.3
OT-N 4	3.7
	3.9
	3.4
	3.5
	3.5
	3.5

Table D. 10 Osteocalcin production (ng ml^{-1}) of osteoblast cells on OT-N samples after 14 days of incubation in culture media. Six measurements were taken per sample.

Sample	Day 14
OT-C 1	3.2
	3.2
	3.1
	3.1
	3.1
	5.9
OT-C 2	5.7
	5.6
	5.7
	5.7
	5.7
	5.7
OT-C 3	5.1
	5.4
	5.4
	5.7
	5.7
	5.7
OT-C 4	3.8
	3.6
	3.6
	3.5
	3.5
	3.5

Table D. 11 Osteocalcin production (ng ml^{-1}) of osteoblast cell on OT-C samples after 14 days of incubation in culture media. Six measurements were taken per sample.

Sample	Day 14
Plastic well	0.182
	0.254
	0.417
	0.364
	0.161
	0.171
OT-T	0.784
	0.525
	0.431
	0.321
	0.268
	0.405
OT-N	0.341
	0.294
	0.469
	0.133
	0.397
	0.201
OT-C	0.194
	0.360
	0.157
	0.293
	0.322
	0.111

Table D. 12 ALP activity (nmol min^{-1} mg^{-1} of protein) of osteoblast cells on plastic culture wells or polymeric tape after 14 days of incubation in culture media. six measurements were taken per sample.

Sample	Day 7	Day 11	Day 14	Day 16
Plastic well	5.60×10^3	7.70×10^3	1.90×10^4	3.33×10^4
	6.70×10^3	1.01×10^4	1.87×10^4	2.99×10^4
	8.00×10^3	9.40×10^3	2.11×10^4	2.77×10^4
	5.20×10^3	8.80×10^3	1.80×10^4	3.40×10^4
	7.90×10^3	7.40×10^3	1.93×10^4	3.50×10^4
	5.90×10^3	6.60×10^3	1.78×10^4	3.50×10^4
OT-T	7.50×10^3	9.40×10^3	1.35×10^4	2.31×10^4
	8.20×10^3	1.18×10^4	1.45×10^4	2.90×10^4
	6.60×10^3	1.02×10^4	1.23×10^4	2.79×10^4
	4.50×10^3	8.90×10^3	1.57×10^4	2.93×10^4
	5.50×10^3	9.70×10^3	1.46×10^4	2.46×10^4
	4.90×10^3	8.50×10^3	9.80×10^4	2.58×10^4
OT-N	7.30×10^3	6.20×10^3	1.33×10^4	1.39×10^4
	6.50×10^3	4.60×10^3	1.18×10^4	1.67×10^4
	5.00×10^3	7.10×10^3	1.27×10^4	1.77×10^4
	3.70×10^3	5.70×10^3	1.03×10^4	1.65×10^4
	5.80×10^3	6.50×10^3	1.25×10^4	1.96×10^4
	4.60×10^3	8.60×10^3	1.39×10^4	1.83×10^4
OT-C	5.80×10^3	6.10×10^3	9.20×10^3	1.50×10^4
	6.90×10^3	7.80×10^3	1.19×10^4	1.37×10^4
	6.00×10^3	7.60×10^3	8.90×10^3	1.69×10^4
	4.11×10^3	8.80×10^3	1.24×10^4	1.43×10^4
	5.82×10^3	5.20×10^3	1.01×10^4	1.21×10^4
	4.95×10^3	4.90×10^3	9.40×10^3	1.46×10^4

Table D. 13 Proliferation of osteoblast cells on plastic culture wells or polymeric tape after 7, 11, 14 and 16 days of incubation in culture media. Six measurements were taken per sample.

Sample	Day 2	Day 4	Day 7	Day 14
Plastic well 1	1.030	1.017	0.888	0.604
	1.031	1.014	0.888	0.604
	1.030	1.014	0.888	0.604
	1.031	1.014	0.888	0.604
	1.030	1.014	0.888	0.604
	1.030	1.014	0.888	0.604
Plastic well 2	1.019	0.971	0.861	0.583
	1.020	0.971	0.861	0.587
	1.021	0.971	0.861	0.587
	1.021	0.971	0.861	0.587
	1.021	0.971	0.861	0.587
Plastic well 3	1.010	0.948	0.790	0.577
	1.012	0.949	0.790	0.577
	1.012	0.949	0.790	0.577
	1.012	0.949	0.790	0.577
	1.012	0.949	0.790	0.577
	1.012	0.949	0.790	0.577
Plastic well 4	0.834	0.874	0.753	0.561
	0.998	0.874	0.753	0.561
	0.997	0.874	0.753	0.561
	0.998	0.874	0.753	0.561
	0.998	0.874	0.753	0.561
	0.998	0.874	0.753	0.561

Table D. 14 Calcium concentration ($mmolL^{-1}$) in the culture media after contact with plastic culture wells in the presence of osteoblast cells after 2,4,7 and 14 days of incubation.

Sample	Day 2	Day 4	Day 7	Day 14
OT-T 1	1.431	1.543	1.844	0.876
	1.431	1.543	1.843	0.876
	1.433	1.544	1.843	0.876
	1.431	1.544	1.843	0.876
	1.431	1.544	1.843	0.876
	1.431	1.544	1.843	0.876
OT-T 2	1.423	1.529	1.759	0.856
	1.425	1.529	1.759	0.856
	1.425	1.529	1.759	0.856
	1.425	1.529	1.759	0.856
	1.425	1.529	1.759	0.856
OT-T 3	1.414	1.500	1.720	0.831
	1.414	1.500	1.720	0.831
	1.414	1.500	1.720	0.831
	1.414	1.500	1.720	0.831
	1.414	1.500	1.720	0.831
	1.414	1.500	1.720	0.831
OT-T 4	1.408	1.498	1.697	0.810
	1.409	1.492	1.697	0.810
	1.409	1.492	1.701	0.810
	1.409	1.492	1.701	0.810
	1.409	1.492	1.701	0.810
	1.409	1.492	1.701	0.810

Table D. 15 Calcium concentration ($mmolL^{-1}$) in the culture media after contact with OT-T samples in the presence of osteoblast cells after 2,4,7 and 14 days of incubation.

Sample	Day 2	Day 4	Day 7	Day 14
OT-T 1	1.440	1.526	1.796	1.025
	1.440	1.526	1.796	1.022
	1.440	1.526	1.796	1.023
	1.440	1.526	1.796	1.023
	1.440	1.526	1.796	1.023
	1.440	1.526	1.738	1.023
OT-T 2	1.420	1.518	1.738	0.976
	1.420	1.518	1.738	0.976
	1.420	1.518	1.738	0.976
	1.420	1.518	1.738	0.976
	1.420	1.518	1.725	0.976
OT-T 3	1.411	1.504	1.725	0.958
	1.411	1.504	1.725	0.958
	1.411	1.504	1.725	0.958
	1.411	1.504	1.725	0.958
	1.411	1.504	1.725	0.958
	1.411	1.504	1.725	0.958
OT-T 4	1.390	1.483	1.713	0.942
	1.391	1.483	1.713	0.942
	1.391	1.483	1.713	0.942
	1.391	1.483	1.713	0.942
	1.391	1.483	1.713	0.942
	1.391	1.483	1.713	0.942

Table D. 16 Calcium concentration ($mmolL^{-1}$) in the culture media after contact with OT-T samples without the presence of osteoblast cells after 2,4,7 and 14 days of incubation.

Sample	Day 2	Day 4	Day 7	Day 14
OT-N 1	1.584	1.607	1.796	1.025
	1.584	1.607	1.796	1.022
	1.584	1.607	1.796	1.023
	1.584	1.607	1.796	1.023
	1.584	1.607	1.796	1.023
	1.584	1.607	1.796	1.023
OT-N 2	1.552	1.585	1.738	0.976
	1.552	1.585	1.738	0.976
	1.552	1.585	1.738	0.976
	1.552	1.585	1.738	0.976
	1.552	1.585	1.738	0.976
OT-N 3	1.536	1.565	1.725	0.958
	1.536	1.565	1.725	0.958
	1.536	1.565	1.725	0.958
	1.536	1.565	1.725	0.958
	1.536	1.565	1.725	0.958
	1.536	1.565	1.725	0.958
OT-N 4	1.519	1.526	1.713	0.942
	1.519	1.527	1.713	0.942
	1.519	1.527	1.713	0.942
	1.519	1.527	1.713	0.942
	1.519	1.527	1.713	0.942
	1.519	1.527	1.713	0.942

Table D. 17 Calcium concentration ($mmolL^{-1}$) in the culture media after contact with OT-N samples in the presence of osteoblast cells after 2,4,7 and 14 days of incubation.

Sample	Day 2	Day 4	Day 7	Day 14
OT-N 1	1.504	1.576	1.786	1.017
	1.504	1.576	1.786	1.017
	1.504	1.576	1.786	1.017
	1.504	1.576	1.786	1.017
	1.504	1.576	1.786	1.017
	1.504	1.576	1.786	1.017
OT-N 2	1.695	1.540	1.749	0.983
	1.695	1.540	1.749	0.983
	1.692	1.540	1.749	0.983
	1.692	1.540	1.749	0.983
	1.692	1.540	1.749	0.983
OT-N 3	1.572	1.521	1.731	0.962
	1.572	1.521	1.731	0.962
	1.572	1.521	1.731	0.962
	1.572	1.521	1.731	0.962
	1.572	1.521	1.731	0.962
	1.572	1.521	1.731	0.962
OT-N 4	1.517	1.541	1.702	0.947
	1.517	1.541	1.702	0.947
	1.517	1.541	1.702	0.947
	1.517	1.541	1.702	0.947
	1.517	1.541	1.702	0.947
	1.517	1.541	1.702	0.947

Table D. 18 Calcium concentration ($mmolL^{-1}$) in the culture media after contact with OT-N samples without the presence of osteoblast cells after 2,4,7 and 14 days of incubation.

Sample	Day 2	Day 4	Day 7	Day 14
OT-C 1	1.060	1.021	0.710	0.581
	1.060	1.021	0.708	0.581
	1.060	1.021	0.708	0.581
	1.060	1.021	0.708	0.581
	1.060	1.021	0.708	0.582
	1.060	1.021	0.708	0.582
OT-C 2	1.037	0.953	0.692	0.579
	1.037	0.953	0.692	0.579
	1.037	0.953	0.692	0.579
	1.037	0.953	0.692	0.579
	1.037	0.953	0.692	0.579
	1.037	0.953	0.692	0.579
OT-C 3	0.998	0.896	0.678	0.561
	0.998	0.896	0.678	0.561
	0.998	0.896	0.678	0.561
	0.998	0.896	0.678	0.561
	0.998	0.896	0.678	0.561
	0.998	0.896	0.678	0.561
OT-C 4	0.942	0.847	0.654	0.544
	0.942	0.847	0.654	0.544
	0.942	0.847	0.654	0.544
	0.942	0.847	0.654	0.544
	0.942	0.847	0.654	0.544
	0.942	0.847	0.654	0.544

Table D. 19 Calcium concentration ($mmolL^{-1}$) in the culture media in contact with OT-C in the presence of osteoblast cells after 2,4,7 and 14 days of incubation.

Sample	Day 2	Day 4	Day 7	Day 14
OT-C 1	0.903	0.903	0.903	0.904
	0.903	0.903	0.903	0.904
	0.903	0.903	0.903	0.904
	0.903	0.903	0.903	0.904
	0.903	0.903	0.903	0.904
	0.903	0.903	0.903	0.904
OT-C 2	0.903	0.903	0.903	0.904
	0.903	0.903	0.903	0.904
	0.903	0.903	0.903	0.904
	0.903	0.903	0.903	0.904
	0.903	0.903	0.903	0.904
OT-C 3	0.903	0.903	0.903	0.904
	0.903	0.903	0.903	0.904
	0.903	0.903	0.903	0.904
	0.903	0.903	0.903	0.904
	0.903	0.903	0.903	0.904
	0.903	0.903	0.903	0.904
OT-C 4	0.903	0.903	0.903	0.904
	0.903	0.903	0.903	0.904
	0.903	0.903	0.903	0.904
	0.903	0.903	0.903	0.904
	0.903	0.903	0.903	0.904
	0.903	0.903	0.903	0.904

Table D. 20 Calcium concentration ($mmolL^{-1}$) in the culture media in contact with OT-C without the presence of osteoblast cells after 2,4,7 and 14 days of incubation.